COMPARATIVE STUDY OF CONVECTIVE AND DIFFUSIVE TRANSPORT PHENOMENA WITHIN THE OPALINUS CLAY OF MONT TERRI

Rapport de thèse

ISRN/IRSN-2017/200
RT/PSE-ENV/2017-0008

Catherine JI YU

Pôle Santé Environnement – Direction de l'Environnement

Service des déchets radioactifs et des transferts dans la géosphère (SEDRE)

Laboratoire d'Etude et de recherche sur les Transferts et les Interactions dans les Sols (LETIS)

Directeur de thèse :   Julio GONÇALVÈS

Co-directeur de thèse :   Jean-Michel MATRAY

Décembre 2017

UNIVERSITE D'AIX-MARSEILLE

ÉCOLE DOCTORALE 251 - SCIENCES DE L'ENVIRONNEMENT

THESE DE DOCTORAT
pour obtenir le titre de
Docteur en Sciences

de l'Université d'Aix-Marseille
Spécialité : Géosciences de l'Environnement

Présentée par
Catherine JI YU

COMPARATIVE STUDY OF CONVECTIVE AND DIFFUSIVE TRANSPORT PHENOMENA WITHIN THE OPALINUS CLAY AT MONT TERRI

Soutenue le 9 Novembre 2017

Devant le jury composé de

Président :	Pr. Philippe COSENZA	Université de Poitiers, France
Rapporteurs :	Pr. Martin MAZUREK	Université de Berne, Suisse
	Dr. HDR, Sébastien SAVOYE	CEA, France
Co-directeurs :	Pr. Julio GONÇALVÈS	Université d'Aix-Marseille, France
	Dr. Jean-Michel MATRAY	IRSN, France
Examinateurs :	Pr. Philippe COSENZA	Université de Poitiers, France
	Dr. Paul MARSCHALL	Nagra, Suisse
Invité :	Dr. David JAEGGI	swisstopo, Suisse

RESUME

La sûreté des installations de stockage profond des déchets radioactifs repose sur l'évaluation des propriétés de confinement de la barrière géologique et des processus qui y régissent le transport de fluide et de solutés. La thèse est menée dans le cadre de l'expérience Deep Borehole du projet Mont Terri, dont l'IRSN est partenaire. Elle vise à renforcer l'évaluation de l'importance relative des phénomènes de transfert convectifs et diffusifs au sein de l'Argile à Opalines et à apporter des éclaircissements concernant l'impact des phénomènes transitoires chimique et hydraulique sur ces tranferts et la génération d'anomalies de pression. Ces anomalies, fréquentes dans les bassins sédimentaires, sont observables au sein des formations argileuses étudiées par l'IRSN, à savoir la formation du Toarcien/Domérien de Tournemire, l'argillite du Callovo-Oxfordien du bassin de Paris, ainsi que l'Argile à Opalines du Mont Terri.

Les travaux présentés ont tout d'abord consisté à acquérir les différentes forces motrices (gradients de pression, de température et de concentration chimique) et les coefficients phénoménologiques intervenant dans les équations de transport généralisées. Ces dernières font intervenir la diffusion de Fick (flux de solutés engendré par un gradient de concentration) et l'advection sensu largo, qui comprend l'advection pure, l'osmose chimique et l'osmose thermique (flux de fluide développés respectivement à partir d'un gradient de pression, de concentration et de température). Les différentes données ont été obtenus à partir d'échantillons de carottes du forage profond incliné BDB-1 et du système hydraulique multi-obturateurs muni de capteurs de pression et de température installés dans ce dernier. Les données de température et de pression, représentatives de la formation, ont révélé un fort gradient géothermique de 8.5 °C 100 m^{-1} et un excès de charge d'au moins 60 m. Les différentes techniques mises en œuvre pour obtenir les paramètres de transport hydraulique (modèle pétrophysique, analyse spectrale des signaux de pression, tests au gaz et à l'eau en cellule Hassler et tests hydrauliques in situ) ont révélés des valeurs de perméabilité de gamme similaire à celles obtenues précédemment au niveau du tunnel. Les valeurs moyennes de conductivité hydraulique obtenues par tests hydrauliques in situ sont toutefois supérieures, de l'ordre de 10^{-12} m s^{-1} dans le faciès argileux de l'Argile à Opalines. Des coefficients d'emmagasinement spécifique homogènes de l'ordre de 10^{-6} m^{-1} ont été déterminés. L'évaluation des concentrations en chlorure le long du forage a été effectuée par essais de lixiviation et diffusion sortante. Le profil obtenu confirme les résultats des études précédentes et révèle une tendance asymétrique avec des concentrations maximales supérieures à 12 g L^{-1} au niveau de la partie basale de la formation argileuse. Différentes expériences de diffusion ont été menées afin d'acquérir les propriétés de transport diffusif de la formation considérée : diffusion sortante ou entrante en configuration cubique et radiale, et diffusion traversante. Le coefficient de diffusion effectif pour le chlorure et le bromure a été évalué de l'ordre de 4·10^{-11} m^2 s^{-1} et un faible rapport d'anisotropie de 2.4 a été estimé pour le facies sableux de l'Argile à Opalines. Les mesures expérimentales de diffusion radiale ont permis de mettre en évidence le phénomène d'exclusion anionique avec un coefficient entre 46 et 60%. Des modèles théoriques basés sur les interactions électrostatiques et la modification des liaisons hydrogène autour des

molécules d'eau proches de la surface des argiles ont été employés pour calculer les paramètres de transport par osmose thermique.

Une inversion bayésienne basée sur un algorithme de Monte-Carlo par chaînes de Markov a été mise en œuvre afin d'établir un scénario paléohydrologique expliquant le profil de chlorinité observé aujourd'hui. Le profil de chlorures obtenu par expériences de diffusion sortante a été interprété à l'aide d'un modèle numérique unidimensionnel diffusif pur. L'hypothèse d'un transport diffusif a été vérifiée en estimant le nombre de Péclet en incluant les processus osmotiques dans le terme advectif. Le scénario considéré consiste en un échange diffusif entre la formation argileuse et les aquifères adjacents, avec une activation différée de ces derniers liée à l'érosion de surface. L'inversion mise en œuvre basée sur les coefficients de diffusion effectifs, la concentration initiale en chlorures et les temps d'exhumation des aquifères a permis d'évaluer le jeu de paramètres permettant les meilleures simulations ainsi que les incertitudes associées.

La contribution des phénomènes de transport osmotique a été déterminée en interprétant le profil de pression. Les cas de solutions à composante monovalente ou divalente ont été considérés pour les calculs des paramètres osmotiques, à partir de données pétrophysiques, de température et de chlorinité. Des simulations transitoires considérant l'évolution temporelle de la chlorinité et de la pression au cours du scénario géologique déterminé au préalable ont été comparées à des simulations en pseudo régime permanent. Ces dernières consistent en de simples calculs faisant l'hypothèse d'un équilibre entre les profils de pression, de température et de chlorinité. Une calibration a été appliquée pour correspondre au mieux aux mesures de pression, en supprimant le caractère membranaire de la formation sus-jacente du Passwang et des coefficients thermo-osmotiques plus réduits dans leur gamme d'incertitude.

Le profil de pression peut être reproduit en évaluant le flux advectif couplé, en prenant en compte les contributions respectives de l'advection de Darcy, la chemo-osmose et la thermo-osmose. Le calcul en hydraulique pure sans osmose permet d'évaluer une vitesse de Darcy de l'ordre de -10^{-14} m s^{-1}, induisant un écoulement descendant. L'osmose chimique contribue à augmenter le flux advectif dans la même direction mais son effet est négligeable comparé à celui de la thermo-osmose. L'étude montre que le sens de l'écoulement s'inverse en introduisant ce dernier processus dans l'équation de transport. La vitesse de Darcy prend alors une valeur de l'ordre de 10^{-13} m s^{-1} et l'écoulement devient ascendant. Le calcul du nombre de Péclet permet néanmoins d'affirmer la dominance de la diffusion par rapport aux phénomènes de transport advectifs pour le transport de fluide et de solutés à travers l'Argile à Opalines du Mont Terri.

Mots-clés : stockage géologique, Mont Terri, Argile à Opalines, paramètres de transport, surpressions, flux couplés, transitoire hydraulique et chimique.

ABSTRACT

The safety of radioactive waste disposal facilities in deep geological formation depends on the evaluation of the rock confining properties and the processes governing fluid and solutes fluxes. The thesis is conducted in the framework of Deep Borehole experiment of the Mont Terri consortium, of which the IRSN is a partner. The purpose of this research is to build confidence with regard to understanding relative importance of diffusive and convective phenomena and to identify the impact of a hydraulic and chemical transient behaviour on the transfers of fluid and solutes, and anomalous pressures generation. These anomalies are frequent in sedimentary basins and can be measured in argillaceous formations studied by the IRSN, such as the Toarcian-Domerian clay rock of Tournemire, the Callovo-Oxfordian formation of the Paris Basin and the Opalinus Clay at Mont Terri.

The first stage of this research work consisted in determining the driving forces (pressure, temperature and solute concentration gradients) and phenomenological coefficients, which are key parameters involved in the global diffusive-advective transport equations. These equations include diffusion defined by Fick's laws (solute flow caused by a concentration gradient), and the advection sensu largo, which corresponds to pure advection coupled with chemical osmosis and thermal osmosis (fluid flow caused respectively by hydraulic, chemical and temperature gradients). Data acquisition was performed with drillcore samples from the BDB-1 deep-inclined borehole and the multi-packer hydraulic system with pressure and temperature sensors installed within the borehole. Representative of the natural formation conditions, temperature and pressure measurements revealed a high geothermal gradient of 8.5 °C 100 m^{-1} and an excess of hydraulic head of at least 60 m. Several methods were used to obtain the hydraulic parameters: petrophysical model, spectral analysis of pressure series, tests using gas or water in Hassler cell, and in situ hydraulic tests. They revealed hydraulic conductivity values virtually in the same range than the ones acquired so far at the tunnel level, but with higher average values in the Opalinus Clay shaly facies, in the order of 10^{-12} m s^{-1}. Specific storage coefficients rather homogeneous in the order of 10^{-6} m^{-1} were determined. Leaching experiments and out diffusion tests were performed to acquire the chloride contents along the borehole. The resulting profile confirms the results of the previous studies and shows an asymmetric curved trend with maximum values superior to 12 g L^{-1} in the basal part of the clay formation. Several experimental setups were used to acquire the Opalinus Clay diffusive parameters: out and in diffusion in cubic or radial configuration and through diffusion. Effective diffusion coefficients for chloride and bromide were estimated in the order of 4·10^{-11} m^2 s^{-1} and a low anisotropy ratio of 2.4 was estimated for chloride effective diffusion coefficient in the Opalinus Clay sandy facies. Radial diffusion measurements enabled to highlight the anion exclusion effect with a coefficient in the range of 46 to 60%. Theoretical models based on electrostatic interactions and the modifications of the hydrogen bounds associated with water molecules near the clay surface were used to compute the osmotic transport parameters.

A Bayesian inversion based on a Monte Carlo Markov Chain algorithm was carried out to obtain a paleohydrological scenario explaining the current chlorinity profile. The chloride profile obtained by out diffusion experiments was interpreted by means of a purely diffusive one-dimensional numerical model. The assumption of purely diffusive mass transport phenomena was verified by estimating the Peclet number including osmotic processes in the advection term. The implemented scenario consists in a diffusive exchange between the argillaceous formation and the adjacent aquifers, with deferred activation times of the fresh-water sources linked to the surface erosion of the geological formations. The implemented inversion based on effective diffusion coefficients, initial value of the chloride concentration and two exhumation and thus, hydraulic activation times for the two bounding aquifers allowed to evaluate the best fit parameter sets and their uncertainties not evaluated so far.

The contribution of osmotic transport phenomena was assessed by interpreting the pressure profile measured in the BDB-1 borehole. Theoretical predictive models were applied to compute the osmotic parameters for monovalent and divalent solutions, based on experimental petrophysical parameters, temperature and chlorinity data. Transient simulations considering the temporal evolution of both chlorinity and pressure with the geological scenario determined using the MCMC scheme, and pseudo steady-state simulations, which are simplified first-order calculations considering equilibrium between pressure, temperature and chlorinity profiles were compared. A calibration was applied assuming no membrane properties for the Passwang Formation and more reduced thermo-osmotic coefficients in their uncertainty range, in order to match the pressure data.

The pressure profile can be reproduced by evaluating the coupled advective flow, by taking into account the respective contributions of pure advection, chemo-osmosis and thermo-osmosis (fluid flows caused respectively by pressure, chlorinity and temperature gradients). Pure hydraulic calculation evaluates a Darcy velocity in the order of -10^{-14} m s^{-1}, related to a downward flow. Chemical osmosis slightly increases the advective flow in the same direction, but its effect is rather minor compared to the one induced by thermo-osmosis. Indeed, the water movement is inverted when considering this latter process in the transport equation. Then, the mean Darcy velocity is in the order of 10^{-13} m s^{-1} and the flow becomes upward. However, the Peclet number calculation enables to confirm the dominance of diffusion with respect to advective transport processes for fluid and solutes fluxes through the Opalinus Clay of Mont Terri.

CONTENTS

LIST OF FIGURES

LIST OF TABLES

INTRODUCTION

Nuclear science has affected our daily life with applications in such various fields as energy production, industrial development, environmental studies, medicine and agriculture. In addition to the profound change on international politics and warfare induced by defence-related industry, accidents in the past decades related to nuclear power generation (Chernobyl, Three Mile Island, Fukushima...) also raised concerns about enhancing nuclear safety and radioprotection.

Radioactive waste is a term describing a substance containing unstable elements, or radionuclides, that decay over time and for which no further use is planned. This type of waste is characterised by the type of radionuclides contained, the associated i) emitted radiation (alpha, beta, gamma and neutron), ii) activity (number of nuclei that spontaneously disintegrate per unit of time) and iii) half-life (time required to decrease by half a population of radioactive nuclei). The activity level and the radioactive half-life are the commonly used criteria to classify radioactive waste. The management of long-lived radioactive waste, presenting a half-life greater than 31 years, remains a long-standing concern, as no sustainable solution has been fully implemented and accepted by the public yet. However, noteworthy lines of research are progressing and aim at ensuring safe future disposal of nuclear waste.

Deep repository of radioactive waste in geological formations has been extensively studied ever since the proposal of this permanent solution by the United States National Academy of Sciences committee on Waste Disposal in 1957. A geological repository is a combination of engineered and natural barriers designed to achieve containment and retention of radionuclides on a geological time period. As the host rock is the final barrier of the system in the event of a radionuclides leakage, the repository performance largely relies on its confinement properties. In most countries where nuclear energy is generated, the suitability of various rock types have been studied, including crystalline rocks (granite and gneiss) as well as sedimentary rocks (clay, carbonates, tuff and salt).

Clay formations were chosen by France (Callovo-Oxfordian), Belgium (Boom Clay) and Switzerland (Opalinus Clay) to install an underground rock laboratory and to evaluate the option to dispose of their Long-Lived, Intermediate and High Level Waste in geological repository. Clays exhibit favourable confinement properties such as low permeability, high retention capacity for radionuclides and other contaminants, lateral continuity, and self-sealing capacity due to swelling after water uptake.

The present study was launched by the Research Laboratory for Migration and Interactions in the Geosphere (LETIS) of the French National Institute for Radioprotection and Nuclear Safety (IRSN). In charge of evaluating the Cigéo French industrial project of geological repository conducted by Andra in a zone located in the Meuse-Haute Marne counties, IRSN is carrying out various studies to assess the containment properties of argillaceous formations. To this end, this public institution developed its own underground rock laboratory at Tournemire (Aveyron, France) to study a Toarcian-Domerian clayrock, and also joined the Mont Terri Consortium (Switzerland), which is devoted to the characterisation of the Opalinus Clay.

Understanding the transport mechanisms of the radionuclides is of utmost importance to assess nuclear waste repository safety performance. In low permeability clay formations, diffusion is assumed to be a significant, if not dominant, transport process with respect to advection. However, advective flows can play a substantial role in fluid movement and induce pressure anomalies within clay formations.

The Mont Terri site is relevant for studying the safety of a repository as it presents an extreme transient situation, the other extreme being the Tournemire site, which has nearly reached hydraulically and hydrochemically steady states. The Bure site is an intermediate situation, as it presents a hydrochemically steady state and is characterized by overpressures and hydraulic properties similar to those of Mont Terri.

The purpose of the thesis project, in the framework of the Deep Borehole experiment, is to clarify the origins of the pressure distribution observed in the Opalinus Clay at Mont Terri and to answer the following questions:
What is the dominant transport phenomenon between convection in its extended formula, including chemical and thermal osmosis, and diffusion in the Opalinus Clay at the Mont Terri rock laboratory and what would be the impact of a hydraulic and chemical transient behavior on the solutes transfer?

This thesis is an element to answer the 9th question of the IRSN scientific strategy in nuclear safety and security: *What are the important phenomena which influence the long-term safety of a geological repository of long-lived low, medium and high-level waste and how to model them?*

The manuscript describes the acquisition of transport parameters, which aims at assessing the Opalinus Clay containment properties. The theoretical framework of the study is introduced in Chapter I, followed by a description of the study site and of the experiment concept in Chapter II. The contribution to the characterization of the Opalinus Clay, including pressure and temperature measurements, acquisition of hydraulic parameters, geochemistry and diffusion coefficients, is detailed in Chapter IV. The final chapter of the manuscript aims at understanding the transport phenomena through the Opalinus Clay by modelling the chloride and pressure profiles.

CHAPTER 1.   STATE OF THE ART

1.1.   WATER AND SOLUTES TRANSFERS IN ARGILLACEOUS MEDIA

1.1.1.   CHARACTERISTICS OF CLAYS AND POROUS MEDIA

1.1.1.1.   Clay rocks properties

Clays composition and structure

The term "clay" refers to a natural occurring material composed primarily of fine-grained minerals inferior to 2 μm in size, which show plastic behaviour at appropriate water contents and harden when dried or fired (Guggenheim and Martin, 1995). Weathering of silicate-rich rock fragments is the main formation process of clay minerals, which are essentially represented by hydrated phyllosilicates. Clay minerals are composed of tetrahedrally (Si, Al) and octahedrally (Al, Fe, Mg) coordinated cations organised to form either sheets or chains. Planes of oxygen atoms surrounding Si^{4+} are referred as tetrahedral (T) or silica sheets, while octahedral (O), alumina or magnesia sheets are composed of individual octahedrons sharing edges made of oxygen atoms or hydroxyl groups (Figure 1.1). Clay layers are comprised of the stacking of basic individual sheets alternating with interlayer spaces: i) a 1:1 or T-O layer (e.g. kaolinite) contains one silica sheet and one octahedral sheet; ii) a 2:1 or T-O-T layer (e.g. illite, smectite) consists of an octahedral sheet between two opposing tetrahedral sheets; iii) a 2:1:1 or T-O-T-O layer (e.g. chlorite) is made of a 2:1 layer with a magnesium dominated octahedral sheet.
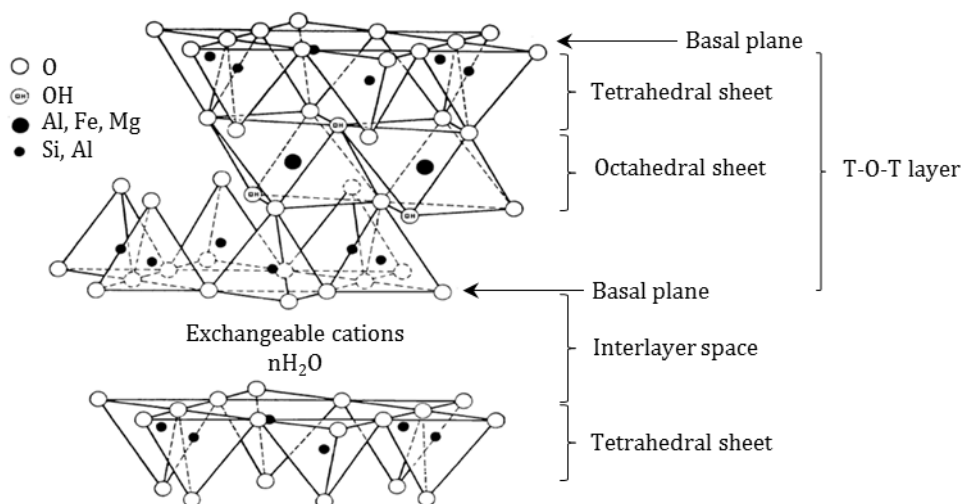
Figure 1.1: Montmorillonite structure (modified from Grim, 1962)

Clay-porewater interactions

Clay basal planes have permanent negative charge sites, owing to a process known as isomorphic substitution. Without changing significantly the crystal structure, central Si- and Al-ions can be substituted for lower positive valence ions differing by less than 10 to 15% in ionic radii. In clay minerals, common isomorphic substitutions are Al^{3+} for Si^{4+} in tetrahedrons, and Mg^{2+}, Fe^{2+}, and Fe^{3+} for Al^{3+} in octahedrons (Bohn et al., 2015).

The hydrolysis of silanol (Si-OH) and aluminol (Al-OH) sites at the external edge of the clay lattice can also lead to the development of negative and positive charges, which are non-permanent and pH-dependant.

The overall charge deficit observed in clays at natural pH is balanced through the adsorption onto the clay surfaces of exchangeable cations, which are termed counterions and contained in the pore water. The cation exchange capacity (CEC) is the total amount of adsorbed cations expressed in milliequivalents per 100 g of dehydrated material.

Adsorption of water molecules by clay mineral is linked to the formation of hydrogen bonds between water molecules and the exposed O^{2-} or HO^- and to the hydration of counterions. Water can come only at the edge of clay particles, as in kaolinite, or also in the interlayer space (smectite) leading to clay swelling.
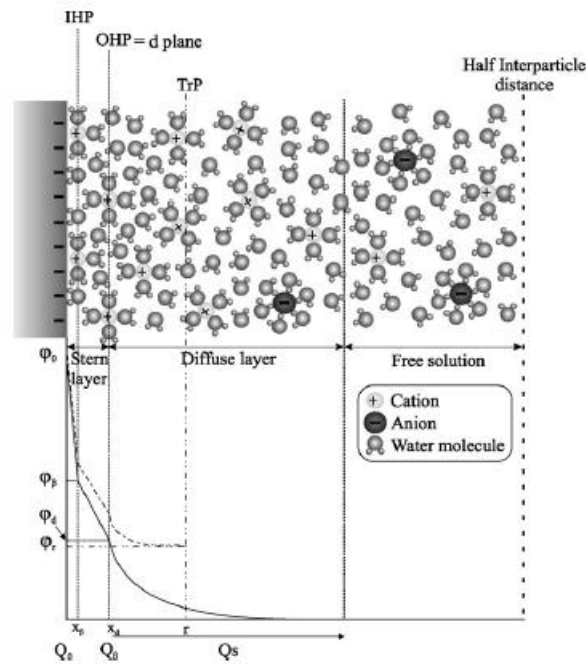
Figure 1.2: Schematic representation of the electrochemical interactions at the surface of a clay particle (Gonçalvès et al., 2007)

The solute distribution and the electrical potential in the pore space can be described by a triple layer electrical model (Figure 1.2), which describes the non-homogeneities in ion distribution. This model considers: i) a compact layer, the Stern layer presenting high solute concentration; ii) a diffuse layer, where the concentration of the counterions decreases towards the middle of

the pore; iii) and the middle of the pore, where the electrical field becomes negligible, and which contain a solution in local equilibrium with pore water.

The passage of anions is restricted when compaction decreases pore size so that the diffuse double layers of two clay particles overlap. This phenomenon is referred as anionic or Donnan exclusion. Since dissociated ions of a salt must move together to ensure electro-neutrality, transport restriction also applies to cationic species. The distribution of electrical charges in solution allows water and non-charged solutes transport, but restricts the passage of charges species through the porous network, conferring to clays semi-permeable membrane behaviour. In such media, osmosis can cause a fluid flow from regions of low salt concentration to regions of high salt concentration, where a fluid pressure build-up is induced.

1.1.1.2. Porous media characteristics

Porous networks in natural media often have complex geometry. Relevant parameters have to be defined to characterise a porous material response to an external sollicitation such as fluid flow or wave propagation.

Several types of porosity are considered depending on the degree of connectivity. Effective porosity or kinematic porosity (ω_c) is the ratio of interconnected pore space, accessible for fluid flow, to the bulk volume of the porous material V_t. This parameter is used to describe advective flow in a porous media (see Equation (1.9)) and can be measured by tracer experiments under a pressure gradient or tidal spectral analysis. Isolated pores are included in the total porosity, or physical porosity ω_t, which represents the ratio of the total pore space of the media V_p to the bulk rock volume. The total porosity can be measured directly, in laboratory, by techniques of measuring volume and weighing after saturation and then after drying, or indirectly, in situ, with geophysical techniques (neutron, gamma-gamma logging).

$$\omega_{tot} = \frac{V_p}{V_t} \tag{1.1}$$

In clay media, an accessible porosity for solute transport can also be defined and can be estimated using diffusion experiments.

A porous material specific surface corresponds to the internal surface of its solid matrix. Symbolised A_s, it is defined as the ratio or the internal surface of the pore space S to the sample volume V_t. Common measurement techniques involving gas adsorption and desorption or microscopic analysis of sections.

$$A_s = \frac{S}{V_t} \tag{1.2}$$

Another parameter is the tortuosity τ, which reflects that a fluid flowing through a porous medium has to cover a longer pathway than the system length.

$$\tau = \left(\frac{L'}{L}\right)^2 \tag{1.3}$$

where L' is the length of a streamline between two points and L is the length of the straight line between these points.

Currently, no technique is available to measure directly this parameter. However, it is supposed to be linked to the material electrical properties. If the material porosity is known and if the solid phase is not conductive, then an electrical tortuosity can be determined by saturating the medium with a conductive fluid. Electric current, which is linked to the displacement of ions in solution, and fluid are assumed to cover the same distance through the material. Hydraulic tortuosity is generally higher than electrical tortuosity according to Walsh and Brace (1984).

A porous medium of electric conductivity σ and saturated by a conducting fluid of conductivity σ_f can be characterized by an adimensional number F called the formation factor:

$$F = \frac{\sigma_f}{\sigma} \tag{1.4}$$

Archie's empirical law (1942) links the formation factor to the medium porosity, independently to the fluid properties:

$$F = \omega^{-m} \tag{1.5}$$

The parameter m is the cementation factor and depends on the nature of the porous material. Ranging between 1.3 and 5.4 (Heitzmann, 2004), m is estimated to be close to 2 for compacted and deeply buried sediments (Ullman and Aller, 1982).

1.1.1.3.   Hydraulic parameters

Hydraulic conductivity, intrinsic permeability and transmissivity

Permeability, also known as hydraulic conductivity and symbolized K, is a material ability to transmit fluid under a hydraulic gradient. Darcy's column experiments showed that the total discharge through a porous medium is proportional to the hydraulic gradient over a given distance (Darcy, 1856).

The resulting law can be written as:

$$Q = -\frac{KA\Delta h}{L} \tag{1.6}$$

where Q [m^3 s^{-1}] is the volumetric flow, K [m s^{-1}] is the porous medium permeability, A [m^2] is the column cross sectional area, Δh [m] is the difference in piezometric head over the length of interest and L [m] is the length of the porous sample.

Piezometric head, or hydraulic head h, is a combined measurement of the elevation and the water pressure above a geodetic datum, and is given by Bernoulli's equation:

$$h = z + \frac{p_f}{\rho_f g} \tag{1.7}$$

where z [m] is the altitude, p_f [Pa] is the fluid pressure and ρ_f [kg m^{-3}] is the fluid volumetric mass.

If i denotes the hydraulic gradient and q the filtration velocity, Darcy's law can also be written as:

$$q = Ki \tag{1.8}$$

When the fluid flow is considered not through the entire sample section but through the material porous network, an effective pore fluid velocity can be defined as follows:

$$u = \frac{q}{\omega_c} \tag{1.9}$$

According to Poiseuille's theory and in the case of a laminar flow, fluid velocity is inversely proportional to its viscosity. Therefore, an intrinsic permeability k can be defined and only depends on the porous media geometrical characteristics. Its relation with hydraulic conductivity writes (Bear and Verruijt, 1987):

$$K = \frac{k\rho_f g}{\mu_f} = \frac{kg}{\eta_f} \tag{1.10}$$

Where μ_f [kg m^{-1} s^{-1}] is the fluid dynamic viscosity, ρ [kg m^{-3}] is the fluid density, g [9.81 m s^{-2}] is the gravity acceleration and η_f [m^2 s^{-1}] is the fluid kinematic viscosity.

Transmissivity T refers to the ability of an aquifer to transmit groundwater through its entire saturated thickness E.

$$T = KE \tag{1.11}$$

Storage and Storativity

Fluid compressibility β_f, expressed in Pa^{-1}, describes a fluid volume variation (and consequently of the associated volumetric mass) caused by a change in pressure. At a given temperature and for a fluid of constant chemical composition and of volume V_f, compressibility coefficient is given by:

$$\beta_f = \frac{1}{V_f}\frac{\partial V_f}{\partial p_f} = \frac{1}{\rho_f}\frac{\partial \rho_f}{\partial p_f} \tag{1.12}$$

An apparent compressibility coefficient α can also be defined for porous media:

$$\alpha = -\frac{1}{V_r}\frac{\partial V_p}{\partial p} \tag{1.13}$$

where V_r [m^3] is the solid matrix volume and V_p [m^3] is the pore volume.

The storage coefficient or storativity is the volume of water an aquifer releases from or takes into storage per unit surface area of the aquifer per unit change in head. It is expressed (Brace et al., 1968; Fischer, 1992a):

$$S = \omega_c \beta_f + \alpha - (1 - \omega_c \beta_s) \tag{1.14}$$

Where ω_c [-] is the effective porosity, α [Pa^{-1}] is the apparent compressibility of the porous medium and β_s [Pa^{-1}] is the solid grain compressibility.

Specific storage coefficient S_s is the ratio between an aquifer storativity and its thickness.

$$S = S_s E \tag{1.15}$$

Taking into account the deformation of the porous medium and the fluid compressibility, S_s also writes (de Marsily, 1986):

$$S_s = \rho_f g \omega_c \left(\frac{\alpha}{\omega_c} + \beta_f - \beta_s \right) \tag{1.16}$$

1.1.2. COUPLED TRANSPORT PHENOMENA IN CLAY ROCKS

1.1.2.1. Terminology

Driving forces for fluid flow (temperature, hydraulic, chemistry or electrical potential gradients) can be described within the framework of the theory of irreversible thermodynamic processes (Table 1.1). A coupled transport process refers to a flow of any kind (heat, fluid, solute or current), which is driven by gradient of a potential not usually associated with that flow, called non-conjugate force.

Table 1.1: Onsager matrix giving the terminology of coupled fluxes (Onsager, 1931a and 1931b). Particular attention is given to the potentially significant processes involved in radionuclides migration (shaded cells).

		Gradient			
		Thermal	**Hydraulic**	**Chemical**	**Electric**
Flux	**Heat**	Thermal conduction	Heat filtration	Dufour effect	Peltier effect
	Fluid	Thermal osmosis	Advection	Chemo-osmosis	Electro-osmosis
	Solute	Soret effect	Ultrafiltration	Diffusion	Electrophoresis
	Electric	Seebeck or Thomson effect	Rouss effect	Diffusion current	Electric conduction

1.1.2.2. Fluid flow processes

Advection

In a classic way, the flow of an incompressible fluid is described by Darcy's law:

$$q = -\frac{k}{\mu_f}\left(\nabla p_f + \rho_f g \nabla z\right) \tag{1.17}$$

where q [m^3 s^{-1}] is the fluid specific discharge, k [m^2] is the intrinsic permeability tensor, μ_f [Pa s] and ρ_f [kg m^{-3}] are respectively the dynamic viscosity and the fluid density, ∇p_f [Pa m^{-1}] is the fluid pressure gradient, g [9.81 m s^{-2}] is the gravity acceleration and ∇z is the vector (0,0,1) if the z-axis is vertical ascending.

Advection is a linear phenomenon, the time required to cover a given distance is proportional to this distance.

Pure advective transport can be expressed by combining Darcy's law and the mass balance equation, also called continuity equation, which writes:

$$div\left(\rho_f q\right) + \frac{\partial\left(\rho_f \omega\right)}{\partial t} + \rho_f q = 0 \tag{1.18}$$

where ω is the tracer accessible porosity.

Within the framework of poro-elasticity (de Marsily, 1986):

$$div\left(\rho_f q\right) = -\frac{S_s}{g}\frac{\partial p}{\partial t} \tag{1.19}$$

If temperature variations in the state equation are taken into account:

$$\frac{d\rho_f}{\rho_f} = \beta_f d\rho_f - \chi_T dT \tag{1.20}$$

where χ_T [K^{-1}] is the coefficient of thermal expansion of water.

Equation (1.19) becomes:

$$div\left(\rho_f q\right) = -\frac{S_s}{g}\frac{\partial p}{\partial t} + \rho_f \omega \chi_T \frac{\partial T}{\partial t} \tag{1.21}$$

If density variations are neglected, the combination of Darcy's law with the continuity equation gives the diffusivity equation:

$$div(K\nabla h) = S_s \frac{\partial h}{\partial t} \tag{1.22}$$

If there is a variation in total stress σ, related to deformation or fracturing of the geological formation, Equation (1.22) rewrites (Schneider et al., 1996; Heitzmann, 2004; Gonçalvès et al., 2004):

$$div\left(\rho_f q\right) = \frac{S_s}{g}\frac{\partial p}{\partial t} - \rho_f \alpha \frac{\partial \sigma}{\partial t} \qquad (1.23)$$

where α [Pa^{-1}] is the compressibility coefficient of the porous medium.

Chemical osmosis

Chemical osmosis refers to the spontaneous passage of solvent through a semi-permeable membrane, resulting from a chemical concentration gradient.

The chemo-osmotic flow can be expressed in terms of a flow similar to Darcy's law:

$$q_\Pi = K_\pi \nabla \Pi_h = \varepsilon K \nabla \Pi_h \qquad (1.24)$$

where K_Π [m s^{-1}] is the coefficient of osmotic permeability and ε is the chemo-osmotic efficiency, also called reflection coefficient or exclusion factor.

The osmotic pressure head is defined as:

$$\Pi_h = \frac{\Pi}{\rho_f g} \qquad (1.25)$$

and the osmotic pressure writes:

$$\Pi = -\frac{RT}{V_w}\ln a_w \qquad (1.26)$$

where Π [Pa] is the osmotic pressure, R [8.32·10^{-3} m^3 Pa K^{-1} mol^{-1}] is the gas constant, T [K] is the temperature, V_w [L mol^{-1}] is the fluid molar volume and a_w is the water activity in solution.

The activity of water can be calculated according to Garrels and Christ (1965):

$$a_w = 1 - V_w \sum_i \frac{c_i}{W_i} \qquad (1.27)$$

where c_i [mol L^{-1}] is the concentration of solute i and W_i [kg mol^{-1}] is the molar mass of solute i.

The osmotic pressure can also be approximated using the Van't Hoff relationship for solutions with concentrations lower than 1 mol L^{-1} (Fritz, 1986).

$$\Pi = -\upsilon RT C_f \qquad (1.28)$$

where υ is the number of dissociated ions in solution (e.g. 2 for NaCl) and C_f [mol L^{-1}] is the solute concentration.

The chemo-osmotic coefficient varies between 0 and 1. Its value equals 0 when the material does not present a membrane behavior, and 1 for an ideal membrane, which totally impedes solute transport.

It can be estimated as a function of the average value of anions concentration in the total porosity $\langle \overline{C^-} \rangle$ and the concentration C_f in the equilibrium solution (out of the electrostatic field influence):

$$\varepsilon = 1 - \frac{\langle \overline{C^-} \rangle}{C_f} \tag{1.29}$$

Based on a diffuse double layer theory, Bresler (1973) numerically computed the osmotic efficiency as a function of the product of the half pore size and the squared root of the concentration. The Bresler's curves shown in Figure 1.3 are common abacus used to predict the osmotic efficiency in argillaceous rocks.
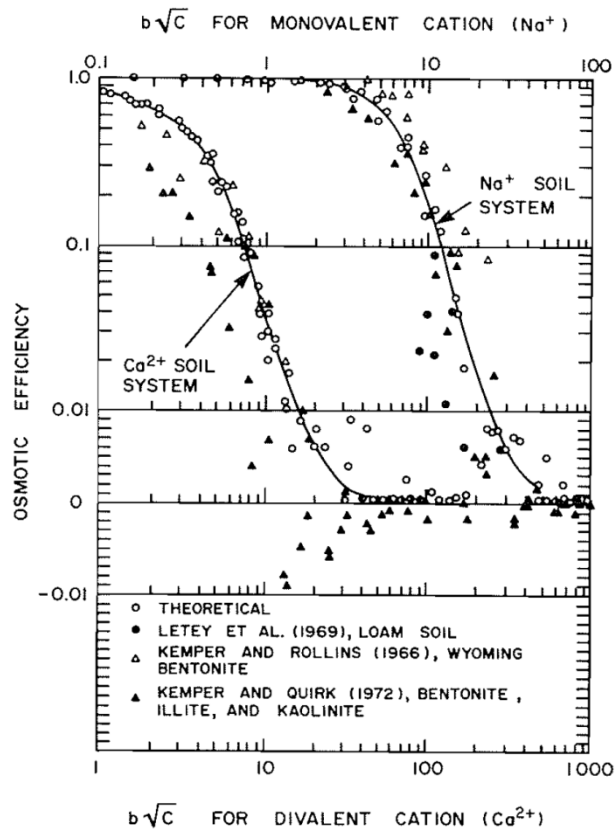
Figure 1.3: Bresler's (1973) curves presenting chemo-osmotic efficiency coefficient for monovalent and divalent solutes, as a function of b√c where b is the half-pore size in Å and c is the solution concentration in normality. Experimental data are taken from Letey et al. (1969), Kemper and Rollins (1966) and Kemper and Quirk (1972).

A numerical approximation for Bresler's monovalent solution was proposed by Bader (2005):

$$\varepsilon_{Bresler} = \frac{1}{2}\left(1 - erf\left[\frac{0.4(v - 7)}{\sqrt{0.9v}}\right]\right) \tag{1.30}$$

and

$$v = b\left(1 - \sqrt{\frac{C_f}{1000M_s}}\right) \tag{1.31}$$

where b is the half pore size (half of the average film thickness between two charged clay platelets), C_f is the solute concentration and M_s is the solute molar mass.

Bolt (1979) proposed a model to calculate ε from the integration of the chemical force for a porous medium:

$$\varepsilon = \frac{\int_0^b \left(1 - \frac{C^-(x)}{C_f}\right)(2b - x^2)dx}{\frac{2b^3}{3}} \tag{1.32}$$

where $C^-(x)$ is the anion concentration in the diffuse layer at a distance x from the beginning of the diffuse layer, C_f is the concentration in equilibrium solution and b is the half-pore size.

C_f corresponds to the concentration obtained by a classical geochemical model. $C^-(x)$ can be calculated using an electrical model (e.g. the triple layer model in Gonçalvès et al., 2007; Tremosa et al. 2012b).

Pore size 2b is determined using a mass balance equation, valid for a parallel-plane conceptual model for the porous network geometry (Neuzil, 2000):

$$b = \frac{\omega}{\rho_s A_s(1 - \omega)} \tag{1.33}$$

where ω [-] is the total porosity, ρ_s [g m^{-3}] is the density of the solid and A_s [m^2 g^{-1}] is the specific surface area.

Thermo-osmosis

Thermo-osmosis refers to a fluid flow q_{TO} occurring through a membrane and driven by a temperature gradient. This phenomenon is a potential origin of abnormal pressures in sedimentary basins (Rousseau-Gueutin, 2008).

It writes:

$$q_{TO} = -\frac{k_T}{\mu_f}\nabla T \tag{1.34}$$

where k_T [m^2 K^{-1} s^{-1}] is the thermo-osmotic permeability, which can be expressed by the following formula.

$$k_T = k\frac{\Delta H}{T} \tag{1.35}$$

where k [m^2] is the intrinsic permeability, ΔH [J m^{-3}] is the macroscopic volume-averaged excess specific enthalpy due to fluid-solid interactions and T [K] is the temperature.

The pioneering theory of thermo-osmosis was proposed within the framework of irreversible thermodynamics by Derjaguin and coworkers in the early 20th century (Derjaguin and Sidorenkov, 1941; Derjaguin et al., 1987; Churaev, 2000).

Gonçalvès et al. (2012) developed a simple heuristic model to estimate the thermo-osmotic permeability based on a theoretical analysis of the change in enthalpy induced by the alteration of hydrogen bonds (HB) in the pore space of clay rocks. The required ΔH can be expressed as:

$$\Delta H = (C_{HB}^b - C_{HB})\Delta H_{HB} \tag{1.36}$$

where C_{HB}^b and C_{HB} [mol m^{-3}] are the HB concentrations in the bulk and the pore fluid and ΔH_{HB} [kJ mol^{-1} of HB] is the energy needed to break one mole of HB, estimated between 6 and 23 kJ mol^{-1} (Hakem et al., 2007).

Hydrogen bond concentrations are calculated for monovalent-divalent system with (Gonçalvès et al., submitted):

$$C_{HB} = N_w^+ C_+ 1/2N_{HB}^+ + N_w^{2+} C_{2+} 1/2N_{HB}^{2+} + N_w^- C_- 1/2N_{HB}^- +$$
$$(C_w - N_w^+ C_+ - N_w^{2+} C_{2+} - N_w^- C_-)\left(\frac{b-b_s}{b}N_{HB}^b + \frac{b_s}{b}N_{HB}^s\right)1/2 \tag{1.37}$$

and
$$C_{HB}^b = N_w^+ c_+ 1/2N_{HB}^+ + N_w^{2+} c_{2+} 1/2N_{HB}^{2+} + N_w^- c_- 1/2N_{HB}^- +$$
$$(c_w - N_w^+ c_+ - N_w^{2+} c_{2+} - N_w^- c_-)N_{HB}^b 1/2 \tag{1.38}$$

where C_w, C_+, C_{2+} and C_- [mol m^{-3}] are the water, monovalent and divalent cations, and anions concentrations in the pore space, c_w, c_+, c_{2+} and c_- [mol m^{-3}] are the water, monovalent and divalent cations, and anions concentrations in the bulk solution, N_w^+, N_w^{2+}, N_w^- are the number of water molecules in the first hydration shell of the monovalent and divalent cations, and of the anion, N_{HB}^+, N_{HB}^{2+}, N_{HB}^- are the mean number of HB per water molecule in the first corresponding hydration shells, b and b_s [m] are the mean half-pore size and the half thickness of highly ordered water, N_{HB}^b and N_{HB}^s are the mean number of HB per water molecule of bulk and highly ordered water.

Ion concentrations are obtained i) based on a Donnan equilibrium formalism for a monovalent-divalent system, ii) assuming a thermodynamic equilibrium between the bulk and the pore fluid solutions and iii) using the electroneutrality equation in the pore.

The chemical potentials of the ions in the bulk solution can be equated to their counterpart i.e. the electrochemical potentials of the ions in the pore space solution of a clay rock assuming thermodynamic equilibrium, yielding:

$$C_{2+}C_-^2 = c_{2+}c_-^2 \tag{1.39}$$

and
$$C_+C_- = c_+c_- \tag{1.40}$$

The electroneutrality equation in the pore is written:

$$2C_{2+} + C_+ = C_- + \frac{Q_v}{e} \tag{1.41}$$

where Q_v [C m⁻³] is the excess charge per unit pore volume to be compensated by counterions and e [1.6·10⁻¹⁹ C] is the elementary charge. Qv is obtained by dividing the excess charge in a unit volume of porous medium by the associated fluid volume yielding (Revil and Leroy, 2004):

$$Q_v = \frac{(1 - \omega)\rho_s CEC \times 96.3}{\omega} \tag{1.42}$$

where ω [-] is the porosity, ρ_s [kg m⁻³] is the grain density and CEC [meq g⁻¹] is the cation exchange capacity.

Using Equations (1.40) and (1.41), Equation (1.41) becomes:

$$C_-^3 + \frac{Q_v}{e} C_-^2 - (c_+ + c_-)C_- - 2c_{2+}c_-^2 = 0 \tag{1.43}$$

Only one of the three roots of Equation (1.43) applies to the problem.

The water molecule concentrations C_w and c_w are calculated using the mass conservation equations (Revil and Leroy, 2004; Gonçalvès and Rousseau-Gueutin, 2008):

$$v_w C_w + v_+ C_+ + v_{2+} C_{2+} + v_- C_- = 1 \tag{1.44}$$

and
$$v_w c_w + v_+ c_+ + v_{2+} c_{2+} + v_- c_- = 1 \tag{1.45}$$

where v_w, v_+, v_{2+} and v_- [m³ mol⁻¹] are respectively the molar volumes of water, monovalent and divalent cations and anion.

This model, presented in detail in Gonçalvès et al. (in review), enables to estimate the thermo-osmotic permeability based on petrophysical parameters commonly measured in clay rocks together with molecular parameters that can be constrained through molecular dynamics simulations.

Electro-osmosis

Electro-osmosis is the flow of fluid resulting of an electrical potential gradient. However, in natural systems, the macroscopic current density J_e is considered null (Bolt, 1979; Revil and Leroy, 2004). The effect of electrical potential gradient is implicitly taken into account at the macroscopic scale in hydraulic and chemo-osmotic terms (Revil and Pessel, 2002). Indeed, most values (e.g. chemical osmotic efficiency) are not measured in short-circuited conditions, which implies that they represent apparent and not absolute values. Therefore, the effects of electro-osmosis on the solute and fluid fluxes are considered in apparent quantities in this research project.

1.1.2.3. Solute flow process: chemical diffusion

Chemical diffusion corresponds to the agitated motion of solutes due to the effect of Brownian movement. It tends to homogenise a medium by displacing solutes from high to low concentration zones. Diffusive transport in a porous medium is ruled by Fick's first law:

$$J_{diff} = -D_e \nabla c \tag{1.46}$$

where J_{diff} [kg m^{-2} s^{-1}] is the diffusive flow, D_e [m^2 s^{-1}] is the effective diffusion coefficient and c [kg m^{-3}] is the solute concentration.

The effective diffusion coefficient D_e can be expressed as a function of structural parameters of the porous medium:

$$D_e = \omega_e \left(\frac{\chi}{\tau^2}\right) D_0 = \frac{D_0}{F} = \frac{D_0}{\omega_e{}^{-m}} = \omega_e D_p \tag{1.47}$$

where ω_e is the diffusion accessible porosity, m is the cementation factor, D_0 [m^2 s^{-1}] is the molecular diffusion coefficient and D_p [m^2 s^{-1}] is the pore diffusion coefficient.

1.1.2.4. General transport equation

Combination of mass balance equation with Fick's second law gives:

$$div(D_e \nabla c - qc) = \omega_c \frac{\partial c}{\partial t} \tag{1.48}$$

where D_e [m^2 s^{-1}] is the effective diffusion coefficient and ∇c [mol m^{-4}] is the concentration gradient, q [m^3 s^{-1}] is the fluid discharge related to advective coupled flows, and ω_c is the kinematic porosity.

The fluid flow equation is extended by combining chemical and thermo-osmosis with the Darcy's flow:

$$q = -\frac{k}{\mu_f}\left(\nabla P + \rho_f g \nabla z\right) + \nu RT\varepsilon \frac{k}{\mu_f}\nabla c - \frac{k_T}{\mu_f}\nabla T \tag{1.49}$$

If the system is considered at equilibrium, so that the variations of pressure, concentration and temperature and with time are assumed null:

$$div(q) = 0 \tag{1.50}$$

Transient state implies the addition of several terms at the right side of Equation (1.50), as presented in part 1.1.2.1.:

$$div(q) = \frac{S_s}{g}\frac{\partial p}{\partial t} - \rho_f \alpha \frac{\partial \sigma}{\partial t}$$

1.2. LONG-TERM TRANSIENT STATES IN ARGILLACEOUS ROCKS

1.2.1. ABNORMAL FLUID PRESSURES

Abnormal pressures are defined as pore pressures above or below hydrostatic pressures (Law and Spencer, 1998). Occuring on all continents and in a wide variety of geological environments, these anomalies first brought interest in the fields of oil and gas resources production. Indeed, costly drilling issues are associated with abnormal pressures, such as borehole collapse, blowout and lost circulation (Fakhry, 2008).

In the context of geological disposal of radioactive waste, pressure anomalies are also considered, since many of the studied clay formations located in shallow environnements exhibit these deviations, as shown in Figure 1.4 and Figure 1.5. Local positive pressure anomalies can enhance radionuclide transport with respect to steady-state flow systems (Bianchi et al., 2015).
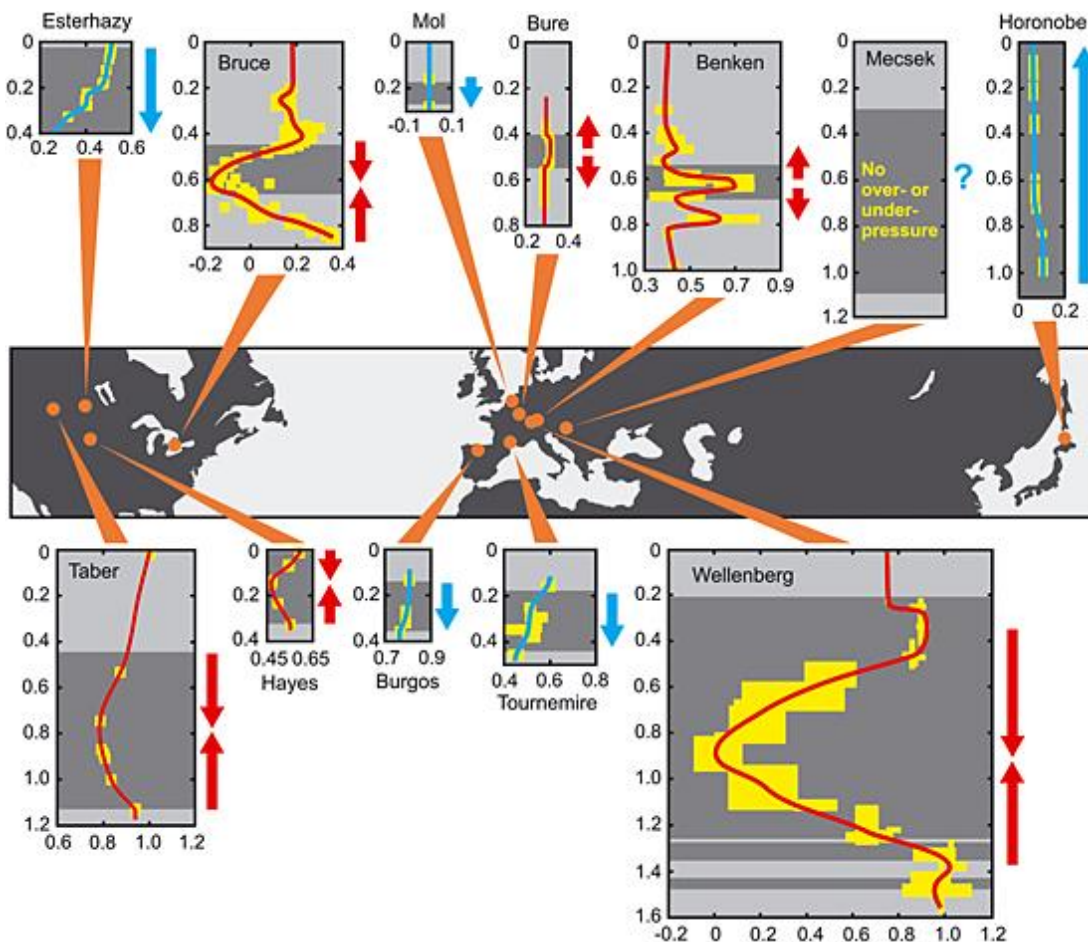
Figure 1.4: Fluid pressure regimes observed in shallow (< ~ 1 km) intraplate argillaceous formations. Pressure profiles and arrows in red denote sites with anomalous pressures, while blue denotes sites without anomalies. Arrows show inferred flow, and argillaceous strata are dark gray. Yellow regions show estimated uncertainty in pressure or range in measured values (Neuzil, 2015).
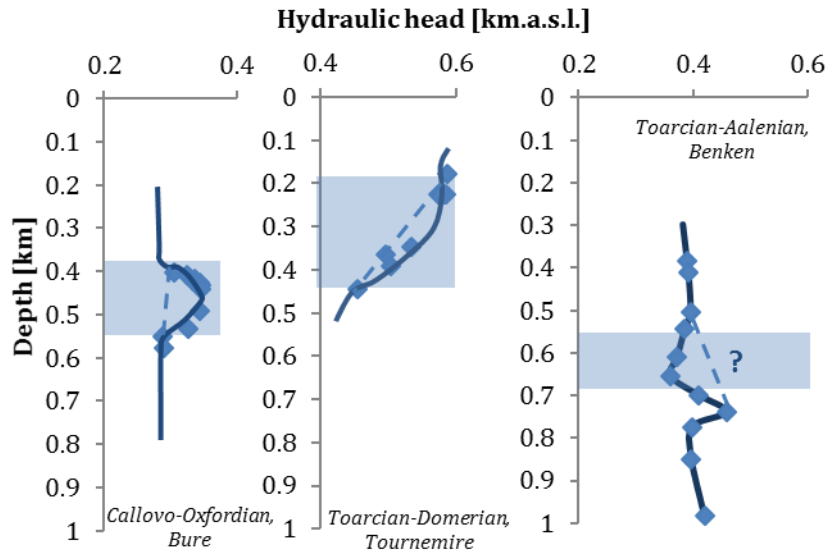
Figure 1.5: Hydraulic head profiles of clay formations studied by IRSN. Argillaceous strata are blue, Blue diamonds denote pressure data. Dashed lines represent inferred steady-state pure hydraulic regimes (Andra, 2005; Trémosa, 2012b; Jäggi and Frieg, 2014).

Anomalous pressures can be explained by three mechanisms: (i) changes in rock porosity volume, (ii) thermomechanical response of the fluid and matrix, (iii) fluid pressure and movements. The main processes mentioned to induce these mechanisms are (Deming, 2001; Trémosa, 2010):

- **Compaction disequilibrium**, linked to high sedimentation or erosion rates associated with a predominance of low-permeability sediments. In these conditions, the porosity reduction is inhibited due to the matrix low permeability, which causes the generation of an abnormal pressure borne by the pore water.

- **Uplift and topographic recharge**, meaning that in the areas of high elevation and descending flow, the fluid pressures are below hydrostatic, whereas in areas of discharge, the fluid pressures ar above hydrostatic. The presence of a seal adjacent to an artesian aquifer can be the cause of underpressures or overpressures.

- **Tectonic constraint**, linked to a lateral compression and frequently found in orogenic belts. In addition to porosity reduction, this process can also lead to the development of overpressure in the core of anticlinal folds by pore fluid squeezing.

- **Clay viscous behaviour**, consisting in a time-dependant deformation at constant load and potentially leading to a porosity reduction.

- **Diagenetic processes**, including mineralogical changesn, dissolution and precipitation, changes in bound water volume and orientation of the load-bearing grains. These processes are commonly envisaged as a secondary cause of overpressures acting during burial.

- **Aquathermal pressuring**, caused in low permeability environments by the coupled increase in pore fluid volume and temperature during sediment burial.

- **Hydrocarbon generation**, caused by the maturation of organic matter. The chemical reaction leading to oil and gas production from kerogen induces a coupled increase of porosity and fluids volume.
- **Osmosis**, related to anion exclusion in clay rocks, defined by a fluid flow driven by a potential gradient other than hydraulic (temperature, chemical or electrical).

1.2.2. NATURAL TRACER PROFILES

The growing interest for argillaceous rocks in the framework of radioactive waste disposal has motivated numerous studies on natural tracer profiles across these formations. The CLAYTRAC project, which results are reported by Mazurek et al (2009), was launched by the Nuclear Energy Agency at the beginning of 2005 and aimed at assessing the potential impacts of geological disposal from the data of nine argillaceous sites.

Natural tracer data are highly relevant because the observed profiles can be considered as large-scale and long-term natural experiments. The interpretation of these profiles by simulating transport scenarios are an interesting complement to laboratory and field experiments for the performance assessment of nuclear disposal facilities.

Figure 1.6 shows the chloride profiles measured in clay formations studied by IRSN: the Callovo-Oxfordian formation at Bure (France), the Toarcian-Domerian clayrock at Tournemire (France) and the Toarcian-Aalenian Formation, also named Opalinus Clay, studied at Benken and at the Mont Terri (Switzerland). These bell-shaped profiles are assumed to be the results of a long-term diffusive exchange between pore water from the aquitard and groundwater of the surrounding aquifers (Andra, 2005; Mazurek et al., 2009; Bensenouci, 2010).
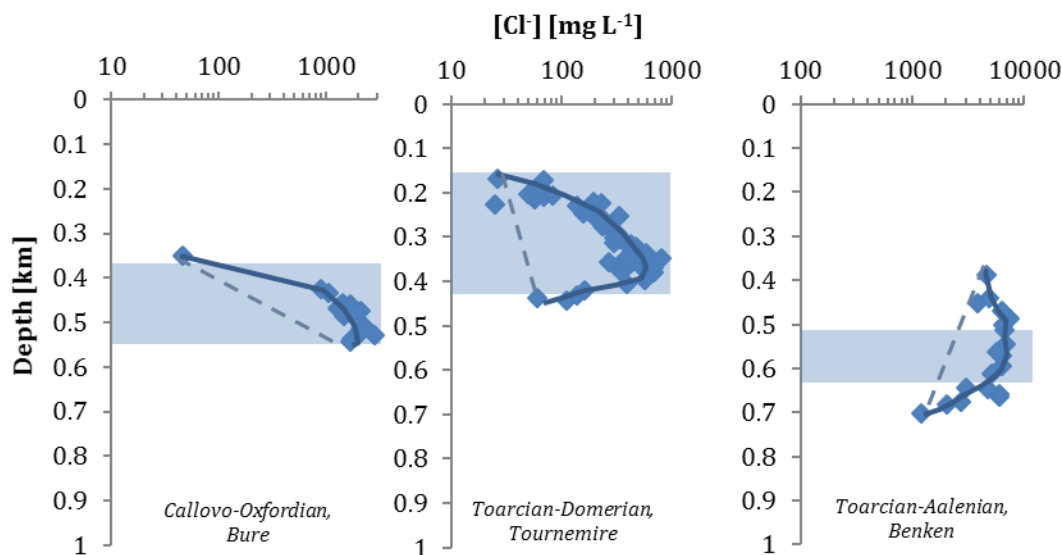
Figure 1.6: Chloride profiles of clay formations studied by IRSN. Argillaceous strata are blue, Blue diamonds denote chloride concentration data. Dashed lines represent steady-state regimes (Andra, 2005; Mazurek et al., 2009; Bensenouci, 2010).

Geochemical and pressure patterns in argillaceous rocks are indicators of formation permeability and flow history. They represent useful tools for understanding transport processes at time and space scales relevant for radionuclide confinement (Neuzil, 2013).

1.3. PRESENTATION OF THE STUDY SITE

1.3.1. THE MONT TERRI UNDERGROUND ROCK LABORATORY

The Opalinus Clay has been identified as a potential host rock formation for the disposal of radioactive waste (Nagra, 2002). This overconsolidated clay shale is studied in an underground rock laboratory (URL) developed in the side gallery of the A16 Transjurane motorway, constructed in the Jura Mountains and located in north-western Switzerland (Figure 1.7). Since 1996, the Mont Terri facility is devoted to the study of the Opalinus Clay geological, geochemical, geomechanical and hydrogeological properties. Operated by the Swiss federal geo-information centre swisstopo as a generic URL, it is one of the most important European underground laboratories in claystones along with the site-specific Meuse/Haute Marne URL (France) operated by ANDRA, the Tournemire URL (France) operated by IRSN, and the site-specific Hades URL (Belgium) operated by SCK·CEN.
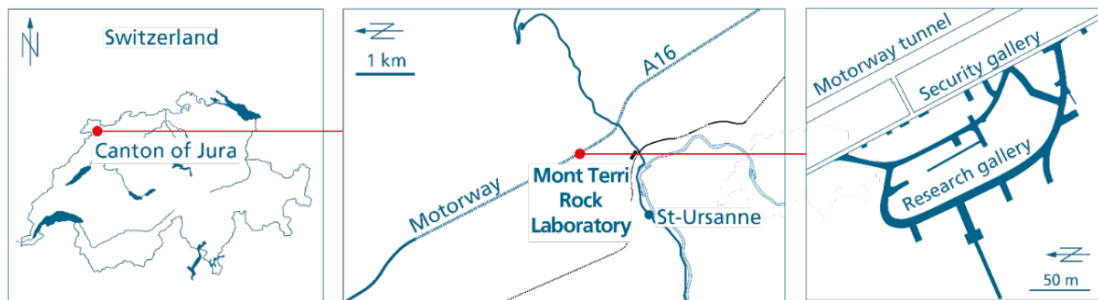
Figure 1.7: Location of the Mont Terri Rock Laboratory in the Folded Jura of north-western Switzerland near the village of St-Ursanne (source: https://www.mont-terri.ch/)

The overburden of the laboratory is 280 m and the tunnel cross-cuts a ca. 240 m section of Opalinus Clay, which dips with an average of 40 degrees towards the south east. Thrusting and faulting in the area caused an increase in formation thickness from true lithological thickness of 90 m to apparent thickness of 160 m. The research galleries in the Opalinus Clay formation extends on about 700 m (Bossart and Thury, 2008; Bossart et al. 2017).

The Mont Terri Consortium consists of 16 partners from Europe, United States, Canada and Japan, who are financing the experiment programs. An average annual budget of about CHF 3 million is allocated for research and operation. Between 1996 and 2016, 138 individual experiments were carried out, including 93 experiments successfully completed by mid-2016. Experiments are in majority focusing in the field of deep geological disposal with 3 major research axes: i) understanding the characteristics, processes and mechanisms in undisturbed claystones, ii) understanding the repository-induced perturbations, and iii) performing experiments related to the demonstration of repository implementation technology. However, an extension to the fields of chemical waste disposal, CO_2 storage and deep geothermal energy has also been developed recently.

1.3.2.   THE OPALINUS CLAY

1.3.2.1.   Geological setting and key characteristics
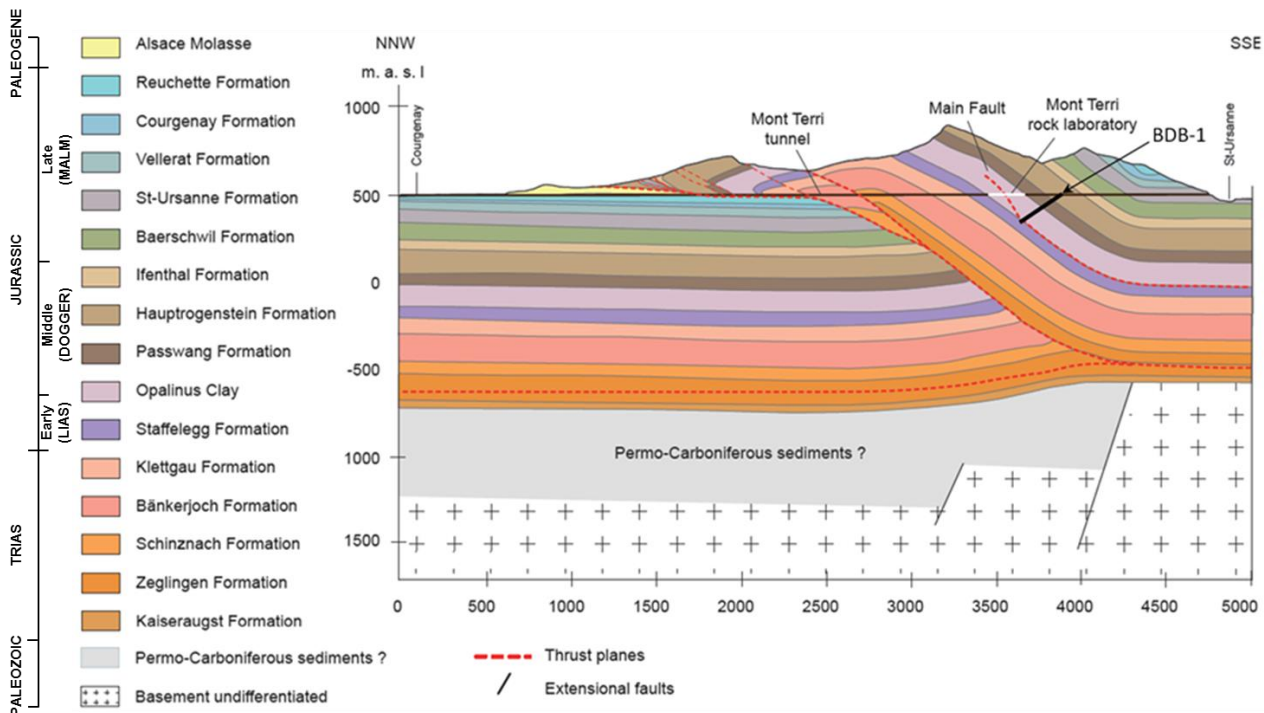
Figure 1.8: Geological cross section of the Mont Terri anticline
(adapted from Nussbaum et al. 2017)

The Opalinus Clay is part of a thick Mesozoic-Cenozoic sedimentary sequence in the Molasse basin, which was deposited in a shallow marine environment (Figure 1.8). Its name comes from the frequent occurrence of the fossil ammonite *Leioceras opalinum*, which aragonite shell presents opalescent effects.

This formation is an indurated clay Aalenian-Toarcian aged (180-170 Ma), overlain by Middle Jurassic karstic aquifers (e.g. Hauptrogenstein) and underlain 800 m of Middle to Late Jurassic limestones (e.g. Gryphaea Limestones), marls and shales, which are only weakly karstified with local water inflows (Pearson et al., 2003). Between the Muschelkalk aquifer below and the Late Jurassic aquifer above, the shale succession from Triassic to Late Jurassic forms a 300 to 450-meter-thick sequence of low to very low permeable rocks (Heitzmann, 2004).

A period of marine regression occurred between 100 and 40 Ma, leading to a subaerial exposure of the top of the Late Jurassic limestone. Starting about 40 Ma, the rifting of the Rhine Graben affected Northern Switzerland, resulting in considerable subsidence of the area in the mid-Tertiary, which brought the Opalinus Clay sequence back to about 500 m depth. According to Clauer et al. (2017), two sea invasions into the Mont Terri area took place during Priabonian (37 to 34 Ma) and during the Rupelian (34 to 28 Ma). Mazurek et al. (2017) proposed that the Malm limestones, represented by the Baerschwil Formation, acted as a fresh-water boundary that

induced a decrease of the Opalinus Clay porewater salinity to half the original value at the end of the Paleogene (23 Ma). Partial evaporation potentially occurred in the Chattian/Aquitanian and afterwards, brines would have diffused in the underlying formation, resulting in a salinity increase in the Opalinus Clay before Late Alpine folding during the late Miocene to Pliocene (about 12 to 3 Ma) that formed the Folded Jura. Erosion exposed the core of the Mont Terri anticline between 6 and 2.5 Ma, and activated the Middle Jurassic limestones aquifer (overlying the Opalinus Clay), causing a porewater flushing. Similarly, infiltration to the Early Jurassic limestones would have started in the Quaternary, between 0.5 and 0.2 Ma ago (Pearson et al., 2003, Mazurek et al., 2011).

Key parameters of the Opalinus clay were summarised by Bossart and Thury (2008), Bossart (2011), and Bossart et al. (2017). The Opalinus Clay presents three major facies (Blaesi et al., 1991; Hosttetler et al., 2017): a shaly facies in the lower half of the sequence, a sandy carbonate-rich facies in the middle, and a sandy facies interstratified with shaly facies in the upper sequence. The shaly facies of the Opalinus Clay mineral composition includes 27-78 % clay minerals (illite, chlorite, kaolinite and illite-smectite mixed layers), 4-29 % carbonates and 10-32 % of quartz and accessory feldspars, pyrite and organic matter. Porosity ranges from 5 to 20 % with the majority of pores in the range of 1 to 25 nm. Several minor tectonic faults and a larger fault zone, called "Main Fault", can be observed in the Opalinus Clay (Nagra, 2002; Nussbaum et al., 2011, Jaeggi et al., 2017). Hydraulic tests indicate that the tectonically disturbed zones are hydraulically similar to the undeformed matrix (Johns et al., 1994; Heitzmann, 2004; Gautschi, 2001, 2017). Hydraulic conductivity values are in the range of $2 \cdot 10^{-14}$ m s^{-1} to $2 \cdot 10^{-12}$ m s^{-1} (Marschall et al., 2005) and diffusion coefficients are estimated from 10^{-12} m s^{-1} to 10^{-11} m s^{-1} for chloride, deuterium and tritium (Van Loon et al., 2004).

1.3.2.2. Previous studies on transport phenomena in the Opalinus Clay

The Swiss National Co-operative for the Disposal of Radioactive Waste (Nagra) has been extensively studying the Opalinus Clay for more than 20 years. Prior to the development of the Mont Terri rock laboratory, investigations were carried out on the Zürcher Weinland in Northern Switzerland, with deep investigation boreholes at Schafisheim, Riniken, Weiach and Benken (Figure 1.9).
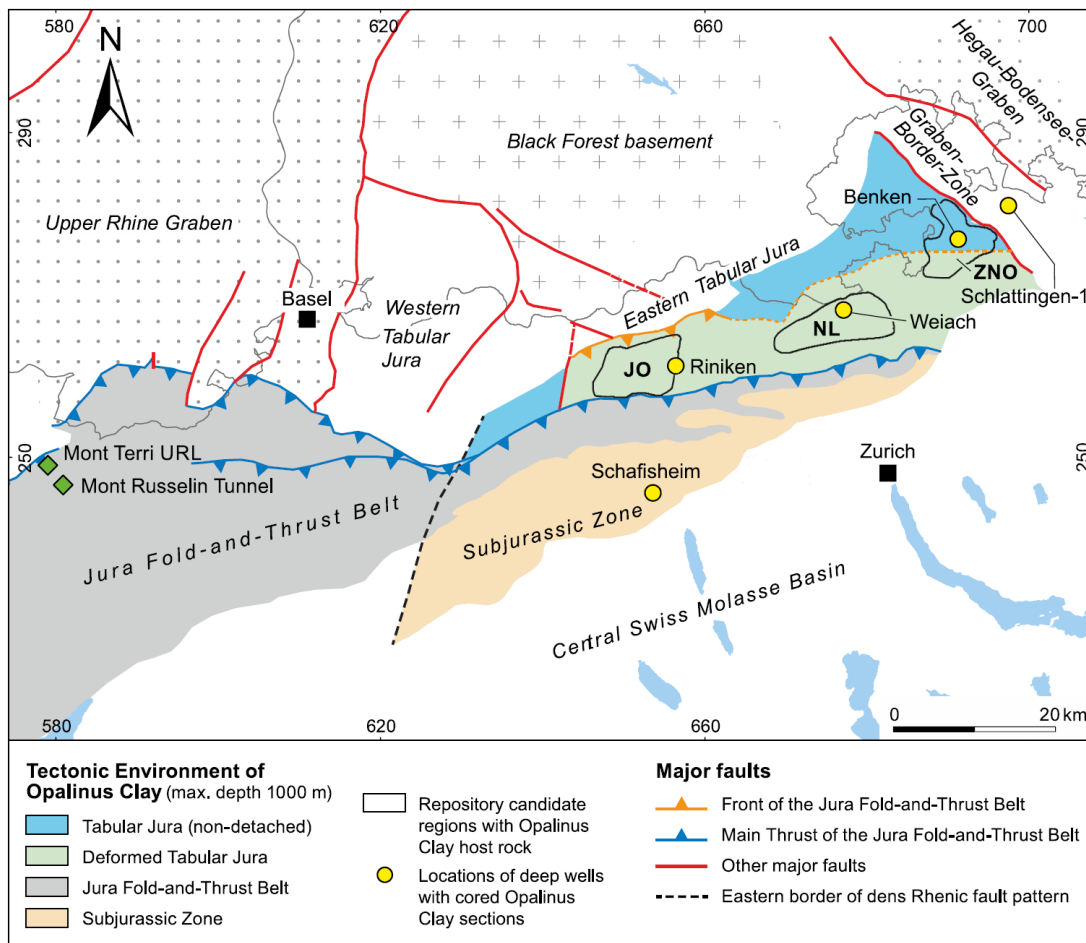
Figure 1.9: Tectonic environment of the Opalinus Clay in Northern Switzerland and location of deep boreholes and tunnel with investigations of the Opalinus Clay (modified after Nagra, 2014b and Gautschi, 2017). Candidate siting regions: Zürich Nordost (ZNO) Nördlinch Lägern (NL), Jura Ost (JO)

Two main reasons are mentioned to justify that diffusion is the main transport process occurring in consolidated argillaceous formations. The first one relies on their very low hydraulic conductivity (in the range of 10^{-14} m s^{-1} to 10^{-12} m s^{-1}) that hinders significant fluid movements. However, long term geological processes can locally enhance fluid flow. Kosakowski (2004) modelled simplified scenarios of enhanced advective transport in the Opalinus Clay induced by tunnel convergence and glaciation. He showed that glaciation-induced flow due to an additional overburden may promote the transport of radionuclides in the geosphere, whereas tunnel convergence has little impact on radionuclide transport.

The second argument for a diffusion-dominated system is based on the analysis of large-scale profiles of natural tracers (chloride, bromide and stable isotopes). At Mont Terri, the halide profile has been specified through several studies, notably the porewater chemistry (PC) experiment (Pearson et al., 2003). It shows the preservation of pore water with a marine origin component, presenting two thirds of the original marine chlorinity (Figure 1.10), which was attributed to a recent dilution by meteoric waters dated in between 5 and 6 Ma by using natural tracers (^{4}He and ^{2}H).
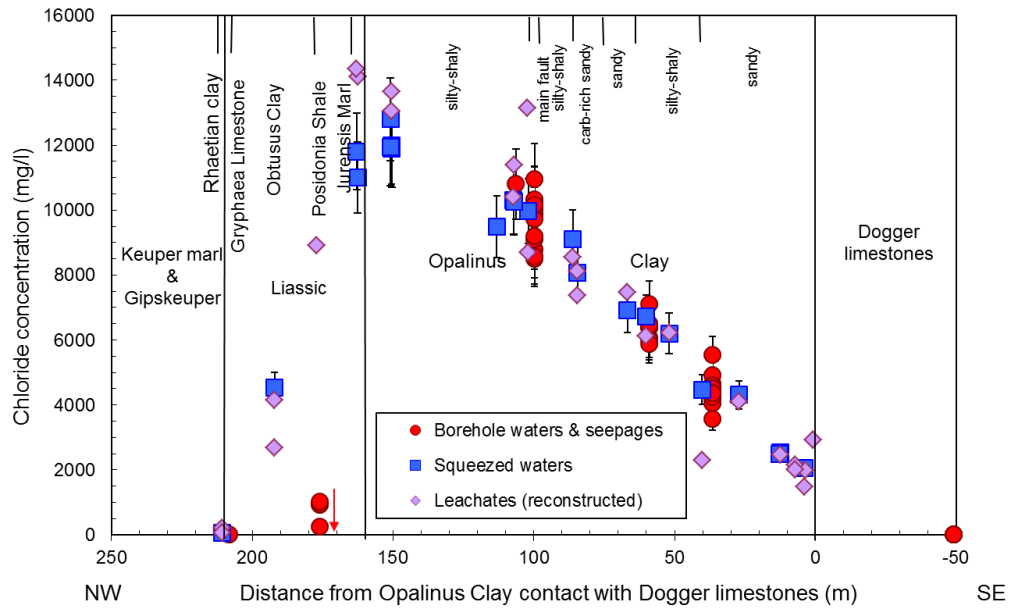
*Figure 1.10: Chloride concentration profile along the Mont Terri rock laboratory
(Pearson et al., 2003)*

The observed chloride profile was modelled by Mazurek et al. (2011), with the following assumptions:

i) an initially Cl⁻ concentration of 18400 mg L⁻¹; ii) a first phase of salinity out diffusion to the overlying limestone aquifer starting 6.5 Ma; iii) and a more recent out-diffusion phase to the underlying aquifer since 0.5 Ma. Erosive activation of the upper aquifer at 6.5 Ma is credible, since the age of thrusting and folding of the Jura Mountains in which the Mont Terri anticline is located is inferior to 10 Ma.

Diffusion properties of Opalinus Clay have been extensively studied in surface laboratories and in the field laboratory at Mont Terri (Van Loon et al., 2012). The panel of studied element includes HTO, D_2O, $H_2^{18}O$, $^{36}Cl^-$, $^{125}I^-$, $^{125}IO_3^-$, $^{35}SO_4^{2-}$, Br^-, $^{22}Na^+$, $^{85}Sr^{2+}$, $^{134}Cs^+$, $^{60}Co^{2+}$, $^{152}Eu^{3+}$, $^{237}Np(V)$ and $^{235}U(VI)$.

Soler (1999) gave a review on coupled transport processes in the Opalinus Clay. The effects of phenomena such as thermal and chemical osmosis, hyperfiltration and thermal diffusion, on water, solute and heat transport were studied. Thermo-osmosis was reported as the only coupled transport mechanism that could significantly affect solute and fluid fluxes. The main conclusion was that coupled processes would have only minor impact on radionuclide transport on a time scale of 1000 years, what is the Swiss Federal Nuclear Safety Inspectorate's (ENSI) requirement for canister failure, although both target and expected lifetimes are 10 000 years in Nagra's current concept. However, the effect of coupled phenomena during the transient phase occurring shortly after the placement of waste canisters still has to be clarified.

Noy et al (2004) reported the results of in situ osmosis experiments performed at the Mont Terri rock laboratory. These experiments consisted in applying a sudden water exchange within

a sealed borehole, using fresh water or hypersaline brine (total dissolved solid of 87.5 g L^{-1}). The chemical gradient induced a significant pressure increase. Pressure transients were modelled using mathematical inversion and revealed low values of osmotic efficiencies (8% with fresh water and 3.6% with brine).

At first, long-term monitoring at the Benken site revealed overpressures overpressures of 0.5 to 1.5 MPa. These anomalies were modelled considering sediment compaction after deposition and ongoing tectonic compression assumed to have begun in the last 5-23 Ma (Bruel and Küpfer, 2002 ; Nagra, 2002, Mazurek et al., 2002, 2006). Calculations indicated that large-scale hydraulic conductivity between 10-16 m s-1 and 10-15 m s-1, lower than the measured ones, are required to explain the preservation of the overpressures over long time scales. However, further measurements obtained after replacing the hydraulic multipacker system in 2009 do not support these interpretations. Indeed, the latest measurements tend to show instead that the Opalinus Clay is underpressured at the Benken site. Compaction disequilibrium (e.g., rebound in response to glacial unloading) and the impact of tectonic strain were suggested as possible causes of the anomalous pressures (Beauheim, 2013).

A complex spatial distribution of porewater pressures within the Opalinus Clay of Mont Terri was given by Croisé et al. (2004), based on a series of boreholes used for long-term pressure monitoring at the Mont Terri tunnel level (Figure 1.11). A cone of depression of hydraulic head towards the laboratory galleries was identified. The highest pressures (> 2 MPa in 2000) were found in the northwestern part of the Opalinus Clay corresponding to the Early Jurassic Limestone, while lower pressures (up to 0.8 MPa in 2000) were measured in the Middle Jurassic Limestone, located in the southwestern part of the tunnel. No abnormal pressure, superior to the one corresponding to the groundwater level above the laboratory was measured.

Pressures in formations adjacent to the Opalinus Clay:
Lias Gryphaea Limestones to the NNW: 2000-2300 kPa
Lower Dogger Blaukalke Limestones to the SSE: 800-1000 kPa

Borehole orientation:
S: slanted / V: vertical / H:horizontal

Simulation parameters:
Hydraulic Conductivity K = 1E-13 m/s
Specific Storage Ss = 1E-6 1/m

Structural elements:
RG: Reconnaissance Gallery
NG: New GalleryEDZ: Excavation Disturbed Zone

Figure 1.11: Pressure observations at the Mont Terri laboratory (mostly on 30.06.2000) and results of numerical simulation according to transient simulation of the flow towards the excavated galleries, along an axis projected perpendicularly through the reconnaissance gallery and the new gallery (Heitzmann, 2004)

CHAPTER 2. EVALUATING THE CONTAINMENT PROPERTIES OF A THICK ARGILLACEOUS LAYER AND ITS SURROUNDING AQUIFERS: MATERIAL AND METHODS

2.1. THE DEEP BOREHOLE EXPERIMENT

Up to the Deep Borehole (DB) experiment, no deep borehole has ever been drilled at the Mont Terri laboratory. The wide variety of experiments has been carried out so far at the tunnel level, which is a hydraulically disturbed zone due to excavation with a radial extension estimated at 2 m (Nussbaum et al., 2011). The DB experiment gave the opportunity to evaluate the properties and processes that define the Opalinus Clay as a confining unit in a hydraulically undisturbed zone.

The goal of the experiment was to develop and validate a methodology for assessing the containment properties of a thick argillaceous unit using the Opalinus Clay as an example. Therefore, the thesis focuses on the determination of the flux of water and solutes between an aquitard and its bounding aquifers. The methodology provides an approach that may be used elsewhere as sites for waste disposal or experimental activities.

In a first step, data collection involved the acquisition of pressure, temperature and chemical gradients through the argillaceous formation and its direct borders, including the Middle Jurassic carbonates and the Early Jurassic marls. The second step consisted in the determination profiles of phenomenological parameters for advective, diffusive and thermo-chemo-osmotic transport processes. The final objective of this research work was to model the flows of water and solutes by coupling all processes possibly affecting the semipermeable formation. The convective contribution to the mass transport in comparison to the diffusion contribution helped estimating the actual containment property of the Opalinus Clay.

Drilling of the BDB-1 deep-inclined borehole was initiated on the 5th December 2013 and was completed at a final depth of 247.5 m on the 30th January 2014 (Fierz and Rösli, 2014). The borehole was cased and drilled with water to a depth of 97.3 m. The uncased borehole section (Opalinus Clay and Staffelegg Formation) was drilled with air. A multi-packer system was successfully installed in BDB-1 just after drilling completion. This system consists of six double packer measuring intervals, an additional interval between the lowest packer and the bottom of the borehole and one interval-port between two double packers. Geology and borehole layout are shown in Figure 2.1.
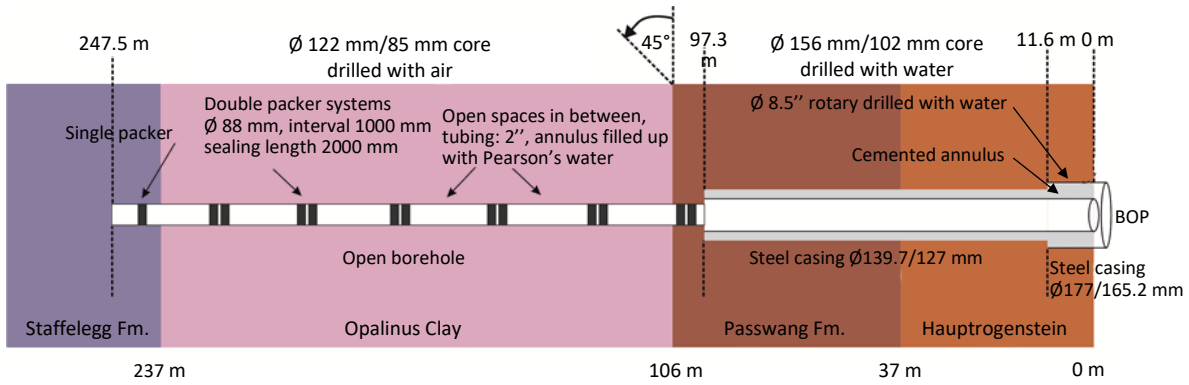
Figure 2.1: Specifications of the BDB-1 borehole (D. Jaeggi, swisstopo)

Intervals were equipped with sensors that enable long term monitoring of pressure and temperature (Table 2.1). Pressure sensors are located at the surface and connected by stainless steel lines to the interval fluids, whereas temperature sensors are located downhole inside the intervals.

Table 2.1: Specifications of the pressure and temperature sensors installed in BDB-1 borehole

Sensor type	Temperature	Pore pressure
Model	IST AG PT1000	Keller AG PAA-33X
Validity	-50 - 650 °C	0 - 50 bars (absolute)
Accuracy	$\pm (0.15 + 0.002 \lvert T \rvert)$ °C	0.05% FS

The whole borehole was cored and drillcores were collected as quickly as possible after their extraction from the rock. To avoid further evaporation and contact with the atmosphere, cores sent for analysis were preserved after nitrogen flushing and sealed with plastic foil in aluminum coated plastic bags after vacuum (Figure 2.2b).
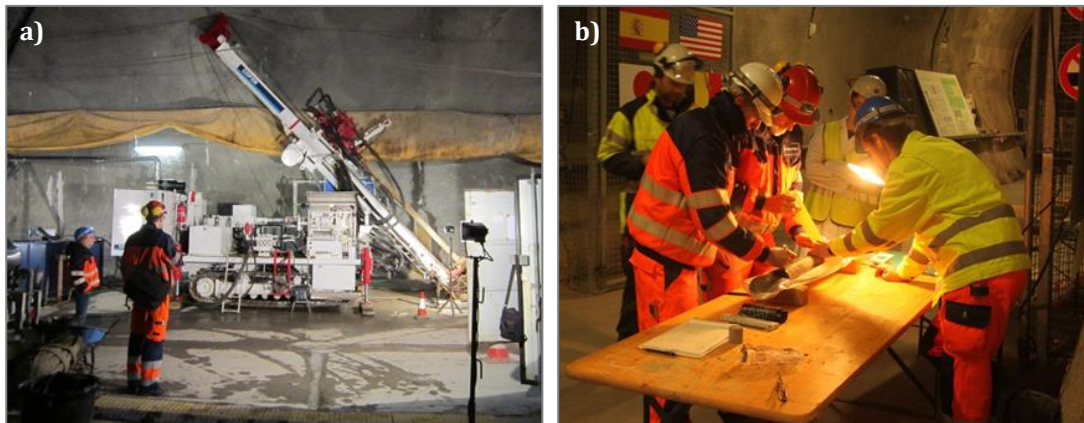
Figure 2.2: a) Drilling of BDB-1 borehole and b) core sampling (D. Jaeggi, swisstopo)

A first set of samples was sent to IRSN, consisting of 2 x 24 core samples, taken every 10 meters along the borehole and each measuring about 25 cm long (Figure 2.3).

Samples were prepared at the LT2S laboratory, located at the IRSN facility in Fontenay-aux-Roses (France), for acquiring petrophysical, mineralogical, geochemical and transport parameters.

Samples 28 and 29, close to the Main Fault, and 25 to 27, from the lower aquifer (Staffelegg Formation), were sent later and remained 10 months unprotected in core boxes, leading to an accentuation of desaturation and oxidation effects for these core samples.

Figure 2.3: Lithostratigraphy of the formations crossed by BDB-1 borehole (adapted from Hostettler et al., 2017), location of the studied samples (represented by red crosses) and measurement chambers

2.2.   METHODOLOGICAL APPROACH

The first part of this research program consisted in acquiring the individual transport parameters along the sedimentary column. Among these phenomena, diffusion is chosen for the solute flows and pure advection, chemical osmosis and thermal osmosis are selected to describe the solutes transport associated with fluid flows. The methodological approach is summarised in Figure 2.4.

Material	**Phenomenological coefficients**
▪ BDB-1 drillcores ▪ In situ multi packer system	Permeability 　　　　　　　　　　Petrophysical model 　　　　　Pressure series spectral analysis 　　　　　　　　　In situ hydraulic tests 　　　　　　　　　　Permeameter tests

Force gradients

Pressure
Temperature   } In situ sensors
Chemical concentration
　　　　　　Geochemical modelling
　　　　▪ Mineralogy
　　　　▪ Leaching
　　　　▪ Out diffusion
　　　　▪ CEC measurements

Diffusion coefficient
　　　　　　　　　　　Out diffusion
　　　　　　　　　　Radial diffusion
　　　　　　　　　Through diffusion
Chemo-osmotic efficiency
　　　　　　　　Bresler (1973) model
Thermo-osmotic permeability
　　　　　　Gonçalvès et al. (2012) model

Figure 2.4: Methodological approach for the analysis of transport processes
in the Opalinus Clay

2.2.1.   MINERALOGY AND ROCK CHEMISTRY

X-ray diffraction (XRD) measurements were performed on BDB-1 samples with a PANalytical X'Pert Pro with Co Kα (λ = 1.54060 Å) radiation operating at 45 kV and 40 mA. Complete mineralogy was obtained by XRD measurement of bulk-rock powder, whereas the clay fraction was determined by XRD of oriented samples of the <2 μm fraction that were air-dried, saturated with ethylene glycol, and heated at 500°C. Mineral identification was performed using HighScore v.3.0 for bulk analysis and MacDiff for fine fraction analysis.

Total carbon and inorganic carbon contents were determined using a ThermoFischer VarioTOC. X-ray fluorescence provided chemical analysis on bulk rock samples and was delivered by the French geological survey (BRGM).

2.2.2.   PETROPHYSICAL MEASUREMENTS

Determination of petrophysical parameters (water contents, porosity, apparent density, degree of saturation etc.) were performed in laboratory on representative element volume samples taken from the central part of the cores. Water contents were determined by weighing before and after oven-drying at 105°C until mass stabilization. Density and degree of saturation were calculated based on Archimede's principle after sample immersion into kerdane (de-aromatized

hydrocarbide), following the experimental protocol first proposed by Monnier et al. (1973) and adapted to Tournemire and Mont Terri claystones (Matray et al., 2007; Matray and Möri, 2012; Ould Bouya, 2014). Grain density was evaluated using a helium pycnometer (Micromeritics Accupyc II 1340) on oven-dried samples. Measurement of pore size distribution and specific surface area was performed by nitrogen adsorption and desorption methods using a Beckman Coulter SA3100 and a Micromeritics 3Flex Surface Characterization Analyzer. The whole experimental procedure and result tables are detailed in Annex I.

2.2.3.   BATCH EXPERIMENTS

2.2.4.1.Leaching experiments

Aqueous leaching was chosen as a porewater extraction technique to acquire the halide profiles along the BDB-1 borehole. The method consists in diluting pore water solutes contained in a powdered rock sample into a leaching solution. The leaching process is a simple method to carry out and is applicable to most rock materials. This technique has been applied on Opalinus Clay samples in the framework of the Water Sampling Experiment at Mont Terri (Pearson et al., 2003) and also by ANDRA on Callovo-Oxfordian claystone samples (Lavastre et al., 2005) and IRSN on Tournemire claystone (Wittebroodt et al., 2007). The main handling difficulty is to avoid contact with open air in order to preserve samples from oxidation and desaturation.

The majority of samples were sawed in the glovebox, using a hand saw. For a technical feasibility reason related to sample hardness, samples 2, 4, 5, 6, 7, 10, 27, 28 and 29 were sawed in the open air using a circular saw. Then, the center parts of the samples were coarsely crushed with a hammer and milled using a laboratory knife mill (IKA M20). For preliminary test purposes, several samples were sieved at different grain sizes (< 100 μm, [100; 200] μm and [200; 500] μm) and the whole sample series at a grain size inferior to 100 μm. Obtained rock powders were packaged in plastic bags and placed in hermetic glass jars for leaching experiments as well as cationic exchange capacity measurements.

Aqueous extractions were performed by adding into a 35 ml centrifuge tube a mass m_{rock} of rock powder and 10 g of leaching solution. Tubes were placed in a hermetic glass jar and stirred out of the glove box using an end-over-end agitator for a known duration $t_{contact}$. Then, samples were centrifuged at 10,000 rpm for 15 minutes and placed again inside the glovebox to be filtered. Filtration of leachates was made using 0.22 μm syringe filter (Figure 2.5).
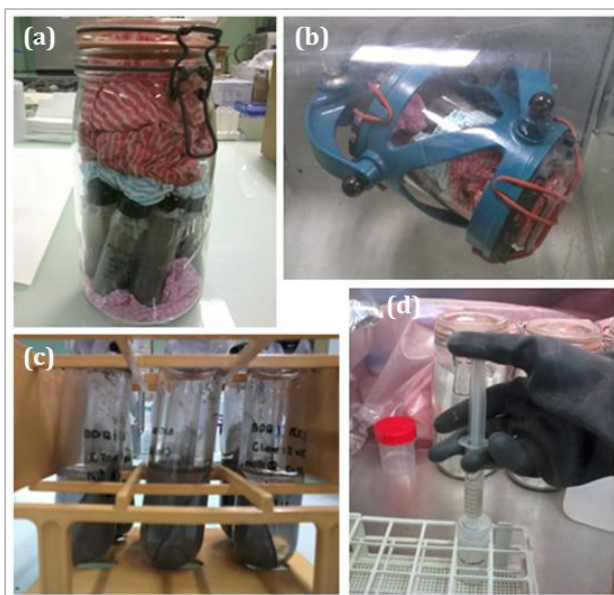
Figure 2.5: Selected leaching experiment steps
(a) centrifuge tubes in hermetic glass jar after placing in contact rock powder with leaching solution
(b) end-over-end agitation
(c) tubes after centrifugation
(d) leachate filtering

As one of the leaching process artefacts is the dissolution of mineral phases leading to biased porewater concentrations, two leaching solutions were tested: milli-Q water made anoxic by bubbling with N_2 for 1h and carbonate saturated water prepared by adding 1 g of fine-grained calcite (Merck) in 2000 ml of the same milli-Q water. The others leaching parameters that were tested are the solid to liquid ratio (0.1, 0.33, 0.5, 1) and the contact time (2h, 24h and 48h). The leaching experiment flowchart is presented in Figure 2.6.
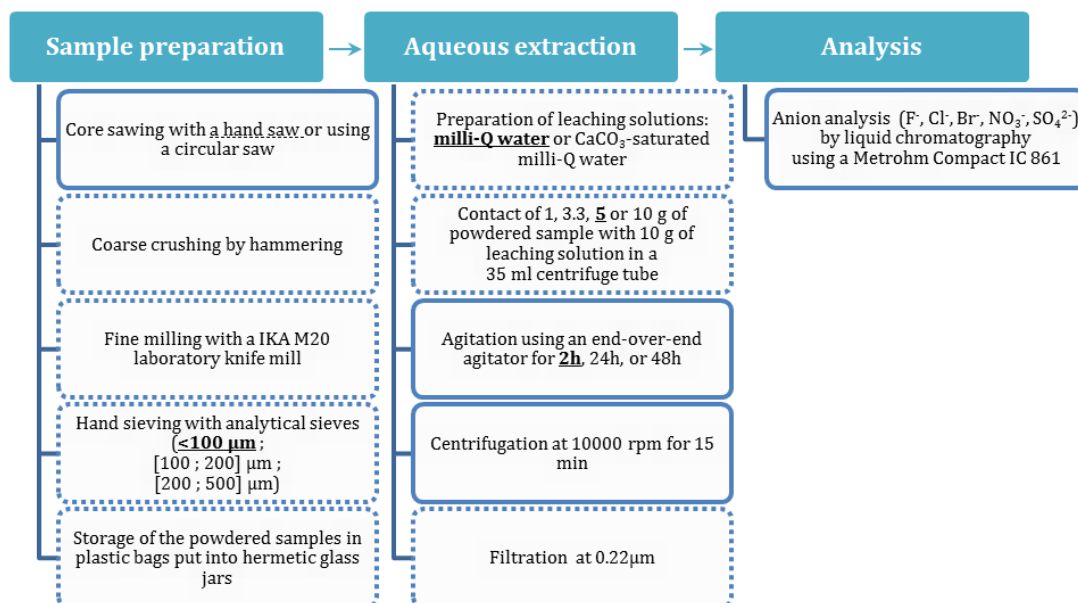
Figure 2.6: Aqueous extraction flowchart used on BDB-1 samples. Dotted steps were done in glovebox (N_2 atmosphere). Underlined options were selected for testing the entire sample series.

A grain size of 100μm, milli-Q water, solid to liquid ratio of 0.5 (m_{rock} = 5 g), and a contact time of 2 hours were eventually chosen for testing the entire sample series. Anions concentrations (F$^-$, Cl$^-$, Br$^-$, NO$_3^-$, SO$_4^{2-}$) were determined by high performance liquid chromatography using a Metrohm Advanced Compact IC 861.

The following formula was used to calculate solute concentrations in porewater:

$$[X]_{PW} = \frac{[X]_l}{\frac{m_r}{m_l} WC_{bulk,wet} P_a} \tag{2.1}$$

where *[X]$_{PW}$* [ppm] and *[X]$_l$* [ppm] are respectively the concentrations of element X in porewater and in leachate, m_l [g] is the mass of liquid (sum of porewater and added leaching solution), m_r [g] is the mass of powdered rock sample, $WC_{bulk,wet}$ [-] is the gravimetric bulk water content and P_a [-] is the ratio between accessible porosity to anions and total porosity.

Water contents were recalculated from laboratory measurements (weighing, drying, density measurements etc.), considering a full saturation state for all samples. This correction was made due to the fact that desaturation of samples during core drilling and sample handling can lead to a strong overestimation of the pore water concentrations.

P_a was assumed to equal 1 in the upper carbonated aquifer (Hauptrogenstein Formation) and 0.55 elsewhere, considering the anion exclusion in clay-bearing formations (Pearson et al., 2003).

2.2.4.2.Cation exchange capacity measurements

Cation exchange capacity and cation occupancies were determined on powdered samples (< 100 μm, refer to 2.2.4.1 for sample preparation) by displacement with two different highly selective cations: Cs$^+$ from cesium chloride (CsCl), or Co(NH$_3$)$_6^{3+}$, referred as Cohex, from cobaltihexamine chloride (Co(NH$_3$)$_6$Cl$_3$). These extractants have been used in previous studies on the Opalinus Clay (Pearson et al., 2003) and on the Toarcian-Domerian clayrock of Tournemire (Trémosa et al., 2012a).

The samples were dried in the glovebox at ambient temperature for two days prior to selective extractions. The concentrations in index cations were chosen in such way that ca. 50% of introduced highly selective cations (index cations) were adsorbed on the rock surface.

$$X_{IC^{n+}} = \frac{m_r CEC M_{IC}}{mV_l C_{IC}} = 50 \tag{2.2}$$

where *X$_{ICm+}$*[%] is the percentage of adsorbed index cation, m_r [g] is the rock sample mass, *CEC* [meq 100 g^{-1}] is the estimated cationic exchange capacity, M_{IC} [g mol^{-1}] is the molar mass of the index cation salt (267.47 g mol^{-1} for cobaltihexamine chloride and 168.36 g mol^{-1} for cesium chloride), *m* is the valence of the index cation, V_l [mL] is the volume of exchange solution and C_{IC} [g L^{-1}] is the initial solution concentration in index cation.

Cation extractions were performed by adding into a 35 ml centrifuge tube a 2 g of rock powder and 15 g of leaching solution (2.64 g L^{-1} for Cohex and 4.98 g L^{-1} for CsCl). Tubes were placed in a hermetic glass jar and stirred out of the glovebox using an end-over-end agitator for one hour. Then, samples were centrifuged at 10,000 rpm for 15 minutes and placed again inside the glovebox to be filtered using 0.2 μm syringe filter. The collected solutions were acidified to pH 1.5 using nitric acid.

Then, cations (Na$^+$, K$^+$, Ca^{2+}, Mg^{2+}, Sr^{2+}, Co(NH$_3$)$_6^{2+}$) were analysed by inductively coupled plasma atomic emission spectrometry, using a Thermo Scientific iCAP 7000 series ICP spectrometer. The technique is based on the excitation of atoms at high temperature plasma. The excited ions emit a radiation with a characteristic wavelength and the emission spectrometer measures the intensity of these radiations to quantify the concentrations contained in the sample. The analytical uncertainties are estimated ± 10 %.

The cation exchange capacity can be calculated from the consumption of a highly selective cation onto the exchangers and also from the sum of cations displaced from the exchange sites into solution. Measured cation concentrations represent the sum of cations displaced from: i) mineral surfaces; ii) dissolution of salts precipitated from porewater; iii) and dissolution of sparsely soluble minerals such as carbonates. Therefore, CEC values calculated from sum of exchanged cations need to be corrected of the contribution of cations from the pore water by substracting the concentrations measured in aqueous leachates. Therefore, the protocol was also applied using milliQ water as contact solution.

The formula used to calculate the concentration of the exchanged index cation is:

$$CEC_{IC} = \frac{[IC]_{initial\ sol} - [IC]_{exchange\ sol}}{\frac{m_r}{m_l} \cdot 10} * m \qquad (2.3)$$

where CEC_{IC} [meq 100g^{-1}] is the cationic exchange capacity calculated from the index cation adsorption, $[IC]_{initial\ sol}$ [ppm] and $[IC]_{exchange\ sol}$ [ppm] are respectively the index cation initial and final concentrations, m_l [g] is the mass of liquid, m_r [g] is the mass of powdered rock sample, and m is the valence of the index cation.

The contribution of individual cations, C_i, is given as follows:

$$C_i = \frac{[X^{n+}]_{exchange\ sol} - [X^{n+}]_{milliQ\ leachate}}{\frac{m_r}{m_l} \cdot 10} * n \qquad (2.4)$$

and
$$CEC_{sum} = \sum_i C_i \qquad (2.5)$$

where CEC_{sum} [meq 100g^{-1}] is the cationic exchange capacity calculated from the sum of exchangeable cations, $[X^{n+}]_{initial\ sol}$ and $[X^{n+}]_{exchange\ sol}$ [ppm] are respectively the concentration of cation X^{n+} in final exchange solution and in milli-Q leachate, m_l [g] is the mass of liquid, m_r [g] is the mass of powdered rock sample, and n is the valence of the exchangeable cation.

Comparison of CEC_{IC} to CEC_{sum} gives information on the system. For example, a higher value for the consumption of the highly selective cation could indicate that an additional cation was exchanged during the experiments and was not analysed for (e.g. NH_4^+). On the other hand, a lower value could suggest substantial contributions of cations from mineral dissolution reactions.

Fractional cation occupancies on the exchanger EX_i are calculated according to:

$$EX_i = \frac{C_i}{CEC} \tag{2.6}$$

where C_i [meq 100g^{-1}] is the quantity of cation (Na^+, K^+, Mg^{2+}, Ca^{2+}, Sr^{2+}) on the permanent charge sites after corrections and CEC [meq 100g^{-1}] is the cation exchange capacity.

2.2.4. PERMEABILITY MEASUREMENTS

2.2.4.1. Petrophysical model

Many permeability models based on porosity and other measurable rock parameters have been proposed during the past century. One of the most well-known relations was developed by Kozeny (1927) and modified later by Carman (1938). They considered a laminar flow ruled by Darcy's law and Poiseuille's equation through a porous media consisting of a bundle of capillary tubes separated by spaces filled of non-porous material. The porosity of such a medium can be defined as:

$$\omega = n_t \pi r^2 \sqrt{\tau} \tag{2.7}$$

where ω is the porosity, n_t is the number of tubes per unit area (A), r is the radius of the capillary tube and τ is the tortuosity.

Darcy's law defines the permeability k as a proportionality coefficient between the average fluid velocity q and a pressure gradient $\frac{dp}{dx}$:

$$q = -\frac{k}{\mu_f}\frac{dp}{dx} \tag{2.8}$$

where μ_f is the fluid dynamic viscosity.

The Poiseuille formula describes laminar flow in a straight channel with a generic cross-sectional shape:

$$q_{channel} = -\frac{A}{\alpha}\frac{1}{\mu_f}\frac{dp}{dx} \tag{2.9}$$

where A is the generic cross-sectional area of the porous channel and α is a dimensionless geometric factor. For cylindrical cross-sections $\alpha = 8\pi$ and $A = \pi r^2$.

If porosity and tortuosity are taken into account:

$$q_{channel} = -\frac{A}{\alpha}\frac{\phi}{\tau}\frac{1}{\mu_f}\frac{dp}{dx}$$ (2.10)

The combination of Poiseuille's equation and Darcy's law gives:

$$k = \frac{\omega r^2}{8\tau} = \frac{r^2}{8F}$$ (2.11)

Assuming a plane-parallel geometry, the intrinsic permeability can be computed across an argillaceous formation following (Kostek et al, 1992; Pape et al., 1999, Tremosa, 2010):

$$k = \frac{b^2}{3F}$$ (2.12)

where k [m^2] is the intrinsic permeability, b [m] is the half-pore size and F [-] is the formation factor, determined by the Archie's law $F = \omega^{-m}$, where ω [-] is the porosity and m [-] is the cementation factor.

The half-pore size can be computed from petrophysical parameters according to Equation (1.33), which is based on a mass balance equation (Neuzil, 2000; Altinier, 2006):

$$b = \frac{\omega}{(1-\omega)\rho_s A_s}$$

where b [m] is the half-pore size, ω [-] is the porosity, ρ_s [g m^{-3}] is the grain density and A_s [m^2 g^{-1}] is the specific surface area.

In a parallel plane geometry, the specific surface area includes inferior and superior platelets. The water volume contained between two platelets can be described as the porosity which equals to the product of 2b (distance between two platelets) and the quantity $(1-\omega)\rho_s A_s$, which represents the contact surface in the medium.

The hydraulic conductivity is deduced from Darcy's law presented in 0. Equation (1.10) is used to compute this parameter from the estimation of the intrinsic permeability.

Fluid dynamic viscosity is determined using the relationship proposed by Mercer et al. (1975):

$$\mu_f = (5.38 + 3.8A - 0.26A^2) \cdot 10^{-3}$$ (2.13)

and
$$A = \frac{T - 150}{100}$$ (2.14)

where μ_f [kg m^{-1} s^{-1}] is the fluid dynamic viscosity and T [°C] is the temperature, which is extrapolated from the measurements performed in the BDB-1 borehole.

The UNESCO equation of state (UNESCO, 1981), which considers the influence of salinity, temperature and pressure on the fluid density, is used to determine this latter parameter.

2.2.4.2. Spectral tidal analysis of pressure time series

The combination of rotational forces and gravitational forces exerted by the sun and the moon on the Earth induce latitudinal and longitudinal strains within the solid matrix and cause slight deformations with two dominant periods: diurnal and semi-diurnal. The pressure oscillations amplitude depends on the poroelastic response of the rock matrix. The tidal gravitational potential can be resolved into a finite set of tidal components described as harmonics, sinusoidal functions of given amplitude and frequency (Doodson and Warburg, 1941; Cutillo and Bredehoeft, 2011).

Five principal components make up about 95% of the tidal potential: the M_2 and N_2 semidiurnal lunar tides, the S_2 semidiurnal solar tide, the O_1 diurnal lunar tide, and the K_1 diurnal lunar-solar tide (Cutillo and Bredehoeft, 2011). The frequencies are known with great precision based on astronomical observations and are common to all ocean and earth tide data, but the amplitude and phase relations are characteristic of each specific data set (Merritt, 2004).

Seasonal or climatic variations, anthropomorphic activities and tidal forces induce changes in the hydraulic pressure in an aquifer. In a confined aquifer, most of the applied stress is absorbed by compression of the pore fluid with a much smaller amount absorbed by matrix or grain deformation. The amplitude of the response is a function of the poroelastic response of the aquifer matrix system. Pressure signal can therefore be used to quantify elastic properties of the rocks if the relationship between the poroelastic and hydraulic pressure responses is known (Hortle et al. 2012). Simplified hydro-mechanical models can be used to characterise quantitatively several hydrogeological properties of a porous medium, such as specific storativity, effective porosity and hydraulic conductivity. The models used in this work are based on Terzaghi's (1936) effective stress concept0 that assumes a constant total stress distributed between grains and fluid effective stress.

The Bredehoeft (1967) model relates specific storage coefficient S_s to tidal strain and relative pressure fluctuations:

$$S_s(f_{M_2}) = \frac{|\Delta\varepsilon|}{\left|\Delta h(f_{M_2})\right|} \tag{2.15}$$

where $|\Delta\varepsilon| = 2.\,10^{-8}$ m^3 m^{-3} is the amplitude of the volumetric strain related to the M_2 semi-diurnal earth tide estimated by Melchior (1978), and $\left|\Delta h(f_{M_2})\right| = 0.10197 * \left|\Delta P(f_{M_2})\right|$ [m] is the amplitude of pressure head fluctuations. $\Delta P(f_{M_2})$ [bar] corresponds to the amplitude of the M_2 tide harmonic found in the Root Mean Square (RMS) spectrum of the pore pressure signal.

The Jacob (1940) formula is used to compute the effective dynamic porosity:

$$\tilde{\phi}_{dyna} = \frac{E_W \tilde{S}_s B}{\rho g} \tag{2.16}$$

where $\tilde{\phi}_{dyna}$ [-] is the effective dynamic porosity, E_W [Pa] is the stiffness modulus of water (ca. 2.05 GPa), $\tilde{S}_s$ [m^{-1}] is the arithmetic mean of the specific storage computed for each member of the couple studied using the M$_2$ earth tide, ρ [kg m^{-3}] is the water density, g [m s^{-2}]is acceleration due to gravity and B [-] is the barometric efficiency which reflects the elastic response of the system and corresponds to the spectral gain (r_g), computed using cross-spectral analysis between two pore pressure sensors.

Two formulations of the vertical effective hydraulic conductivity are proposed by Boldt-Leppin et al. (2003) to estimate hydraulic conductivity: one using the amplitude found at M$_2$ harmonic, $\tilde{K}_v^{Ampl.}(f_{M_2})$, and the other using the phase shift, $\tilde{K}_v^{\Delta\varphi}(f_{M_2})$:

$$\tilde{K}_v^{Ampl.}(f_{M_2}) = \tilde{S}_s(f_{M_2}) \frac{\pi(z_1 - z_2)^2}{(f_{M_2})^{-1}} \left[ln\left(\frac{A_{z_1}(f_{M_2})}{A_{z_2}(f_{M_2})}\right)\right]^{-2} \tag{2.17}$$

and

$$\tilde{K}_v^{\Delta\varphi}(f_{M_2}) = \tilde{S}_s(f_{M_2}) \frac{\pi}{(f_{M_2})^{-1}} \left[\frac{(z_1 - z_2)}{\Delta\varphi(f_{M_2})}\right]^2 \tag{2.18}$$

where $\tilde{K}_v^{Ampl.}(f_{M_2})$ [m s^{-1}] is the vertical "Amplitude effective hydraulic conductivity", z_1 and z_2 [m] are respectively the depth of the sensor 1 and of the sensor 2, $A_{z_1}(f_{M_2})$ and $A_{z_2}(f_{M_2})$ [kPa], are the earth tide amplitude found at M$_2$ respectively for the sensor 1 and the sensor 2, $\tilde{S}_s(f_{M_2})$ [m^{-1}] is the arithmetic mean of the effective specific storativity coefficients obtained for the sensor 1 and the sensor 2, f_{M_2}[s^{-1}] is the frequency of the M$_2$ earth tide, $\tilde{K}_v^{\Delta\varphi}(f_{M_2})$ [m s^{-1}] is the vertical "Phase effective hydraulic conductivity", and $\Delta\varphi$ [rad] is the spectral phase shift found at M$_2$.

2.2.4.3.In situ determination by well testing

Well testing is one of the most used techniques to acquire the hydraulic parameters of a geological formation from the inversion of its response to a hydraulic disturbance. Traditional well tests include pulse tests, slug test, constant rate or constant pressure tests. A pulse test is a well-test in which a sudden change of pressure is created by injecting or pumping a volume of water during a nearly instantaneous time interval in an isolated portion of a borehole. This method is similar to the slug test, with the difference being that the latter is conducted in open-hole conditions. Hydraulic parameters can also be determined by injecting or withdrawing fluid at a constant pressure or constant flowrate and monitoring the drawdown in the well during the test and the recovery phase. Two kinds of well tests were performed in the BDB-1 deep borehole: pulse withdrawal tests and constant flow withdrawal tests (Figure 2.7). A schematic view of test equipment is presented in Figure 2.8.
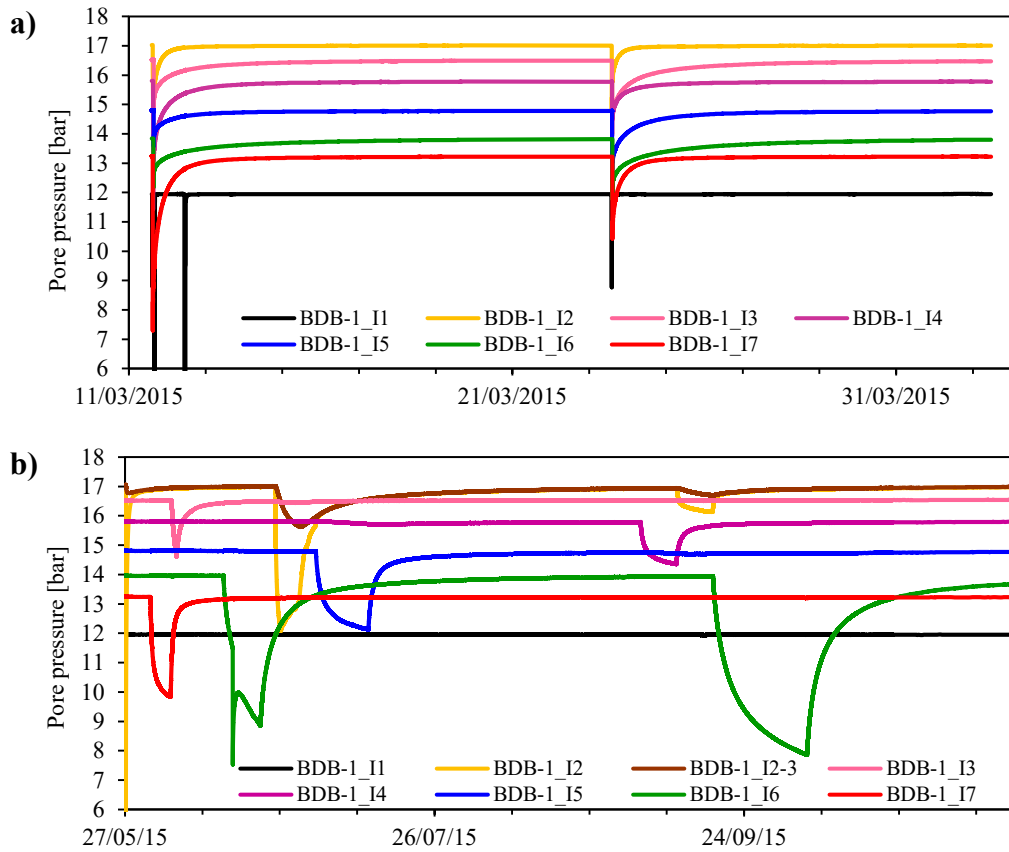
Figure 2.7: Records of pore pressure responses in the seven intervals of BDB-1 borehole to a) *pulse tests and b) constant rate withdrawal tests.*
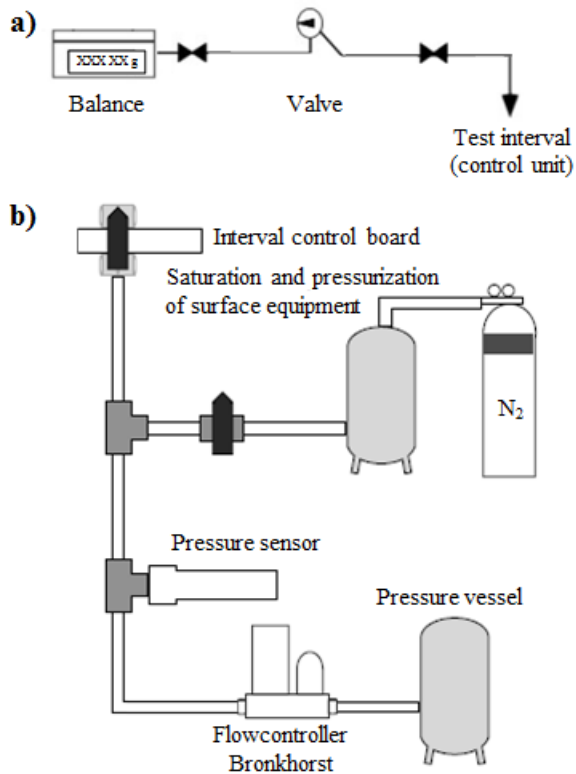
Figure 2.8: Experimental setup for a) pulse test and b) constant rate withdrawal test

Pulse withdrawal tests

Hydraulic testing in BDB-1 deep borehole was launched on March 11th 2015, with a first series of pulse-withdrawal tests. These tests are preferred as initial phase because they: i) draw water from the formation into the borehole rather than forcing particulate-bearing borehole fluid into the formation; ii) provide an immediate measurement of the system compressibility C_{tz} that is necessary for test analysis and provides evidence of the presence or absence of gas and other unusual conditions; iii) can be concluded quickly if the hydraulic conductivity K is high, providing information to define and leaving time to perform, subsequent test phases; and iv) can be continued for as long as necessary, up to the total time available to obtain a reliable analysis if K is low.

The following procedure was used for the pulse withdrawal tests:
- Connect a saturated water line to the correspondent closed valve at the control unit.
- Open valve and wait until pulse pressure is reached
  (differential pressure in the range of 1 to 6 bars).
- Close valve and measure the withdrawn water volume.

The recording rate of the data acquisition system was optimised for each test phase to obtain sufficient data for a proper test analysis. Given its quick hydraulic response, performing more pulse tests on Interval 1 (Staffelegg Formation) was possible. For each of the other intervals, two pulse tests were carried out. The tests were conducted between March 11th and April 2nd, 2015 (Figure 2.7a).

Constant flowrate withdrawal tests

Pulse tests interpretation gave a first estimation of hydraulic parameters, enabling to propose a configuration for constant flowrate withdrawal tests. The argillaceous formation permeability being inferior to 10^{-10} m s^{-1}, very low pumping flow rates have to be applied to avoid desaturation of the measuring intervals and extreme drops in pressure. Therefore, a flowmeter able to sustain a pumping rate of 5 μL min^{-1} for several days (Bronkhorst® μ-flow L01) was used to test intervals 2 to 7, for which the hydraulic responses to pulse testing were the slowest. Interval 1 was tested with a higher flow rate of 5 mL min^{-1} using a Bronkhorst® Liqui-Flow L10.

Constant rate withdrawal tests were launched on May 27th 2015 by Solexperts and it was intended to perform one test per interval. However, due to several technical failures affecting flowmeters, data acquisition system and control unit, testing had to be repeated on intervals 2 and 6. Figure 2.7b shows the evolution of pore pressures in the different measuring intervals.

2.2.4.4. Permeameter tests

Permeameter tests were carried out on Opalinus Clay samples using Hassler Cell at the French Institute of Petroleum and New Energies (IFPen). The Hassler Cell permeameter is a quick-loading core holder that applies a confining pressure to a cylindrical rock sample (40 mm or 15 mm diameter), mimicking the in situ conditions. This experimental arrangement for measuring intrinsic permeability involves measuring the water (synthetic porewater) or gas (nitrogen) flow through a specimen of uniform cross-sectional area with the surfaces parallel to the direction of flow being sealed. The Steady State method consists in maintaining several pressure gradients over a sample and measuring the resulting fluid flows (Boulin et al., 2010). Cylindrical core specimens are held within a sleeve of nitrile rubber that acts as a barrier between the fluid flowing through the core and the pressurized fluid in the outer chamber of the cell (Cerny and Rovnanikova, 2002). The experimental setup is illustrated in Figure 2.9.
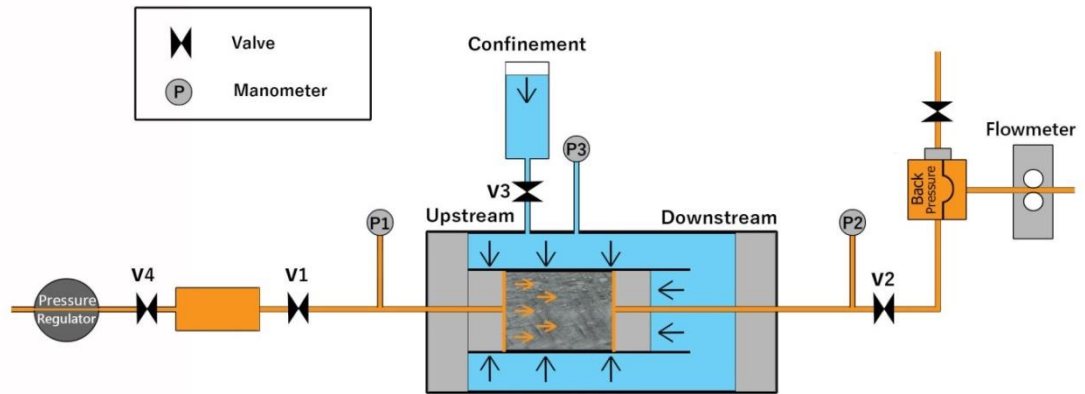
Figure 2.9: Experimental set up used for performing Steady State method in Hassler cell (Al Reda, 2016)

Based on Darcy's law, the apparent intrinsic permeability can be estimated from the relationship (Al Reda, 2016):

$$k_a = \frac{Q}{A} \frac{\mu_f LP}{\left(P_u{}^2 - P_d{}^2\right)} \tag{2.19}$$

where k_a [m^2] is the apparent intrinsic permeability, Q [m^3 s^{-1}] is the flow rate, A [m^2] is the sample surface, μ_f [Pa s] is the fluid dynamic viscosity, L [m] is the sample length, P [Pa] is the measured flow pressure fixed at $1.022 \cdot 10^5$ Pa absolute, P_u and P_d [Pa] are respectively the upstream and downstream pressures.

For measurements involving liquid flow, apparent intrinsic permeability corresponds to the sample intrinsic permeability. In the case of gas permeability measurements, a process called "Klinkenberg effect" or "gas slippage" induces for low pore pressure a non zero gas velocity in the direction of the flow and in the vicinity of pore walls, contributing to a higher quantity of gas flowing through the pores (Klinkenberg, 1941; McPhee and Arthur, 1995; Letham and Bustin, 2015).

In order to correct the apparent permeability overestimated due to slippage effect, Klinkenberg gave the following relation:

$$k_a = \beta k \frac{1}{P_m} + k \qquad (2.20)$$

where k_a [m²] and k [m²] are respectively the apparent intrinsic permeability and the real intrinsic permeability, β [-] is the Klinkenberg slippage parameter and P_m [Pa] is the arithmetic mean pressure between the upstream and downstream pressures.

Permeability measurement for plugs drilled parallel to the bedding plane could not be made due to the presence of micro-cracks. Therefore, these samples were coated with epoxy resin in order to fill the micro-cracks and enable permeability measurements.

2.2.5. DIFFUSION EXPERIMENTS

Three experimental setups were used at laboratory scale in order to acquire the diffusive parameters of the BDB-1 samples and to evaluate the diffusion anisotropy.

2.2.4.5. Out diffusion and in diffusion

In or out diffusion is referred to, depending on the solutes migration direction: in diffusion occurs when the tracer diffuses from the test solution to the sample and conversely, out diffusion is referred to when the tracer diffuses from the sample to the test solution.

Parallelepiped configuration

The experiment consists in immersing a cuboid-shaped sample (side of ca. 5 cm, cut using a diamond wire saw) into a synthetic solution and sampling the solution until reaching a concentration equilibrium state (Figure 2.10). The method has been used on claystone from Tournemire rock laboratory (France) by Patriarche (2001) and Bachir Bey (2013). It enables the estimation of halide concentrations in porewater as well as pore diffusion coefficient of the tested sample.
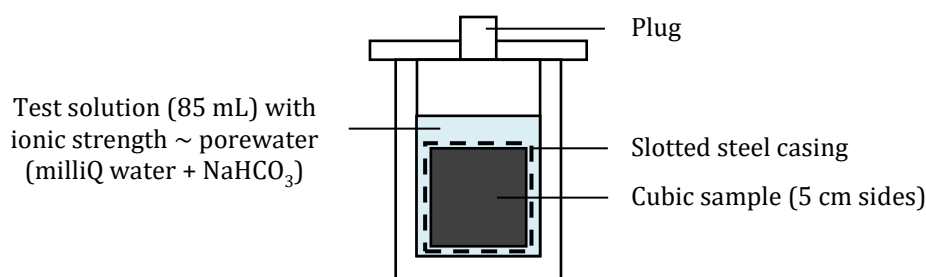
Figure 2.10: Schematic cross-section view of a cubic out diffusion cell

Results can be biased by several artefacts linked to the composition of the test solution. Pure water can be aggressive towards mineral phases and induce dissolution reactions. Moreover, osmotic effects can happen due to the chemical gradient between test solution and porewater and cause the sample to swell (Savoye, 2008).

The experiment was designed to limit these effects by: i) constraining the rock sample by placing it inside a metallic grid, after coating the sample with epoxy resin on four faces to impose a single diffusion direction (perpendicular or parallel to bedding planes); and ii) by using a test solution with a similar ionic strength to the porewater one.

Test solution was prepared by adding a known amount of NaHCO3 into milli-Q water. The salt quantities were determined according to the chloride contents estimated from leaching experiments.

The test solution volume was minimised based on the diffusion cells dimension (5.6 x 5.6 x 9.4 cm) and a planned total number of samples (20 x 2 mL), and optimised not to desaturate the sample for the whole experiment duration. Initial solid to liquid ratio were in the range of 3.32 to 4.50. Sampling was performed using 0.2 μm filter syringes.

The evolution of diffusive transfer was monitored by regular sampling of the test solution. Halides (Cl-, Br-) and sulphate concentrations were determined by ionic chromatography using a Metrohm Advanced Compact IC 861. Figure 2.11 shows pictures of the experimental protocol.
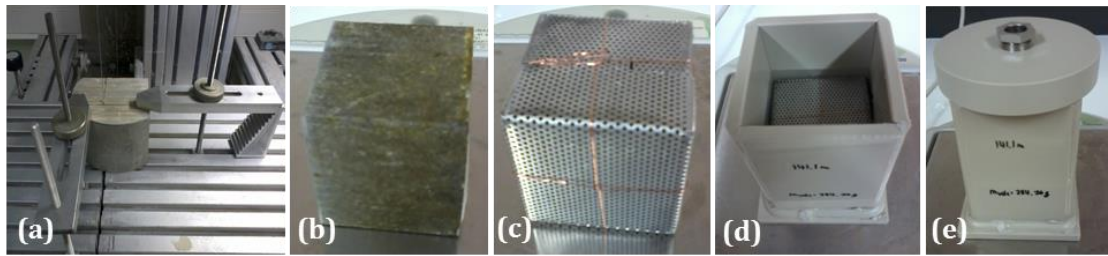
Figure 2.11: Preparation steps of out diffusion experiment
(a) Core sawing using a diamond wire saw (b) Resin-coated cuboid sample
(c) Sample placed in stainless steel grid bound with copper wire
(d) Sample in diffusion cell in contact with test solution
(e) Closed diffusion cell

The mass balance equation of the system writes:

$$C_{pw}m_{pwa} = (m_{ftw} + m_{pwa})C_{eq} + \sum_{i=1}^{n} m_i C_i \qquad (2.21)$$

where C_{pw} [ppm] is the solute concentration in pore water, m_{pwa} [mg] is the mass of pore water accessible to anions, m_{ftw} [mg] is the final mass of test solution, C_{eq} [ppm] is the equilibrium concentration, n [-] is the number of samples, m_i [mg] is the mass of sample i and C_i [ppm] is the concentration of sample i.

In the same way as for leaching experiments, the mass of accessible porewater was corrected for desaturation.

Pore diffusion coefficients were estimated by modelling the experiment with the transport code HYTEC.

Radial configuration

Radial diffusion experiment consists in diffusive equilibrium between pore water and a test solution with known composition placed in a reservoir drilled in a core sample (Van der Kamp et al., 1996a; Savoye et al., 2006a; Savoye et al., 2006b). The sample consists of a core portion with a diameter of 10.2 cm or 8.5 cm and a length between 6.7 and 10 cm, cut with a circular saw. A 24 mm diameter reservoir was drilled in each sample, in which was inserted a 22 mm outer diameter copper tube with horizontal slots in order to limit sample swelling. A 18 mm diameter polytetrafluoroethylene (PTFE) rod was also placed in the reservoir to minimise the solution volume used for the experiment and the time required to reach diffusive equilibrium.

After drilling, reservoirs were filled with solutions of compositions as close as possible to porewater, for a resaturation phase of seven weeks. Theoretical chemical concentrations were obtained by coupling: chloride determination using leaching and out diffusion, cationic exchange capacity measurements and geochemical modelling. Isotopic compositions were extrapolated from measurements on BDB-1 samples by vacuum distillation, squeezing and diffusive exchange (Mazurek et al., 2016). For the diffusion phase, reservoirs were drained and filled with a solution depleted in heavy isotopes (-205‰ SMOW in ^{2}H and -26‰ SMOW in ^{18}O) and enriched in bromide (approximatively 100 mg L^{-1}). A volume of 500 µL was regularly sampled and filtered using 0.2 µm filter syringe in each diffusion cells. Solutions were analysed for anions (Cl$^-$, SO$_4^{2-}$ and Br$^-$) by ionic chromatography using a DIONEX ICS-1000, and for isotopes (^{18}O and ^{2}H) using a laser water isotope analyser Las Gatos Research LWIA-24IEP.

A schematic representation and pictures of the experimental setup are respectively given in Figure 2.12 and Figure 2.13.
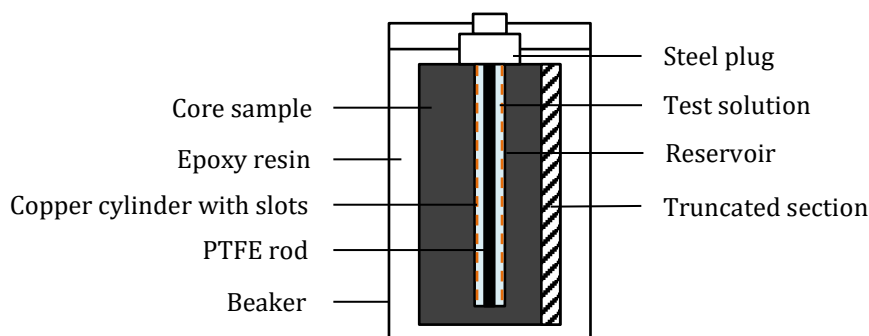
Figure 2.12: Schematic ross-section view of a radial diffusion cell

Figure 2.13: Preparation steps of radial diffusion experiments
(a) Core sawing using a circular saw (b) Plug fixation on the core
(c) Resin-coated core sample in a beaker
(d) Reservoir drilling (e) Empty reservoir (f) Insertion of the copper tube
(g) Insertion of the PTFE rod
(h) Pouring of the resaturating solution

The diffusion equation describing the solute transport in the core sample in radial coordinates writes:

$$\omega_e \frac{\partial C}{\partial t} = \frac{1}{r}\frac{\partial C}{\partial r}\left(r D_e \frac{\partial C}{\partial r}\right) \qquad r_R < r < r_c \tag{2.22}$$

where C [mol L^{-1}] is the solute concentration in pore-water that is accessible for tracer E, r [m] is the radial distance from the centre of the reservoir (with r_R [m] radius of the reservoir and r_c [m] radius of the core sample), ω_e [-] is the porosity accessible to the tracer E, D_p [m] is the effective diffusion coefficient.

Initial conditions for Equation (2.22) are:

$$C(r,0) = C_{PW}^E\big|_{t=0} \tag{2.23}$$
$$C(R,0) = C_{TW}^E\big|_{t=0} \tag{2.24}$$

where $C_{TW}^E\big|_{t=0}$ and $C_{PW}^E\big|_{t=0}$ are respectively the initial tracer E concentration in the reservoir test solution and the initial tracer E concentration in pore-water.

Boundary conditions for Equation (2.22) are:

$$C(R,t) = C(r_R,t) \tag{2.25}$$
$$\frac{\partial C}{\partial r}(r_c,t) = 0 \tag{2.26}$$

The semi-analytical solution is given by Novakowski and Van der Kamp (1996) and Savoye et al. (2006a):

$$\hat{F}(p) = \left\langle \frac{\hat{c}}{C^E_{TW}\big|_{t=0}} \right\rangle (p)$$

$$= \frac{C^E_{PW}\big|_{t=0}}{C^E_{TW}\big|_{t=0} \cdot p} + \tag{2.27}$$

$$\frac{\left(C^E_{TW}\big|_{t=0} - C^E_{PW}\big|_{t=0}\right) \cdot \left[K_1(\sqrt{p}\cdot r_{DC}) \cdot I_0(\sqrt{p}) + I_1(\sqrt{p}\cdot r_{DC}) \cdot K_0(\sqrt{p})\right]}{C^E_{TW}\big|_{t=0} \cdot \left[K_1(\sqrt{p}\cdot r_{DC}) \cdot \{pI_0(\sqrt{p}) - \beta\sqrt{p}I_1(\sqrt{p})\} + I_1(\sqrt{p}\cdot r_{DC}) \cdot \{pK_0(\sqrt{p}) + \beta\sqrt{p}K_1(\sqrt{p})\right]}$$

$$\hat{F}(p) = \left\langle \frac{\hat{c}}{C^E_{PW}\big|_{t=0}} \right\rangle (p) \qquad\qquad = \frac{1}{p} +$$

$$\frac{\left(C^E_{TW}\big|_{t=0} - C^E_{PW}\big|_{t=0}\right) \cdot \left[K_1(\sqrt{p}\cdot r_{DC}) \cdot I_0(\sqrt{p}) + I_1(\sqrt{p}\cdot r_{DC}) \cdot K_0(\sqrt{p})\right]}{C^E_{PW}\big|_{t=0} \cdot \left[K_1(\sqrt{p}\cdot r_{DC}) \cdot \{pI_0(\sqrt{p}) - \beta\sqrt{p}I_1(\sqrt{p})\} + I_1(\sqrt{p}\cdot r_{DC}) \cdot \{pK_0(\sqrt{p}) + \beta\sqrt{p}K_1(\sqrt{p})\}\right]} \tag{2.28}$$

where the hat denotes Laplace transformed quantities, I_0, I_1, K_0 and K_1 are respectively modified Bessel functions of the first and second kind, p is the Laplace variable, β [-] is the capacity ratio equal to $2\omega_e$, r_{DC} [-] is the r_c over r_R ratio, $C^E_{TW}\big|_{t=0}$ and $C^E_{PW}\big|_{t=0}$ are respectively the initial tracer E concentration of test water in the reservoir and the initial tracer E concentration in pore-water.

A numerical inversion of the Laplace transformis was developed by Savoye et al. (2006a) using Mathematica 5.2 and the De Hoog et al. (1982) algorithm. The script was adapted to take into account the core truncation, the PTFE rod and the copper cylinder. The method enables simultaneous measurement of diffusion parameters (effective porosity and diffusion coefficient) parallel to the bedding plane.

2.2.4.6. Through diffusion

The through diffusion cell consists of a polypropylene sample holder, two polypropylene reservoirs for liquid phase (upstream and downstream, with respective capacities of 180 mL and 90 mL), two supporting grids and two sampling openings (Figure 2.14).
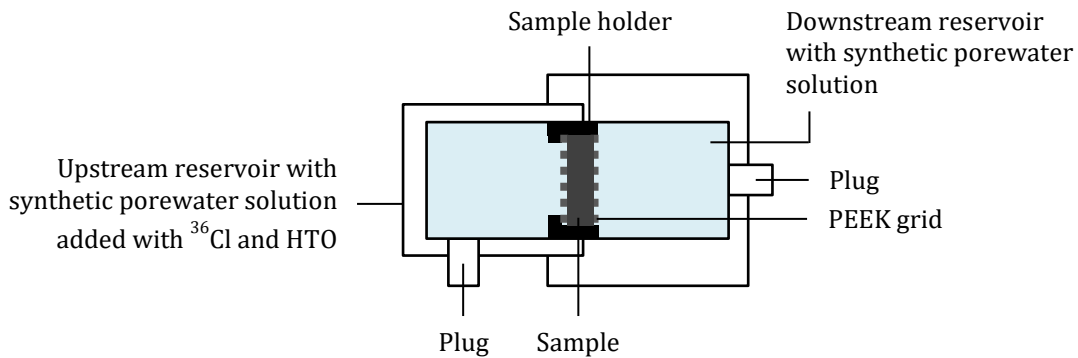
Figure 2.14: Schematic cross-section view of a through diffusion cell

Cylindrical samples of approximatively 10 mm thickness and 30 mm diameter were prepared from core samples by sawing with a diamond wire saw. These samples were confined between porous polyether ether ketone (PEEK) grids in order to control clay mineral swelling and the assembly was fixed to the sample holder using Sikadur® epoxy adhesive. Pictures of the experimental protocol are shown in Figure 2.15.
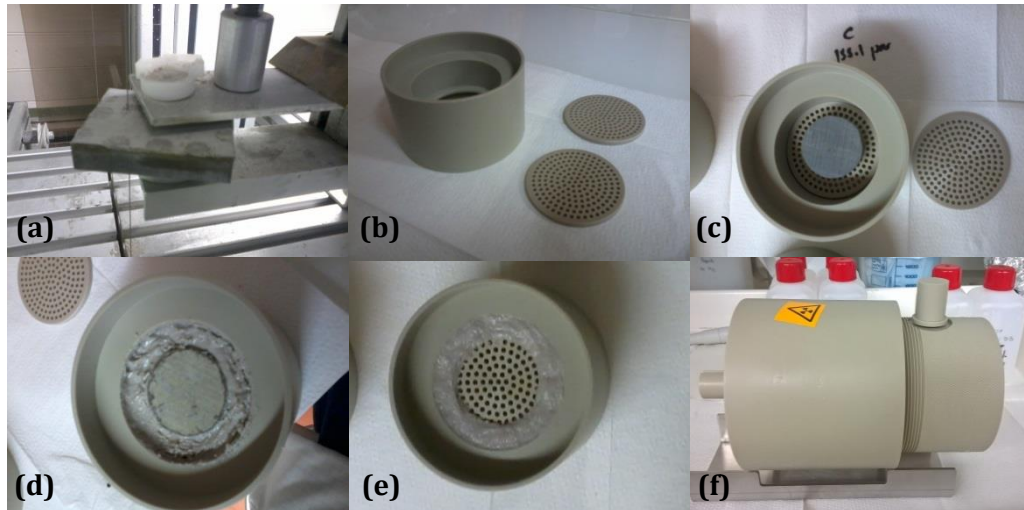
Figure 2.15: Preparation steps of through diffusion experiments
(a) Sample preparation using a diamond wire saw (b) Sample holder and PEEK grids
(c) Sample mounting in the sample holder
(d) Sample fixation using Sikadur® epoxy adhesive
(e) Final sample holder (f) Through diffusion cell containing the sample holder

Similarly to radial diffusion experiments, the sample underwent a resaturation phase of three months, in which the two reservoirs were filled with synthetic porewater. Chemical compositions of the reservoirs were analysed using ionic chromatography in order to ensure that equilibrium was reached.

To initialise the diffusion phase, reservoirs were drained and the upstream reservoir was filled with a synthetic porewater doped with radioactive tracers (^{36}Cl and HTO, 375 kBq L^{-1} for each tracer), while the downstream reservoir was filled with an untraced synthetic solution.

The flux of radioactive species between the reservoirs was monitored as a function of time by liquid scintillation using a Packard Tri-carb 3100 TR counter. For each sampling, the sampled volumes in the upstream reservoir and the downstream reservoir were respectively of 0.5 mL and 5 mL. Sampled volumes were replaced by the same volume of initial solutions in order to keep the reservoir volumes and limit conditions constant. All radioactive activity measurements were corrected for radioactive decay.

Pore diffusion coefficients were estimated by modelling the experiment with the transport code HYTEC.

2.2.6. MODELLING TOOLS

2.2.6.1. HYTEC and CHESS

HYTEC (HYdrological Transport coupled with Equilibrium Chemistry) is a coupled reactive transport code developed since 1993 at Mines ParisTech (Van der Lee et al., 2003). This simulation tool solves coupled equations describing mass conservation and solute transport. It takes into account variations of hydrodynamic parameters such as porosity, permeability, reactive surface area and diffusion coefficient, as well as chemical reactions between solution, gas or mineral phases (e.g. dissolution, precipitation and sorption). HYTEC applications covers impact studies of polluting deposits, safety assessment of nuclear waste disposal, geological gas storage, material and structure durability studies.

The modelling platform is based on the geochemical module CHESS (Chemical Equilibrium of Species and Surfaces), which is optimized for coupling with several transport models (METIS, R2D2 and RT1D). Simulation results can be visualized with the post-processor HYPE.

The transport equation writes:

$$\frac{\partial \omega c_i}{\partial t} = \text{div}\left(D_e(\omega)\nabla c_i\right) - \frac{\partial \omega \overline{c_i}}{\partial t} \qquad (2.29)$$

where c_i is the mobile fraction of the total concentration of component i and $\overline{c_i}$ is the immobile fraction, D_e [m^2 s^{-1}] is the effective diffusion coefficient and ω [-] is the porosity.

The feedback of chemistry on mass transport is modelled by using a modified version of the Archie's law:

$$D_e(\omega) = D_e(\omega_0)\left(\frac{\omega - \omega_c}{\omega_0 - \omega_c}\right)^m \qquad (2.30)$$

where ω_0 [-] is the initial porosity, D_e [m^2 s^{-1}] is the effective diffusion coefficient, ω_c [-] is the critical porosity threshold under which diffusion stops, and m [-] is Archie's empirical coefficient.

HYTEC was used in this study for the interpretation of cubic out diffusion and through diffusion experiments.

2.2.6.2. PHREEQC

Geochemical modelling was performed using PHREEQC Interactive 3.1.4 calculation code (Parkhurst and Appelo, 1999), using sit.dat thermodynamic database (Duro et al., 2007). PHREEQC is an open source computer program developed by the United-States Geological Survey (USGS). Written in the C-programming language, the code is able to compute equilibrium chemistry of aqueous solutions interacting with minerals, gases, solid solutions, exchangers, and sorption surfaces. Speciation computing can be coupled with a mass transfer module to simulate one-dimensional transport (advection, dispersion and diffusion). PHREEQC can also model kinetic reactions and enable inverse-modelling.

2.2.6.3.nSIGHTS

Hydraulic tests were analysed using Sandia National Laboratories well-test simulator nSIGHTS (n-dimensional Statistical Inverse Graphical Hydraulic Test Simulator). This open source numerical tool was developed by INTERA, based on the well-test analysis code GTFM (Graph Theoretic Field Model). GTFM was developed from 1983 to 1996 and extensively used in the Swiss, Swedish and French nuclear waste programs, as well as at the DOE's Waste Isolation Pilot Plant in New Mexico (Roberts et al. 1999; Bowman and Roberts, 2009).

nSIGHTS is suited to analyse well tests in various media because it is not based on analytical solutions that require ideal conditions such as an initial assumption of radial flow. Inverse simulations involve optimizing the hydraulic parameters that provides the best fit to the measured data. The conceptual flow model can be validated if the function residuals are minimized and defined as normally distributed. The code also quantifies the uncertainty associated with the fitting parameters, by performing random perturbation analyses to determine if the nonlinear regression algorithm is converging to a unique global minimum, or if the results are obtained from local minima. Moreover, nSIGHTS generates multiple specialized plots such as pressures derivatives, Horner, Ramey A, B and C, deconvolved pulse response and flow dimension diagnostic plots.

In a generalized system of flow dimension n, the equation from Barker (1988) describes flow that occurs radially toward or away from a well in a homogeneous, isotropic aquifer and fills a n-dimensional space:

$$S_s \frac{\partial h}{\partial t} = \frac{K}{r^{n-1}} \frac{\partial}{\partial r}\left(r^{n-1}\frac{\partial h}{\partial r}\right) \qquad (2.31)$$

where S_s [m^{-1}] is the specific storage coefficient, h [m] is the hydraulic head, t [s] is the elapsed time, K [m s^{-1}] is the hydraulic conductivity, r [m] is the radial distance from borehole, and n [-] is the flow dimension.
The flow area is defined as:

$$A(r) = b^{3-n}\frac{2\pi^{n/2}}{\Gamma^{n/2}}r^{n-1} \qquad (2.32)$$

where b [m] is the extent of the flow zone, and Γ is the gamma function.

2.2.6.4. MuSTAT

Spectral analysis of the pressure dataset in BDB-1 borehole was performed using the Multi-STatistical Analysis Tool (MuSTAT), jointly developed by the IRSN and the INPT (Fatmi, 2009; Ababou et al., 2012; Bailly et al., 2014). MuSTAT consists in a Python code associated with toolboxes programmed in Matlab. The package provides an automatic and controlled preprocessing and processing step of time series. Preprocessing includes time gap and spurious value detection as well as data reconstruction by autoregressive first order process.

Spectral analysis

Fourier spectral analysis decomposes a signal $X(t)$ into periodic functions expressed in the frequency domain. The dimensional spectrum of the time series is expressed as the Fourier transform of the covariance function:

$$R_{XX}(j) = \frac{1}{\sigma_X^2} \frac{1}{N-1} \sum_{n=1}^{n=N-j} (X(t_n) - \bar{X})(X(t_{n+j}) - \bar{X}) \tag{2.33}$$

And
$$S_{XX}(f_i) = 2\Delta t\, \sigma_X \sigma_X \left[R_{XX}(0) + 2 \sum_{j=1}^{M} D_j(\tau_j)\, R_{XX}(\tau_j) \cos(2\pi\, \tau_j\, f_i) \right] \tag{2.34}$$

where $R_{XX}[-]$ is the normalised auto-covariance function also named auto-correlation function, σ_X [unit$_X$] is the standard deviation of the signal, N [-] is the total number of data contained in the time series, $\bar{X}$ [unit$_X$] is the mean of $X(t)$, S_{XX}[unit$_X^2$ s] is the dimensional spectrum, $f_i = \frac{1}{2M\Delta t_i}$ [Hz] is the discrete positive dimensional frequency, Δt [s] is the homogeneous time step, M [-] is the maximum (M = N-1) or total number of time lags considered, $D_j = \left(1 + cos\left(\frac{\pi j}{M}\right)\right)/2$ is the Tuckey filter, and $\tau_j = j\Delta t$ [s] is the discrete lag time.

A Root Mean Square (RMS) amplitude spectrum is defined as a function of the discrete frequency interval Δf [Hz], in order to obtain a frequency dependent measure of fluctuations, directly in the unit of the signal:

$$S_{XX}^{RMS}(f_i) = 2\sqrt{S_{XX}(f_i)\, \Delta f} \tag{2.35}$$

Co-spectral analysis

Cross-analysis of two signals enables to identify the common harmonics and to detect the potential causal relationship between them. The dimensional cross-spectrum of two signals $X(t)$ and $Y(t)$ is described as follows:

$$S_{XY}(f_i) = |S_{XY}(f_i)|e^{-\varphi_{XY}(f_i)} = S_{Re}(f_i) + iS_{Im}(f_i) \tag{2.36}$$

With
$$S_{Re}(f_i) = 2\Delta t \sigma_X \sigma_Y \left[R_{XY}(0) \right.$$
$$\left. + \sum_{j=1}^{M} \left(R_{XY}(j) + R_{YX}(j) \right) D_j \cos(2\pi\Delta t\, f_i) \right] \tag{2.37}$$

And
$$S_{Im}(f_i) = 2\Delta t \sigma_X \sigma_Y \left[\sum_{j=1}^{M} \left(R_{XY}(j) - R_{YX}(j) \right) D_j \sin(2\pi \Delta t \ f_i) \right] \qquad (2.38)$$

where S_{Re} [unit$_X$·unit$_Y$·s]and S_{Im} [unit$_X$·unit$_Y$·s]are respectively the real and the imaginary part of the cross-spectrum, f_i [Hz] is a given discrete frequency, $|S_{XY}(f_i)| = \sqrt{S_{Re}^2(f_i) + S_{Im}^2(f_i)}$ [unit$_X$·unit$_Y$·s] is the amplitude cross-spectrum, and $\varphi_{XY}(f_i) = sign\left(S_{im}(f_i)\right)cos^{-1}\left(\frac{S_{Re}(f_i)}{|S_{XY}(f_i)|}\right)$ [radians] is the phase cross-spectrum defined in [-π,+π].

A dimensional Root Mean square cross amplitude spectrum can also be defined:

$$S_{XY}^{RMS}(f_i) = 2\sqrt{S_{XY}(f_i)\,\Delta f} \qquad (2.39)$$

The spectral coherence function computes the correlation between two signals for a given harmonic:

$$Coh_{XY}^{RMS}(f_i) = \frac{|S_{XY}^{RMS}(f_i)|}{\sqrt{S_{XX}^{RMS}(f_i) + S_{YY}^{RMS}(f_i)}} \qquad (2.40)$$

The spectral causal gain $G_c(f_i)$ [unit$_Y$/ unit$_X$] or [unit$_X$/unit$_Y$], and reduced causal gain $g_c(f_i)$ [-] reflect the effects of the input signal on the output signal:

$$G_c(f_i) = G_{XY}(f_i) \ \ if \ \ \varphi_{XY}(f_i) \geq 0 \ \ and \ \ G_c(f_i)$$
$$= G_{YX}(f_i) \ \ if \ \ \varphi_{XY}(f_i) < 0 \qquad (2.41)$$

$$g_c(f_i) = g_{XY}(f_i) \ \ if \ \ \varphi_{XY}(f_i) \geq 0 \ \ and \ \ g_c(f_i) \qquad (2.42)$$
$$= g_{YX}(f_i) \ \ if \ \ \varphi_{XY}(f_i) < 0$$

where $G_{XY}(f_i) = |S_{XY}(f_i)|/S_{XX}(f_i), \quad G_{YX}(f_i) = /|S_{XY}(f_i)|/S_{YY}(f_i), \quad g_{XY}(f_i) = G_{XY}(f_i).(\sigma_X/\sigma_Y)$ and $g_{YX}(f_i) = G_{YX}(f_i).(\sigma_Y/\sigma_X)$.

CHAPTER 3.   CHARACTERISATION OF THE OPALINUS CLAY AND ITS BOUNDING FORMATIONS

3.1.   HYDRAULIC HEAD AND TEMPERATURE PROFILES

3.1.1.   PRESSURE MEASUREMENTS AND ASSOCIATED HYDRAULIC HEAD PROFILE

Porewater pressure and packer pressure were monitored in eight measuring interval of the BDB-1 deep borehole (Figure 3.1). The installation of the multipacker system induced significant pressure variations in early February 2014, related to the saturation of hydraulic lines and the packers inflation. The monitored pressures reached stabilized values more or less rapidly depending on the interval. The first interval, located in the Staffelegg Formation below the Opalinus Clay, had the fastest hydraulic response. No significant difference was seen between the upper part of the Opalinus Clay and the bottom part of its overlying aquifer in terms of hydraulic response.
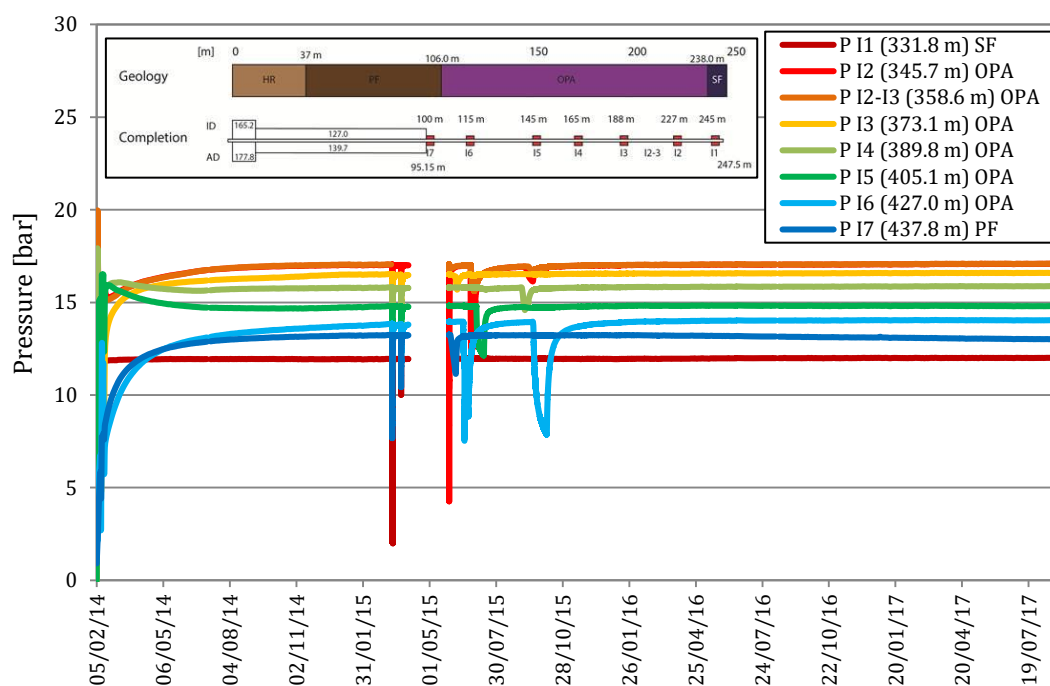
Figure 3.1: Pore pressure evolution measured in BDB-1 borehole (sensors at gallery level) from February 2014 to September 2017 with the elevation of the intervals given in the legend.

Pressure anomalies within argillaceous rocks have an impact on radionuclide transport from the repository to the biosphere. Inward flow induced by underpressures in the host rock can delay radionuclide transport, whereas the presence of overpressures can enhance the process. Pressure monitoring in the BDB-1 deep borehole revealed anomalous overpressures up to 0.59 MPa in the Opalinus Clay of Mont Terri (Figure 3.2). Prior studies at the Benken site also showed porewater overpressures of 0.5 to 1.5 MPa (Nagra, 2002), which were explained as being remnants from the maximum burial in the Miocene or resulting from an ongoing lateral thrust,

during which porewater drainage and compaction have not yet reached an equilibrium state. However, long term monitoring after hydraulic system replacement at Benken revealed underpressures between 0.22 and 0.33 MPa (Beauheim, 2013; Jäggi et al., 2014), which origins are not clearly established.
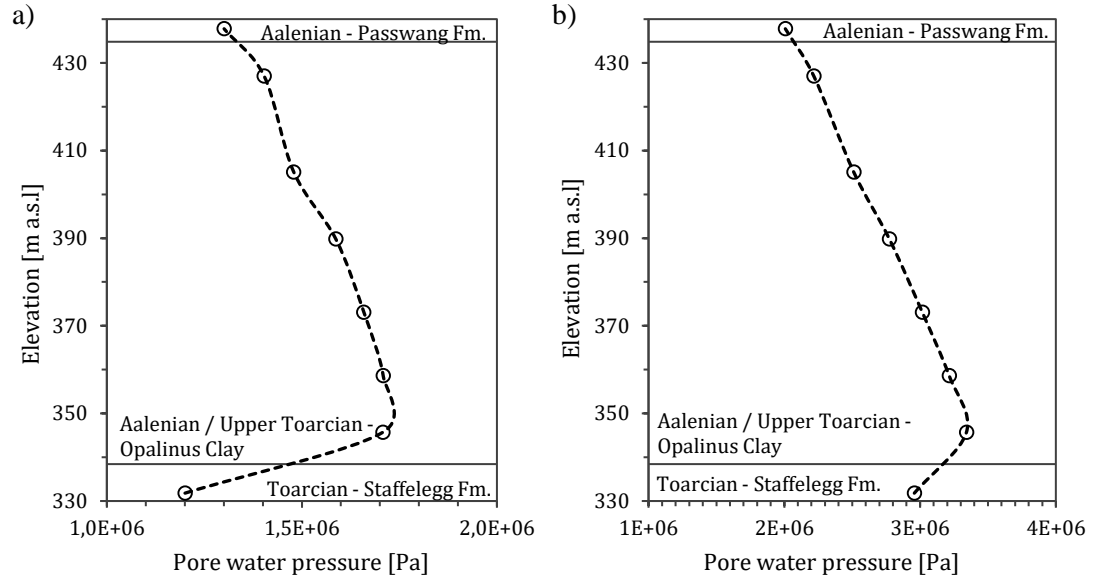
Figure 3.2: a) Porewater pressure profile across the Opalinus Clay measured at the gallery level in BDB-1 borehole as of September 5th 2017; b) Porewater pressure profile corrected for sensors elevation.

Pore pressure measurements were used to calculate a hydraulic head profile across the Opalinus Clay of Mont Terri. The hydraulic head was calculated and corrected for barometric pressure and density variations according to the following formula:

$$h = \frac{P_0 + \rho_f g(z_0 - z) - P_{atmo}}{\rho_f \times g} + z \qquad (3.1)$$

where *h* [m.a.s.l.] is the hydraulic head, P_0 and *Patmo* [Pa] are respectively the pore pressure of the measured at the borehole head and the atmospheric pressure, ρ_f [kg m^{-3}] is the porewater density, *g* [9.81 m s^{-2}] is the gravity acceleration, z_0 and *z* [m.a.s.l.] are respectively the Mont Terri gallery level and the measured point elevation.

The results are presented in Figure 3.3 and Table 3.1. The hydraulic head profile indicates an excess head up to ca. 50 m with respect to the linear evolution of the surrounding formations. The maximum value is found in the lower part of the argillaceous formation. The hydraulic gradient is globally oriented vertically upward. The measured excess head in the Opalinus Clay is of the same order of magnitude as the 20 to 40 m measured in the Toarcian claystone (Tournemire, France) and as the 40 to 60 m found in the Callovo-Oxfordian formation (Bure, France)(Tremosa, 2010). The reference head of the underlying aquifer (Trias Marl and Limestone) was modelled at ca. 600 m (Kuhlmann et al., 2011; Figure 3.4) and can be evaluated in the range of 500 to 530 m considering the BDB-1 borehole measurements and with the

uncertainties related to the upper boundary of the lower aquifer, which would suggest an even higher value of pressure anomaly in the order of 130 m.
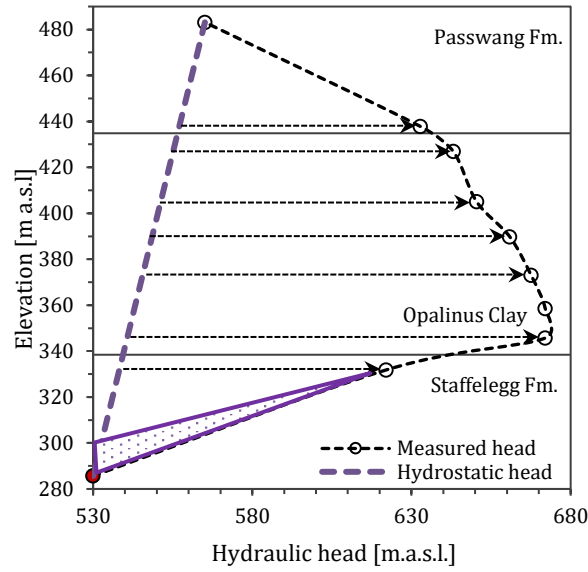
Figure 3.3: Hydraulic head profile across the Opalinus Clay measured in BDB-1 borehole as of September 5th 2017. The dotted area represents the uncertainty domain for the lower aquifer hydraulic head.

Table 3.1: Hydraulic head and elevation of the BDB-1 borehole measurement chambers

Chamber	Elevation [m.a.s.l.]	Depth along BDB-1 z-axis [m]	Hydraulic head [m]	Hydrostatic head [m]	Indicative overpressure [MPa]
I_1	331.8	247.5 – 244.62	622.02	538.21	83.81
I_2	345.7	226.17 – 227.17	672.01	540.68	131.32
I_{2-3}	358.6	196.37 – 196.92	672.01	542.98	129.03
I_3	373.1	188.17 – 189.17	667.56	545.55	122.00
I_4	389.8	164.72 – 165.72	660.88	548.52	112.35
I_5	405.1	144.27 – 145.27	650.46	551.24	99.21
I_6	427	114.82 – 115.82	643.09	555.14	87.95
I_7	437.8	100.37 – 101.37	632.82	557.06	75.76
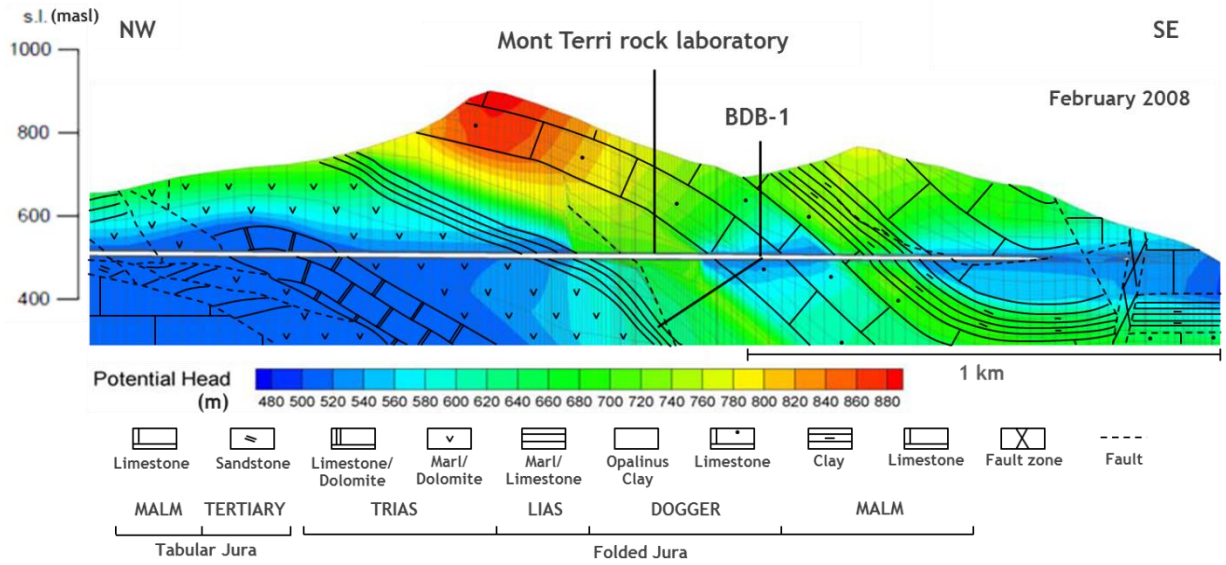
Figure 3.4: Modelled hydraulic head distribution at the Mont Terri underground laboratory, as of February 2008 and associated geological cross section (modified from Freivogel and Huggenberger, 2003 and Kuhlmann et al., 2011)

3.1.2. TEMPERATURE PROFILE

The establishment of a temperature profile is of main interest since temperature is the driving force for thermo-osmosis. The temperature evolution measured in the different intervals of BDB-1 borehole is reported in Figure 3.5.
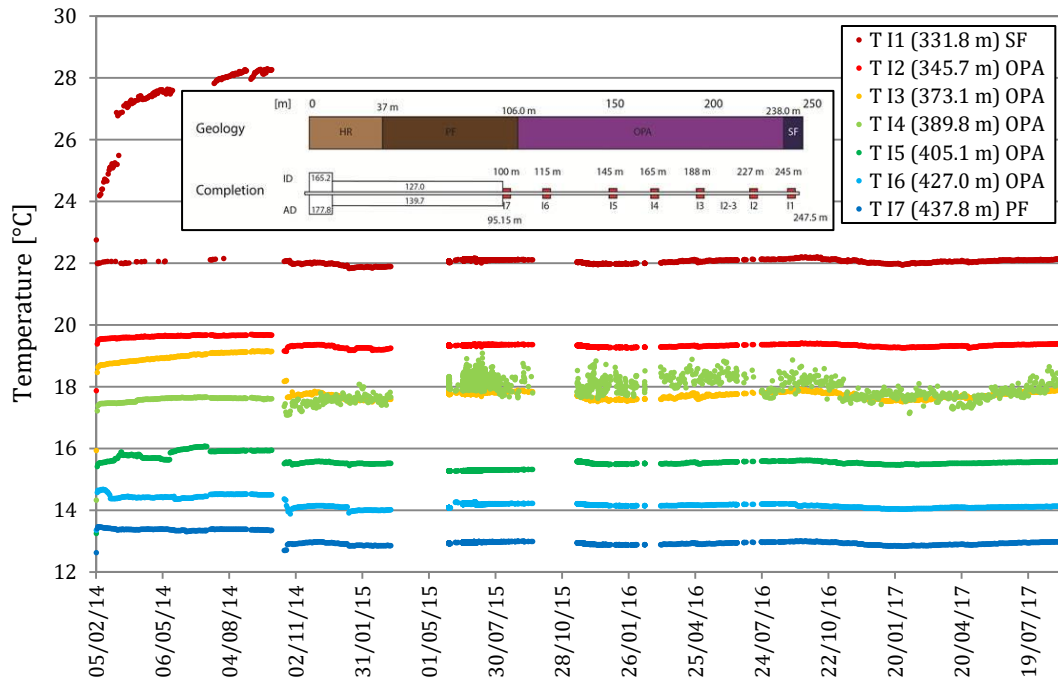
Figure 3.5: Temperature evolution in BDB-1 borehole from February 2014 to September 2017 with the elevation of the interval. given in the legend.

Signal problems with temperature sensors were observed in the beginning of the monitoring. The T1 sensor, located in the deepest part of the BDB-1 borehole, showed significant outliers up to 6°C from actual values. Several technical issues were investigated (amplifier or electrical interface internal problems). In 2014 October 14th, technical change on the interface was performed. Since then, the sensors present reasonable values, except for the T4 sensor which shows a noised signal fluctuating between 17.5°C and 18.2°C. This anomaly is possibly due to a coupling issue between steel casing and sensor.

Temperature varies in between 12.9 °C at the boundary between the Passwang Formation and the Opalinus Clay boundary to 21.9 °C in the Staffelegg Formation. Therefore, a high geothermal gradient of 8.5 °C per 100 m can be seen across the Opalinus Clay (Figure 3.6). This value is nearly three times higher compared to the average geothermal gradient of 3 °C per 100 m found in the Swiss Molasse Basin.

Prior studies in deep boreholes carried out by Nagra at Riniken, Weiach and Benken in northern Switzerland, revealed low thermal conductivity values in the Opalinus Clay (globally inferior to 2.5 W m^{-1} K^{-1}), consistent with the heat accumulation and increased temperatures observed in this formation (Table 3.2).

Temperature profiles measured in deep investigation boreholes are controlled by several factors: current geothermal state conditions (basal heat flow, surface temperature, thermal conductivity profile, groundwater flow) and climate changes on a geological time scale.

Apatite fission-track analysis, petrographic and isotopic studies of diagenetic cements and fluid inclusions showed that the maximum temperature reached by the Opalinus Clay is ca. 85°C during the Cretaceous, while temperatures related to the Miocene burial were ca. 65° (Mazurek et al., 2002).
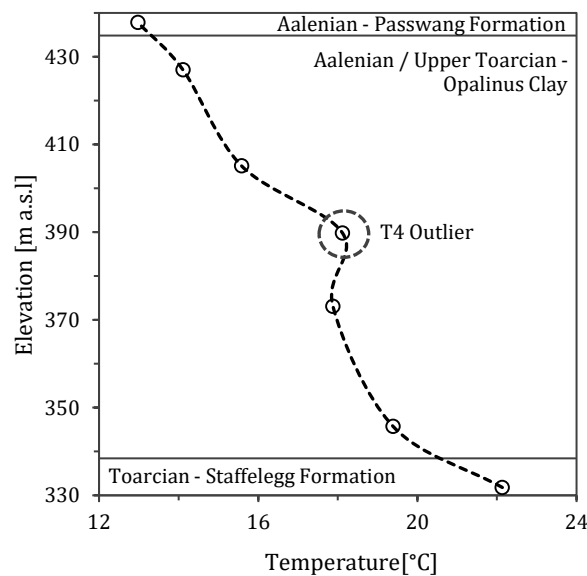
Figure 3.6: Geothermal gradient across the Opalinus clay measured in BDB-1 borehole as of September 5th 2017

Table 3.2: Measured thermal conductivity, temperatures and geothermal gradients in the Opalinus Clay (Bossart and Thury, 2008; Papafotiou and Senger, 2014a and 2014b; *this study)

Location	OPA thermal conductivity [W·m⁻¹·K⁻¹]	OPA top temperature [°C]	OPA bottom temperature [°C]	Temperature gradient [°C / 100 m]
Weiach	2.0	32	39	4.4
Benken	Upper OPA (538-625 m): 3.2 (horizontal) 1.8 (vertical) Lower OPA (625-652 m): 2.0 (horizontal) 1.3 (vertical)	30	38	4.3
Riniken	n.a.	26.8	35.5	7.8
Mont Terri	2.1 (horizontal) 1.2 (vertical)	12.9*	21.9*	8.5*

3.2. MINERALOGY

3.2.1. MINERAL CONTENTS ACQUIRED BY X-RAY DIFFRACTION ON BULK ROCK POWDERS

The mineralogical profile (Figure 3.7) was acquired by Ould Bouya (2014) 0 and suggests that the Opalinus Clay is composed of 35 to 66 % of phyllosilicates (illite, kaolinite and chlorite), 4 to 32 % of calcite, 0 to 3 % of dolomite/ankerite, 13 to 38 % of quartz, 0 to 7 % of feldspars and 0 to 3 % of pyrite. In the Middle Jurassic overlying formations, the carbonated phase varies between 72 % in the Hauptrogenstein and 58 % in the Passwang Formation. The clay fraction does not exceed 11% in these formations. Detailed mineral contents are reported in Table 3.3 and Table 3.4. These data were obtained by traditional Reference Intensity Ratio method, which suffer from limitations such as effects caused by variations in mineral crystallinity, preferred orientation in the sample mount and differential absorption of X-rays by minerals in the mixture.
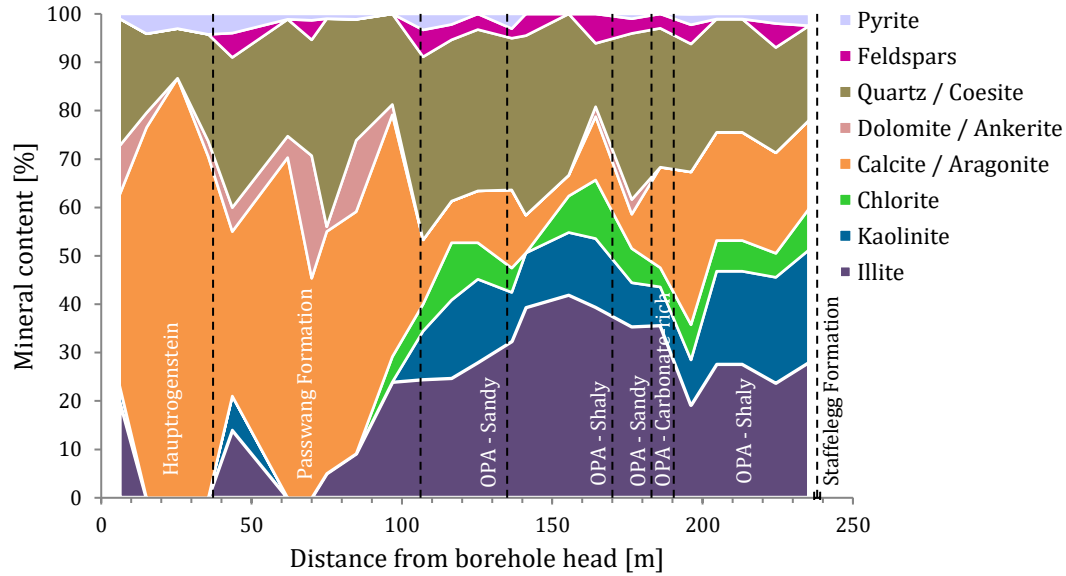
Figure 3.7: Mineralogical profile acquired by XRD on bulk rock samples along the BDB-1 borehole (modified from Ould Bouya, 2014)

Table 3.3: Mineral contents [wt%] obtained by XRD on bulk rock samples of Middle Jurassic Carbonates (Ould Bouya, 2014)

Formation	Hauptrogenstein				Passwang Formation					
Distance (m)	6	15.1	25.3	35.58	43.52	62.08	70.03	75.03	84.98	96.9
Quartz / Coesite	26	16	10	22	31	24	24	43	25	19
Feldspars	0	0	0	0	5	0	4	0	0	0
Silty fraction	**26**	**16**	**10**	**22**	**36**	**24**	**28**	**43**	**25**	**19**
Calcite /Aragonite	39	77	87	71	34	70	45	50	50	50
Dolomite /Ankerite	10	3	0	3	5	4	25	1	15	2
Carbonate fraction	**49**	**80**	**87**	**74**	**39**	**75**	**71**	**51**	**65**	**52**
Illite	20	0	0	0	14	0	0	5	9	24
Kaolinite	0	0	0	0	7	0	0	0	0	0
Chlorite	0	0	0	0	0	0	0	0	0	5
Clay fraction	**24**	**0**	**0**	**0**	**21**	**0**	**0**	**5**	**9**	**29**
Pyrite	1	4	3	4	4	1	1	1	1	0
TOTAL	**100**	**100**	**100**	**100**	**100**	**100**	**100**	**100**	**100**	**100**

Table 3.4: Mineral contents [wt%] obtained by XRD on bulk rock samples of Opalinus Clay (Ould Bouya, 2014)

Formation	OPA sandy			OPA shaly				OPA Sandy	OPA Carb-rich	OPA Shaly				
Distance [m]	107.2	116.5	125.4	136.6	141.4	156	165	176.7	186.2	196.4	205	213.5	224.7	235.7
Quartz / Coesite	38	33	33	31	37	33	13	34	29	26	23	23	22	20
Feldspars	6	3	3	2	4	0	6	3	3	4	0	0	5	0
Silty fraction	**43**	**37**	**37**	**33**	**42**	**33**	**19**	**37**	**32**	**30**	**23**	**23**	**27**	**20**
Calcite /Aragonite	13	9	11	16	8	4	13	7	21	32	22	22	21	18
Dolomite /Ankerite	0	0	0	0	0	0	2	3	0	0	0	0	0	0
Carbonate fraction	**13**	**9**	**11**	**16**	**8**	**4**	**15**	**10**	**21**	**32**	**22**	**22**	**21**	**18**
Illite	24	25	28	32	39	42	39	35	36	19	28	28	24	28
Kaolinite	10	16	17	10	11	13	14	9	8	9	19	19	22	23
Chlorite	6	12	8	5	0	8	12	7	4	7	6	6	5	9
Clay fraction	**40**	**53**	**53**	**47**	**51**	**62**	**66**	**52**	**48**	**36**	**53**	**53**	**50**	**60**
Pyrite	3	2	0	3	0	0	0	1	0	2	1	1	2	2
TOTAL	**100**	**100**	**100**	**100**	**100**	**100**	**100**	**100**	**100**	**100**	**100**	**100**	**100**	**100**

Additional XRD analysis, selective extractions with phosphoric acid and microscopic observations were performed on the same Opalinus Clay samples by BRGM (Lerouge, 2014) to precise the parameter lattices and the contents of carbonated mineral phases. The clay mineral contents (Table 3.5) are globally in good agreement, although illite/smectite mixed layers were identified by Lerouge. Carbonates are present through the Opalinus Clay as calcite, dolomite/ankerite assemblage, and siderite. Calcite appears in bioclasts, micrite, euhedral grains and sparite in silty quartz/feldspaths layers. Dolomite $(Ca_{0.50}(Fe_{0.02},Mg_{0.48})(CO_3)_2)$ is quite pure and only present in core of euhedral grains and cements. Ankerite $(Ca_{0.53}(Fe_{0.14},Mg_{0.33})(CO_3)_2)$ is always present as coronas surrounding dolomite grains. Siderite $(Ca_{0.10}(Fe_{0.73},Mg_{0.17})CO_3)$ appears as 100 µm-sized masses and as impregnation of layers.

Table 3.5: Mineral contents [wt%] obtained by XRD on bulk rock samples of Opalinus Clay (Lerouge, 2014. Collaborative work between BRGM and University of Bern, unpublished)

Formation	OPA sandy			OPA shaly				OPA Sandy	OPA Carb-rich	OPA Shaly				
Distance [m]	107.2	116.5	125.4	136.6	141.4	156	165	176.7	186.2	196.4	205	213.5	224.7	235.7
Quartz	33	32	38	26	22	18	21	32	42	14	13	13	12	11
Microcline	4	3	3	2	2	1	1	3	3	< 1	< 1	< 1	1	< 1
Plagioclase	4	2	2	3	3	3	3	3	3	3	2	2	2	2
Silty fraction	**41**	**37**	**43**	**31**	**27**	**22**	**25**	**38**	**48**	**17**	**15**	**15**	**15**	**13**
Calcite	11	7	8	21	3	3	5	8	16	8	13	12	15	22
Dolomite /Ankerite	0	0	0	0	0	0	0	9	7	0	2	2	1	1
Siderite	0	0	4	4	5	9	4	3	1	3	2	2	2	0
Carbonate fraction	**11**	**7**	**12**	**25**	**8**	**12**	**9**	**20**	**24**	**11**	**17**	**16**	**18**	**23**
Kaolinite	10	9	8	8	16	15	16	9	7	17	16	15	15	15
Illite Mica	20	21	18	16	27	28	23	14	7	27	26	27	26	25
Chlorite	2	5	4	3	2	2	3	1	3	4	3	3	3	3
Mixed layers I/S	12	15	13	11	16	18	20	14	9	19	18	19	18	18
Clay fraction	**44**	**50**	**43**	**38**	**61**	**63**	**62**	**38**	**26**	**67**	**63**	**64**	**62**	**61**
Anatase	1	3	1	1	3	3	3	2	2	3	3	3	3	2
Apatite OH	0	0	0	3	0	0	0	< 1	1	0	0	0	0	0
Pyrite	3	3	1	2	1	0	1	2	1	2	2	2	2	1
TOTAL	**100**	**100**	**100**	**100**	**100**	**100**	**100**	**100**	**102**	**100**	**100**	**100**	**100**	**100**

3.2.2. CLAY MINERAL CONTENTS ACQUIRED BY X-RAY DIFFRACTION ON CLAY FRACTION

Further characterization of the clay fraction in samples from BDB-1 borehole was carried out by N'Guessan (2015) and is presented in Table 3.6.

Table 3.6: Clay minerals contents [wt%] obtained by XRD on clay fractions (< 2 µm) of BDB-1 borehole samples. Results in shaded boxes are to be taken with caution due to low intensity peaks on the associated diffractogram (N'Guessan, 2015)

Formation	Passwang Formation	OPA Sandy	OPA Shaly	OPA Sandy	OPA Carbonate-rich sandy	OPA - Shaly			Staffelegg Formation		
Distance [m]	74.9	125.3	141.2	176.6	186.1	204.9	225.5	230.7	238.2	241.9	243.9
I/S R1	9	10	24	38	30	12	14	31	2	23	2
Illite	34	34	27	27	24	37	38	33	34	41	80
Chlorite	41	23	21	2	19	24	4	8	26	13	14
Kaolinite	16	33	29	32	27	27	44	29	37	23	3
Total	**100**	**100**	**100**	**100**	**100**	**100**	**100**	**100**	**100**	**100**	**100**

The clay fraction in the Opalinus Clay is composed of illite, kaolinite, chlorite and R1 type illite-smectite (I/S) mixed layers (80% illite, 20% smectite). Coupling the clay fraction results with bulk rock oxide analysis by X-Ray fluorescence (see Annex V), the following mean composition of the Opalinus Clay was determined: 16 % illite, 11 % I/S mixed layers, 7 % chlorite, 15 % kaolinite, 16 % carbonates, 13 % feldspars and 24 % quartz.
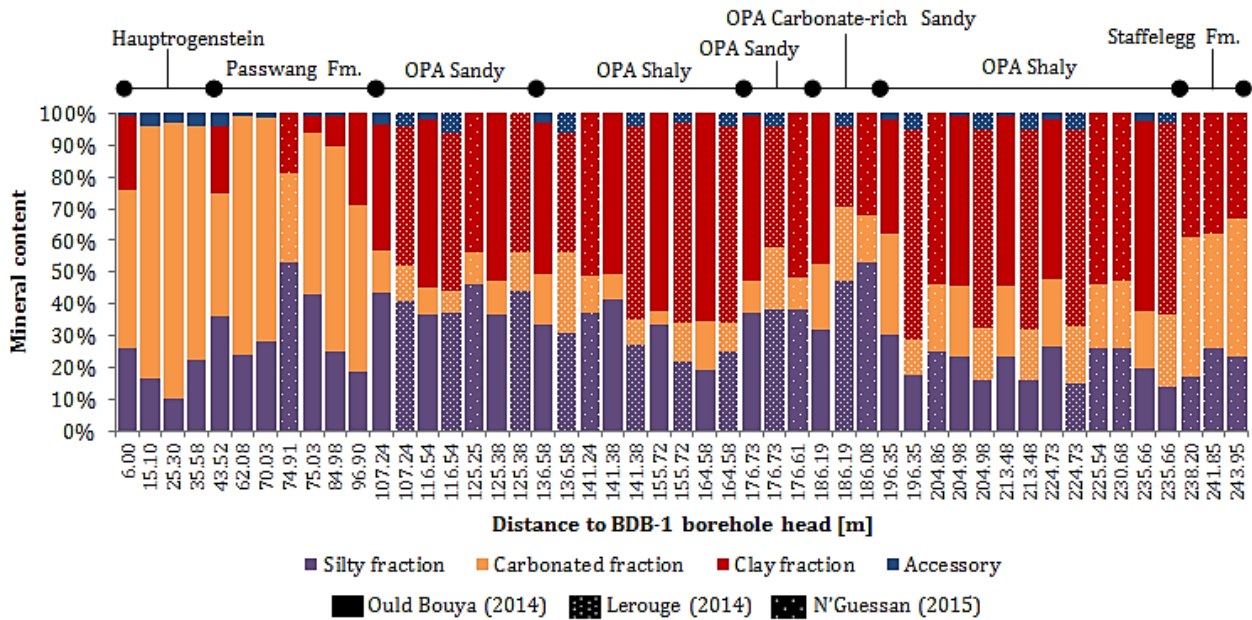
Figure 3.8: Mineral characterisation carried out on BDB-1 borehole samples (compiled from Ould Bouya, 2014; Lerouge, 2014; and N'Guessan, 2015)

3.3.   PETROPHYSICAL PARAMETERS

Gravimetric water contents in the Opalinus Clay do not exceed 5 % with a mean value of 4.9 %, which is higher than the values obtained in the carbonated upper aquifer (0.6 to 3 %), represented by the Hauptrogenstein Formation.

Grain densities obtained by helium pycnometry have a mean value of 2.74 g cm^{-3} in the Opalinus Clay overlying formations and of 2.72 g cm^{-3} in the argillaceous layer. Higher carbonate proportions and presence of sulphide minerals can explain higher density values (e.g. 2.71 g cm^{-3} for calcite, 2.83 g cm^{-3} for dolomite, 5.02 g cm^{-3} for pyrite). The lowest grain densities are found in the bituminous facies of the Staffelegg Formation (Rietheim Member), ranging between 2.3 and 2.4 g cm^{-3}. These low values are probably linked to the presence of organic matter.

The Passwang Formation, which directly overlays the Opalinus Clay, does not reveal clear petrophysical differences with the clay formation except for the specific surface area. This parameter has an average value of 13 m^2 g^{-1} in the carbonated section of the borehole and shows significant fluctuations linked to the marly composition of the Passwang Formation. A higher mean value of 29 m^2 g^{-1} characterises the Opalinus Clay.

The water accessible porosity is 13.0 % in the Opalinus Clay, lower than the mean value of 18 % suggested by previous studies performed at the tunnel level. The discrepancy may reflect the deconfinement and relaxation of stresses occurring in this perturbed zone. The Passwang Formation presents slightly lower porosity values ranging between 8.1 % and 14.6 % with a mean value of 12.2 %. The Hauptrogenstein is characterized by the lowest porosity with a mean value of 3.9 %.

Except for bulk densities, petrophysical parameters measured in the Opalinus Clay show lower values in the carbonated facies than in the shaly facies. Results are presented in Figure 3.9.
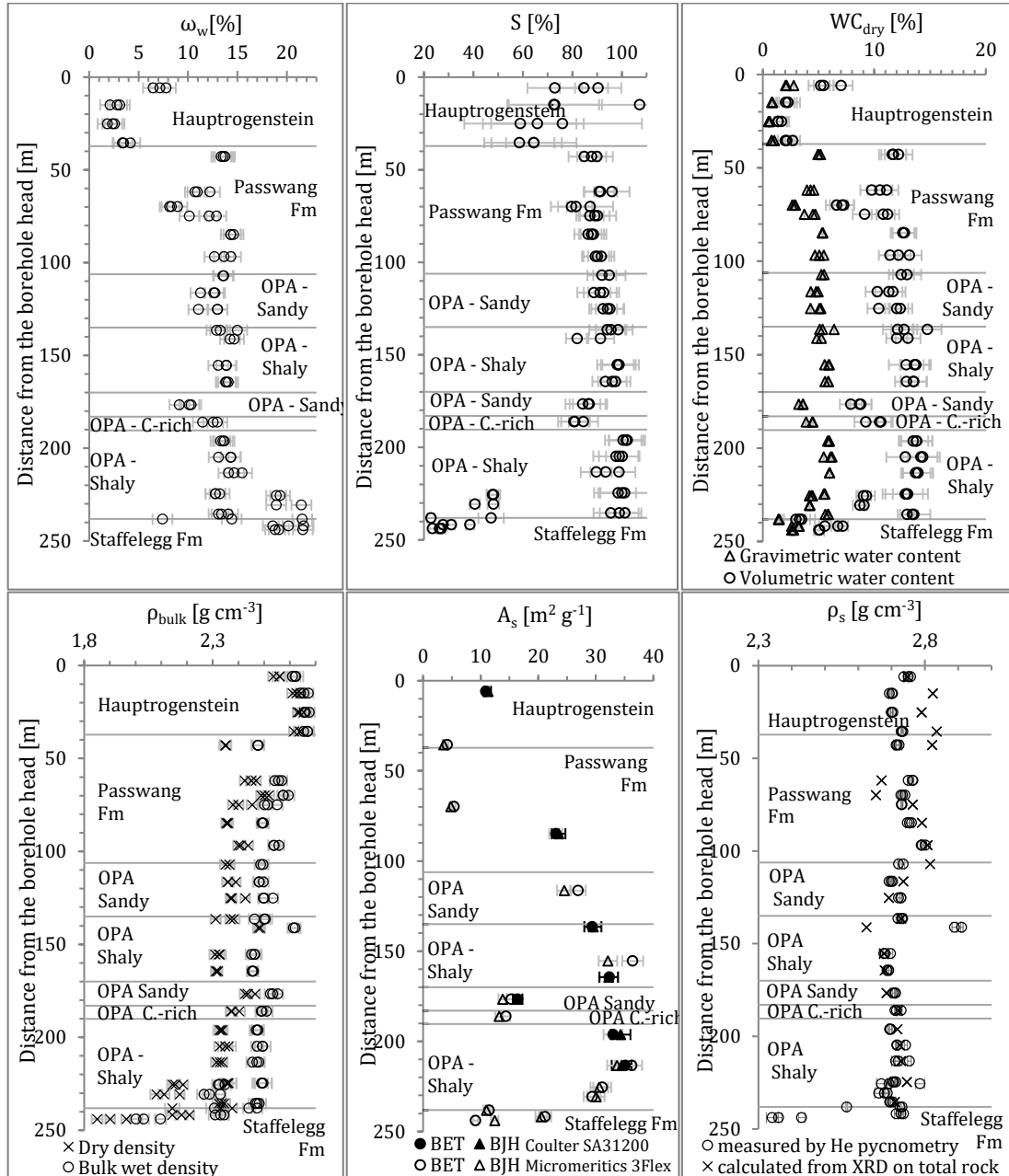
Figure 3.9: Profiles of petrophysical parameters acquired on BDB-1 borehole samples (water loss porosity ω_w, degree of saturation S, dry mass based water content WC_{dry}, bulk density ρ_{bulk}, specific surface area A_s, grain density ρ_s).

The Opalinus Clay is also characterised by a low pore size. The analysis of nitrogen adsorption and desorption isotherms revealed that 70 to 93 % of the connected porous network is constituted of mesopores (pore diameter between 2 and 50 nm), with a mean size of 13 nm (Figure 3.10). Calculation of the half-pore size from petrophysical parameters, following Equation (1.33), reveals mean pore sizes in the range of 3.11 to 7.28 nm.
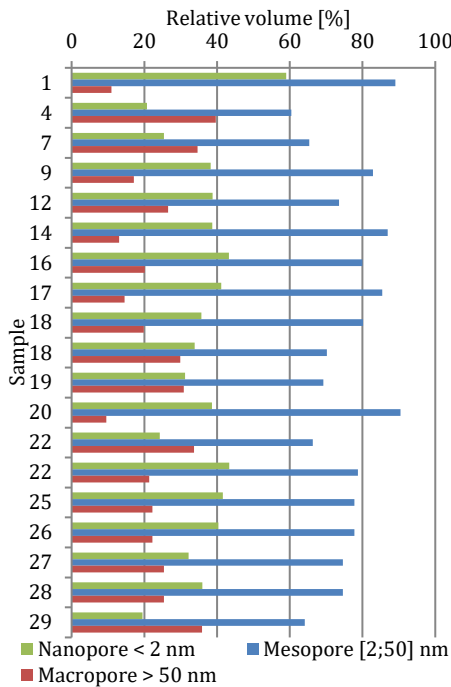
Figure 3.10: Pore relative volume distribution measured by BJH on BDB-1 samples
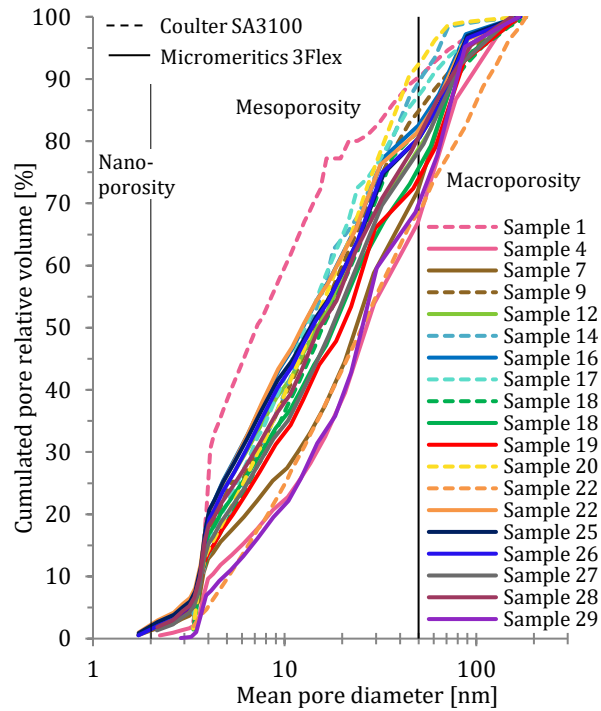
Figure 3.11: Cumulated pore relative volume measured by BJH on BDB-1 samples

Petrophysical parameters obtained on BDB-1 borehole samples are globally in good agreement with the results reported in the literature (Table 3.7).

Table 3.7: Comparison of the Opalinus Clay petrophysical characteristics obtained from several studies at the Mont Terri underground laboratory

	Previous studies (Bossart, 2011)		DB experiment (this study)	
Parameter	Range	Mean	Range	Mean
Bulk saturated density [g cm^{-3}]	2.40 – 2.53	2.45	2.45 – 2.62	2.47 ± 0.024
Bulk dry density [g cm^{-3}]	2.28 – 2.32	2.31	2.31 – 2.48	2.33 ± 0.022
Grain density [g cm^{-3}]	2.70 – 2.77	2.74	2.67 – 2.91	2.72 ± 0.0057
Water content [saturated weight %]	5.0 – 8.9	6.6	3.1 – 6.0	4.90 ± 0.0066
Water content [dry weight %]	5.3 – 9.8	7	3.22 – 6.4	5.16 ± 0.0073
Porosity, total physical [vol%]	14.0 – 24.7	18.3	9.1 – 21.5	14.1 ± 0.97
Specific surface area [m^2 g^{-1}]	24 - 37	31	15 – 35	29 ± 5

3.4. NATURAL TRACERS CONCENTRATIONS

3.4.1. ANION CONCENTRATIONS

The effects of several leaching parameters were tested on the Opalinus Clay shaly facies (sample 16) and its sandy facies (sample 18).

Halides and sulphate concentrations obtained in aqueous leachates with different leaching solutions, contact times and grains sizes are presented in Figure 3.12. The experiments revealed that a contact time of 2 hours is sufficient, since it gives similar results to those obtained by stirring the samples for 24 hours and 48 hours.

The use of carbonate-saturated water did not change significantly the obtained concentrations in leachates. Therefore, dissolution of carbonate mineral phases seems to have limited impact on the porewater elements that are studied, supporting that halides and sulphate are free elements in the experiment set-up.

The Br^-/Cl^- molar ratios virtually correspond to seawater ratio of $1.52 \cdot 10^{-3}$ (Fontes and Matray, 1993). SO_4^{2-}/Cl^- ratios are four times higher than the $5.16 \cdot 10^{-2}$ seawater ratio for the two considered samples (Figure 3.13), even though particular care was given to avoid reactions leading to sulphate release in the pore water.

Sample 16 (Opalinus Clay shaly facies)

Sample 18 (Opalinus Clay sandy facies)
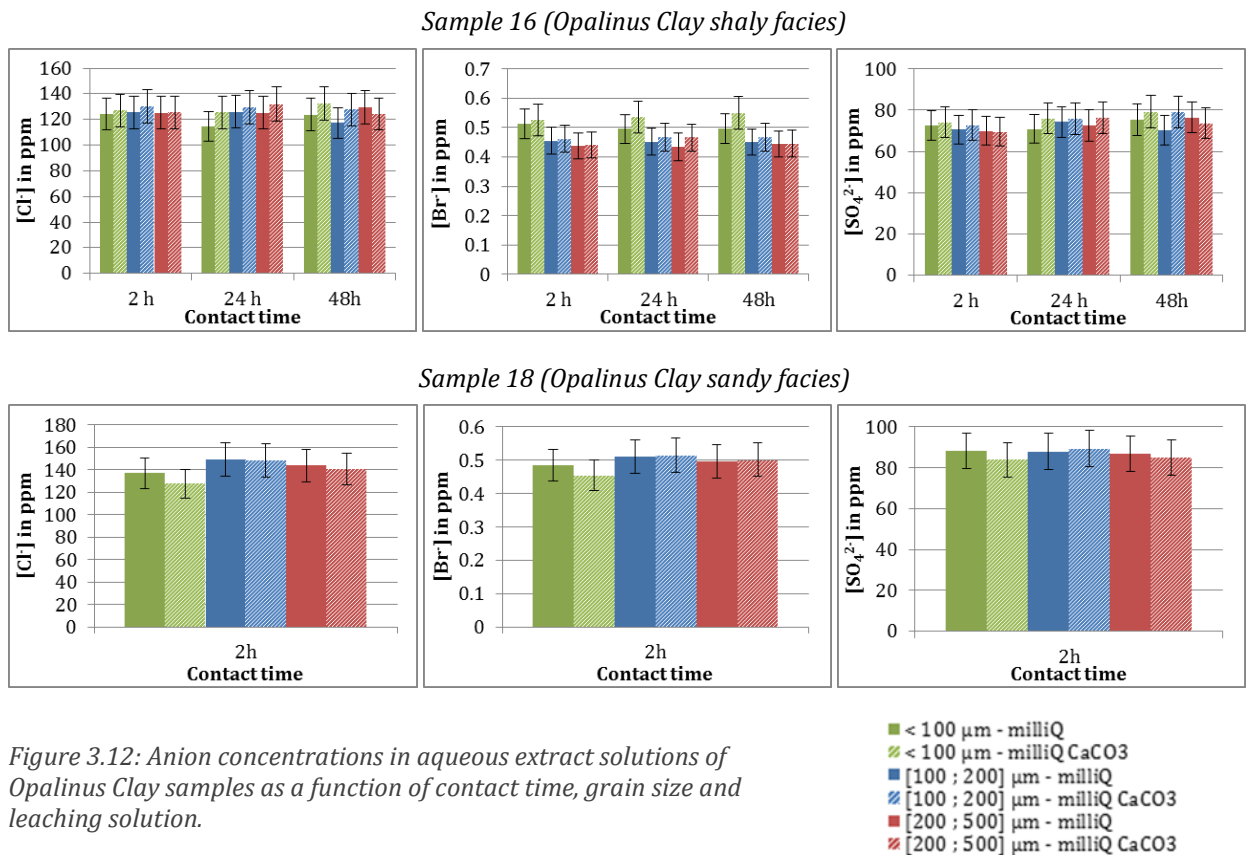
Figure 3.12: Anion concentrations in aqueous extract solutions of Opalinus Clay samples as a function of contact time, grain size and leaching solution.
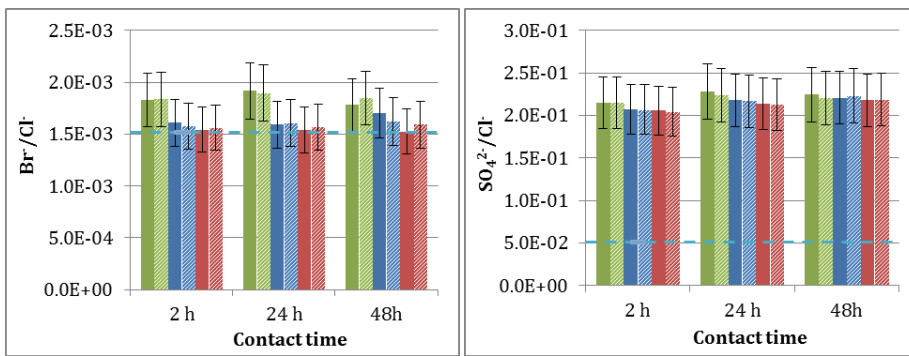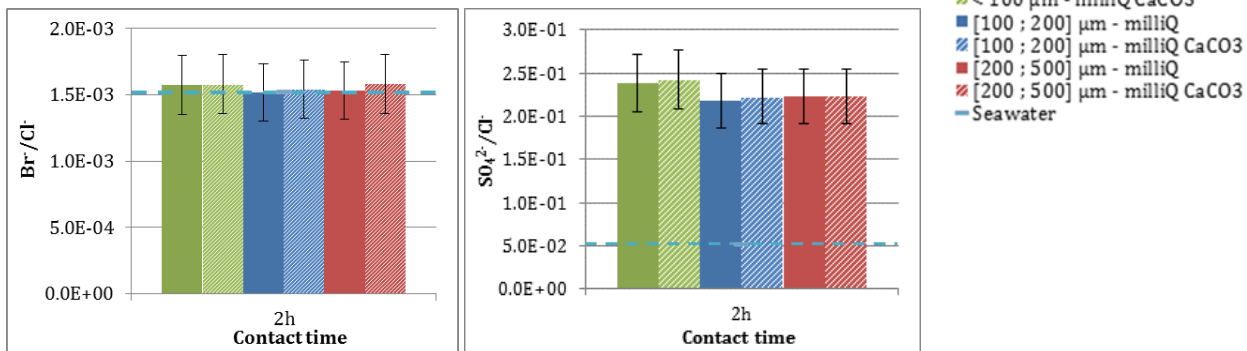
- < 100 μm - milliQ
- < 100 μm - milliQ CaCO3
- $[100 ; 200]$ μm - milliQ
- $[100 ; 200]$ μm - milliQ CaCO3
- $[200 ; 500]$ μm - milliQ
- $[200 ; 500]$ μm - milliQ CaCO3

Sample 16 (Opalinus Clay shaly facies)

Sample 18 (Opalinus Clay sandy facies)

Figure 3.13: Anion molar ratios in aqueous extract solutions of Opalinus clay samples as a function of contact time, grain size and leaching solution.

The plots of the anion concentrations of the leachates against their solid to liquid ratios are presented in Figure 3.13. The logarithmic scale is used as concentrations show a wide range of values. Linear regression lines have been calculated for each solute and are also shown in the figures with their equations and correlation coefficients. Concentrations and solid to liquid ratios are strongly correlated for halides and sulphate whereas the linear behaviour is less strong for fluoride. This element seems to have a constant concentration when solid to liquid ratio gets superior to 0.33 (Figure 3.14).

Sample 16 (Opalinus Clay shaly facies)   *Sample 18 (Opalinus Clay sandy facies)*
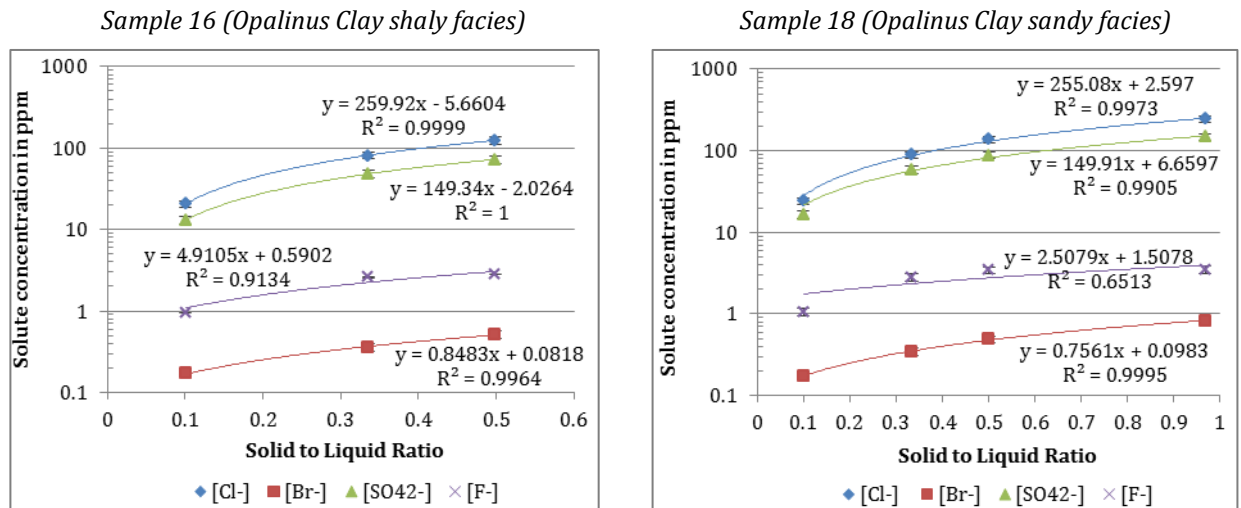
Figure 3.14: Anion concentrations in aqueous extract solutions of Opalinus clay samples as a function of solid to liquid ratios.

Chloride, bromide and sulphate profiles acquired by leaching and out diffusion experiments on BDB-1 samples are presented in Figure 3.15 and confirm the vertical variability of porewater composition along the sedimentary column.

Chloride is the major anion with concentrations obtained by leaching experiments ranging from 2.5 ± 0.26 g L^{-1} to 16.1 ± 1.7 g L^{-1} in the Opalinus Clay. Out diffusion experiments give a range between 2.1 ± 0.3 g L^{-1} and 14.4 ± 1.0 g L^{-1} for chloride contents. Maximum concentrations are found in the basal shaly facies. Bromide and chloride concentrations are characterised by a similar bell-shaped curve profile. The depth profile of bromide shows scatter possibly due to the difficulty to quantify low bromide concentrations by ionic chromatography. High chloride contents found by leaching experiments in the calcareous lithologies (Hauptrogenstein and Passwang Formation) are probably due to the decrepitation of saline fluid inclusions during crushing of the rock. Aqueous extraction by leaching also provides higher concentrations than those evaluated by out diffusion in the clay-rich lithologies, indicating that the liberation of chloride from additional reservoir during the leaching experiments may also be considered in the Opalinus Clay.

Bensenouci (2010) performed leaching experiments as well as radial diffusive exchange on Tournemire clay rock samples (France), and also found that anion concentrations obtained from leaching were higher than those calculated from radial diffusion or determined on fracture fluids. The same analysis has been echoed by Bachir-Bey (2013), who acquired concentrations by leaching three times higher than those obtained by out diffusion.

In leaching experiment, samples are reduced to a low grain size (< 100 μm) and put into contact with pure water. This extraction process: i) highly increases the reactive surface area; potentially ii) opens closed porosity which can contains fluid inclusions; iii) induces release of elements from mineral dissolution. Although diffusion experiments require a longer period of implementation than leaching tests, this method should be preferred for the analysis of porewater composition, as it has a non-destructive design.
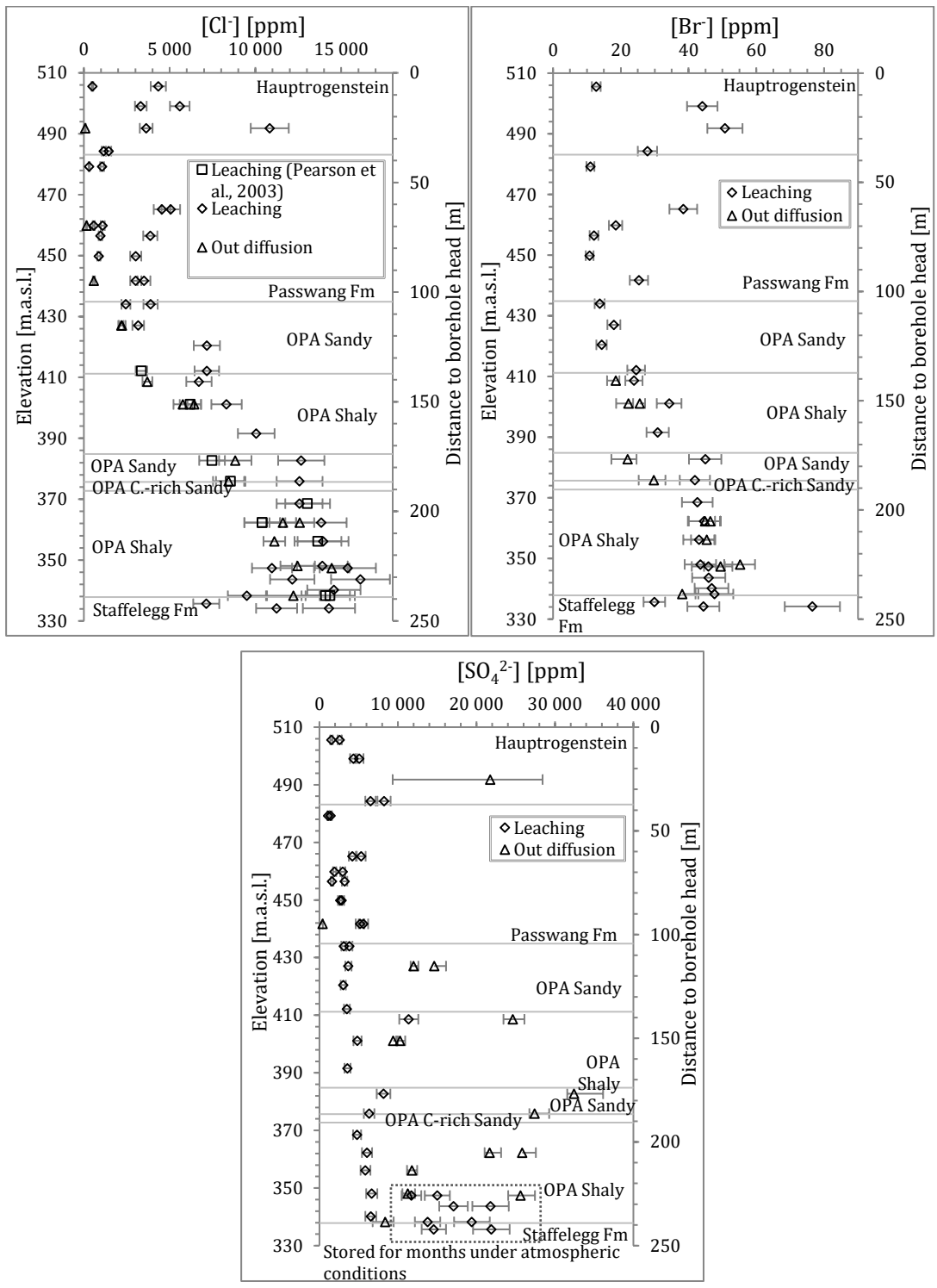
Figure 3.15: Chloride, bromide and sulphate profiles acquired along BDB-1 borehole

Sulphate profile along BDB-1 borehole also shows an increasing trend with depth, but even when extraction was performed under anoxic conditions, oxidation had a major effect on measured concentrations. Moreover, sample storage for samples in the deepest part of the borehole, under atmospheric conditions prior to processing and analysis led to large overestimations of sulphate concentrations in porewater. The rock being the main reservoir of sulphur in the water-rock system, even a minor contribution of mineral dissolution such as pyrite or traces of sulphur minerals has a major impact on concentrations in solution.

Results of leaching and out diffusion experiments on BDB-1 borehole samples, reported in Annex II.2, are globally consistent with those obtained so far at the Mont Terri tunnel level (Pearson et al., 2003) from leaching, squeezing and analyses of borehole waters. Previous studies also concluded to a maximum value for chloride content (from 13.6 to 14.4 g L^{-1}) found at the limit between the Opalinus Clay and the Staffelegg Formation.

Halide concentration ratios are consistent with a marine origin of the Opalinus Clay porewater (Figure 3.16). Sulphate to chloride ratios are much higher than the marine ratio, due to a clear overestimation of sulphate contents following oxidation during sampling and processing.
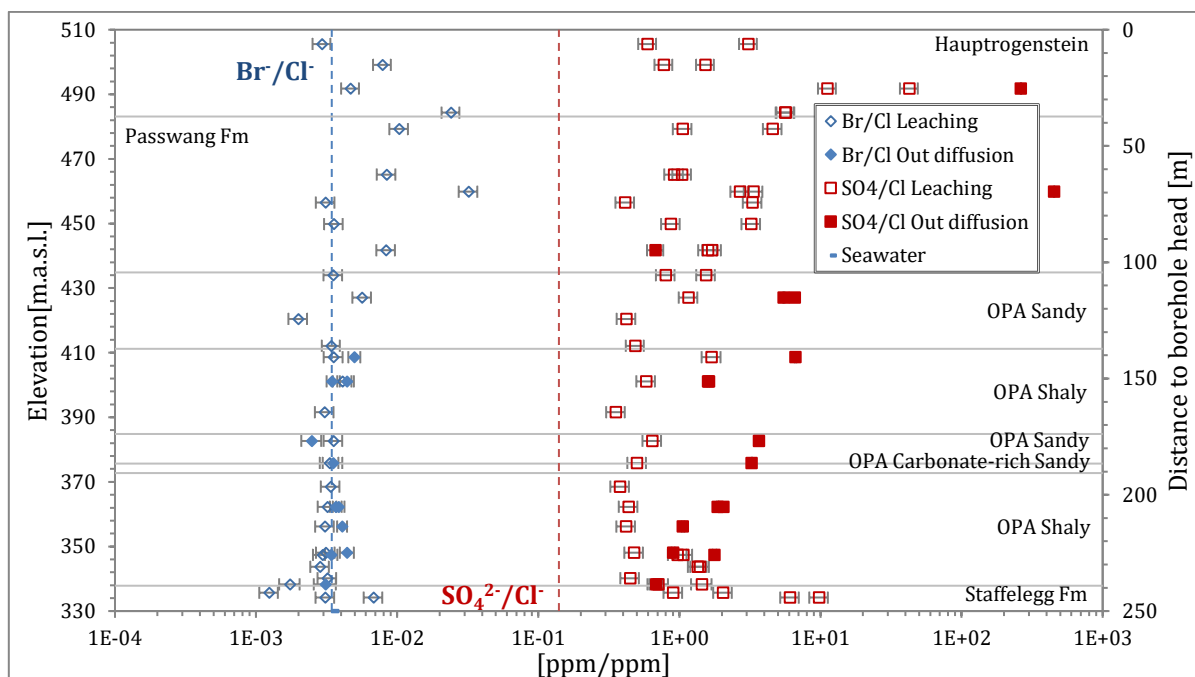
Figure 3.16: Anion massic ratios in porewater acquired by leaching and out diffusion experiments on BDB-1 samples

An inter-comparison of chemical and isotopic pore-water compositions determined by different laboratories using a variety of techniques was performed within the DB-A Experiment. The obtained chloride and bromide profiles are shown in Figure 3.17. Out diffusion experiments gave more consistent results than leaching experiments, compared to aqueous leaching. A coarser grain size (> mm) should be used to obtain more reliable values, in order to limit the contribution of anion sources other than connected porewater. More detailed results and interpretation on the inter-comparison can be found in Mazurek et al. (2016).
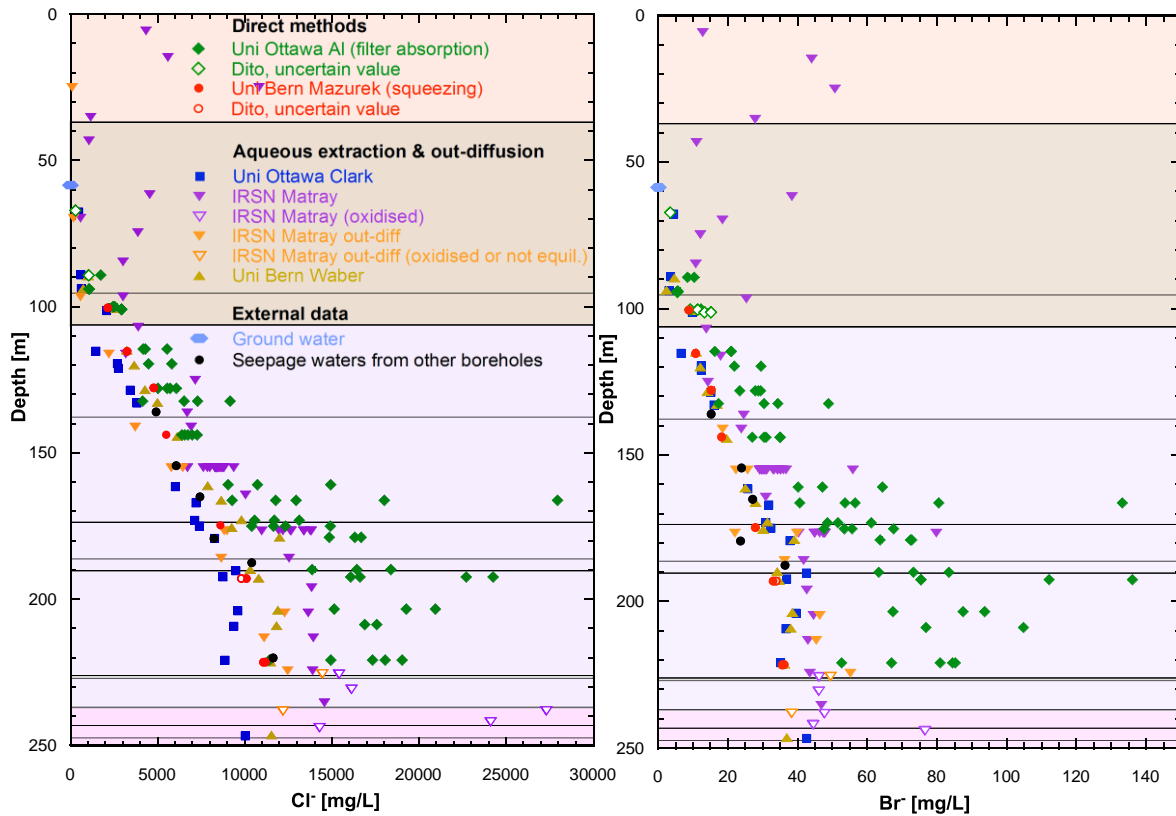
Figure 3.17: Chloride and bromide concentrations in anion-accessible porewater based on direct and indirect extraction techniques, groundwater and in porewater obtained by long-term in-situ sampling elsewhere in the rock laboratory (Mazurek et al., 2016)

3.4.2.   STABLE ISOTOPES CONCENTRATIONS

Within the DB-A Experiment, vacuum distillation at 150 °C, diffusive isotope exchange and squeezing were performed on BDB-1 samples at the University of Bern (Switzerland) and the University of Ottawa (Canada) to obtain stable water isotopes profiles (Figure 3.18). Diffusive exchange and squeezing methods enabled the acquisition of consistent, smooth, lithology independent and bell-shaped profiles, with data fitting well along the meteoric line (Figure 3.19). These profiles were used to prepare synthetic solutions for radial diffusion experiments.
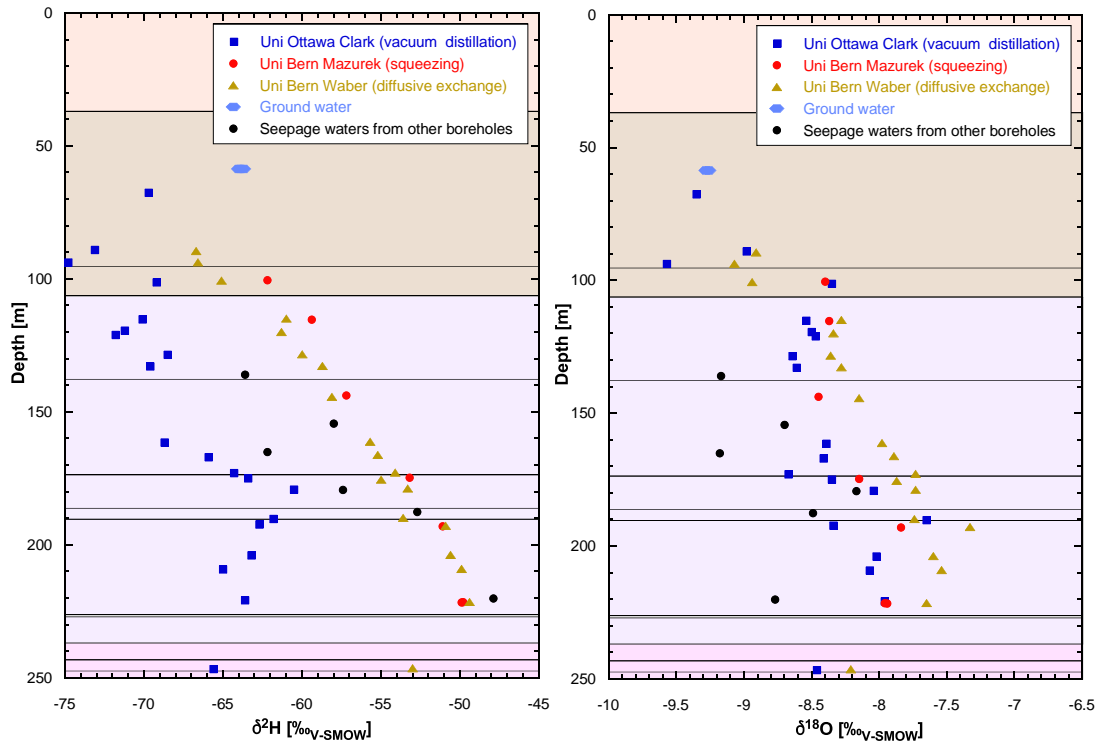
Figure 3.18: Profiles of δ²H and δ¹⁸O in porewater acquired on BDB-1 samples (Mazurek et al., 2016)
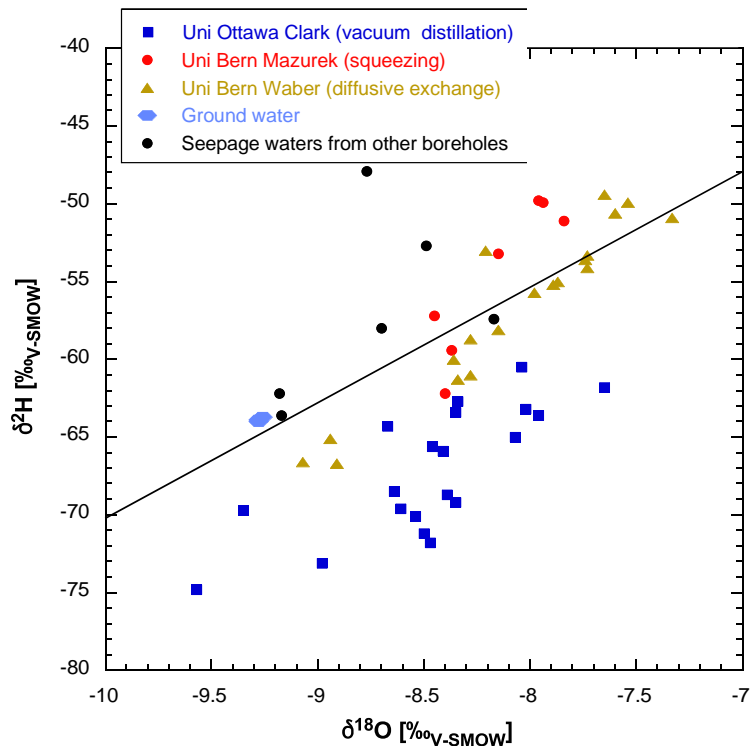
Figure 3.19: δ²H vs δ¹⁸O in porewater acquired on BDB-1 samples (Mazurek et al., 2016). Local meteoric water line (δ²H = 7.55 δ¹⁸O + 4.8) according to Kullin and Schmassmann (1991)

3.5. CATION EXCHANGE CAPACITY

3.5.1. CEC RESULTS

Results of CEC calculations using either cobaltihexamine chloride (Cohex) or cesium chloride are presented in Figure 3.20 and in Annex II.3. For most of the samples, the sum of exchanged cations is inferior to the amount of consumed highly selective cations. The uncertainties calculated by error propagation are higher for the CEC based on index cation than the one based on sum of exchanged cations, since the initial solutions are quite concentrated.

The highest discrepancies are associated to the use of cobaltihexamine as extractant. Indeed, consumption of cobaltihexamine quantified by ICP-AES can reach twice the sum of cations originally present onto the clay sites with values between 0.92 ± 3.62 and 21.11 ± 2.69 meq $100g^{-1}$. The analytical technique enables the measurement of total cobalt which should correspond to the quantity of Cohex ions. The overestimation is probably related to enhanced complexation reaction between cobaltihexamine and organic matter.

Given the relative consistency between CEC values obtained with cesium chloride (index cation based and sum of cations based) and the sum of exchanged cations using cobaltihexamine chloride, the estimation based on cobalt concentrations cannot be considered as representative of the CEC.
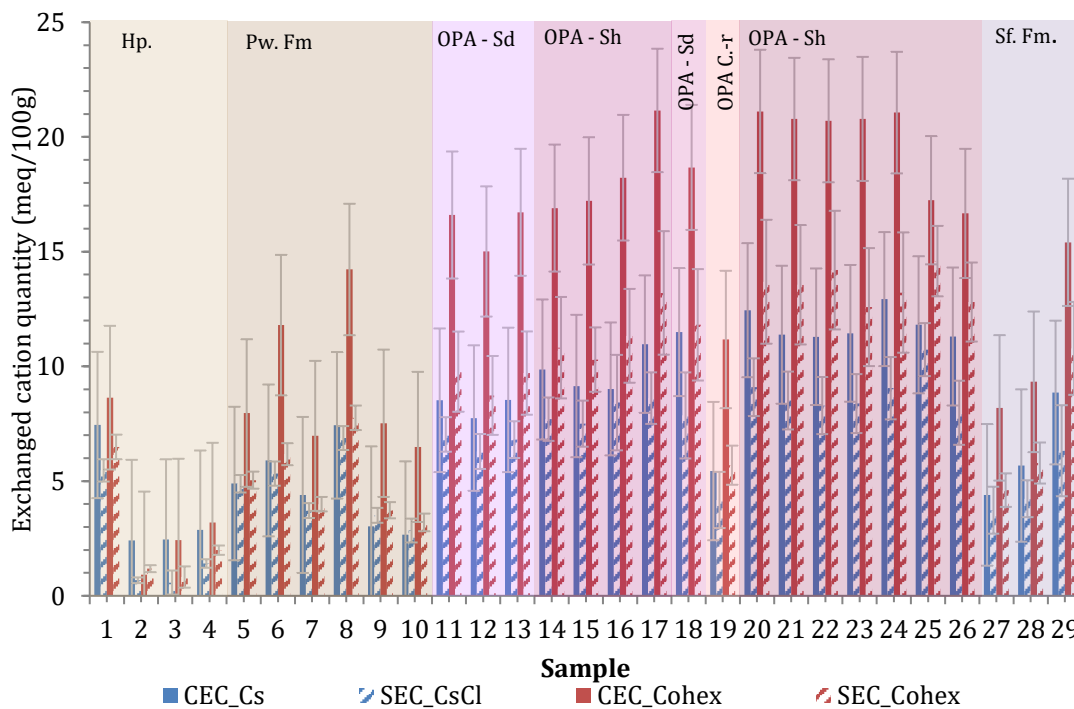
Figure 3.20: Cationic exchange capacity calculated from displacement of highly selective cation

The CEC is positively correlated with the total clay content of the samples. Indeed, the lowest values are observed in the Middle Jurassic carbonates and in the Staffelegg Formation (CEC_{sum} from 1.18 ± 0.15 to 10.51 ± 1.98 meq 100g^{-1}). Based on cesium consumption, the basal shaly facies of the Opalinus Clay is characterised by the highest values of CEC, between 11.3 ± 3.0 to 12.93 ± 2.9 meq 100g^{-1}, with an associated sum of exchanged cations ranging from 7.87 ± 1.40 to 10.65 ± 1.16 meq 100g^{-1}. These values are consistent with the mean CEC value of 11.1 meq 100g^{-1} reported in the literature (Bossart, 2011). Results are quite homogeneous in the Opalinus Clay except in the carbonate-rich facies, where the quantity of exchanged cations is lower (CEC_{sum} of 3.93 ± 0.75 meq 100g^{-1} and CEC_{Cs} of 5.39 ± 3.34 meq 100g^{-1}).

3.5.2. SELECTIVITY COEFFICIENTS

Figure 3.21 shows the calculated cation occupancies obtained along the BDB-1 borehole. The largest cation inventory is for calcium in all investigated samples, followed by sodium. Sodium occupancy is lower than the range of 3.61 to 6.37 meq 100g^{-1} reported in literature (Bossart, 2011), with a mean value of 1.87 ± 0.32 meq 100g^{-1} for the Opalinus Clay shaly facies. Magnesium inventories determined with cobaltihexamine are higher than the ones acquired with cesium chloride. This could be related to a preferential exchange of cobaltihexamine with magnesium from brucite layers (Mg(OH)$_2$) in chlorites (Waber et al., 2003). Indeed, brucite shows high sorption properties in relation to ions of heavy metals in aqueous medium.

Mean values of individual cation occupancies and fractional cation occupancies obtained for each facies encountered along the BDB-1 borehole are reported in Table 3.9 and Table 3.10. The values obtained are quite different from results of previous studies (Table 3.8). Indeed, sodium fractional occupancies are lower and calcium is correspondingly higher.

Table 3.8: Exchangeable cation populations and total cation exchange capacities measured on sample from Mont Terri (Pearson et al., 2003)

		UniBern		PSI	CIEMAT		BRGM		
		<0.2 mol Cl$^-$							Without NH$_4^+$
		Mean	SD		Mean	SD	Mean	SD	
K$^+$	meq kg rock^{-1}	7.9	1.1	5.4	8.4	0.6	15.5	0.4	15.5
NH$_4^+$	meq kg rock^{-1}						34.9	15.8	
Na$^+$	meq kg rock^{-1}	58.5	7.3	48.1	28.7	3.7	56.6	2.3	56.6
Ca^{2+}	meq kg rock^{-1}	32.3	4.9	25.4	56.2	4.1	34.9	2.4	34.9
Mg^{2+}	meq kg rock^{-1}	21.5	2.5	15.6	24.4	1.5	27.4	2.1	27.4
Sr^{2+}	meq kg rock^{-1}	1.2	0.2	0.0	0.8	0.1			
Total CEC	meq kg rock^{-1}	121.4	15.8	94.5	118.3	10.0	169.2	9.3	134.4
K+	Equ. fraction	0.07	0.01	0.06	0.07	0.01	0.09	0.00	0.12
NH$_4^+$	Equ. fraction						0.21	0.10	
Na$^+$	Equ. fraction	0.48	0.06	0.51	0.24	0.03	0.33	0.01	0.42
Ca^{2+}	Equ. fraction	0.27	0.04	0.27	0.48	0.04	0.21	0.01	0.26
Mg^{2+}	Equ. fraction	0.18	0.02	0.17	0.21	0.01	0.16	0.01	0.20
Sr^{2+}	Equ. fraction	0.010	0.002		0.007	0.001			

Figure 3.21: Individual cation occupancies (Ca²⁺, Na⁺, Mg²⁺, K⁺, Sr²⁺) obtained by exchange with cesium chloride (CsCl) solution and cobaltihexamine chloride (CoHex) solution on BDB-1 borehole samples.

Table 3.9: Mean values of exchangeable cation populations acquired on BDB-1 borehole samples by exchange with a cesium chloride solution.

Formation	meq·kg$_{rock}^{-1}$							% cation occupancies - Index cation based CEC					% cation occupancies - Cation sum based CEC				
	Na	K	Mg	Ca	Sr	Sum	Cs	Na	K	Mg	Ca	Sr	Na	K	Mg	Ca	Sr
Hauptrogenstein	0.3±0.1	2.1±0.2	2.4±0.9	15.4±1.6	0.1±0.0	20.3±1.9	37.9±17.1	1.0±0.8	4.6±2.6	5.9±3.4	33.6±17.4	0.4±0.3	3.2±1.8	9.8±2.4	5.4±13.3	80.7±30.3	0.9±0.2
Passwang Fm.	1.5±0.7	7.2±0.4	8.2±0.9	26.3±1.2	2.5±0.1	45.7±1.7	46.1±13.8	3.0±2.7	17.2±8.7	18.0±7.9	62.3±33.7	5.6±2.8	5.1±1.8	16.0±1.1	17.4±2.0	58.2±3.5	5.3±0.3
OPA - Sandy	8.3±3.8	11.4±0.8	10.9±1.05	34.0±2.0	2.1±0.1	66.7±4.5	82.7±18.2	10.0±5.1	13.8±3.2	13.2±3.2	41.1±11.2	2.5±0.6	12.4±5.8	17.1±1.6	16.4±1.9	51.0±4.5	3.1±0.3
OPA - Shaly	14.4±4.7	13.2±0.7	12.3±1.0	37.5±1.9	1.6±0.1	66.7±5.2	82.7±15.2	14.1±5.1	13.1±2.1	12.3±2.2	37.1±5.9	1.6±0.3	18.0±6.1	16.7±1.4	15.7±1.7	47.5±3.9	2.1±0.2
OPA - Sandy	15.2±9.7	12.5±1.4	9.5±1.6	35.3±3.5	1.4±0.1	74.0±10.5	97.6±30.7	15.6±11.1	12.8±4.3	10.2±6.6	36.2±12.0	1.4±0.5	20.6±13.4	16.9±3.0	12.9±2.8	47.7±8.3	3.0±1.9
OPA - Carbonate rich	3.0±7.1	0.3±0.6	5.5±1.0	23.2±2.4	1.4±0.1	39.3±7.53	53.9±33.4	5.6±13.5	11.5±7.2	9.9±1.1	43.0±27.0	2.6±1.7	7.6±18.0	15.7±3.6	14.0±3.6	59.0±12.8	2.7±3.6
OPA - Shaly	21.2±4.5	13.9±0.6	11.7±0.7	40.0±1.5	1.1±0.0	87.7±4.8	118.0±11.2	17.9±4.2	11.8±1.2	9.9±1.1	9.2±3.5	1.0±0.1	23.6±5.4	15.9±1.1	13.3±1.1	45.9±3.2	1.1±1.3
Staffelegg Fm.	-	6.9±0.7	5.9±3.3	34.9±3.8	0.6±0.1	46.0±7.5	65.7±18.9	-	11.1±4.0	9.6±5.1	26.5±15.3	0.9±0.3	-	16.0±2.5	13.8±5.7	20.4±13.0	1.3±0.2

Table 3.10: Mean values of exchangeable cation populations acquired on BDB-1 borehole samples by exchange with a cobaltihexamine chloride solution.

Formation	meq·kg$_{rock}^{-1}$							% cation occupancies - Index cation based CEC					% cation occupancies - Cation sum based CEC				
	Na	K	Mg	Ca	Sr	Sum	Co	Na	K	Mg	Ca	Sr	Na	K	Mg	Ca	Sr
Hauptrogenstein	0.3±0.1	0.6±0.3	5.4±0.5	19.7±1.8	0.2±0.0	26.2±1.9	37.9±17.2	1.4±3.4	2.3±1.6	12.1±16.3	43.7±24.6	0.7±0.9	1.9±1.0	3.4±1.6	15.4±2.1	81.5±20.6	1.0±0.2
Passwang Fm.	1.2±0.7	3.5±0.5	15.1±0.7	27.2±1.3	2.9±0.1	49.9±1.69	91.6±12.9	1.3±0.9	3.9±0.9	15.7±2.6	30.4±5.2	3.1±0.5	2.5±1.8	7.2±1.2	28.6±1.6	56.0±3.3	5.6±0.3
OPA - Sandy	12.0±4.1	9.9±1.4	17.1±10.0	41.8±2.5	2.4±0.1	83.2±5.1	161.1±16.1	7.4±2.7	6.1±1.1	10.6±1.2	25.9±3.0	1.5±0.2	14.4±5.1	11.9±1.8	20.6±1.8	50.2±4.3	2.9±0.3
OPA - Shaly	20.5±5.2	12.6±1.5	20.9±1.1	46.2±2.4	2.1±0.1	102.1±6.0	183.7±13.7	11.0±3.0	6.9±1.0	11.4±1.1	25.1±2.3	1.1±0.1	19.8±5.2	12.4±1.6	20.5±1.6	45.2±3.5	2.0±0.2
OPA - Sandy	23.3±11.1	11.7±2.7	19.5±2.0	46.9±4.8	1.9±0.2	103.2±12.5	186.7±27.3	12.5±6.2	6.3±1.7	10.4±1.9	25.1±4.5	1.0±0.2	22.5±11.1	11.4±3.0	18.9±3.0	45.4±7.2	1.8±0.3
OPA - Carbonate rich	7.3±7.7	4.9±1.36	12.4±1.3	30.7±3.2	1.7±0.2	56.9±8.5	111.7±29.9	6.5±7.1	4.4±1.7	11.1±3.2	27.4±7.9	1.5±0.4	12.8±13.7	8.6±2.7	21.7±3.9	53.9±9.8	3.0±0.5
OPA - Shaly	32.2±5.2	13.8±1.2	21.8±0.8	54.2±2.1	1.5±0.1	123.5±5.8	197.7±10.3	16.6±2.9	7.0±0.7	11.3±0.8	27.7±3.4	0.8±0.1	25.9±4.5	11.2±1.1	17.6±1.1	44.0±2.9	1.3±0.1
Staffelegg Fm.	2.3±5.9	5.6±1.2	15.1±1.2	45.5±4.5	0.8±0.1	69.3±7.6	109.8±17.4	2.4±5.0	5.4±1.5	14.2±2.8	39.1±7.1	0.7±0.1	4.0±8.0	8.9±2.0	23.2±2.7	62.7±7.9	1.2±0.1

3.6. GEOCHEMICAL MODELLING

3.6.1. CONSTRAINTS TO MODEL POREWATER AT THE MONT TERRI SITE

Geochemical modelling is an indirect approach to obtain the porewater composition by considering it as a result of water-rock interactions. The characterisation of the geochemical system is based on selected properties of the rock and the solution (mineralogy, petrology, cation exchange properties, mobile anions concentrations, pH or CO_2 partial pressure).

Thermodynamic models for the porewater composition of Opalinus Clay were first developed by Bradbury and Baeyens (1997-1998, 1998) and Pearson et al. (2003) for the Mont Terri locality. A comprehensive review of the modelling approaches developed within the Mont Terri Underground Rock Laboratory scientific programs was given by Pearson et al. (2011). Modelling of porewater chemistry was performed on BDB-1 data with PhreeqC v.3.1.4., using the sit.dat thermodynamic database. The major constraints are summarised in Table 3.11.

Table 3.11: Models for porewater at the Mont Terri Underground Rock Laboratory (adapted from Pearson et al., 2011)

Parameter	Bradbury and Baeyens (1998)	Pearson et al. (2003)	Pearson et al. (2011)	Present study
Database	Pearson and Berner (1991); Pearson et al. (1992)	Nagra/PSI Hummel et al. (2002)	THERMODDEM http://thermoddem.brgm.fr/index.asp?langue=GB	sit.dat ~ANDRA ThermoChimie v7.b (Duro et al., 2007)
Cl	Fixed at average values measured in borehole samples			
S^{VI} (total)	Calculated using bulk rock content from leaching and several estimated values of anion-accessible porosity. Decreased as necessary to avoid gypsum oversaturation	Fixed at SO4/Cl ratio in seawater or calculated from celestite saturation and Na-Sr exchange	Fixed at SO4/Cl ratio in seawater	
Log[P_{CO2}]	Fixed at generic value; Carbonate species and TIC calculated from CO_3^{2-}, P_{CO2}, and carbonate equilibria	Fixed at generic value		
pH		Solution electroneutrality	Kaolinite, illite-Mg, Illite-ltm2, Mg-montmorillonite, chlorite, daphnite or siderite saturation	Solution electroneutrality
Eh,pe		SO_4^{2-}/S^{2-} couple at pyrite and siderite, goethite or Fe(OH)$_3$ (mic) saturation	SO_4^{2-}/S^{2-} couple at pyrite and siderite saturation	
Ca^{2+}	Na-Ca exchange	Calcite saturation	Na-Ca exchange	Calcite saturation
Mg^{2+}	Dolomite saturation	Dolomite saturation and Na-Mg exchange		
Na^+	Solution electroneutrality	Na-Ca exchange	Solution electroneutrality	
K^+	Na-K exchange			
Sr^{2+}		Na-Sr exchange	Celestite saturation	Na-Sr exchange and celestite saturation
Si	Chalcedony saturation	Quartz saturation		
F^-	Fluorite saturation			
Al		Kaolinite or halloysite saturation	Kaolinite, illite-Mg, Illite-Imt2, Mg-montmorillonite	
Fe^{2+}		Siderite, goethite or Fe(OH)$_3$ saturation	Siderite saturation	
U		UO$_2$(s) saturation		

Two models were chosen to describe cation exchange reactions on clay minerals: the one-site model used by Pearson et al. (2003) and the multi-site model developed by Tremosa et al. (2012a). According to the first one, all cation exchanges occur on an undifferentiated site, whereas the second one distributes the exchange reactions on different sites located on illite and smectite mineral phases. Following the multi-site model of Bradbury and Baeyens (2000), three classes of surface sites can be considered for cation exchange on illite. The "planar sites" (Xp) are linked to the fixed negative charge resulting of isomorphic substitution in tetrahedral and octahedral layers. These sites account for 80% of the illite exchange capacity and present a low affinity for cations. The "type-II sites" (Xii) and the "frayed-edge sites" (Xfes), located at the edge of the interlayer with "type-II sites" in the wedge, are high affinity sites with respective distributions of approximatively 80% and 0.25% of the illite total CEC. For steric reasons, only monovalent cations exchange on the latter sites. A fourth site with low affinity and high capacity (Z) is considered on smectite phase. Selectivity coefficients for the exchange reactions are reported in Table 3.12.

Table 3.12: Exchange reactions for the different site classes for illite and smectite considered in the models and their associated selectivity coefficients in the Gaines and Thomas (1953) convention.

Exchange reaction	Log K	Reference
One site model		
$NaXp + K^+ = KXp + Na^+$	0.70	Appelo and Postma (1993)
$2NaXp + Ca^{2+} = CaXp_2 + 2Na^+$	0.80	Appelo and Postma (1993)
$2NaXp + Mg^{2+} = MgXp_2 + 2Na^+$	0.60	Appelo and Postma (1993)
$2NaXp + Sr^{2+} = SrXp_2 + 2Na^+$	0.91	Appelo and Postma (1993)
Multi-site model		
Illite planar site Xp		
$NaXp + K^+ = KXp + Na^+$	1.11	Bradbury and Baeyens (2000)
$2NaXp + Ca^{2+} = CaXp_2 + 2Na^+$	1.04	Baeyens and Bradbury (2004)
$2NaXp + Mg^{2+} = MgXp_2 + 2Na^+$	1.04	Baeyens and Bradbury (2004)
$2NaXp + Sr^{2+} = SrXp_2 + 2Na^+$	1.44	Missana et al. (2008)
Ilite type II site Xii		
$NaXii + K^+ = KXii + Na^+$	2.1	Bradbury and Baeyens (2000)
Illite frayed-edge-site Xfes		
$NaXfes + K^+ = KXfes + Na^+$	2.4	Bradbury and Baeyens (2000)
Smectite site Z		
$NaZ + K^+ = KZ + Na^+$	0.82-0.88	Tournassat et al. (2009)
$2NaZ + Ca^{2+} = CaZ_2 + 2Na^+$	0.53-0.7	Tournassat et al. (2009)
$2NaZ + Mg^{2+} = MgZ_2 + 2Na^+$	0.47-0.62	Tournassat et al. (2009)
$2NaZ + Sr^{2+} = SrZ_2 + 2Na^+$	0.14-0.19	Tournassat et al. (2009)

The determination of the amount of each type of exchange site includes a first calculation of the proportion of illite and smectite, based on rock contents measured by XRD in illite and illite/smectite (I/S) mixed layers. It was assumed that there is 80% of illite in the I/S mixed layers, in accordance to results presented in Section 3.2.2, and that the charge of smectite and illite are respectively 0.75 and 0.2 $mmol_c$ kg^{-1} (Tournassat et al., 2009). The total amount of exchange sites, represented by the measured CEC, is converted from charges per mass of rock to charges per mass of porewater accounting for porosity and grain density. The amount of each

type of exchange sites is obtained by combining the proportion of charges associated with illite and smectite and the total amount of exchange sites. Eventually, the exchanger composition is calculated for the considered cations (Na^+, K^+, Ca^{2+}, Mg^{2+}, Sr^{2+}) with the fractional occupancies.

Anions contents were fixed based on the marine SO_4^{2-}/Cl^- ratio and the laboratory measurements of chloride concentrations obtained by out diffusion experiments. The partial pressure of CO_2 was fixed at $10^{-2.2}$ bars, as in Nagra (2002), and controls the pH with calcite equilibrium. Pyrite and siderite were included in order to calculate the redox potential. Thermodynamic equilibrium with calcite, dolomite, quartz, and celestite was enforced after initialising the solutions with ion exchanges. Calculations were performed at temperatures extrapolated from measurements in BDB-1 borehole (12.2 to 21.6 °C), although there is a lack of temperature dependency coefficients available in the thermodynamic database.

3.6.2. RESULTS AND SENSITIVITY ANALYSIS

Figure 3.22 and Figure 3.23 are Schoeller diagrams that compare the modelling results in the OPA shaly facies and the composition of borehole samples measured at the rock laboratory level. Na^+ is the dominant cation and is followed by Ca^{2+} and Mg^{2+}. While Na+ balances virtually the entire Cl^- charge in borehole samples, modelling gives lower concentrations of Na^+ and higher concentrations of Ca^{2+}. This discrepancy is probably linked to the higher selectivity coefficient for Na-Ca exchange obtained by CEC measurements on BDB-1 samples. The one-site model tends to heighten the phenomena and also gives higher contents of K^+ compared to the multi-site model. The concentration in K^+ is sensitive to illite proportion in I/S mixed layers, as it slightly decreases when increasing the proportion from 70% to 80%. This observation supports the importance of illite high affinity sites for the adsorption of monovalent cations. Retrieving dolomite and siderite as equilibrium phases lowers the resulting concentration in K^+.
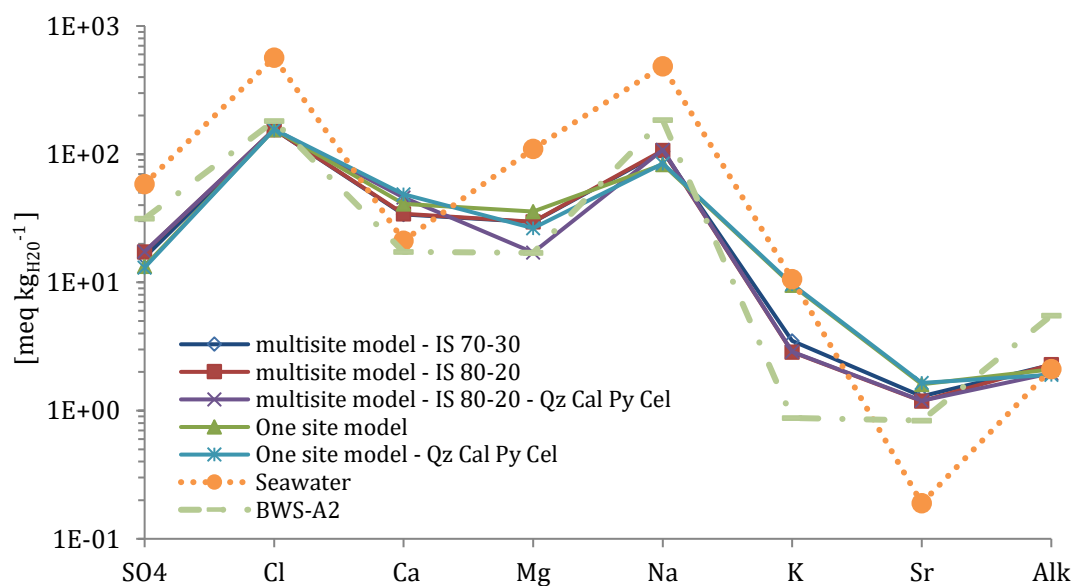
Figure 3.22: Schoeller diagram illustrating modelled compositions with different constraints of OPA top shaly facies porewater
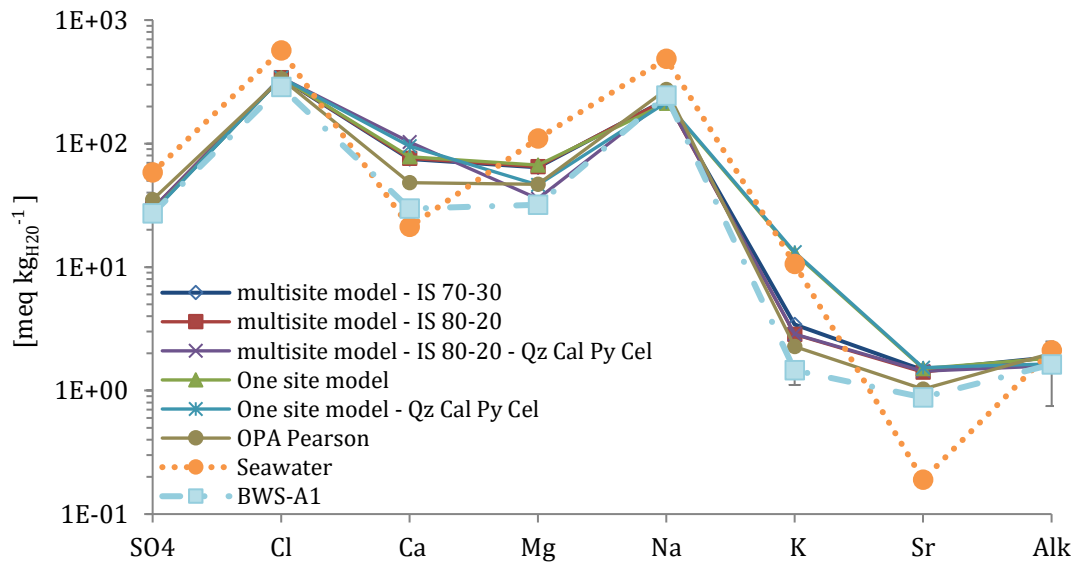
Figure 3.23: Schoeller diagram illustrating modelled compositions with different constraints of OPA basal shaly facies porewater

The porewater composition profile obtained along BDB-1 borehole using the multi-site model is presented in Figure 3.24. The modelled pH ranges between 6.93 in the Staffelegg Formation and 7.37 in the Passwang Formation, which is consistent with the critical range of 6.80 to 8.17 reported in the literature Nagra (2002). Except for K^+, ion concentrations tend to increase with depth and a slight variation is observed at the carbonate-rich sandy facies level, where Ca^{2+}, Mg^{2+} and Sr^{2+} contents increase with a higher slope.
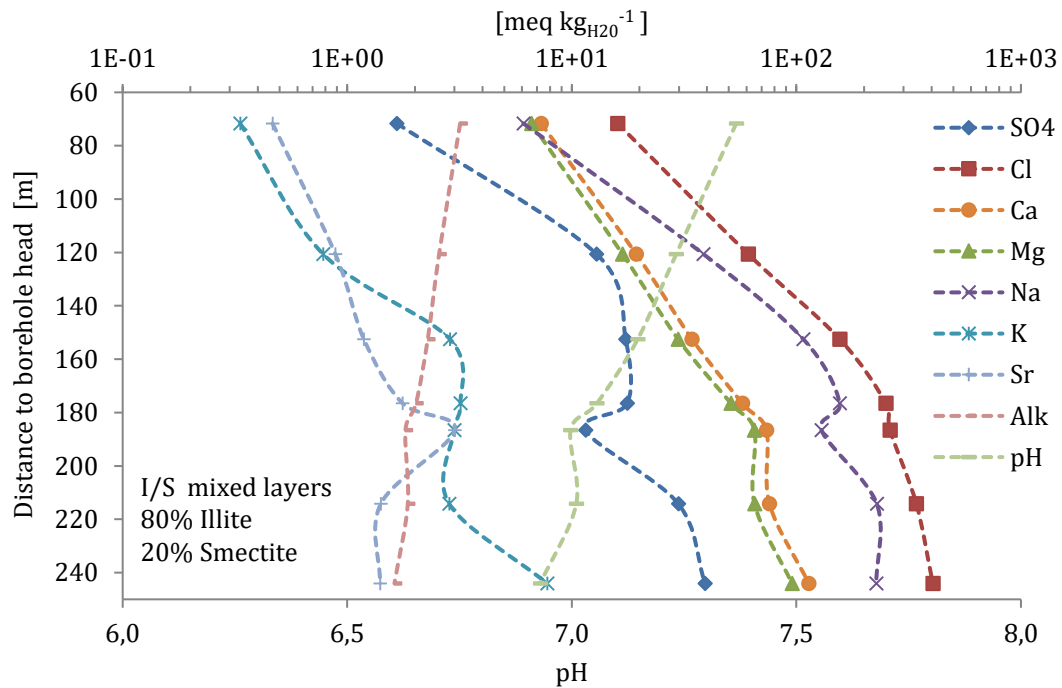
Figure 3.24: Porewater composition profile across the BDB-1 borehole deduced from the multi-site model by using measured clay-rock parameters.

3.7. ACCESSIBLE POROSITIES AND DIFFUSION COEFFICIENTS

The results presented in this section were obtained by fitting experimental data of diffusion experiment numerically with HYTEC v.3.6 (out diffusion and through diffusion experiments) or semi-analytically with the computer algebra program Mathematica v.5.2 (radial diffusion experiments). The fitting plots and complete result tables can be found in Annex III.

3.7.1. ACCESSIBLE POROSITIES TO ANIONS AND WATER STABLE ISOTOPES

Diffusion accessible porosities obtained on BDB-1 samples are reported in Figure 3.25.

Except for the carbonate-rich sandy facies, porosity values obtained by radial diffusion for stable water isotopes in the Opalinus Clay (up to 22 %) are higher than the values obtained by density measurements (maximum value of 15 %). Sample preparation steps, such as drilling, may bring additional porosity by creating microcracks. Values obtained for ^2H and ^{18}O are globally comparable and the anion exclusion (ratio of anion to water accessible porosities) is in the range of 51 % to 55 % in the OPA shaly facies and between 45 % and 51 % in the sandy facies.

Chloride and bromide diffusion accessible porosities are also comparable with values comprised between 6 % and 12 % with a best estimate at 8%.
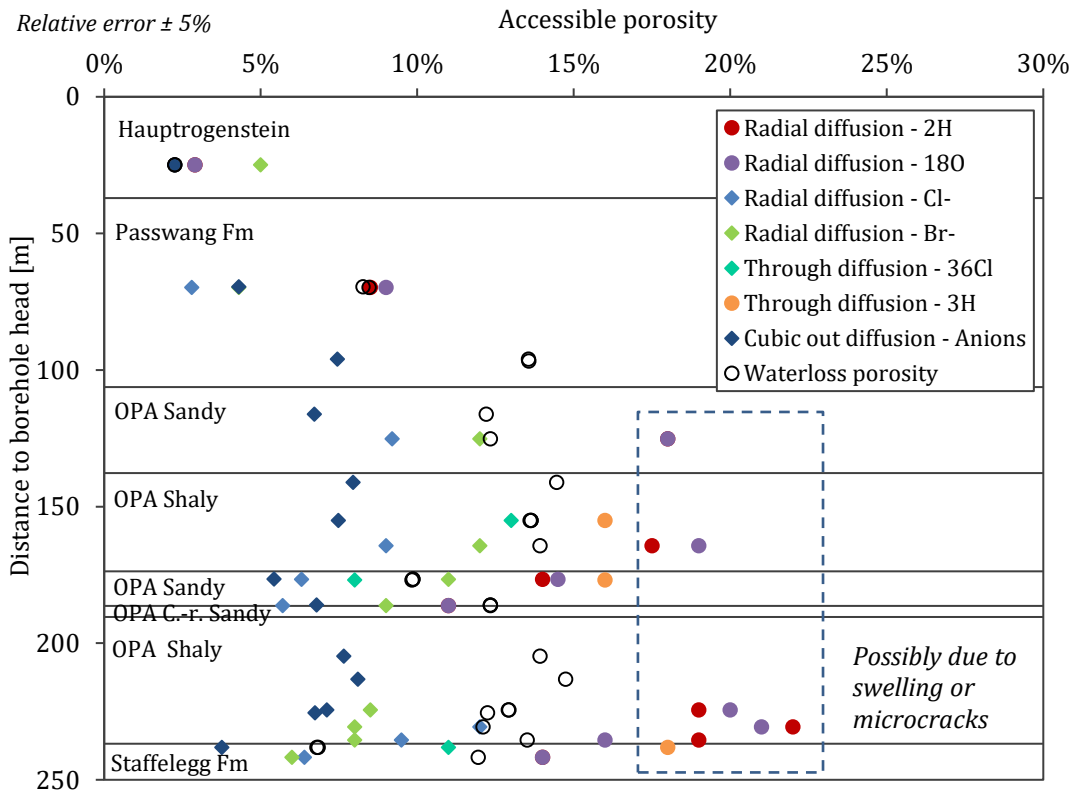
Figure 3.25: Accessible porosity obtained on BDB-1 samples. Values for cubic out diffusion were arbitrarily set at 55% of total porosity except for the Hauptrogenstein Formation.

3.7.2. EFFECTIVE DIFFUSION COEFFICIENTS

Figure 3.26 shows the effective diffusion coefficients obtained with the three diffusion experimental setups. Diffusion parameters are also reported in Table 3.13

Deduced from radial diffusion experiments, chloride and bromide effective diffusion coefficient parallel to the bedding are in the order of $4 \cdot 10^{-11}$ m² s⁻¹ in the Opalinus Clay, which is in good agreement with the range of $1.7 \cdot 10^{-11}$ to $4.5 \cdot 10^{-11}$ m² s⁻¹ for bromide and $1.8 \cdot 10^{-11}$ to $6.8 \cdot 10^{-11}$ m² s⁻¹ for chloride reported in previous studies (Bossart et al., 2011). Reasonable values from $3.0 \cdot 10^{-11}$ to $1.13 \cdot 10^{-10}$ m² s⁻¹ are obtained for stable water isotopes, covering a larger range than the interval of $4.0 \cdot 10^{-11}$ to $1.0 \cdot 10^{-10}$ m² s⁻¹ obtained at the rock laboratory level. Diffusion coefficients in the Opalinus Clay shaly facies obtained on BDB-1 samples by radial and cubic out diffusion are probably overestimated due to an unsufficient containment against swelling.

The values obtained by through diffusion experiments are also in good agreement with literature data. In the OPA shaly facies, values of $9.6 \cdot 10^{-11}$ m² s⁻¹ for tritium and $1.43 \cdot 10^{-11}$ m² s⁻¹ for ³⁶Cl are obtained parallel to the bedding. In the OPA sandy facies, simulations give $1.87 \cdot 10^{-11}$ m² s⁻¹ for tritium and $5.12 \cdot 10^{-12}$ m² s⁻¹ for ³⁶Cl perpendicular to the bedding.

Another formula for the anion exclusion ratio can be expressed as (Jacquier et al., 2013):

$$P_a = \frac{D_e[HTO]/D_e[^{36}Cl^-]}{D_0[HTO]/D_0[^{36}Cl^-]} \tag{2.43}$$

where D_e [m² s⁻¹] is the effective diffusion coefficient and D_0 [m² s⁻¹] is the diffusion coefficient in free water ($2.008 \cdot 10^{-9}$ m² s⁻¹ for HTO and $1.771 \cdot 10^{-9}$ m² s⁻¹ for Cl⁻ at 25°C according to Mills and Lobo, 1989).

Using Equation (2.43), the anion exclusion deduced from through diffusion experiment is equal to 5.9 in the OPA shaly facies, and 3.2 in the OPA sandy facies.
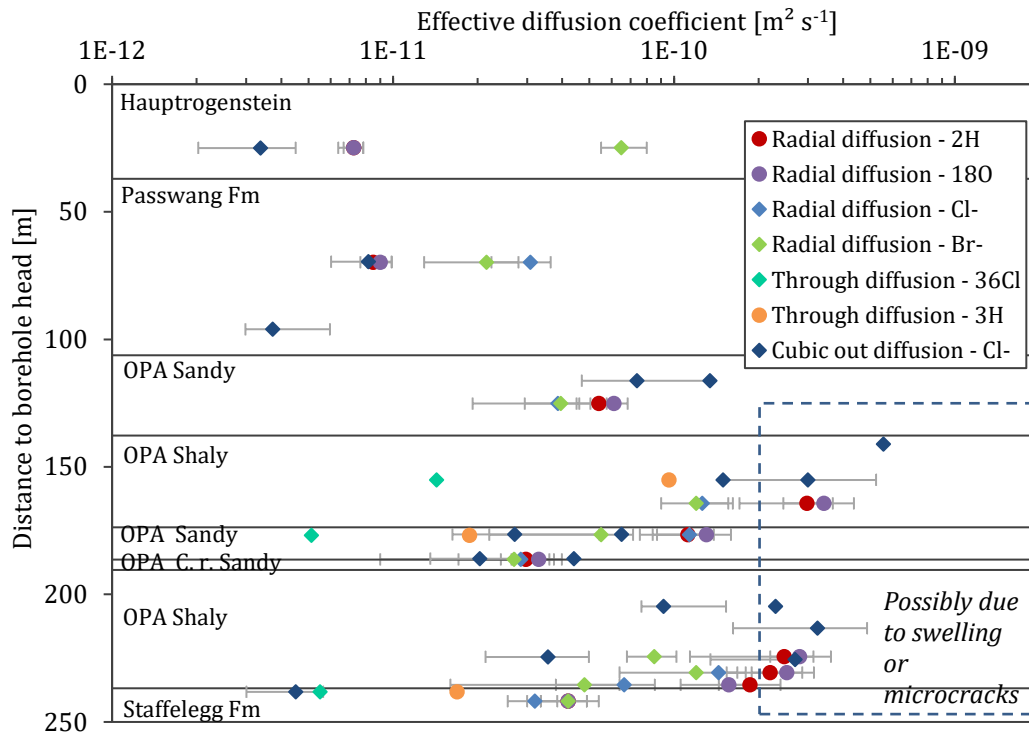
Figure 3.26: Effective diffusion coefficients acquired on BDB-1 samples

The diffusion anisotropy ratio is the ratio between the effective diffusion coefficient for diffusion parallel to the bedding and the diffusion coefficient perpendicular to the bedding. A low anisotropy ratio of 2.4 was estimated for chloride effective diffusion coefficient in the Opalinus Clay sandy facies (Figure 3.27), which is lower than the value of 4 reported by Van Loon et al. (2004) on a shaly facies sample. Anisotropy of diffusive parameters was impossible to determine in the shaly facies due to sample cracking and other unloading artefacts. Diffusion anisotropy ratios were also determined in a field scale experiment at Mont Terri within the Diffusion and Retention Experiment and revealed values of 3.8 for iodide and 2.56 for bromide, lower than the ratios of 5.06 derived for HTO in the same experiment (Gimmi et al., 2014).
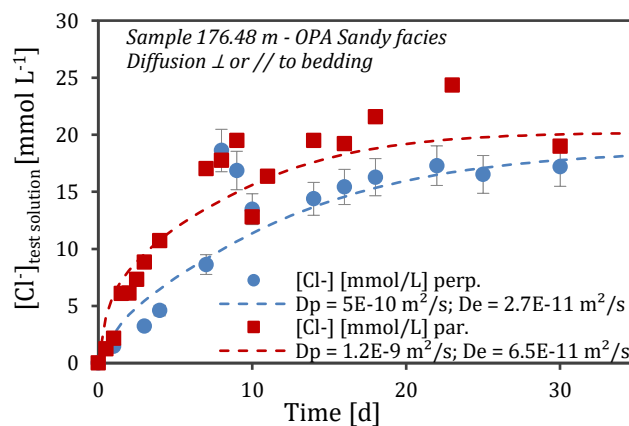
Figure 3.27: Chloride effective diffusion coefficients determination by out diffusion on an Opalinus Clay sandy facies sample

Table 3.13: Effective diffusion coefficients De and accessible porosity ω for HDO, H2180, Cl-, Br-, 36Cl- and HTO acquired on BDB-1 samples. D.O. stands for Diffusion Orientation with respect to the bedding plane. Shaded numbers are probably affected by experimental artefacts. Values with an asterisk were retained for chloride profile modelling.

Distance to borehole head [m]	Formation	Tracer	D.O.	D_e [m²/s](×10⁻¹²)	ω	Acquisition method
24.95	Hauptrogenstein	HDO	∥	0.725±0.058	0.029	Radial out diffusion
24.95		$H_2^{18}O$	∥	0.725±0.0725	0.029	Radial out diffusion
24.95	Passwang Formation	Br⁻	∥	6.5±1.25	0.05	Radial in diffusion
24.98		Cl⁻	⊥	0.34±0.12	0.022	Cubic out diffusion
69.6		Cl⁻	⊥	0.817*±0.19	0.083	Cubic out diffusion
69.78		HDO	∥	0.85±0.085	0.085	Radial out diffusion
69.78	OPA – Sandy facies	$H_2^{18}O$	∥	0.9±0.09	0.09	Radial out diffusion
69.78		Cl⁻	∥	3.08±0.08	0.028	Radial out diffusion
69.78		Br⁻	∥	2.15±0.75	0.043	Radial in diffusion
96.07		Cl⁻	⊥	0.373±0.15	0.136	Cubic out diffusion
116.24		Cl⁻	⊥	7.38*±4.36	0.122	Cubic out diffusion
116.24		Cl⁻	∥	13.4±6.71	0.122	Cubic out diffusion
125.21		HDO	∥	5.4±0.63	0.18	Radial out diffusion
125.21		$H_2^{18}O$	∥	6.12±0.9	0.18	Radial out diffusion
125.21	OPA – Shaly facies	Cl⁻	∥	3.86±0.63	0.092	Radial out diffusion
125.21		Br⁻	∥	3.96±1.8	0.12	Radial in diffusion
141.1		Cl⁻	⊥	55.6	0.145	Cubic out diffusion
155.1		Cl⁻	⊥	29.9±18.7	0.136	Cubic out diffusion
155.1		Cl⁻	∥	15.0±7.48	0.136	Cubic out diffusion
155.1		³⁶Cl⁻	∥	1.43*	0.13	Through diffusion
155.1		HTO	∥	9.6	0.16	Through diffusion
164.29		HDO	∥	29.8±6.13	0.175	Radial out diffusion
164.29	OPA – Shaly facies	$H_2^{18}O$	∥	34.2±13.3	0.19	Radial out diffusion
164.29		Cl⁻	∥	12.6±6.13	0.09	Radial out diffusion
164.29		Br⁻	∥	12.0±7.8	0.12	Radial in diffusion
176.48		Cl⁻	⊥	2.71*±1.9	0.099	Cubic out diffusion
176.48		Cl⁻	∥	6.51±1.36	0.099	Cubic out diffusion
176.60		HDO	∥	11.2±2.45	0.14	Radial out diffusion
176.60	OPA – Sandy facies	$H_2^{18}O$	∥	13.1±3.63	0.145	Radial out diffusion
176.60		Cl⁻	∥	11.3±2.45	0.063	Radial out diffusion
176.60		Br⁻	∥	5.5±2.4	0.11	Radial in diffusion

Distance to borehole head [m]	Formation	Tracer	D.O.	D_e [m²/s](×10⁻¹²)	ω	Acquisition method
176.84	OPA Sandy facies	³⁶Cl⁻	∥	1.43	0.08	Through diffusion
176.84		HTO	∥	9.6	0.16	Through diffusion
185.97		Cl⁻	⊥	2.04±0.68	0.123	Cubic out diffusion
185.97		Cl⁻	∥	4.41±2.04	0.123	Cubic out diffusion
186.27		HDO	∥	2.97±0.33	0.11	Radial out diffusion
186.27	OPA – Carbonate-rich sandy facies	$H_2^{18}O$	∥	3.3±0.66	0.11	Radial out diffusion
186.27		Cl⁻	∥	2.85±0.33	0.057	Radial out diffusion
186.27		Br⁻	∥	2.7±1.35	0.09	Radial in diffusion
204.73		Cl⁻	⊥	9.19±3.83	0.139	Cubic out diffusion
204.73		Cl⁻	∥	23.0±11.5	0.139	Cubic out diffusion
213.23		Cl⁻	⊥	32.4±16.2	0.147	Cubic out diffusion
224.40		HDO	∥	24.7±9.98	0.19	Radial out diffusion
224.40		$H_2^{18}O$	∥	28.0±7.1	0.20	Radial out diffusion
224.40	OPA – Shaly facies	Br⁻	∥	8.5±1.7	0.085	Radial in diffusion
224.49		Cl⁻	⊥	3.56*±1.42	0.129	Cubic out diffusion
225.5		Cl⁻	⊥	27.0	0.123	Cubic out diffusion
230.64		HDO	∥	22.0±6.6	0.22	Radial out diffusion
230.64		$H_2^{18}O$	∥	25.2±6.3	0.21	Radial out diffusion
230.64		Cl⁻	∥	14.4±6.6	0.12	Radial out diffusion
230.64		Br⁻	∥	12.0±5.2	0.08	Radial in diffusion
235.48		HDO	∥	18.6±4.75	0.19	Radial out diffusion
235.48		$H_2^{18}O$	∥	15.7±4.4	0.16	Radial out diffusion
235.48		Cl⁻	∥	6.65±4.75	0.095	Radial out diffusion
235.48		Br⁻	∥	4.8±2.4	0.08	Radial in diffusion
238.2	Staffelegg Formation	Cl⁻	⊥	0.451*±0.132	0.068	Cubic out diffusion
238.2		³⁶Cl⁻	⊥	0.55	0.11	Through diffusion
238.2		HTO	⊥	1.69	0.18	Through diffusion
241.83		HDO	∥	4.2±0.77	0.14	Radial out diffusion
241.83		$H_2^{18}O$	∥	4.2±0.77	0.14	Radial out diffusion
241.83		Cl⁻	∥	3.2±0.77	0.064	Radial out diffusion
241.83		Br⁻	∥	4.2±1.2	0.06	Radial in diffusion

3.8. HYDRAULIC PARAMETERS

The hydraulic parameter determination presented in the following section is detailed in Yu et al. (2017a) (see Annex VI).

3.8.1. PETROPHYSICAL MODEL RESULTS

The petrophysical model described in 2.2.4.1 was applied to the Opalinus Clay. The model is adapted to rock type with parallel-planed geometry porous network. The cementation factor is the only parameter that has to be chosen arbitrarily. Ranging between 1.3 and 5.4 (Horseman et al., 1996), it is estimated to be close to 2 for compacted and deeply buried sediment (Ullman and Aller, 1982). Based on conductivity logging in BDB-1 borehole and by combining the formation factor formula with the cementation factor (Eq. (1.4) and (1.5)), computed cementation factors are lower and range between 0.90 and 1.71.

The intrinsic permeability profiles (Figure 3.28a) show a low vertical variability through the Opalinus Clay, where it ranges between $1.8 \cdot 10^{-21}$ and $6.1 \cdot 10^{-20}$ m^2 if a cementation factor varying between 2 and 3 is taken. For a cementation factor of 2.5, the mean intrinsic permeability is $7.7 \cdot 10^{-21}$ m^2 for the Opalinus Clay shaly facies and $7.9 \cdot 10^{-21}$ m^2 for its sandy facies. These values are in good agreement with the range of $1 \cdot 10^{-21}$ and $6 \cdot 10^{-20}$ m^2 obtained by gas injection experiments performed at the Mont Terri laboratory (Marschall et al. 2005). Based on the same cementation factor, difference can be seen in the carbonate-rich sandy facies, where values are about three times higher than in the shaly and the sandy facies. With a higher exponent m = 3, the resulting intrinsic permeability has a mean value of $7.6 \cdot 10^{-21}$ m^2 and no clear distinction arises between the different facies. The intrinsic permeability values computed in the Passwang Formation and the Staffelegg Formation are much more heterogeneous and vary between $1.5 \cdot 10^{-21}$ and $5.8 \cdot 10^{-20}$ m^2.

The corresponding hydraulic conductivity profiles are presented in Figure 3.28b and show similar trends compared with the intrinsic permeability profiles. The hydraulic conductivity obtained for the Opalinus Clay ranges between $1.9 \cdot 10^{-14}$ and $5.8 \cdot 10^{-13}$ m s-1 for a cementation factor varying between 2 and 3. For a cementation factor of 2.5, the formation is characterised by a mean hydraulic conductivity of $8.3 \cdot 10^{-14}$ m s^{-1}. No clear discrepancy between the shaly facies and the sandy facies is revealed, with respective mean values of $7.3 \cdot 10^{-14}$ and $6.9 \cdot 10^{-14}$ m s^{-1}. These values are consistent with the range of $2 \cdot 10^{-14}$ to $1 \cdot 10^{-12}$ m s^{-1} reported in previous studies (Bossart et al., 2011). The Passwang Formation and the Staffelegg Formation present a various range of hydraulic conductivities between $1.6 \cdot 10^{-14}$ and $6.1 \cdot 10^{-13}$ m s^{-1}.

The computation of intrinsic permeability using variable cementation factors in the Opalinus Clay gives higher values in the range of $4.0 \cdot 10^{-20}$ to $1.9 \cdot 10^{-19}$ m^2, corresponding to hydraulic conductivity values ranging between of $4.1 \cdot 10^{-13}$ to $1.7 \cdot 10^{-12}$ m s^{-1}.
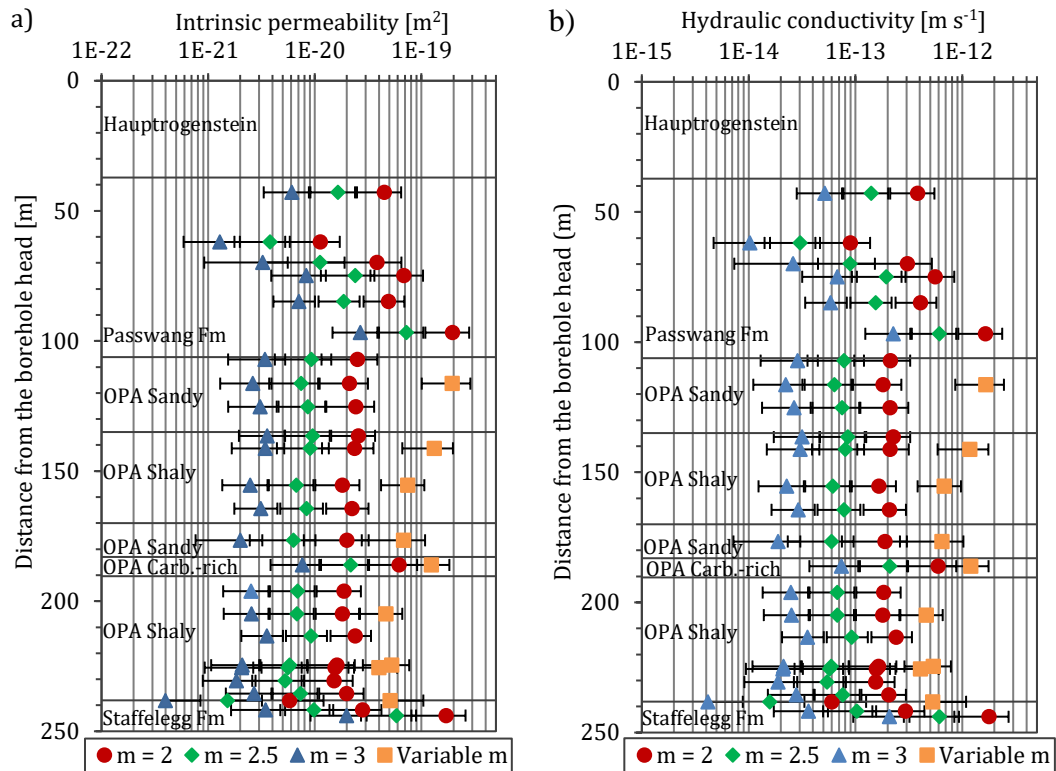
Figure 3.28: a) Intrinsic permeability profile and b) hydraulic conductivity profile computed across the Opalinus Clay (OPA) and the Passwang Formation for cementation factor (m) of 2, 2.5 and 3. Square symbols represent values for variable m computed based on conductivity logging measurements across the OPA.

3.8.2. PERMEAMETER TESTS IN HASSLER CELLS

Intrinsic permeability measurements were performed using the steady state method described in section 2.2.4, mainly using nitrogen as flowing fluid. Sets of samples were prepared in order to test either perpendicular or parallel flow to the bedding. Since drilling induced cracks, especially in the parallel to the bedding plugs, epoxy resin was used to coat the samples, thus filling the fractures and enabling permeability measurements.

Intrinsic permeability values in the Opalinus Clay range between $6.9 \cdot 10^{-21}$ and $4.0 \cdot 10^{-19}$ m^2, corresponding to a range in hydraulic conductivities of $6.9 \cdot 10^{-14}$ to $3.7 \cdot 10^{-12}$ m^2 s^{-1} (Figure 3.29). Estimation of permeability anisotropy was complicated by the great brittleness of the Opalinus Clay, when the material is unloaded, and resin coating has certainly an effect on permeability measurements. For example, a test was performed on the same sample before and after coating, resulting in a significant difference in permeability ($1.0 \cdot 10^{-21}$ m^2 with resin coating versus $4.0 \cdot 10^{-19}$ m^2 without coating). It can be assumed that results from coated samples underestimate the sample real permeability to an unknown extent, while there is an overestimation for permeability measurements on uncoated samples.
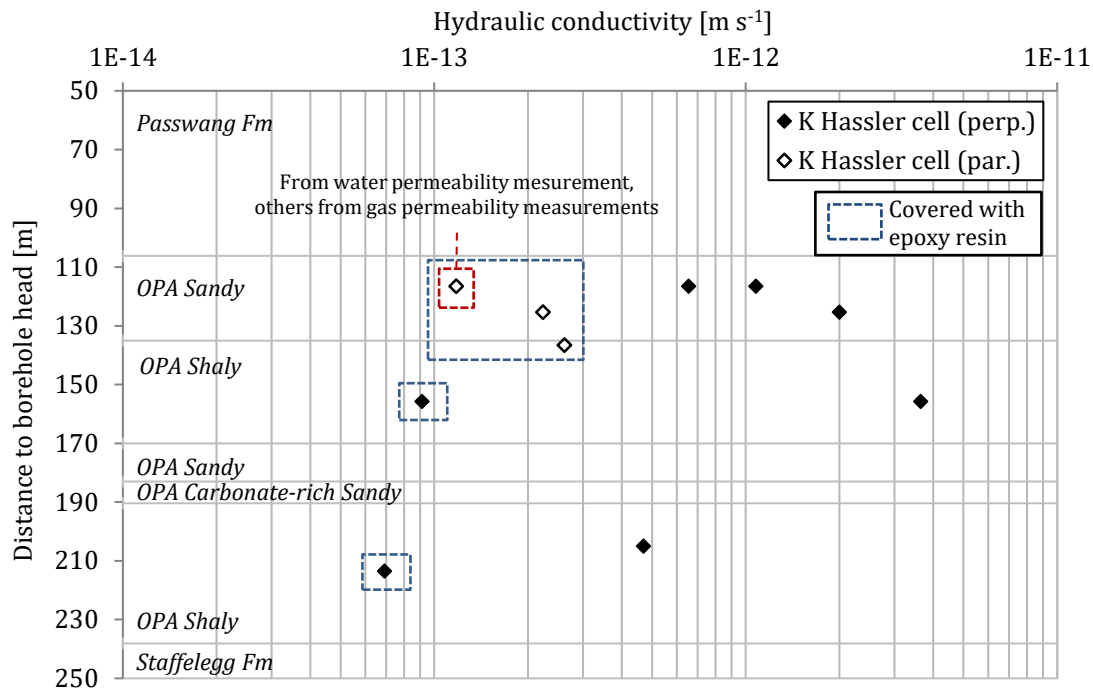
Figure 3.29: Hydraulic conductivity results using the steady state method in Hassler Cell

Microtomography results performed at IRSN on four samples covered with resin using a Bruker Skyscan 1173, show that epoxy resin has entirely filled micro-cracks for three samples (Figure 3.30). For the fourth one, microtomography was not able to show very fine micro-cracks because of voxel resolution (25.01 μm).
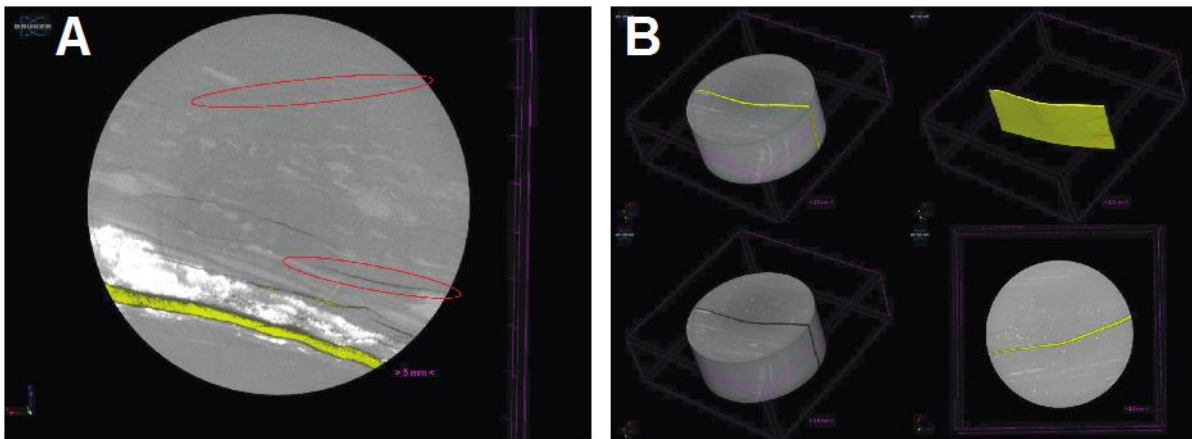
Figure 3.30: Micro-computed tomography on two Opalinus Clay samples, yellow colour represents epoxy resin: A) the sample M12D (OPA shaly facies) shows micro-cracks filled with resin, but resolution is not sufficient to see if resin entered the fine micro-cracks surrounded with red ellipses, this sample gave a non-satisfactory permeability result, B) Permeability result of the sample M14c (OPA Sandy facies) is satisfactory, micro-computed tomography shows epoxy resin filling the crack.

3.8.3. RESULTS OF HYDRAULIC TESTING ON BDB-1 BOREHOLE

Numerical analyses of test events result in wide range of estimated formation parameters. The interpretation plots and result tables are given in Annex IV.

The application of a composite model, which takes into account a damaged skin zone, is required for most of the test analyses. Taking as an example the first pulse test carried out on BDB-1 borehole Interval 2, Figure 3.31 shows a comparison of the residuals (measured value minus simulated value) to that of a normal distribution using a homogeneous model and a composite one. The homogeneous model appears to be unsatisfactory because the residuals are not normally distributed, which indicates the presence of a systematic error.
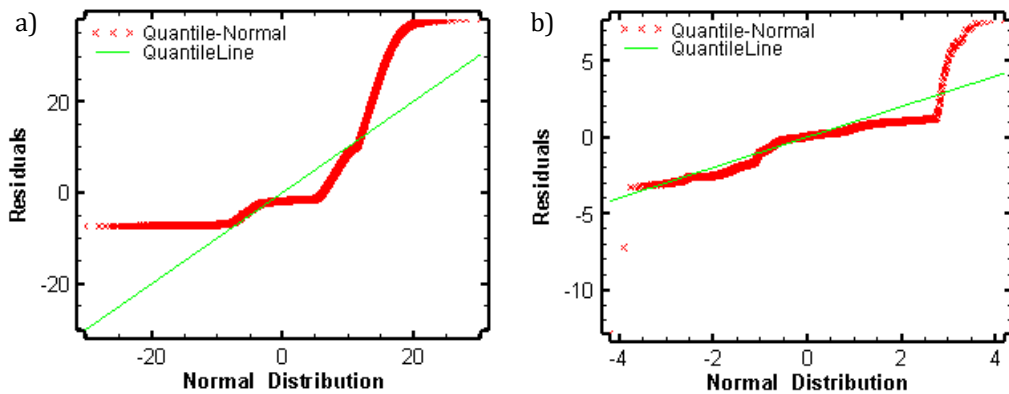
Figure 3.31: Example of residual plots for the optimization of Interval 2 (OPA shaly facies) pulse sequence fits to the Cartesian pressure response (test C2-1).
a) homogeneous model b) composite model with skin.

The plausibility ranges for fitted parameters are set as follows:
- Formation hydraulic conductivity from 10^{-13} to 10^{-8} m s^{-1} for Interval 1 located in the Staffelegg Formation; and from 10^{-14} and 10^{-11} m s^{-1} for Intervals 2 to 7 (located in the Opalinus Clay and the Passwang Formation); skin zone conductivity ranges are higher of one order of magnitude.
- Formation and skin specific storage from 10^{-8} to 10^{-4} m^{-1}
- Flow dimension between 1 and 3.5
- Skin thickness from 0.5 to 30 cm.
- Flow external boundary radius between 0.2 and 5 m

Pulse tests and constant rate pumping tests results are respectively compiled in Table 3.14.

Table 3.14: Parameter estimates from BDB-1 borehole pulse withdrawal tests and constant rate (CR) withdrawal tests (K [m s⁻¹]: hydraulic conductivity; S_s [m⁻¹]: specific storage; n: flow dimension; t_s [cm]: skin thickness). Empty cells represent unrealistically wide range of uncertainties.

Test	Interval	t_s [cm]	K [m·s⁻¹] Formation Range	K [m·s⁻¹] Formation Best fit	K Skin Best fit	S_s [m⁻¹] Formation Range	S_s [m⁻¹] Formation Best fit	S_s Skin Best fit	n Range	n Best fit
Pulse										
C1-1	I$_1$	-	$1 \cdot 10^{-10}$ - $3.5 \cdot 10^{-10}$	$2.1 \cdot 10^{-10}$	-	$6 \cdot 10^{-9}$ -	$1.4 \cdot 10^{-8}$	-	1.9 - 2.7	2.2
C1-2	I$_1$	-	$1 \cdot 10^{-11}$ - $1 \cdot 10^{-7}$	$4.2 \cdot 10^{-10}$	-		$1.4 \cdot 10^{-6}$	-		2.0
C1-3	I$_1$	-	$1 \cdot 10^{-11}$ - $1 \cdot 10^{-7}$	$5.6 \cdot 10^{-10}$			$6.3 \cdot 10^{-8}$	-		2.4
C1-6	I$_1$	-	$3 \cdot 10^{-11}$ - $1 \cdot 10^{-8}$	$5.9 \cdot 10^{-9}$	-		$8.3 \cdot 10^{-7}$	-		2.0
C2-1	I2	0.5	$2 \cdot 10^{-12}$ - $3 \cdot 10^{-11}$	$3.1 \cdot 10^{-12}$	$7.8 \cdot 10^{-12}$	$1 \cdot 10^{-7}$ - $3 \cdot 10^{-5}$	$5.2 \cdot 10^{-6}$	$4.3 \cdot 10^{-5}$	1.8 - 3.0	2.8
C2-2	I2	0.5	$2 \cdot 10^{-12}$ - $1 \cdot 10^{-10}$	$7.3 \cdot 10^{-12}$	$1.0 \cdot 10^{-11}$	$1 \cdot 10^{-7}$ - $2 \cdot 10^{-5}$	$3.0 \cdot 10^{-6}$	$4.7 \cdot 10^{-5}$	1.4 - 2.9	2.0
C3-1	I3	0.5	$1 \cdot 10^{-13}$ - $3 \cdot 10^{-12}$	$5.1 \cdot 10^{-13}$	$1.6 \cdot 10^{-12}$	$5 \cdot 10^{-7}$ - $3 \cdot 10^{-5}$	$3.7 \cdot 10^{-6}$	$1.2 \cdot 10^{-5}$	1.4 - 3.1	2.1
C3-2	I3	0.5	$2 \cdot 10^{-13}$ - $2 \cdot 10^{-12}$	$4.9 \cdot 10^{-13}$	$1.6 \cdot 10^{-12}$	$2 \cdot 10^{-6}$ - $3 \cdot 10^{-5}$	$1.1 \cdot 10^{-5}$	$1.5 \cdot 10^{-5}$	1. 4 - 3.4	2.5
C4-1	I4	0.5	$1 \cdot 10^{-12}$ - $9 \cdot 10^{-12}$	$2.3 \cdot 10^{-12}$	$5.7 \cdot 10^{-12}$	$2 \cdot 10^{-6}$ - $1 \cdot 10^{-5}$	$6.4 \cdot 10^{-6}$	$5.5 \cdot 10^{-5}$	1. 7 - 3	2.3
C4-2	I4	2.0	$7 \cdot 10^{-13}$ - $1 \cdot 10^{-11}$	$4.2 \cdot 10^{-12}$	$2.7 \cdot 10^{-11}$	$1 \cdot 10^{-6}$ - $2 \cdot 10^{-5}$	$2.2 \cdot 10^{-6}$	$9.7 \cdot 10^{-6}$	1.5 - 3	2.0
C5-1	I5	0.5	$4 \cdot 10^{-13}$ - $4 \cdot 10^{-12}$	$1.6 \cdot 10^{-12}$	$1.4 \cdot 10^{-12}$	$3 \cdot 10^{-7}$ - $8 \cdot 10^{-6}$	$1.0 \cdot 10^{-6}$	$2.6 \cdot 10^{-5}$	1.8 - 2.9	1.9
C5-2	I5	0.5	$4 \cdot 10^{-13}$ - $3 \cdot 10^{-12}$	$1.0 \cdot 10^{-12}$	$2.7 \cdot 10^{-12}$	$1 \cdot 10^{-6}$ - $3 \cdot 10^{-5}$	$8.5 \cdot 10^{-6}$	$4.7 \cdot 10^{-5}$	1 - 3	2.5
C6-1	I6	1.5	$8 \cdot 10^{-14}$ - $8 \cdot 10^{-13}$	$1.9 \cdot 10^{-13}$	$1.4 \cdot 10^{-11}$	$8 \cdot 10^{-7}$ - $1 \cdot 10^{-5}$	$6.6 \cdot 10^{-6}$	$6.6 \cdot 10^{-6}$	1.7 - 3	2.6
C6-2	I6	0.5	$2 \cdot 10^{-13}$ - $6 \cdot 10^{-13}$	$2.7 \cdot 10^{-13}$	$5.4 \cdot 10^{-12}$	$1 \cdot 10^{-6}$ - $2 \cdot 10^{-5}$	$1.7 \cdot 10^{-5}$	$2.9 \cdot 10^{-5}$	1.7 - 3	2.8
C7-1	I7	0.5	$3 \cdot 10^{-13}$ – $4.4.5 \cdot 10^{-12}$	$5.8 \cdot 10^{-13}$	$3.7 \cdot 10^{-13}$	$4 \cdot 10^{-7}$ - $2 \cdot 10^{-5}$	$3.7 \cdot 10^{-6}$	$1.9 \cdot 10^{-6}$	1.9 – 3.5	3.0
C7-2	I7	0.5	$4 \cdot 10^{-13}$ - $2 \cdot 10^{-12}$	$1.4 \cdot 10^{-12}$	$8.6 \cdot 10^{-12}$	10^{-9} - $2 \cdot 10^{-5}$	$1.2 \cdot 10^{-6}$	$9.4 \cdot 10^{-7}$	2.1 – 2.6	2.3
CR										
C1-7	I1	4.3		$5.0 \cdot 10^{-10}$	$5.7 \cdot 10^{-9}$	$1 \cdot 10^{-8}$ - $1 \cdot 10^{-4}$	$8.2 \cdot 10^{-6}$	$6.2 \cdot 10^{-5}$	2.0 - 3.0	2.1
C2-2	I2	14.2	$4 \cdot 10^{-13}$ - $8 \cdot 10^{-11}$	$3.9 \cdot 10^{-12}$	$3.5 \cdot 10^{-11}$		$1.2 \cdot 10^{-6}$	$9.0 \cdot 10^{-5}$	1.4 - 2.7	1.95
C3-3	I3	0.7	$1 \cdot 10^{-13}$ - $2 \cdot 10^{-12}$	$9.9 \cdot 10^{-13}$	$1.6 \cdot 10^{-12}$	$3 \cdot 10^{-8}$ - $6 \cdot 10^{-5}$	$1.5 \cdot 10^{-5}$	$4.9 \cdot 10^{-5}$	1.5 - 3.0	1.9
C4-3	I4	1.4	$4 \cdot 10^{-14}$ - $5 \cdot 10^{-12}$	$2.4 \cdot 10^{-12}$	$3.0 \cdot 10^{-12}$	$4 \cdot 10^{-8}$ - $3 \cdot 10^{-4}$	$1.2 \cdot 10^{-5}$	$4.0 \cdot 10^{-5}$	1.9 – 3.0	2.1
C5-3	I5	1.8	$7 \cdot 10^{-14}$ - $9 \cdot 10^{-12}$	$8.1 \cdot 10^{-13}$	$1.5 \cdot 10^{-11}$	$1 \cdot 10^{-7}$ - $3 \cdot 10^{-5}$	$8.9 \cdot 10^{-5}$	$2.4 \cdot 10^{-5}$	1.9 - 3.0	2.3
C6-3	I6	0.5	$1 \cdot 10^{-14}$ - $4 \cdot 10^{-12}$	$2.2 \cdot 10^{-13}$	$1.1 \cdot 10^{-12}$	$1 \cdot 10^{-7}$ - $2 \cdot 10^{-5}$	$7.7 \cdot 10^{-6}$	$9.9 \cdot 10^{-5}$	1.5 - 2.9	2.5
C7-3	I7	0.6	$1 \cdot 10^{-13}$ - $1 \cdot 10^{-12}$	$4.4 \cdot 10^{-13}$	$8.2 \cdot 10^{-13}$	$3 \cdot 10^{-8}$ - $4 \cdot 10^{-6}$	$8.5 \cdot 10^{-6}$	$2.3 \cdot 10^{-5}$	2.1 - 3.0	2.7

Pulse testing revealed the highest hydraulic conductivity values in the Staffelegg Formation (Interval 1, see Figure 2.3) with best fit values ranging from $2.1 \cdot 10^{-10}$ to $5.9 \cdot 10^{-10}$ m s⁻¹. Located in the basal shaly facies of Opalinus Clay (Interval 2), the bottom part of the main fault zone is characterised by conductivity values from $3.1 \cdot 10^{-12}$ to $7.3 \cdot 10^{-12}$ m s⁻¹ and do not differ from the upper shaly facies represented by Interval 4 and 5, whose best estimates are up to $4.2 \cdot 10^{-12}$ m s⁻¹. The lowest values are found in the sandy facies (Interval 6, best fit values up to $2.7 \cdot 10^{-13}$ m s⁻¹), and the carbonate-rich sandy facies (Interval 3, best fit values up to $5.1 \cdot 10^{-13}$ m s⁻¹). The basal part of the Passwang Formation, represented by Interval 7, shows similar hydraulic conductivity values to Opalinus Clay ($5.8 \cdot 10^{-13}$ to $1.4 \cdot 10^{-12}$ m s⁻¹).

The analyses results of the constant flowrate withdrawal tests are quite consistent with those obtained from pulse tests. Indeed, a similar trend can be observed with slightly higher permeability values in the shaly facies than in the sandy facies of the Opalinus Clay.

Specific storage and flow dimension estimates are highly variable. One of the issues with single well hydraulic testing is that the volume of tested rock is limited to the immediate vicinity of the

well. For specific storage estimation, the method involving tidal analysis may be more representative since the deformation is applied to the entire rockmass.

Additional numerical interpretations were performed by AF Consult (2016) on the hydraulic tests carried out in the seven intervals of BDB-1 borehole. The numerical tool Multisim, which has similar working principle with nSIGHTS, was used. The results are reported in Table 3.15 and are globally in good accordance with the results presented above.

Table 3.15: Comparison of numerical interpretation results using nSIGHTS and Multisim

	nSIGHTS (Pulse and CR)						Multisim (CR) (AF Consult, 2016)					
	K_{min}	K_{max}	Ref. value	$S_{s\,min}$	$S_{s\,max}$	Ref. value	K_{min}	K_{max}	Ref. value	$S_{s\,min}$	S_{smax}	Ref value
	[m s^{-1}]			[m^{-1}]			[m s^{-1}]			[m^{-1}]		
I1	$2.1\cdot10^{-10}$	$5.9\cdot10^{-9}$	$5.0\cdot10^{-10}$	$1.4\cdot10^{-8}$	$8.2\cdot10^{-6}$	$8.2\cdot10^{-6}$	$2.5\cdot10^{-9}$	$2.8\cdot10^{-9}$	$2.5\cdot10^{-9}$	$1.0\cdot10^{-6}$	$2.2\cdot10^{-6}$	$2.2\cdot10^{-6}$
I2	$3.1\cdot10^{-12}$	$7.3\cdot10^{-12}$	$3.9\cdot10^{-12}$	$1.2\cdot10^{-6}$	$5.2\cdot10^{-6}$	$5.2\cdot10^{-6}$	$1.0\cdot10^{-12}$	$2.2\cdot10^{-12}$		$1.6\cdot10^{-6}$	$2.0\cdot10^{-5}$	$8.1\cdot10^{-6}$
I3	$4.9\cdot10^{-13}$	$9.9\cdot10^{-13}$	$9.9\cdot10^{-13}$	$3.7\cdot10^{-6}$	$1.5\cdot10^{-5}$	$1.5\cdot10^{-5}$	$4.5\cdot10^{-13}$	$9.0\cdot10^{-13}$	$4.5\cdot10^{-13}$	$4.0\cdot10^{-6}$	$8.5\cdot10^{-6}$	$1.0\cdot10^{-6}$
I4	$2.3\cdot10^{-12}$	$4.2\cdot10^{-12}$	$2.4\cdot10^{-12}$	$2.2\cdot10^{-6}$	$1.2\cdot10^{-5}$	$5.0\cdot10^{-6}$	$2.6\cdot10^{-12}$	$3.7\cdot10^{-12}$	$3.7\cdot10^{-12}$	$8.0\cdot10^{-7}$	$5.0\cdot10^{-6}$	$5.0\cdot10^{-6}$
I5	$8.1\cdot10^{-13}$	$1.6\cdot10^{-12}$	$8.1\cdot10^{-13}$	$1.0\cdot10^{-6}$	$8.9\cdot10^{-5}$	$8.9\cdot10^{-6}$	$2.0\cdot10^{-12}$	$2.2\cdot10^{-12}$	$4.0\cdot10^{-12}$	$9.0\cdot10^{-7}$	$4.1\cdot10^{-6}$	$5.0\cdot10^{-6}$
I6	$2.2\cdot10^{-13}$	$2.7\cdot10^{-13}$	$2.2\cdot10^{-13}$	$6.6\cdot10^{-6}$	$1.7\cdot10^{-5}$	$7.7\cdot10^{-6}$	$4.8\cdot10^{-13}$	$8.0\cdot10^{-13}$	$6.7\cdot10^{-13}$	$9.9\cdot10^{-7}$	$5.0\cdot10^{-6}$	$2.0\cdot10^{-6}$
I7	$4.4\cdot10^{-13}$	$8.6\cdot10^{-12}$	$4.4\cdot10^{-13}$	$1.2\cdot10^{-6}$	$8.5\cdot10^{-6}$	$8.5\cdot10^{-6}$	$2.1\cdot10^{-12}$	$3.3\cdot10^{-12}$	$1.8\cdot10^{-12}$	$1.0\cdot10^{-6}$	$6.0\cdot10^{-6}$	$5.5\cdot10^{-7}$

3.8.4. SPECTRAL TIDAL ANALYSIS

The detection of tidal components was performed on the pore pressure time series monitored by the sensors placed in BDB-1 borehole, with an acquisition time step set at 15 minutes. The time series were preprocessed in order to obtain reconstituted signals without time gaps and spurious values, which are linked to system technical issues. The length of the time series was chosen to be as long as possible without accounting for the disturbances caused by the multipacker system installation.

The four largest amplitude tidal components, O_1, K_1, S_2 and M_2 appear on all processed signal at the exact expected frequencies for time series between September 1st 2014 and March 10th 2015 (Figure 3.32 and Table 3.16). Therefore, the hydraulic system can be considered at equilibrium with the rockmass. This detection also gives confidence that there is no trapped air bubble in the system, which would have disturbed the signals.

Tide types can be quantitatively classified by the form ratio F_t, which is defined as the sum of the amplitudes of the two main diurnal components (K_1 and O_1) divided by the sum of the amplitudes of the two main semi-diurnal components (M_2 and S_2) (Wiegel, 1964).

$$F_t = \frac{K_1 + O_1}{M_2 + S_2}$$

3.

If F_t is less than 0.25, the tidal current is considered semi-diurnal, mixed but mainly semi-diurnal if it is between 0.25 and 1.5, mixed but mainly diurnal if it is between 1.5 and 3, and diurnal if it is greater than 3.
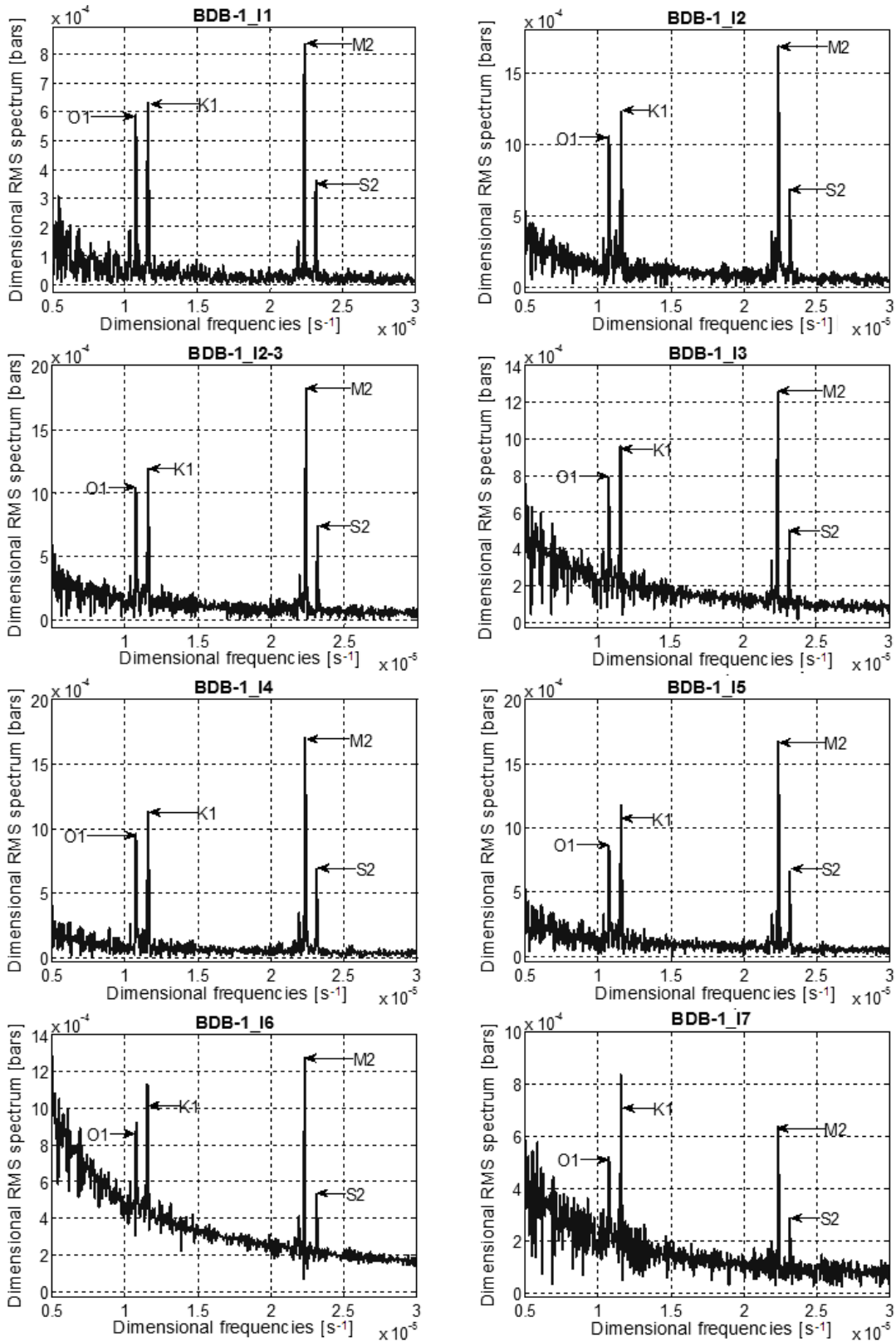
Figure 3.32: Estimated Root Mean Square spectrum of pore pressure time series measured in BDB-1 borehole between 01/09/2014 and 10/03/2015. The following tides are observable: principal lunar semidiurnal tide M₂ (2.236 · 10⁻⁵ Hz) and solar semidiurnal tide S₂ (2.315 · 10⁻⁵ Hz), lunar diurnal tides K₁ (1.161 · 10⁻⁵ Hz) and O₁ (1.076 · 10⁻⁵ Hz), and the solar diurnal components S₁ (1.157 · 10⁻⁵ Hz) and P₁ (1.154 · 10⁻⁵ Hz).

Table 3.16: RMS Amplitude of the tidal components observed on the BDB-1 borehole pore pressure signals between 01/09/2014 and 10/03/2015

Formation / associated chamber	Amplitude on the RMS spectrum [bar]				Form ratio
	O_1 ($1.076 \cdot 10^{-5}$ Hz)	K_1 ($1.161 \cdot 10^{-5}$ Hz)	S_2 ($2.315 \cdot 10^{-5}$ Hz)	M_2 ($2.236 \cdot 10^{-5}$ Hz)	
Staffelegg Formation / I_1	$5.886 \cdot 10^{-4}$	$6.326 \cdot 10^{-4}$	$3.606 \cdot 10^{-4}$	$8.353 \cdot 10^{-4}$	1.02
OPA – Shaly facies / I_2	$1.054 \cdot 10^{-3}$	$1.230 \cdot 10^{-3}$	$6.848 \cdot 10^{-4}$	$1.696 \cdot 10^{-3}$	0.96
OPA – Shaly facies / I_{2-3}	$1.041 \cdot 10^{-3}$	$1.192 \cdot 10^{-3}$	$7.390 \cdot 10^{-4}$	$1.823 \cdot 10^{-3}$	0.87
OPA – Carbonate-rich facies / I_3	$7.905 \cdot 10^{-4}$	$9.553 \cdot 10^{-4}$	$5.014 \cdot 10^{-4}$	$1.255 \cdot 10^{-3}$	0.99
OPA – Shaly facies / I_4	$9.560 \cdot 10^{-4}$	$1.133 \cdot 10^{-3}$	$6.838 \cdot 10^{-4}$	$1.701 \cdot 10^{-3}$	0.88
OPA – Shaly facies / I_5	$8.591 \cdot 10^{-4}$	$1.084 \cdot 10^{-4}$	$6.546 \cdot 10^{-4}$	$1.670 \cdot 10^{-3}$	0.84
OPA – Sandy facies / I_6	$8.637 \cdot 10^{-4}$	$1.205 \cdot 10^{-3}$	$5.329 \cdot 10^{-4}$	$1.278 \cdot 10^{-3}$	1.04
Passwang Formation / I_7	$5.200 \cdot 10^{-4}$	$7.206 \cdot 10^{-4}$	$2.825 \cdot 10^{-4}$	$6.360 \cdot 10^{-4}$	1.35

The tidal deformation through the Opalinus Clay at Mont Terri is characterized by a form ratio varying between 0.84 and 1.04, which indicates a mixed, mainly semi-diurnal tide. The maximum value is found in the Passwang Formation, for which the diurnal components have slightly higher amplitudes than the semi-diurnal ones. Except for this interval, the M_2 tide has the highest amplitude values among the four major tides.

3.8.4.1. Specific storage coefficient

The results of S_s computation based on Equation (2.15) are given in Table 3.17. Specific storage values are ranging between $1.08 \cdot 10^{-6}$ and $1.56 \cdot 10^{-6}$ m^{-1} in the Opalinus Clay and are higher for the adjacent formations ($2.35 \cdot 10^{-6}$ m^{-1} for the Middle Jurassic limestone and $3.08 \cdot 10^{-6}$ m^{-1} for the Early Jurassic aquifer). These estimates are consistent with the range given in the literature, deduced from in situ packer tests and permeameter tests for the Opalinus Clay shaly facies ([$1 \cdot 10^{-7}$; $1 \cdot 10^{-4}$] m^{-1}, with best estimate at $2 \cdot 10^{-6}$ m^{-1} (Bossart et al., 2011).

Table 3.17: Specific storage coefficients (S_s) estimated from absolute pore pressure signals for BDB-1 borehole measuring intervals with corresponding formations and amplitude of pressure head fluctuations Δh.

Formation	Chamber	Δh [bar]	Δh [m]	S_s [m^{-1}]
Up. Toarcian - Staffelegg Formation	I_1	$8.353 \cdot 10^{-4}$	$8.52 \cdot 10^{-3}$	$2.35 \cdot 10^{-6}$
Up. Toarcian / Low. Aalenian - Opalinus Clay – Shaly facies	I_2	$1.696 \cdot 10^{-3}$	$1.73 \cdot 10^{-2}$	$1.16 \cdot 10^{-6}$
Up. Toarcian / Low. Aalenian - Opalinus Clay – Shaly facies	I_{2-3}	$1.823 \cdot 10^{-3}$	$1.86 \cdot 10^{-2}$	$1.08 \cdot 10^{-6}$
Lower Aalenian - Opalinus Clay – Carbonate-rich facies	I_3	$1.255 \cdot 10^{-3}$	$1.28 \cdot 10^{-2}$	$1.56 \cdot 10^{-6}$
Lower Aalenian Opalinus Clay – Shaly facies	I_4	$1.701 \cdot 10^{-3}$	$1.73 \cdot 10^{-2}$	$1.15 \cdot 10^{-6}$
Middle Aalenian - Opalinus Clay – Shaly facies	I_5	$1.670 \cdot 10^{-3}$	$1.70 \cdot 10^{-2}$	$1.17 \cdot 10^{-6}$
Up. Aalenian - Opalinus Clay – Sandy facies	I_6	$1.278 \cdot 10^{-3}$	$1.32 \cdot 10^{-2}$	$1.53 \cdot 10^{-6}$
Up. Aalenian - Passwang Formation	I_7	$6.360 \cdot 10^{-4}$	$6.49 \cdot 10^{-3}$	$3.08 \cdot 10^{-6}$

3.8.4.2. Effective dynamic porosity

Effective dynamic porosity values obtained using the M_2 tide (Table 3.18) are globally in well agreement with water loss porosity obtained from petrophysical measurements. Indeed, coherent values between 8% and 24% are obtained by cross-analyses of measuring intervals located in the Opalinus Clay. Statistical analysis carried out in previous studies on Mont Terri samples (Fatmi, 2009; Matray and Bailly, 2015) revealed values of very low range between 1% and 4% that could be related to the hydraulically disturbed state of the studied area.

Except for the value of 24%, obtained by cross-analysis between the chamber located in the Main Fault and the interval port above, values of effective porosity are below the total porosity values acquired in laboratory by water loss and density measurements. This is expected since kinematic porosity is the porous volume available for fluid advective displacement, corresponding to the total porosity minus i) the adsorbed water on minerals surface, ii) the water absorbed in the clay-mineral lattice, iii) the unconnected pore volume and iv) the dead-end pore volume. Spectral analysis on BDB-1 borehole pressure data suggests that the effective porosity in the Opalinus Clay represents 51 % to 84 % of thewater loss porosity, with the higher values obtained for cross-analysis with pressure data monitored in the sandy facies of the OPA.

In comparison, an effective porosity corresponding to 50 % of the total porosity and obtained by tracing experiments was retained for the safety assessment of the Callovo-Oxfordian Formation in France (ANDRA, 2005c). Desbois et al (2010) estimated the effective porosity to represent that 70% to 90% of total porosity on Boom Clay samples based on imaging techniques.

Table 3.18: Spectral coherence function (Coh), spectral gain (r_g), arithmetic mean of the specific storativity coefficient ($\tilde{S}_s$) and effective dynamic porosity ($\widetilde{\omega}_{dyna}$) obtained for the M_2 earth tide for different couples of sensors in BDB-1 borehole. Mean water loss porosity (ω_{wl}) is given for purposes of comparison.

Chamber	Coh [-]	r_g [-]	$\tilde{S}_s$ [m^{-1}]	$\widetilde{\omega}_{dyn}$ [-]	ω_{wl} [-]	$\widetilde{\omega}_{dyn}/\omega_{wl}$
I_1 vs. I_2	0.9985	0.252	$1.752 \cdot 10^{-6}$	0.09	0.18	0.51
I_2 vs. I_{2-3}	0.9992	1.035	$1.116 \cdot 10^{-6}$	0.24	0.15	
I_{2-3} vs. I_3	0.9986	0.3949	$1.319 \cdot 10^{-6}$	0.11	0.13	0.84
I_3 vs. I_4	0.9977	4.681	$1.358 \cdot 10^{-6}$	*1.33 (outlier)*	0.12	
I_4 vs. I_5	0.993	0.4758	$1.164 \cdot 10^{-6}$	0.12	0.14	0.83
I_5 vs. I_6	0.9965	0.2889	$1.355 \cdot 10^{-6}$	0.08	0.13	0.63
I_6 vs. I_7	0.9965	1.629	$2.309 \cdot 10^{-6}$	*0.79 (outlier)*	0.13	

3.8.4.3. Effective hydraulic conductivity

Vertical hydraulic conductivity values obtained by spectral analysis and reported in Table 3.19 are much higher than those obtained by other techniques. Indeed, unrealistically high conductivities ranging between $5.66 \cdot 10^{-5}$ m s^{-1} and $1.40 \cdot 10^{-7}$ m s^{-1} are found in the Opalinus Clay. These values are 6 to 8 orders of magnitude higher than the range expected from literature data: [$2 \cdot 10^{-14}$; $1 \cdot 10^{-12}$] m s^{-1} (Bossart et al., 2011).

Table 3.19: Spectral coherence function (Coh), arithmetic mean of the specific storativity coefficient ($\tilde{S}_s$), RMS amplitude of the pressure pore signal 1 (A_{z_1}), and of the pore pressure signal 2 (A_{z_2}), vertical effective amplitude hydraulic conductivity ($\tilde{K}_v^{Ampl.}$) and vertical effective phase hydraulic conductivity ($\tilde{K}_v^{\Delta\varphi}$) obtained for the M_2 earth tide for different couples of sensors in BDB-1 borehole.

	Coh [-]	$\tilde{S}_s$ [m^{-1}]	A_{z_1} [bar]	A_{z_2} [bar]	$\Delta\varphi$ [rad]	$\tilde{K}_v^{Ampl.}$ [m s^{-1}]	$\tilde{K}_v^{\Delta\varphi}$ [m s^{-1}]
I_1 vs. I_2	0.9985	$1.752 \cdot 10^{-6}$	$8.35 \cdot 10^{-4}$	$1.70 \cdot 10^{-3}$	-0.1822	$4.74 \cdot 10^{-8}$	$7.17 \cdot 10^{-7}$
I_2 vs. I_{2-3}	0.9992	$1.116 \cdot 10^{-6}$	$1.70 \cdot 10^{-3}$	$1.82 \cdot 10^{-3}$	0.03573	$2.50 \cdot 10^{-6}$	$1.02 \cdot 10^{-5}$
I_{2-3} vs. I_3	0.9986	$1.319 \cdot 10^{-6}$	$1.82 \cdot 10^{-3}$	$1.26 \cdot 10^{-3}$	0.07658	$1.40 \cdot 10^{-7}$	$3.32 \cdot 10^{-6}$
I_3 vs. I_4	0.9977	$1.358 \cdot 10^{-6}$	$1.26 \cdot 10^{-3}$	$1.70 \cdot 10^{-3}$	-0.06768	$2.88 \cdot 10^{-7}$	$5.81 \cdot 10^{-6}$
I_4 vs. I_5	0.993	$1.164 \cdot 10^{-6}$	$1.70 \cdot 10^{-3}$	$1.67 \cdot 10^{-3}$	0.02158	$5.66 \cdot 10^{-5}$	$4.11 \cdot 10^{-6}$
I_5 vs. I_6	0.9965	$1.355 \cdot 10^{-6}$	$1.67 \cdot 10^{-3}$	$1.28 \cdot 10^{-3}$	-0.05037	$6.38 \cdot 10^{-7}$	$1.80 \cdot 10^{-5}$
I_6 vs. I_7	0.9965	$2.309 \cdot 10^{-6}$	$1.28 \cdot 10^{-3}$	$6.36 \cdot 10^{-3}$	0.5081	$3.89 \cdot 10^{-8}$	$7.33 \cdot 10^{-8}$

Bailly and Matray (2015) performed statistical analysis on pore pressure time series acquired in the BCD-3 borehole located at the Mont Terri tunnel level. They found hydraulic conductivities ranging in [$1.9 \cdot 10^{-10}$; $7.5 \cdot 10^{-11}$] m s^{-1} using the same method not on the M_2 earth tide, which was not found in their pore pressure time series, but on the S_1 solar diurnal tide. The study also suggested that the structures observed in this borehole were hydraulically conductive, meaning that the Opalinus Clay true permeability should be even lower than the range given by statistical results.

Boldt-Leppin et al. (2003) studied the King site claystone formation and obtained differences of one to three orders of magnitude between laboratory hydraulic conductivity results and results using tidal analysis. These discrepancies were explained by scale factor effects and presence of fractured area.

3.8.5. COMPILATION OF HYDRAULIC CONDUCTIVITY RESULTS ACQUIRED ON BDB-1 BOREHOLE

Reliable estimates of permeability and specific storage that describe the bulk hydraulic behaviour are needed for the evaluation of radionuclide transport in geological formations. Linking the results of laboratory tests to bulk characteristics at the regional scale is not straightforward and the meaning of measured values has to be interpreted. Sedimentary rocks are generally associated with anisotropic properties such as permeability, diffusion coefficient and mechanical features. In the Opalinus Clay, which is an overconsolidated clay, a moderate permeability anisotropy ratio of 5.5 was estimated based on laboratory permeameter tests (Fernàndez et al., 2007). The Steady State method using Hassler cell was implemented in our study with the objective to acquire the permeability anisotropy, but a relevant evaluation was not obtained due to sample brittleness. When this latter characteristic can be limited by resin injection then Hassler cell can be a satisfactory mean for determining parameters such as anisotropy and kinematic porosity, which are difficult to obtain in situ.

The petrophysical model is based on a conceptual parallel plane geometry which would be associated to a flow orientation parallel to bedding planes. Since BDB-1 borehole was drilled perpendicular to bedding plane, the main solicited direction for fluid flow during hydraulic testing is also parallel to stratification. For its part, tidal analysis is mainly based on gravitational forces that propagate radially from the center of the Earth and should result, given the setting of the Mont Terri anticline, in composite values of parallel and perpendicular to bedding permeabilities.

Although the petrophysical model may be unsuited to carbonated formations, calculation was also performed on the Passwang Formation and the Staffelegg Formation, which shows similar petrophysical parameters. Another questionable point is the use of a constant value for the Archie's exponent since this parameter depends on the nature of the porous medium. Conductivities values obtained in BDB-1 with variable cementation factor are only indicative and not quality-assured, given the uncertainties linked to data acquisition. Indeed, the Opalinus Clay was in the air-drilled section of the borehole, giving constraints for in-situ determination of cementation factor.

The Main Fault that intersects the laboratory does not impact the barrier function of the Opalinus Clay. Indeed, the sealing of fault planes by calcite shear fibres and clay minerals induce small effect of tectonic deformation on the hydraulic properties of the Opalinus Clay (Nussbaum et al, 2011). This observation is supported by the consistency between the hydraulic tests performed in the intact shaly facies and those carried out in the interval crossing the fault zone. Similarly, no contrast can be identified on the different profiles obtained with the petrophysical model.

Hydraulic permeability measurements performed on BDB-1 borehole samples are compiled in Figure 3.33 and result tables can be found in Annex IV.
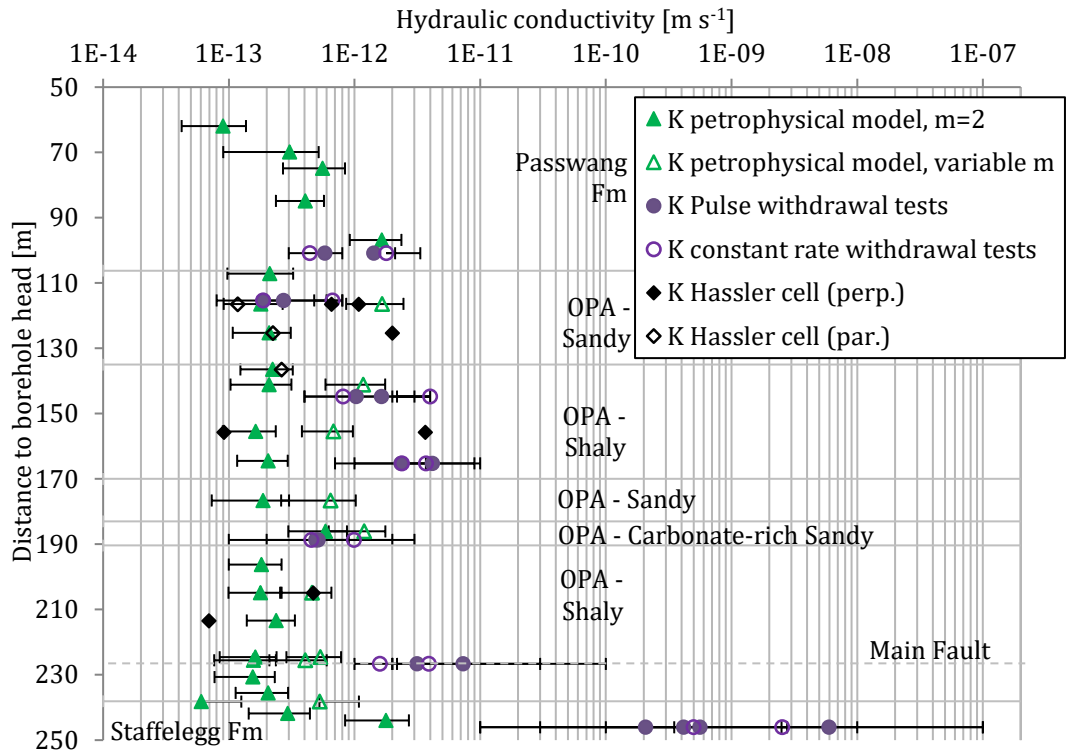
Figure 3.33: Comparison of hydraulic conductivity measurements acquired on BDB-1 borehole using different approaches (petrophysical model, in situ hydraulic tests and laboratory permeameter tests)

CHAPTER 4.   TRANSPORT MODELLING

4.1.   CHLORIDE PROFILE MODELLING

A more extended version of this section can be found in Yu et al., 2017b (see Annex VI)..

4.1.1.   MODELLING ASSUMPTIONS AND SCENARIO

Although the predominant character of diffusion among other transport processes in low permeability formations is generally claimed, such assumption, which greatly simplifies transport numerical calculations, must be verified using the Peclet number (Soler, 2001):

$$Pe = \frac{\langle q \rangle L}{\langle D_e \rangle} \tag{4.1}$$

where $\langle q \rangle$ [m s^{-1}] is the average specific discharge (Darcy's velocity), L [m] is a characteristic distance for transport, here taken to be the geological formation half thickness, and $\langle D_e \rangle$ [m^2 s^{-1}] is the harmonic mean of effective diffusion coefficients. It is classically stated that for Pe < 1, diffusion dominates over advection and advection is dominant over chemical diffusion if Pe > 1. However, in their discussion of transport phenomena in low permeability environments, Huysmans and Dassargues (2005) show that for Peclet numbers (Eq. (4.1)) as high as 10, numerically simulated chlorinity profiles considering advection and diffusion or diffusion alone only differed by 10% pointing to a negligible advective contribution. Consequently, one can consider that below a value of 10 for Pe, diffusion models are sufficiently accurate for chlorinity profile interpretations.

The Opalinus Clay is characterised by maximum pressures (or hydraulic head h), temperature and chlorinity values within the formation yielding corresponding differences with the surrounding aquifers of at least 5 bars (Δh = 50 m), ΔT = 4°C, and Δc = 0.42 mol L^{-1} respectively. Note that in fact, a monotonic cross-formational temperature difference of 8.5°C per 100 m is observed.

Considering that osmotic processes are at work in the Opalinus Clay, the 1D Darcy's velocity accounting for osmotic terms can be expressed as (Gonçalvès et al., 2015):

$$q = -K \frac{\partial h}{\partial z} + \frac{\nu R T \varepsilon_c K}{\rho_f g} \frac{\partial c}{\partial z} - \frac{\varepsilon_T}{\rho_f g} K \frac{\partial T}{\partial z} \tag{4.2}$$

where K [m s^{-1}] is the cross-formational hydraulic conductivity, z is the axis perpendicular to the bedding, h [m] is the hydraulic head, ρ_f is the porewater density [kg m^{-3}], g [9.81 m s^{-2}] is the gravitational acceleration, ε_c[-] and ε_T [Pa K^{-1}] are respectively the chemical osmotic efficiency and the thermo-osmotic coefficient, ν is the number of dissociated species for a salt (e.g. 2 for NaCl), R [8.32 m^3 Pa K^{-1} mol^{-1}] is the gas constant, T [K] is the temperature, and c [mol m^{-3}] is the

chloride concentration. Note that for this first-order calculation, no gravity effect due to salinity is considered enabling the use of the hydraulic head h.

The first term in the right-hand side of Eq. (4.2) is related to purely darcian fluid flow, the second and third terms to the chemical and thermal osmosis, i.e. fluid flow driven by salinity and temperature gradients. The petrophysical parameters of the Opalinus Clay together with the thermo-osmotic model by Gonçalvès et al. (2015) points to a thermo-osmotic coefficient ε_T in the order of 10^5 Pa K^{-1}. For the two remaining terms, simple gradients given by $\Delta h/L$, $\Delta c/L$, and $\Delta T/L$ can be introduced in Eq. (4.1) and (4.2).

Peclet calculations require equivalent transport parameters (harmonic means across the formation, perpendicular to the bedding). Using the data described in Sections 3.7.2 and 3.8, a harmonic mean of 10^{-11} m^2 s^{-1} and 1.85×10^{-13} m s^{-1} is found for D_e and K. Using these values for an equivalent NaCl ($\nu = 2$) system, $\varepsilon_T = 10^5$ Pa K^{-1}, and ε_c between 0.036 and 0.081 (Noy et al., 2004) yields a Peclet number of between 1.3 and 1.5. It can thus be concluded that transport is likely dominated by diffusion for the Opalinus Clay. Therefore, mass transport calculations can be made by solving Eq. (4.3) using a simple and robust finite difference numerical scheme.

$$\omega \frac{\partial c}{\partial t} = \frac{\partial}{\partial z}(D_e(\omega)\nabla c) \tag{4.3}$$

The paleohydrogeological evolution was chosen accordingly to the conclusions of Bossart and Wermeille (2003), who constrained the erosion and thus the exhumation of the Middle Jurassic limestone overlying the Opalinus Clay between 10.5 and 1.2 Ma (time t_0 hereafter). At that time, the subsequent rapid flushing of the Middle Jurassic limestone pore water by meteoritic water brought the chlorinity to zero which constitutes a boundary condition for the transport model. The activation of the Early Jurassic limestone aquifer underlying the Opalinus Clay occurred between 0.5 and 0.2 Ma (time t_1). A plausible range between 14 and 23 g L^{-1} was chosen for the initial chlorinity C_0 prior to the Jura Mountains folding (Mazurek et al., 2011).

Cross-formational diffusive transport parameters, namely effective diffusion coefficient and diffusion accessible porosity, were deduced from laboratory experiments carried out on BDB-1 samples and described in Sections 2.2.4 and 2.2.5. Exhumation times t_0 and t_1 together with the initial chlorinity are used for boundary and initial conditions definition of the 1D diffusion model. At initial time t_0, the chlorinity is set to C_0 within the Opalinus clay, the upper and lower concentration boundary conditions are 0 and C_0, respectively. Then, when the simulation time reaches t_1, the lower boundary condition is set to zero. These boundary conditions allow simulating diverging diffusive mass transport from the Opalinus Clay towards first the upper aquifer alone then towards both aquifers. The model takes into accounts seven formations showing different properties listed in Table 4.1. A Bayesian inversion using a Monte Carlo Markov Chain (MCMC) method (Tarantola, 2005) was used to identify model parameters.

Table 4.1: *Input parameters and associated uncertainties involved in the MCMC inversion process. Accessible porosities and formation thicknesses were kept constant. CI stands for Confidence Interval.*

Formation	Thickness [m]	ω [vol.%]	De [m² s⁻¹] (·10⁻¹¹)		
			Measurements	*A priori*	*A posteriori* Mean and 95% CI
Passwang Formation	69	7.5	D_e^7: 0.817 ± 0.2	$[10^{-1}\text{-}20]$	2.66 [1.51; 4.81]
OPA – Sandy facies	29	6.9	D_e^6: 7.38 ± 4.36	$[10^{-1}\text{-}20]$	6.55 [3.92; 11.61]
OPA – Shaly facies	35	7.6	D_e^5: 0.597 ± 0.2	$[10^{-1}\text{-}20]$	0.30 [0.18; 0.41]
OPA – Sandy facies	14	5.4	D_e^4: 2.71 ± 1.9	$[10^{-1}\text{-}20]$	1.91 [0.59; 4.12]
OPA – Carbonate-rich Sandy facies	6	6.8	D_e^3: 2.04 ± 0.68	$[10^{-1}\text{-}20]$	2.91 [0.39; 4.84]
OPA – Shaly facies	47	7.7	D_e^2: 3.56 ± 1.42	$[10^{-1}\text{-}20]$	0.33 [0.04; 0.62]
Staffelegg Formation	63	4.5	D_e^1: 0.451 ± 0.132	$[10^{-1}\text{-}20]$	0.59 [0.15; 1.04]

Parameter	Value	Range			
	A priori				*A posteriori*
Activation time [Ma]					
Middle Jurassic aquifer t_0 (upper boundary)	-5	[-10.5; -1.2]			-4.54 [-6.77; 1.7]
Early Jurassic aquifer t_1 (lower boundary)	-0.25	[-0.5; -0.2]			-0.24 [-0.3; -0.2]
Initial chlorinity C_0 [g L⁻¹]	19	[14;23]			19 [17.3; 22]

4.1.2. MCMC MODELLING RESULTS

The parameters to be calibrated must be chosen carefully since for more than 10 parameters, implementing MCMC methods becomes hazardous (large time- and cpu-consuming, convergence issues). However, under the assumption of purely diffusive mass transport, since the porosity intrinsically appears ($D_e = \omega D_p$) in both sides of Eq. (4.3), this parameter does not impact calculated chlorinity profiles which are only controlled by the pore diffusion coefficient. Therefore, porosity was not considered in our inverse modelling and was kept constant for each formation. From a practical standpoint, the calibrated parameters were the cross-formational effective diffusion coefficient for each of the seven formations D_e values (in fact D_p since ω is fixed, see above), t_0, t_1 and C_0 which are all considered uncertain. Uniform *a priori* distributions were considered for these ten parameters using lower and upper boundaries described in Section 4.1.1 for t_0, t_1 and C_0, and boundaries encompassing the measurements for the seven formation D_e values (Table 4.1).
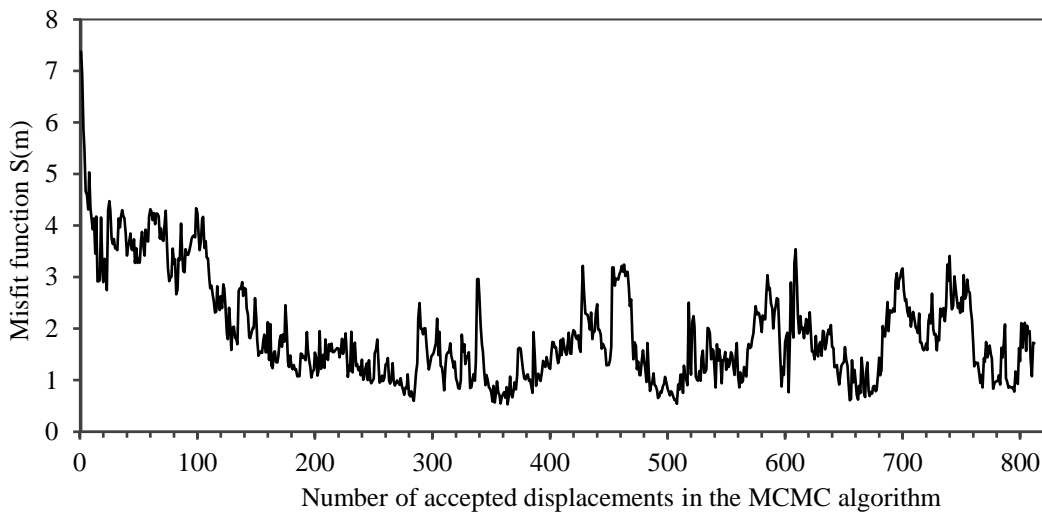
Figure 4.1: Misfit function as a function of the number of accepted displacements in the MCMC algorithm.

In the course of the MCMC inversion process involving ten parameters (a priori values in Table 4.1), the misfit function reached a plateau after about 2000 iterations for 100000 performed iterations. The convergence of the MCMC approach is characterised by a sharp decrease of the misfit function value from almost 7 to 1.5 on average after 2000 iterations (almost 200 accepted movements) of the random walk as shown in Figure 4.1. Only about 800 random moves were accepted, indicating a relatively low number of parameter sets that fit the experimental data. The sets of parameters leading to the 5% lower misfit values were used to establish the *a posteriori* marginal distributions of the ten parameters shown in Figure 4.2.
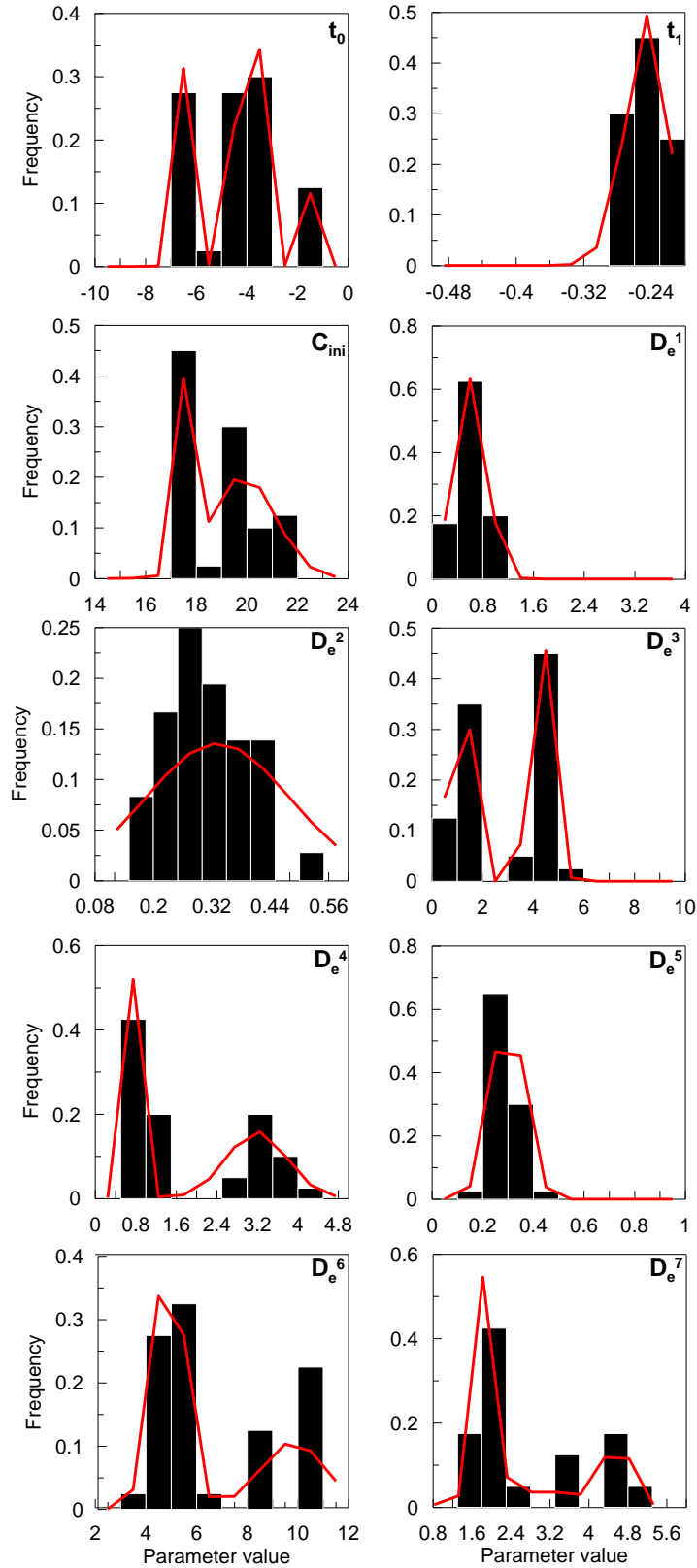
Figure 4.2: A posteriori distributions (pdfs) for each parameter of the diffusion model. Parameters values in [×10⁻¹¹ m² s⁻¹] for D_e, [g L⁻¹] for C_0, and [Ma] for t_0 and t_1. The histograms results from the MCMC approach (Section 3.5). In red, the fitted theoretical distributions (Gaussian mixtures: t_0, C_0, D_{e3}, D_{e4}, D_{e6}, and D_{e7}, Gaussian: D_{e1}, D_{e2}, and D_{e5}, and Lognormal: t_1)

Both multimodal and unimodal distributions are obtained. Multimodal distributions were fitted by gaussian mixture distributions, all unimodal variables were fitted by a gaussian model except for C_0 that is described by a log normal distribution. Mean values and 95% confidence intervals for each parameter were calculated using the fitted distributions (see Table 4.1).

Multimodal distributions were fitted by gaussian mixture distributions:

$$\alpha G(\mu_1, \sigma_1) \ + \ \beta G(\mu_2, \sigma_2) \ + \ \gamma G(\mu_3, \sigma_3) \qquad\qquad (4.4)$$

where $G(\mu_i, \sigma_i)_{i=\{1,..3\}}$ are Gaussian distributions and α, β, and γ are the respective weights. The fitted distribution parameters are listed in Table 4.2.

Table 4.2: Parameters of fitted pdf with effective diffusion coefficients D_e [× 10^{-11} m^2 s^{-1}], activation times t_0 and t_1 [Ma], and initial chloride concentration C_0 [g L^{-1}].

Variable	α	β	γ	μ_1	σ_1	μ_2	σ_2	μ_3	σ_3
t_0	0.32	0.56	0.12	-6.45	-3.95	-1.78	0.19	0.22	0.10
$Log(-t_1)$	1	0	0	-0.61	0.04	-	-	-	-
C_0	0.37	0.63	0	17.48	19.87	1.22	0.09	-	-
D_e^1	1	0	0	0.60	0.22	-	-	-	-
D_e^2	1	0	0	0.33	0.14	-	-	-	-
D_e^3	0.16	0.3	0.54	0.48	1.74	4.33	0.08	0.08	0.3
D_e^4	0.53	0.47	0	0.75	3.18	0.57	0.10	-	-
D_e^5	1	0	0	0.3	0.06	-	-	-	-
D_e^6	0.67	0.33	0	4.91	9.83	1.24	0.55	-	-
D_e^7	0.58	0.22	0.2	1.86	3.08	4.58	0.14	1.19	0.14

For multimodal distributions, the weights and means of each fitted normal distribution component are used to calculate an "overall mean" for a given parameter as the weighted average of the mean values. Therefore, the relative importance of each gaussian distribution within the gaussian mixture is respected. Note that the low number of sampled values in the parameter space is likely a limitation for the *a posteriori* marginal pdfs identification method described in Section 3.5. However, taking more samples (40% of accepted displacements) yields the same type of marginal distributions but with slightly different statistical parameters and a larger misfit when the mean parameters values are used in a direct simulation.

As shown in Figure 4.3a, the simulation of diffusion for chloride matches fairly well the experimental data considering the mean a posteriori values for the parameters (Table 4.1). Except for two diffusion coefficients values (Passwang Formation and Opalinus Clay basal shaly facies), the fitted parameters are highly consistent with the measurements and exhumation time expectations (Figure 4.3b). The misfit for diffusion coefficients can be due to an imperfect mechanical confining of the Opalinus Clay sample leading to an overestimation of the measured D_e for the Opalinus Clay shaly facies. On the other hand, the Passwang Formation is more heterogeneous compared to the different facies of the Opalinus Clay. Lithostratigraphic investigation carried out by Hostettler et al. (2017) on BDB-1 drillcores showed that this

formation exhibits variable lithology (silty to fine sandy marls, quartz sand and biodetrital sandy limestones, ferruginous limestones, iron oolithic marls and limestones). The number of samples investigated in laboratory-scale diffusion experiments was likely insufficient to reflect this variability in the present study.

Figure 4.3: Comparison between a) experimental and simulated chloride profile obtained with the mean a priori and a posteriori values for the parameters and b) experimental and fitted diffusion coefficients, error bars represent 95% confidence interval. Z denotes the orthogonal distance to the Staffelegg Formation base.

The sensitivity of the MCMC model was assessed and devoted to the analysis of the influence of the fitted parameters and the effect of their uncertainties. The uncertainty range for each parameter listed in Table 4.1 was independently tested. The resulting plots are presented in Figure 4.4. With a time range of several million years, changes in activation time for the upper aquifer (t_0) induce moderated effect on the envelope profiles, relatively to variations of the lower aquifer activation time (t_1), which only extend on 300 thousand years. In the lower part of the stratigraphic column, the simulated chloride profile is mainly constrained by the lower boundary condition and the Staffelegg Formation effective diffusion coefficient (D_e^1), as experimental data are lacking in this section. For a same authorized variation range of effective diffusion coefficients ($1 \cdot 10^{-12}$ to $2 \cdot 10^{-10}$ m^2 s^{-1}), the most pronounced impact of parameter change on the fit is observed for the Staffelegg Formation and the upper part of the column (D_e^5 and D_e^6 in the Opalinus Clay, and D_e^7 in the Passwang Formation).
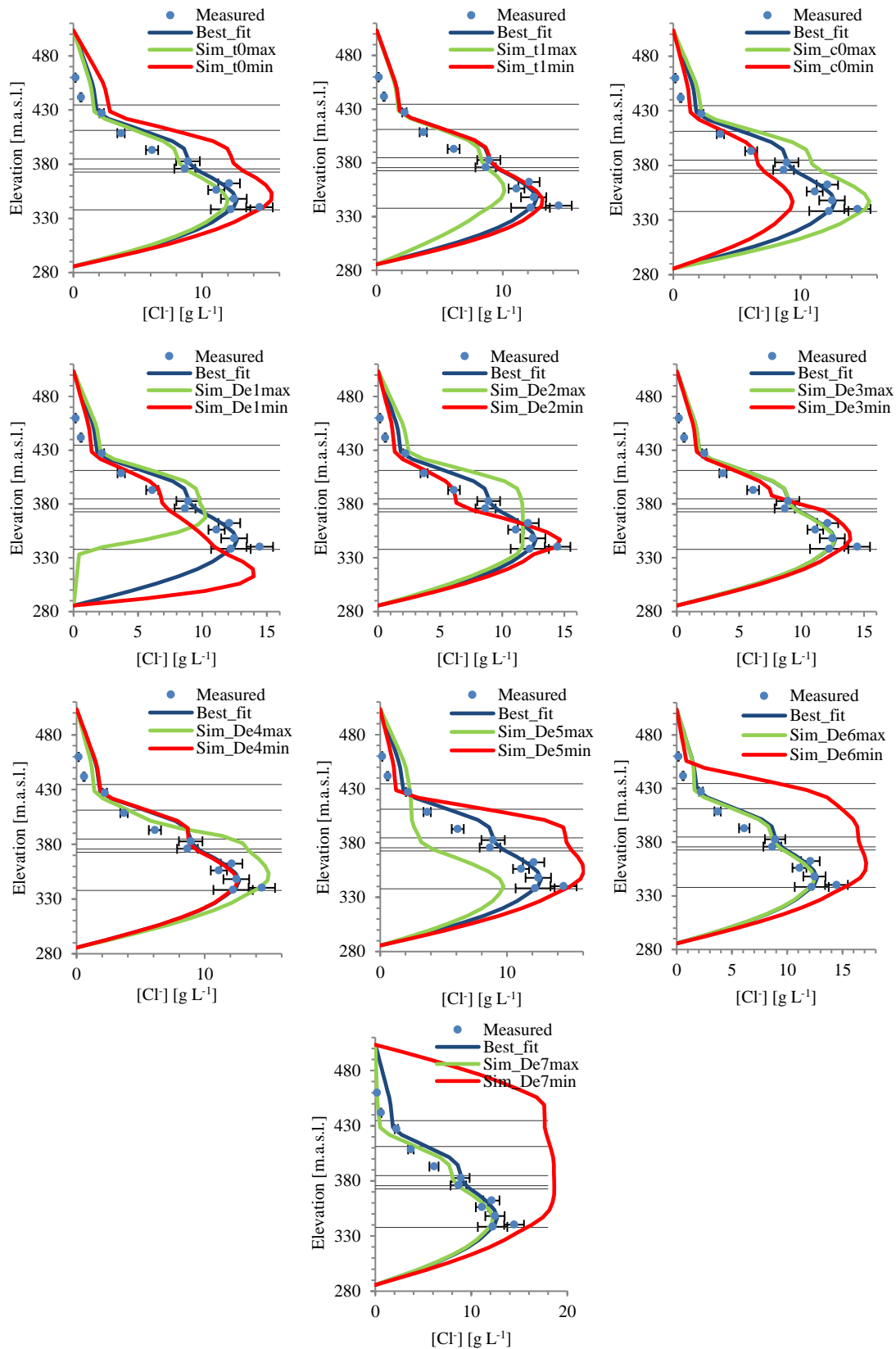
Figure 4.4: Results of the sensitivity analysis on the fitted parameters: influence of the aquifers activation times, initial concentration and effective diffusion coefficients on the simulated chloride profile. Z denotes the orthogonal distance to the Staffelegg Formation base.

The modelling results are globally consistent with previous studies carried out at the Mont Terri rock laboratory. A lower equivalent effective diffusion coefficient for anions of $4.6 \cdot 10^{-12}$ m^2 s^{-1} was used in Mazurek et al. (2011) for the Opalinus Clay and the directly adjacent formations, whereas different diffusion coefficient values were considered for each unit along the rock sequence in the present study. A higher cross-formational equivalent diffusion coefficient of $6.3 \cdot 10^{-12}$ m^2 s^{-1} for the Opalinus Clay explains the shorter time obtained for the adjacent aquifers activation in comparison with the study of Mazurek et al. (2011): 4.5 Ma compared to 6 Ma for the upper aquifer and 0.246 Ma compared to 0.5 Ma for the lower aquifer. However, the activation age at -4.54 Ma proposed here is close to one of the major morpho-tectonic event proposed by Kuhlemann and Rahn (2013) at -4.2 Ma.

An integrated study from BDB-1 borehole samples characterisation on the Opalinus Clay transport capabilities and transport modelling was performed. Petrophysical analysis enabled the acquisition of water accessible porosity, grain density and water contents along the rock sequence. Out diffusion and aqueous leaching techniques were used to obtain chloride concentrations of porewater in the Opalinus Clay and its bounding formations. Effective diffusion coefficients and diffusion accessible porosities were also investigated by radial diffusion and through diffusion experiments.

The measured chloride contents are in good agreement with previous investigation performed at the Mont Terri tunnel level, and show an asymmetric bell-shaped trend increasing to a high chloride concentration of 14.4 g L^{-1} towards the bottom of the Opalinus Clay. Moreover, chloride to bromide ratios reflect a marine signature in the clay rock. The chloride profile suggests a diffusive exchange between the argillaceous formation and the adjacent aquifers, with deferred activation times of the fresh-water sources linked to the surface erosion of the geological formations. This scenario was implemented in a Monte Carlo Markov Chain algorithm, which enabled to assess the best fitting set of parameters (initial chloride content, aquifer activation times and diffusion coefficients) and associated confidence intervals explaining the present-day chloride profile. Experimental and simulated data are comparable for respective diffusion times of 4.54 Ma and 0.246 Ma between the Opalinus Clay and the Middle Jurassic (overlying) and Early Jurassic (underlying) limestones.

The present study confirms the paleohydrogeological evolution of the Mont Terri site from the folding of the Jura Mountains. This scenario is fundamental to constrain the transient modelling of the overpressure regime observed in the Opalinus Clay to fully characterise transport processes in this formation.

4.2. OSMOTIC INTERPRETATION OF THE PRESSURE PROFILE

4.2.1. TRANSIENT SIMULATIONS

4.2.1.1. Mathematical formulation

Fluid flow and transport processes are calculated in the cross-formational direction, denoted Z, corresponding to the maximum driving forces (pressure, salinity, temperature gradients) and thus presumably constituting a main direction for fluxes.

Taking into account osmotic processes, Darcy's velocity in the Z direction writes:

$$q = -\frac{k}{\mu_f}\left(\frac{\partial p}{\partial Z} + \rho_f g cos(\alpha)\right) + \frac{kvRT\varepsilon_c}{\mu_f}\frac{\partial c}{\partial Z} - \frac{k\varepsilon_T}{\mu_f}\frac{\partial T}{\partial Z} \qquad (4.5)$$

where k [m^2] is the cross-formational intrinsic permeability, μ_f [Pa s] the dynamic viscosity of the fluid, p [Pa] the pressure, ρ_f [kg m^{-3}] the density of the fluid, g [9.81 m^2 s^{-1}] the acceleration due to gravity, α is the slope of the Opalinus Clay formation, v is a parameter describing the total ionic concentration of a dissolved salt, R [8.31 10^3 Pa K^{-1} mol^{-1}] is the gas constant, T [K] the temperature, ε_c is the chemical osmotic efficiency, c [mol m^{-3}] the chloride concentration in the bulk solution, found in adjacent aquifers or macropores, and ε_T [Pa K^{-1}] is the thermo-osmotic coefficient. If c denotes the chloride concentration, the total ionic concentration for a NaCl salt is $2c$ and $v = 2$, while for a CaCl$_2$ salt, $v = 1.5$ and the total concentration equals to $1.5c$.

The first term in the right-hand side of Equation (4.5) is the classical Darcy's law in pressure where $\rho g cos(\alpha)$ is the gravity effect along the Z axis. The second and third terms represent the chemical and thermal osmosis, respectively.

Equation (4.5) is introduced and the mass balance equation:

$$\frac{\partial}{\partial Z}\left(\rho_f q\right) = -\frac{S_s}{g}\frac{\partial p}{\partial t} \qquad (4.6)$$

yields:

$$\frac{\partial}{\partial Z}\left(\rho_f\left(-\frac{k}{\mu_f}\left(\frac{\partial p}{\partial Z} + \rho g cos(\alpha)\right) + \frac{kvRT\varepsilon_c}{\mu_f}\frac{\partial c}{\partial Z} - \frac{k\varepsilon_T}{\mu_f}\frac{\partial T}{\partial Z}\right)\right) = -\frac{S_s}{g}\frac{\partial p}{\partial t} \qquad (4.7)$$

where S_s [m^{-1}] is the specific storage coefficient accounting for the hydro-mechanical behavior of the porous media. Solving Equation (4.7) requires knowing $c(Z)$ and $T(z)$ and thus solving mass and heat transport equations. For the sake of simplicity, a time constant geothermal gradient $\partial T/\partial Z$ is assumed considering that the two exhumation stages slightly modified the absolute temperatures but not the temperature gradient. Consequently, heat transport is not calculated and an average temperature of 300 K is considered for thermo-osmotic coefficient calculations.

The transient chlorinity profile is calculated by solving the mass transport equation:

$$\frac{\partial}{\partial Z}\left(D_e \frac{\partial c}{\partial Z} - qc\right) = \omega_e \frac{\partial c}{\partial t} \tag{4.8}$$

The resolution of Equation (4.7) requires the concentration profile to be known while solving Equation (4.8) involves the specific discharge q in the advective term. Equations (4.7) and (4.8) have to be solved simultaneously, whence the coupled flow processes.

4.2.1.2. Numerical resolution

Based on geological and petrophysical description of BDB-1, seven formations are considered in the 1D model. Equations (4.7) and (4.8) are solved using a finite differences method where the advection term in the transport equation is treated by an upwind scheme. In order to reduce the computation times, the advective term is discretised explicitly while the diffusion term is implicit. This requires small time steps in comparison to the characteristic time of the system for a numerical resolution where Equations (4.7) and (4.8) can thus be solved successively. The fluid density and dynamic viscosity are kept constant assuming weak chlorinity and temperature effects on fluid flow in comparison to the other processes taken into account here. A regular mesh spacing of 2 m and time spacing of 1000 yrs were used.

To simulate the temporal variation of both chlorinity and pressure, a geological scenario has to be considered. The simulation is started at the exhumation time of the overlying aquifer (-4.4 Ma) at constant chlorinity C_{ini} = 19 g L^{-1} immediately followed by a groundwater flushing by meteoritic waters which established the topography-driven hydrodynamics and related aquifer pressures and the zero-concentration upper boundary condition (see Section 4.1). Pressure initial and boundary conditions are set as follows: i) a time constant upper pressure boundary condition equal to the present-day value (8.04 bars); ii) an initial hydrostatic pressure across the Opalinus Clay based on the upper value and iii) a constant lower boundary condition equal to its initial value until the second exhumation time. At the lower aquifer exhumation time (-0.24 Ma), the lower boundary conditions (pressure, chlorinity) are set to the present-day values of the lower aquifer, 24.85 bar and 0 g L^{-1}, respectively. The lower pressure boundary condition was deduced from the hydraulic heads of the underlying aquifer.

4.2.2. PSEUDO STEADY-STATE (PSS) SIMULATIONS

Alternatively to transient models which necessitate cost-consuming simulations of the geological evolution of the system, simplified first-order calculations can be proposed. Although a priori questionable, the reliability of quasi steady-state simulations while the chlorinity profile is not at equilibrium can be envisaged for the reasons detailed below. Considering a steady-state in osmotic flows means an equilibrium between pressure, temperature and chlorinity profiles. The temperature profile across the Opalinus Clay is at quasi thermal diffusion equilibrium characterised by a near linear shape, as in many sedimentary basins. This is obviously not the case for the chlorinity profile which is characterized by a maximum value within the Opalinus

formation decreasing to its boundaries. However, it was shown that diffusion controls chemo-osmotic processes with a characteristic time far larger than the hydraulic one (Rousseau-Gueutin et al., 2008; Gonçalvès et al., 2012; Trémosa et al., 2012b; Neuzil, 2015). Consequently, the pressure profile adjusts itself to the chlorinity profile roughly instantaneously in a succession of quasi-equilibrium states. Therefore, it can be assumed that a steady-state calculation based on the present state (chlorinity and temperature profiles) will bring some reliable information. The main interest relies in the rapidity and simplicity of such calculation.
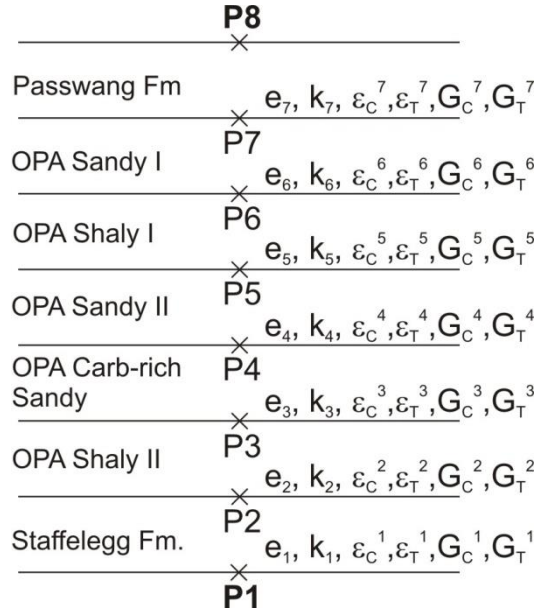
Figure 4.5: Geometrical framework for pseudo steady-state calculations. P1 and P8 are prescribed boundary conditions. G_c^i, G_T^i, ε_C^i, ε_T^i are respectively the chlorinity and temperature gradient, the chemo- and thermo-osmotic coefficients of formation i, e_i and k_i are the thickness and intrinsic permeability of formation i.

The steady-state requires q to be constant. For each layer i depicted in Figure 4.5, the constant q writes:

$$q = -\frac{k_i}{\mu_f}\left(\frac{P_{i+1} - P_i}{e_i} + \rho g cos(\alpha)\right) + \frac{k_i \nu RT \varepsilon_c^i}{\mu_f}G_c^i - \frac{k_i \varepsilon_T^i}{\mu_f}G_T^i \qquad (4.9)$$

The system of seven equations and seven unknowns (q, $P_{i=2,..,7}$) can be written in the following form:

$$q = \frac{1}{\mu_f \sum_{i=1}^{7}\frac{e_i}{k_i}}\left(P_1 - P_8 + \nu RT\sum_i \varepsilon_c^i G_c^i e_i - \sum_i \varepsilon_T^i G_T^i e_i - \rho g cos(\alpha)\sum_i e_i\right) \qquad (4.10)$$

and

$$P_i = P_{i-1} + \left(\frac{-q\mu_f}{k_{i-1}} + \nu RT \varepsilon_c^i G_c^i - \varepsilon_T^i G_T^i - \rho_f g cos(\alpha)\right) e_i \qquad (4.11)$$

for i = 2,…, 7.

Solving Equations (4.10) and (4.11) is straightforward and only requires knowing the chlorinity gradients G_c^i, temperature gradients G_T^i and the average chlorinity for each formation (to compute ε_T^i, ε_c^i). All these quantities are identified on the measured chlorinity and temperature profile. In addition, a constant value G_T (-0.08 °C m^{-1}) for the temperature gradient can be considered.

4.2.3.   PARAMETER VALUES

For transient simulations, the effective diffusion coefficients obtained from the calibration of a purely diffusive transport model for the chlorine profile are used. Time-varying chemical osmotic efficiency and thermo-osmotic parameter due to their dependency to the natural tracer concentration are calculated using theoretical expressions by Bresler (1973) and Gonçalvès et al. (2012), respectively using petrophysical parameters by formation (*CEC*, A_s, porosity) for monovalent and divalent solutions. Average measured intrinsic permeability values and specific storage coefficients are used (Yu et al., 2017). This parametrisation, together with the initial and boundary conditions, and exhumation scenario forms the base-case simulation.

For pseudo steady-state calculations, measured intrinsic permeabilities and expressions by Bresler (1973) and Gonçalvès et al. (2012) for the osmotic coefficients are also used. For such simulations, there is no need to characterise mass or heat transport since the chlorinity, temperature and their gradients are directly deduced from the measured profiles. Similarly to transient simulations, an average temperature of 300 K is considered for thermo-osmotic coefficient calculations.

The parameter values are given in Table 4.3.

Table 4.3: Parameters values used in the pressure profile simulations: formation and facies thickness (t), intrinsic permeability (k), half-pore size (b), specific surface area (A_s), total porosity (ω), chloride accessible porosity (ω_{Cl}), cation exchange capacity (CEC). Mean chloride concentration ($[Cl^-]_m$), chemo-osmotic efficiency (ε_c) and thermo-osmotic coefficient (ε_T) in monovalent and divalent cases are given for the pseudo steady-state simulation. The thermo-osmotic coefficients were divided by 1.3 for calibration purpose.

	t	k	b	A_s	ω	ω_{Cl}	CEC	$[Cl^-]_m$	ε_{c_mono}	ε_{c_div}	ε_{T_mono}	ε_{T_div}
	[m]	[m^2]	[nm]	[m^2 g^{-1}]	[%]	[%]	[meq g^{-1}]	[mol L^{-1}]	[-]	[-]	[Pa/K]	[Pa/K]
Passwang Fm.	69	1.00E-19	3.38	5.37	12.17	7.5	0.0470	0.03	0.037	0.011	0.00E+00	0.00E+00
OPA Sandy I	29	3.74E-21	2.07	26.89	12.6	6.9	0.0797	0.06	0.646	0.297	2.10E+05	1.31E+05
OPA Shaly I	35	4.76E-20	1.85	36.41	13.9	7.6	0.0948	0.14	0.488	0.176	1.83E+05	1.08E+05
OPA Sandy II	14	3.74E-21	2.46	15.28	9.9	5.4	0.0934	0.24	0.073	0.013	3.68E+05	2.71E+05
OPA – Carbonate-rich Sandy	6	9.06E-21	3.45	14.38	12.3	6.8	0.0480	0.24	0.023	0.009	7.56E+04	5.50E+04
OPA Shaly II	47	7.80E-20	1.73	32.24	13.3	7.7	0.1103	0.28	0.222	0.051	2.36E+05	1.60E+05
Staffelegg Fm.	63	9.80E-18	3.37	13.92	9.5	4.5	0.0584	0.17	0.109	0.024	2.06E+05	1.45E+05

4.2.4. MODELLING RESULTS

In natural clay rock, divalent cations such as Ca^{2+} are present in the pore fluid. It was shown that a small amount of divalent cations decreases osmotic coefficients to their purely divalent value (Trémosa, 2010; Gonçalvès et al., in review). For chemical osmosis, this dramatically decreases the ability of such process to produce overpressures (Trémosa, 2010). Osmotic coefficients are thus calculated firstly for divalent solutions. The validity of any comparison between pseudo steady-state (PSS) pressure outputs (based on the present-day chlorinity profile) and transient ones requires that the calculated final chlorinity profile matches as closely as possible the observed chlorinity profile. In any case, this is a natural expectation for the transient model.

4.2.4.1. Transient simulation results

Despite some discrepancy, the first base case run using the transient model without any calibration process produces final simulations close, at first order, to measurements especially for pressure. However, the apparent relatively good agreement between the calculated pressures at the end of the transient simulation and the data shown in Figure 4.6b has to be moderated because of the discrepancy between calculated and measured chlorinity (Figure 4.6a).
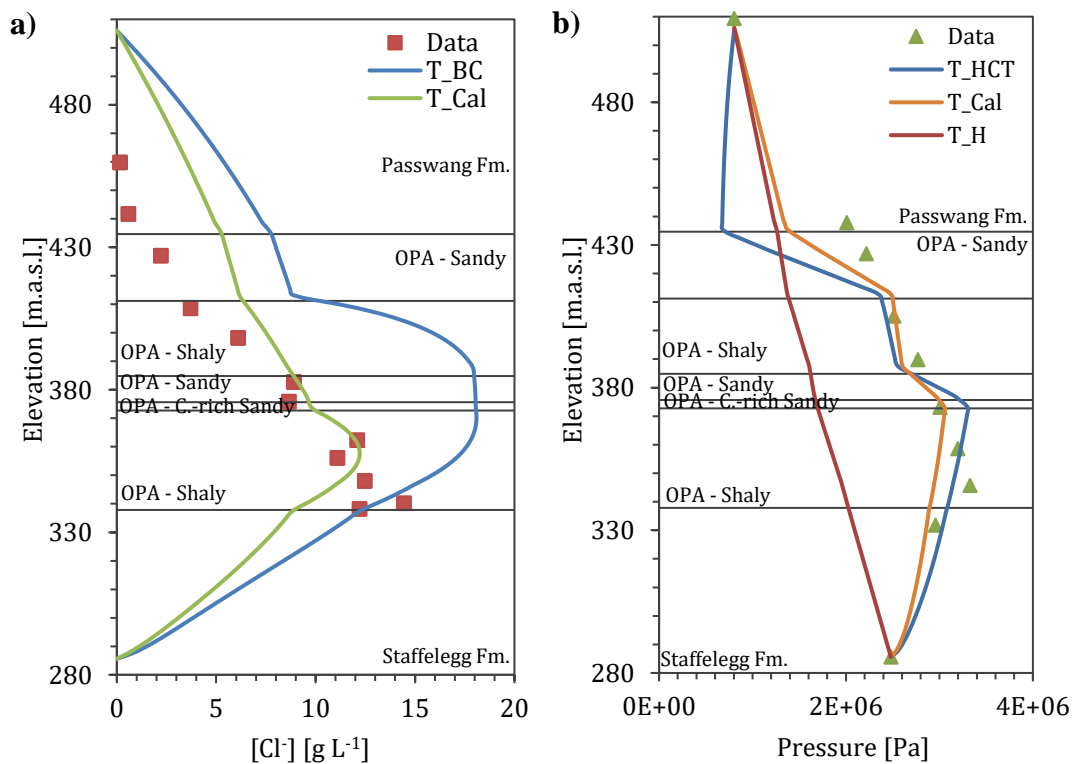
Figure 4.6: a) present-day simulated and measured chlorinity profile in the transient base-case (T_BC) and using calibrated D_e values (T_Cal); b) calculated present-day pressure profile using transient model (T in legend). The simulation considering purely hydraulics (no osmosis) is labeled 'H', and the simulation including hydraulics chemical and thermo-osmosis 'HCT' using the base case, the calibrated simulation for both ε_T and D_e is labeled T_Cal.

According to our simulations, the advective flow is dominated by thermo-osmosis (see below). Higher calculated concentrations due to the advection causes lower values for the thermal osmotic coefficients and thus lower pressures. In other words, if a better agreement between calculated salinities and data was obtained, higher pressures would have been calculated at the end of the transient simulation. In order to confirm the potential role of osmotic processes and especially thermal osmosis, some modelling refinement using parsimonious calibration within the uncertainty range of parameters has to be made.

The most sensitive parameters for the transport model (among the ten parameters previously used in the purely diffusive model) are the effective diffusion coefficients which must be increased to match the chlorinity data. However, when larger D_e values are used to obtained lower calculated salinities, larger ε_T values are calculated in the model increasing calculated pressures and thus the deviation from the pressure data. Therefore, increasing D_e values must be accompanied by a decrease of ε_T within the identified uncertainty range of the thermo-osmotic permeability model associated with molecular parameters ($\pm$ 0.3 in $\log(\varepsilon_T)$).

In the upper part of the Opalinus Clay, pressures calculated by a simple purely hydraulic simulation follows more closely the pressure data, suggesting that the Passwang Formation has no membrane behaviour. The slight calibration using a simple gradient method is based on the following constraints: i) no membrane properties (ε_T = 0) is considered for the Passwang Formation, ii) in order to match the pressure data, all the remaining thermo-osmotic coefficients have to be divided at most by a factor 2 (the above-mentioned uncertainty), and iii) higher effective diffusion coefficients.

The best agreement between simulation outputs and data shown in Figure 4.6 is obtained by dividing the osmotic permeability coefficient by 1.3 and using the D_e values in Table 4.4. It is noteworthy that the factor 1.3 is very weak when considering the classical uncertainty of one order of magnitude for hydraulic conductivity. The mean error between simulated chlorinity and data is 2 g L^{-1} while it was 0.9 g L^{-1} for the purely diffusive model. The thermo-osmosis dominated the advection process with an average Darcy velocity in the order of 10^{-13} m s^{-1} (upward flow) while purely hydraulic calculation predicts a value in the order of -10^{-14} m s^{-1} (downward flow).

Table 4.4: Effective diffusion coefficients values [$\times 10^{-11}$ m^2 s^{-1}] from laboratory experiments, Monte Carlo Markov Chain pure diffusion modelling, and calibrated for advection-diffusion pressure modelling.

Formation - Facies	Measurements	Pure diffusion values	Advection-Diffusion Calibrated values
Passwang Formation	0.817	2.66	**3.00**
OPA – Sandy facies	7.38	6.55	6.55
OPA – Shaly facies	0.597	0.3	**2.30**
OPA – Sandy facies	2.71	1.91	1.91
OPA – Carbonate-rich Sandy facies	2.04	2.91	2.91
OPA – Shaly facies	3.56	0.33	**0.47**
Staffelegg Formation	0.451	0.59	**1.24**

4.2.4.2. Pseudo steady-state simulation results

In order to check the ability of the PSS solution to provide relevant results, calculations are performed under the same conditions than for the transient model: no membrane properties for the Passwang Formation and reduced ε_T values. Figure 4.7a illustrates that when the chlorinity is correctly reproduced, despite some overestimation, simple and fast PSS simulations provide a fairly good estimate of the osmotic effects, in few seconds compared to the few hours duration for transient ones. Pseudo steady-state simulations shown in Figure 4.7a confirm the expectation of a negligible chemical osmosis contribution to the overpressures in the divalent case, the main contribution would be thermal-osmosis making this process a plausible candidate to explain overpressures. The corresponding simulated profiles for hydraulic head are shown in Figure 4.8

The PSS solution is used to compare monovalent- and divalent-based calculations of the overpressure. This comparison depicted in Figure 4.7b shows that higher overpressures of about 0.5 MPa are obtained. In monovalent-based calculation, a higher contribution of the chemical osmosis is computed especially at the bottom of the Opalinus Clay (about 0.2 MPa). However, chemical osmosis alone does not allow explaining the pressure profile. In this case again, thermo-osmosis seems the dominant advective process.
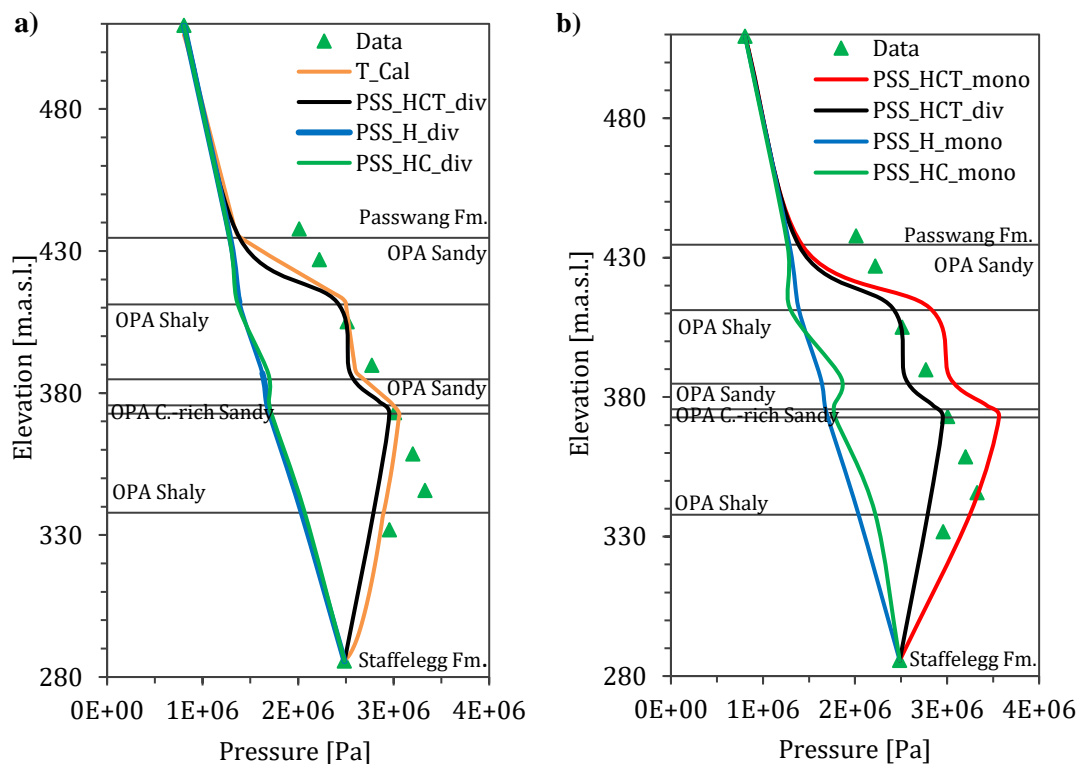
Figure 4.7: a) Calculated present-day pressure profile using PSS calculations for divalent osmotic parameters. The calibrated transient simulation (T_Cal) is also shown for comparison. Purely hydraulics (no osmosis) is labeled 'H', hydraulics and chemo-osmosis is denoted 'HC' and the simulation including hydraulics, chemical and thermo-osmosis 'HCT'; b) same as a) using monovalent osmotic parameters.
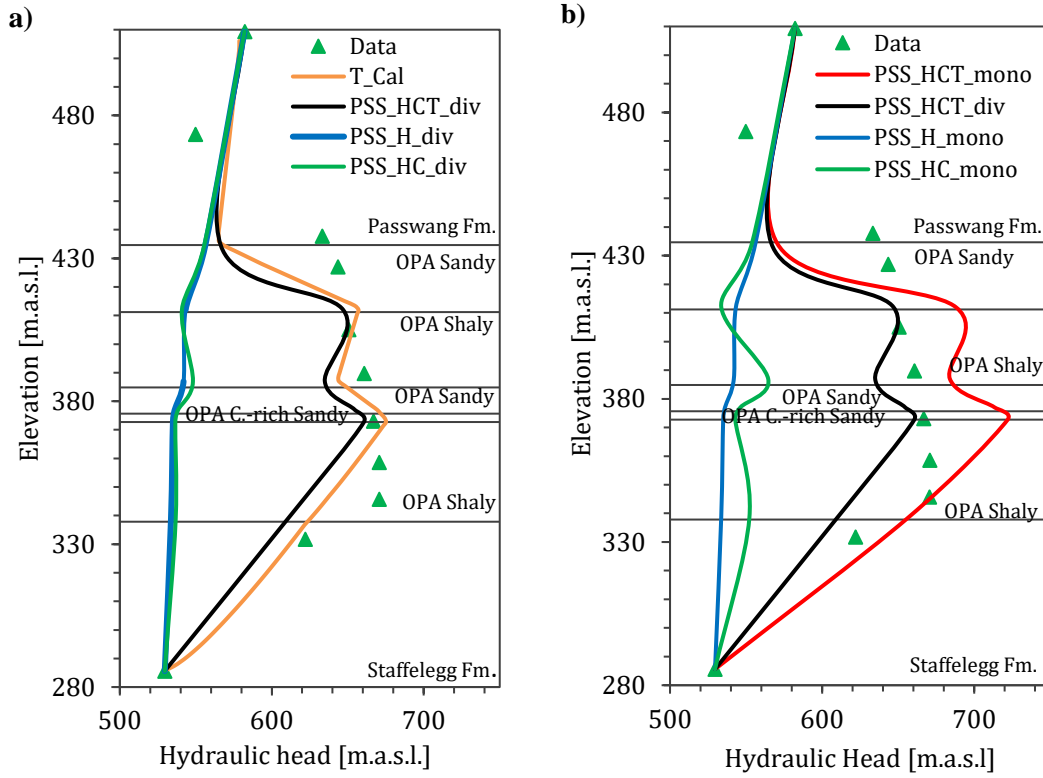
Figure 4.8: a) Calculated present-day hydraulic head profile using PSS calculations for divalent osmotic parameters. The calibrated transient simulation (T_Cal) is also shown for comparison. Purely hydraulics (no osmosis) is labeled 'H', hydraulics and chemo-osmosis is denoted 'HC' and the simulation including hydraulics, chemical and thermo-osmosis 'HCT'; b) same as a) using monovalent osmotic parameters.

4.2.5. DISCUSSION

Diffusion is currently considered the dominant transport process in clay rocks. The relative importance of advection and diffusion must be discussed in the light of our calculations.

The deviation from the purely diffusion due to the advective process can be quantitatively described using:

$$f = \frac{\int_{Z=0}^{Z=L}(C(Z)-C_D(Z))dZ}{\int_{Z=0}^{Z=L}(C_{Adv}(Z)-C_D(Z))dZ} \tag{4.12}$$

where $C(Z)$ is the chlorinity calculated by the advection-diffusion model, $C_D(Z)$ and $C_{Adv}(Z)$ are the calculated salinities in purely diffusive and purely advective transport, respectively. A value of 0 for f denotes a purely diffusive transport while $f = 1$ corresponds to a purely advective profile. Note that purely diffusive calculations were made using the D_e values of Table 4.4.
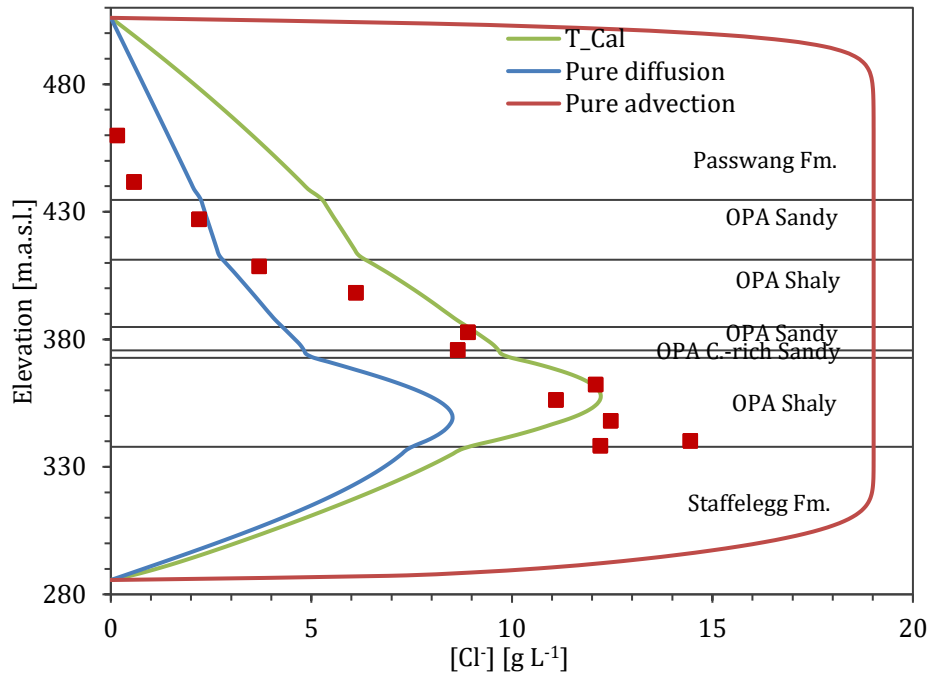
Figure 4.9: Chlorinity profile at the end of the calibrated transient simulation also showing diffusive and purely advective transport calculation derived from simulation T_Cal.

According to the simulations shown in Figure 4.9, a *f* value of 0.18 is found suggesting that transport is mostly diffusive (explaining 82% of the profile) but is slightly modified (18%) by advection. Note that the almost homogeneous result for advection shown in Figure 4.9 is due to the fact that during most of the simulation time (between -4.4 Ma and -0.246 Ma), salt is transported upward from the bottom boundary condition at $c = c_{ini}$ by advection.

In order to identify the prominent transport process usually one uses the Peclet number P_e defined by Equation (4.1). Using the calibrated values of D_e reported in Table 4.4 yields a harmonic mean of $1.3 \cdot 10^{-11}$ m^2 s^{-1}. Introducing this value, L = 263 m, corresponding to the half-thickness of the studied stratigraphic column, which is the characteristic transport distance (distance between maximum and minimum concentration areas), and a Darcy's velocity computed by PSS simulations yields a P_e in the range of 0.15 to 2.3 for the monovalent case and in the range of 0.15 to 1.4 for the divalent case (Table 4.5). Although values higher than one are obtained, diffusion remains the dominant transport process in such clay-rich material as suggested by Huysmans and Dassargues (2005).

Table 4.5: Steady state Darcy velocities q and corresponding Peclet number P_e in monovalent and divalent cases. Purely hydraulics (no osmosis) is labeled 'H', hydraulics and chemo-osmosis is denoted 'HC' and the simulation including hydraulics, chemical and thermo-osmosis 'HCT'.

	PSS_H	PSS_HC	PSS_HT	PSS_HCT
$q_{monovalent}$ [m s^{-1}]	-1.5E-14	-4.7E-14	2.2E-13	1.9E-13
P_e	0.15	0.48	2.3	1.9
$q_{divalent}$ [m s^{-1}]	-1.5E-14	-2.5E-14	1.5E-13	1.3E-13
P_e	0.15	0.25	1.5	1.4
	Dominant diffusion		Diffusion and contribution of advection	

More simple and faster PSS simulations provide a first order valuable estimate of the overpressures expected from osmotic processes. The major interest of these simulations relies in the fact that there is no need for a sometimes uncertain or controversial geological scenario and that far less time-consuming calculations are required. The calibration implemented in our simulations is preliminary and can be refined.

Chemical osmosis has attracted almost exclusive attention despite the fact that the highly plausible presence of divalent ions in natural media dramatically decreases osmotic coefficient and thus the overpressuring potential of shales as discussed by Trémosa et al (2010). Conversely, the presence of divalent cations causes only a slight reduction of the thermal osmotic flow making this process an interesting candidate to explain overpressures. Already proposed to explain some part of the overpressures in the Callovo-Oxfordian formation (Gonçalvès et al., 2012), thermo-osmotic processes in the Opalinus Clay can also be regarded as a plausible explanation for the pressures measured in the BDB-1 deep borehole at Mont Terri. Therefore, within the range of uncertainty of thermal osmosis coefficients, simulations in fairly good agreement with both chlorinity and pressure data are obtained pointing to a prominent role of this process.

According to Neuzil (2015), the characteristic time t_{diss} for dissipating an existing anomaly to half of its initial magnitude in the case of one-dimensional flow can be approximated as:

$$t_{diss} = 0.4 \frac{L^2 S_s}{K} \tag{4.13}$$

where L [m] is the minimum flow distance to dissipate the anomaly (generally half the formation thickness), K [m s^{-1}] is the hydraulic conductivity and S_s [m^{-1}] is the specific storage.

For the Opalinus Clay at Benken, t_{diss} was estimated to range between $9.24 \cdot 10^{-3}$ and 1.8 Ma, which is consistent with the conclusion of Horseman et al. (1991) stating that geological events at times significantly greater than 2 Ma from the present day are unlikely to be responsible for abnormal pressures in the Opalinus Clay. With the values used in our modelling (L = 131.5 m, K = $1.85 \cdot 10^{-13}$ m s^{-1}, S_s = 10^{-6} m^{-1}), a characteristic time of approximatively 1200 years is found. More resilient processes than tectonic or hydrologic change, such as osmotic processes, have to be invoked to explain the overpressures currently measured in the Opalinus Clay.

CONCLUSIONS AND OUTLOOKS

In the framework of geological disposal of radioactive wastes, the aims of this thesis was to characterise the Opalinus Clay at Mont Terri using a methodology that may be used at sites for waste disposal or experimental activities, and to clarify the origins of the overpressures observed in this argillaceous formation. Coupled transport processes and their relative contributions to the mass transport were studied, with a focus on the main processes for solute (diffusion) and fluid flows (advection and osmotic processes).

The Deep Borehole experiment enabled the acquisition of data in a hydraulically undisturbed zone of the Opalinus Clay, i.e. unaffected by the drainage effects of underground structures happening at the tunnel level. Several studies have been carried out to deepen the knowledge about this argillaceous formation. The BDB-1 borehole is a 247.5 m deep-inclined borehole, that provided core samples normal to the bedding and yielded excellent material especially to assess the spatial distribution of petrophysics, mineralogy, porewater geochemistry and put constrains on stratigraphy and facies limits. Temperature and pressure data collected in the BDB-1 borehole represent the natural formation conditions. The temperature profile was established and reveals a linear trend and a high geothermal gradient of 8.5 °C 100 m^{-1}. The hydraulic head profile obtained from pressure measurements indicates an excess head of at least 60 m and possibly up to 130 m depending on the location of the lower aquifer boundary. The formations underlying the Opalinus Clay were only crossed by the BDB-1 borehole on a few meters, leading to uncertainties concerning the lower aquifer and the pressure distribution in this section.

Petrophysical measurements were performed in laboratory on the borehole core samples and gave consistent results with the findings obtained at the gallery level of the Mont Terri rock laboratory.

Concerning geochemistry acquisition, out diffusion technique gave satisfactory results in terms of porewater chloride concentrations. But sample swelling prevented the possibility to get a full set of proper values for diffusion coefficients. Avoiding deformation by constraining more efficiently the studied samples could improve the experimental procedures. Concentrations acquired by leaching experiments were higher than the ones obtained by out diffusion, probably due to opening of chloride reservoirs during milling or dissolution of chloride-bearing minerals. The resulting chlorinity profile confirms the previous studies and shows an asymmetric curved trend with maximum values superior to 12 g L^{-1} in the basal part of the Opalinus Clay. The acquisition of cationic exchange properties enabled to test a multi-site model to establish the porewater composition profile by geochemical modelling. This method considers the interactions at thermodynamic equilibrium occurring between the rock and the pore water, and parameters characterising the geochemical system.

Diffusion coefficients and accessible porosities to anions and water isotopes were acquired by cubic out diffusion, radial diffusion and through diffusion. Effective diffusion coefficients for chloride and bromide were estimated in the order of $4 \cdot 10^{-11}$ m^2 s^{-1} and a low anisotropy ratio of 2.4 was estimated for chloride effective diffusion coefficient in the Opalinus Clay sandy facies. Difficulties were encountered to obtain the anisotropy in the shaly facies due to sample cracking and other unloading artefacts. Anionic exclusion was estimated by radial diffusion between 46 and 60 %.

Estimating hydraulic and chemical parameters in low permeability media remains challenging. A model that links intrinsic permeability to petrophysical parameters gives values in the order of 10^{-20} m^2, corresponding to hydraulic conductivities in the order of 10^{-13} m s^{-1}. Tidal analysis has revealed itself not to be an appropriate method to compute hydraulic conductivity, giving values overestimated of several orders of magnitudes. On the other hand, this technique, which inverts the rockmass poro-elastic response, gives reasonable values for specific storage and effective porosity. As a third method, in situ hydraulic testing was performed using the multipacker system installed within BDB-1 borehole. The values obtained by numerical inversion from pulse tests are consistent with those deduced from constant rate withdrawal tests and suggest a slight vertical variability across the formation in the range of $1 \cdot 10^{-13}$ m s^{-1} to $7 \cdot 10^{-12}$ m s^{-1}, possibly due to local variations of the matrix structure, composition and cementation, or the presence of fractures. These results are also supported by tests performed at laboratory scale using Hassler cell, although they might be influenced by drilling and sample preparation artefacts.

Chloride is a conservative natural tracer that gives precious information on transport phenomena. Therefore, a relevant interpretation of the chloride profile is crucial for water flow and flow characterisation. The chloride profile obtained by out diffusion experiments was interpreted by means of a purely diffusive one-dimensional numerical model. The assumption of purely diffusive mass transport phenomena was verified by estimating the Peclet number including osmotic processes in the advection term. The scenario implemented with a Monte Carlo Markov Chain (MCMC) inversion algorithm consists in a diffusive exchange between the argillaceous formation and the adjacent aquifers, with deferred activation times of the fresh-water sources linked to the surface erosion of the geological formations. A Bayesian inversion based on effective diffusion coefficients, initial value of the chloride concentration and two exhumation and thus, hydraulic activation times for the two bounding aquifers (ten parameters) allowed to evaluate the best fit parameter sets and their uncertainties not evaluated so far.

The contribution of osmotic transport phenomena was assessed by interpreting the pressure profile measured in the BDB-1 borehole. Theoretical predictive models were applied to compute the osmotic parameters for monovalent and divalent solutions, based on experimental petrophysical parameters, temperature and chlorinity data. Two types of simulation were carried out: i) transient simulations considering the temporal evolution of both chlorinity and pressure with the geological scenario determined using the MCMC scheme, and ii) pseudo steady-state simulations, which are simplified first-order calculations considering an

equilibrium between pressure, temperature and chlorinity profiles. A calibration was applied assuming no membrane properties for the Passwang Formation and reduced thermo-osmotic coefficients, in order to match the pressure data.

The pressure profile can be reproduced by evaluating the coupled advective flow, by taking into account the respective contributions of pure advection, chemo-osmosis and thermo-osmosis (fluid flows caused respectively by pressure, chlorinity and temperature gradients). Pure hydraulic calculation evaluates a Darcy velocity in the order of -10^{-14} m s^{-1}, related to a downward flow. Chemical osmosis slightly increases the advective flow in the same direction but its effect is rather minor compared to the one induced by thermo-osmosis. Indeed, the water movement is inverted when considering thermo-osmosis in the transport equation. Then, the mean Darcy velocity is in the order of 10^{-13} m s^{-1} and the flow becomes upward. This conclusion for the Opalinus Clay at Mont Terri is consistent with the findings of a similar study focused on the Toarcian-Domerian clayey formation of Tournemire (France). It is also noteworthy that since many sedimentary basins are at thermal equilibrium (with a linear geothermal gradient associated to thermal diffusion), calculations using pseudo steady-state for the analysis of thermo-osmosis can thus be implemented more easily.

Three osmotic processes have been identified in clay rocks. Although thermo-osmosis seems a reasonable candidate for overpressure generation and could potentially have a significant effect on solute and fluid transport in a repository, the importance of this process remains neglected. Thermo-osmosis in natural clay rocks is poorly investigated and experimental data are lacking to properly assess and calibrate predictive models. To better constrain experimental uncertainties, improvements can be made at laboratory scale when inducing a temperature gradient and measuring the pressure development at steady state in saturated clay rocks. Further studies under strictly controlled conditions are required to improve the characterisation of this transport process.

This thesis focused on the impact of transport processes in an argillaceous formation over the long term and pointed to the prominent role of thermo-osmosis in the generation of pressure anomalies in clay rocks. Modelling at a lower time scale from 1000 to 10 000 years, corresponding to the expected time of waste canister failure, would be necessary to understand the effects of hydraulic, thermal and chemical transient states induced at the vicinity of radioactive wastes repository. The effect of temperature gradient on fluid flow has been highlighted by our study. The impact of this driving force on solute flux has not been investigated in our work and could retain some attention since transient thermal state is expected with the installation of high level and exothermic radioactive waste canisters in a deep geological repository. This should require some experimental works to assess the impact of such transport phenomenon.

The results of this study suggest that the overpressured state of the Opalinus Clay has no significant impact on the solute transfer since natural tracer profile can be mostly explained by a pure diffusive transport model. However, in case of a containment default of the natural or the engineered barriers within the framework of a deep geological repository, the advective contribution may become important and enhance the radionuclide leakage. Thus, safety assessment for a geological disposal installation should take into account such overpressures.

REFERENCES

Ababou, R., Fatmi, H., Matray, J.-M., Nussbaum, C., Bailly, D., 2012. Statistical analyses of Pore Pressure Signals in Claystone During Excavation Works at the Mont Terri Underground Research Laboratory. Chap. 17 *Radioactive Waste*. InTech, ISBN: 979-953-307-274-5, 373-430

AF Consult, 2016. DB Experiment: Analysis of hydraulic tests carried out in the 7 intervals of the BDB-1 borehole. *Mont Terri TN* 2017-05, Draft version, 121p.

Al Reda, M., 2016. Comparative study of methods for assessing permeability on Opalinus Clay samples. *Master thesis*, Université Paris-Sud 11, Orsay, France.

Altinier, M.V., 2006. Etude de la composition isotopique des eaux porales de l'argilite de Tournemire : inter-comparaison des méthodes de mesure et relations avec les paramètres pétrophysiques. *Thèse*, Université Paris-Sud 11, Orsay, France.

ANDRA, 2005c. Safety Evaluation of a Geological Repository. s.l: Agence Nationale des Déchets Radioactifs, 784p.

Appelo, C.A.J., and Postma, D., 1993. Geochemistry, Groundwater and Pollution. Balkema, Rotterdam, 526p.

Archie, G.E., 1942. The Electrical Resistivity Log as an Aid in Determining Some Reservoir Characteristics. *Trans. A.I.M.E.*, 146, 54-62

Bachir-Bey, N., 2013. Origine des halogénures (Cl- et Br-) et de leurs isotopes stables (δ37Cl) dans la couche argileuse de Tournemire. Approche expérimentale et numérique. *Mémoire de Master*, Université Paris-Sud 11, Orsay, France.

Bader S, 2005. Osmosis in groundwater: chemical and electrical extensions to Darcy's Law. *PhD thesis*, Delft University of Technology, Netherlands, 198p.

Modelling coupled chemico-osmotic and advective-diffusive transport of nitrate salts in the Callovo-Oxfordian Clay (PDF Download Available). Available from: https://www.researchgate.net/publication/258606112_Modelling_coupled_chemico-osmotic_and_advective-diffusive_transport_of_nitrate_salts_in_the_Callovo-Oxfordian_Clay?ev=prf_high [accessed Sep 8, 2017].

Baeyens, B., Bradbury, M.H., 2004. Cation exchange capacity measurements on illite using the sodium and cesium isotope dilution technique: effects of the index cation, electrolyte concentration and competition: modelling. *Clays Clay Miner*. 52, 421–431.

Bailly, D., Matray, J.-M., Ababou, R., 2014. Temporal behavior of a ventilated claystone at the Tournemire URL: Cross-spectral analyses focused on daily harmonics. *Eng. Geol.* 183, 137-158

Bailly, D., Matray, J.-M., 2015. LP-A Experiment: Phase 20, Statistical analysis of time series acquired in the EZ-B Niche and at the Main fault. *Mont Terri TN* 2014-59, 77p.

Barker, J.A., 1988. A Generalized Radial-Flow Model for Hydraulic Tests in Fractured Rock. *Water Resour. Res*. 24(10), 1796-1804

Bear, J., Verruijt, A., 1987. Modeling groundwater flow and pollution. D. Reidel Publishing Company, Dordrecht, Netherlands, 414p.

Beauheim, R.L., 2013. Hydraulic conductivity and head distributions in the host rock formations of the proposed siting regions. Nagra Interner Bericht, 13-13. Nagra, Wettingen, Switzerland. <www.nagra.ch>

Bensenouci, F., 2010. Apport des traceurs naturels à la compréhension des transferts au sein des formations argileuses compactées. *Thèse*, Université Paris-Sud XI, Orsay, France.

Bianchi, M., Liu, H.H., Birkholzer, J.T., 2015. Radionuclide transport behavior in a generic geological radioactive waste repository. Groundwater, 53(3), 440-451.

Blaesi, H.-R., Peters, T. J., Mazurek, M., 1991. Der Opalinus-Ton des Mt. Terri (Kanton Jura): Lithologie, Mineralogie und physiko-chemische Gesteinsparameter. *Nagra Interner Bericht*, 90-60. Nagra, Wettingen, Switzerland. <www.nagra.ch>

Bohn, H.L., Strawn, D.G., O'Connor, G.A., 2015. Soil Chemistry. John Wiley & Sons, 4th edition, 392p.

Boldt-Leppin, B.E.J., Hendry, J., 2003. Application of Harmonic Analysis of Water Levels to Determine Vertical Hydraulic Conductivities in *Clay-Rich Aquitards*. Vol. 41, No. 4 – Ground Water, 514-522.

Bolt, G. H., 1979. Soil Chemistry, B. Physico-Chemical models. Elsevier, Amsterdam.

Bossart, P., Wermeille, S., 2003. Paleohydrological study of the Mont Terri rock laboratory. In: Heitmann, P., Tripet, J.P. (Eds.), Mont Terri Project-Geology, paleohydrogeoogy and stress field of the Mont Terri

region. *Reports of the FOWG*, n°4, Bern, Switzerland, 45-64. <www.swisstopo.admin.ch>

Bossart, P., Thury, M., 2008. Mont Terri Rock Laboratory – Project, programme 1996 to 2007 and results, no. 3, Swiss Geological Survey, Wabern.

Bossart, P., 2011. Characteristics of the Opalinus clay at Mont Terri. http://www.mont-terri.ch/internet/mont-terri/fr/home/geology/key_characteristics.parsys.49924 .DownloadFile.tmp/characteristicsofopa.pdf

Bossart, P., Bernier, F., Birkholzer, J., Bruggeman, C., Connolly, P., Dewonck, S., Fukaya, M., Herfort, M., Jensen, M., Matray, J.-M., Mayor, J.C., Moeri, A., Oyama, T., Schuster, K., Shigeta, N., Vietor, T., Wieczorek, K., 2017. Mont Terri rock laboratory, 20 years of research: introduction, site characteristics and overview of experiments. *Swiss J. Geosci.*, 110, doi:10.1007/s00015-016-0236-1

Bowman, D.O., Roberts, R.M., 2009. Analysis of Culebra and Magenta Hydraulic Tests Performed Between January 2005 and August 2008. *Analysis Report for AP-070*, WIPP:1.4.2.3, 108p.

Brace W.F., Walsh J.B. & Frangos W.T., 1968. Permeability of granite under high pressure, *J. Geoph. Res*, 73 (6), p. 2225-2236.

Bradbury, M.H., Baeyens, B., Pearson, F.J., Berner, U., 1997-1998. Derivation of In Situ Opalinus Clay Porewater Compositions from Experimental and Geochemical Modelling Studies with Addendum. Wettingen, Switzerland, *Nagra, Technical Report* 97-07.

Bradbury, M.H., Baeyens, B., 1998. A physiochemical characterisation and geochemical modelling approach for determining porewater chemistries in argillaceous rocks. *Geochim. Cosmochim. Acta* 62, 783–795.

Bradbury, M.H., Baeyens, B., 2000. A generalised sorption model for the concentration dependent uptake of caesium by argillaceous rocks. *J. Contam. Hydrol.* 42, 141–163.

Bresler, E., 1973. Anion Exclusion and Coupling Effects in Nonsteady Transport Trhough Unsaturated Soils: I. Theory. *Soil Sci. Soc. Am. Proc.*, *37 (5)*, 663-669.

Boulin, P.F., Bretonnier, P. Gland, N., Lombard, J.M., 2010. Low water permeability measurements of clay samples. Contribution of steady state method compared to transient methods. *Int. Symp. Soc. of Core Analysts*, Halifax, Nova Scotia, Canada, 4-7 October, 12p.

Bredehoeft, J.D., 1967. Response of Well-aquifer Systems to Earth Tides. U.S.G.S., Washington, D.C., 20242

Bruel, D., Küpfer, T., 2002. Modelling the overpressure regime in the Opalinus clay, at Benken (CH): Implications for the present day hydrogeological parameters. *Clays in Nat. and Eng. Barriers for Radioact. Waste Confinement*, ANDRA, Reims, France, 155-156.

Carman, P.C., 1938. Fundamental principal of industrial filtration – A critical review of present knowledge. *Trans. Inst. Chem. Eng.*, 16: 168-188

Cerny, R., Rovnanikova, P., 2002. Transport Processes in Concrete. CRC Press, ISBN 9780415242646 560p.

Clauer, N., Techer, I., Nussbaum, C., Laurich, B., 2017. Geochemical signatures of paleofluids in microstructures from Main Fault of the Opalinus Clay, Mont Terri rock laboratory, (Switzerland). *Swiss J. Geosci.*, 110, doi:10.1007/s00015-016-0253-0

Croisé, J., Schilckenrieder, L., Marschall, P., Boisson, J.Y., Vogel, P., Yamamoto, S., 2004. Hydrogeological investigations in a low permeability claystone formation: the Mont Terri Rock Laboratory. *Phys. and Chem. Earth*, 29, 3-15

Cutillo, P.A., Bredehoeft, J.D., 2011. Estimating Aquifer Properties from the Water Level Response to earth Tides. *Ground Water*, 49(4), 600-610

Churaev, N.V., 2000. Liquid and Vapour Flows in Porous Bodies: Surface Phenomena. 319 Taylor & Francis, London.

Darcy, H., 1856. Les fontaines publiques de la ville de Dijon. Paris: Dalmont.

De Hoog, F.R., Knight, J.H., Stokes, A.N., 1982. An improved method for numerical inversion of Laplace transform. SIAM *J. Sci. Statist. Comput.* 3, 357–366.

Deming, D., 2001. Abnormal fluid pressures. Chapter 8 in: An Introduction to Hydrogeology, McGraw-Hill Science/Engineering/Math, 480p.

Derjaguin, B.V., and G.P. Sidorenkov, 1941. On thermo-osmosis of liquid in porous glass. *C.R. Acad. Sci.*, U.R.S.S. 32, 622-626.

Derjaguin, B.V., Churaev, N.V., Muller, V.M., 1987. Surface Forces. 1st Ed. ed. Kitchener, J.A., New York: Consultants Bureau.

Desbois, G., Urai, J.L., Houben, M.E., Sholokhova, Y., 2010. Typology, morphology and connectivity of pore space in claystones from reference site for research using BIB, FIB and cryo-SEM methods. EPJ Web of Conferences 6, 22005

Doodson, A.T., Warburg, H.D., 1941. Admiralty manual of tides. Her Majesty's Stationary Office, London, xii, 270p.

Duro, L., Grivé, M., Domènech, C., Gaona, X., Colás, E., Montoya, V., Bruno, J., 2007. Development of the ThermoChimie thermodynamic database. *ANDRA Report* C.RP.0ENQ.07.0001.

Fakhry, A.A., 2008. Field Methods for Petroleum Geologists: A Guide to Computerized Lithostratigraphic Correlation Charts Case Study: Northern Africa. Springer Science & Business Media, 112p.

Fatmi, H., Ababou, R., Matray, J.-M., 2008. Statistical pre-processing analyses of hydrometeorological time series in a geological clay site (methodology and first results for Mont Terri's PP experiment). *Phys. Chem. Earth Lett.* A/B/C 33 (Suppl. 1), S14-S23

Fatmi, H., 2009. Méthodologie d'analyse des signaux et caractérisation hydrogéologique : application aux chroniques de données obtenues aux laboratoires souterrains du Mont Terri, Tournemire et Meuse/Haute-Marne. *Thèse*, Université de Toulouse, 249p.

Fernàndez, D., Gómez-Hernández, J.J, Mayor, J.C., 2007. Estimating hydraulic conductivity of the Opalinus Clay at the regional scale: combined effect of desaturation and EDZ. *Phys. Chem. Earth* (Parts A/B/C), 32 (8-14), pp. 639-645

Fierz, T., and Rösli, U., 2014. DB Experiment Installation of a 7-interval multi-packer system into borehole BDB-1. *Mont Terri TN* 2014-23, 37p.

Fischer G.J., 1992a. The determination of permeability and storage capacity: Pore pressure oscillation method, in Fault Mechanics and Transport Properties of Rocks, eds. B. Evans and T.-F. Wong, Academic Press, London, 187-211 (Chapter 8).

Fontes, J.C., Matray, J.M., 1993. Geochemistry and origin of formation brines from the Paris Basin, France. 1. Brines associated with Triassic salts. Chemical Geology, 109, 149-175.

Freivogel, M., and Huggenberger, P., 2003. Modellierung bilanzierter Profile im Gebiet Mont Terri La Croix (Kanton Jura). In: Heitzmann, P., et Tripet, J.P. (eds) Mont Terri Project Geology, Paleohydrology and Stress Field of the Mont Terri Region. *Reports of the FOWG.* Geology Series 4, 7-43.

Fritz, S. J., 1986. Ideality of clay membranes in osmotic processes: A Review. *Clays and Clay Miner.* 34, 2, 214-223.

Gaines, G.I., Thomas, H.C., 1953. Adsorption studies on clay minerals. II. A formulation of the thermodynamics of exchange adsorption. *J. Phys. Chem*. 21, 714–718.

Garrels, R.M., and Christ, C.L., 1965. Solutions, minerals and equilibria. Harper and Row, New York, 450p.

Gautschi, A., 2001. Hydrogeology of a fractured shale (Opalinus Clay): Implications for the deep disposal of radioactive wastes. Hydrogeol. J., 9, 97-107.

Gautschi, A., 2017. Safety-relevant hydrogeological properties of the claystone barrier of a Swiss radioactive waste repository: An evaluation using multiple lines of evidence. *Grundwasser*, Zeitschrift der Fachsektion Hydrogeologie, 13 p. doi:10.1007/s00767-017-0364-1

Gimmi, T., Leupin, O.X., Eikenberg, J., Glaus, M.A., Van Loon, L.R., Waber, H.N., Wersin, P., Wang, H.A.O., Grolimund, D., Borca, C.N., Dewonck, S., Wittebroodt, C., 2014. Anisotropic diffusion at the field scale in a 4-year multi-tracer diffusion and retention experiment – I: Insights from the experimental data. Geochemica et Cosmochimica Acta, 125, pp. 373-393.

Gonçalvés, J., Violette, S., Wending, J., 2004. Analytical and numerical solutions for alternative overpressuring processes: Application to the Callovo-Oxfordian sedimentary sequence in the Paris basin, France. *J. Geophy. Res.* 109, Issue B2, 1978-2012

Gonçalvés, J., Rousseau-Gueutin, P., Revil, 2007. Introducing interacting diffuse layer in TLM calculations. A reappraisal of the influence of the pore size on the swelling pressure and the osmotic efficiency of compacted bentonites. . *J. Colloid and Interface Sci.* 316, 92-99.

Gonçalvès, J., and Rousseau-Gueutin, P., 2008. Molecular-scale model for the mass density of electrolyte solutions bound by clay surfaces: Application to bentonites. *J. Colloid Interface Sci. 320*, 590-598.

Gonçalvès, J., Rousseau-Gueutin, P., De Marsily, G., Cosenza, P., Violette, S., 2010. What is the significance of pore pressure in a saturated shale layer? *Water Resour. Res.* 46 (2010), W04514, doi: 10.1029/2009WR008090.

Gonçalvès, J., de Marsily G., Tremosa, J., 2012. Importance of thermo-osmosis for fluid flow and transport in clay formations hosting a nuclear waste repository. *Earth Planet. Sci. Lett.* 339–340, 1–10.

Gonçalvès, J., Adler, P.M., Cosenza, P., Pazdniakou, A., de Marsily, G., 2015. Semi-permeable membrane properties

and chemo-mechanical coupling in clay barriers. *Nat. Eng. Clay Barriers*, pp. 269-327.

Gonçalvès, J., Ji Yu, C., Matray, J.M., Trémosa, J., in review. Thermo-osmotic permeability of clays, submitted to *Geophy. Res. Let.*

Grim, R.E., 1962. Applied Clay Mineralogy. McGraw Hill, New York

Guggenheim, S., Martin, R.T., 1995. Definition of Clay and Clay Mineral. Joint Report of the AIPEA Nomenclature and CMS Nomenclature Committees. *Clays clay miner.* 43: 255-256.

Hakem, I.F., A. Boussaid, H. Benchouk-Taleb, and M.R. Bockstaller, 2007. Temperature, pressure, and isotope effects on the structure and properties of liquid water: A lattice approach. *J. Chem. Phys. 127*, 224106(1-10).

Heitzmann, P. (Ed.), 2004. Mont Terri Project – Hydrogeological Synthesis, Osmotic Flow. *Report of the FOWG*, N°6, Geology Series.

Horseman, S.T., Alexander, J., Holmes, D.C., 1991. Implications of long-term transient flow, coupled flow and borehole effects on hydrogeological testing in the Opalinus Clay: Preliminary study with scoping calculations. Nagra Technical Report 91-16, 135p.

Horseman, S.T., Higgo, J. J. W., Alexander, J., and Harrington, J. F., 1996. Water, Gas and Solute Movement Trough Argillaceous Media. NEA, 306 pp.

Hortle, A., Trefry, M., Michael, K., 2012. Signal processing of hydrographs for monitoring the integrity of freshwater aquifers near the Otway CO_2 storage site. Cooperative Research Centre for Greenhouse Gas Technologies, Canberra, Australia, *CO2CRC Report* No RPT12-3856

Hostettler, B., Reisdorf, A. G., Jaeggi, D., Deplazes, G., Bläsi, H.-R., Morard, A., Feist-Burkhardt, S., Waltschew, A., Dietze, V., Menkveld-Gfeller, U., 2017. Litho- and biostratigraphy of the Opalinus Clay and bounding formations in the Mont Terri rock laboratory (Switzerland). *Swiss J. Geosci.*, 110, doi:10.1007/s00015-016-0250-3

Hummel, W., Berner, U., Curti, E., Pearson, F.J., Thoenen, T., 2002. Nagra/PSI Chemical Thermodynamic Data Base 01/01. Parkland, Florida, Universal Publishers/uPublish.com. (Also Published as Wettingen, Switzereland, *Nagra Technical Report* NTB 02-16).

Huysmans, M., Dassargues, A., 2005. Review of the use of Péclet numbers to determine the relative importance of advection and diffusion in low permeability environments. *Hydrogeol. J.*, 13 (5–6), 895–904.

Jacob, C.E., 1940. On the flow of water in an artesian aquifer. *Trans. Am. Geophys. Union*, 2, 574-786

Jacquier, P., Hainos, D., Robinet, J.C., Herbette, M., Grenut, B., Bouchet, A., Ferry, C., 2013. The influence of mineral variability of Callovo-Oxfordian clay rocks on radionuclide transfer properties. *Appl. Clay Sci.* 83-84, 129-136.

Jaeggi, D., Laurich, B., Nussbaum, C., Kristof Schuster, Connolly, P., 2017. Tectonic structure of the "Main Fault" in the Opalinus Clay, Mont Terri rock laboratory (Switzerland). *Swiss J. of Geosci.*, 110, doi: 10.1007/s00015-016-0243-2

Jäggi, K., SJ GeoTec AG, Frieg, B., 2014. OPA: Sondierbohrung Benken. Langzeitbeobachtung 2013 Dokumentation der Messdaten. *Nagra Arbeitsbericht* NAB 14-15, 51p.

Johns, R. T., Vomvoris, S. G., Löw, S., 1995. Review of hydraulic field tests in the Opalinus Clay of Northern Switzerland. Hydraul. and hydrochem. Charact. of argillaceous rocks. NEA.

Kemper, W. D., and Evans, N. A., 1966. Movement of Water as Effected by Free Energy and Pressure Gradients III. Restriction of Solutes by Membranes. Soil Sci. Soc. Am. Proc., 27, 5, 485-490.

Kemper, W. D., and Quirk, J. P., 1972. Ion Mobilities and Electric Charge of external Clay Surfaces Inferred from Potential Differences and Osmotic Flow. Soil Sci. Soc. Am. Proc., 36, 426-433.

Klinkenberg, L.J., 1941. The permeability of porous media to liquids and gases. Drilling and production practice, *Am. Pet. Inst.*

Kosakowski, G., 2004. Time-dependant Flow and Transport Calculations for Project Opalinus Clay (Entsorgungsnachweis). *PSI Bericht* Nr. 04-10, ISSN 1019-0643, 83p.

Kostek, S., Schwartz, L., and Johnson, D., 1992. Fluid permeability in porous media: Comparison of electrical estimates with hydrodynamical calculations. *Phys. Rev.* B 45(1), 186-194.

Kozeny, J., 1927. Über kapillare Leitung des Wassers im Boden. Akademie des Wissesschaften. Wien, 136 (2a): 271

Kuhlemann, J., Rahn, M., 2013. Plio-Pleistocene landscape evolution in Northern Switzerland. *Swiss. J. Geosci.*, 106, 451-467.

Kuhlmann, U., Ballmer, M., Marschall, P., 2011. HA Experiment: Phase 12 Hydrogeologic analysis and synthesis. Complementary modelling of Mont Terri site. *Mont Terri TN* 2007-41, 48p.

Kullin, M. and Schmassmann, H., 1991. Isotopic composition of modern recharge. In: Pearson, F.J., Balderer, W., Loosli, H.H., Lehmann, B.E., Matter, A., Peters, T., Schmassmann, H. & Gautschi, A.: Applied isotope hydrogeology. A case study in northern Switzerland. Elsevier, Amsterdam, The Netherlands and *Nagra Technical Report* NTB 88-01, Nagra, Wettingen, Switzerland, 65–89.

Lavastre, V., Jendrzejewski, N., Agrinier, P., Javoy, M., Evrard, M., 2005. Chlorine Transfer Out of a Very Low Permeability Clay Sequence (Paris Basin, France): ^{35}Cl and ^{37}Cl evidence. Geochemica et Cosmochimica Acta., Vol. 69, No. 21, 4949-4961.

Law, B.E., Spencer, C.W., 1998. Abnormal Pressure in Hydrocarbon Environments. Chapt. 1 from AAPG Memoir 70: Abnormal Pressure in Hydrocarbon Environments, Ed. by B.E. Law, G.F. Ulmishek and V.I. Slavin. *Am. Ass; of Petr. Geol*, 1-11.

Letey, J., and Kemper, W. D., 1969. Movement of Water and Salt through a Clay-Water System: Experimental Verification of Onsager Reciprocal Relation. Soil Sci. Soc. Am. Proc., 33, 25-29.

Letham, E.A., and Bustin, R.M., 2015. Klinkenberg gas slippage measurements as a mean for shale pore structure characterization. *Geofluids*, Vol. 7, 1-5.

Marsily, G. de, 1986. Quantitative Hydrogeology, *Groundw. Hydrol. Eng.* (Academic Press).

Marschall, P., Horseman, S., Gimmi, T., 2005. Characterisation of gas transport properties of the Opalinus Clay, a potential host rock formation for radioactive waste disposal. *Oil Gas Sci. Technol*., 60, No. 1, 121-139

Matray, J.M., Savoye, S., Cabrera, J., 2007. Desaturation and structure relationships around drifts excavated in the well-compacted Tournemire's argillite (Aveyron, France). *Eng. Geol*. 90, 1-16.

Matray, J.M., and Möri, A., 2012. Petrophysical measurements on BCD-3 core samples from the Mont Terri rock laboratory. *Note technique* IRSN/PRP-DGE/2012-00020, 24 p.

Matray, J.-M., and Bailly, D., 2015. LP-A Experiment: Phase 20 Statistical analysis of time series acquired in

the EZ-B Niche and at the Main fault. *Mont Terri TN* 2014-59, 77 p.

Mazurek, M., Elie, M., Hurford, A., Leu, W., Gautschi, A., 2002. Burial History of Opalinus Clay. Clays in Natural And Engineered Barriers For Radioactive Waste Confinement, Int. Meeting, Reims, France.

Mazurek, M., Hurford, A., Leu, W., 2006. Unravelling the multi-stage burial history of the Swiss Molasse Basin: intergration of apatite fission track, vitrinite reflectance and biomarker isomerisation analysis. Basin Res., 18, 27-50.

Mazurek, M., Alt-Epping, P., Bath, A., Gimmi, T., & Waber, H. N., 2009. Natural tracer profiles across argillaceous formations: The CLAYTRAC Project (p. 365). Paris: Nuclear Energy Agency report, OECD.

Mazurek, M., Alt-Epping, P., Bath, A., Gimmi, T., Waber, H.N., Buschaert, S., De Cannière, P., De Craen, M., Gautschi, A., Savoye, S., Vinsot, A., Wemaere, I., Wouters, L., 2011. Natural tracer profiles across argillaceous formations. *Appl. Geochem.*, 1035-1064

Mazurek, M., Al, T., Celejewski, M., Clark, I.D., Fernandez, A.M., Kennel-Morrison, L., Matray, J.M., Murseli, S., Oyama, T., Qiu, S., Rufer, D., St-Jean, G., Waber H.N., Yu, C., 2016. Mont Terri Project: Comparison of pore-water investigations conducted by several laboratories on materials from the BDB-1 borehole. *Mont Terri TN*, draft version.

Mazurek, M., de Haller, A., 2017. Pore-water evolution and solute-transport mechanisms in Opalinus Clay at Mont Terri and Mont Russelin (Canton Jura, Switzerland). *Swiss J. Geosci.*, 110, doi:10.1007/s00015-016-0249-9.

McPhee, C.A., and Arthur, K.G., 1995. Relative permeability measurements: an inter-laboratory comparison. *Eur. Pet. Conf.*, Soc. of Pet. Eng..

Melchior, P., 1978. The Tides of the Planet Earth. Pergamon Press, Paris, 609 p.

Mercer, J. W., Pinder, G. F., and Donalson, I. G., 1975. A Galerkin-finite element analysis of the hydrothermal system at Wairakei, New-Zealand. *J. Geophys. Res.* 80, 2608-2621.

Merritt, M.L., 2004. Estimating hydraulic properties of the Floridan aquifer system by analysis of earth-tide, ocean-tide, and barometric effects. Collier and Hendry Counties, Florida. *U.S.G.S. Water-resour. investigations Report* 03-4267, vi, 70 p.

Mills, R.L., and Lobo, V.M.M., 1989. Self-diffusion in Electrolyte Solutions - A Critical Examination of Data Compiled from the Literature. Elsevier.

Missana, T., García-Gutiérrez, M., Alonso, U., 2008. Sorption of strontium onto illite/smectite mixed clays. *Phys. Chem. Earth* 33, S156–S162.

Monnier, G., Stengel, P., Fies, J.C., 1973. Une méthode de mesure de la densité apparente de petits agglomérats terreux. Application à l'analyse de système de porosité du sol. *Ann. Agron.* 24, 533-545.

Munro, R. G., 2004. Analytical representations of elastic moduli data with simultaneous dependence on temperature and porosity. *J. Res. Nat. Inst. Stand. and Technol.* 109, 497-503.

Nagra, 2002. Project Opalinus Clay: Safety Report, Demonstration of disposal feasibility for spent fuel, vitrified high-level waste and long-lived intermediate-level waste (Entsorgungsnachweis). *Technical Report* 02-05, 472 p.

Jäggi, K., Frieg, B., 2014. OPA: Sondierbohrung Benken Langzeitbeobachtung 2013 Dokumentation des Messdaten. *Nagra Arbeitsbericht* NAB 14-15, 51p.

Nagra, 2014b. SGT Etappe 2: Vorschlag weiter zu untersuchender geologischer Standortgebiete mit zugehörigen Standortarealen für die Oberflächenanlage. Geologische Grundlagen. Dossiers I – VII. Technical Report NTB 14-02, 64 p.

Neuzil, C. E., 2000. Osmotic generation of "anomalous" fuid pressures in geological environments. *Nature,* 403, 182-184.

Neuzil, C., and Provost, A., 2009. Recent experimental data may point to a greater role for osmotic pressures in the subsurface. *Water Resour. Res.* 45, W03410, doi:10.1029/2007WR006450.

Neuzil, C.E., 2013. Can Shale Safely Host U.S. Nuclear Waste? EOS, Trans., *Am. Geophy. Union*, Vol.94. 261-268.

Neuzil, C.E., 2015. Interpreting fluid pressure anomalies in shallow intraplate argillaceous formations. *Geophys. Res. Lett.*, 42., 4801-4808

N'Guessan, E.N., 2015. Analyse de la fraction fine de roches argileuses et de calcaires jurassiques par diffraction des rayons X (DRX) : vers une meilleure modélisation de la composition des eaux porales. *Mémoire de Master*, Université Paris-Sud 11, Orsay, France.

Novakowski, K.S., Van der Kamp, G., 1996. The radial diffusion method 2. A Semianalytical model for the determination of effective diffusion coefficients, porosity and adsorption. *Water Resour. Res.*, 32, No. 6, 1823-1830.

Noy, D., Horseman, S., Harrington, J., Bossart, P., Fisch, H., 2004. An Experimental and modelling study of chemico-osmotic effects in the Opalinus Clay of Switzerland. In: Heitzmann, P. ed. (2004) Mont Terri Project - Hydrogeological Synthesis, Osmotic Flow. *Reports of the FOWG*, Geology Series (6), 95–126.

Nussbaum, C., Bossart, P., Amann, F., & Aubourg, C., 2011. Analysis of tectonic structures and excavation induced fractures in the Opalinus Clay, Mont Terri underground rock laboratory (Switzerland). *Swiss J. Geosci.*, 104, 187-210.

Nussbaum, C., Kloppenburg, A., Caer, T., Bossart, P., 2017. Tectonic evolution of the Mont Terri anticline based on forward modelling. *Swiss J. Geosci.*, 110, doi:10.1007/s00015-016-0248-x.

Onsager, L, 1931a. Reciprocal relations in irreversible processes, I, *Phys. Rev.* 37, 405.

Onsager, L., 1931b. Reciprocal relations in irreversible processes, II, *Phys. Rev.* 38, 2265.

Ould Bouya, M.L., 2014. Acquisition d'un profil de perméabilité intrinsèque au sein de l'Argile à Opalines du Mont Terri par analyse minéralogique et pétrophysique. *Mémoire de Master*, Université Paris-Sud 11, Orsay, France.

Parkhurst, D.L., Appelo, C.A.J., 1999. User's guide to PHREEQC (version 2) A computer program for speciation, batch-reaction, one-dimensional transport, and inverse geochemical calculations. *Water Resour. Investigations Report* 99-4259. U.S. Geological Survey.

Papafotiou, A., Senger, R., 2014a. Thermo-hydraulic modelling of the temperature distribution in the siting region Jura Ost. *Nagra Arbeitsbericht* NAB 14-39, 70 p.

Papafotiou, A., Senger, R., 2014b. Thermo-hydraulic modelling of the temperature distribution in the siting region Nördliche Lägern. *Nagra Arbeitsbericht* NAB 13-56, 70 p.

Pape, H., Clauser, C., and Iffland, J., 1999. Permeability prediction based on fractal pore-space geometry. *Geophysics 1447-1460*, 64.

Patriarche, D., 2001. Caractérisation et modélisation des transferts de traceurs naturels dans les argilites de Tournemire. *Thesis*, Ecole des Mines, Paris

Pearson Jr., F.J., Berner, U., 1991. Nagra Thermochemical Data Base I. Core Data, Wettingen, Switzerland, *Nagra Technical Report* NTB 91-17.

Pearson F.J., Berner U., Hummel W., 1992. Nagra Thermochemical Data Base II. Supplemental Data 05/92. Wettingen, Switzerland, *Nagra Technical Report* NTB 91-18.

Pearson, F.J., Arcos, D., Boisson, J-Y., Fernández, A. M., Gäbler, H. E., Gaucher, E., Gautschi, A., Griffault, L., Hernán, P., Waber, N., 2003. Mont Terri Project - Geochemistry of water in the Opalinus Clay Formation at the Mont Terri Rock Laboratory. *Report of the FOWG*, N°5, Geology Series.

Pearson, F.J., Tournassat, C., Gaucher, E.C., 2011. Biogeochemical processes in a clay formation *in situ* experiment: Part E – Equilibrium controls on chemistry of pore water from the Opalinus Clay, Mont Terri Underground Research Laboratory, Switzerland. *Appl. Geochem.* 26, 990-1008

Revil, A., and Pessel, M., 2002. Electroosmotic flow and the validity of the classical Darcy equation in silty shales. Geophys. Res. Lett., 29-9, pp. 14-1-14-4(4).

Revil, A., and Leroy, P., 2004. Constitutive equations for ionic transport in porous shales. *J. Geophy. Res.* 109, B013208, doi: 10.1029/2003JB002755

Roberts, R.M., Beauheim, R.L, Domski, P.S., 1999. Hydraulic Testing of Salado Formation Evaporites at the Waste Isolation Pilot Plant Site: Final Report, SAND98-2537, Albuquerque, NM: Sandia National Laboratories.

Rousseau-Gueutin, P., 2008. Les processus couplés dans les argilites du Callovo-Oxfordien sur le site de Bure : implications pour les mouvements de fluide et de solutés. *Thèse*, Université Pierre et Marie Curie, Paris VI, France.

Rousseau-Gueutin, P., Gonçalvès, J., Violette, S., 2008. Osmotic efficiency in Callovo-Oxfordian argillites: Experimental vs. theoretical models. *Phys. Chem. Earth*, *33*, s106-s113.

Savoye, S., Michelot, J-L., Wittebroodt, C., Altinier, M. V., 2006a. Contribution of the exchange diffusive method to the characterization of pore-water in the consolidated argillaceous rocks. *J. Cont. Hydrol*. 86, 87-104.

Savoye, S., Michelot, J.L., Wittebroodt, C., 2006b. Evaluation of the reversibility of iodide uptake by argillaceous rocks by the radial diffusion method. *Radiochi. Acta* 94, 699-704.

Savoye, S., 2008. Apport des traceurs à la compréhension des processus de transport au sein des formations argileuses indurées, *HDR*, Université Paris-Sud 11, Orsay, France

Schneider, F., Potdevin, J. L., Wolf, S., and Faille, I., 1996. Mechanical and chemical compaction model for sedimentary basin simulators. *Tectonophysics 263*, 307-317.

Soler, J.M., 1999. Coupled Transport Phenomena in the Opalinus Clay: Implications for Radionuclide Transport. *Nagra Technical Report* 99-09

Soler, J.M., 2001. The effect of coupled transport phenomena in the Opalinus Clay and implications for radionuclide transport. *J. Contam. Hydrol.*, 53, 63–84

Tarantola, A., 2005. Monte Carlo Methods. Chapter 2 in Inverse Problem Theory and Methods for Model Parameter Estimation. Soc. for Ind. and Appl. Math., 41-56.

Terzaghi, V.K., 1936. The Sheering Resistance of Saturated Soils and the Angle between the Planes of Shear. First International Conference of Soil Mechanics, Harvard University, Vol. 1, 54-46

Tournassat, C., Gailhanou, H., Crouzet, C., Braibant, G., Gautier, A., Gaucher, E.C., 2009. Cation exchange selectivity coefficient values on smectite and mixed-layer illite/smectite minerals. *Soil Sci. Soc. Am. J.* 73, 928–942.

Tremosa, J., 2010. Influence of osmotic processes on the excess-hydraulic head measured in the Toarcian/Domerian argillaceous formation of Tournemire. *Thèse*, Université Pierre et Marie Curie, Paris VI, France.

Tremosa, J., Arcos, D., Matray, J.M., Bensenouci, F., Gaucher, E.C., Tournassat, C., Hadi, J., 2012a. Geochemical characterization and modelling of the Toarcian/Domerian porewater at the Tournemire nderground research laboratory. *Appl. Geochem.*, 27, 1417-1431.

Tremosa, J., Gonçalvès, J., Matray, J.M., 2012b. Natural conditions for more limited osmotic abnormal fluid pressures in sedimentary basins. *Water Resour. Res.*, Vol. 48, W04530.

Ullman, W.J. et Aller, R.C., 1982. Diffusion Coefficients in Nearshore Marine Sediments. *Limnol. and Oceanogr.* 27, 552-556.

Unesco, 1981. Tenth report on the joint panel on oceanographic tables and standard. Sidney, BC, Canada. 1-5 september 1980. *Unesco technical paper in mar. sci.* 36, 28 pp.

Van der Lee, J., De Windt, L., Lagneau, V. and Goblet, P., 2003. Module-oriented modeling of reactive transport with HYTEC. *Comput. & Geosci.*, 29-3, 265-275

Van der Kamp, G., Van Stempvoort, D.R., Wassenaar, L.I., 1996a. The radial diffusion method 1. Using intact cores to determine isotopic composition, chemistry, and effective porosities for groundwater in aquitards. *Water Resour. Res.*, 32, No. 6, 1815-1822.

Van der Kamp, G., Novakowski, K.S., 1996. The radial diffusion method 2. A Semianalytical model for the determination of effective diffusion coefficients, porosity and adsorption. *Water Resour. Res.*, 32, No. 6, 1823-1830.

Van Loon, L.R., Soler, J., Müller, W. and Bradbury, M. H., 2004. Anisotropic diffusion in layered Argillaceous Rocks: a case study with Opalinus clay. *Environ. Sci. Technol.* 38, 5721–5728.

Van Loon, L.R., Glaus, M., Ferry, C., Latrille, C., 2012. Studying radionuclide migration on different scales: the complementary roles of laboratory and in situ experiments. In: Radionuclide behaviour in the natural environment: science, implications and lessons for the nuclear industry, Woodhead Publishing Series in Energy, No. 42, 446-483.

Waber, H.N., Gaucher, E.C., Fernandez, A.M., Bath, A., 2003. Aqueous Leachates and Cation Exchange Properties of Mont Terri Claystones. Annex 3 in Pearson (2003), *Report of the FOWG*, N°5, Geology Series.

Walsh J.B. & Brace W.F., 1966, Elasticity of rock: A review of recent theoritical studies, Rock *Mech. Eng. Geol.*, 4, p. 283.

Wiegel, R.L., 1964. Tsunamis, storm surges, and harbour oscillations. Ch. 5 in Oceanographical Engineering, Prentice Hall, Englewood Cliffs, New Jersey, 95-127.

Wittebroodt, C., Savoye, S., Jacquier, P., Beaucaire, C., Bensenouci, F., Pitsch, H., Gouze, P., Michelot, J.L., 2007. Comparison between radial diffusion and leaching for determining chloride and sulphate in Tournemire argillite pore water. Int. Meeting, 17-18 Sept, Clays in Nat. & Eng. Barriers for Rad. Waste Conf., 485-486.

Yu, C., Matray, J.M., Gonçalvès, J., Jaeggi, D., Gräsle, W., Wieczorek, K., Vogt, T., Sykes, E., 2017a. Comparative study of methods to estimate hydraulic parameters in the hydraulically undisturbed Opalinus Clay (Switzerland). *Swiss J. Geosci.*, 110, doi: 10.1007/s00015-016-0257-9h

Yu, C., Gonçalvès, J., Matray, J.M., 2017b. Bayesian inversion of a chloride profile obtained in the hydraulically undisturbed Opalinus Clay: mass transport and paleo-hydrological implications, Applied Geochemistry, in press, corrected proof, doi: 10.1016/j.apgeochem.2017.11.004

AI-1 Specific Surface Area Measurement

AI-1-1 BET Method

The BET method was developed by Brunauer, Emett and Teller (1938) and enables specific surface area measurement by gas adsorption (Brunauer et al. 1940). The protocol used in the present study is the one described by Alcade et al. (2013). It is based on the determination of gas quantity necessary to cover the external surface and internal pores of a solid by a complete monolayer. The method is applicable on powdered solid sample which particle diameter does not exceed 2 mm and which specific surface area is greater than 0.2 $m^2\,g^{-1}$.

The sample is placed in an oven at 105°C, crushed and put into a glass sample holder. In order to empty the sample porosity of water and air that it mays contain and enable fixation of N_2 gas, the powdered sample is degassed at 105°C for 120 minutes and cooled in a bath of liquid nitrogen at a temperature of 77 K, to avoid gas condensation with increasing temperature.

Helium, a gas that will not fix on the sample surface, is injected into the sample holder to measure the volume which is not occupied by the sample. After helium evacuation, nitrogen is injected by successive steps, enabling the apparatus to measure the pressure in the sample holder. The partial pressure regularly measured and in the range of 0 to 0.995 enables to determine the quantity of adsorbed nitrogen. Results are processed using the equation of Brunauer, Emmett and Teller:

$$\frac{P_s/P_0}{n_a(1-P_s/P_0)} = \frac{1}{n_m C} + \left(\frac{C-1}{n_m C}\right)P_s/P_0 \qquad \text{(AI-1-1)}$$

where P_s [Pa] is the pressure of adsorption gas in equilibrium with the adsorbate gas, P_0 [Pa] is the saturation vapour pressure of the adsorption gas, P_s/P_0 [-] is the relative pressure of the adsorption gas, n_a [mol g^{-1}] is the specific adsorbed gas quantity, n_m [mol g^{-1}] is the molecular coverage capacity, quantity of adsorbed gas necessary to cover a unit surface with a complete monolayer and C [-] is the BET constant.

Graphically, the quantity $\frac{P_s/P_0}{n_a(1-P_s/P_0)}$ is represented in function of relative pressure P_s/P_0. When P_s/P_0 is in the range 0.05 to 0.35, equation (AI-1-1) is a linear function $y = ax + b$

with slop $\qquad a = \left(\frac{C-1}{n_m C}\right) \qquad$ (AI-1-2) $\qquad$ and y-intercept $\qquad b = \frac{1}{n_m C} \qquad$ (AI-1-3)

Thus, BET constant writes:

$$C = \frac{a}{b} + 1 \qquad \text{(AI-1-4)}$$

And the monolayer volume is given by:

$$V_M = \frac{1}{a+b} \tag{AI-1-5}$$

The corresponding specific surface area is deduced with the following relation:

$$A_s = \frac{V_M}{V_m m_s} S_{Ad} NA \tag{AI-1-6}$$

where A_s [m^2 g^{-1}] is the specific surface area of the solid, V_M [cm^3] is the volume of the adsorbed gas monolayer, S_{Ad} [m^2] is the area of the efficient section per adsorbate molecule, V_m [22414 cm^3 mol^{-1} at P = 1 atm and T = 25°C] is the volume of a molecular gram, M_s [g] is the mass of the sample after degassing, and NA [6.022·10^{23} atomes mol^{-1}] is the Avogadro constant.

AI-1-2 BJH Method

The BJH technique enables to obtain specific surface area and pore size distribution. The theory was proposed by Barrett, Joy and Halenda in 1951. Its principle is based on the analysis of isotherm of adsorption and desorption of nitrogen at 77 K, showing a hysteresis loop. In this method, calculation of the specific surface area is done on the desorption part which is supposed to be the most representative of the equilibrium between gaseous nitrogen and condensed nitrogen by capillarity. Pores are considered to be filled at the equilibrium pressure for which a saturation plateau or an inflexion point can be seen. According to Brunauer classification, the shape of the hysteresis loop gives information on pore size and shape.

References:

Alcade, G., Barker, E., et Bassot, S., 2013. Document IRSN/PRP-DGE/SRTG/LAME, BET/MOP-01. Mode Opératoire de la mesure de la surface spécifique d'un solide pulvérulent par adsorption de l'azote par modèle BET, 13p.

Barrett, E.P., Joyner, L.G., Halenda, P.P., 1951. The determination of pore volume and area distributions in porous substances. I. Computations from nitrogen isotherms. Journal of the American Chemical Society, Vol. 73, No. 1, pp. 373-380

Brunauer, S., Emmett, P.H., et Teller, E., 1938. Adsorption of gases in multimolecular layers. J. Amer. Chem. Soc. 60, 309-319

Brunauer, S., Deming, L.S.; Deming, W.S., Teller, E., 1940. On a Theory of the Van der Waals Adsorption of Gases. Journal of the American Chemical Society, Vol. 62, No. 7, 1723-1732

AI-2 Grain density determination

Grain density is determined using helium pycnometry. The apparatus is an AccuPyc II 1340. Protocol is described in Alcade et al. (2013). The technique enables to measure volumetric mass of a bulk or powdered solid, of regular or irregular shape from the measure of real

volume V_s of a dried sample (but it does include closed porosity), which mass M_s is known by weighing on a precision balance.

Sample is placed in a helium cell which volume V_{cell} is known, at a known pressure P_1 and known ambient temperature T_a.

The apparatus consists in two cells: the measuring cell and the expansion cell. The sample volume should neither be less than 10% of the measuring cell neither superior than 90% of it. Valve is closed and expansion cell with known volume V_{exp} is put into contact with helium with known pressure P_a and temperature T_a. Then, valve is open and the two cells are communicating with a pressure of equilibrium P_2.
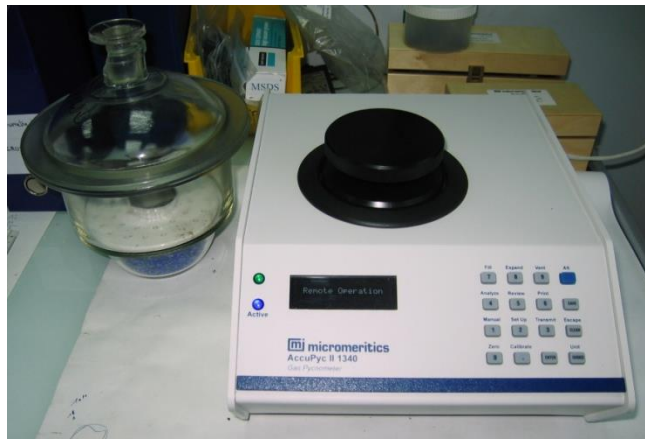
Figure A.I.1: AccuPyc II 1340 Helium-pycnometer

According to the ideal gas law:

$$P_1(V_{cell} - V_{sample}) = n_{cell}RT_a \qquad \text{(AI-2-1)}$$

$$P_aV_{exp} = n_{exp}RT_a \qquad \text{(AI-2-2)}$$

$$P_2(V_{cell} - V_{sample} + V_{exp}) = (n_{cell} + n_{exp})RT_a \qquad \text{(AI-2-3)}$$

By replacing the right member of (AI-2-3) by the left members of (AI-2-1) and (AI-2-2), the following equation is obtained:

$$V_{sample} = V_{cell} - \frac{P_2 - P_a}{P_1 - P_2}V_{exp} \qquad \text{(AI-2-4)}$$

The sample grain density ρ_S is given by:

$$\rho_S = \frac{M_s}{V_s} \qquad \text{(AI-2-5)}$$

References:

Alcade, G., Barker, E., et Bassot, S., 2013. Document IRSN / PRP-DGE / SRTG / LAME, BET/MOP-01. Utilisation du pycnomètre à hélium AccuPyc II 1340, 19p.

AI-3 Determination of water content, degree of saturation and total physical porosity

AI-3-1 Definitions

Definitions proposed in this document are consistent to those proposed in Appendix 10 of Pearson et al. (2003). Several parameters have to be determined to obtain the volumetric water content.

- The total or physical porosity, n_{tot} [-], is the ratio of the pore volume V_{pores} [m³] to total apparent volume V_{tot} [m³]:

$$n_{tot} = \frac{V_{pores}}{V_{tot}} \quad \text{(AI-1)} \qquad V_{pores} = V_{tot} - V_s \quad \text{(AI-2)} \qquad V_{pores} = V_{tot} - \frac{M_s}{\rho_s} \quad \text{(AI-3)}$$

Where M_s [g] is the oven-dried at temperature T=105°C sample mass and ρ_S [g cm⁻³] is the grain density measured by helium pycnometry on oven-dried samples.

- The gravimetric water content WC [-] is described on a mass basis relative to either the dry mass, M_s [g], or the total mass of the humid sample M_{tot} [g]. M_w [g] is the mass of water contained in the sample.

$$WC_{dry} = \frac{M_w}{M_s} \quad \text{and} \quad WC_{wet} = \frac{M_w}{M_{tot}} \qquad \text{(AI-4)}$$

$$WC_{dry} = \frac{M_{tot} - M_s}{M_s} \qquad \text{(AI-5)}$$

- The degree of saturation, S [-], is the ratio of water-filled to total pore space [cm³]. ρ_W [g cm⁻³] is the porewater density.

$$S = \frac{V_W}{V_{pores}} = \frac{M_{tot} - M_s}{\rho_w} \qquad \text{(AI-6)}$$

- The volumetric moisture content, ϑ [-], is the ratio of water-filled pore space, V_w [cm³], to total volume, V_{tot} [cm³].

$$\vartheta = \frac{V_W}{V_{tot}} = S n_{tot} \qquad \text{(AI-7)}$$

The following protocol was proposed by Matray et al. (2007) and used on Opalinus Clay samples by Matray and Möri (2012).

AI-3-2 Determination of V_{tot}

Measurement of the apparent sample volume is based on Archimedes' principle (Monnier et al, 1973). The solid sample immersed in a liquid is subject to a force called upthrust buoyancy (Figure A.I.2). The value of this force is equal to the weight of liquid displaced by the sample measured on a scale.

Figure A.I.2: Upthrust Buoyancy

The buoyancy is equal to the difference between the mass of the solid in the air and the mass of the solid in the liquid, according to the equation:

$$G_h = m_{sa} - m_{sl} = m_{dl} \qquad \text{(AI-8)}$$

Where G_h [g] is the buoyancy, m_{sa} [g] is the mass of the solid in the air, m_{sl} [g] is the mass of the solid in the liquid and m_{dl} [g] is the mass of the displaced liquid.
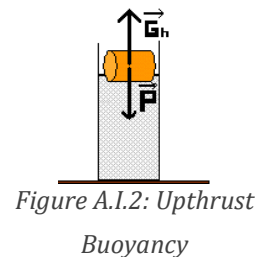
The measured thrust is equal to the mass of liquid displaced. Knowing the density of the liquid, we can deduce the precise volume of displaced liquid equivalent to the total apparent volume of the sample:

$$V_{ld} = \frac{m_{dl}}{\rho_{liq}} = \frac{G_h}{\rho_{liq}}$$ (AI-9)

where ρ_{liq} [g cm⁻³] is the liquid density and V_{liq} [cm³] is the volume of displaced liquid.

The volume of liquid displaced is equivalent to the apparent volume of the immersed solid V_s [cm³]:

$$V_{ld} = V_s = \frac{m_{dl}}{\rho_{liq}}$$ (AI-10)

Then, knowing the mass of the solid in the air, density of the solid is calculated as follows:

$$\rho_s = \frac{m_{sa}}{V_s}$$ (AI-11)   or $$\rho_s = \frac{m_{sa}\rho_{liq}}{m_{sa} - m_{sl}}$$ (AI-12)

Where V_s [cm³] is the apparent volume of solid, ρ_S [g·cm⁻³] is the solid density, m_{sa} [g] is the mass of the solid in the air and m_{sl} [g] is the mass of the solid in the liquid.

The solid sample is assumed constituted of three phases: water, air and solid. The determination of the total apparent volume of the sample requires first a full saturation of all pores after immersion in a liquid that must meet certain requirements:

- it must have a good affinity with the rock type in order to easily migrate within it to fill the voids during immersion;
- it should be immiscible with the water present in the solid;
- it should not cause swelling of the sample; and
- it must not be volatile.

The liquid used is generally a denatured de-aromatised petroleum commercially known as Kerdane, Zibro.

Due to the saturation of the solid, rock masses measured during the experiment must be saturated by the liquid immersion. The density of the saturated solid is defined by:

$$\rho_h = \frac{w_a\rho_w}{w_a - w_p}$$ (AI-13)

where ρ_h [g cm⁻³] is the density of the saturated solid, w_a [g] is the mass of the sample saturated in the air, ρ_w [g cm⁻³] is the porewater density and w_p [g] is the mass of the sample saturated in the liquid.

Then the total apparent volume becomes:

$$V_{tot} = \frac{w_a}{\rho_h}$$ (AI-14)

Several factors affect measurement:

- Air density during the sample weighing in the air

Correction to be applied is as follows:

$$\rho_h = \frac{w_a(\rho_w - \rho_a)}{w_a - w_p} + \rho_a$$ (AI-15)

where ρ_a [0.0012 g·cm⁻³ at 20°C and 1 bar] is the air density.

- Stem volume of the sample holder

With this device, during immersion of the sample, it is necessary to take into account the additional buoyancy created by the diving support rods. The thrust depends on the height of the liquid level elevation.

Since the sample volume V_s is equal to the volume of displaced liquid V_{lq}:

$$\frac{w_a - w_p}{\rho_p} = \pi R^2 h \qquad \text{(AI-16)}$$

Where h [m] is the height of the liquid elevation and R [m] is the beaker radius.

- Buoyancy caused by the two rods G_{2rods} :

$$G_{2rods} = 2V_{rod}\rho_w \qquad \text{(AI-17)}$$

Thus,
$$G_{2rods} = 2\pi r^2 h \rho_w \qquad \text{(AI-18)}$$

where r [m] is the rods radius.

Substituting in the formula h by the expression (AI-16):

$$G_{2rods} = 2\pi r^2 \frac{w_a - w_p}{\rho_w \pi R^2}\rho_w = 2r^2 \frac{w_a - w_p}{R^2} \qquad \text{(AI-19)}$$

The value of this thrust caused by the immersion is subtracted from the measured thrust:

$$G_{real} = G_h - G_{2rods} \qquad \text{(AI-20)}$$

$$G_{real} = \left(w_a - w_p\right) - \left(\left(w_a - w_p\right)2\pi \frac{r^2}{R^2}\right) \qquad \text{(AI-21)}$$

$$G_{real} = \left(w_a - w_p\right)\left(1 - 2\frac{r^2}{R^2}\right) \qquad \text{(AI-22)}$$

For a beaker diameter of 76 mm, $\qquad G_{real} = G_h \cdot 0.99983 \qquad \text{(AI-23)}$

The expression of the density is: $\quad \rho_h = \dfrac{w_a(\rho_p - \rho_a)}{(w_a - w_p) \cdot 0.99983} + \rho_a \qquad \text{(AI-24)}$

Therefore, taking into account the two factors described above, the formula used to calculate the apparent volume of solid by this method will be:

$$V_{tot} = \frac{w_a}{\rho_h} = \frac{w_a}{\dfrac{w_a(\rho_p - \rho_a)}{(w_a - w_p) \cdot 0.99983} + \rho_a} \qquad \text{(AI-25)}$$

The liquid phase employed at IRSN is a denatured de-aromatised oil commercially known as Zibro. Zibro is a KRISTAL mark containing aromatic hydrocarbon content less than 0.007% and with a flash point above 65 °C.

The device used is named YDK 01 from Sartorius©. It aims at measuring the density of a solid or liquid sample by means of an accurate scale. It consists of a swing, a beaker and a bridge.

The swing is placed on the tray using different adapters depending on the scale. The bridge allows not taking into account the beaker containing the immersion liquid during weighing.
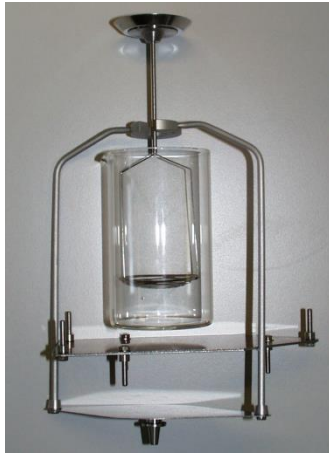
Figure A.I.3: YDK 01 device suitable for Sartorius scales LA/LP and LE

The following steps are necessary:

- place the beaker of 76 mm diameter in the middle of the metal bridge;
- fill the beaker so as to obtain during measurement a level of oil located 5 mm above the sample;
- place a thermometer in another beaker and record the temperature of the oil during the experiment;
- place the swing adapted to the sample (sample will sink or float depending on the difference in density between the sample and the oil);
- saturate the samples in the oil until there is no more air bubbles, 2 hours should be sufficient;
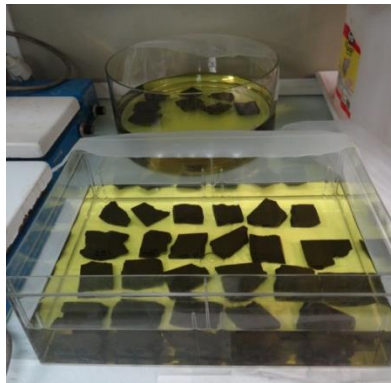
Figure A.I.4: Samples dumped into Zibro (de-aromatised petroleum) for resaturation prior determination of the apparent sample volume

- remove the excess oil on the sample with clean paper;
- place the sample on the top shelf of the suspension system and measure the mass of the solid in the saturated air w_a (Figure A.I.5);
- place the sample in the swing and read the value of the mass of the solid in the saturated liquid w_p;

Figure A.I.5: Measurement of w_a
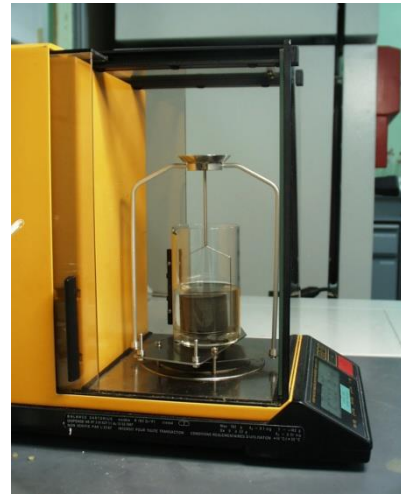
Figure A.I.6: Measurement of w_p

- then, calculate the apparent volume.

The beaker must be placed in the axis of the swing to avoid the sample contacts the edge. When diving the sample in the beaker, there should not be air bubble trapped under the basket, which would tend to distort the measurement.

AI-3-2 Determination of M_{tot}, M_s, ρ_s, ρ_w, ρ_p

M_{tot} and M_s are measured on the same accurate SARTORIUS R180D scale respectively on the same hydrated and oven-dried samples. The estimated repeatability is maximized at 0.002 g. The grain density and its error (ρ_s, $\sigma_{\rho s}$) is obtained for each piece of rock by using an AccuPyc II1340 Helium-pycnometer from Micrometrics. Porewater density and its error (ρ_w, $\sigma_{\rho w}$) can either be measured or calculated from a geochemical model. Petroleum density and its error (ρ_p, σ_{pp}) is a function of temperature. Two functions are proposed for Zibro, a denatured petroleum, with the temperature range (Figure A.I.7). Error was estimated at -0.0007.
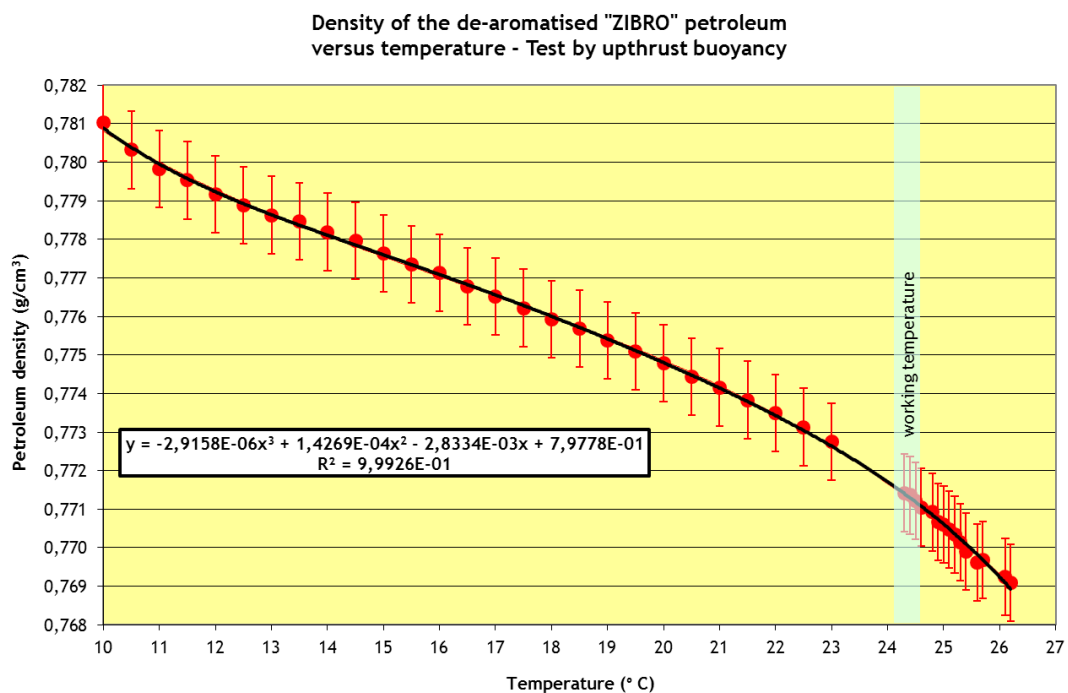
Figure 7: Density vs temperature relationship for Zibro obtained at the IRSN laboratory

Air density and its error (ρ_a, $\sigma_{\rho a}$) may be considered as constant. One cm^3 of air is weighing about 1.2 mg at 20°C and 1 bar. Considering these conditions close to the experimental one, ρ_a was taken equal to 0.0012 g cm^{-3} with a nil error.

AI-3-2 Errors associated to functions

Errors on functions U=F(V1, V2,...) are estimated by propagation of the analytical errors variances following the classical Gauss formula (in Theoria combinationis, 1821):

$$\sigma_0^2 = \sigma_{V_1}^2 \left(\frac{dF}{dV_1}\right)^2 + \sigma_{V_2}^2 \left(\frac{dF}{dV_2}\right)^2 + \cdots$$

- Bulk wet density [g cm^{-3}]: ρ_h

$$\rho_h = \frac{w_a(\rho_{liq} - \rho_{air})}{0.999983 \cdot G} + \rho_a$$

where w_a [g] is the mass of the sample saturated in the air, w_p [g] is the mass of the sample saturated in the liquid, G is the upthrust buoyancy, ρ_p [g cm^{-3}] is the density of petroleum at temperature T [°C] and ρ_a [0.0012 g cm^{-3} at STP conditions] is the air density.

0.999983 represents the correction of the thrust due to the rods' immersion.

Error on ρ_h:

$$\sigma_{\rho_h}{}^2 = \sigma_{w_a}{}^2 \left(\frac{\partial \rho_h}{\partial w_a}\right)^2 + \sigma_{\rho_p}{}^2 \left(\frac{\partial \rho_h}{\partial \rho_p}\right)^2 + \sigma_{\rho_a}{}^2 \left(\frac{\partial \rho_h}{\partial \rho_a}\right)^2 + \sigma_{w_l}{}^2 \left(\frac{\partial \rho_h}{\partial w_l}\right)^2$$

With:
$$\frac{\partial \rho_h}{\partial w_a} = -\frac{(\rho_p - \rho_a) \cdot w_p}{0.99983(w_a - w_p)^2} \quad ; \quad \frac{\partial \rho_h}{\partial \rho_p} = \frac{w_a}{0.99983(w_a - w_p)}$$

$$\frac{\partial \rho_h}{\partial \rho_a} = -\frac{w_a}{0.99983(w_a - w_p)} \quad ; \quad \frac{\partial \rho_h}{\partial w_p} = \frac{(\rho_p - \rho_a) \cdot w_a}{0.99983(w_a - w_p)^2}$$

- Total apparent volume of the humid sample [cm^3]: V_{tot}

$$V_{tot} = \frac{w_a}{\rho_h}$$

Error on V_{tot}:

$$\sigma_{V_{tot}}{}^2 = \sigma_{\rho_h}{}^2 \left(\frac{\partial V_h}{\partial \rho_h}\right)^2 + \sigma_{M_h}{}^2 \left(\frac{\partial \rho_h}{\partial M_h}\right)^2 \quad \text{with} \quad \frac{\partial V_h}{\partial \rho_h} = -\frac{w_a}{\rho_h{}^2} \quad \text{and} \quad \frac{\partial V_h}{\partial M_h} = \frac{1}{\rho_h}$$

- Gravimetric water content, dry mass basis [%]: WC_d

$$WC_d = 100 \left(\frac{M_h}{M_t} - 1\right)$$

Error on WC_d:

$$\sigma_{WC_d}{}^2 = \sigma_{M_h}{}^2 \left(\frac{\partial WC_d}{\partial M_h}\right)^2 + \sigma_{M_t}{}^2 \left(\frac{\partial WC_d}{\partial M_t}\right)^2 \quad \text{with} \quad \frac{\partial WC_d}{\partial M_h} = \frac{100}{M_t} \quad \text{and} \quad \frac{\partial WC_d}{\partial M_t} = -\frac{100M}{M_t{}^2}$$

- Water volume [cm^3]: V_w

$$V_w = \frac{M_h - M_t}{\rho_w}$$

Error on V_w

$$\sigma_{V_w}{}^2 = \sigma_{M_h}{}^2 \left(\frac{\partial V_w}{\partial M_h}\right)^2 + \sigma_{M_t}{}^2 \left(\frac{\partial V_w}{\partial M_t}\right)^2 + \sigma_{\rho_w}{}^2 \left(\frac{\partial V_w}{\partial \rho_w}\right)^2$$

with $\qquad \dfrac{\partial V_w}{\partial M_h} = \dfrac{1}{\rho_w} \qquad ; \qquad \dfrac{\partial V_w}{\partial M_t} = -\dfrac{1}{\rho_w} \qquad ; \qquad \dfrac{\partial V_w}{\partial \rho_w} = \dfrac{M_t - M_h}{\rho_w{}^2}$

- Solid volume [cm³]: V_s

$$V_s = \frac{M_t}{\rho_s}$$

Error on V_s:

$$\sigma_{V_s}{}^2 = \sigma_{M_t}{}^2 \left(\frac{\partial V_s}{\partial M_t}\right)^2 + \sigma_{\rho_s}{}^2 \left(\frac{\partial V_s}{\partial \rho_s}\right)^2 \qquad \text{with} \qquad \frac{\partial V_s}{\partial M_t} = \frac{1}{\rho_s} \qquad \text{and} \qquad \frac{\partial V_s}{\partial \rho_s} = -\frac{M_t}{\rho_s{}^2}$$

- Pore volume [cm³]: V_{pore}

$$V_{pore} = V_{tot} - \frac{M_t}{\rho_s}$$

Error on V_{pore}:

$$\sigma_{V_{pore}}{}^2 = \sigma_{V_{tot}}{}^2 \left(\frac{\partial V_{pore}}{\partial V_{tot}}\right)^2 + \sigma_{M_t}{}^2 \left(\frac{\partial V_{pore}}{\partial M_t}\right)^2 + \sigma_{\rho_s}{}^2 \left(\frac{\partial V_{pore}}{\partial \rho_s}\right)^2$$

with $\qquad \dfrac{\partial V_{pore}}{\partial V_{tot}} = 1 \qquad ; \qquad \dfrac{\partial V_{pore}}{\partial M_t} = -\dfrac{1}{\rho_s} \qquad ; \qquad \dfrac{\partial V_{pore}}{\partial \rho_s} = \dfrac{M_t}{\rho_s{}^2}$

- Degree of saturation [-]: S

$$S = \frac{V_w}{V_{pore}}$$

Error on S:

$$\sigma_S{}^2 = \sigma_{V_w}{}^2 \left(\frac{\partial S}{\partial V_w}\right)^2 + \sigma_{V_{pore}}{}^2 \left(\frac{\partial S}{\partial V_{pore}}\right)^2 \qquad \text{with} \qquad \frac{\partial S}{\partial V_w} = \frac{1}{V_{pore}} \qquad \text{and} \qquad \frac{\partial S}{\partial V_{pore}} = -\frac{V_w}{V_{pore}{}^2}$$

- Dry density [g cm⁻³]: ρ_d

$$\rho_d = \frac{M_t}{V_h}$$

Error on ρ_d:

$$\sigma_{\rho_d}{}^2 = \sigma_{M_t}{}^2 \left(\frac{\partial \rho_d}{\partial M_t}\right)^2 + \sigma_{V_h}{}^2 \left(\frac{\partial \rho_d}{\partial V_h}\right)^2 \qquad \text{with} \qquad \frac{\partial \rho_d}{\partial M_t} = \frac{1}{V_h} \qquad \text{and} \qquad \frac{\partial \rho_d}{\partial V_h} = -\frac{M_t}{V_h{}^2}$$

- Total porosity [%]: n_{tot}

$$n_{tot} = 100 \cdot \frac{V_{pore}}{V_{tot}}$$

Error on n_{tot}:

$$\sigma_{n_{tot}}{}^2 = \sigma_{V_{pore}}{}^2 \left(\frac{\partial n_{tot}}{\partial V_{pore}}\right)^2 + \sigma_{V_{tot}}{}^2 \left(\frac{\partial n_{tot}}{\partial V_{tot}}\right)^2$$

with $\qquad \dfrac{\partial n_{tot}}{\partial V_{pore}} = \dfrac{100}{V_{tot}} \qquad \text{and} \qquad \dfrac{\partial n_{tot}}{\partial V_{tot}} = -\dfrac{100 V_{pore}}{V_{tot}{}^2}$

- <u>Volumetric water content [-]</u>: ϑ

$$\vartheta = Sn_{tot}$$

Error on ϑ:

$$\sigma_\vartheta{}^2 = \sigma_S{}^2 \left(\frac{\partial \vartheta}{\partial S}\right)^2 + \sigma_{n_{tot}}{}^2 \left(\frac{\partial \vartheta}{\partial n_{tot}}\right)^2 \quad \text{with} \quad \frac{\partial \vartheta}{\partial S} = n_{tot} \quad \text{and} \quad \frac{\partial \vartheta}{\partial n_{tot}} = S$$

<u>References</u>:

Gauss, C.F., 1821. Theoria combinationis observationum erroribus minimis obnoxiae, Werke, vol. 4, 1-94

Matray, J.M., Savoye, S. & Cabrera, J., 2007. Desaturation and structure relationships around drifts excavated in the well-compacted Tournemire's argillite (Aveyron, France) / Engineering Geology 90, 1-16

Matray, J.-M., and Möri, A., 2012. Petrophysical measurements on BCD-3 core samples from the Mont Terri rock laboratory. Note technique IRSN/PRP-DGE/2012-00020, 24 p.

Monnier, G., Stengel, P. & Fies, J.C., 1973. Une méthode de mesure de la densité apparente de petits agglomérats terreux. Application à l'analyse de système de porosité du sol. Ann. Agron. 24, 533–545

Pearson, F. J., Arcos, D., Boisson, J-Y., Fernández, A. M., Gäbler, H. E., Gaucher, E., Gautschi, A., Griffault, L., Hernán, P., Waber, N., 2003. Mont Terri Project - Geochemistry of water in the Opalinus Clay Formation at the Mont Terri Rock Laboratory. Annex 10: Porosity and Water Content of Mont Terri Mudrocks. Report of the FOWG, N°5, Geology Series, 22 p.

AI-4 Results tables

Sample ID	Distance		Formation	Specific surface area (Coulter SA3100 apparatus)			Specific surface area (Micromeritics 3Flex apparatus)			Chlorinity from out diffusion experiments and water density			Grain densities			Zibro (Petroleum)		
Sample ID	minimum distance	maximum distance	Formation	BET	Error on As BET	BJH	BET	Error on As BET	BJH	Chlorinity	Water density	Error on rw	measured from He pycnometry	Error on srs	calculated from XRD total rock	Zibro temperature	Zibro density	Error on rp
				As BET	s AsBET	As BJH	As BET	s AsBET	As BJH	Cl⁻	r_w	sr_w	r_s	sr_s	r_s	t	r_p	sr_p
	m	m		m²/g	m²/g	m²/g	m²/g	m²/g	m²/g	mg/l	g/cm³	g/cm³	g/cm3	g/cm3	g/cm3	°C	g/cm³	g/cm³
1a	5.8	6	Hauptrogenstein (carbonates)	10.911	0.546	11.242				8.1	0.9999	0.0002	2.7575	0.0026	2.7478	23	0.77262	0.002
1b	5.8	6		10.911	0.546					8.1	0.9999	0.0002	2.7366	0.0014	2.7478	23	0.77262	0.002
1c	5.8	6		10.911	0.546					8.1	0.9999	0.0002	2.7499	0.0012	2.7478	23	0.77262	0.002
2a	14.84	15.1		3.084	0.154					43.19	0.9999	0.0002	2.6935	0.0023	2.8239	23	0.77262	0.002
2b	14.84	15.1		3.084	0.154					43.19	0.9999	0.0002	2.7006	0.0015	2.8239	23	0.77262	0.002
2c	14.84	15.1		3.084	0.154					43.19	0.9999	0.0002	2.7034	0.0025	2.8239	23	0.77262	0.002
3a	24.98	25.3		3.155	0.158					82.54	1.0000	0.0002	2.7046	0.002	2.7904	23	0.77262	0.002
3b	24.98	25.3		3.155	0.158					82.54	1.0000	0.0002	2.6998	0.0039	2.7904	23	0.77262	0.002
3c	24.98	25.3		3.155	0.158					82.54	1.0000	0.0002	2.6994	0.0023	2.7904	23	0.77262	0.002
4a	35.35	35.58		10.434	0.522		4.209	0.210	3.576	100.1	1.0000	0.0002	2.7341	0.0029	2.835	23	0.77262	0.002
4b	35.35	35.58		10.434	0.522					100.1	1.0000	0.0002	2.7294	0.0015	2.835	23	0.77262	0.002
4c	35.35	35.58		10.434	0.522					100.1	1.0000	0.0002	2.7316	0.002	2.835	23	0.77262	0.002
5a	42.28	42.52	Passwang Formation (marl and limestone)	21.345	1.067					111.8	1.0000	0.0002	2.7143	0.0077	2.822	23	0.77262	0.002
5b	42.28	42.52		21.345	1.067					111.8	1.0000	0.0002	2.7167	0.0068	2.822	23	0.77262	0.002
5c	42.28	42.52		21.345	1.067					111.8	1.0000	0.0002	2.723	0.0084	2.822	23	0.77262	0.002
6a	61.75	62.08		28.760	1.438					144.9	1.0001	0.0002	2.7505	0.0035	2.6693	23	0.77262	0.002
6b	61.75	62.08		28.760	1.438					144.9	1.0001	0.0002	2.7626	0.0032	2.6693	23	0.77262	0.002
6c	61.75	62.08		28.760	1.438					144.9	1.0001	0.0002	2.7641	0.0025	2.6693	23	0.77262	0.002
7a	69.76	70.03		8.513	0.426		5.372	0.269	4.795	158	1.0001	0.0002	2.7405	0.002	2.6528	23	0.77262	0.002
7b	69.76	70.03		8.513	0.426					158	1.0001	0.0002	2.7333	0.0012	2.6528	23	0.77262	0.002
7c	69.76	70.03		8.513	0.426					158	1.0001	0.0002	2.7281	0.0016	2.6528	23	0.77262	0.002
8a	74.78	75.03		12.982	0.649					237.1	1.0002	0.0002	2.7313	0.0028	2.7631	23	0.77262	0.002
8b	74.78	75.03		12.982	0.649					237.1	1.0002	0.0002	2.7302	0.0023	2.7631	23	0.77262	0.002
8c	74.78	75.03		12.982	0.649					237.1	1.0002	0.0002	2.7299	0.0021	2.7631	23	0.77262	0.002
9a	84.73	84.98		23.062	1.153	23.545				393.4	1.0005	0.0002	2.7472	0.0055	2.7911	23	0.77262	0.002
9b	84.73	84.98		23.062	1.153					393.4	1.0005	0.0002	2.7603	0.0059	2.7911	23	0.77262	0.002
9c	84.73	84.98		23.062	1.153					393.4	1.0005	0.0002	2.7539	0.0008	2.7911	23	0.77262	0.002
10a	96.7	96.9		10.045	0.502					581	1.0008	0.0002	2.7915	0.0042	2.8082	23	0.77262	0.002
10b	96.7	96.9		10.045	0.502					581	1.0008	0.0002	2.8017	0.0032	2.8082	23	0.77262	0.002
10c	96.7	96.9		10.045	0.502					581	1.0008	0.0002	2.7893	0.0025	2.8082	23	0.77262	0.002
11b	107	107.24	OPA (sandy)	28.505	1.425					1435	1.0018	0.0002	2.7213	0.0031	2.816	23	0.77262	0.002
11c	107	107.24		28.505	1.425					1435	1.0018	0.0002	2.7351	0.004	2.816	23	0.77262	0.002
12a	116.24	116.54		25.214	1.261		26.892	1.345	24.487	2202	1.0027	0.0002	2.6925	0.0022	2.7349	24.4	0.77124	0.002
12b	116.24	116.54		25.214	1.261					2202	1.0027	0.0002	2.7037	0.0033	2.7349	24.4	0.77124	0.002
12c	116.24	116.54		25.214	1.261					2202	1.0027	0.0002	2.6988	0.0027	2.7349	24.4	0.77124	0.002
13a	125.12	125.38		24.048	1.202					2737	1.0033	0.0002	2.7212	0.0033	2.6922	24.4	0.77124	0.002
13b	125.12	125.38		24.048	1.202					2737	1.0033	0.0002	2.728	0.0029	2.6922	24.4	0.77124	0.002
13c	125.12	125.38		24.048	1.202					2737	1.0033	0.0002	2.7283	0.0031	2.6922	24.4	0.77124	0.002
14a	136.33	136.58	OPA (shaly)	29.373	1.469	29.511				3414	1.0041	0.0002	2.7194	0.0064	2.7289	24.4	0.77124	0.002
14b	136.33	136.58		29.373	1.469					3414	1.0041	0.0002	2.7331	0.0041	2.7289	24.4	0.77124	0.002
14c	136.33	136.58		29.373	1.469					3414	1.0041	0.0002	2.7305	0.0036	2.7289	24.4	0.77124	0.002
15a	141.1	141.38		31.661	1.583					3703	1.0044	0.0002	2.8892	0.0082	2.625	24.4	0.77124	0.002
15b	141.1	141.38		31.661	1.583					3703	1.0044	0.0002	2.9108	0.0034	2.625	24.4	0.77124	0.002
16a	155.1	155.72		34.286	1.714		36.406	1.820	32.109	6106	1.0072	0.0002	2.6764	0.012	2.677	24.4	0.77124	0.002
16b	155.1	155.72		34.286	1.714					6106	1.0072	0.0002	2.6811	0.0068	2.677	24.4	0.77124	0.002
16c	155.1	155.72		34.286	1.714					6106	1.0072	0.0002	2.6971	0.0065	2.677	24.4	0.77124	0.002
17a	164.3	164.58		32.360	1.618	32.225				7295	1.0086	0.0002	2.6862	0.0055	2.6793	24.4	0.77124	0.002
17b	164.3	164.58		32.360	1.618					7295	1.0086	0.0002	2.6919	0.0059	2.6793	24.4	0.77124	0.002
17c	164.3	164.58		32.360	1.618					7295	1.0086	0.0002	2.6909	0.0067	2.6793	24.4	0.77124	0.002
18a	176.48	176.73	OPA (sandy)	16.428	0.821	16.026	15.281	0.764	13.790	8897	1.0106	0.0002	2.7054	0.0031	2.6846	24.4	0.77124	0.002
18b	176.48	176.73		16.428	0.821					8897	1.0106	0.0002	2.7121	0.0021	2.6846	24.4	0.77124	0.002
18c	176.48	176.73		16.428	0.821					8897	1.0106	0.0002	2.7107	0.0009	2.6846	24.4	0.77124	0.002
19a	185.97	186.19	OPA (carb.-rich)	15.008	0.750		14.383	0.719	13.209	8652	1.0103	0.0002	2.7152	0.002	2.7194	24.4	0.77124	0.002
19b	185.97	186.19		15.008	0.750					8652	1.0103	0.0002	2.7108	0.0018	2.7194	24.4	0.77124	0.002
19c	185.97	186.19		15.008	0.750					8652	1.0103	0.0002	2.7286	0.0031	2.7194	24.4	0.77124	0.002
20a	196.08	196.35	OPA (shaly)	32.997	1.650	34.306				10508	1.0125	0.0002	2.6956	0.0059	2.7173	24.4	0.77124	0.002
20b	196.08	196.35		32.997	1.650					10508	1.0125	0.0002	2.6947	0.005	2.7173	24.4	0.77124	0.002
20c	196.08	196.35		32.997	1.650					10508	1.0125	0.0002	2.697	0.0033	2.7173	24.4	0.77124	0.002
21a	204.73	204.98		35.660	1.783					12089	1.0144	0.0002	2.716	0.0044	2.725	24.4	0.77124	0.002
21b	204.73	204.98		35.660	1.783					12089	1.0144	0.0002	2.7427	0.0048	2.725	24.4	0.77124	0.002
21c	204.73	204.98		35.660	1.783					12089	1.0144	0.0002	2.7173	0.0037	2.725	24.4	0.77124	0.002
22a	213.23	213.48		35.093	1.755		36.225	1.811	33.665	11100	1.0131	0.0002	2.7535	0.0056	2.728	24.4	0.77124	0.002
22b	213.23	213.48		35.093	1.755					11100	1.0131	0.0002	2.7206	0.0109	2.728	24.4	0.77124	0.002
22c	213.23	213.48		35.093	1.755					11100	1.0131	0.0002	2.7121	0.0122	2.728	24.4	0.77124	0.002
23a	224.48	224.73		32.211	1.611					12462	1.0147	0.0002	2.7132	0.0044	2.7458	24.4	0.77124	0.002
23b	224.48	224.73		32.211	1.611					12462	1.0147	0.0002	2.7035	0.0069	2.7458	24.4	0.77124	0.002
23c	224.48	224.73		32.211	1.611					12462	1.0147	0.0002	2.7075	0.0045	2.7458	24.4	0.77124	0.002
25a	225.45	225.63		31.120	1.556		31.120	1.556	30.600	14446	1.0172	0.0002	2.6931	0.0064		22.5	0.77305	0.002
25b	225.45	225.63		31.120	1.556					14446	1.0172	0.0002	2.6699	0.0152		22.5	0.77305	0.002
25c	225.45	225.63		31.120	1.556					14446	1.0172	0.0002	2.7857	0.0134		22.5	0.77305	0.002
26a	230.6	230.75		29.372	1.469		29.372	1.469	30.020	13539	1.0159	0.0002	2.6784	0.0105		22.5	0.77305	0.002
26b	230.6	230.75		29.372	1.469					13539	1.0159	0.0002	2.6876	0.0082		22.5	0.77305	0.002
26c	230.6	230.75		29.372	1.469					13539	1.0159	0.0002	2.6618	0.0129		22.5	0.77305	0.002
24a	235.41	235.66		32.193	1.610					12681	1.0146	0.0002	2.6972	0.0057	2.7093	24.4	0.77124	0.002
24b	235.41	235.66		32.193	1.610					12681	1.0146	0.0002	2.7034	0.0089	2.7093	24.4	0.77124	0.002
24c	235.41	235.66		32.193	1.610					12681	1.0146	0.0002	2.6947	0.0028	2.7093	24.4	0.77124	0.002
27a	238.15	238.25	Staffelegg Formation (marly limestone)	11.467	0.573		11.467	0.573	10.982	12210	1.0139	0.0002	2.7251	0.0035		22.5	0.77305	0.002
27b	238.15	238.25		11.467	0.573					12210	1.0139	0.0002	2.7313	0.0054		22.5	0.77305	0.002
27c	238.15	238.25		11.467	0.573					12210	1.0139	0.0002	2.5656	0.0026		22.5	0.77305	0.002
28a	241.8	241.9		21.189	1.059		21.189	1.059	20.540	12142	1.0136	0.0002	2.7364	0.005		22.5	0.77305	0.002
28b	241.8	241.9		21.189	1.059					12142	1.0136	0.0002	2.7277	0.0072		22.5	0.77305	0.002
28c	241.8	241.9		21.189	1.059					12142	1.0136	0.0002	2.7137			22.5	0.77305	0.002
29a	243.9	244		9.102	0.455		9.102	0.455	12.438	12103	1.0134	0.0002	2.3606	0.0097		22.5	0.77305	0.002
29b	243.9	244		9.102	0.455					12103	1.0134	0.0002	2.43	0.0096		22.5	0.77305	0.002
29c	243.9	244		9.102	0.455					12103	1.0134	0.0002	2.3416	0.0179		22.5	0.77305	0.002

Sample ID	min. distance (m)	max. distance (m)	Formation	M_{tot} (g)	sM_{tot} (g)	M_{cupel} (g)	W_a (g)	sW_a (g)	W_p (g)	sW_p (g)	r_h (g/cm³)	sr_h (g/cm³)	V_{total} (cm³)	sV_{total} (cm³)	Mt_x (g)	σMt (g)
1a	5.8	6	Hauptrogenstein (carbonates)	25.605	0.002	1.1777	25.708	0.002	18.141	0.050	2.623	0.030	9.803	0.111	25.0951	0.002
1b	5.8	6		66.076	0.002	1.1737	66.236	0.002	46.729	0.050	2.621	0.019	25.272	0.180	64.6980	0.002
1c	5.8	6		56.447	0.002	1.1722	56.523	0.002	39.806	0.050	2.610	0.020	21.657	0.167	54.9310	0.002
2a	14.84	15.1		59.938	0.002	1.1806	60.153	0.002	42.577	0.050	2.642	0.020	22.770	0.170	59.4270	0.002
2b	14.84	15.1		71.982	0.002	1.1861	72.149	0.002	51.309	0.050	2.672	0.018	26.998	0.185	71.3724	0.002
2c	14.84	15.1		66.066	0.002	1.1756	66.248	0.002	46.986	0.050	2.655	0.019	24.954	0.178	65.5529	0.002
3a	24.98	25.3		59.300	0.002	1.1783	59.455	0.002	42.302	0.050	2.675	0.020	22.222	0.167	58.9876	0.002
3b	24.98	25.3		46.696	0.002	1.1766	46.877	0.002	33.278	0.050	2.661	0.022	17.618	0.148	46.4541	0.002
3c	24.98	25.3		68.735	0.002	1.1704	68.958	0.002	48.915	0.050	2.656	0.020	25.966	0.181	68.2972	0.002
4a	35.35	35.58		52.276	0.002	1.1712	52.471	0.002	37.298	0.050	2.669	0.021	19.656	0.157	51.8771	0.002
4b	35.35	35.58		68.459	0.002	1.1888	68.739	0.002	48.742	0.050	2.653	0.019	25.906	0.181	67.7658	0.002
4c	35.35	35.58		45.929	0.002	1.1888	46.071	0.002	32.749	0.050	2.670	0.023	17.258	0.147	45.5549	0.002
5a	42.28	42.52	Passwang Formation (marl and limestone)	49.003	0.002	1.1738	49.169	0.002	33.847	0.050	2.477	0.020	19.850	0.164	46.6764	0.002
5b	42.28	42.52		40.717	0.002	1.1742	40.824	0.002	28.099	0.050	2.477	0.022	16.484	0.149	38.7126	0.002
5c	42.28	42.52		38.363	0.002	1.1689	38.509	0.002	26.497	0.050	2.475	0.023	15.562	0.144	36.5544	0.002
6a	61.75	62.08		55.389	0.002	1.1626	55.431	0.002	38.692	0.050	2.556	0.020	21.685	0.168	53.1137	0.002
6b	61.75	62.08		56.178	0.002	1.1805	56.318	0.002	39.217	0.050	2.542	0.020	22.154	0.171	53.7199	0.002
6c	61.75	62.08		58.329	0.002	1.1891	58.404	0.002	40.857	0.050	2.569	0.020	22.732	0.172	56.1107	0.002
7a	69.76	70.03		48.702	0.002	1.1769	48.821	0.002	34.296	0.050	2.595	0.021	18.816	0.155	47.3685	0.002
7b	69.76	70.03		56.867	0.002	1.1820	57.118	0.002	39.984	0.050	2.573	0.020	22.197	0.170	55.2535	0.002
7c	69.76	70.03		48.142	0.002	1.1677	48.283	0.002	33.808	0.050	2.575	0.021	18.752	0.156	46.8994	0.002
8a	74.78	75.03		55.260	0.002	1.1694	55.400	0.002	38.392	0.050	2.514	0.020	22.034	0.171	52.8837	0.002
8b	74.78	75.03		54.013	0.002	1.1752	54.234	0.002	37.494	0.050	2.501	0.020	21.686	0.170	51.5832	0.002
8c	74.78	75.03		50.430	0.002	1.1849	50.555	0.002	35.254	0.050	2.551	0.021	19.821	0.161	48.6192	0.002
9a	84.73	84.98		53.087	0.002	1.1845	53.337	0.002	36.812	0.050	2.492	0.020	21.407	0.170	50.3686	0.002
9b	84.73	84.98		43.812	0.002	1.1809	44.036	0.002	30.416	0.050	2.496	0.022	17.644	0.153	41.5881	0.002
9c	84.73	84.98		53.393	0.002	1.1735	53.651	0.002	37.067	0.050	2.497	0.020	21.484	0.170	50.6933	0.002
10a	96.7	96.9		58.637	0.002	1.1720	58.780	0.002	41.044	0.050	2.558	0.019	22.978	0.174	56.0124	0.002
10b	96.7	96.9		53.429	0.002	1.1766	53.564	0.002	37.269	0.050	2.537	0.020	21.109	0.167	50.6524	0.002
10c	96.7	96.9		52.729	0.002	1.1699	52.908	0.002	36.824	0.050	2.539	0.020	20.836	0.166	50.1903	0.002
11b	107	107.24	OPA (sandy)	42.112	0.002	1.1676	42.233	0.002	29.125	0.050	2.487	0.022	16.982	0.151	39.9149	0.002
11c	107	107.24		50.412	0.002	1.1653	50.540	0.002	34.908	0.050	2.496	0.020	20.250	0.165	47.8939	0.002
12a	116.24	116.54		54.155	0.002	1.1775	54.260	0.002	37.516	0.050	2.497	0.020	21.731	0.171	51.9217	0.002
12b	116.24	116.54		40.143	0.002	1.1704	40.281	0.002	27.769	0.050	2.481	0.023	16.237	0.147	38.3070	0.002
12c	116.24	116.54		50.706	0.002	1.1789	50.826	0.002	35.043	0.050	2.481	0.020	20.484	0.166	48.3125	0.002
13a	125.12	125.38		60.007	0.002	1.1665	60.115	0.002	41.560	0.050	2.496	0.019	24.081	0.180	57.0332	0.002
13b	125.12	125.38		63.235	0.002	1.1833	63.333	0.002	44.080	0.050	2.535	0.020	24.987	0.182	60.6344	0.002
13c	125.12	125.38		58.815	0.002	1.1795	58.957	0.002	40.786	0.050	2.500	0.019	23.583	0.178	55.9791	0.002
14a	136.33	136.58	OPA (shaly)	48.345	0.002	1.1797	48.399	0.002	33.253	0.050	2.462	0.020	19.656	0.163	45.4383	0.002
14b	136.33	136.58		38.451	0.002	1.1879	38.492	0.002	26.652	0.050	2.505	0.023	15.365	0.143	36.5880	0.002
14c	136.33	136.58		50.486	0.002	1.1847	50.572	0.002	34.984	0.050	2.500	0.020	20.230	0.165	47.9177	0.002
15a	141.1	141.38		53.201	0.002	1.1830	53.310	0.002	37.591	0.050	2.613	0.021	20.399	0.162	50.5401	0.002
15b	141.1	141.38		55.836	0.002	1.1787	56.180	0.002	39.661	0.050	2.620	0.020	21.439	0.166	53.2559	0.002
16a	155.1	155.72		34.236	0.002	1.1943	34.352	0.002	23.610	0.050	2.464	0.024	13.942	0.137	32.4388	0.002
16b	155.1	155.72		43.006	0.002	1.1882	43.096	0.002	29.549	0.050	2.451	0.022	17.580	0.155	40.5843	0.002
16c	155.1	155.72		43.708	0.002	1.1759	43.761	0.002	30.069	0.050	2.463	0.021	17.769	0.155	41.2802	0.002
17a	164.3	164.58	OPA (sandy)	51.664	0.002	1.1681	51.770	0.002	35.515	0.050	2.454	0.020	21.096	0.170	48.7970	0.002
17b	164.3	164.58		61.673	0.002	1.1721	61.906	0.002	42.506	0.050	2.459	0.018	25.177	0.186	58.4103	0.002
17c	164.3	164.58		54.085	0.002	1.1922	54.199	0.002	37.177	0.050	2.454	0.020	22.090	0.174	51.0819	0.002
18a	176.48	176.73		49.331	0.002	1.1624	49.544	0.002	34.421	0.050	2.524	0.021	19.627	0.161	47.6149	0.002
18b	176.48	176.73		56.923	0.002	1.1676	57.119	0.002	39.877	0.050	2.553	0.020	22.376	0.172	55.1475	0.002
18c	176.48	176.73		60.793	0.002	1.1833	61.015	0.002	42.460	0.050	2.534	0.019	24.081	0.179	58.6631	0.002
19a	185.97	186.19	OPA (carb.-rich)	44.322	0.002	1.1787	44.554	0.002	30.874	0.050	2.510	0.022	17.754	0.154	42.6693	0.002
19b	185.97	186.19		47.673	0.002	1.1900	47.894	0.002	33.065	0.050	2.489	0.021	19.244	0.161	45.6227	0.002
19c	185.97	186.19		47.297	0.002	1.1677	47.531	0.002	32.837	0.050	2.493	0.021	19.069	0.160	45.2821	0.002
20a	196.08	196.35	OPA (shaly)	45.712	0.002	1.1745	45.761	0.002	31.521	0.050	2.476	0.021	18.481	0.158	43.1999	0.002
20b	196.08	196.35		37.888	0.002	1.1765	37.958	0.002	26.111	0.050	2.469	0.021	15.375	0.144	35.7574	0.002
20c	196.08	196.35		40.764	0.002	1.1678	40.817	0.002	28.107	0.050	2.475	0.022	16.495	0.149	38.4709	0.002
21a	204.73	204.98		43.395	0.002	1.1904	43.419	0.002	29.889	0.050	2.473	0.022	17.559	0.154	40.8615	0.002
21b	204.73	204.98		27.950	0.002	1.1857	27.977	0.002	19.335	0.050	2.495	0.027	11.215	0.122	26.3471	0.002
21c	204.73	204.98		25.946	0.002	1.1789	25.978	0.002	17.949	0.050	2.493	0.028	10.420	0.117	24.6037	0.002
22a	213.23	213.48		33.139	0.002	1.1638	33.200	0.002	22.849	0.050	2.472	0.025	13.433	0.134	31.2630	0.002
22b	213.23	213.48		46.482	0.002	1.1648	46.530	0.002	32.074	0.050	2.480	0.020	18.762	0.159	43.8513	0.002
22c	213.23	213.48		44.040	0.002	1.1656	44.069	0.002	30.233	0.050	2.454	0.021	17.957	0.156	41.5572	0.002
23a	224.48	224.73		40.446	0.002	1.1659	40.507	0.002	27.971	0.050	2.490	0.023	16.269	0.147	38.3132	0.002
23b	224.48	224.73		20.577	0.002	1.1864	20.618	0.002	14.242	0.050	2.492	0.031	8.274	0.104	19.5102	0.002
23c	224.48	224.73		23.144	0.002	1.1756	23.178	0.002	16.022	0.050	2.496	0.030	9.286	0.111	21.9345	0.002
25a	225.45	225.63		39.993	0.002	1.1911	40.089	0.002	27.701	0.050	2.499	0.023	16.040	0.146	38.3874	0.002
25b	225.45	225.63		36.119	0.002	1.1703	36.210	0.002	24.970	0.050	2.488	0.024	14.554	0.139	34.6084	0.002
25c	225.45	225.63		35.056		1.1827	35.155	0.002	24.249	0.050	2.490	0.024	14.120	0.137	33.5578	0.002
26a	230.6	230.75		46.190	0.002	1.1854	46.348	0.002	31.772	0.050	2.456	0.020	18.872	0.160	44.3127	0.002
26b	230.6	230.75		32.470	0.002	1.1765	32.609	0.002	22.377	0.050	2.462	0.025	13.247	0.133	31.1671	0.002
26c	230.6	230.75		28.381		1.1786	28.474	0.002	19.545	0.050	2.463	0.026	11.561	0.124	27.2274	0.002
24a	235.41	235.66		35.725	0.002	1.1728	35.808	0.002	24.688	0.050	2.481	0.024	14.432	0.139	33.8286	0.002
24b	235.41	235.66		38.006	0.002	1.1682	38.105	0.002	26.195	0.050	2.465	0.023	15.456	0.144	35.9067	0.002
24c	235.41	235.66		47.563	0.002	1.1800	47.601	0.002	32.769	0.050	2.473	0.021	19.249	0.161	44.9206	0.002
27a	238.15	238.25	Staffelegg Formation (marly limestone)	42.957	0.002	1.1815	43.148	0.002	30.304	0.050	2.595	0.023	16.630	0.146	42.3509	0.002
27b	238.15	238.25		21.479	0.002	1.1874	21.614	0.002	15.165	0.050	2.589	0.032	8.349	0.103	21.1807	0.002
27c	238.15	238.25		54.904	0.002	1.1840	55.133	0.002	38.727	0.050	2.596	0.020	21.242	0.165	54.0974	0.002
28a	241.8	241.9		32.173	0.002	1.1858	32.427	0.002	22.372	0.050	2.491	0.025	13.018	0.131	31.1807	0.002
28b	241.8	241.9		31.445	0.002	1.1894	31.615	0.002	21.934	0.050	2.522	0.026	12.535	0.128	30.6494	0.002
28c	241.8	241.9		54.902	0.002	1.1886	55.211	0.002	37.818	0.050	2.452	0.019	22.519	0.175	53.1551	0.002
29a	243.9	244		26.269	0.002	1.1734	26.480	0.002	16.982	0.050	2.153	0.022	12.296	0.137	25.5599	0.002
29b	243.9	244		36.522	0.002	1.1894	36.828	0.002	24.014	0.050	2.220	0.021	16.591	0.157	35.5972	0.002
29c	243.9	244		35.383	0.002	1.1753	35.633	0.002	22.810	0.050	2.146	0.021	16.600	0.160	34.4492	0.002

Calculated parameters

Sample ID	min distance (m)	max distance (m)	Formation	WC$_{dry,105°}$ (DS)	σWC$_{dry,105°}$ (DS)	V$_w$ (cm³)	σV$_w$ (cm³)	V$_s$ (cm³)	σV$_s$ (cm³)	V$_{pores}$ (cm³)	σV$_{pores}$ (cm³)	S (DS)	σS (DS)	r$_d$ (g/cm3)	σr$_d$ (g/cm3)	n$_{tot}$ (DS)	σn$_{tot}$ (DS)	WC$_{wet,25°}$ (DS)	σWC$_{wet,25°}$ (DS)	WC$_{wet,25°}$ full sat (DS)	q (DS)	σq (DS)	b (m)	σb (m)
1a	5.8	6	Hauptrogenstein (carbonates)	0.020	0.000114	0.510	0.0028	9.101	0.00861	0.70	0.11	0.727	0.115	2.560	0.029	0.072	0.0114	1.99%	1.09E-04	2.72%	0.052	0.0117		
1b	5.8	6		0.021	0.000044	1.378	0.0028	23.642	0.01212	1.63	0.18	0.845	0.094	2.560	0.018	0.065	0.0072	2.09%	4.24E-05	2.46%	0.055	0.0085		
1c	5.8	6		0.028	0.000052	1.516	0.0028	19.976	0.00875	1.68	0.17	0.902	0.090	2.536	0.020	0.078	0.0077	2.69%	4.94E-05	2.97%	0.070	0.0098		
2a	14.84	15.1		0.009	0.000048	0.511	0.0028	22.063	0.01885	0.71	0.17	0.724	0.175	2.610	0.019	0.031	0.0075	0.85%	4.70E-05	1.17%	0.022	0.0077		
2b	14.84	15.1		0.009	0.000040	0.610	0.0028	26.428	0.01470	0.57	0.19	1.070	0.348	2.644	0.018	0.021	0.0069	0.85%	3.91E-05	0.79%	0.023	0.0104		
2c	14.84	15.1		0.008	0.000043	0.513	0.0028	24.248	0.02244	0.71	0.18	0.727	0.185	2.627	0.018	0.028	0.0072	0.78%	4.26E-05	1.06%	0.021	0.0074		
3a	24.98	25.3		0.005	0.000048	0.312	0.0028	21.810	0.01615	0.41	0.17	0.758	0.308	2.654	0.020	0.019	0.0075	0.53%	4.76E-05	0.69%	0.014	0.0081		
3b	24.98	25.3		0.005	0.000061	0.242	0.0028	17.206	0.02487	0.41	0.15	0.588	0.215	2.637	0.022	0.023	0.0085	0.52%	6.04E-05	0.88%	0.014	0.0071		
3c	24.98	25.3		0.006	0.000042	0.437	0.0028	25.301	0.02157	0.67	0.18	0.657	0.181	2.630	0.021	0.026	0.0070	0.64%	4.10E-05	0.96%	0.017	0.0065		
4a	35.35	35.58		0.008	0.000055	0.399	0.0028	18.974	0.02014	0.68	0.16	0.584	0.135	2.639	0.021	0.035	0.0080	0.76%	5.39E-05	1.30%	0.020	0.0066		
4b	35.35	35.58		0.010	0.000042	0.693	0.0028	24.828	0.01366	1.08	0.13	0.643	0.109	2.616	0.018	0.042	0.0070	1.01%	4.11E-05	1.57%	0.027	0.0064		
4c	35.35	35.58		0.008	0.000062	0.374	0.0028	16.677	0.01223	0.58	0.15	0.644	0.163	2.640	0.022	0.034	0.0085	0.81%	6.13E-05	1.26%	0.022	0.0078		
5a	42.28	42.52	Passwang Formation (marl and limestone)	0.050	0.000062	2.326	0.0029	17.196	0.04879	2.65	0.17	0.877	0.062	2.351	0.019	0.134	0.0087	4.75%	5.64E-05	5.38%	0.117	0.0107	2.66E-09	1.02E-09
5b	42.28	42.52		0.052	0.000075	2.005	0.0029	14.250	0.03568	2.23	0.17	0.897	0.061	2.349	0.021	0.136	0.0094	4.92%	6.78E-05	5.46%	0.122	0.0118	2.70E-09	1.02E-09
5c	42.28	42.52		0.049	0.000079	1.808	0.0029	13.424	0.04142	2.14	0.15	0.846	0.059	2.349	0.022	0.137	0.0097	4.71%	7.20E-05	5.52%	0.116	0.0116	2.74E-09	1.02E-09
6a	61.75	62.08		0.043	0.000054	2.275	0.0029	19.311	0.02458	2.37	0.17	0.958	0.069	2.449	0.019	0.110	0.0079	4.11%	5.00E-05	4.28%	0.105	0.0107	1.55E-09	7.21E-10
6b	61.75	62.08		0.046	0.000054	2.458	0.0029	19.445	0.02254	2.71	0.17	0.908	0.058	2.425	0.019	0.122	0.0078	4.38%	4.93E-05	4.80%	0.111	0.0100	1.75E-09	7.28E-10
6c	61.75	62.08		0.040	0.000051	2.218	0.0029	20.300	0.01837	2.43	0.17	0.912	0.065	2.468	0.019	0.107	0.0077	3.80%	4.76E-05	4.15%	0.099	0.0099	1.51E-09	7.15E-10
7a	69.76	70.03		0.028	0.000061	1.333	0.0028	17.285	0.01264	1.53	0.16	0.870	0.091	2.517	0.021	0.081	0.0083	2.74%	5.73E-05	3.13%	0.071	0.0102	3.80E-09	2.37E-09
7b	69.76	70.03		0.029	0.000052	1.613	0.0028	20.215	0.00891	1.98	0.17	0.814	0.070	2.489	0.019	0.089	0.0077	2.84%	4.90E-05	3.46%	0.073	0.0088	4.21E-09	2.39E-09
7c	69.76	70.03		0.026	0.000061	1.242	0.0028	17.191	0.01011	1.56	0.16	0.796	0.080	2.501	0.020	0.083	0.0084	2.58%	5.80E-05	3.22%	0.066	0.0094	3.91E-09	2.39E-09
8a	74.78	75.03		0.045	0.000055	2.376	0.0029	19.362	0.01986	2.67	0.17	0.889	0.057	2.400	0.019	0.121	0.0079	4.30%	5.01E-05	4.81%	0.108	0.0099	3.89E-09	1.63E-09
8b	74.78	75.03		0.047	0.000056	2.429	0.0029	18.894	0.01593	2.79	0.17	0.870	0.053	2.379	0.019	0.129	0.0080	4.50%	5.12E-05	5.14%	0.112	0.0097	4.17E-09	1.60E-09
8c	74.78	75.03		0.037	0.000059	1.811	0.0029	17.810	0.01372	2.01	0.16	0.900	0.072	2.453	0.020	0.101	0.0082	3.59%	5.51E-05	3.97%	0.091	0.0104	3.19E-09	1.60E-09
9a	84.73	84.98		0.054	0.000058	2.717	0.0029	18.335	0.03671	3.07	0.17	0.884	0.050	2.353	0.019	0.144	0.0082	5.12%	5.19E-05	5.75%	0.127	0.0102	2.65E-09	9.39E-10
9b	84.73	84.98		0.053	0.000070	2.222	0.0029	15.067	0.03221	2.58	0.16	0.862	0.052	2.357	0.020	0.146	0.0090	5.08%	6.29E-05	5.84%	0.126	0.0109	2.69E-09	9.41E-10
9c	84.73	84.98		0.053	0.000057	2.698	0.0029	18.408	0.00540	3.08	0.17	0.877	0.048	2.360	0.019	0.143	0.0090	5.06%	5.17E-05	5.72%	0.126	0.0098	2.63E-09	9.35E-10
10a	96.7	96.9		0.047	0.000052	2.622	0.0029	20.065	0.03020	2.91	0.18	0.900	0.054	2.438	0.018	0.127	0.0077	4.48%	4.72E-05	4.95%	0.114	0.0098	5.18E-09	2.07E-09
10b	96.7	96.9		0.055	0.000057	2.774	0.0029	18.079	0.02066	3.03	0.17	0.916	0.052	2.400	0.019	0.144	0.0080	5.20%	5.16E-05	5.65%	0.131	0.0104	5.95E-09	2.11E-09
10c	96.7	96.9		0.051	0.000058	2.537	0.0029	17.994	0.01614	2.84	0.17	0.893	0.052	2.409	0.019	0.136	0.0081	4.82%	5.24E-05	5.36%	0.122	0.0101	5.64E-09	2.10E-09
11b	107	107.24	OPA (sandy)	0.055	0.000073	2.193	0.0029	14.668	0.01672	2.31	0.15	0.948	0.062	2.350	0.021	0.136	0.0090	5.22%	6.54E-05	5.49%	0.129	0.0120	2.03E-09	7.63E-10
11c	107	107.24		0.053	0.000061	2.513	0.0029	17.511	0.02562	2.74	0.17	0.917	0.056	2.365	0.020	0.135	0.0083	4.99%	5.47E-05	5.42%	0.124	0.0107	2.01E-09	7.56E-10
12a	116.24	116.54		0.043	0.000056	2.227	0.0029	19.284	0.01557	2.45	0.17	0.910	0.064	2.389	0.019	0.113	0.0079	4.12%	5.12E-05	4.51%	0.102	0.0102	1.87E-09	8.43E-10
12b	116.24	116.54		0.048	0.000076	1.831	0.0029	14.168	0.01731	2.07	0.15	0.885	0.064	2.359	0.021	0.127	0.0092	4.57%	6.89E-05	5.14%	0.113	0.0115	2.14E-09	8.59E-10
12c	116.24	116.54		0.050	0.000060	2.387	0.0029	17.901	0.01792	2.58	0.17	0.924	0.060	2.359	0.019	0.126	0.0082	4.72%	5.45E-05	5.09%	0.117	0.0107	2.12E-09	8.56E-10
13a	125.12	125.38		0.052	0.000051	2.964	0.0029	20.959	0.02543	3.12	0.18	0.949	0.055	2.368	0.018	0.130	0.0076	4.96%	4.60E-05	5.21%	0.123	0.0102	2.28E-09	8.91E-10
13b	125.12	125.38		0.043	0.000048	2.592	0.0029	22.227	0.02364	2.76	0.18	0.939	0.050	2.427	0.018	0.110	0.0074	4.11%	4.38E-05	4.37%	0.101	0.0098	1.89E-09	8.69E-10
13c	125.12	125.38		0.051	0.000052	2.827	0.0029	20.518	0.02332	3.07	0.18	0.922	0.054	2.374	0.018	0.130	0.0077	4.82%	4.69E-05	5.21%	0.120	0.0100	2.28E-09	8.90E-10
14a	136.33	136.58	OPA (shaly)	0.064	0.000064	2.895	0.0029	16.709	0.03933	2.95	0.17	0.982	0.056	2.312	0.019	0.150	0.0086	6.01%	5.68E-05	6.11%	0.147	0.0119	2.21E-09	7.52E-10
14b	136.33	136.58		0.051	0.000079	1.856	0.0028	13.387	0.02010	1.98	0.14	0.938	0.068	2.381	0.022	0.129	0.0095	4.85%	7.18E-05	5.15%	0.121	0.0125	1.84E-09	7.32E-10
14c	136.33	136.58		0.054	0.000061	2.558	0.0029	17.549	0.02315	2.68	0.17	0.954	0.059	2.369	0.019	0.133	0.0083	5.09%	5.46E-05	5.32%	0.126	0.0111	1.90E-09	7.32E-10
15a	141.1	141.38		0.053	0.000057	2.649	0.0029	17.493	0.04965	2.91	0.17	0.911	0.055	2.478	0.020	0.142	0.0084	5.00%	5.19E-05	5.46%	0.130	0.0107	1.82E-09	6.50E-10
15b	141.1	141.38		0.048	0.000054	2.568	0.0029	18.296	0.02138	3.14	0.17	0.817	0.043	2.484	0.019	0.147	0.0090	4.62%	4.95E-05	5.60%	0.120	0.0090	1.86E-09	6.47E-10
16a	155.1	155.72		0.055	0.000090	1.784	0.0028	12.120	0.05435	1.82	0.15	0.980	0.079	2.327	0.023	0.131	0.0106	5.25%	8.05E-05	5.35%	0.128	0.0147	1.64E-09	6.48E-10
16b	155.1	155.72		0.060	0.000072	2.405	0.0028	15.137	0.03840	2.44	0.16	0.984	0.064	2.309	0.020	0.139	0.0091	5.63%	6.39E-05	5.72%	0.137	0.0127	1.76E-09	6.47E-10
16c	155.1	155.72		0.059	0.000071	2.410	0.0028	15.305	0.03689	2.46	0.16	0.978	0.063	2.323	0.020	0.139	0.0091	5.55%	6.29E-05	5.67%	0.136	0.0125	1.74E-09	6.42E-10
17a	164.3	164.58		0.059	0.000060	2.843	0.0029	18.166	0.03720	2.93	0.17	0.970	0.054	2.313	0.019	0.139	0.0083	5.55%	5.32E-05	5.71%	0.135	0.0113	1.86E-09	6.81E-10
17b	164.3	164.58		0.056	0.000050	3.235	0.0029	21.699	0.04756	3.48	0.19	0.930	0.051	2.320	0.017	0.138	0.0077	5.29%	4.47E-05	5.67%	0.129	0.0101	1.84E-09	6.77E-10
17c	164.3	164.58		0.059	0.000057	2.978	0.0029	18.983	0.04727	3.11	0.17	0.958	0.056	2.312	0.019	0.141	0.0084	5.55%	5.09E-05	5.78%	0.135	0.0111	1.88E-09	6.81E-10
18a	176.48	176.73	OPA (sandy)	0.036	0.000060	1.698	0.0028	17.600	0.02018	2.03	0.16	0.838	0.067	2.426	0.020	0.103	0.0083	3.48%	5.63E-05	4.12%	0.087	0.0098	2.59E-09	1.28E-09
18b	176.48	176.73		0.032	0.000052	1.756	0.0028	20.334	0.01576	2.04	0.17	0.860	0.073	2.465	0.019	0.091	0.0077	3.12%	4.89E-05	3.61%	0.077	0.0094	2.53E-09	1.25E-09
18c	176.48	176.73		0.036	0.000049	2.107	0.0028	21.641	0.00722	2.44	0.18	0.864	0.065	2.436	0.018	0.101	0.0075	3.50%	4.57E-05	4.03%	0.088	0.0091	2.53E-09	1.27E-09
19a	185.97	186.19	OPA (carb.-rich)	0.039	0.000068	1.636	0.0028	15.715	0.01160	2.04	0.15	0.802	0.061	2.403	0.021	0.115	0.0087	3.73%	6.26E-05	4.61%	0.092	0.0099	3.18E-09	1.41E-09
19b	185.97	186.19		0.045	0.000063	2.030	0.0029	16.830	0.01120	2.41	0.16	0.841	0.054	2.371	0.020	0.125	0.0094	4.30%	5.81E-05	5.07%	0.105	0.0100	3.53E-09	1.43E-09
19c	185.97	186.19		0.044	0.000064	1.994	0.0028	16.595	0.01887	2.47	0.16	0.806	0.052	2.375	0.020	0.130	0.0085	4.26%	5.85E-05	5.23%	0.105	0.0097	3.64E-09	1.43E-09
20a	196.08	196.35	OPA (shaly)	0.058	0.000067	2.481	0.0028	16.026	0.03508	2.45	0.16	1.010	0.067	2.338	0.020	0.133	0.0088	5.49%	6.02E-05	5.44%	0.134	0.0126	1.72E-09	6.62E-10
20b	196.08	196.35		0.060	0.000081	2.104	0.0028	13.270	0.02463	2.11	0.15	0.999	0.068	2.326	0.022	0.137	0.0096	5.62%	7.26E-05	5.63%	0.137	0.0135	1.78E-09	6.68E-10
20c	196.08	196.35		0.060	0.000076	2.265	0.0028	14.264	0.01747	2.33	0.15	1.015	0.068	2.332	0.021	0.135	0.0092	5.63%	6.75E-05	5.55%	0.137	0.0131	1.76E-09	6.64E-10
21a	204.73	204.98		0.062	0.000071	2.497	0.0028	15.045	0.02438	2.51	0.16	0.993	0.062	2.327	0.020	0.143	0.0090	5.84%	6.33E-05	5.87%	0.142	0.0125	1.73E-09	6.16E-10
21b	204.73	204.98		0.061	0.000111	1.580	0.0028	9.606	0.01683	1.61	0.12	0.982	0.075	2.349	0.026	0.143	0.0111	5.73%	9.83E-05	5.83%	0.141	0.0153	1.71E-09	6.17E-10
21c	204.73	204.98		0.055	0.000118	1.323	0.0028	9.054	0.01235	1.37	0.12	0.969	0.084	2.361	0.027	0.131	0.0114	5.17%	1.06E-04	5.33%	0.127	0.0156	1.56E-09	6.14E-10
22a	213.23	213.48		0.060	0.000093	1.852	0.0029	11.354	0.02310	2.08	0.14	0.891	0.058	2.327	0.020	0.155	0.0102	5.66%	8.30E-05	6.31%	0.138	0.0124	1.89E-09	6.30E-10
22b	213.23	213.48		0.060	0.000066	2.597	0.0028	16.118	0.04686	2.64	0.17	0.982	0.064	2.337	0.020	0.141	0.0092	5.66%	5.92E-05	5.76%	0.138	0.0124	1.72E-09	6.25E-10
22c	213.23	213.48		0.060	0.000070	2.451	0.0028	15.323	0.06893	2.63	0.18	0.930	0.052	2.314	0.020	0.147	0.0092	5.64%	6.24E-05	6.03%	0.136	0.0126	1.81E-09	6.33E-10
23a	224.48	224.73		0.056	0.000076	2.102	0.0028	14.121	0.02291	2.15	0.15	0.978	0.068	2.355	0.021	0.132	0.0092	5.27%	6.81E-05	5.38%	0.129	0.0127	1.74E-09	6.74E-10
23b	224.48	224.73		0.055	0.000149	1.051	0.0028	7.217	0.01843	1.06	0.11	0.994	0.100	2.358	0.030	0.128	0.0129	5.18%	1.34E-04	5.21%	0.127	0.0181	1.68E-09	6.87E-10
23c	224.48	224.73		0.055	0.000133	1.192	0.0028	8.101	0.01349	1.18	0.11	1.006	0.095	2.362	0.028	0.128	0.0121	5.22%	1.19E-04	5.20%	0.128	0.0171	1.68E-09	6.82E-10
25a	225.45	225.63		0.042	0.000075	1.578	0.0028	14.254	0.03188	1.79	0.15	0.884	0.074	2.393	0.022	0.111	0.0094	4.01%	6.93E-05	4.52%	0.098	0.0117	1.50E-09	6.87E-10
25b	225.45	225.63		0.044	0.000084	1.485	0.0028	12.962	0.07380	1.59	0.15	0.933	0.092	2.378	0.023	0.109	0.0099	4.18%	7.67E-05	4.47%	0.104	0.0143	1.48E-09	7.00E-10
25c	225.45	225.63		0.045	0.000062	1.473	0.0020	12.046	0.05795	2.07	0.15	0.710	0.051	2.377	0.023	0.147	0.0106	4.27%	5.71E-05	5.91%	0.104	0.0106	1.99E-09	7.00E-10
26a	230.6	230.75		0.042	0.000065	1.848	0.0028	16.544	0.06486	2.33	0.17	0.794	0.059	2.348	0.020	0.123	0.0092	4.06%	6.00E-05	5.07%	0.098	0.0103	1.79E-09	7.43E-10
26b	230.6	230.75		0.042	0.000093	1.282	0.0028	11.597	0.03539	1.65	0.14	0.777	0.065	2.353	0.024	0.125	0.0105	4.01%	8.54E-05	5.10%	0.097	0.0115	1.80E-09	7.45E-10
26c	230.6	230.75		0.042	0.000077	1.135	0.0020	10.229	0.04958	1.33	0.13	0.852	0.086	2.355	0.025	0.115	0.0116	4.06%	7.05E-05	4.73%	0.098	0.0140	1.67E-09	7.51E-10
24a	235.41	235.66		0.056	0.000086	1.870	0.0028	12.542	0.02652	1.89	0.13	0.990	0.074	2.344	0.023	0.131	0.0099	5.31%	7.71E-05	5.36%	0.130	0.0138	1.74E-09	6.80E-10
24b	235.41	235.66		0.058	0.000081	2.069	0.0028	13.282	0.04373	2.17	0.15	0.952	0.066	2.323	0.022	0.141	0.0098	5.52%	7.24E-05	5.79%	0.134	0.0132	1.88E-09	6.87E-10
24c	235.41	235.66		0.059	0.000065	2.604	0.0028	16.670	0.01734	2.68	0.16	1.010	0.064	2.330	0.020	0.134	0.0085	5.56%	5.78E-05	5.50%	0.135	0.0121	1.86E-09	6.78E-10
27a	238.15	238.25	Staffelegg Formation (marly limestone)	0.014	0.000067	0.597	0.0028	15.541	0.01997	1.09	0.17	0.548	0.074	2.547	0.022	0.065	0.0089	1.41%	6.54E-05	2.54%	0.036	0.0069	2.24E-09	1.74E-09
27b	238.15	238.25		0.014	0.000134	0.294	0.0028	7.755	0.02158	0.59	0.10	0.494	0.087	2.547	0.031	0.071	0.0125	1.39%	1.31E-04	2.77%	0.035	0.0067	2.45E-09	1.78E-09
27c	238.15	238.25		0.015	0.000053	0.795	0.0028	21.086	0.02138	0.16	0.19	5.102	5.459	2.547	0.007	0.007	0.0089	1.47%	5.11E-05	0.29%	0.037	0.0566	5.21E-10	1.73E-09
28a	241.8	241.9		0.032	0.000092	0.979	0.0028	11.395	0.02083	1.62	0.13	0.603	0.049	2.395	0.024	0.125	0.0103	3.09%	8.66E-05	5.01%	0.075	0.0087	2.46E-09	1.01E-09
28b	241.8	241.9		0.026	0.000093	0.785	0.0028	11.336	0.02977	1.30	0.13	0.605	0.061	2.445	0.023	0.103	0.0102	2.53%	8.88E-05	4.12%	0.063	0.0090	2.00E-09	9.93E-10
28c	241.8	241.9		0.033	0.000054	1.724	0.0028	19.588	0.03610	2.93	0.18	0.588	0.036	2.360	0.018	0.130	0.0080	3.18%	5.07E-05	5.29%	0.077	0.0066	2.60E-09	1.02E-09
29a	243.9	244		0.028	0.000112	0.699	0.0028	10.828	0.04450	1.47	0.14	0.476	0.047	2.079	0.023	0.119	0.0118	2.70%	1.06E-04	5.50%	0.057	0.0079	6.31E-09	2.74E-09
29b	243.9	244		0.026	0.000080	0.912	0.0028	14.649	0.05788	1.94	0.17	0.470	0.041	2.146	0.020	0.117	0.0102	2.53%	7.65E-05	5.24%	0.055	0.0067	5.99E-09	2.64E-09
29c	243.9	244		0.027	0.000083	0.921	0.0028	14.712	0.11247	1.89	0.20	0.488	0.051	2.075	0.020	0.114	0.0118	2.64%	7.89E-05	5.26%	0.055	0.0082	6.02E-09	2.77E-09

Sample ID	min distance (m)	max distance (m)	Formation	k₂.₀ (m²)	σk2.0 (m²)	k₂.₀ mean (m²)	σk2.0mean (m²)	k₂.₅ (m²)	σk2.5 (m²)	k₂.₅ mean (m²)	σk2.5mean (m²)	k₃ (m²)	σk3 (m²)	k₃ mean (m²)	σk3mean (m²)
1a	5.8	6	Hauptrogenstein (carbonates)												
1b	5.8	6													
1c	5.8	6													
2a	14.84	15.1													
2b	14.84	15.1													
2c	14.84	15.1													
3a	24.98	25.3													
3b	24.98	25.3													
3c	24.98	25.3													
4a	35.35	35.58													
4b	35.35	35.58													
4c	35.35	35.58													
5a	42.28	42.52	Passwang Formation (marl and limestone)	4.22E-20	3.27E-20			1.54E-20	1.21E-20			5.65E-21	4.45E-21		
5b	42.28	42.52		4.47E-20	3.44E-20	4.47E-20	1.98E-20	1.65E-20	1.28E-20	1.65E-20	7.37E-21	6.06E-21	4.75E-21	6.06E-21	2.74E-21
5c	42.28	42.52		4.72E-20	3.59E-20			1.75E-20	1.34E-20			6.48E-21	5.04E-21		
6a	61.75	62.08		9.66E-21	9.07E-21			3.20E-21	3.02E-21			1.06E-21	1.01E-21		
6b	61.75	62.08		1.53E-20	1.29E-20	1.12E-20	5.94E-21	5.36E-21	4.53E-21	3.80E-21	2.03E-21	1.87E-21	1.60E-21	1.29E-21	6.98E-22
6c	61.75	62.08		8.67E-21	8.31E-21			2.83E-21	2.74E-21			9.27E-22	9.02E-22		
7a	69.76	70.03		3.19E-20	4.03E-20			9.09E-21	1.16E-20			2.59E-21	3.33E-21		
7b	69.76	70.03		4.72E-20	5.42E-20	3.81E-20	2.68E-20	1.41E-20	1.63E-20	1.11E-20	7.90E-21	4.21E-21	4.91E-21	3.25E-21	2.33E-21
7c	69.76	70.03		3.53E-20	4.37E-20			1.02E-20	1.27E-20			2.94E-21	3.70E-21		
8a	74.78	75.03		7.42E-20	6.30E-20			2.59E-20	2.21E-20			9.00E-21	7.75E-21		
8b	74.78	75.03		9.61E-20	7.68E-20	6.84E-20	3.51E-20	3.45E-20	2.77E-20	2.38E-20	1.24E-20	1.24E-20	1.00E-20	8.30E-21	4.40E-21
8c	74.78	75.03		3.49E-20	3.54E-20			1.11E-20	1.13E-20			3.54E-21	3.65E-21		
9a	84.73	84.98		4.80E-20	3.45E-20			1.82E-20	1.32E-20			6.90E-21	5.04E-21		
9b	84.73	84.98		5.14E-20	3.65E-20	4.89E-20	2.02E-20	1.96E-20	1.41E-20	1.86E-20	7.75E-21	7.51E-21	5.44E-21	7.06E-21	2.97E-21
9c	84.73	84.98		4.73E-20	3.40E-20			1.79E-20	1.30E-20			6.78E-21	4.95E-21		
10a	96.7	96.9		1.43E-19	1.16E-19			5.11E-20	4.17E-20			1.82E-20	1.49E-20		
10b	96.7	96.9		2.43E-19	1.75E-19	1.95E-19	8.58E-20	9.22E-20	6.67E-20	7.20E-20	3.20E-20	3.49E-20	2.55E-20	2.67E-20	1.20E-20
10c	96.7	96.9		1.97E-19	1.49E-19			7.28E-20	5.53E-20			2.69E-20	2.06E-20		
11b	107	107.24	OPA (sandy)	2.56E-20	1.95E-20			9.45E-21	7.26E-21			3.49E-21	2.71E-21		
11c	107	107.24		2.46E-20	1.87E-20	2.51E-20	1.35E-20	9.04E-21	6.94E-21	9.24E-21	5.02E-21	3.32E-21	2.58E-21	3.41E-21	1.87E-21
12a	116.24	116.54		1.48E-20	1.35E-20			4.95E-21	4.55E-21			1.66E-21	1.54E-21		
12b	116.24	116.54		2.48E-20	2.02E-20	2.11E-20	1.04E-20	8.86E-21	7.29E-21	7.42E-21	3.69E-21	3.16E-21	2.63E-21	2.61E-21	1.31E-21
12c	116.24	116.54		2.38E-20	1.95E-20			8.45E-21	6.96E-21			3.00E-21	2.49E-21		
13a	125.12	125.38		2.90E-20	2.30E-20			1.05E-20	8.33E-21			3.76E-21	3.02E-21		
13b	125.12	125.38		1.46E-20	1.35E-20	2.43E-20	1.18E-20	4.85E-21	4.52E-21	8.61E-21	4.22E-21	1.61E-21	1.51E-21	3.06E-21	1.52E-21
13c	125.12	125.38		2.92E-20	2.31E-20			1.05E-20	8.37E-21			3.79E-21	3.04E-21		
14a	136.33	136.58	OPA (shaly)	3.65E-20	2.52E-20			1.41E-20	9.85E-21			5.48E-21	3.85E-21		
14b	136.33	136.58		1.87E-20	1.51E-20	2.55E-20	1.13E-20	6.72E-21	5.48E-21	9.53E-21	4.27E-21	2.41E-21	1.99E-21	3.57E-21	1.62E-21
14c	136.33	136.58		2.12E-20	1.65E-20			7.73E-21	6.07E-21			2.82E-21	2.23E-21		
15a	141.1	141.38		2.23E-20	1.62E-20			8.43E-21	6.16E-21			3.18E-21	2.35E-21		
15b	141.1	141.38		2.49E-20	1.75E-20	2.36E-20	1.19E-20	9.53E-21	6.73E-21	8.98E-21	4.56E-21	3.65E-21	2.60E-21	3.42E-21	1.75E-21
16a	155.1	155.72		1.53E-20	1.23E-20			5.51E-21	4.50E-21			1.99E-21	1.65E-21		
16b	155.1	155.72		1.98E-20	1.48E-20	1.82E-20	8.05E-21	7.40E-21	5.58E-21	6.71E-21	3.00E-21	2.76E-21	2.10E-21	2.48E-21	1.12E-21
16c	155.1	155.72		1.94E-20	1.45E-20			7.23E-21	5.46E-21			2.69E-21	2.05E-21		
17a	164.3	164.58		2.22E-20	1.65E-20			8.26E-21	6.18E-21			3.08E-21	2.32E-21		
17b	164.3	164.58		2.15E-20	1.60E-20	2.23E-20	9.55E-21	8.01E-21	6.00E-21	8.33E-21	3.59E-21	2.98E-21	2.25E-21	3.11E-21	1.35E-21
17c	164.3	164.58		2.33E-20	1.71E-20			8.74E-21	6.46E-21			3.28E-21	2.44E-21		
18a	176.48	176.73	OPA (sandy)	2.39E-20	2.38E-20			7.67E-21	7.71E-21			2.46E-21	2.50E-21		
18b	176.48	176.73		1.41E-20	1.59E-20	2.00E-20	1.21E-20	4.26E-21	4.82E-21	6.30E-21	3.85E-21	1.29E-21	1.47E-21	1.99E-21	1.23E-21
18c	176.48	176.73		2.19E-20	2.22E-20			6.98E-21	7.10E-21			2.22E-21	2.28E-21		
19a	185.97	186.19	OPA (carb.-rich)	4.46E-20	4.01E-20			1.51E-20	1.37E-20			5.12E-21	4.69E-21		
19b	185.97	186.19		6.52E-20	5.37E-20	6.14E-20	2.98E-20	2.31E-20	1.91E-20	2.17E-20	1.06E-20	8.18E-21	6.84E-21	7.64E-21	3.80E-21
19c	185.97	186.19		7.43E-20	5.92E-20			2.68E-20	2.15E-20			9.64E-21	7.81E-21		
20a	196.08	196.35	OPA (shaly)	1.74E-20	1.36E-20			6.36E-21	5.00E-21			2.32E-21	1.84E-21		
20b	196.08	196.35		1.99E-20	1.52E-20	1.87E-20	8.33E-21	7.37E-21	5.66E-21	6.88E-21	3.09E-21	2.73E-21	2.12E-21	2.53E-21	1.15E-21
20c	196.08	196.35		1.88E-20	1.45E-20			6.92E-21	5.36E-21			2.55E-21	1.99E-21		
21a	204.73	204.98		2.03E-20	1.47E-20			7.70E-21	5.62E-21			2.91E-21	2.15E-21		
21b	204.73	204.98		2.01E-20	1.48E-20	1.81E-20	7.91E-21	7.62E-21	5.68E-21	6.78E-21	3.00E-21	2.89E-21	2.18E-21	2.54E-21	1.14E-21
21c	204.73	204.98		1.39E-20	1.12E-20			5.02E-21	4.11E-21			1.82E-21	1.51E-21		
22a	213.23	213.48		2.87E-20	1.94E-20			1.13E-20	7.73E-21			4.44E-21	3.08E-21		
22b	213.23	213.48		1.95E-20	1.44E-20	2.39E-20	9.81E-21	7.33E-21	5.47E-21	9.19E-21	3.82E-21	2.75E-21	2.07E-21	3.54E-21	1.49E-21
22c	213.23	213.48		2.34E-20	1.67E-20			8.96E-21	6.45E-21			3.43E-21	2.50E-21		
23a	224.48	224.73		1.76E-20	1.39E-20			6.40E-21	5.08E-21			2.32E-21	1.87E-21		
23b	224.48	224.73		1.54E-20	1.30E-20	1.61E-20	7.62E-21	5.51E-21	4.71E-21	5.79E-21	2.78E-21	1.97E-21	1.72E-21	2.08E-21	1.01E-21
23c	224.48	224.73		1.53E-20	1.28E-20			5.45E-21	4.62E-21			1.95E-21	1.68E-21		
25a	225.45	225.63		9.24E-21	8.63E-21			3.08E-21	2.91E-21			1.03E-21	9.81E-22		
25b	225.45	225.63		8.70E-21	8.42E-21	1.54E-20	7.90E-21	2.87E-21	2.82E-21	5.61E-21	2.96E-21	9.51E-22	9.44E-22	2.05E-21	1.12E-21
25c	225.45	225.63		2.83E-20	2.04E-20			1.09E-20	7.90E-21			4.16E-21	3.07E-21		
26a	230.6	230.75		1.62E-20	1.37E-20			5.69E-21	4.85E-21			2.00E-21	1.72E-21		
26b	230.6	230.75		1.68E-20	1.42E-20	1.51E-20	7.58E-21	5.93E-21	5.06E-21	5.26E-21	2.67E-21	2.09E-21	1.81E-21	1.84E-21	9.46E-22
26c	230.6	230.75		1.23E-20	1.13E-20			4.16E-21	3.90E-21			1.41E-21	1.34E-21		
24a	235.41	235.66		1.72E-20	1.37E-20			6.23E-21	5.02E-21			2.25E-21	1.84E-21		
24b	235.41	235.66		2.33E-20	1.73E-20	1.98E-20	8.85E-21	8.74E-21	6.57E-21	7.31E-21	3.29E-21	3.28E-21	2.49E-21	2.69E-21	1.23E-21
24c	235.41	235.66		1.90E-20	1.47E-20			6.96E-21	5.41E-21			2.55E-21	2.00E-21		
27a	238.15	238.25	Staffelegg Formation (marly limestone)	7.19E-21	1.13E-20			1.84E-21	2.93E-21			4.71E-22	7.57E-22		
27b	238.15	238.25		1.01E-20	1.52E-20	5.77E-21	6.31E-21	2.70E-21	4.11E-21	1.51E-21	1.68E-21	7.21E-22	1.12E-21	3.97E-22	4.49E-22
27c	238.15	238.25		1.13E-24	1.58E-23			9.70E-26	1.36E-24			8.31E-27	1.18E-25		
28a	241.8	241.9		3.13E-20	2.63E-20			1.11E-20	9.39E-21			3.90E-21	3.36E-21		
28b	241.8	241.9		1.43E-20	1.45E-20	2.79E-20	1.42E-20	4.60E-21	4.72E-21	9.82E-21	5.07E-21	1.48E-21	1.54E-21	3.45E-21	1.81E-21
28c	241.8	241.9		3.82E-20	3.03E-20			1.38E-20	1.10E-20			4.98E-21	4.00E-21		
29a	243.9	244		1.89E-19	1.69E-19			6.55E-20	5.92E-20			2.26E-20	2.08E-20		
29b	243.9	244		1.64E-19	1.47E-19	1.70E-19	8.94E-20	5.61E-20	5.08E-20	5.81E-20	3.10E-20	1.92E-20	1.76E-20	1.99E-20	1.08E-20
29c	243.9	244		1.56E-19	1.48E-19			5.28E-20	5.05E-20			1.78E-20	1.73E-20		

Sample ID	Distance		Formation	Calculated parameters																	
Sample ID	minimum distance	maximum distance	Formation	T	σT	A	σA	μ	σμ	K2.0	σK2.0	K2.0 Mean	σK2.0 mean	K2.5	σK2.5	K2.5 mean	σK2.5 mean	K3	σK3	K3 mean	σK3 mean
	m	m		°C	°C			Pa*s	Pa*s	m/s	m/s	m/s	m/s	m/s	m/s	m/s	m/s	m/s	m/s	m/s	m/s
1a	5.8	6	Hauptrogenstein (carbonates)	13.69				1.86E-04	#######												
1b	5.8	6		13.69				1.86E-04	#######												
1c	5.8	6		13.69				1.86E-04	#######												
2a	14.84	15.1		13.79				1.86E-04	#######												
2b	14.84	15.1		13.79				1.86E-04	#######												
2c	14.84	15.1		13.79				1.86E-04	#######												
3a	24.98	25.3		13.85				1.86E-04	#######												
3b	24.98	25.3		13.85				1.86E-04	#######												
3c	24.98	25.3		13.85				1.86E-04	#######												
4a	35.35	35.58		13.96				1.86E-04	#######												
4b	35.35	35.58		13.96				1.86E-04	#######												
4c	35.35	35.58		13.96				1.86E-04	#######												
5a	42.28	42.52	Passwang Formation (marl and limestone)	13.97	0.2	-1.360	0.002	1.16E-03	6.29E-06	3.59E-13	2.78E-13			1.31E-13	1.02E-13			4.79E-14	3.78E-14		
5b	42.28	42.52		13.97	0.2	-1.360	0.002	1.16E-03	6.29E-06	3.80E-13	2.92E-13	3.79E-13	1.68E-13	1.40E-13	1.08E-13	1.40E-13	6.26E-14	5.14E-14	4.03E-14	5.14E-14	2.33E-14
5c	42.28	42.52		13.97	0.2	-1.360	0.002	1.16E-03	6.29E-06	4.00E-13	3.05E-13			1.48E-13	1.14E-13			5.50E-14	4.27E-14		
6a	61.75	62.08		11.6	0.2	-1.384	0.002	1.23E-03	7.03E-06	7.67E-14	7.20E-14			2.54E-14	2.40E-14			8.40E-15	8.00E-15		
6b	61.75	62.08		11.6	0.2	-1.384	0.002	1.23E-03	7.03E-06	1.22E-13	1.02E-13	8.91E-14	4.72E-14	4.25E-14	3.60E-14	3.02E-14	1.61E-14	1.49E-14	1.27E-14	1.02E-14	5.54E-15
6c	61.75	62.08		11.6	0.2	-1.384	0.002	1.23E-03	7.03E-06	6.89E-14	6.60E-14			2.25E-14	2.17E-14			7.37E-15	7.16E-15		
7a	69.76	70.03		11.8	0.2	-1.382	0.002	1.23E-03	6.96E-06	2.55E-13	3.22E-13			7.26E-14	9.25E-14			2.07E-14	2.66E-14		
7b	69.76	70.03		11.8	0.2	-1.382	0.002	1.23E-03	6.96E-06	3.77E-13	4.33E-13	3.05E-13	2.14E-13	1.13E-13	1.30E-13	8.89E-14	6.31E-14	3.37E-14	3.92E-14	2.60E-14	1.86E-14
7c	69.76	70.03		11.8	0.2	-1.382	0.002	1.23E-03	6.96E-06	2.82E-13	3.49E-13			8.14E-14	1.01E-13			2.35E-14	2.95E-14		
8a	74.78	75.03		12.2	0.2	-1.378	0.002	1.21E-03	6.83E-06	6.00E-13	5.09E-13			2.09E-13	1.78E-13			7.28E-14	6.26E-14		
8b	74.78	75.03		12.2	0.2	-1.378	0.002	1.21E-03	6.83E-06	7.77E-13	6.21E-13	5.53E-13	2.84E-13	2.79E-13	2.24E-13	1.92E-13	1.00E-13	1.00E-13	8.11E-14	6.71E-14	3.55E-14
8c	74.78	75.03		12.2	0.2	-1.378	0.002	1.21E-03	6.83E-06	2.82E-13	2.86E-13			8.97E-14	9.71E-14			2.86E-14	2.95E-14		
9a	84.73	84.98		12.9	0.2	-1.371	0.002	1.19E-03	6.61E-06	3.96E-13	2.85E-13			1.50E-13	1.09E-13			5.68E-14	4.15E-14		
9b	84.73	84.98		12.9	0.2	-1.371	0.002	1.19E-03	6.61E-06	4.24E-13	3.01E-13	4.03E-13	1.67E-13	1.62E-13	1.16E-13	1.53E-13	6.39E-14	6.19E-14	4.48E-14	5.82E-14	2.45E-14
9c	84.73	84.98		12.9	0.2	-1.371	0.002	1.19E-03	6.61E-06	3.90E-13	2.81E-13			1.48E-13	1.07E-13			5.59E-14	4.08E-14		
10a	96.7	96.9		13.6	0.2	-1.364	0.002	1.17E-03	6.40E-06	1.21E-12	9.78E-13			4.29E-13	3.50E-13			1.53E-13	1.26E-13		
10b	96.7	96.9		13.6	0.2	-1.364	0.002	1.17E-03	6.40E-06	2.05E-12	1.47E-12	1.64E-12	7.21E-13	7.75E-13	5.60E-13	6.05E-13	2.69E-13	2.94E-13	2.14E-13	2.24E-13	1.01E-13
10c	96.7	96.9		13.6	0.2	-1.364	0.002	1.17E-03	6.40E-06	1.66E-12	1.25E-12			6.12E-13	4.65E-13			2.26E-13	1.73E-13		
11b	107	107.24	OPA (sandy)	13.5	0.2	-1.365	0.002	1.17E-03	6.43E-06	2.15E-13	1.64E-13	2.11E-13	1.13E-13	7.93E-14	6.09E-14	7.76E-14	4.21E-14	2.93E-14	2.27E-14	2.86E-14	1.57E-14
11c	107	107.24		13.5	0.2	-1.365	0.002	1.17E-03	6.43E-06	2.06E-13	1.57E-13			7.58E-14	5.83E-14			2.79E-14	2.16E-14		
12a	116.24	116.54		14	0.2	-1.360	0.002	1.15E-03	6.29E-06					4.22E-14	3.88E-14			1.42E-14	1.31E-14		
12b	116.24	116.54		14	0.2	-1.360	0.002	1.15E-03	6.29E-06	2.11E-13	1.72E-13	1.80E-13	8.84E-14	7.55E-14	6.21E-14	6.32E-14	3.14E-14	2.69E-14	2.24E-14	2.22E-14	1.12E-14
12c	116.24	116.54		14	0.2	-1.360	0.002	1.15E-03	6.29E-06	2.03E-13	1.66E-13			7.20E-14	5.93E-14			2.55E-14	2.12E-14		
13a	125.12	125.38		14.4	0.2	-1.356	0.002	1.14E-03	6.17E-06	2.50E-13	1.98E-13			9.00E-14	7.17E-14			3.24E-14	2.60E-14		
13b	125.12	125.38		14.4	0.2	-1.356	0.002	1.14E-03	6.17E-06	1.26E-13	1.16E-13	2.09E-13	1.01E-13	4.17E-14	3.89E-14	7.41E-14	3.63E-14	1.39E-14	1.30E-14	2.63E-14	1.31E-14
13c	125.12	125.38		14.4	0.2	-1.356	0.002	1.14E-03	6.17E-06	2.51E-13	1.99E-13			9.07E-14	7.21E-14			3.27E-14	2.62E-14		
14a	136.33	136.58	OPA (shaly)	15.2	0.2	-1.348	0.002	1.12E-03	5.96E-06	3.22E-13	2.22E-13			1.25E-13	8.68E-14			4.82E-14	3.39E-14		
14b	136.33	136.58		15.2	0.2	-1.348	0.002	1.12E-03	5.96E-06	1.65E-13	1.33E-13	2.25E-13	9.91E-14	5.91E-14	4.83E-14	8.40E-14	3.76E-14	2.12E-14	1.75E-14	3.14E-14	1.43E-14
14c	136.33	136.58		15.2	0.2	-1.348	0.002	1.12E-03	5.96E-06	1.87E-13	1.46E-13			6.81E-14	5.34E-14			2.48E-14	1.96E-14		
15a	141.1	141.38		15.3	0.2	-1.347	0.002	1.12E-03	5.93E-06	1.97E-13	1.43E-13			7.45E-14	5.44E-14			2.81E-14	2.07E-14		
15b	141.1	141.38		15.3	0.2	-1.347	0.002	1.12E-03	5.93E-06	2.20E-13	1.54E-13	2.09E-13	1.05E-13	8.42E-14	5.95E-14	7.93E-14	4.03E-14	3.22E-14	2.30E-14	3.02E-14	1.55E-14
16a	155.1	155.72		16.3	0.2	-1.337	0.002	1.09E-03	5.67E-06	1.39E-13	1.12E-13			5.01E-14	4.10E-14			1.81E-14	1.50E-14		
16b	155.1	155.72		16.3	0.2	-1.337	0.002	1.09E-03	5.67E-06	1.80E-13	1.35E-13	1.65E-13	7.32E-14	6.73E-14	5.08E-14	6.10E-14	2.73E-14	2.51E-14	1.91E-14	2.26E-14	1.02E-14
16c	155.1	155.72		16.3	0.2	-1.337	0.002	1.09E-03	5.67E-06	1.76E-13	1.32E-13			6.57E-14	4.97E-14			2.45E-14	1.87E-14		
17a	164.3	164.58		17	0.2	-1.330	0.002	1.07E-03	5.51E-06	2.05E-13	1.53E-13			7.66E-14	5.73E-14			2.85E-14	2.16E-14		
17b	164.3	164.58		17	0.2	-1.330	0.002	1.07E-03	5.51E-06	2.00E-13	1.49E-13	2.07E-13	8.86E-14	7.43E-14	5.56E-14	7.73E-14	3.33E-14	2.76E-14	2.08E-14	2.88E-14	1.25E-14
17c	164.3	164.58		17	0.2	-1.330	0.002	1.07E-03	5.51E-06	2.16E-13	1.59E-13			8.11E-14	5.99E-14			3.04E-14	2.27E-14		
18a	176.48	176.73	OPA (sandy)	17.5	0.2	-1.325	0.002	1.05E-03	5.39E-06					7.22E-14	7.26E-14			2.32E-14	2.35E-14		
18b	176.48	176.73		17.5	0.2	-1.325	0.002	1.05E-03	5.39E-06	1.33E-13	1.49E-13	1.88E-13	1.14E-13	4.01E-14	4.54E-14	5.93E-14	3.62E-14	1.21E-14	1.38E-14	1.87E-14	1.16E-14
18c	176.48	176.73		17.5	0.2	-1.325	0.002	1.05E-03	5.39E-06	2.06E-13	2.09E-13			6.57E-14	6.68E-14			2.09E-14	2.14E-14		
19a	185.97	186.19	OPA (carb.-rich)	18.2	0.2	-1.318	0.002	1.03E-03	5.23E-06					1.45E-13	1.31E-13			4.90E-14	4.49E-14		
19b	185.97	186.19		18.2	0.2	-1.318	0.002	1.03E-03	5.23E-06	6.24E-13	5.14E-13	5.88E-13	2.85E-13	2.21E-13	1.83E-13	2.07E-13	1.02E-13	7.83E-14	6.55E-14	7.32E-14	3.64E-14
19c	185.97	186.19		18.2	0.2	-1.318	0.002	1.03E-03	5.23E-06	7.12E-13	5.67E-13			2.56E-13	2.06E-13			9.23E-14	7.48E-14		
20a	196.08	196.35		18.8	0.2	-1.312	0.002	1.02E-03	5.10E-06	1.70E-13	1.33E-13			6.20E-14	4.87E-14			2.26E-14	1.79E-14		
20b	196.08	196.35		18.8	0.2	-1.312	0.002	1.02E-03	5.10E-06	1.94E-13	1.48E-13	1.83E-13	8.12E-14	7.18E-14	5.52E-14	6.71E-14	3.01E-14	2.66E-14	2.07E-14	2.47E-14	1.12E-14
20c	196.08	196.35		18.8	0.2	-1.312	0.002	1.02E-03	5.10E-06	1.83E-13	1.41E-13			6.75E-14	5.23E-14			2.48E-14	1.94E-14		
21a	204.73	204.98		19.3	0.2	-1.307	0.002	1.01E-03	5.00E-06	2.01E-13	1.46E-13			7.61E-14	5.56E-14			2.88E-14	2.13E-14		
21b	204.73	204.98		19.3	0.2	-1.307	0.002	1.01E-03	5.00E-06	1.99E-13	1.47E-13	1.79E-13	7.82E-14	7.54E-14	5.62E-14	6.70E-14	2.96E-14	2.86E-14	2.16E-14	2.51E-14	1.13E-14
21c	204.73	204.98		19.3	0.2	-1.307	0.002	1.01E-03	5.00E-06	1.37E-13	1.11E-13			4.96E-14	4.06E-14			1.79E-14	1.49E-14		
22a	213.23	213.48	OPA (shaly)	19.8	0.2	-1.302	0.002	9.94E-04	4.89E-06	2.87E-13	1.94E-13			1.13E-13	7.73E-14			4.43E-14	3.08E-14		
22b	213.23	213.48		19.8	0.2	-1.302	0.002	9.94E-04	4.89E-06	1.95E-13	1.44E-13	2.39E-13	9.80E-14	7.33E-14	5.47E-14	9.19E-14	3.82E-14	2.75E-14	2.07E-14	3.54E-14	1.49E-14
22c	213.23	213.48		19.8	0.2	-1.302	0.002	9.94E-04	4.89E-06	2.34E-13	1.67E-13			8.96E-14	6.45E-14			3.43E-14	2.50E-14		
23a	224.48	224.73	OPA (shaly)	20.4	0.2	-1.296	0.002	9.79E-04	4.78E-06	1.79E-13	1.41E-13			6.50E-14	5.16E-14			2.36E-14	1.90E-14		
23b	224.48	224.73		20.4	0.2	-1.296	0.002	9.79E-04	4.78E-06	1.57E-13	1.32E-13	1.64E-13	7.75E-14	5.60E-14	4.79E-14	5.88E-14	2.82E-14	2.00E-14	1.74E-14	2.11E-14	1.03E-14
23c	224.48	224.73		20.4	0.2	-1.296	0.002	9.79E-04	4.78E-06	1.55E-13	1.30E-13			5.54E-14	4.70E-14			1.98E-14	1.71E-14		
25a	225.45	225.63		20.6	0.2	-1.294	0.002	9.75E-04	4.74E-06					3.16E-14	2.98E-14			1.05E-14	1.00E-14		
25b	225.45	225.63		20.6	0.2	-1.294	0.002	9.75E-04	4.74E-06	8.90E-14	8.62E-14	1.58E-13	8.08E-14	2.94E-14	2.88E-14	5.74E-14	3.03E-14	9.73E-15	9.66E-15	2.10E-14	1.15E-14
25c	225.45	225.63		20.6	0.2	-1.294	0.002	9.75E-04	4.74E-06	2.90E-13	2.09E-13			1.11E-13	8.09E-14			4.26E-14	3.14E-14		
26a	230.6	230.75		20.9	0.2	-1.291	0.002	9.67E-04	4.68E-06	1.67E-13	1.41E-13			5.86E-14	4.99E-14			2.06E-14	1.77E-14		
26b	230.6	230.75		20.9	0.2	-1.291	0.002	9.67E-04	4.68E-06	1.73E-13	1.46E-13	1.55E-13	7.81E-14	6.11E-14	5.21E-14	5.42E-14	2.75E-14	2.16E-14	1.86E-14	1.89E-14	9.74E-15
26c	230.6	230.75		20.9	0.2	-1.291	0.002	9.67E-04	4.68E-06	1.26E-13	1.17E-13			4.29E-14	4.02E-14			1.46E-14	1.38E-14		
24a	235.41	235.66		21	0.2	-1.290	0.002	9.65E-04	4.66E-06	1.77E-13	1.42E-13			6.42E-14	5.18E-14			2.32E-14	1.90E-14		
24b	235.41	235.66		21	0.2	-1.290	0.002	9.65E-04	4.66E-06	2.40E-13	1.79E-13	2.05E-13	9.12E-14	9.01E-14	6.77E-14	7.54E-14	3.40E-14	3.38E-14	2.57E-14	2.78E-14	1.27E-14
24c	235.41	235.66		21	0.2	-1.290	0.002	9.65E-04	4.66E-06	1.96E-13	1.51E-13			7.18E-14	5.59E-14			2.63E-14	2.06E-14		
27a	238.15	238.25	Staffelegg Formation (marly limestone)	21.3	0.2	-1.287	0.002	9.58E-04	4.61E-06	7.46E-13	1.18E-13			1.91E-14	3.04E-14			4.89E-15	7.85E-15		
27b	238.15	238.25		21.3	0.2	-1.287	0.002	9.58E-04	4.61E-06	1.05E-13	1.57E-13	5.99E-13	6.55E-14	2.80E-14	4.26E-14	1.57E-14	1.74E-14	7.48E-15	1.16E-14	4.12E-15	4.66E-15
27c	238.15	238.25		21.3	0.2	-1.287	0.002	9.58E-04	4.61E-06	1.01E-17	1.42E-16			1.01E-18	1.42E-17			8.62E-20	1.22E-18		
28a	241.8	241.9		21.6	0.2	-1.284	0.002	9.51E-04	4.55E-06	3.27E-13	2.75E-13			1.15E-13	9.81E-14			4.08E-14	3.51E-14		
28b	241.8	241.9		21.6	0.2	-1.284	0.002	9.51E-04	4.55E-06	1.49E-13	1.51E-13	2.92E-13	1.49E-13	4.81E-14	4.93E-14	1.03E-13	5.30E-14	1.55E-14	1.61E-14	3.61E-14	1.90E-14
28c	241.8	241.9		21.6	0.2	-1.284	0.002	9.51E-04	4.55E-06	4.00E-13	3.16E-13			1.44E-13	1.15E-13			5.20E-14	4.18E-14		
29a	243.9	244		21.8	0.2	-1.282	0.002	9.47E-04	4.51E-06	1.99E-12	1.77E-12			6.87E-13	6.21E-13			2.37E-13	2.18E-13		
29b	243.9	244		21.8	0.2	-1.282	0.002	9.47E-04	4.51E-06	1.72E-12	1.54E-12	1.78E-12	9.38E-13	5.89E-13	5.33E-13	6.10E-13	3.25E-13	2.01E-13	1.85E-13	2.09E-13	1.13E-13
29c	243.9	244		21.8	0.2	-1.282	0.002	9.47E-04	4.51E-06	1.64E-12	1.55E-12			5.54E-13	5.30E-13			1.87E-13	1.82E-13		

AII-1 Out diffusion experiments

AII-1-1 Synthetic solutions preparation

Table AII-1: Salt concentrations used for out diffusion test solutions calculated from chloride content estimated from leaching experiments on BDB-1 borehole samples.

Formation	Distance [m]	$[Cl^-]$ [mol L^{-1}]	Ionic strength [mol L^{-1}]	$[NaHCO_3]$ [g L^{-1}]
Hauptrogenstein	24.98	0.306	0.398	25.67
Passwang Formation	96.07	0.085	0.109	7.14
OPA - Sandy	116.24	0.089	0.114	7.48
OPA - Shaly	141.1	0.195	0.252	16.38
OPA - Shaly	155.1	0.234	0.303	19.66
OPA - Sandy	176.48	0.357	0.466	29.99
OPA - Carbonate-rich	185.97	0.354	0.462	29.74
OPA - Shaly	204.73	0.384	0.503	32.26
OPA - Shaly	213.23	0.393	0.515	33.01
Staffelegg Formation	238.2	0.414	0.543	34.78

AII-1-2 Out diffusion results

Sample	Diff. Orient.	n_{tot}	σ_{ntot}	P_{acc}	σ_{acc}	n_{acc}	σ_{nacc}	$WC_{grav, wet}$	$WC_{grav, wet, fullS}$	M_{rock} [g]	M_{sol} [g]	M_{pwacc} [g]	σ_{pwacc} [g]	$M_{pwacc,fullS}$ [g]	$\sigma_{pwacc, fullS}$ [g]
24.98	⊥	0.023	0.005	1.00	0.29	0.023	0.005	0.50%	0.80%	326.78	79.98	1.63	0.48	2.61	0.76
69.6	⊥	0.083	0.005	0.52	0.04	0.043	0.003	2.70%	3.20%	304.61	85.05	4.28	0.36	5.07	0.42
96.07	⊥	0.136	0.005	0.55	0.03	0.075	0.003	4.80%	5.30%	286.04	61.08	7.55	0.38	8.34	0.41
116.24	⊥	0.122	0.005	0.55	0.03	0.067	0.003	4.60%	5.00%	300.27	84.17	7.60	0.45	8.26	0.49
116.24	//	0.122	0.005	0.55	0.03	0.067	0.003	4.60%	5.00%	303.4	84.46	7.68	0.46	8.34	0.50
141.1	⊥	0.145	0.006	0.55	0.03	0.079	0.003	5.00%	5.40%	283.58	83.06	7.80	0.46	8.42	0.49
155.1	⊥	0.136	0.006	0.55	0.03	0.075	0.003	5.60%	5.60%	302.34	85.03	9.31	0.57	9.31	0.57
155.1	//	0.136	0.006	0.55	0.03	0.075	0.003	5.60%	5.60%	293.97	84.96	9.05	0.55	9.05	0.55
176.48	⊥	0.099	0.005	0.55	0.04	0.054	0.003	3.50%	4.00%	304.21	86.11	5.86	0.40	6.69	0.45
176.48	//	0.099	0.005	0.55	0.04	0.054	0.003	3.50%	4.00%	299.09	84.96	5.76	0.39	6.58	0.44
185.97	⊥	0.123	0.005	0.55	0.03	0.068	0.003	4.30%	5.00%	290.93	86	6.88	0.41	8.00	0.47
185.97	//	0.123	0.005	0.55	0.03	0.068	0.003	4.30%	5.00%	297.07	85	7.03	0.42	8.17	0.48
204.73	⊥	0.139	0.007	0.55	0.04	0.077	0.004	5.70%	5.80%	298.87	85.14	9.37	0.62	9.53	0.64
204.73	//	0.139	0.007	0.55	0.04	0.077	0.004	5.70%	5.80%	298.91	85.2	9.37	0.62	9.54	0.64
213.23	⊥	0.147	0.006	0.55	0.03	0.081	0.003	5.70%	6.00%	282.63	85.11	8.86	0.50	9.33	0.53
224.49	⊥	0.129	0.007	0.55	0.04	0.071	0.004	5.20%	5.20%	290.55	85.17	8.31	0.67	8.31	0.67
225.5	⊥	0.123	0.006	0.55	0.04	0.067	0.003	4.40%	4.93%	309.25	85.1	7.48	0.53	8.39	0.60
238.2	⊥	0.068	0.006	0.55	0.07	0.038	0.003	1.40%	2.70%	300.68	85.09	2.32	0.29	4.47	0.56

Sample	Diff. Orient.	$[Cl^-]_{pw, fullS}$ [mM]	$\sigma_{[Cl-]pw, fullS}$ [mM]	$[Br^-]_{pw, fullS}$ [mM]	$\sigma_{[Br-]pw, fullS}$ [mM]	$[SO_4^{2-}]_{pw, fullS}$ [mM]	$\sigma_{[SO42-], fullS}$ [mM]	Molar Br/Cl	$\sigma_{Br/Cl}$
24.98	⊥	2.33	0.71	0.00	0.00	226.56	69.38	na	na
69.6	⊥	4.47	0.52	0.00	0.00	747.03	222.74	na	na
96.07	⊥	16.40	1.69	0.00	0.00	4.11	0.42	na	na
116.24	⊥	61.62	3.68	0.00	0.00	125.05	6.20	na	na
116.24	//	62.60	5.98	0.00	0.00	152.19	15.74	na	na
141.1	⊥	104.47	8.11	0.231	0.014	256.69	15.15	0.00221	2.16E-04
155.1	⊥	181.45	11.10	0.28	0.02	107.15	6.57	0.00154	1.33E-04
155.1	//	162.98	15.64	0.32	0.02	97.94	6.00	0.00196	2.24E-04
176.48	⊥	248.87	26.63	0.28	0.03	337.71	38.49	0.00111	1.78E-04
176.48	//	253.01	25.26	0.50	0.05	192.53	20.29	0.00197	2.84E-04
185.97	⊥	237.95	25.64	0.37	0.04	285.48	19.20	0.00156	2.47E-04
185.97	//	250.10	24.31	0.53	0.05	202.47	20.86	0.00213	2.98E-04
204.73	⊥	327.08	21.91	0.56	0.04	225.80	15.13	0.00171	1.62E-04
204.73	//	354.89	23.78	0.58	0.04	269.01	18.01	0.00164	1.55E-04
213.23	⊥	313.09	17.80	0.57	0.03	122.64	6.97	0.00181	1.46E-04
224.49	⊥	351.51	28.32	0.69	0.06	117.40	9.32	0.00196	2.24E-04
225.5	⊥	407.46	29.08	0.62	0.04	266.93	18.86	0.00152	1.53E-04
238.2	⊥	344.41	43.36	0.48	0.06	87.41	11.00	0.00138	2.46E-04

Sample	Distance	Formation	Real state of samples		Recalculated for full saturation				Grain size	Leaching solution	Time	M_solid	σsolid	M_Mpw	σMpw	M_A,d,leach,sol	σM,A,d,leach,sol	M_liq	σMliq	S/L	σS/L
	m		WC_bulk,wet	σWC_bulk,wet	WC_bulk,wet	σWC_bulk,wet	PCl	σPCl	μm			g	g	g	g	g	g	g	g		
Seawater										MilliQ water CaCO3											
Blank										MilliQ water											
Blank																					
1	5.8	Hauptrogenstein (limestone)	0.027	5.0E-05	0.027	5.0E-05	1	0.02	<100	MilliQ water	2h	5.009	0.002	0.1352	0.0003	10	0.002	10.1352	0.002	0.49	2.20E-04
2	14.84		0.008	4.0E-05	0.010	4.0E-05	1	0.02	<102	MilliQ water	2h	4.995	0.002	0.0500	0.0002	9.993	0.002	10.0430	0.002	0.50	2.23E-04
3	24.98		0.005	6.0E-05	0.008	6.0E-05	1	0.02	<104	MilliQ water	2h	4.999	0.002	0.0400	0.0003	10.052	0.002	10.0920	0.002	0.50	2.22E-04
4	35.35		0.008	6.0E-05	0.012	6.0E-05	1	0.02	<106	MilliQ water	2h	4.997	0.002	0.0600	0.0003	10.003	0.002	10.0630	0.002	0.50	2.22E-04
5	43.27		0.047	7.0E-05	0.054	7.0E-05	0.55	0.02	<108	MilliQ water	2h	5.008	0.002	0.2704	0.0004	10.103	0.002	10.3734	0.002	0.48	2.15E-04
6	61.75	Passwang Formation (marl and limestone)	0.041	5.0E-05	0.045	5.0E-05	0.55	0.02	<110	MilliQ water	2h	4.991	0.002	0.2246	0.0003	10.007	0.002	10.2316	0.002	0.49	2.18E-04
7	69.76		0.027	6.0E-05	0.032	6.0E-05	0.55	0.02	<112	MilliQ water	2h	5.001	0.002	0.1600	0.0003	10.181	0.002	10.3410	0.002	0.49	2.15E-04
8	74.78		0.043	5.0E-05	0.048	5.0E-05	0.55	0.02	<114	MilliQ water	2h	5.018	0.002	0.2409	0.0003	10.018	0.002	10.2589	0.002	0.49	2.17E-04
9	84.73		0.051	6.0E-05	0.058	6.0E-05	0.55	0.02	<116	MilliQ water	2h	4.994	0.002	0.2897	0.0003	10.066	0.002	10.3557	0.002	0.48	2.15E-04
10	96.7		0.048	5.0E-05	0.053	5.0E-05	0.55	0.02	<118	MilliQ water	2h	4.997	0.002	0.2648	0.0003	9.986	0.002	10.2508	0.002	0.49	2.17E-04
11	107	OPA (sandy)	0.05	5.0E-05	0.054	5.0E-05	0.55	0.02	<120	MilliQ water	2h	5.009	0.002	0.2705	0.0003	10.003	0.002	10.2735	0.002	0.49	2.17E-04
12	116.21		0.046	7.0E-05	0.050	7.0E-05	0.55	0.02	<100	MilliQ water	2h	5.003	0.002	0.2502	0.0004	9.993	0.002	10.2432	0.002	0.49	2.18E-04
13	125.12		0.048	5.0E-05	0.052	5.0E-05	0.55	0.02	<100	MilliQ water	2h	4.999	0.002	0.2599	0.0003	10.013	0.002	10.2729	0.002	0.49	2.17E-04
14	136.33		0.051	5.0E-05	0.053	5.0E-05	0.55	0.02	<100	MilliQ water	2h	4.996	0.002	0.2648	0.0003	9.996	0.002	10.2608	0.002	0.49	2.17E-04
15	141.1		0.05	5.0E-05	0.054	5.0E-05	0.55	0.02	<100	MilliQ water	2h	4.988	0.002	0.2694	0.0003	10.006	0.002	10.2754	0.002	0.49	2.17E-04
16	155.1	OPA (shaly)	0.056	6.0E-05	0.056	6.0E-05	0.55	0.02	<100	MilliQ water	2 h	1.008	0.002	0.0564	0.0001	10.015	0.002	10.0714	0.002	0.10	2.00E-04
16	155.1		0.056	6.0E-05	0.056	6.0E-05	0.55	0.02	<100	MilliQ water	2 h	3.354	0.002	0.1878	0.0002	9.988	0.002	10.1758	0.002	0.33	2.07E-04
16	155.1		0.056	6.0E-05	0.056	6.0E-05	0.55	0.02	<100	MilliQ water	2 h	5.002	0.002	0.2801	0.0003	10.025	0.002	10.3051	0.002	0.49	2.16E-04
16	155.1		0.056	6.0E-05	0.056	6.0E-05	0.55	0.02	[100 : 200]	MilliQ water	2 h	5.002	0.002	0.2801	0.0003	10.003	0.002	10.2831	0.002	0.49	2.17E-04
16	155.1		0.056	6.0E-05	0.056	6.0E-05	0.55	0.02	[200 : 500]	MilliQ water	2 h	4.995	0.002	0.2797	0.0003	9.985	0.002	10.2647	0.002	0.49	2.17E-04
16	155.1		0.056	6.0E-05	0.056	6.0E-05	0.55	0.02	<100	MilliQ water CaCO3	2 h	4.998	0.002	0.2799	0.0003	9.992	0.002	10.2719	0.002	0.49	2.16E-04
16	155.1		0.056	6.0E-05	0.056	6.0E-05	0.55	0.02	[100 : 200]	MilliQ water CaCO3	2 h	5.005	0.002	0.2803	0.0003	10.03	0.002	10.3103	0.002	0.49	2.16E-04
16	155.1		0.056	6.0E-05	0.056	6.0E-05	0.55	0.02	[200 : 500]	MilliQ water CaCO3	2 h	5	0.002	0.2800	0.0003	10.042	0.002	10.322	0.002	0.48	2.16E-04
16	155.1		0.056	6.0E-05	0.056	6.0E-05	0.55	0.02	<100	MilliQ water	24 h	5.009	0.002	0.2805	0.0003	9.983	0.002	10.2628	0.002	0.49	2.17E-04
16	155.1		0.056	6.0E-05	0.056	6.0E-05	0.55	0.02	[100 : 200]	MilliQ water	24 h	4.997	0.002	0.2798	0.0003	10.04	0.002	10.3209	0.002	0.49	2.16E-04
16	155.1		0.056	6.0E-05	0.056	6.0E-05	0.55	0.02	[200 : 500]	MilliQ water	24 h	5.016	0.002	0.2809	0.0003	10.026	0.002	10.3059	0.002	0.48	2.16E-04
16	155.1		0.056	6.0E-05	0.056	6.0E-05	0.55	0.02	<100	MilliQ water CaCO3	24 h	4.998	0.002	0.2799	0.0003	10.003	0.002	10.2577	0.002	0.44	2.14E-04
16	155.1		0.056	6.0E-05	0.056	6.0E-05	0.55	0.02	[100 : 200]	MilliQ water CaCO3	24 h	5.005	0.002	0.2803	0.0003	9.975	0.002	10.2553	0.002	0.49	2.18E-04
16	155.1		0.056	5.0E-05	0.057	5.0E-05	0.55	0.02	[200 : 500]	MilliQ water CaCO3	24 h	5.025	0.002	0.2814	0.0003	9.975	0.002	10.2648	0.002	0.49	2.17E-04
16	155.1		0.056	6.0E-05	0.056	6.0E-05	0.55	0.02	<100	MilliQ water	48h	5.005	0.002	0.2803	0.0003	10.03	0.002	10.3103	0.002	0.49	2.16E-04
16	155.1		0.056	6.0E-05	0.056	6.0E-05	0.55	0.02	[100 : 200]	MilliQ water	48h	4.999	0.002	0.2799	0.0003	10.029	0.002	10.3089	0.002	0.48	2.16E-04
16	155.1		0.056	6.0E-05	0.056	6.0E-05	0.55	0.02	[200 : 500]	MilliQ water	48h	5.026	0.002	0.2815	0.0003	9.981	0.002	10.2625	0.002	0.49	2.18E-04
16	155.1		0.056	6.0E-05	0.056	6.0E-05	0.55	0.02	<100	MilliQ water CaCO3	48h	5.013	0.002	0.2807	0.0003	9.989	0.002	10.2697	0.002	0.48	2.17E-04
16	155.1		0.056	6.0E-05	0.056	6.0E-05	0.55	0.02	[100 : 200]	MilliQ water CaCO3	48h	4.548	0.002	0.2547	0.0003	10.003	0.002	10.2577	0.002	0.44	2.14E-04
16	155.1		0.056	6.0E-05	0.056	6.0E-05	0.55	0.02	[200 : 500]	MilliQ water CaCO3	48h	4.997	0.002	0.2798	0.0003	9.985	0.002	10.2648	0.002	0.49	2.17E-04
17	164.3		0.056	5.0E-05	0.057	5.0E-05	0.55	0.02	<100	MilliQ water	48h	5.014	0.002	0.2858	0.0003	10.04	0.002	10.3258	0.002	0.49	2.16E-04
18	176.6	OPA (sandy)	0.035	5.0E-05	0.04	5.0E-05	0.55	0.02	<100	MilliQ water	48h	1.006	0.002	0.0402	0.0001	10.05	0.002	10.0902	0.002	0.10	1.99E-04
18	176.6		0.035	5.0E-05	0.04	5.0E-05	0.55	0.02	[100 : 200]	MilliQ water	48h	3.33	0.002	0.1332	0.0002	9.99	0.002	10.1232	0.002	0.33	2.08E-04
18	176.6		0.035	5.0E-05	0.04	5.0E-05	0.55	0.02	[200 : 500]	MilliQ water	48h	5.041	0.002	0.2016	0.0003	10.062	0.002	10.2636	0.002	0.49	2.17E-04
18	176.6		0.035	5.0E-05	0.04	5.0E-05	0.55	0.02	<100	MilliQ water CaCO3	48h	9.833	0.002	0.3933	0.0005	10.164	0.002	10.5573	0.002	0.93	2.63E-04
18	176.6		0.035	5.0E-05	0.04	5.0E-05	0.55	0.02	<100	MilliQ water CaCO3	2h	5.011	0.002	0.2004	0.0003	10.698	0.002	10.8984	0.002	0.46	2.02E-04
18	176.6		0.035	5.0E-05	0.04	5.0E-05	0.55	0.02	[100 : 200]	MilliQ water	2h	4.996	0.002	0.1998	0.0003	9.994	0.002	10.1938	0.002	0.49	2.19E-04
18	176.6		0.035	5.0E-05	0.04	5.0E-05	0.55	0.02	[200 : 500]	MilliQ water	2h	5.004	0.002	0.2002	0.0003	10.073	0.002	10.2732	0.002	0.49	2.17E-04
18	176.6		0.035	5.0E-05	0.04	5.0E-05	0.55	0.02	[100 : 200]	MilliQ water CaCO3	2h	5.009	0.002	0.2004	0.0003	10.047	0.002	10.2474	0.002	0.49	2.18E-04
18	176.6		0.035	5.0E-05	0.04	5.0E-05	0.55	0.02	[200 : 500]	MilliQ water CaCO3	2h	5.011	0.002	0.2004	0.0003	10.32	0.002	10.5204	0.002	0.48	2.11E-04
19	185.97	OPA (carb-rich)	0.043	6.0E-05	0.050	6.0E-05	0.55	0.02	<100	MilliQ water	2h	4.988	0.002	0.2494	0.0003	10.018	0.002	10.2674	0.002	0.49	2.17E-04
20	196.08		0.056	6.0E-05	0.055	6.0E-05	0.55	0.02	<100	MilliQ water	2h	4.995	0.002	0.2747	0.0003	10.065	0.002	10.3397	0.002	0.48	2.15E-04
21	204.73		0.057	8.0E-05	0.057	8.0E-05	0.55	0.02	<100	MilliQ water	2h	5.002	0.002	0.2851	0.0004	10.09	0.002	10.3751	0.002	0.48	2.15E-04
22	213.23	OPA (shaly)	0.057	8.0E-05	0.060	8.0E-05	0.55	0.02	<100	MilliQ water	2h	5.008	0.002	0.3005	0.0004	10.2	0.002	10.5005	0.002	0.48	2.12E-04
23	224.48		0.052	1.3E-04	0.052	1.3E-04	0.55	0.02	<100	MilliQ water	2h	4.998	0.002	0.2599	0.0007	9.996	0.002	10.2559	0.002	0.49	2.19E-04
25	225.45		0.042	6.0E-05	0.049	6.0E-05	0.55	0.02	<100	MilliQ water	2h	5.008	0.002	0.2470	0.0003	10.005	0.002	10.252	0.002	0.49	2.18E-04
26	230.6		0.041	7.0E-05	0.049	7.0E-05	0.55	0.02	<102	MilliQ water	2h	4.995	0.002	0.2468	0.0004	9.993	0.002	10.2398	0.002	0.49	2.18E-04
24	235.41		0.055	7.0E-05	0.055	7.0E-05	0.55	0.02	<104	MilliQ water	2h	4.992	0.002	0.2746	0.0004	10.08	0.002	10.3546	0.002	0.48	2.15E-04
27	238.15	Staffelegg (marly limestone)	0.014	1.3E-03	0.027	1.3E-03	0.55	0.02	<105	MilliQ water	2h	5.002	0.002	0.1332	0.0065	10.004	0.002	10.1372	0.007	0.49	3.85E-04
28	241.8		0.031	9.0E-05	0.048	9.0E-05	0.55	0.02	<107	MilliQ water	2h	5.005	0.002	0.2414	0.0005	10.146	0.002	10.3874	0.002	0.48	2.15E-04
29	243.9		0.026	8.0E-05	0.053	8.0E-05	0.55	0.02	<100	MilliQ water	2h	5.004	0.002	0.2659	0.0004	10.045	0.002	10.3109	0.002	0.49	2.16E-04

Leachate concentrations (Raw data)

Sample	Distance (m)	Formation	F^- ppm	σ_{F^-}	F^- mmol/L	σ_{F^-}	Cl^- ppm	σ_{Cl^-}	Cl^- mmol/l	σ_{Cl^-}	Br^- ppm	σ_{Br^-}	Br^- mmol/l	σ_{Br^-}	NO_3^- ppm	$\sigma_{NO_3^-}$	NO_3^- mmol/l	$\sigma_{NO_3^-}$	SO_4^{2-} ppm	$\sigma_{SO_4^{2-}}$	SO_4^{2-} mmol/l	$\sigma_{SO_4^{2-}}$
Seawater			0.135	0.013	0.007	0.001	0.294	0.029	0.008	0.001	0.000	0.000	0.000	0.0E+00	0.225	0.022	0.004	0.000	0.150	0.015	0.002	0.000
Blank			0.000	0.000	0.000	0.000	0.000	0.000	0.000	0.000	0.000	0.000	0.000	0.0E+00	0.000	0.000	0.000	0.000	0.000	0.000	0.000	0.000
1	5.8	Hauptrogenstein (limestone)	1.507	0.151	0.079	0.008	57.890	5.789	1.633	0.163	0.170	0.017	0.002	2.1E-04	17.959	1.796	0.290	0.029	34.542	3.454	0.359	0.036
2	14.84		0.614	0.061	0.032	0.003	27.796	2.780	0.784	0.078	0.201	0.020	0.003	2.7E-04	7.702	0.770	0.124	0.012	21.627	2.163	0.225	0.023
3	24.98		0.475	0.048	0.025	0.003	42.929	4.293	1.211	0.121	0.166	0.017	0.002	2.1E-04	17.436	1.744	0.281	0.028	481.740	48.174	5.013	0.501
4	35.35		1.669	0.167	0.088	0.009	6.888	0.689	0.194	0.019	0.158	0.016	0.002	2.0E-04	0.500	0.050	0.008	0.001	38.750	3.875	0.403	0.040
5	43.27		3.956	0.396	0.208	0.021	15.256	1.526	0.430	0.043	0.464	0.046	0.006	5.8E-04	5.734	0.573	0.092	0.009	16.135	1.614	0.168	0.017
6	61.75	Passwang Formation (marl and limestone)	1.485	0.149	0.078	0.008	55.013	5.501	1.552	0.155	0.157	0.016	0.002	2.0E-04	3.604	0.360	0.058	0.006	50.577	5.058	0.526	0.053
7	69.76		3.449	0.345	0.182	0.018	4.887	0.489	0.138	0.014	0.156	0.016	0.002	2.0E-04	0.456	0.046	0.007	0.001	16.448	1.645	0.171	0.017
8	74.78		3.044	0.304	0.160	0.016	49.997	5.000	1.410	0.141	0.166	0.017	0.002	2.1E-04	16.061	1.606	0.259	0.026	20.725	2.073	0.216	0.022
9	84.73		3.129	0.313	0.165	0.016	46.501	4.650	1.312	0.131	0.360	0.036	0.005	4.5E-04	13.642	1.364	0.220	0.022	40.595	4.060	0.422	0.042
10	96.7		3.455	0.346	0.182	0.018	42.981	4.298	1.212	0.121	0.199	0.020	0.002	2.5E-04	0.827	0.083	0.013	0.001	73.527	7.353	0.765	0.077
11	107	OPA (sandy)	6.281	0.628	0.331	0.033	56.286	5.629	1.588	0.159	0.241	0.024	0.003	3.0E-04	9.436	0.944	0.152	0.015	45.194	4.519	0.470	0.047
12	116.21		5.320	0.532	0.280	0.028	42.544	4.254	1.200	0.120	0.199	0.020	0.003	2.5E-04	0.855	0.086	0.014	0.001	49.550	4.955	0.516	0.052
13	125.12		4.475	0.448	0.236	0.024	99.751	9.975	2.814	0.281	0.348	0.035	0.004	4.4E-04	13.572	1.357	0.219	0.022	42.195	4.220	0.439	0.044
14	136.33		3.649	0.365	0.192	0.019	95.210	9.521	2.686	0.269	0.344	0.034	0.004	4.3E-04	5.103	0.510	0.082	0.008	49.652	4.965	0.517	0.052
15	141.1		3.394	0.339	0.179	0.018	99.907	9.991	2.818	0.282	0.172	0.017	0.002	2.2E-04	6.366	0.637	0.103	0.010	164.112	16.411	1.708	0.171
16	155.1	OPA (shaly)	0.942	0.094	0.050	0.005	20.703	2.070	0.584	0.058	0.355	0.036	0.004	4.4E-04	0.518	0.052	0.008	0.001	12.997	1.300	0.135	0.014
16	155.1		2.587	0.259	0.136	0.014	81.129	8.113	2.288	0.229	0.512	0.051	0.006	6.4E-04	1.005	0.101	0.016	0.002	48.142	4.814	0.501	0.050
16	155.1		2.835	0.284	0.149	0.015	124.321	12.432	3.507	0.351	0.455	0.046	0.006	5.7E-04	1.557	0.156	0.025	0.003	72.477	7.248	0.754	0.075
16	155.1		2.987	0.299	0.157	0.016	125.440	12.544	3.538	0.354	0.442	0.044	0.005	5.5E-04	0.624	0.062	0.010	0.001	70.571	7.057	0.734	0.073
16	155.1		3.283	0.328	0.173	0.017	125.315	12.531	3.535	0.353	0.526	0.053	0.007	6.6E-04	0.614	0.061	0.010	0.001	69.822	6.982	0.727	0.073
16	155.1		2.809	0.281	0.148	0.015	127.181	12.718	3.587	0.359	0.461	0.046	0.006	5.8E-04	1.647	0.165	0.027	0.003	74.091	7.409	0.771	0.077
16	155.1		2.997	0.300	0.158	0.016	129.952	12.995	3.665	0.367	0.442	0.044	0.006	5.5E-04	1.084	0.108	0.017	0.002	72.812	7.281	0.758	0.076
16	155.1		3.299	0.330	0.174	0.017	114.603	11.460	3.233	0.323	0.495	0.050	0.006	6.2E-04	1.763	0.176	0.028	0.003	70.849	7.085	0.737	0.074
16	155.1		2.861	0.286	0.151	0.015	125.962	12.596	3.553	0.355	0.452	0.045	0.006	5.7E-04	0.584	0.058	0.009	0.001	74.360	7.436	0.774	0.077
16	155.1		2.878	0.288	0.151	0.015	125.341	12.534	3.535	0.354	0.445	0.045	0.006	5.6E-04	1.824	0.182	0.029	0.003	76.057	7.606	0.791	0.079
16	155.1		2.646	0.265	0.139	0.014	129.270	12.927	3.646	0.365	0.536	0.054	0.007	6.7E-04	0.790	0.079	0.013	0.001	75.911	7.591	0.790	0.079
16	155.1		2.878	0.288	0.151	0.015	132.013	13.201	3.724	0.372	0.468	0.047	0.006	5.9E-04	0.829	0.083	0.013	0.001	76.127	7.613	0.792	0.079
16	155.1		3.574	0.357	0.188	0.019	123.811	12.381	3.492	0.349	0.466	0.047	0.006	5.8E-04	9.816	0.982	0.158	0.016	75.328	7.533	0.784	0.078
16	155.1		3.049	0.305	0.160	0.016	117.273	11.727	3.308	0.331	0.497	0.050	0.006	6.2E-04	0.502	0.050	0.008	0.001	70.227	7.023	0.731	0.073
16	155.1		2.829	0.283	0.149	0.015	129.377	12.938	3.649	0.365	0.450	0.045	0.006	5.6E-04	1.718	0.172	0.028	0.003	76.466	7.647	0.796	0.080
17	164.3	OPA (sandy)	3.279	0.328	0.173	0.017	132.302	13.230	3.732	0.373	0.445	0.045	0.006	5.6E-04	0.986	0.099	0.016	0.002	148.080	14.808	1.541	0.154
18	176.6		3.484	0.348	0.183	0.018	127.814	12.781	3.605	0.361	0.467	0.047	0.006	5.8E-04	0.885	0.089	0.014	0.001	77.313	7.731	0.805	0.080
18	176.6		2.831	0.283	0.149	0.015	124.404	12.440	3.509	0.351	0.446	0.045	0.006	5.6E-04	1.923	0.192	0.031	0.003	73.616	7.362	0.766	0.077
18	176.6		3.225	0.323	0.170	0.017	143.902	14.390	4.059	0.406	0.497	0.050	0.006	6.2E-04	0.792	0.079	0.013	0.001	54.494	5.449	0.567	0.057
18	176.6		3.224	0.322	0.170	0.017	148.277	14.828	4.182	0.418	0.515	0.052	0.006	6.4E-04	2.020	0.202	0.033	0.003	86.846	8.685	0.904	0.090
18	176.6		3.421	0.342	0.180	0.018	140.678	14.068	3.968	0.397	0.501	0.050	0.006	6.3E-04	0.542	0.054	0.009	0.001	89.238	8.924	0.929	0.093
18	176.6		3.215	0.322	0.169	0.017	24.064	2.406	0.679	0.068	0.175	0.018	0.002	2.2E-04	0.459	0.046	0.007	0.001	85.009	8.501	0.885	0.088
18	176.6		1.051	0.105	0.055	0.006	88.382	8.838	2.493	0.249	0.343	0.034	0.004	4.3E-04	0.541	0.054	0.009	0.001	16.489	1.649	0.172	0.017
18	176.6		2.826	0.283	0.149	0.015	136.917	13.692	3.862	0.386	0.485	0.049	0.006	6.1E-04	0.513	0.051	0.008	0.001	58.969	5.897	0.614	0.061
18	176.6		3.425	0.343	0.180	0.018	246.145	24.615	6.943	0.694	0.828	0.083	0.010	1.0E-03	2.134	0.213	0.034	0.003	88.210	8.821	0.918	0.092
19	185.97	OPA (carb.-rich)	3.499	0.350	0.184	0.018	167.968	16.797	4.738	0.474	0.559	0.056	0.007	7.0E-04	0.436	0.044	0.007	0.001	148.080	14.808	1.541	0.154
20	196.08	OPA (shaly)	3.457	0.346	0.182	0.018	202.249	20.225	5.705	0.570	0.622	0.062	0.008	7.8E-04	4.751	0.475	0.077	0.008	83.859	8.386	0.873	0.087
21	204.73		3.100	0.310	0.163	0.016	206.077	20.608	5.813	0.581	0.673	0.067	0.008	8.4E-04	7.322	0.732	0.118	0.012	88.011	8.801	0.916	0.092
22	213.23		3.224	0.322	0.170	0.017	219.417	21.942	6.189	0.619	0.677	0.068	0.008	8.5E-04	1.045	0.105	0.017	0.002	92.322	9.232	0.961	0.096
23	224.48		3.478	0.348	0.183	0.018	193.714	19.371	5.464	0.546	0.606	0.061	0.008	7.6E-04	6.146	0.615	0.099	0.010	92.857	9.286	0.966	0.097
25	225.45		4.202	0.420	0.221	0.022	203.820	20.382	5.749	0.575	0.607	0.061	0.008	7.6E-04	7.208	0.721	0.116	0.012	198.944	19.894	2.070	0.207
26	230.6		3.399	0.340	0.179	0.018	213.715	21.372	6.028	0.603	0.609	0.061	0.008	7.6E-04	5.614	0.561	0.091	0.009	289.004	28.900	3.007	0.301
24	235.41		4.951	0.495	0.261	0.026	212.534	21.253	5.995	0.599	0.682	0.068	0.009	8.5E-04	5.586	0.559	0.090	0.002	95.402	9.540	0.993	0.099
27	238.15	Staffelegg (marly limestone)	1.625	0.163	0.086	0.009	197.138	19.714	5.561	0.556	0.344	0.034	0.004	4.3E-04	30.809	3.081	0.497	0.050	140.340	14.034	1.460	0.146
28	241.8		1.422	0.142	0.075	0.007	308.129	30.813	8.691	0.869	0.382	0.038	0.005	4.8E-04	57.370	5.737	0.925	0.093	279.939	27.994	2.913	0.291
29	243.9		0.646	0.065	0.034	0.003	202.551	20.255	5.713	0.571	0.629	0.063	0.008	7.9E-04	0.748	0.075	0.012	0.001	1985.279	198.528	20.658	2.067

Sample	Distance m	Formation	F^- ppm	σ_{F-}	F^- mmol/l	σ_{F-}	Cl^- ppm	σ_{Cl-}	Cl^- mmol/l	σ_{Cl-}	Br^- ppm	σ_{Br-}	Br^- mmol/l	σ_{Br-}	NO_3^- ppm	σ_{NO3-}	NO_3^- mmol/l	σ_{NO3-}	SO_4^{2-} ppm	σ_{SO42-}	SO_4^{2-} mmol/l	σ_{SO42-}	Br/Cl	$\sigma_{Br/Cl}$	SO_4^{2-}/Cl	$\sigma_{SO4/Cl}$
Seawater							20082350		565.7		68714		0.86						2806120		29.2		1.52E-03		5.16E-02	
Blank																										
Blank																										
1	5.8	Hauptrogenstein (limestone)	112.9	11.5	5.9	0.6	4338.3	442.5	122.4	12.5	12.7	1.3	0.2	0.0	1345.9	137.3	21.7	2.2	2588.6	264.0	26.9	2.7	1.30E-03	1.84E-04	2.20E-01	3.11E-02
2	14.84		123.5	12.6	6.5	0.7	5588.7	570.4	157.6	16.1	44.0	4.5	0.6	0.1	1548.6	158.0	25.0	2.5	4348.3	443.8	45.3	4.6	3.50E-03	4.94E-04	2.87E-01	4.06E-02
3	24.98		119.9	12.3	6.3	0.6	10833.1	1107.8	305.6	31.2	50.7	5.2	0.6	0.1	4400.0	449.9	71.0	7.3	121567.2	12431.1	1265.5	129.4	2.08E-03	2.94E-04	4.14E+00	5.86E-01
4	35.35		280.1	28.6	14.7	1.5	1155.9	118.0	32.6	3.3	27.9	2.8	0.3	0.0	83.9	8.6	1.4	0.1	6502.9	664.0	67.7	6.9	1.07E-02	1.51E-03	2.08E+00	2.94E-01
5	43.27		275.9	29.4	14.5	1.5	1064.0	113.2	30.0	3.2	11.0	1.2	0.1	0.0	399.9	42.6	6.4	0.7	1125.3	119.7	11.7	1.2	4.60E-03	6.50E-04	3.90E-01	5.52E-02
6	61.75	Passwang Formation (marl and limestone)	123.0	13.1	6.5	0.7	4556.7	484.9	128.5	13.7	38.4	4.1	0.5	0.1	298.5	31.8	4.8	0.5	4189.2	445.8	43.6	4.6	3.74E-03	5.29E-04	3.39E-01	4.80E-02
7	69.76		405.2	43.1	21.3	2.3	574.2	61.1	16.2	1.7	18.4	2.0	0.2	0.0	53.6	5.7	0.9	0.1	1932.4	205.7	20.1	2.1	1.43E-02	2.02E-03	1.24E+00	1.76E-01
8	74.78		235.7	25.1	12.4	1.3	3871.8	412.0	109.2	11.6	12.1	1.3	0.2	0.0	1243.8	132.4	20.1	2.1	1604.9	170.8	16.7	1.8	1.38E-03	1.96E-04	1.53E-01	2.16E-02
9	84.73		203.4	21.6	10.7	1.1	3022.7	321.7	85.3	9.1	10.8	1.1	0.1	0.0	886.8	94.4	14.3	1.5	2638.8	280.8	27.5	2.9	1.58E-03	2.24E-04	3.22E-01	4.56E-02
10	96.7		243.1	25.9	12.8	1.4	3024.7	321.9	85.3	9.1	25.3	2.7	0.3	0.0	58.2	6.2	0.9	0.1	5174.4	550.6	53.9	5.7	3.72E-03	5.26E-04	6.31E-01	8.93E-02
11	107	OPA (sandy)	433.7	46.2	22.8	2.4	3887.0	413.6	109.6	11.7	13.7	1.5	0.2	0.0	651.6	69.3	10.5	1.1	3121.0	332.1	32.5	3.5	1.57E-03	2.22E-04	2.96E-01	4.19E-02
12	116.21		396.1	42.1	20.8	2.2	3167.4	337.1	89.3	9.5	17.9	1.9	0.2	0.0	63.7	6.8	1.0	0.1	3689.0	392.6	38.4	4.1	2.51E-03	3.57E-04	4.30E-01	6.08E-02
13	125.12		321.5	34.2	16.9	1.8	7167.4	762.7	202.2	21.5	14.3	1.5	0.2	0.0	975.2	103.8	15.7	1.7	3031.8	322.6	31.6	3.4	8.85E-04	1.26E-04	1.56E-01	2.21E-02
14	136.33		257.1	27.4	13.5	1.4	6708.1	713.8	189.2	20.1	24.5	2.6	0.3	0.0	359.5	38.3	5.8	0.6	3498.3	372.3	36.4	3.9	1.62E-03	2.31E-04	1.92E-01	2.72E-02
15	141.1		235.4	25.1	12.4	1.3	6929.6	737.4	195.5	20.8	23.9	2.5	0.3	0.0	441.6	47.0	7.1	0.8	11382.9	1211.3	118.5	12.6	1.53E-03	2.17E-04	6.06E-01	8.57E-02
16	155.1	OPA (shaly)	305.6	32.5	16.1	1.7	6716.1	714.8	189.4	20.2	55.8	5.9	0.7	0.1	168.0	17.9	2.7	0.3	4216.2	448.7	43.9	4.7	3.69E-03	5.21E-04	2.32E-01	3.28E-02
16	155.1		254.8	27.1	13.4	1.4	7991.6	850.4	225.4	24.0	35.0	3.7	0.4	0.0	99.0	10.5	1.6	0.2	4742.2	504.6	49.4	5.3	1.94E-03	2.75E-04	2.19E-01	3.10E-02
16	155.1		189.6	20.2	10.0	1.1	8315.8	884.9	234.6	25.0	34.2	3.6	0.4	0.0	104.1	11.1	1.7	0.2	4848.0	515.9	50.5	5.4	1.83E-03	2.58E-04	2.18E-01	3.04E-02
16	155.1		199.4	21.2	10.5	1.1	8372.7	891.0	236.2	25.1	30.4	3.2	0.4	0.0	41.6	4.4	0.7	0.1	4710.4	501.2	49.0	5.2	1.61E-03	2.28E-04	2.08E-01	2.94E-02
16	155.1		219.0	23.3	11.5	1.2	8361.1	889.7	235.8	25.1	29.1	3.1	0.4	0.0	41.0	4.4	0.7	0.1	4658.6	495.7	48.5	5.2	1.54E-03	2.18E-04	2.06E-01	2.91E-02
16	155.1		187.4	19.9	9.9	1.0	8486.4	903.1	239.4	25.5	35.1	3.7	0.4	0.0	109.9	11.7	1.8	0.1	4943.9	526.1	51.5	5.5	1.84E-03	2.60E-04	2.15E-01	3.04E-02
16	155.1		200.4	21.3	10.6	1.1	8691.6	924.9	245.2	26.1	30.8	3.2	0.4	0.0	72.5	7.7	1.2	0.1	4869.9	518.2	50.7	5.4	1.57E-03	2.23E-04	2.07E-01	2.92E-02
16	155.1		221.1	23.5	11.6	1.2	8413.3	895.3	237.3	25.3	29.6	3.2	0.4	0.0	31.0	3.3	0.5	0.1	4658.0	495.7	48.5	5.2	1.56E-03	2.21E-04	2.04E-01	2.89E-02
16	155.1		190.3	20.2	10.0	1.1	7621.9	811.1	215.0	22.9	32.9	3.5	0.4	0.0	117.3	12.5	1.9	0.2	4711.9	501.4	49.1	5.2	1.92E-03	2.71E-04	2.18E-01	3.23E-02
16	155.1		191.9	20.4	10.1	1.1	8399.4	893.8	236.9	25.2	30.1	3.2	0.4	0.0	38.9	4.1	0.6	0.1	4958.5	527.6	51.6	5.5	1.59E-03	2.25E-04	2.18E-01	3.08E-02
16	155.1		234.1	24.9	12.3	1.3	8374.1	891.1	236.2	25.1	29.1	3.1	0.4	0.0	30.9	3.3	0.5	0.1	4848.3	515.9	50.5	5.4	1.54E-03	2.18E-04	2.14E-01	3.02E-02
16	155.1		177.1	18.9	9.3	1.0	8391.3	892.9	236.7	25.2	35.9	3.8	0.4	0.0	122.1	13.0	2.0	0.2	5091.9	541.8	53.0	5.6	1.90E-03	2.68E-04	2.17E-01	3.17E-02
16	155.1		191.5	20.4	10.1	1.1	8599.8	915.1	242.6	25.8	31.1	3.3	0.4	0.0	52.6	5.6	0.8	0.1	5037.4	536.8	52.6	5.6	1.61E-03	2.27E-04	2.17E-01	3.06E-02
16	155.1		236.8	25.2	12.5	1.3	8748.3	930.9	246.8	26.3	30.9	3.3	0.4	0.0	33.3	3.5	0.5	0.1	5044.8	536.8	52.5	5.6	1.57E-03	2.22E-04	2.13E-01	3.01E-02
16	155.1		203.9	21.7	10.7	1.1	8280.8	881.2	233.6	24.9	33.2	3.5	0.4	0.0	114.9	12.2	1.9	0.2	5038.2	536.1	52.4	5.6	1.78E-03	2.52E-04	2.25E-01	3.17E-02
16	155.1		189.4	20.2	10.0	1.1	7852.0	835.5	221.5	23.6	30.1	3.2	0.4	0.0	66.0	7.0	1.1	0.1	4702.0	500.4	48.9	5.2	1.70E-03	2.41E-04	2.21E-01	3.12E-02
16	155.1		217.4	23.1	11.4	1.2	8577.0	912.7	241.9	25.7	29.5	3.1	0.4	0.0	58.7	6.2	0.9	0.1	5069.3	539.4	52.8	5.6	1.53E-03	2.16E-04	2.18E-01	3.08E-02
17	164.3		231.7	24.7	12.2	1.3	8799.9	936.4	248.2	26.4	36.6	3.9	0.5	0.0	127.9	13.6	2.1	0.2	5262.8	560.0	54.8	5.8	1.85E-03	2.61E-04	2.21E-01	3.12E-02
18	176.6	OPA (sandy)	207.3	22.1	10.9	1.2	9359.6	996.0	264.0	28.1	34.2	3.6	0.4	0.0	58.0	6.2	0.9	0.1	5661.5	602.5	58.9	6.3	1.62E-03	2.29E-04	2.23E-01	3.16E-02
18	176.6		215.1	22.9	11.3	1.2	8297.1	882.9	234.0	24.9	29.7	3.2	0.4	0.0	55.3	5.9	0.9	0.1	4909.8	522.5	51.1	5.4	1.59E-03	2.25E-04	2.18E-01	3.09E-02
18	176.6		204.1	21.7	10.7	1.1	10046.0	1069.0	283.4	30.2	30.9	3.3	0.4	0.0	644.8	68.6	10.4	1.1	3579.7	380.9	37.3	4.0	1.36E-03	1.94E-04	1.32E-01	1.86E-02
18	176.6	OPA (shaly)	479.2	51.0	25.2	2.7	10971.1	1167.7	309.5	32.9	79.8	8.5	1.0	0.1	209.3	22.3	3.4	0.4	7517.5	800.1	78.3	8.3	3.23E-03	4.56E-04	2.53E-01	3.58E-02
18	176.6		390.5	41.6	20.6	2.2	12212.8	1299.6	344.5	36.7	47.4	5.0	0.6	0.1	74.8	8.0	1.2	0.1	8148.4	867.1	84.8	9.0	1.72E-03	2.44E-04	2.46E-01	3.48E-02
18	176.6		317.0	33.7	16.7	1.8	12671.2	1348.4	357.4	38.0	44.9	4.8	0.6	0.1	47.5	5.1	0.8	0.1	8163.6	868.7	85.0	9.0	1.57E-03	2.22E-04	2.38E-01	3.36E-02
18	176.6		170.8	18.2	9.0	1.0	12012.6	1278.3	338.8	36.1	40.4	4.3	0.5	0.1	104.1	11.1	1.7	0.2	7226.7	769.0	75.2	8.0	1.49E-03	2.11E-04	2.22E-01	3.14E-02
18	176.6		341.8	36.4	18.0	1.9	12641.0	1345.2	356.6	37.9	43.1	4.6	0.5	0.1	43.1	4.6	0.7	0.1	8290.2	882.2	86.3	9.2	1.58E-03	2.23E-04	2.42E-01	3.42E-02
18	176.6		203.9	21.7	10.7	1.1	13428.6	1429.0	378.8	40.3	44.0	4.8	0.5	0.1	31.1	3.3	0.5	0.1	8104.3	862.4	84.4	9.0	1.52E-03	2.15E-04	2.23E-01	3.15E-02
18	176.6		287.5	30.6	15.1	1.6	13841.9	1473.0	390.4	41.5	47.4	5.0	0.6	0.1	187.3	19.9	3.0	0.3	8162.6	868.6	85.0	9.0	1.52E-03	2.15E-04	2.18E-01	3.08E-02
18	176.6		300.9	32.0	15.8	1.7	13788.1	1467.3	388.9	41.4	47.9	5.1	0.6	0.1	50.4	5.4	0.8	0.1	8298.3	883.1	86.4	9.2	1.53E-03	2.17E-04	2.23E-01	3.14E-02
18	176.6		306.8	32.6	16.1	1.7	13425.0	1428.6	378.7	40.3	47.8	5.0	0.6	0.1	43.4	4.6	0.7	0.1	8112.4	863.3	84.5	9.0	1.58E-03	2.23E-04	2.23E-01	3.15E-02
19	185.97	OPA (carb-rich)	184.1	19.6	9.7	1.0	12572.7	1337.9	354.6	37.7	41.8	4.5	0.5	0.1	355.6	37.8	5.7	0.6	6329.8	673.6	65.9	7.0	1.48E-03	2.10E-04	1.86E-01	2.63E-02
20	196.08		228.6	24.3	12.0	1.3	13839.4	1472.7	390.4	41.5	42.6	4.5	0.5	0.1	501.0	53.3	8.1	0.9	4794.7	510.2	49.9	5.3	1.36E-03	1.94E-04	1.28E-01	1.81E-02
21	204.73		260.0	27.7	13.7	1.5	13634.6	1450.9	384.6	40.9	44.5	4.7	0.6	0.1	69.1	7.4	1.1	0.1	6059.3	644.8	63.1	6.7	1.45E-03	2.05E-04	1.64E-01	2.32E-02
22	213.23	OPA (shaly)	212.9	22.7	11.2	1.2	13941.2	1483.6	393.2	41.8	43.0	4.6	0.5	0.1	390.5	41.6	6.3	0.7	5865.9	624.2	61.1	6.5	1.37E-03	1.95E-04	1.55E-01	2.20E-02
23	224.48		301.5	32.1	15.9	1.7	13898.6	1479.3	392.0	41.7	43.5	4.6	0.5	0.1	517.2	55.0	8.3	0.9	6662.3	709.1	69.4	7.4	1.39E-03	1.97E-04	1.77E-01	2.50E-02
25	225.45		256.5	27.3	13.5	1.4	15382.7	1636.9	433.9	46.2	45.8	4.9	0.6	0.1	423.7	45.1	6.8	0.7	15014.7	1597.8	156.3	16.6	1.26E-03	1.88E-04	3.60E-01	5.09E-02
26	230.6		262.4	27.9	13.8	1.5	16121.8	1715.6	454.7	48.4	45.9	4.9	0.6	0.1	421.4	44.8	6.8	0.7	21801.3	2320.0	227.0	24.2	1.26E-03	1.80E-04	4.99E-01	7.06E-02
24	235.41		339.5	36.1	17.9	1.9	14573.4	1550.8	411.1	43.7	46.8	5.0	0.6	0.1	77.0	8.2	1.2	0.1	6541.7	696.1	68.1	7.2	1.42E-03	2.03E-04	1.66E-01	2.34E-02
27	238.15	Staffelegg (marly limestone)	224.9	26.3	11.8	1.4	27288.0	3194.9	769.7	90.1	47.6	5.6	0.6	0.1	4264.6	499.3	68.8	8.1	19426.0	2274.4	202.2	23.7	7.74E-04	1.10E-04	2.63E-01	3.71E-02
28	241.8		111.3	11.8	5.9	0.6	24107.7	2565.6	680.0	72.4	29.9	3.2	0.4	0.0	4488.6	477.7	72.4	7.7	21902.1	2330.9	228.0	24.3	5.50E-04	7.82E-05	3.35E-01	4.74E-02
29	243.9		45.6	4.8	2.4	0.3	14282.7	1519.9	402.9	42.9	44.4	4.7	0.6	0.1	52.7	5.6	0.9	0.1	139989.9	14897.4	1457.3	155.1	1.38E-03	1.96E-04	3.62E+00	5.11E-01

AII-3 Cationic Exchange Capacity measurements

AII-3-1 Raw data

Concentrations in final exchange solution

Sample	Distance	Formation	M_{solid}	σ_{Msolid}	M_{liquid}	$\sigma_{Mliquid}$	S/L	$\sigma_{S/L}$	pH	Cs^+ ppm	σ_{Cs+}	mmol/L	σ_{Cs+}	Ca^{2+} ppm	σ_{Ca2+}	mmol/l	σ_{Ca2+}	K^+ ppm	σ_{K+}	mmol/l	σ_{K+}	Mg^{2+} ppm	σ_{Mg2+}	mmol/l	σ_{Mg2+}	Na^+ ppm	σ_{Na+}	mmol/l	σ_{Na+}	Sr^{2+} ppm	σ_{Sr2+}	mmol/l	σ_{Sr2+}
			g	g	g	g				ppm	/	mmol/L		ppm		mmol/l	<0.002	ppm		mmol/l	0.0	ppm		mmol/l	<0.002	ppm		mmol/l	<0.0152	ppm	/	mmol/l	/

(Full numeric data table — see source for complete values.)

Concentrations in final exchange solution

Sample	Distance	Formation	M_{solid}	σ_{Msolid}	M_{liquid}	$\sigma_{Mliquid}$	S/L	$\sigma_{S/L}$	pH	Co^{3+}	Ca^{2+}	K^+	Mg^{2+}	Na^+	Sr^{2+}

(Full numeric data table — see source for complete values.)

Sample	Distance [m]	Formation	M_{solid} [g]	σ_{Msolid} [g]	M_{liquid} [g]	$\sigma_{Mliquid}$ [g]	WCdry	S/L	σ_{SL}	pH	Ca^{2+} ppm	σ_{Ca2+}	Ca^{2+} mmol/l	σ_{Ca2+}	K^+ ppm	σ_{K+}	K^+ mmol/l	σ_{K+}	Mg^{2+} ppm	σ_{Mg2+}	Mg^{2+} mmol/l	σ_{Mg2+}	Mg^{2+} meq/100g	σ_{Mg2+}	Na^+ ppm	σ_{Na+}	Na^+ mmol/l	σ_{Na+}	Sr^{2+} ppm	σ_{Sr2+}	Sr^{2+} mmol/l	σ_{Sr2+}
Blank											1.9	0.2	0.0	0.0	2.0	0.2	0.1	0.0	< 0.08	0.2	< 0.003	0.0	0.1	0.0	0.7	0.1	0.0	0.0	< 0.08	0.0	< 0.0009	/
1	5.8	Hauptrogenstein (limestone)	2.012	0.007	14.995	0.007	2.81%	0.13	4.71E-04	9.36	9.41	0.9	0.2	0.0	4.8	0.5	0.1	0.0	2.1	0.2	0.1	0.0	0.1	0.0	1.7	0.2	0.1	0.0	0.1	0.0	0.0	0.0
2	14.84		2.007	0.007	14.99	0.007	1.03%	0.13	4.71E-04	9.67	9.82	1.0	0.2	0.0	3.4	0.3	0.1	0.0	1.2	0.1	0.0	0.0	0.1	0.0	2.1	0.2	0.1	0.0	0.2	0.0	0.0	0.0
3	24.98		2.017	0.007	14.982	0.007	0.86%	0.13	4.71E-04	9.01	76.26	7.6	1.9	0.2	5.5	0.6	0.1	0.0	4.6	0.5	0.2	0.0	0.3	0.0	2.5	0.2	0.1	0.0	0.9	0.1	0.0	0.0
4	35.35		2.002	0.007	15.057	0.007	1.40%	0.13	4.69E-04	9.68	9.01	0.9	0.2	0.0	6.1	0.6	0.2	0.0	1.8	0.2	0.1	0.0	0.1	0.0	2.2	0.2	0.1	0.0	0.6	0.1	0.0	0.0
5	43.27	Passwang Formation (marl and limestone)	1.998	0.007	15.005	0.007	5.77%	0.13	4.71E-04	9.75	6.38	0.6	0.2	0.0	7.3	0.7	0.2	0.0	2.5	0.3	0.1	0.0	0.2	0.0	3.3	0.3	0.1	0.0	1.0	0.1	0.0	0.0
6	61.75		2.012	0.007	14.993	0.007	4.64%	0.13	4.71E-04	9.24	11.75	1.2	0.3	0.0	6.9	0.7	0.2	0.0	4.6	0.5	0.2	0.0	0.3	0.0	6.6	0.7	0.3	0.0	1.4	0.1	0.0	0.0
7	69.76		1.997	0.007	15.115	0.007	3.38%	0.13	4.67E-04	9.62	6.61	0.7	0.2	0.0	6.8	0.7	0.2	0.0	2.1	0.2	0.1	0.0	0.1	0.0	7.4	0.7	0.3	0.0	1.2	0.1	0.0	0.0
8	74.78		2.005	0.007	15.022	0.007	4.89%	0.13	4.70E-04	9.73	3.43	0.3	0.1	0.0	5.9	0.6	0.2	0.0	1.3	0.1	0.0	0.0	0.1	0.0	17.0	1.7	0.7	0.1	0.8	0.1	0.0	0.0
9	84.73		2.003	0.007	14.989	0.007	6.14%	0.13	4.71E-04	9.59	5.13	0.5	0.1	0.0	12.0	1.2	0.3	0.0	1.0	0.1	0.0	0.0	0.1	0.0	19.4	1.9	0.8	0.1	0.7	0.1	0.0	0.0
10	96.7	OPA (sandy)	1.999	0.007	15.014	0.007	5.63%	0.13	4.70E-04	9.39	6.60	0.7	0.2	0.0	9.5	0.9	0.2	0.0	0.9	0.1	0.0	0.0	0.1	0.0	27.8	2.8	1.2	0.1	0.8	0.1	0.0	0.0
11	107		2.009	0.007	14.994	0.007	5.44%	0.13	4.71E-04	10.01	1.14	0.1	0.0	0.0	5.9	0.6	0.2	0.0	0.4	0.0	0.0	0.0	0.0	0.0	54.4	5.4	2.4	0.2	0.1	0.0	0.0	0.0
12	116.21		1.998	0.007	15.017	0.007	5.17%	0.13	4.70E-04	10.03	1.33	0.1	0.0	0.0	5.1	0.5	0.1	0.0	0.3	0.0	0.0	0.0	0.0	0.0	58.7	5.9	2.6	0.3	0.1	0.0	0.0	0.0
13	125.12	OPA (shaly)	2.007	0.007	15.012	0.007	5.21%	0.13	4.70E-04	10.01	1.18	0.1	0.0	0.0	6.1	0.6	0.2	0.0	0.4	0.0	0.0	0.0	0.0	0.0	60.0	6.0	2.6	0.3	< 0.08	/	< 0.0009	/
14	136.33		2.013	0.007	15.027	0.007	5.88%	0.13	4.70E-04	10.01	1.25	0.1	0.0	0.0	5.0	0.5	0.1	0.0	0.2	0.0	0.0	0.0	0.0	0.0	70.6	7.1	3.1	0.3	< 0.08	/	< 0.0009	/
15	141.1		2.009	0.007	14.984	0.007	5.81%	0.13	4.71E-04	9.87	1.47	0.1	0.0	0.0	7.8	0.8	0.2	0.0	0.3	0.0	0.0	0.0	0.0	0.0	81.0	8.1	3.5	0.4	< 0.08	/	< 0.0009	/
16	155.1		2.003	0.007	15.002	0.007	6.06%	0.13	4.71E-04	9.99	1.19	0.1	0.0	0.0	4.9	0.5	0.1	0.0	0.3	0.0	0.0	0.0	0.0	0.0	82.2	8.2	3.6	0.3	< 0.08	/	< 0.0009	/
17	164.3	OPA (sandy)	2.003	0.007	14.989	0.007	5.50%	0.13	4.71E-04	10.02	1.06	0.1	0.0	0.0	5.5	0.5	0.1	0.0	0.3	0.0	0.0	0.0	0.0	0.0	78.0	7.8	3.4	0.3	< 0.08	/	< 0.0009	/
18	176.6	OPA (sandy)	1.993	0.007	14.999	0.007	4.28%	0.13	4.71E-04	10.06	1.09	0.1	0.0	0.0	4.4	0.4	0.1	0.0	0.3	0.0	0.0	0.0	0.0	0.0	79.5	8.0	3.5	0.3	< 0.08	/	< 0.0009	/
19	185.97	OPA (carbonate-rich)	2.004	0.007	15.278	0.007	5.56%	0.13	4.62E-04	10.01	1.81	0.2	0.0	0.0	4.8	0.5	0.1	0.0	0.3	0.0	0.0	0.0	0.0	0.0	70.7	7.1	3.1	0.3	0.1	0.0	0.0	0.0
20	196.08	OPA (shaly)	2.003	0.007	15.005	0.007	6.04%	0.13	4.71E-04	9.96	1.14	0.1	0.0	0.0	4.9	0.5	0.1	0.0	0.2	0.0	0.0	0.0	0.0	0.0	90.0	9.0	3.9	0.4	< 0.08	/	< 0.0009	/
21	204.73		2.014	0.007	14.992	0.007	6.03%	0.13	4.71E-04	9.96	1.17	0.1	0.0	0.0	4.7	0.5	0.1	0.0	0.2	0.0	0.0	0.0	0.0	0.0	94.6	9.5	4.1	0.4	< 0.08	/	< 0.0009	/
22	213.23		2.001	0.007	14.981	0.007	6.44%	0.13	4.72E-04	9.96	1.22	0.1	0.0	0.0	5.0	0.5	0.1	0.0	0.2	0.0	0.0	0.0	0.0	0.0	97.0	9.7	4.2	0.4	< 0.08	/	< 0.0009	/
23	224.48		1.996	0.007	14.977	0.007	5.57%	0.13	4.72E-04	10.05	1.40	0.1	0.0	0.0	4.9	0.5	0.1	0.0	0.2	0.0	0.0	0.0	0.0	0.0	100.2	10.0	4.4	0.4	< 0.08	/	< 0.0009	/
25	225.45		2.008	0.007	14.99	0.007	9.55%	0.13	4.71E-04	9.99	1.25	0.1	0.0	0.0	5.6	0.6	0.1	0.0	0.2	0.0	0.0	0.0	0.0	0.0	104.2	10.4	4.5	0.5	< 0.08	/	< 0.0009	/
26	230.6		2.007	0.007	14.984	0.007	9.90%	0.13	4.67E-04	9.93	0.47	0.0	0.0	0.0	2.8	0.3	0.1	0.0	0.1	0.0	0.0	0.0	0.0	0.0	38.9	3.9	1.7	0.2	< 0.08	/	< 0.0009	/
24	235.41		2.006	0.007	15.115	0.007	5.89%	0.13	4.71E-04	9.83	1.90	0.2	0.0	0.0	10.7	1.1	0.3	0.0	0.4	0.0	0.0	0.0	0.0	0.0	119.7	12.0	5.2	0.5	< 0.08	/	< 0.0009	/
27	238.15	Staffelegg (marly limestone)	2.015	0.007	14.986	0.007	6.57%	0.13	4.71E-04	9.98	2.62	0.3	0.1	0.0	10.1	1.0	0.3	0.0	0.4	0.0	0.0	0.0	0.0	0.0	65.9	6.6	2.9	0.3	< 0.08	/	< 0.0009	/
28	241.8		1.998	0.007	14.999	0.007	9.42%	0.13	4.71E-04	9.88	3.18	0.3	0.1	0.0	11.2	1.1	0.3	0.0	0.6	0.1	0.0	0.0	0.0	0.0	79.4	7.9	3.5	0.3	0.1	0.0	0.0	0.0
29	243.9		2.011	0.007	15.019	0.007	10.55%	0.13	4.70E-04	8.45	110.46	11.0	2.8	0.3	25.9	2.6	0.7	0.1	15.4	1.5	0.6	0.0	0.9	0.1	157.9	15.8	6.9	0.7	3.2	0.3	0.0	0.0

AII-3-2 Calculated data

CsCl

Sample	Distance (m)	Formation	Ca²⁺ meq/100g	σCa2+	E_Ca	σE_Ca	K⁺ meq/100g	σK+	E_K	σE_K	Mg²⁺ meq/100g	σMg2+	E_Mg	σE_Mg	Na⁺ meq/100g	σNa+	E_Na	σE_Na	Sr²⁺ meq/100g	σSr2+	E_Sr	σE_Sr	Cs⁺ meq/100g	σCs+	SEC meq/100g	σSEC
1	5.8	Hauptrogenstein (limestone)	4.07	0.44	0.74	0.10	0.53	0.07	0.10	0.01	0.81	0.20	0.15	0.04	0.03	0.02	0.01	0.00	0.02	0.00	0.00	0.00	7.44	3.19	5.47	0.49
2	14.84		0.55	0.10	0.82	0.21	0.05	0.02	0.07	0.03	0.04	0.07	0.06	0.11	0.02	0.02	0.05	0.03	0.00	0.00	0.01	0.00	2.41	3.52	0.68	0.12
3	24.98		0.56	0.44	0.96	1.16	0.04	0.03	0.08	0.08	-0.05	0.29	-0.09	0.50	0.00	0.02	0.05	0.06	0.00	0.00	0.03	0.01	2.45	3.50	0.58	0.52
4	35.35		0.99	0.13	0.70	0.13	0.21	0.04	0.15	0.04	0.15	0.12	0.11	0.09	0.03	0.02	0.02	0.02	0.03	0.00	0.02	0.00	2.87	3.47	1.41	0.19
5	43.27	Passwang Formation (marl and limestone)	2.43	0.26	0.50	0.07	1.28	0.15	0.26	0.04	0.89	0.23	0.18	0.05	0.04	0.04	0.02	0.01	0.02	0.02	0.04	0.01	4.89	3.34	4.88	0.38
6	61.75		3.32	0.37	0.62	0.09	0.62	0.08	0.12	0.02	1.07	0.35	0.20	0.07	0.08	0.02	0.02	0.01	0.02	0.02	0.03	0.01	5.90	3.31	5.33	0.53
7	69.76		2.25	0.25	0.61	0.09	0.47	0.07	0.13	0.02	0.62	0.18	0.17	0.05	0.09	0.04	0.04	0.02	0.21	0.02	0.06	0.01	4.40	3.40	3.72	0.33
8	74.78		3.76	0.39	0.55	0.07	0.76	0.09	0.11	0.02	1.39	0.25	0.20	0.04	0.22	0.06	0.06	0.03	0.53	0.05	0.08	0.01	7.43	3.19	6.88	0.52
9	84.73		1.98	0.21	0.57	0.08	0.70	0.11	0.20	0.04	0.55	0.16	0.16	0.04	0.19	0.02	0.06	0.01	0.19	0.02	0.06	0.01	3.03	3.48	3.51	0.33
10	96.7		2.05	0.23	0.66	0.11	0.46	0.08	0.15	0.03	0.41	0.10	0.13	0.03	0.26	0.01	0.08	0.08	0.16	0.02	0.05	0.01	2.03	3.53	3.11	0.36
11	107.00	OPA (sandy)	3.49	0.35	0.50	0.07	1.24	0.14	0.18	0.03	1.20	0.20	0.17	0.03	0.62	0.11	0.09	0.09	0.25	0.03	0.04	0.01	8.52	3.13	7.03	0.75
12	116.21		3.34	0.34	0.53	0.08	0.93	0.11	0.15	0.02	1.06	0.17	0.17	0.03	0.65	0.12	0.10	0.11	0.20	0.02	0.03	0.01	7.75	3.17	6.29	0.76
13	125.12		3.36	0.34	0.49	0.08	1.26	0.14	0.18	0.03	1.03	0.17	0.15	0.03	0.69	0.14	0.10	0.10	0.17	0.02	0.03	0.00	8.54	3.15	6.81	0.80
14	136.33		3.71	0.37	0.48	0.08	1.32	0.15	0.17	0.03	1.21	0.20	0.16	0.03	0.83	0.16	0.11	0.10	0.18	0.02	0.02	0.00	9.86	3.05	7.70	0.95
15	141.1	OPA (shaly)	3.46	0.35	0.46	0.08	1.33	0.15	0.18	0.03	1.42	0.23	0.19	0.04	0.90	0.14	0.12	0.12	0.15	0.02	0.02	0.00	9.14	3.10	7.50	1.00
16	155.1		3.94	0.39	0.48	0.08	1.16	0.13	0.14	0.02	1.25	0.20	0.15	0.03	1.00	0.19	0.12	0.12	0.17	0.02	0.02	0.00	10.54	3.01	8.15	1.10
17	164.3		3.90	0.39	0.45	0.07	1.47	0.16	0.17	0.03	1.05	0.17	0.12	0.03	0.97	0.20	0.11	0.12	0.15	0.01	0.02	0.00	10.97	3.00	8.62	1.12
18	176.6	OPA (sandy)	3.53	0.35	0.47	0.08	1.25	0.14	0.17	0.03	0.95	0.16	0.13	0.03	1.03	0.23	0.20	0.13	0.14	0.01	0.02	0.00	9.76	3.07	7.47	1.05
19	185.97	OPA (carb-rich)	2.32	0.23	0.59	0.13	0.62	0.08	0.16	0.04	0.55	0.09	0.14	0.04	0.70	0.08	0.18	0.18	0.14	0.01	0.04	0.01	5.39	3.34	3.94	0.75
20	196.08	OPA (shaly)	4.27	0.43	0.47	0.08	1.18	0.13	0.13	0.02	1.36	0.22	0.15	0.03	1.16	0.23	0.13	0.13	0.12	0.01	0.01	0.00	12.45	2.92	9.09	1.26
21	204.73		3.91	0.39	0.46	0.08	1.40	0.15	0.16	0.03	1.03	0.17	0.12	0.03	1.18	0.23	0.14	0.14	0.12	0.01	0.01	0.00	11.38	3.01	8.51	1.26
22	213.23		3.88	0.39	0.47	0.08	1.48	0.16	0.18	0.03	1.00	0.16	0.12	0.03	1.16	0.21	0.14	0.14	0.12	0.01	0.01	0.00	11.29	2.98	8.29	1.25
23	224.48		3.91	0.39	0.47	0.09	1.45	0.16	0.18	0.03	1.02	0.17	0.12	0.03	1.20	0.21	0.15	0.15	0.11	0.01	0.01	0.00	11.44	2.98	8.38	1.29
25	225.45		4.17	0.42	0.46	0.08	1.35	0.15	0.15	0.03	1.33	0.22	0.15	0.03	1.26	0.22	0.14	0.14	0.12	0.01	0.01	0.00	12.93	2.92	9.05	1.36
26	230.6		3.90	0.39	0.36	0.05	1.51	0.16	0.14	0.02	1.26	0.20	0.12	0.02	1.06	0.36	0.10	0.11	0.10	0.01	0.01	0.00	11.81	2.99	10.73	1.16
24	235.41		3.89	0.39	0.49	0.10	1.35	0.16	0.17	0.04	1.16	0.19	0.15	0.04	1.32	0.17	0.17	0.18	0.10	0.01	0.01	0.00	11.30	3.01	7.98	1.40
27	238.15		2.10	0.22	0.63	0.14	0.65	0.09	0.19	0.05	0.52	0.09	0.16	0.04	0.60	0.01	0.18	0.27	0.04	0.00	0.01	0.00	5.18	3.36	3.35	0.65
27	238.15	Staffelegg (marly limestone)	1.89	0.30	0.51	0.16	0.61	0.12	0.16	0.06	0.40	0.08	0.11	0.04	0.97	0.21	0.21	0.21	0.04	0.00	0.01	0.00	4.40	3.09	3.73	1.02
28	241.8		2.58	0.27	0.61	0.13	0.76	0.11	0.18	0.04	0.74	0.13	0.18	0.05	0.06	0.17	0.06	0.06	0.06	0.01	0.02	0.01	5.68	3.32	4.23	0.80
29	243.9		5.79	1.07	0.92	0.33	0.65	0.16	0.10	0.04	0.51	0.98	0.08	0.16	-0.75	0.22	-0.12	0.22	0.09	0.02	0.01	0.01	8.86	3.13	6.32	1.98

CoHex

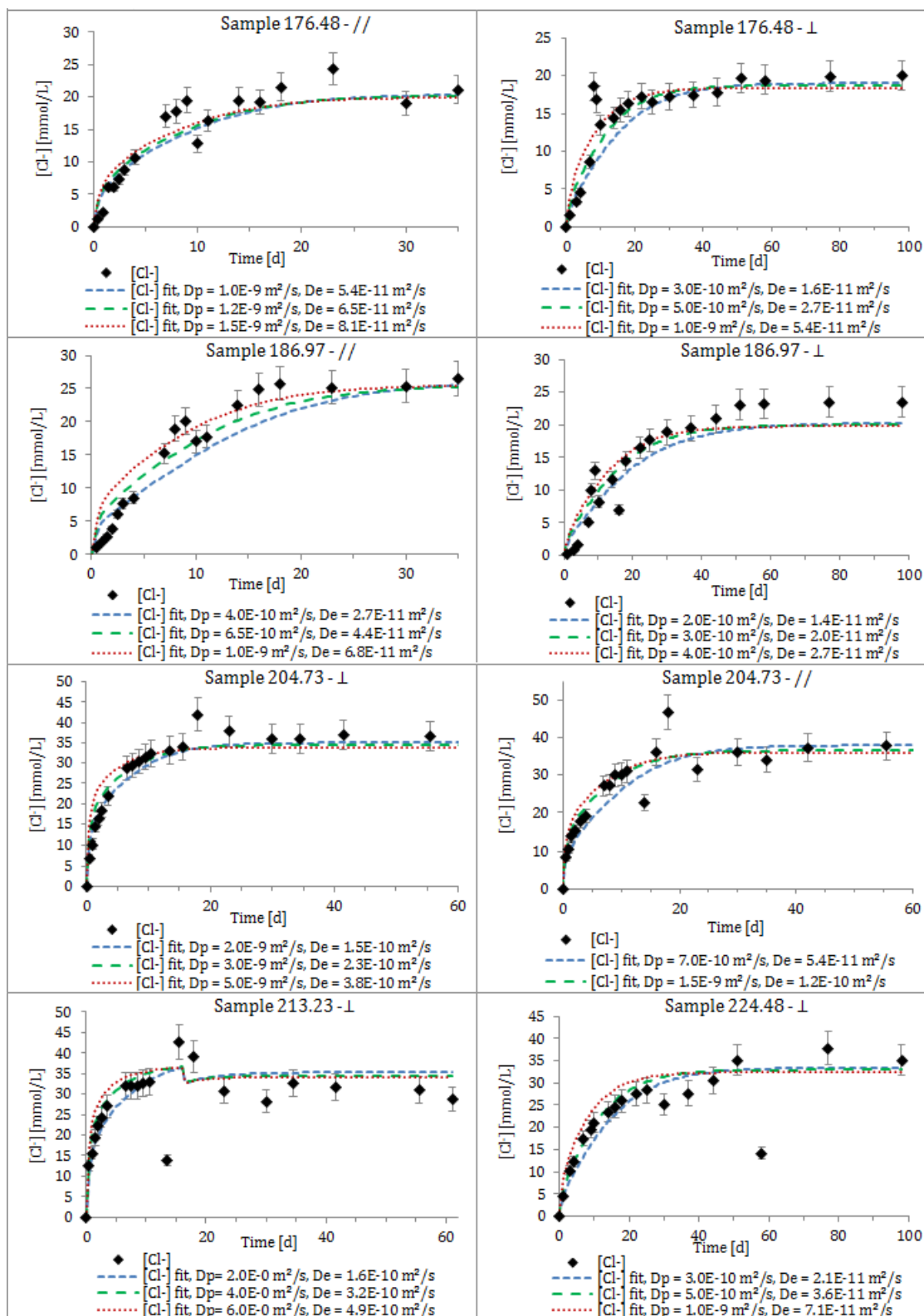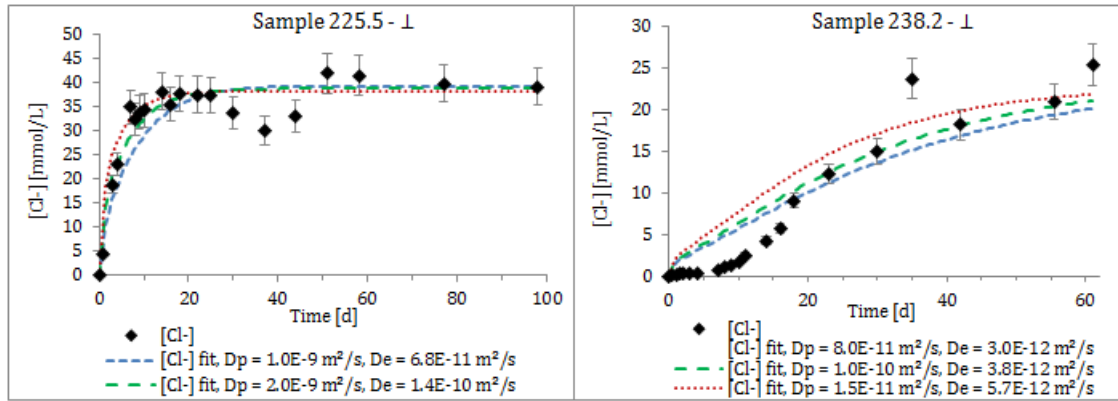| Sample	Distance (m)	Formation	Ca²⁺ meq/100g	σCa2+	E_Ca	σE_Ca	K⁺ meq/100g	σK+	E_K	σE_K	Mg²⁺ meq/100g	σMg2+	E_Mg	σE_Mg	Na⁺ meq/100g	σNa+	E_Na	σE_Na	Sr²⁺ meq/100g	σSr2+	E_Sr	σE_Sr	Co³⁺ meq/100g	σCo3+	SEC meq/100g	σSEC
1	5.8	Hauptrogenstein (limestone)	4.61	0.50	0.71	0.10	0.24	0.09	0.04	0.01	1.59	0.24	0.24	0.03	0.03	0.02	0.01	0.00	0.03	0.00	0.00	0.00	8.64	3.13	6.49	0.54
2	14.84		1.02	0.15	0.86	0.16	-0.02	0.03	-0.02	0.03	0.15	0.12	0.12	0.03	0.02	0.02	0.03	0.02	0.01	0.00	0.01	0.00	0.92	3.62	1.18	0.15
3	24.98		0.78	0.46	0.95	0.78	-0.04	0.04	-0.04	0.05	0.05	0.19	0.06	0.06	0.02	0.02	0.03	0.03	0.01	0.00	0.03	0.00	2.43	3.54	0.82	0.46
4	35.35		1.47	0.19	0.74	0.12	0.06	0.06	0.03	0.02	0.38	0.05	0.19	0.05	0.05	0.02	0.02	0.02	0.05	0.01	0.06	0.01	3.19	3.48	1.99	0.20
5	43.27	Passwang Formation (marl and limestone)	2.67	0.29	0.53	0.07	0.33	0.12	0.07	0.02	1.74	0.34	0.34	0.05	0.23	0.04	0.04	0.01	0.02	0.04	0.04	0.01	7.97	3.22	5.04	0.37
6	61.75		3.42	0.36	0.55	0.08	0.34	0.12	0.06	0.02	2.14	0.24	0.35	0.05	0.22	0.07	0.04	0.01	0.03	0.06	0.06	0.01	11.80	3.06	6.17	0.48
7	69.76		2.30	0.26	0.58	0.08	0.25	0.10	0.06	0.02	1.15	0.13	0.29	0.04	0.24	0.08	0.06	0.02	0.03	0.06	0.09	0.01	6.97	3.27	3.99	0.31
8	74.78		3.68	0.38	0.47	0.06	0.55	0.15	0.07	0.02	2.60	0.27	0.34	0.04	0.67	0.19	0.09	0.03	0.07	0.09	0.01	0.01	14.22	2.86	7.76	0.53
9	84.73		2.12	0.24	0.66	0.11	0.41	0.11	0.11	0.04	0.87	0.09	0.23	0.03	0.21	0.12	0.06	0.02	0.21	0.02	0.06	0.01	7.52	3.21	3.73	0.35
10	96.7		2.12	0.24	0.66	0.11	0.23	0.11	0.07	0.03	0.54	0.06	0.17	0.03	0.18	0.27	0.04	0.09	0.18	0.02	0.06	0.01	6.49	3.27	3.20	0.38
11	107.00	OPA (sandy)	4.39	0.45	0.45	0.09	1.00	0.24	0.10	0.03	1.81	0.18	0.19	0.04	0.69	0.28	0.07	0.07	0.28	0.03	0.03	0.01	16.60	2.77	9.77	1.75
12	116.21		3.83	0.39	0.44	0.10	0.84	0.21	0.10	0.03	1.72	0.17	0.20	0.04	0.70	0.24	0.12	0.08	0.24	0.02	0.02	0.01	15.01	2.84	8.73	1.72
13	125.12		4.32	0.44	0.44	0.09	1.14	0.27	0.12	0.04	1.59	0.16	0.16	0.03	0.76	0.21	0.14	0.08	0.21	0.02	0.02	0.00	16.72	2.77	9.71	1.82
14	136.33		4.52	0.46	0.42	0.10	1.24	0.29	0.12	0.04	1.72	0.17	0.16	0.04	0.92	0.20	0.16	0.09	0.20	0.02	0.02	0.00	16.90	2.77	10.81	2.21
15	141.1	OPA (shaly)	4.05	0.41	0.39	0.07	1.28	0.31	0.12	0.03	2.63	0.27	0.26	0.04	0.99	0.19	0.15	0.10	0.19	0.02	0.02	0.00	17.21	2.77	10.30	1.40
16	155.1		4.64	0.47	0.41	0.08	1.17	0.27	0.10	0.03	2.02	0.20	0.18	0.04	1.10	0.22	0.19	0.10	0.22	0.02	0.02	0.00	18.22	2.74	11.33	2.04
17	164.3		5.25	0.53	0.40	0.09	1.35	0.31	0.10	0.03	1.96	0.20	0.15	0.03	1.16	0.21	0.20	0.10	0.21	0.02	0.02	0.00	21.16	2.69	13.20	2.69
18	176.6	OPA (sandy)	4.69	0.48	0.40	0.09	1.17	0.27	0.10	0.03	1.95	0.20	0.17	0.04	1.11	0.19	0.20	0.14	0.19	0.02	0.02	0.00	18.67	2.73	11.81	2.43
19	185.97	OPA (carb-rich)	3.06	0.32	0.54	0.10	0.49	0.14	0.09	0.03	1.24	0.13	0.22	0.04	0.77	0.17	0.13	0.11	0.17	0.02	0.03	0.01	11.17	2.99	5.69	0.85
20	196.08	OPA (shaly)	5.61	0.57	0.41	0.09	1.39	0.32	0.10	0.03	1.84	0.19	0.13	0.03	1.33	0.16	0.22	0.11	0.16	0.02	0.02	0.00	21.11	2.69	13.69	2.70
21	204.73		5.38	0.54	0.40	0.09	1.32	0.30	0.10	0.03	1.95	0.20	0.14	0.03	1.40	0.16	0.24	0.11	0.16	0.02	0.02	0.00	20.78	2.67	13.56	2.60
22	213.23		6.26	0.63	0.44	0.09	1.40	0.32	0.10	0.03	1.93	0.19	0.14	0.03	1.37	0.15	0.21	0.10	0.15	0.02	0.02	0.00	20.71	2.68	14.20	2.59
23	224.48		4.92	0.50	0.39	0.09	1.30	0.30	0.11	0.03	2.01	0.20	0.16	0.04	1.35	0.15	0.21	0.12	0.15	0.02	0.02	0.00	20.79	2.70	12.58	2.57
25	225.45		4.95	0.50	0.37	0.08	1.46	0.33	0.11	0.03	2.17	0.22	0.16	0.04	1.44	0.17	0.22	0.12	0.17	0.02	0.02	0.00	21.06	2.65	13.22	2.62
26	230.6		5.23	0.53	0.36	0.05	1.41	0.31	0.10	0.03	2.54	0.26	0.17	0.03	1.26	0.14	0.34	0.09	0.14	0.01	0.01	0.00	17.24	2.80	14.59	1.53
24	235.41		5.61	0.57	0.44	0.07	1.38	0.34	0.11	0.03	2.79	0.28	0.22	0.04	1.55	0.14	0.22	0.12	0.14	0.01	0.01	0.00	16.67	2.81	12.80	1.72
27	238.15		2.61	0.27	0.57	0.11	0.49	0.16	0.11	0.04	1.16	0.12	0.25	0.05	0.64	0.05	0.05	0.14	0.05	0.01	0.01	0.00	8.19	3.17	4.61	0.73
28	241.8	Staffelegg (marly limestone)	3.24	0.34	0.56	0.10	0.56	0.18	0.10	0.03	1.52	0.16	0.26	0.05	0.78	0.06	0.06	0.14	0.07	0.01	0.01	0.00	9.33	3.06	5.79	0.90
29	243.9		7.81	1.26	0.72	0.18	0.64	0.26	0.06	0.03	1.86	0.30	0.17	0.04	1.46	0.01	0.01	0.14	0.12	0.02	0.02	0.00	15.41	2.77	10.78	2.02

AIII-1 Out diffusion

AIII-1-1 Modelling of halide contents evolution in test solutions using HYTEC 3.6
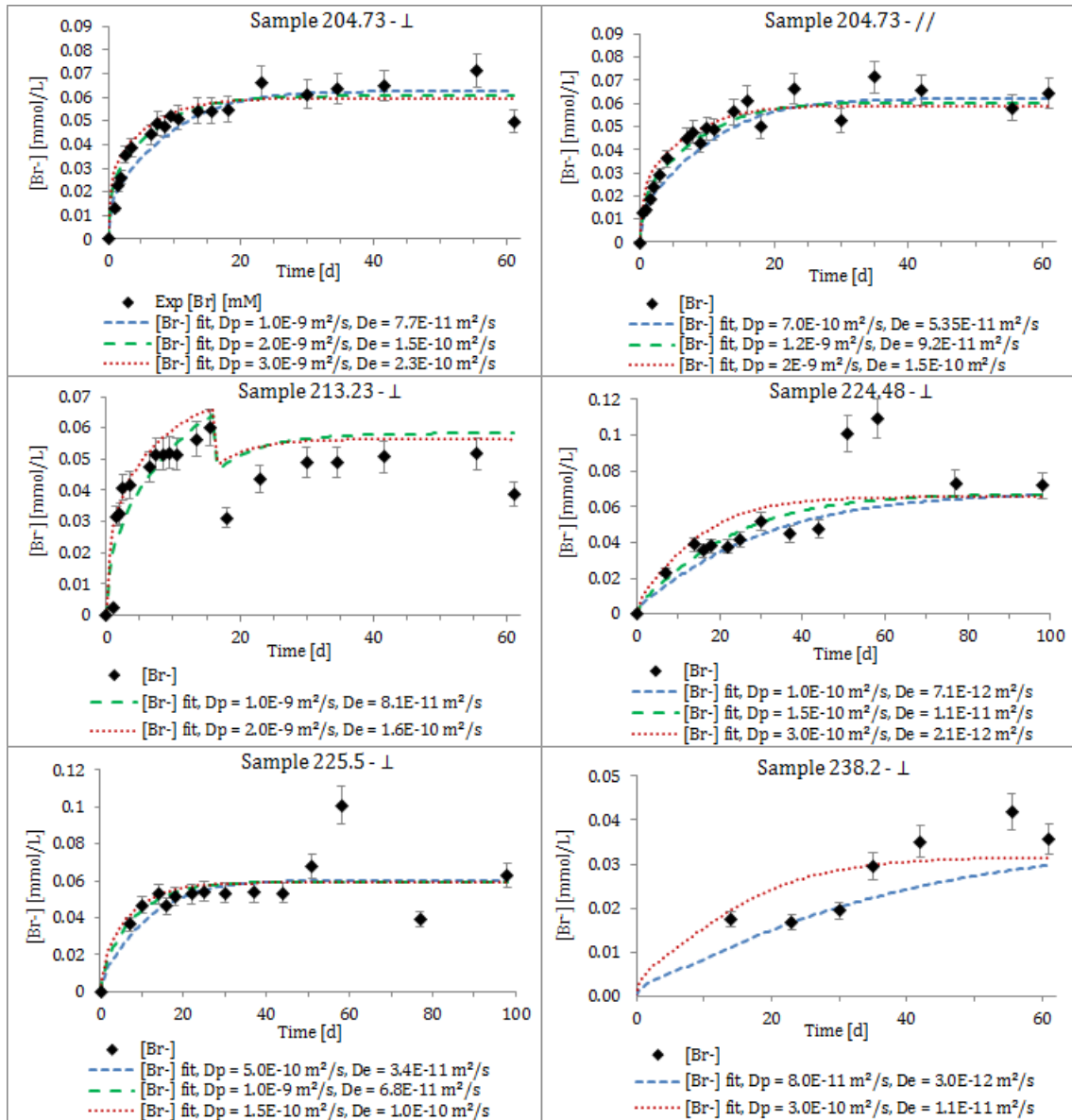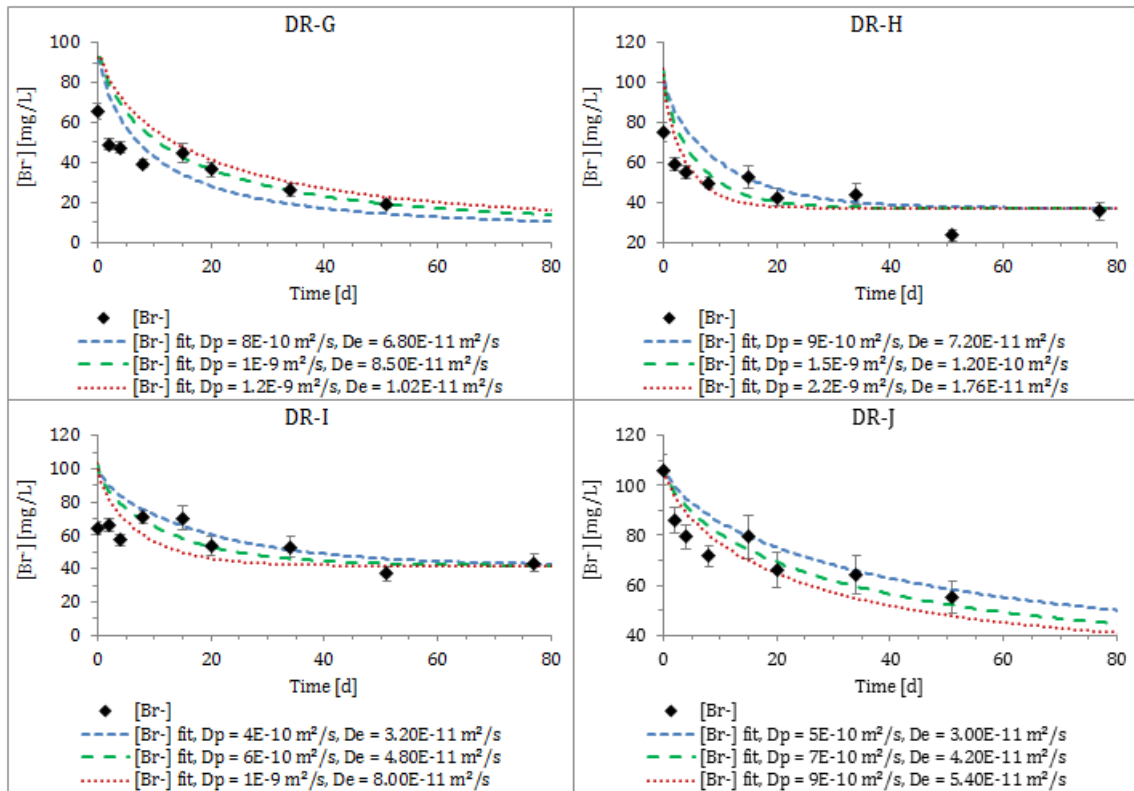
Chloride diffusion coefficients

Bromide diffusion coefficients

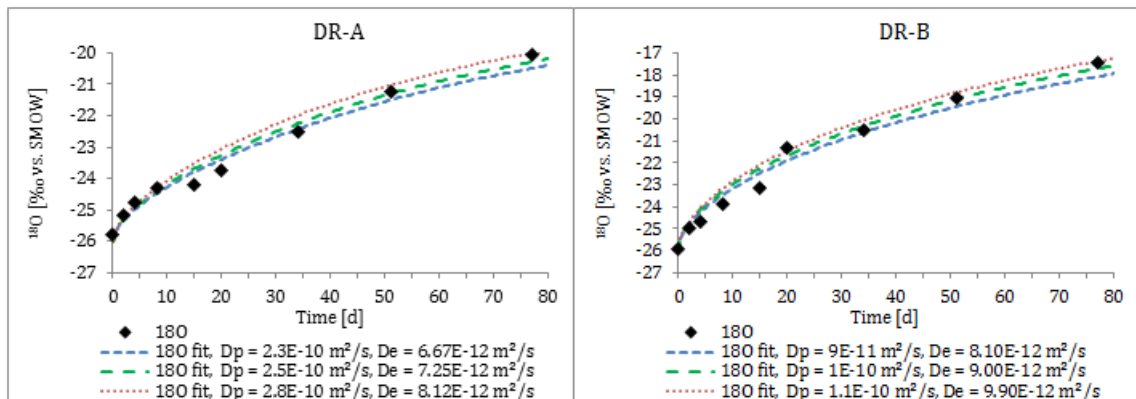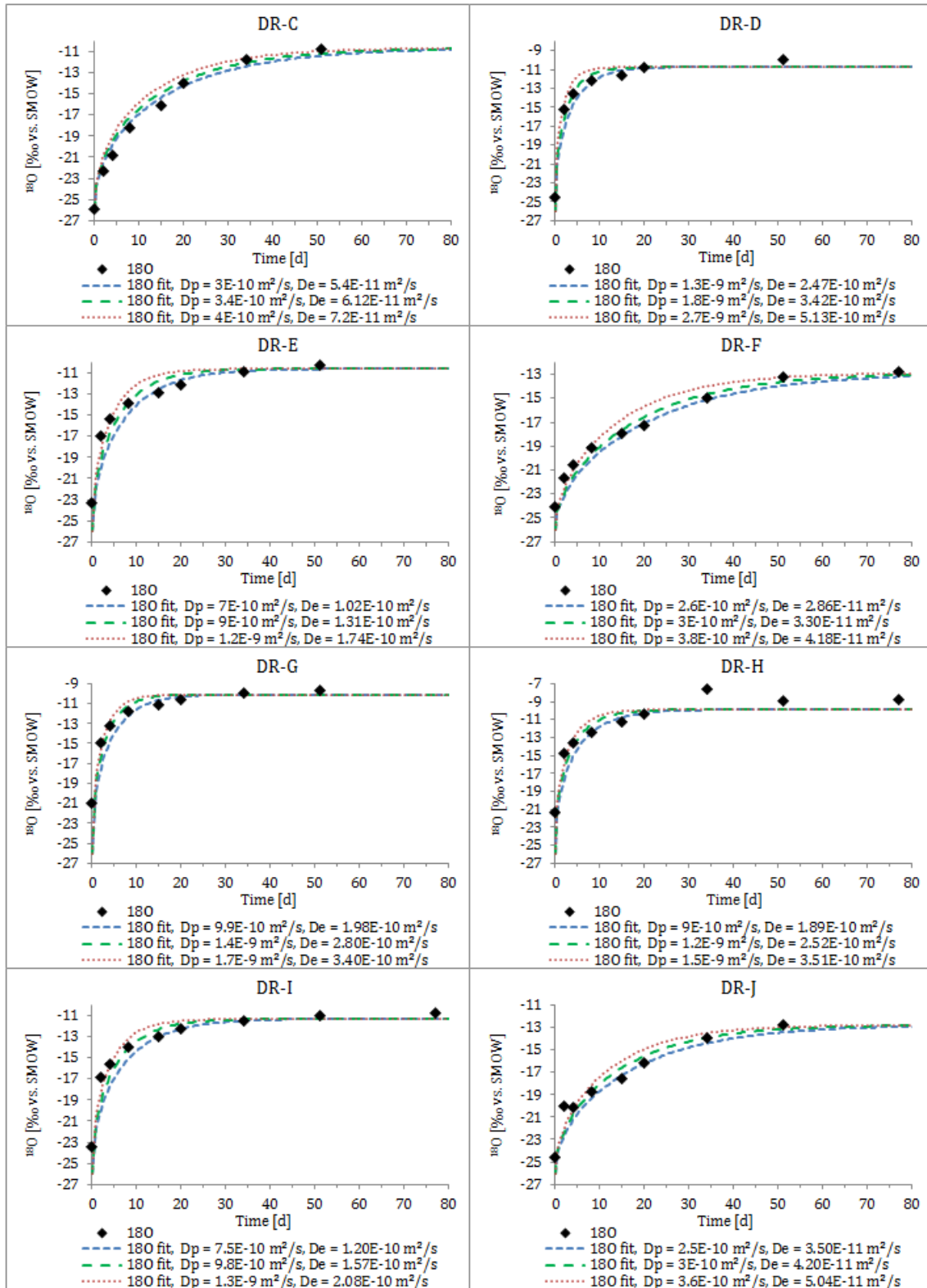**Sample 204.73 - ⊥**

$[Br^-]$ [mmol/L] vs Time [d]

◆ Exp [Br] [mM]
- - - - [Br-] fit, Dp = 1.0E-9 m²/s, De = 7.7E-11 m²/s
- - - - [Br-] fit, Dp = 2.0E-9 m²/s, De = 1.5E-10 m²/s
········ [Br-] fit, Dp = 3.0E-9 m²/s, De = 2.3E-10 m²/s

Sample 204.73 - //

$[Br^-]$ [mmol/L] vs Time [d]

◆ [Br-]
- - - - [Br-] fit, Dp = 7.0E-10 m²/s, De = 5.35E-11 m²/s
- - - - [Br-] fit, Dp = 1.2E-9 m²/s, De = 9.2E-11 m²/s
········ [Br-] fit, Dp = 2E-9 m²/s, De = 1.5E-10 m²/s

Sample 213.23 - ⊥

$[Br^-]$ [mmol/L] vs Time [d]

◆ [Br-]
- - - - [Br-] fit, Dp = 1.0E-9 m²/s, De = 8.1E-11 m²/s
········ [Br-] fit, Dp = 2.0E-9 m²/s, De = 1.6E-10 m²/s

Sample 224.48 - ⊥

$[Br^-]$ [mmol/L] vs Time [d]

◆ [Br-]
- - - - [Br-] fit, Dp = 1.0E-10 m²/s, De = 7.1E-12 m²/s
- - - - [Br-] fit, Dp = 1.5E-10 m²/s, De = 1.1E-11 m²/s
········ [Br-] fit, Dp = 3.0E-10 m²/s, De = 2.1E-12 m²/s

Sample 225.5 - ⊥

$[Br^-]$ [mmol/L] vs Time [d]

◆ [Br-]
- - - - [Br-] fit, Dp = 5.0E-10 m²/s, De = 3.4E-11 m²/s
- - - - [Br-] fit, Dp = 1.0E-9 m²/s, De = 6.8E-11 m²/s
········ [Br-] fit, Dp = 1.5E-10 m²/s, De = 1.0E-10 m²/s

Sample 238.2 - ⊥

$[Br^-]$ [mmol/L] vs Time [d]

◆ [Br-]
- - - - [Br-] fit, Dp = 8.0E-11 m²/s, De = 3.0E-12 m²/s
········ [Br-] fit, Dp = 3.0E-10 m²/s, De = 1.1E-11 m²/s

AIII-1-2 Result table for chloride

Sample	Elevation	Diff Orient.	n_{tot}	σ_{ntot}	P_{acc}	σ_{acc}	n_{acc}	Perpendicular to bedding De [m²/s]	min	max	Parallel to bedding De [m²/s]	min	max	anisotropy
24.98	491.92	⊥	0.023	0.005	1.00	0.21	0.023	3.38E-12	2.03E-12	4.50E-12				
69.6	459.83	⊥	0.083	0.005	0.52	0.03	0.043	8.17E-12	6.02E-12	9.89E-12				
96.07	442.27	⊥	0.136	0.005	0.55	0.02	0.075	3.73E-12	2.98E-12	5.96E-12				
116.24	427.17	⊥	0.122	0.005	0.55	0.02	0.067	7.38E-11	4.70E-11	1.34E-10				
116.24	427.17	//	0.122	0.005	0.55	0.02	0.067				1.34E-10	6.71E-11	2.01E-10	1.82E+00
141.1	408.72	⊥	0.145	0.006	0.55	0.02	0.079	5.56E-10						
155.1	398.42	⊥	0.136	0.006	0.55	0.02	0.075	2.99E-10	1.50E-10	5.24E-10				
155.1	398.42	//	0.136	0.006	0.55	0.02	0.075				1.50E-10	7.48E-11	2.25E-10	5.00E-01
176.48	382.81	⊥	0.099	0.005	0.55	0.03	0.054	2.71E-11	1.63E-11	5.42E-11				
176.48	382.81	//	0.099	0.005	0.55	0.03	0.054				6.51E-11	5.42E-11	8.14E-11	2.40E+00
185.97	375.93	⊥	0.123	0.005	0.55	0.02	0.068	2.04E-11	1.36E-11	2.71E-11				
185.97	375.93	//	0.123	0.005	0.55	0.02	0.068				4.41E-11	2.71E-11	6.78E-11	2.17E+00
204.73	362.39	⊥	0.139	0.007	0.55	0.03	0.077	9.19E-11	7.66E-11	1.53E-10				
204.73	362.39	//	0.139	0.007	0.55	0.03	0.077				2.30E-10	1.53E-10	3.83E-10	2.50E+00
213.23	356.26	⊥	0.147	0.006	0.55	0.02	0.081	3.24E-10	1.62E-10	4.87E-10				
224.49	348.15	⊥	0.129	0.007	0.55	0.03	0.071	3.56E-11	2.13E-11	4.98E-11				
225.5	347.42	⊥	0.123	0.006	0.55	0.03	0.067	2.70E-10	1.35E-10	0.00E+00				
238.2	338.28	⊥	0.068	0.006	0.55	0.05	0.038	4.51E-12	3.01E-12	5.64E-12				

AIII-2 Radial diffusion

AIII-2-1 Solutions preparation

Target recipes for resaturation solutions

Sample	BDB1-Depth [m]	[Cl⁻] [g/kg]	[Cl⁻] [mol/kg]	Salinity [g/kg]	Ionic strength [mol/kg]	[²H] [SMOW]	[¹⁸O] [SMOW]	Resaturation Phase solutions — Mass of anhydrous salts							pH
								NaCl [g/kg]	KCl [g/kg]	MgCl₂ [g/kg]	CaCl₂ [g/kg]	SrCl₂ [g/kg]	Na₂SO₄ [g/kg]	NaHCO₃ [g/kg]	
DR-A	24.9 - 25.0	0.08	0.002	0.18	0.003	-66.5	-9.72	0.000	0.000	0.000	0.286	0.001	0.017	0.263	7.39
DR-B	69.725 - 69.825	0.17	0.005	0.33	0.006	-63.9	-9.5	0.050	0.023	0.244	0.181	0.025	0.015	0.742	7.24
DR-C	125.155 - 125.255	3.00	0.085	5.45	0.109	-60	-8.4	2.191	0.125	0.533	1.857	0.078	1.017	0.179	7.38
DR-D	164.24 - 164.34	7.09	0.200	12.82	0.258	-55	-7.9	6.606	0.197	1.819	1.819	0.110	1.300	0.182	7.10
DR-E	176.55 - 176.65	8.90	0.251	16.09	0.326	-54	-7.8	10.454	0.112	1.509	2.076	0.100	1.554	0.204	7.15
DR-F	186.22 - 186.32	8.65	0.244	15.65	0.316	-52.5	-7.75	7.555	0.085	2.464	3.263	0.211	0.812	0.163	7.04
DR-G	224.35 - 224.45	12.46	0.352	22.52	0.459	-49	-7.6	14.011	0.267	2.250	3.287	0.090	2.474	0.170	7.07
DR-H	230.6 - 230.68	12.44	0.351	22.49	0.458	-50.5	-7.9	14.011	0.267	2.250	3.287	0.090	2.474	0.170	7.07
DR-I	235.43 - 235.53	13.54	0.382	24.48	0.500	-51	-7.8	7.792	0.203	5.310	7.325	0.189	1.664	0.125	6.89
DR-J	241.8 - 241.867	11.56	0.326	20.89	0.425	-52	-8.1	1.393	0.345	6.351	8.915	0.198	1.637	0.117	6.84

Evolution of chloride and sulphate contents during resaturation phase

Sample	Target values mg/L		Calculated values from salts mg/L		Measured (April) mg/L		Measured (10/05/2016) mg/L		Measured (30/05/2016) mg/L			Resaturation period	
	SO₄²⁻	Cl⁻	SO₄²⁻	Cl⁻	SO₄²⁻	Cl⁻	SO₄²⁻	Cl⁻	SO₄²⁻	Cl⁻	Br⁻	Start	End
DR-A	12	71	11	184	10	128	303	146	706	134	0	13/04/2016	30/05/2016
DR-B	529	178	10	350	62	500	208	480	608	143	0	08/04/2016	30/05/2016
DR-C	688	3018	688	3009	1010	3656	1648	4009	2759	3075	10	08/04/2016	30/05/2016
DR-D	879	7100	879	6672	1170	6347	1064	6448	1330	7070	6	11/04/2016	30/05/2016
DR-E	1050	8911	1051	8895	1519	9340	1847	8228	4367	9402	6	11/04/2016	30/05/2016
DR-F	549	8662	549	8644	839	7732	1444	5128	2305	8974	7	11/04/2016	30/05/2016
DR-G	1672	12461	1673	12451	2254	12495	3142	13266	3054	12620	5	13/04/2016	30/05/2016
DR-H	1672	12461	1673	12451	2194	12303	1989	13675	2893	14818	8	13/04/2016	30/05/2016
DR-I	1125	13561	1125	13555	1666	11438	1414	12324	3246	11820	11	13/04/2016	30/05/2016
DR-J	1106	11573	1107	11538	1675	11581	1493	9574	1813	9906	28	13/04/2016	30/05/2016

AIII-2-2 Modelling of Cl⁻, Br⁻, ^{18}O and ^{2}H evolution in test solutions using Mathematica v.5.2

Chloride diffusion coefficients

Annex III – Diffusion experiments

DR-I — [Cl-] vs Time [d]
- ♦ [Cl-]
- [Cl-] fit, Dp = 5.0E-10 m²/s, De = 4.75E-11 m²/s
- [Cl-] fit, Dp = 7.0E-10 m²/s, De = 6.65E-11 m²/s
- [Cl-] fit, Dp = 1.0E-9 m²/s, De = 9.50E-11 m²/s

DR-J — [Cl-] vs Time [d]
- ♦ [Cl-]
- [Cl-] fit, Dp = 4.0E-10 m²/s, De = 2.56E-11 m²/s
- [Cl-] fit, Dp = 5.0E-10 m²/s, De = 3.20E-11 m²/s
- [Cl-] fit, Dp = 6.0E-10 m²/s, De = 3.84E-11 m²/s

Bromide diffusion coefficients

DR-A — [Br-] vs Time [d]
- ♦ [Br-]
- [Br-] fit, Dp = 1E-9 m²/s, De = 5.00E-11 m²/s
- [Br-] fit, Dp = 1.3E-9 m²/s, De = 6.50E-11 m²/s
- [Br-] fit, Dp = 1.5E-9 m²/s, De = 7.50E-11 m²/s

DR-B — [Br-] vs Time [d]
- ♦ [Br-]
- [Br-] fit, Dp = 3.5E-10 m²/s, De = 1.51E-11 m²/s
- [Br-] fit, Dp = 5E-10 m²/s, De = 2.15E-11 m²/s
- [Br-] fit, Dp = 7E-10 m²/s, De = 3.01E-11 m²/s

DR-C — [Br-] vs Time [d]
- ♦ [Br-]
- [Br-] fit, Dp = 2E-10 m²/s, De = 2.40E-11 m²/s
- [Br-] fit, Dp = 3.3E-10 m²/s, De = 3.96E-11 m²/s
- [Br-] fit, Dp = 5E-10 m²/s, De = 6.00E-11 m²/s

DR-E — [Br-] vs Time [d]
- ♦ [Br-]
- [Br-] fit, Dp = 3.5E-10 m²/s, De = 3.85E-11 m²/s
- [Br-] fit, Dp = 5E-10 m²/s, De = 5.50E-11 m²/s
- [Br-] fit, Dp = 8E-10 m²/s, De = 8.80E-11 m²/s

DR-F — [Br-] vs Time [d]
- ♦ [Br-]
- [Br-] fit, Dp = 2E-10 m²/s, De = 1.80E-11 m²/s
- [Br-] fit, Dp = 3E-10 m²/s, De = 2.70E-11 m²/s
- [Br-] fit, Dp = 5E-10 m²/s, De = 4.50E-11 m²/s

DR-G — [Br-] vs Time [d]
- ♦ [Br-]
- [Br-] fit, Dp = 8E-10 m²/s, De = 6.80E-11 m²/s
- [Br-] fit, Dp = 1E-9 m²/s, De = 8.50E-11 m²/s
- [Br-] fit, Dp = 1.2E-9 m²/s, De = 1.02E-11 m²/s

DR-G, DR-H, DR-I, DR-J — [Br⁻] diffusion plots

DR-G
[Br⁻] fit, Dp = 8E-10 m²/s, De = 6.80E-11 m²/s
[Br⁻] fit, Dp = 1E-9 m²/s, De = 8.50E-11 m²/s
[Br⁻] fit, Dp = 1.2E-9 m²/s, De = 1.02E-11 m²/s

DR-H
[Br⁻] fit, Dp = 9E-10 m²/s, De = 7.20E-11 m²/s
[Br⁻] fit, Dp = 1.5E-9 m²/s, De = 1.20E-10 m²/s
[Br⁻] fit, Dp = 2.2E-9 m²/s, De = 1.76E-11 m²/s

DR-I
[Br⁻] fit, Dp = 4E-10 m²/s, De = 3.20E-11 m²/s
[Br⁻] fit, Dp = 6E-10 m²/s, De = 4.80E-11 m²/s
[Br⁻] fit, Dp = 1E-9 m²/s, De = 8.00E-11 m²/s

DR-J
[Br⁻] fit, Dp = 5E-10 m²/s, De = 3.00E-11 m²/s
[Br⁻] fit, Dp = 7E-10 m²/s, De = 4.20E-11 m²/s
[Br⁻] fit, Dp = 9E-10 m²/s, De = 5.40E-11 m²/s

²H diffusion coefficients

DR-A, DR-B, DR-C, DR-D — ²H diffusion plots

DR-A
2H fit, Dp = 2.3E-10 m²/s, De = 6.67E-12 m²/s
2H fit, Dp = 2.5E-10 m²/s, De = 7.25E-12 m²/s
2H fit, Dp = 2.7E-10 m²/s, De = 7.83E-12 m²/s

DR-B
2H fit, Dp = 1.1E-10 m²/s, De = 7.65E-12 m²/s
2H fit, Dp = 1.0E-10 m²/s, De = 8.50E-12E-11 m²/s
2H fit, Dp = 9E-11 m²/s, De = 9.35E-12 m²/s

DR-C
2H fit, Dp = 2.8E-10 m²/s, De = 5.04E-11 m²/s
2H fit, Dp = 3.0E-10 m²/s, De = 5.40E-11 m²/s
2H fit, Dp = 3.5E-10 m²/s, De = 6.30E-11 m²/s

DR-D
2H fit, Dp = 1.3E-9 m²/s, De = 2.28E-10 m²/s
2H fit, Dp = 1.7E-9 m²/s, De = 2.98E-10 m²/s
2H fit, Dp = 2.0E-9 m²/s, De = 3.50E-10 m²/s

18O diffusion coefficients

AIII-2-3 Result tables

^2H

Sample	Formation	Distance	Elevation	D_e ($m^2\,s^{-1}$)	Min	Max	D_p	Min	Max	ω
DR-A	Hauptrogenstein	24.95	491.94	7.25E-12	6.67E-12	7.83E-12	2.50E-10	2.30E-10	2.70E-10	2.9%
DR-B	Passwang Formation	69.78	459.83	8.50E-12	7.65E-12	9.35E-12	1.00E-10	9.00E-11	1.10E-10	8.5%
DR-C	OPA Sandy	125.21	420.48	5.40E-11	5.04E-11	6.30E-11	3.00E-10	2.80E-10	3.50E-10	18.0%
DR-D	OPA Shaly	164.29	391.70	2.98E-10	2.28E-10	3.50E-10	1.70E-09	1.30E-09	2.00E-09	17.5%
DR-E	OPA Sandy	176.60	382.72	1.12E-10	9.10E-11	1.40E-10	8.00E-10	6.50E-10	1.00E-09	14.0%
DR-F	OPA C-r Sandy	186.27	375.72	2.97E-11	2.64E-11	3.30E-11	2.70E-10	2.40E-10	3.00E-10	11.0%
DR-G	OPA Shaly	224.40	362.63	2.47E-10	1.81E-10	3.80E-10	1.30E-09	9.50E-10	2.00E-09	19.0%
DR-H	OPA Shaly	230.64	343.72	2.20E-10	1.54E-10	2.86E-10	1.00E-09	7.00E-10	1.30E-09	22.0%
DR-I	OPA Shaly	235.48	340.24	1.86E-10	1.33E-10	2.28E-10	9.80E-10	7.00E-10	1.20E-09	19.0%
DR-J	Staffelegg Formation	241.83	335.68	4.20E-11	3.50E-11	5.04E-11	3.00E-10	2.50E-10	3.60E-10	14.0%

^{18}O

Sample	Formation	Distance	Elevation	D_e ($m^2\,s^{-1}$)	Min	Max	D_p	Min	Max	ω
DR-A	Hauptrogenstein	24.95	491.94	7.25E-12	6.67E-12	8.12E-12	2.50E-10	2.30E-10	2.80E-10	2.9%
DR-B	Passwang Formation	69.78	459.83	9.00E-12	8.10E-12	9.90E-12	1.00E-10	9.00E-11	1.10E-10	9.0%
DR-C	OPA Sandy	125.21	420.48	6.12E-11	5.40E-11	7.20E-11	3.40E-10	3.00E-10	4.00E-10	18.0%
DR-D	OPA Shaly	164.29	391.70	3.42E-10	2.47E-10	5.13E-10	1.80E-09	1.30E-09	2.70E-09	19.0%
DR-E	OPA Sandy	176.60	382.72	1.31E-10	1.02E-10	1.74E-10	9.00E-10	7.00E-10	1.20E-09	14.5%
DR-F	OPA C-r Sandy	186.27	375.72	3.30E-11	2.86E-11	4.18E-11	3.00E-10	2.60E-10	3.80E-10	11.0%
DR-G	OPA Shaly	224.40	362.63	2.80E-10	1.98E-10	3.40E-10	1.40E-09	9.90E-10	1.70E-09	20.0%
DR-H	OPA Shaly	230.64	343.72	2.52E-10	1.89E-10	3.15E-10	1.20E-09	9.00E-10	1.50E-09	21.0%
DR-I	OPA Shaly	235.48	340.24	1.57E-10	1.20E-10	2.08E-10	9.80E-10	7.50E-10	1.30E-09	16.0%
DR-J	Staffelegg Formation	241.83	335.68	4.20E-11	3.50E-11	5.04E-11	3.00E-10	2.50E-10	3.60E-10	14.0%

Br^-

Sample	Formation	Distance	Elevation	D_e ($m^2\,s^{-1}$)	Min	Max	D_p	Min	Max	ω
DR-A	Hauptrogenstein	24.95	491.94	6.50E-11	5.00E-11	7.50E-11	1.30E-09	1.00E-09	1.50E-09	5.0%
DR-B	Passwang Formation	69.78	459.83	2.15E-11	1.51E-11	3.01E-11	5.00E-10	3.50E-10	7.00E-10	4.3%
DR-C	OPA Sandy	125.21	420.48	3.96E-11	2.40E-11	6.00E-11	3.30E-10	2.00E-10	5.00E-10	12.0%
DR-D	OPA Shaly	164.29	391.70	1.20E-10	8.40E-11	2.40E-10	1.00E-09	7.00E-10	2.00E-09	12.0%
DR-E	OPA Sandy	176.60	382.72	5.50E-11	3.85E-11	8.80E-11	5.00E-10	3.50E-10	8.00E-10	11.0%
DR-F	OPA C-r Sandy	186.27	375.72	2.70E-11	1.80E-11	4.50E-11	3.00E-10	2.00E-10	5.00E-10	9.0%
DR-G	OPA Shaly	224.40	362.63	8.50E-11	6.80E-11	1.02E-10	1.00E-09	8.00E-10	1.20E-09	8.5%
DR-H	OPA Shaly	230.64	343.72	1.20E-10	7.20E-11	1.76E-10	1.50E-09	9.00E-10	2.20E-09	8.0%
DR-I	OPA Shaly	235.48	340.24	4.80E-11	3.20E-11	8.00E-11	6.00E-10	4.00E-10	1.00E-09	8.0%
DR-J	Staffelegg Formation	241.83	335.68	4.20E-11	3.00E-11	5.40E-11	7.00E-10	5.00E-10	9.00E-10	6.0%

Cl^-

Sample	Formation	Distance	Elevation	D_e ($m^2\,s^{-1}$)	Min	Max	D_p	Min	Max	ω
DR-A	Hauptrogenstein	24.95	491.94							
DR-B	Passwang Formation	69.78	459.83	3.08E-11	2.52E-11	3.92E-11	1.10E-09	9.00E-10	1.40E-09	0.028
DR-C	OPA Sandy	125.21	420.48	3.86E-11	3.13E-11	4.78E-11	4.20E-10	3.40E-10	5.20E-10	9.2%
DR-D	OPA Shaly	164.29	391.70	1.26E-10	9.00E-11	1.62E-10	1.40E-09	1.00E-09	1.80E-09	9.0%
DR-E	OPA Sandy	176.60	382.72	1.13E-10	8.82E-11	1.51E-10	1.80E-09	1.40E-09	2.40E-09	6.3%
DR-F	OPA C-r Sandy	186.27	375.72	2.85E-11	1.71E-11	3.99E-11	5.00E-10	3.00E-10	7.00E-10	5.7%
DR-G	OPA Shaly	224.40	362.63							
DR-H	OPA Shaly	230.64	343.72	1.44E-10	1.08E-10	3.00E-10	1.20E-09	9.00E-10	2.50E-09	12.0%
DR-I	OPA Shaly	235.48	340.24	6.65E-11	4.75E-11	9.50E-11	7.00E-10	5.00E-10	1.00E-09	9.5%
DR-J	Staffelegg Formation	241.83	335.68	3.20E-11	2.56E-11	3.84E-11	5.00E-10	4.00E-10	6.00E-10	6.4%

AIII-3 Through diffusion

AIII-3-1 Resaturation solutions

	Formation	Sample	Expected Concentration from salts [ppm]							Measured concentration [ppm]			
			Cl	SO$_4$	Ca	Na	K	Mg	Sr	Cl	+/-	SO$_4$	+/-
TD-A	Passwang Fm	96.7	568	81	141	160	5	77	17	580	60	86	9
TD-B-C	OPA Shaly	155.1	3046	701	307	1864	29	52	16	3080	310	740	80
TD-D	OPA Sandy	176.84	8891	1050	750	4672	59	386	55	9100	1000	1080	110
TD-E	OPA Carb. Rich Sandy	186.08	8638	549	1176	3279	44	631	117	8900	900	580	60
TD-F	Staffelegg Fm	238.2	12169	1766	2585	4127	90	844	59	12400	1300	1800	190

AIII-3-2 Experimental plots and HYTEC simulations where possible

TD-D

TD-E

TD-F
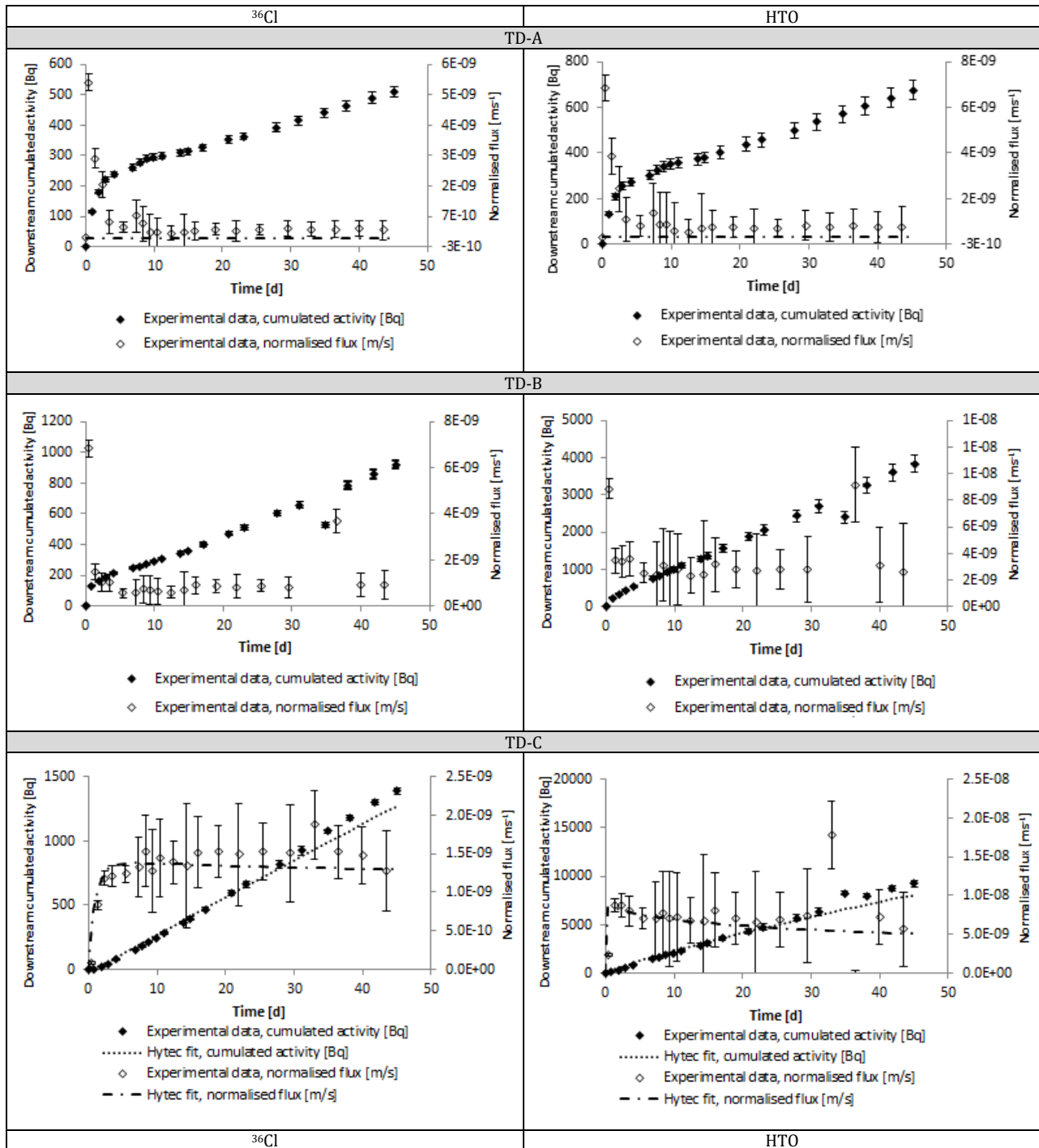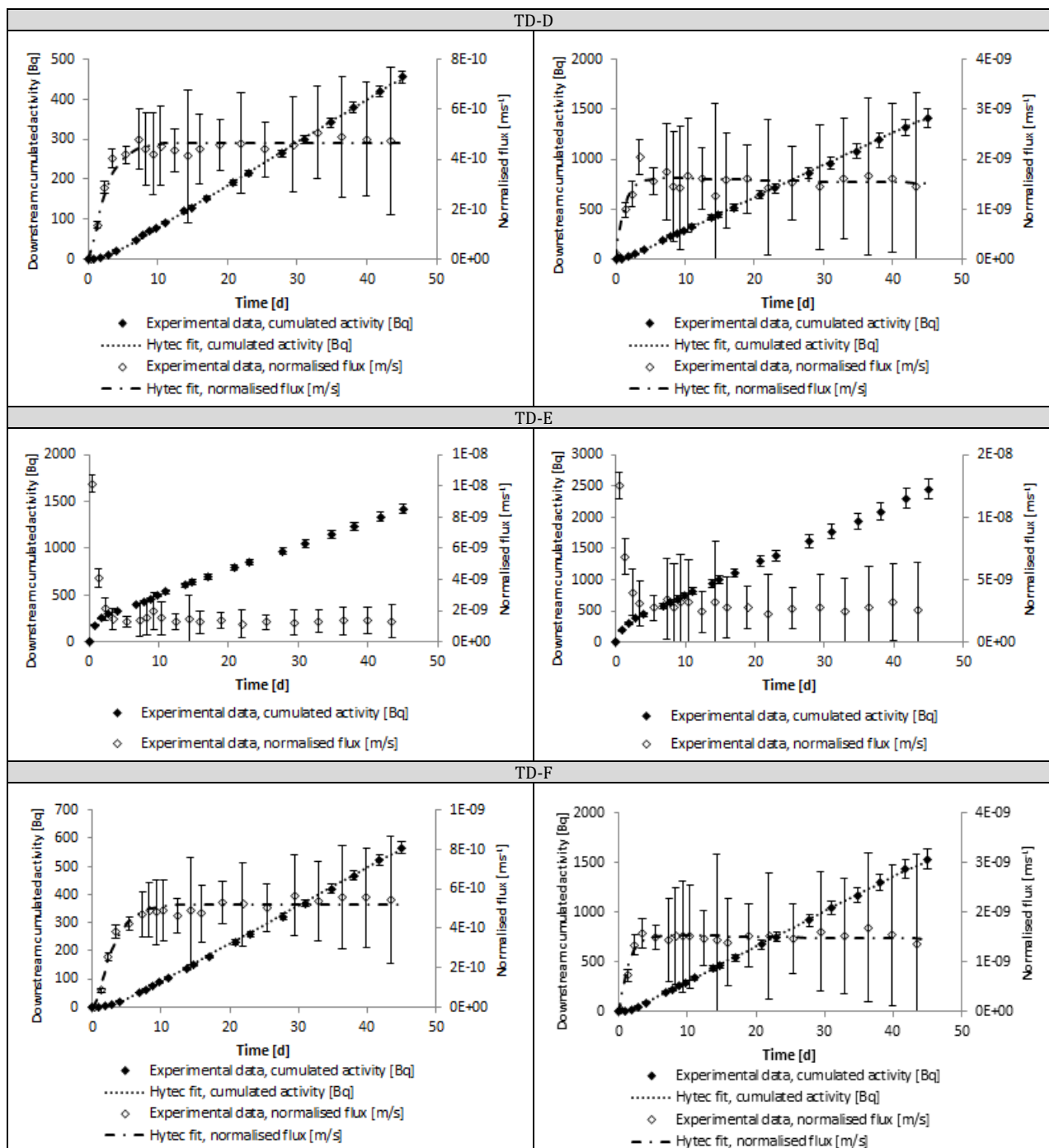
AIII-3-3 Results table

Formation	Sample	Elevation	Diffusion orientation / bedding	Cell	Element	HYTEC simulation results		
						D_e [m²/s]	ω	Exclusion factor
OPA shaly	155.1	398.42	//	TD-C	³⁶Cl	1.43E-11	13.0%	0.81
	155.1	398.42			HTO	9.60E-11	16.0%	
OPA sandy	176.84	382.55	⊥	TD-D	³⁶Cl	5.12E-12	8.0%	0.50
	176.84	382.55			HTO	1.87E-11	16.0%	
Staffelegg	238.2	338.28	⊥	TD-F	³⁶Cl	5.50E-12	11.0%	0.61
	238.2	338.28			HTO	1.69E-11	18.0%	

AIV-1 Results tables of in situ hydraulic tests numerical interpretation

AIV-1-1 Pulse withdrawal tests

Tested Interval		Unit	BDB-1 Int1	BDB-1 Int1	BDB-1 Int1	BDB-1 Int2	BDB-1 Int3	BDB-1 Int4	BDB-1 Int5	BDB-1 Int6	BDB-1 Int7
Test Parameters:			Pulse	Pulse	Pulse	Pulse	Pulse	Pulse	Pulse	Pulse	Pulse
Borehole radius		[m]	0.061	0.061	0.061	0.061	0.061	0.061	0.061	0.061	0.061
Interval depth	from	[m]	244.62	244.62	244.62	226.17	188.17	164.72	144.27	114.82	100.37
	to	[m]	247.5	247.5	247.5	227.17	189.17	165.72	145.27	115.82	101.37
Interval length		[m]	2.88	2.88	2.88	1	1	1	1	1	1
System volume		[m³]	3.588E-2	3.588E-2	3.588E-2	9.351E-3	9.007E-3	8.795E-3	8.610E-3	8.343E-3	8.213E-3
Initial pressure		[kPa]	1195	1195	1195	1703	1652	1581	1480	1384	1324
Reference			C1-1	C1-2	C1-3	C2-1	C3-1	C4-1	C5-1	C6-1	C7-1
Test Performance:											
Withdrawn volume		[m³]	1.98E-7	6.73E-7	2.12E-5	5.33E-6	1.58E-6	8.02E-6	1.19E-6	1.69E-6	4.49E-6
Pressure difference		[kPa]	22.7	156.9	314.6	350.6	179.3	438.2	121.7	166.6	594.2
Wellbore storage coeff.		[m³·Pa⁻¹]	9.11E-12	4.29E-11	6.73E-11	1.52E-11	8.84E-12	1.83E-11	9.80E-12	1.02E-11	7.56E-12
Compressibility C_{tz}		[Pa⁻¹]	2.54E-10	1.19E-09	1.87E-09	1.63E-09	9.81E-10	2.08E-09	1.14E-09	1.22E-09	9.20E-10
Analysis Results, best fit:											
K		[m·s⁻¹]	**2.07E-10**	**4.16E-10**	**5.58E-10**	**3.13E-12**	**5.13E-13**	**2.34E-12**	**1.64E-12**	**1.88E-13**	**5.78E-13**
T		[m²·s⁻¹]	**5.96E-10**	**1.20E-09**	**1.61E-09**	**3.13E-12**	**5.13E-13**	**2.34E-12**	**1.64E-12**	**1.88E-13**	**5.78E-13**
Ss		[m⁻¹]	**1.35E-08**	**1.36E-06**	**6.34E-08**	**5.23E-06**	**3.69E-06**	**6.38E-06**	**1.04E-06**	**6.58E-06**	**3.72E-06**
K_skin		[m·s⁻¹]				7.8E-12	1.63E-12	5.70E-12	1.38E-12	1.40E-11	3.72E-13
Ss_skin		[m⁻¹]				4.3E-05	1.17E-05	5.45E-05	2.56E-05	6.55E-06	1.91E-06
R_skin		cm				**0.5**	**0.5**	**0.5**	**0.5**	**1.5**	**0.5**
n			**2.25**	**2.04**	**2.39**	**2.75**	**2.13**	**2.29**	**1.90**	**2.57**	**3.04**
Reference					C1-6	C2-2	C3-2	C4-2	C5-2	C6-2	C7-2
Test Performance:											
Withdrawn volume		[m³]			1.97E-5	3.66E-6	3.97E-6	3.41E-6	5.20E-6	3.55E-6	2.45E-6
Pressure difference		[kPa]			316.9	221.8	249.3	183.8	251.8	203.5	279.4
Wellbore storage coeff.		[m³·Pa⁻¹]			6.23E-11	1.65E-11	1.59E-11	1.85E-11	2.06E-11	1.74E-11	8.75E-12
Compressibility C_{tz}		[Pa⁻¹]			1.74E-09	1.77E-09	1.77E-09	2.11E-09	2.40E-09	2.09E-09	1.07E-09
Analysis Results, best fit:											
K		[m·s⁻¹]			**5.94E-09**	**7.28E-12**	**4.92E-13**	**4.15E-12**	**1.03E-12**	**2.71E-13**	**1.42E-12**
T		[m²·s⁻¹]			**1.70E-09**	**7.28E-12**	**4.92E-13**	**4.15E-12**	**1.03E-12**	**2.71E-13**	**1.42E-12**
Ss		[m⁻¹]			**8.27E-07**	**2.97E-06**	**1.10E-05**	**2.18E-06**	**8.51E-06**	**1.71E-05**	**1.24E-06**
K_skin		[m·s⁻¹]				1.03E-11	1.63E-12	2.73E-11	2.65E-12	5.37E-12	8.55E-12
Ss_skin		[m⁻¹]				4.70E-05	1.48E-05	9.70E-06	4.68E-05	2.93E-05	9.42E-07
R_skin		cm				0.5	0.5	2.01	0.5	0.5	0.5
n					1.99	2	2.47	1.89	2.51	2.77	2.27

AIV-1-2 Constant rate withdrawal tests

Tested Interval		Unit	BDB-1 Int1	BDB-1 Int2	BDB-1 Int3	BDB-1 Int4	BDB-1 Int5	BDB-1 Int6	BDB-1 Int7
Test Parameters:			Constant rate	Constant rate	Constant rate	Constant rate	Constant rate	Constant rate	Constant rate
Borehole radius		[m]	0.061	0.061	0.061	0.061	0.061	0.061	0.061
Interval depth	from	[m]	244.62	226.17	188.17	164.72	144.27	114.82	100.37
	to	[m]	247.5	227.17	189.17	165.72	145.27	115.82	101.37
Interval length		[m]	2.88	1	1	1	1	1	1
Initial pressure		[kPa]	1196.1	1703	1652	1581	1480	1384	1324
Reference			C1-7	C2-3	C3-3	C4-3	C5-3	C6-3	C7-3
Test Performance:									
Flowrate		[ml·min⁻¹]	- 5	- 0.005	- 0.005	- 0.005	- 0.005	- 0.005	- 0.005
Pumping duration		[hours]	2.18	162.9	23.10	166.23	243.32	437.76	121.36
Pressure difference		[kPa]	163.7	82.0	189.6	143.5	266.7	609.0	331.2
Analysis Results, best fit:									
K		[m·s⁻¹]	**4.97E-10**	**3.91E-12**	**9.85E-13**	**2.38E-12**	**8.10E-13**	**2.23E-13**	**4.39E-13**
T		[m²·s⁻¹]	**1.73E-10**	**3.91E-12**	**9.85E-13**	**2.38E-12**	**8.10E-13**	**2.23E-13**	**4.39E-13**
Ss		[m⁻¹]	**8.2E-07**	**1.2E-06**	**1.49E-06**	**1.18E-06**	**8.86E-07**	**7.70E-07**	**8.47E-07**
K_skin		[m·s⁻¹]	**5.65E-09**	**3.5E-11**	**1.61E-12**	**2.96E-12**	**1.49E-11**	**1.12E-12**	**8.24E-13**
Ss_skin		[m⁻¹]	**6.24E-06**	**6.2E-05**	**4.92E-05**	**3.97E-05**	**2.39E-05**	**9.9E-05**	**2.25E-05**
R_skin		cm	**4.25**	**4.83**	**0.70**	**1.41**	**1.79**	**0.81**	**0.61**
n			**2.11**	**1.95**	**1.9**	**2.12**	**2.33**	**2.55**	**2.66**

AIV-2 Result table of intrinsic permeability measurements in Hassler cell

Distance to borehole head		Formation	Plug ID	Width		Length		Orientation with respect to the bedding		Fluid	Resin coating	Permeability measurements			
Minimum distance	Maximum distance			Width	Error on W	Length	Error on L	Perpendicular	Parallel			Apparent permeability	Error on k_g	Intrinsic permeability	Error on k_l
				W	σ_W	L	σ_L					k_g	σ_{kg}	k_l	σ_{kl}
m	m			mm	mm	mm	mm					m^2	m^2	m^2	m^2
116.24	116.54		M12a	39.53	0.001	25.76	0.002	⊥		$N_{2(g)}$		1.92E-19	3.06E-11	1.26E-19	1.25E-31
116.24	116.54		M12b	39.52	0.001	27.67	0.002	⊥		$N_{2(g)}$		1.17E-19	1.68E-11	7.70E-20	7.60E-32
116.24	116.54	OPA	M12c	39.6	0.001	55.08	0.002		//	$N_{2(g)}$	X	3.38E-18	3.36E-10	2.59E-18	2.56E-30
116.24	116.54	(sandy)	M12c	39.6	0.001	55.08	0.002		//	$H_2O_{(l)}$				1.38E-20	1.90E-22
125.12	125.38		M13a	39.51	0.001	29.79	0.002	⊥		$N_{2(g)}$		3.08E-19	3.36E-11	2.31E-19	2.28E-31
125.12	125.38		M13b	39.6	0.001	42.16	0.002		//	$N_{2(g)}$	X	4.93E-20	6.91E-12	2.58E-20	2.55E-32
136.33	136.58	OPA	M14c	39.5	0.001	30.23	0.002		//	$N_{2(g)}$	X	9.77E-20	2.27E-11	2.96E-20	2.92E-32
155.1	155.72	(shaly)	M16b	39.65	0.001	29.39	0.002	⊥		$N_{2(g)}$		4.71E-19	4.34E-11	4.05E-19	3.99E-31
204.73	204.98	OPA	M21a	39.78	0.001	12.29	0.002	⊥		$N_{2(g)}$		6.71E-20	5.92E-12	4.74E-20	4.68E-32
213.23	213.48	(shaly)	M22a	39.49	0.001	7.34	0.002	⊥		$N_{2(g)}$		1.88E-20	3.26E-12	6.91E-21	6.82E-33

ANNEX V: X-RAY FLUORESCENCE AND LOSS ON IGNITION AT 1000 °C RESULTS (BRGM)

Sample ID	Distance	Formation	Composition										
	[m]		[%]										
			Al_2O_3	CaO	Fe_2O_3	K_2O	MgO	MnO	Na2O	P_2O_5	LOI	SiO_2	TiO_2
BDB 1 - 08	74.905	Passwang Fm.	6.9	14.3	5.07	2.18	1.4	0.08	0.2	< DL	13.97	53.8	0.58
BDB 1 - 13	125.25	OPA (sandy)	14.6	5.1	4.93	2.84	1.6	0.05	0.4	0.24	9.13	59.6	0.9
BDB 1 - 15	141.24	OPA (shaly)	17	4.9	6.19	2.99	1.9	0.08	0.4	0.26	10.61	53.1	0.94
BDB 1 - 18	176.61	OPA (sandy)	17.1	4	6.12	3.06	2	0.04	0.4	0.42	9.63	54.8	0.92
BDB 1 - 19	186.08	OPA (carbonate-rich sandy)	11.2	6.6	4.46	2.22	1.9	0.05	0.5	0.26	10.09	60.7	0.71
BDB 1 - 21	204.86		19.7	8.1	6.02	3.19	2.4	0.06	0.4	0.21	13.64	44.2	0.87
BDB 1 - 25	225.54	OPA (shaly)	19	9.1	5.78	3.07	2.4	0.05	0.4	0.23	14.18	43.7	0.84
BDB 1 - 26	230.67		18.8	9.6	5.55	3.11	2.4	0.05	0.4	0.24	14.49	43.7	0.83
BDB 1 - 27	238.2		6.8	37.4	2.83	0.98	1.9	0.07	0.2	0.09	32.8	15.3	0.29
BDB 1 - 28	241.85	Staffelegg Fm.	12.4	19.9	4.07	2.28	3.4	0.09	0.5	0.15	21.57	32.5	0.54
BDB 1 - 29	243.95		7.2	23.2	7.99	1.73	1.6	0.05	0.4	0.27	25.86	24.9	0.35

Comparative study of methods to estimate hydraulic parameters in the hydraulically undisturbed Opalinus Clay (Switzerland)

Catherine Yu[1,2] · Jean-Michel Matray[1] · Julio Gonçalvès[2] · David Jaeggi[3] ·
Werner Gräsle[4] · Klaus Wieczorek[5] · Tobias Vogt[6] · Erik Sykes[7]

Abstract The deep borehole (DB) experiment gave the opportunity to acquire hydraulic parameters in a hydraulically undisturbed zone of the Opalinus Clay at the Mont Terri rock laboratory (Switzerland). Three methods were used to estimate hydraulic conductivity and specific storage values of the Opalinus Clay formation and its bounding formations through the 248 m deep borehole BDB-1: application of a Poiseuilletype law involving petrophysical measurements, spectral analysis of pressure time series and in situ hydraulic tests. The hydraulic conductivity range inthe OpalinusClay given by the first method is 2×10^{-14}–6×10^{-13} m s^{-1} for a cementation factor ranging between 2 and 3. These results show low

Editorial handling: P. Bossart and A. G. Milnes.

This is paper #4 in the Mont Terri Special Issue of the Swiss Journal of Geosciences (see Bossart et al. 2017, Table 3 and Fig. 7).

✉ Catherine Yu
catherine.jiyu@irsn.fr

[1] Institut de Radioprotection et de Sûreté Nucléaire, 31 Allée du Général Leclerc, 92260 Fontenay-aux-Roses, France

[2] Aix Marseille Université UMR 6635 CEREGE Technopôle Environnement Arbois-Méditerranée, BP80,
13545 Aix-en-Provence Cedex 4, France

[3] Federal Office of Topography Swisstopo, Seftigenstrasse 264, 3084 Wabern, Switzerland

[4] Federal Institute for Geosciences and Natural Resources (BGR), Stilleweg 2, 30655 Hannover, Germany

[5] Global Research for Safety (GRS), Schwertnergasse 1, 50667 Cologne, Germany

[6] National Cooperative for the Disposal of Radioactive Waste (Nagra), Hardstrasse 73, 5430 Wettingen, Switzerland

[7] Nuclear Waste Management Organization, 22 St. Clair Ave. E., Toronto, ON, Canada

vertical variability whereas in situ hydraulic tests suggest higher values up to $7 \times 9 \ 10^{-12}$ m s^{-1}. Core analysis provides economical estimates of the homogeneous matrix hydraulic propertiesbut do not account for heterogeneities at larger scale such as potential tectonic conductive features. Specific storage values obtained by spectral analysis are consistent and in the order of 10^{-6} m^{-1}, while formulations using phase shift and gain between pore pressure signals were found to be inappropriate to evaluate hydraulic conductivity in the Opalinus Clay. The values obtained are globally in good agreement with the ones obtained previously at the rock laboratory.

1 Introduction

Based on favourable confining properties, such as low permeability, strong retention and self-sealing capacities, clay formations are the preferred host rock option for a deep geological repository of long-lived, intermediate and high level radioactive waste in several countries including France, Belgium and Switzerland. In the latter country, the Opalinus Clay (OPA) has been selected as a potential host rock for a disposal facility (Nagra 2002) and has been studied at the Mont Terri rock laboratory since 1996. The laboratory is located at a depth of ca. 280 m, in the security gallery of the A16 Transjurane motorway, which crosses the Jura Mountains in north-western Switzerland.

The accurate hydraulic characterisation of low permeability formations is of high importance to ensure

the safety of a geological repository. Hydraulic properties can be estimated by various laboratory and field experiments (Van der Kamp 2001; Yu et al. 2013), including empirical methods based on the rock matrix properties (Chapuis and Aubertin 2003), falling head or constant head permeameter tests in laboratory (Boulin et al. 2012), and in situ field tests that rely on measurement of pore pressure or water level changes due to tidal natural loading (Bredehoeft 1967; Merritt 2004; Jiang et al. 2013) or artificial application of an hydraulic pressure different from the static formation pressure (Neuzil 1982; Butler 1998; Mejías et al. 2009). As these methods are carried out from sub-millimetre to hectometre investigation scales, scale dependency can affect the results (Keller et al. 1989; Neuzil 1994).

This paper compares three different techniques to estimate hydraulic properties of the Opalinus Clay: application of a Poiseuille-type law involving petrophysical measurements, in situ packer tests and spectral analysis of pore pressure time series.

2 Geological setting

The Opalinus Clay at the Mont Terri site is an overconsolidated claystone of Aalenian-Toarcian age, overlain by 800 m of Middle to Late Jurassic limestones, marls and shales, and underlain by 400 m of Early Jurassic to Triassic marls and limestones, dolomites and anhydrites (Fig. 1). The thickness of the Opalinus Clay in the Mont

Terri anticline varies between 130 m in the BDB-1 borehole and 160 m at rock laboratory level, depending on the tectonic contribution. This corresponds to a sedimentary thickness of about 120 m, when corrected for tectonic overthrusting. The Opalinus Clay reached a burial depth of 1350 m about 120 Ma ago during early Cretaceous, which resulted in a maximum temperature of 80–90 C (Mazurek et al. 2006). A period of marine regression occurred between 100 and 40 Ma, leading to a subaerial exposure of the top of the Malm limestone. Starting about 40 Ma, the rifting of the Rhine Graben affected Northern Switzerland, resulting in considerable subsidence of the area in the mid-Tertiary, which brought the Opalinus Clay sequence back to about 500 m depth. Two sea invasions into the Mont Terri area took place during Priabonian (37–34 Ma) and during the Rupelian (34–28 Ma) (Clauer et al. 2017). Late Alpine folding during the late Miocene to Pliocene (about 12–3 Ma) formed the Folded Jura. Erosion exposed the core of the Mont Terri anticline towards 2.5 Ma, and allowed fresh water infiltration to the Middle Jurassic limestones. Similarly, infiltration to the Early Jurassic limestones would have started in the Quaternary, around 350 thousand years ago (Pearson et al. 2003).

Three main facies were identified within the Opalinus Clay (Blaesi et al. 1991): a shaly facies in the lower part of the sequence, a thin carbonate-rich sandy facies in the
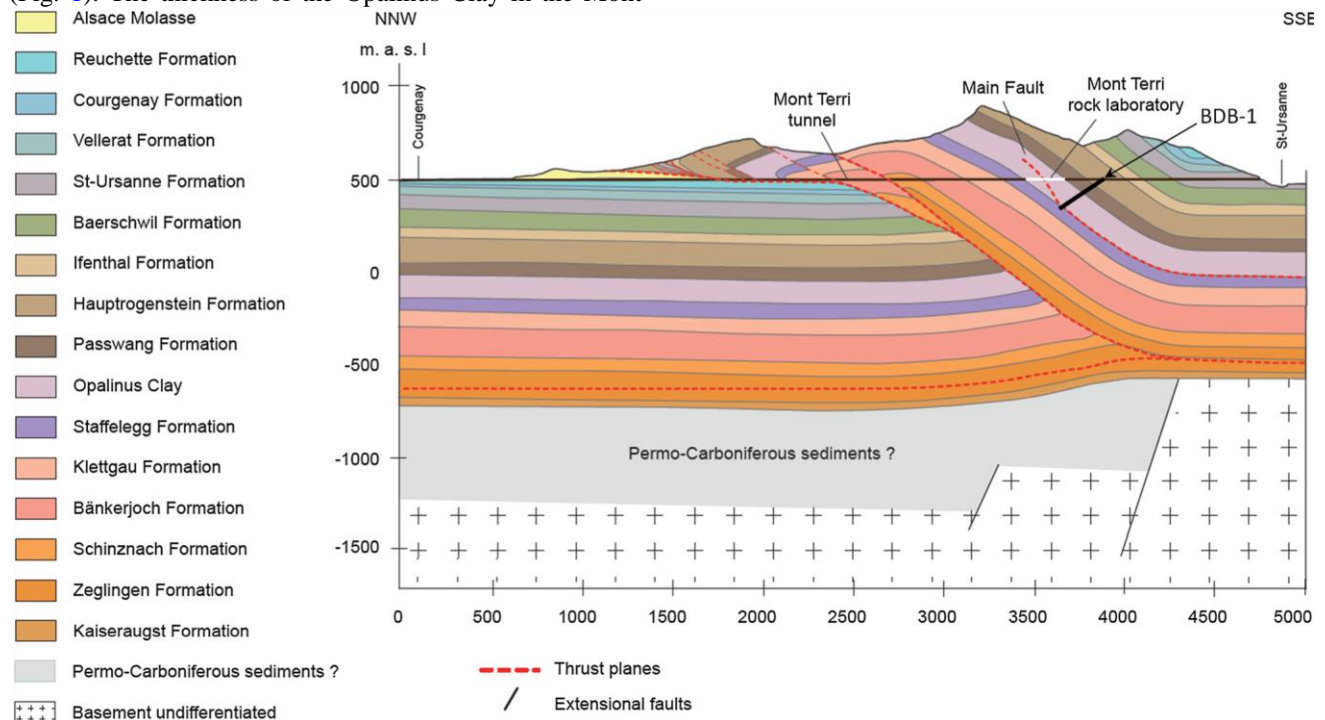
Fig. 1 Geological cross-section of the Mont Terri anticline. Location the Dogger aquifer, the entire Opalinus Clay formation and the upper of the rock laboratory is indicated by a white line. The BDB-1 deep part of the Liassic marls (adapted from Nussbaum et al. 2017) borehole, represented by a thick black line, crosses the lower part of of the Dogger aquifer, the entire Opalinus Clay formation and the upper part of the Liassic marls.
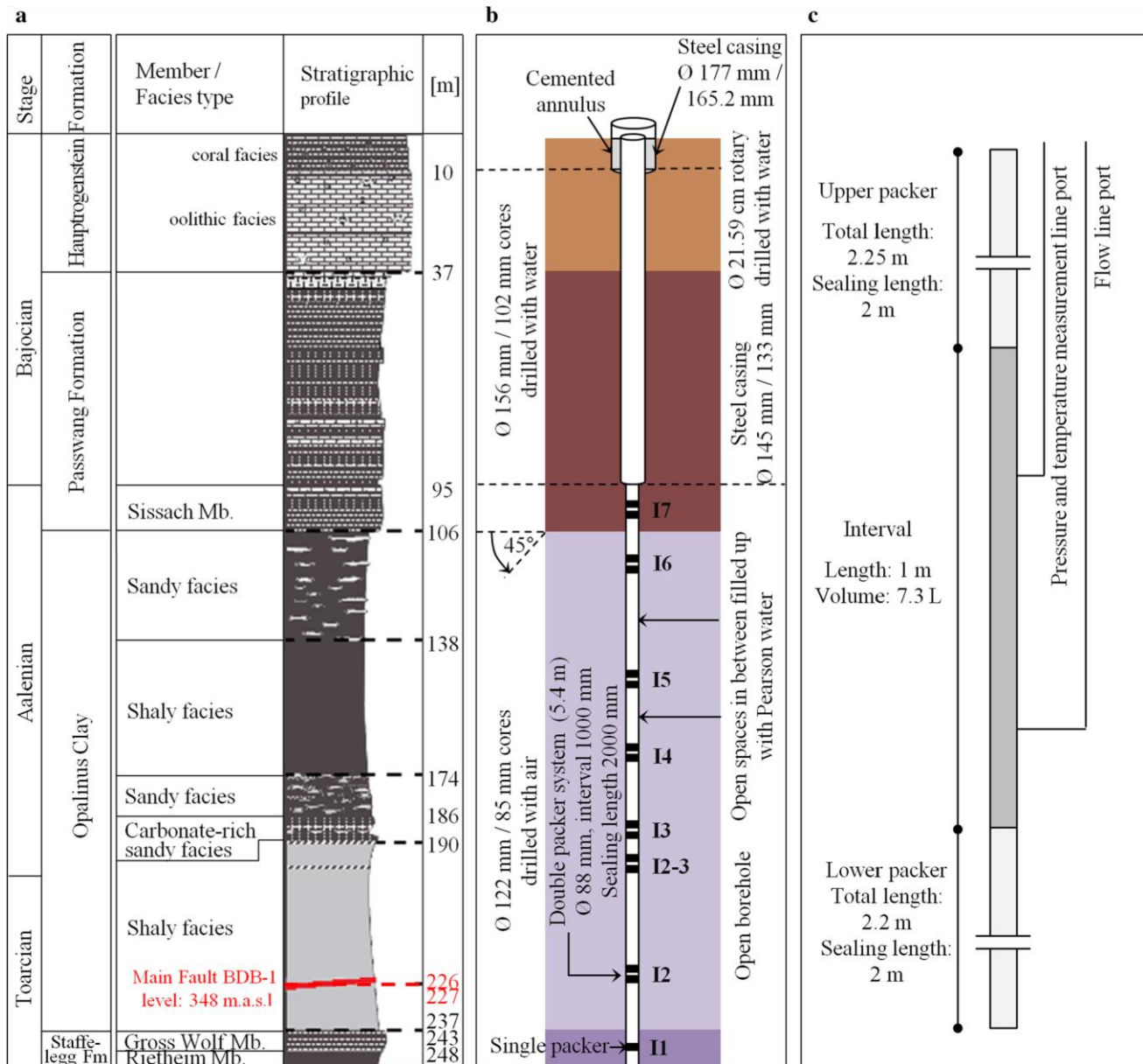
Fig. 2 a Stratigraphic sequence along the BDB-1 borehole; **b** BDB-1 borehole layout; **c** Layout of double packer elements (adapted from Hostettler et al. 2017)

middle part of the formation, and a sandy facies interstratified with shaly facies in the upper sequence. The shaly facies mineral composition includes 27–78% of clay minerals (illite, chlorite, kaolinite and illite–smectite mixed layers), 4–29% of carbonates, 10–32% of quartz, and accessory feldspars, pyrite and organic matter (Bossart and Thury 2008). Several minor tectonic faults and a larger fault zone called ''Main Fault'' can be observed in the Opalinus Clay (Nussbaum et al. 2011). Nagra's investigations in deep boreholes at Riniken, Weiach, Schafisheim and Benken revealed that the

tectonically disturbed zones are hydraulically similar to the undeformed matrix (Johns et al. 1995; Gautschi 2001). Based on permeameter tests and in situ packer tests, hydraulic conductivity values in tectonically disturbed zones are in the range of 2×10^{-14} to 2×10^{-12} m s^{-1}, and specific storage ranges from 2×10^{-7} to 1.7×10^{-4} m^{-1} (Marschall et al. 2005).

3 BDB-1 deep borehole

The deep borehole experiment (DB) aims at evaluating the hydrogeological properties and processes of undisturbed Opalinus Clay at the Mont Terri rock laboratory. For the

Table 1 Specifications of the pressure and temperature sensors installed in BDB-1 borehole

Sensor type	Temperature	Pore pressure
Model	IST AG PT1000	Keller AG PAA-33X
Validity range	-50 to 650 C	0–50 bars (absolute)
Accuracy	$\pm (0.15 + 0.002 \, |T|)$ C	0.05% FS

first time in this laboratory, a 247.5 m long 45 downward inclined borehole has been drilled through the Opalinus Clay and the bounding formations. The stratigraphic sequence crossed by the borehole is presented in Fig. 2a and is described in detail in Hostettler et al. (2017). The borehole was entirely cored for stratigraphic, petrophysical, mineralogical and geochemical studies. The Opalinus Clay section was drilled with air as drilling fluid. Drilling was immediately followed by the installation of a multipacker system (Fierz and Rösli 2014) consisting in five double packer measuring intervals and an interval port within the Opalinus Clay, a single packer in the Staffelegg Formation at the bottom of the borehole, and a further

double packer interval isolating the lowermost zone of the Passwang Formation (Fig. 2b, c). Intervals were equipped with sensors that enable long term monitoring of pressure and temperature (Table 1). Pressure sensors are located at the surface and connected by stainless steel lines to the interval fluids, whereas temperature sensors are located downhole inside the intervals.

4 Techniques for hydraulic parameters evaluation

4.1 Petrophysical model

Assuming a plane-parallel geometry, the intrinsic permeability can be computed across an argillaceous formation using a semi-empirical Poiseuille-type law (Kostek et al. 1992; Pape et al. 1999; Tremosa 2010):

$$k = \frac{b^2}{3F} \tag{1}$$

where k is the intrinsic permeability [m²], b is the half-pore size [m] and F is the formation factor [-], which accounts for the tortuosity of the porous media and can be determined using the Archie's law (Archie 1942):

$$F = \omega^{-m} \tag{2}$$

where ω is the porosity [-] and m is the cementation factor. The formation factor can also be related to diffusion parameters (Boving and Grathwohl 2001; Van Loon and Mibus 2015) or electrical properties (Archie 1942), following Eqs. (3) and (4):

$$F = \frac{D_w}{D_e} \tag{3}$$

where D_w is the diffusion coefficient in pure water [m² s⁻¹] and D_e is the effective diffusion coefficient [m² s⁻¹].

$$F = \frac{R_0}{R_w} \tag{4}$$

where R_0 is the rock resistivity [ohm m] saturated with a brine of resistivity R_w [ohm m].

The half-pore size can be computed from petrophysical parameters according to the following relation based on a mass balance equation (Neuzil 2000; Altinier 2006):

$$b = \frac{\omega}{(1 - \omega)\rho_s A_s} \tag{5}$$

where b is the half-pore size [m], ω is the porosity [-], ρ_s is the grain density [g m⁻³] and A_s is the specific surface area [m² g⁻¹].

Intrinsic permeability and hydraulic conductivity are linked according to:

$$K = \frac{k\rho_f g}{\mu_f} \tag{6}$$

where K is the hydraulic conductivity [m s⁻¹], ρ_f is the fluid density [kg m⁻³], g is the gravity acceleration [m s⁻²] and μ_f is the fluid dynamic viscosity [Pa s].

Fluid dynamic viscosity was estimated according to Mercer et al. (1975):

$$\mu_f = (5.38 + 3.8A - 0.26A^2) \times 10^{-3} \tag{7}$$

with

$$A = \frac{T - 150}{100} \tag{8}$$

where μ_f is the fluid dynamic viscosity [Pa s] and T is the temperature [C].

The Unesco equation of state (1981) was used to determine the fluid density as a function of salinity, temperature and pressure.

Determination of petrophysical parameters were performed in laboratory on representative element volume samples taken from the central part of BDB-1 drillcores. Porosity and water contents were determined by weighing before and after oven-drying at 105 C until mass stabilisation. Density and degree of saturation were calculated based on Archimede's principle after sample immersion into kerdane following the experimental protocol first proposed by Monnier et al. (1973) and later adapted by Matray et al. (2007) for argillite samples. Grain density was evaluated using a helium pycnometer (Micromeritics AccuPyc II 1340) on oven-dried samples and also recalculated from results of X-Ray diffraction measurements on bulk samples.
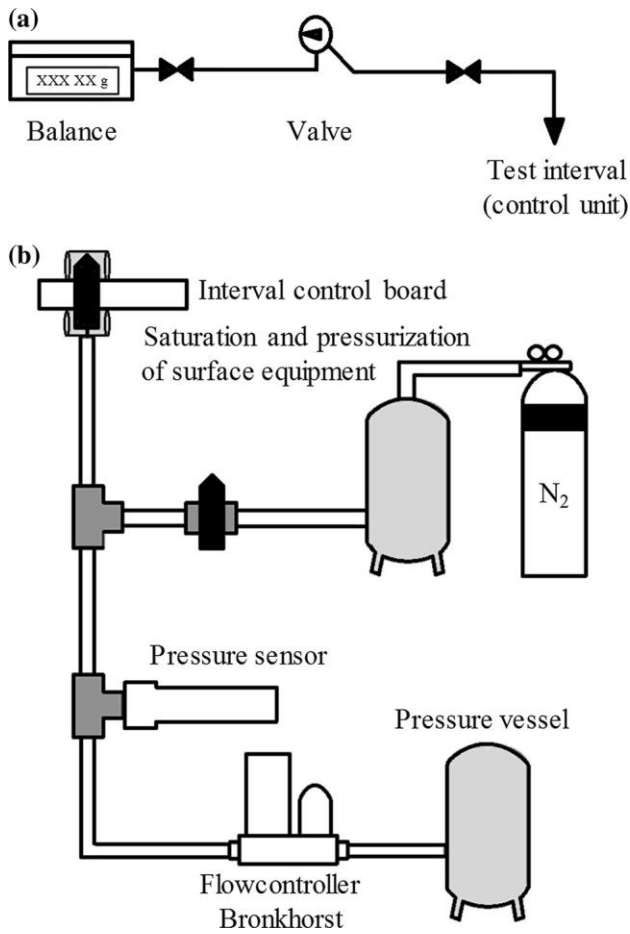
Fig. 3 Experimental set up for: **a** pulse withdrawal tests; **b** constant rate pumping tests performed on BDB-1 borehole (Solexperts)

4.2 In-situ hydraulic testing experiments

Hydraulic in situ testing in boreholes, also referred as well testing, is the most common method used in groundwater and oil industries to acquire the hydraulic properties of geological formations. Pulse withdrawal tests and constant rate withdrawal tests were conducted in BDB-1 borehole, from March 11th to November 16th 2015. During a withdrawal pulse test, pressure is lowered abruptly by opening and closing the downhole shut-in valve

(Bredehoeft and Papadopoulos 1980; Neuzil 1982). These tests are preferred as initial phase because they give an immediate measurement of the system compressibility and generally require shorter time frame than pumping tests. Given its quick hydraulic response, performing more pulse tests on interval 1 (Staffelegg Formation, Fig. 2b) was possible, whereas two pulse tests were carried out on each of the other intervals.

Constant rate withdrawal test parameters such as flow rate and flow duration must be chosen with caution. In low permeability media, high flow rates can lead to desaturation of the measuring intervals and extreme drops in pressure. Therefore, a flowmeter able to sustain a very low pumping rate of 0.3 g h^{-1} for several days (Bronkhorstl-flow L01) was used to test intervals 2 to 7 (Fig. 2b), for which the hydraulic responses to pulse testing were the slowest. Interval 1 was tested with a higher flow rate of 5 ml min^{-1} using a Bronkhorst Liqui-Flow L10. Experimental setups for both kind of tests and associated hydraulic responses are respectively reported in Figs. 3 and 4. Flowmeter failed during the testing of intervals 2 and 6 and approximatively two months of pressure recovery were required before performing a second test on these test chambers.

Hydraulic test data were analysed using the well-test interpretation program nSIGHTS, which was developed by INTERA for Sandia National Laboratories (Beauheim and Roberts 2004). The code is based on Barker's equation (1988), which describes flow in an n-dimensional space, and does not restrict to integer dimensions (Beauheim et al. 2004).

$$S_s \frac{\partial h}{\partial t} = \frac{K}{r^{n-1}} \frac{\partial}{\partial r}\left(r^{n-1}\frac{\partial h}{\partial r}\right) \tag{9}$$

where S_s is the specific storage coefficient [m^{-1}], h is the hydraulic head [m], t is the elapsed time [s], K is the
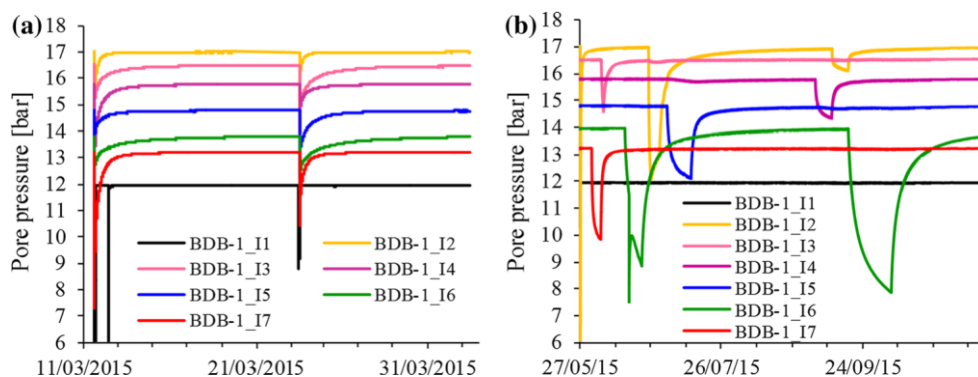
Fig. 4 Records of pore pressure responses in the seven intervals of BDB-1 borehole to: **a** pulse tests; **b** constant rate withdrawal tests

Table 2 Plausibility ranges set in nSIGHTS for fitted parameters

Fitted parameter	Plausibility range
K [m s^{-1}]	
Interval 1	10^{-13}–10^{-8}
Interval 2 to 7	10^{-13}–10^{-11}
S$_s$ [m^{-1}]	10^{-8}–10^{-4}
Flow dimension [-]	1–3.5
Skin thickness [cm]	0.5–30
External boundary radius [m]	0–5

K stands for hydraulic conductivity and Ss for specific storage. Skin zone conductivity ranges were set one order of magnitude higher compared to intact rock

hydraulic conductivity [m s^{-1}], r is the radial distance from borehole [m], and n is the flow dimension [-]. The flow area is defined as

$$A(r) = b^{3-n} \frac{2\pi^{n/2}}{\Gamma^{n/2}} r^{n-1} \tag{10}$$

where b is the extent of the flow zone [m], and C is the gamma function [-].

nSIGHTS is able to take account of borehole inclination by adjusting parameters such as formation thickness or capacitive effect. Equations are programmed as functions of pressure and the code uses unsensitively pressure or hydraulic head data according to user configuration. Flow is simulated in saturated conditions under a pressure gradient between the well and the external boundary of the model following Dupuit conditions. Density effects do not intervene directly in the equation system, as density is considered constant in the test interpretation.

Uncertainties associated with the fitted parameters are evaluated by performing random perturbation analyses. Plausibility ranges for fitted parameters were defined prior to the parameter optimisation procedure (Table 2). During the inverse parameter estimation, nSIGHTS provides bestfit results within these pre-defined ranges. Optimisation was performed using a simplex approach. Uncertainties associated with the fitted parameters are evaluated by performing random perturbation analyses (not detailed in this paper).

4.3 Tidal analysis on pore pressure time series

Rotational and gravitational forces exerted by the sun and the moon on the Earth induce latitudinal and longitudinal strains within the solid matrix and cause deformations with two dominant periods: diurnal and semi-diurnal. The tidal gravitational potential can be resolved into a finite set of tidal components described as harmonics, which are sinusoidal functions of given amplitude and frequency (Doodson and Warburg 1941; Cutillo and Bredehoeft 2011). Five main components account for about 95% of the tidal potential: the M$_2$ and N$_2$ semidiurnal lunar tides, the S$_2$ semidiurnal solar tide, the O$_1$ diurnal lunar tide, and the K$_1$ diurnal lunar-solar tide.

Seasonal or climatic variations, anthropogenic activities and tidal forces induce hydraulic pressure changes in geological formations. The amplitude of the pressure response depends on the poroelastic response of the aquifer matrix. Pressure signal can therefore be analysed to determine hydrogeological properties, such as specific storage, effective porosity and hydraulic conductivity. The models used in this work are based on Terzaghi's (1936) effective stress concept, which assumes a constant total stress distributed between grains and fluid stress. Bredehoeft (1967) related tidal strain to specific storage:

$$S_s = \frac{|\Delta\varepsilon|}{|\Delta h|} \tag{11}$$

where S_s is the specific storage [m^{-1}], |De| is the amplitude of volumetric strain fluctuation fixed at 2 9 10^{-8} for the M$_2$ tide (Melchior 1978), and |Dh| is the amplitude of relative pressure head fluctuations [m].

Jacob's (1940) formula was used to compute the porosity:

$$\omega = \frac{E_W S_s B}{\rho_f g} \tag{12}$$

where ω correspond to the porosity [-], E_W is the stiffness modulus of water, equal to 2.05 GPa, S_s is the specific storage [m^{-1}], B is the barometric efficiency [-], which reflects the elastic response of the system, ρ_f is the fluid density, and g is the gravity acceleration equal to 9.81 m s^{-2}.

Hydraulic conductivity was estimated with formulations using the M$_2$ harmonic amplitude and phase shift (Boldt-Leppin and Hendry 2003; Timms and Acworth 2005), measured at two depths, z$_1$ and z$_2$ [m]:

$$K_v^{Amp}(f_{M_2}) = S_s(f_{M_2}) \frac{\pi (z_1 - z_2)^2}{(f_{M_2})^{-1}} \left[ln\left(\frac{A_{z_1}(f_{M_2})}{A_{z_2}(f_{M_2})}\right) \right]^{-2} \tag{13}$$

$$K_v^{\Delta\varphi}(f_{M_2}) = S_s(f_{M_2}) \frac{\pi}{(f_{M_2})^{-1}} \left[\frac{(z_1 - z_2)}{\Delta\varphi(f_{M_2})} \right]^2 \tag{14}$$

where K_v^{Amp} is the "amplitude effective hydraulic conductivity", A$_{z1}$ and A$_{z2}$ [kPa], are the M$_2$ earth tide amplitude associated to the sensors, S$_s$ [m^{-1}] is the arithmetic mean of the effective specific storage coefficients obtained individually for the two sensors, f$_{M2}$ [s^{-1}] is the frequency of the M$_2$ earth tide equal to 2.236 × 10^{-5} Hz, $K_t^{\Delta\varphi}$ [m s^{-1}] is the "phase effective hydraulic

conductivity'', and $\Delta\varphi$ [rad] is the spectral phase shift between the sensors.

Spectral analysis of BDB-1 borehole pressure dataset was performed using the Multi-Statistical Analysis Tool (MuSTAT v1), jointly developed by the Institut de Radioprotection et de Suˆreté Nucléaire and the Institut National Polytechnique de Toulouse (Fatmi et al. 2008; Ababou et al. 2012; Bailly et al. 2014). Consisting in a Python code associated with toolboxes programmed in Matlab, the package provides automatic features: (a) preprocessing of time series, that enables the detection of time gaps and spurious values, as well as data reconstruction by autoregressive first order process; (b) processing of a single time series; (c) cross-analysis of two time series.

5 Results at various scales of investigation

5.1 Sub-millimeter to centimeter scale

5.1.1 Petrophysical parameters

The petrophysical parameters necessary for the computation of intrinsic permeability are presented in Fig. 5 as a function of distance along BDB-1 borehole.

The mean water accessible porosity is 13.0% in the Opalinus Clay, with a lower average porosity of 12.0% in the sandy facies compared to the shaly facies, which exhibit a mean porosity of 13.5%. These values are lower than the mean value of 18% suggested by previous studies performed at the Mont Terri tunnel level.

The Passwang Formation presents slightly lower porosity values ranging between 8.1 and 14.6% with a mean value of 12.2%. The Hauptrogenstein is characterised by the lowest porosity with a mean value of 3.9%.

Grain densities obtained by helium pycnometry have a mean value of 2.74 g cm^{-3} in the Opalinus Clay overlying formations and of 2.72 g cm^{-3} in the argillaceous layer. The lowest grain densities are found in the bituminous Rietheim Member of the Staffelegg Formation (see Fig. 1a), ranging between 2.3 and 2.4 g cm^{-3}. These low values are probably linked to the presence of organic matter.

The Passwang Formation, which directly overlays the Opalinus Clay, does not reveal clear petrophysical discrepancies with the clay formation except for the specific surface area. This parameter has an average value of 13 m^2 g^{-1} in the carbonated section of the borehole and shows significant fluctuations linked to the marly composition of the Passwang Formation. A higher mean value of 29 m^2 g^{-1} characterises the Opalinus Clay.

The Opalinus Clay is also characterised by a low pore size. Analyses of nitrogen adsorption and desorption isotherms show that 70 to 93% of the connected porous network is constituted of mesopores (pore diameter between 2 and 50 nm), with a mean size of 13 nm. Calculation of the half-pore size from petrophysical parameters, following Eq. (5), gives mean pore sizes in the range of 3.1 to 7.3 nm.
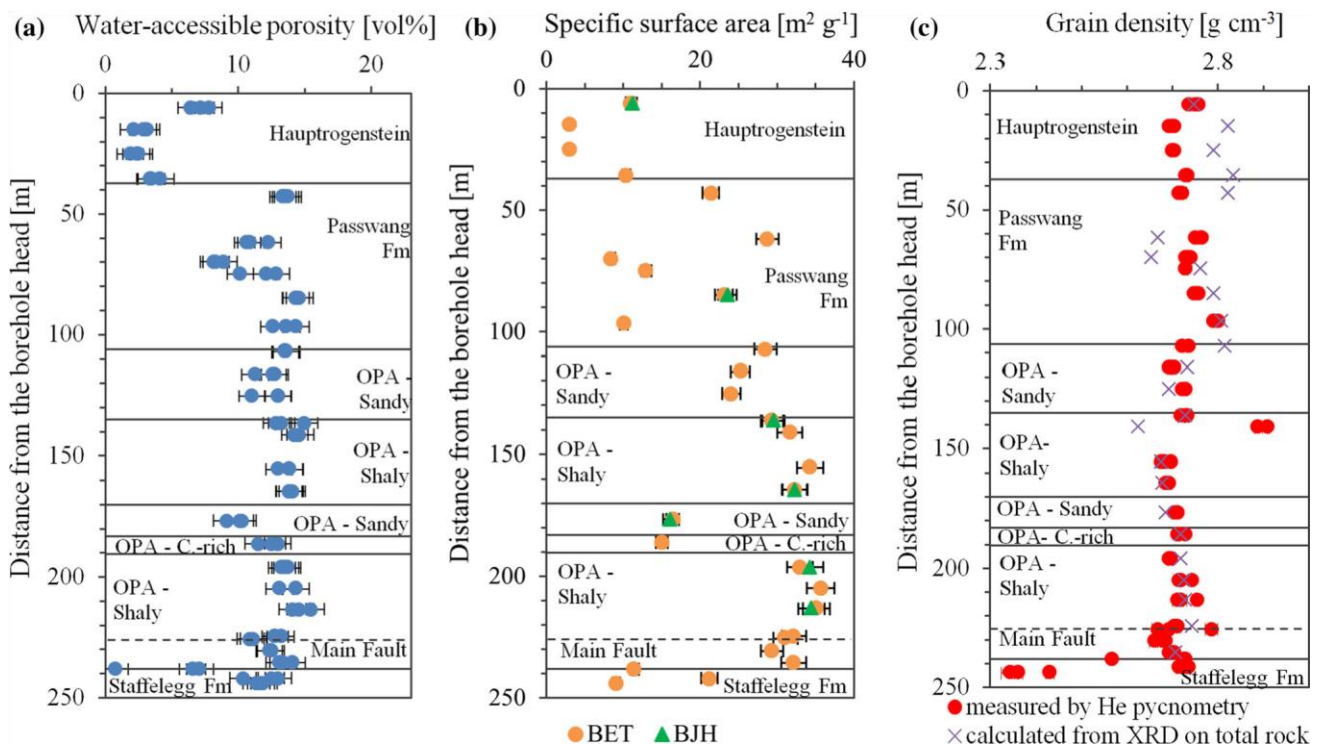
Fig. 5 Petrophysical parameters acquired along BDB-1 borehole: **a** Water accessible porosity acquired by oven-drying at 105 C; **b** Specific surface area obtained by BJH and BET methods; **c** Grain density estimated by helium pycnometry on oven dried samples
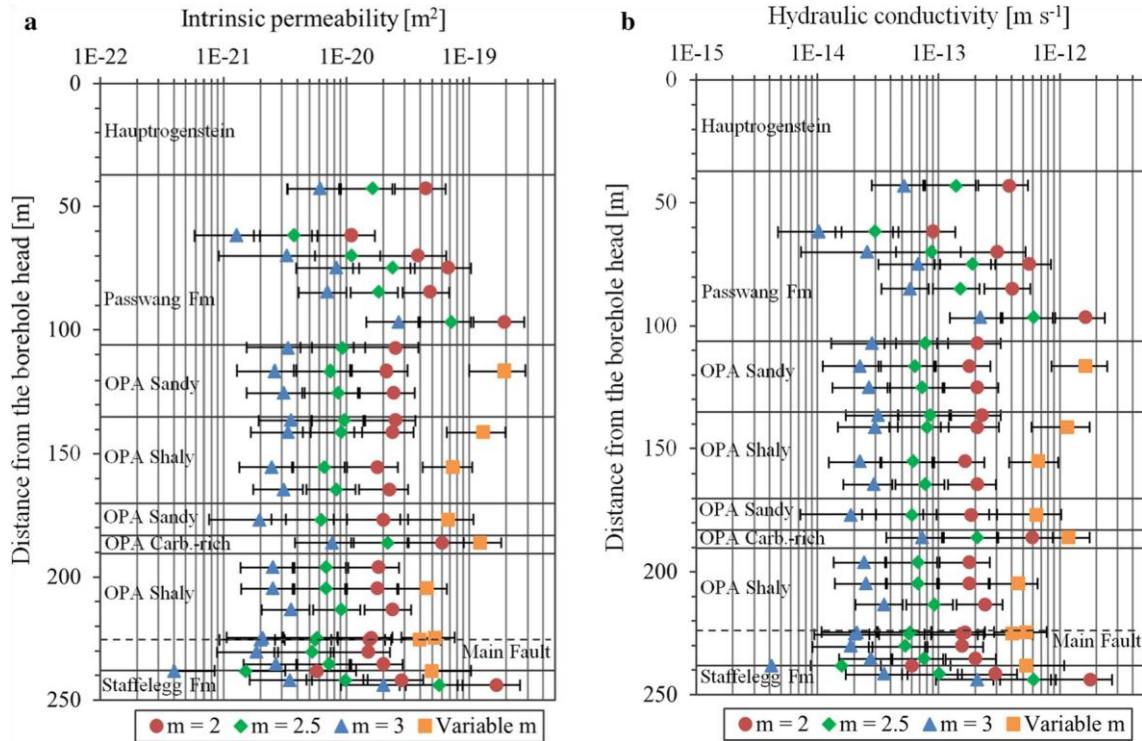
Fig. 6 a Intrinsic permeability profile and **b** hydraulic conductivity profile computed across the Opalinus Clay (OPA) and the Passwang Formation for cementation factor (m) of 2, 2.5 and 3.

Square symbols represent values for variable m computed based on conductivity logging measurements across the Opalinus Clay

Ranging between 1.3 and 5.4 (Horseman et al. 1996), the cementation factor was estimated to be close to 2 for compacted and deeply buried sediments (Ullman and Aller 1982; Tremosa 2010). Van Loon et al. (2003) related the effective diffusion coefficient of tritium measured in the Opalinus Clay to its porosity using a cementation factor of 2.5. An attempt was made to compute cementation factors from conductivity values obtained by borehole logging in BDB-1 and water-accessible porosity determined at laboratory scale. No real conductivity of formation fluid was acquired in the Opalinus Clay, as this part of the borehole was drilled with air. Therefore, fluid conductivity values were estimated based on chlorinity data acquired on BDB1 core samples (not detailed in this paper). Low values of cementation factors are thus obtained and range between 0.9 and 1.7.

5.1.2 Intrinsic permeability and hydraulic conductivity

The intrinsic permeability profiles (Fig. 6a) show a low vertical variability through the Opalinus Clay, where it ranges between 1.8×10^{-21} and 6.1×10^{-20} m^2 if a cementation factor varying between 2 and 3 is taken. For a cementation factor of 2.5, the mean intrinsic permeability is 7.7×10^{-21} m^2 for the Opalinus Clay shaly facies and 7.9×10^{-21} m^2 for its sandy facies. These values are in good agreement with the range of 1×10^{-21} and 6×10^{-20} m^2 obtained by gas injection experiments performed at the

Mont Terri laboratory (Marschall et al. 2005). Based on the same cementation factor, difference can be seen in the carbonate-rich sandy facies, where values are about three times higher than in the shaly and the sandy facies. With a higher exponent m = 3, the resulting intrinsic permeability has a mean value of 7.6×10^{-21} m^2 and no clear distinction arises between the different facies. The intrinsic permeability values computed in the Passwang Formation and the Staffelegg Formation are much more heterogeneous and vary between 1.5×10^{-21} and 5.8×10^{-20} m^2.

The corresponding hydraulic conductivity profiles are presented in Fig. 6b and show similar trends compared with the intrinsic permeability profiles. The hydraulic conductivity obtained for the Opalinus Clay ranges between 1.9×10^{-14} and 5.8×10^{-13} m s^{-1} for a cementation factor varying between 2 and 3. For a cementation factor of 2.5, the formation is characterised by a mean hydraulic conductivity of 8.3×10^{-14} m s^{-1}. No clear discrepancy between the shaly facies and the sandy facies is revealed, with respective mean values of 7.3×10^{-14} and 6.9×10^{-14} m s^{-1}. These values are consistent with the range of 2×10^{-14}–1×10^{-12} m s^{-1} reported in previous studies (Bossart and Thury 2008). The Passwang Formation and the Staffelegg Formation present a various range of hydraulic conductivities between 1.6×10^{-14} and 6.1×10^{-13} m s^{-1}.
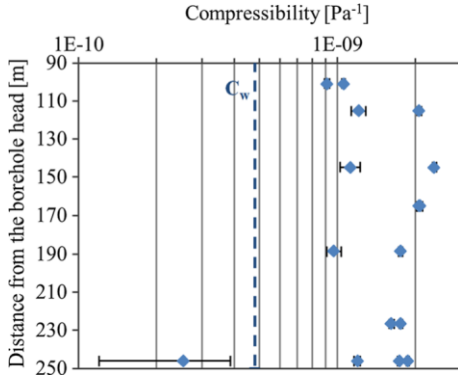
Fig. 7 System compressibility computed from pulse testing in BDB1 borehole. *Dashed line* represents the water compressibility at 10 °C. The outlier in the *lower* part of the borehole is due to a very low withdrawn volume

The computation of intrinsic permeability using variable cementation factors in the Opalinus Clay gives higher values in the range of 4.0×10^{-20} to 1.9×10^{-19} m², corresponding to hydraulic conductivity values in the range of 4.1×10^{-13}–1.7×10^{-12} m s⁻¹.

5.2 Decimeter to meter scale: in situ hydraulic tests results

Pore pressure should be fully recovered from artificial disturbance induced by the installation procedure (e.g., drilling, logging, equipment installation) before starting a hydraulic test. Steady state was considered to be reached when the tidal components were detected on all pore pressure time series acquired in BDB-1 borehole, which indicate that the system is fully pressurised and saturated (see Sect. 5.3.1).

The observed compressibility of the test zone (C_{tz}) was deduced from pulse tests and computed according to:

$$C_{tz} = \frac{1}{V_{tz}} \frac{dV}{dP} \tag{14}$$

where V_{tz} [m³] is the shut-in volume, dV [m³] is the withdrawn volume and dP [Pa] is the pressure variation. Test zone compressibility in BDB-1 borehole varies between 9.1×10^{-10} and 2.4×10^{-9} Pa⁻¹ (Fig. 7), approximately up to a factor of 5 larger than water compressibility, which is equal to 4.8×10^{-10} Pa⁻¹ at 10 °C (Kell 1975). The discrepancy can be attributed to the mechanical compliance of the equipment.

Semi-logarithmic plots presented in Fig. 8 give a qualitative comparison of the hydraulic behaviours characterising the different tested intervals. Degree of pore

pressure dissipation (U) and normalised drawdown pressure (U_{norm}) are respectively defined by the following equations:

$$U = \frac{U_t - U_0}{U_{min} - U_0} \tag{15}$$

$$U_{norm} = \frac{U_t - U_{min}}{U_0 - U_{min}} \tag{16}$$

where U_t [kPa] is the pore pressure at time t, U_0 [kPa] is the hydrostatic pore pressure in situ and U_{min} [kPa] is the pore pressure reached after pulse application or at the end of the pumping phase.

Discrepancies in the degree of dissipation can be observed between tests performed on a same interval (Fig. 8a). Constant rate withdrawal tests were carried out using the same flow rate of 0.3 g h⁻¹ for different durations. To compare the evolution of pore pressures in the measuring intervals during pumping phase, P_{min} was taken to correspond to the shortest pumping duration in the calculation of U_{norm}. If specific storage is assumed homogeneous through the Opalinus Clay, the order from left to right on Fig. 8b gives an indication of decreasing permeability.

The application of a composite model, which takes into account a damaged skin zone, was required for most of the test numerical interpretations. Taking as an example the first pulse test carried out on BDB-1 Interval 2, Fig. 9 shows a comparison of the residuals (measured value minus simulated value) to that of a normal distribution, using a homogeneous model and a composite one. The homogeneous model appears to be unsatisfactory because the residuals are not normally distributed, which indicates the presence of a systematic error.

Pulse tests and constant rate pumping tests results are respectively compiled in Table 3. Pulse testing revealed the highest hydraulic conductivity values in the Staffelegg Formation (Interval 1, see Fig. 2b) with best fit values ranging from 2.1×10^{-10} to 5.9×10^{-10} m s⁻¹. Located in the basal shaly facies of Opalinus Clay (Interval 2), the bottom part of the main fault zone is characterised by conductivity values from 3.1×10^{-12} to 7.3×10^{-12} m s⁻¹ and do not differ from the upper shaly facies represented by Interval 4 and 5 (Fig. 10), whose best estimates are up to 4.2×10^{-12} m s⁻¹. The lowest values are found in the sandy facies (Interval 6, best fit values up to 2.7×10^{-13} m s⁻¹), and the carbonate-rich sandy facies (Interval 3, best fit values up to 5.1×10^{-13} m s⁻¹).
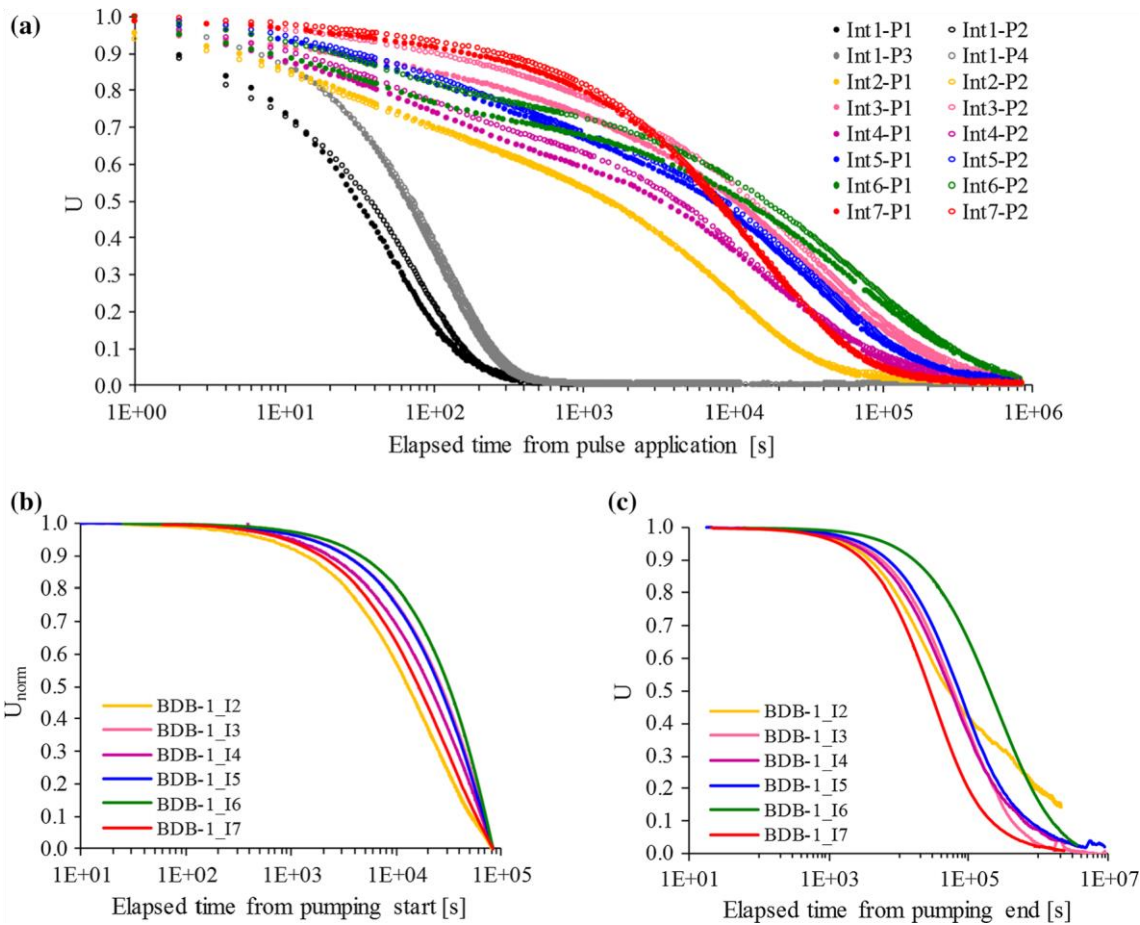
Fig. 8 Comparison of the different tests performed on BDB-1 constant rate withdrawal tests and c degree of dissipation following borehole: **a** degree of dissipation associated to the recovery phases the end of the withdrawal phase of pulse withdrawal tests; **b** normalised pressure drawdown during
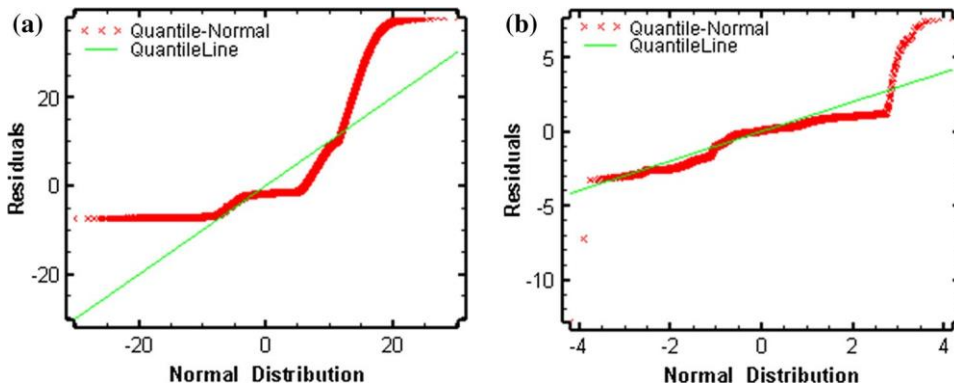
Fig. 9 Example of residual plots for the optimization of Interval 2 (Opalinus Clay shaly facies) pulse sequence fit to the Cartesian pressure response using **a** an homogeneous model and **b** a composite model with skin

The basal part of the Passwang Formation, represented by Interval 7, shows similar hydraulic conductivity values to Opalinus Clay.

The analyses results of the constant flowrate withdrawal tests are quite consistent with those obtained from pulse tests. Indeed, a similar trend can be observed with slightly higher $(5.8 \times 10^{-13}$–1.4×10^{-12} m s$^{-1})$.

Table 3 Parameter estimates from BDB-1 borehole pulse withdrawal tests and constant rate (CR) withdrawal tests (K [m s^{-1}]: hydraulic conductivity; S$_s$ [m^{-1}]: specific storage; n: flow dimension; t$_s$ [cm]: skin thickness)

Test	Interval	T$_s$ [cm]	K [m s^{-1}] Formation Range	Formation Best fit	Skin Best fit	S$_s$ [m^{-1}] Formation Range	Formation Best fit	Skin Best fit	n Range	n Best fit
Pulse										
C1–1	I$_1$	–	1×10^{-10}–3.5×10^{-10}	2.1×10^{-10}	–	$6\ 9\ 10^{-9}$–$6.3\ 9\ 10^{-8}$	1.4×10^{-8}	–	1.9–2.7	2.2
C1–2	I$_1$	–	1×10^{-11}–1×10^{-7}	$4.2\ 9\ 10^{-10}$	–		1.4×10^{-6}	–		2.0
C1–3	I$_1$	–	1×10^{-11}–1×10^{-7}	5.6×10^{-10}	–		6.3×10^{-8}	–		2.4
C1–6	I$_1$	–	3×10^{-11}–1×10^{-8}	5.9×10^{-9}	–		8.3×10^{-7}	–		2.0
C2–1	I$_2$	0.5	2×10^{-12}–3×10^{-11}	3.1×10^{-12}	7.8×10^{-12}	$1\ 9\ 10^{-7}$–$3\ 9\ 10^{-5}$	5.2×10^{-6}	4.3×10^{-5}	1.8–3.0	2.8
C2–2	I$_2$	0.5	2×10^{-12}–1×10^{-10}	7.3×10^{-12}	1.0×10^{-11}	$1\ 9\ 10^{-7}$–$9\ 10^{-5}$	3.0×10^{-6}	4.7×10^{-5}	1.4–2.9	2.0
C3–1	I$_3$	0.5	1×10^{-13}–3×10^{-12}	5.1×10^{-13}	1.6×10^{-12}	$5\ 9\ 10^{-7}$–$3\ 9\ 10^{-5}$	3.7×10^{-6}	1.2×10^{-5}	1.4–3.1	2.1
C3–2	I$_3$	0.5	2×10^{-13}–2×10^{-12}	4.9×10^{-13}	1.6×10^{-12}	$2\ 9\ 10^{-6}$–$9\ 10^{-5}$	1.1×10^{-5}	1.5×10^{-5}	1.4–3.4	2.5
C4–1	I$_4$	0.5	$1\ 9\ 10^{-12}$–$9\ 9\ 10^{-12}$	$2.3\ 9\ 10^{-12}$	$5.7\ 9\ 10^{-12}$	$2\ 9\ 10^{-6}$–$1\ 9\ 10^{-5}$	6.4×10^{-6}	5.5×10^{-5}	1.7–3	2.3
C4–2	I$_4$	2.0	7×10^{-13}–1×10^{-11}	4.2×10^{-12}	2.7×10^{-11}	$1\ 9\ 10^{-6}$–$9\ 10^{-5}$	2.2×10^{-6}	9.7×10^{-6}	1.5–3	2.0
C5–1	I$_5$	0.5	4×10^{-13}–4×10^{-12}	1.6×10^{-12}	1.4×10^{-12}	$3\ 9\ 10^{-7}$–$8\ 9\ 10^{-6}$	1.0×10^{-6}	2.6×10^{-5}	1.8–2.9	1.9
C5–2	I$_5$	0.5	4×10^{-13}–3×10^{-12}	1.0×10^{-12}	2.7×10^{-12}	$1\ 9\ 10^{-6}$–$3\ 9\ 10^{-5}$	8.5×10^{-6}	4.7×10^{-5}	1–3	2.5
C6–1	I$_6$	1.5	8×10^{-14}–8×10^{-13}	1.9×10^{-13}	1.4×10^{-11}	$8\ 9\ 10^{-7}$–$1\ 9\ 10^{-5}$	6.6×10^{-6}	6.6×10^{-6}	1.7–3	2.6
C6–2	I$_6$	0.5	2×10^{-13}–6×10^{-13}	2.7×10^{-13}	5.4×10^{-12}	$1\ 9\ 10^{-6}$–$9\ 10^{-5}$	1.7×10^{-5}	2.9×10^{-5}	1.7–3	2.8
C7–1	I$_7$	0.5	3×10^{-13}–4.5×10^{-12}	5.8×10^{-13}	3.7×10^{-13}	$4\ 9\ 10^{-7}$–$2\ 9\ 10^{-5}$	3.7×10^{-6}	1.9×10^{-6}	1.9–3.5	3.0
C7–2	I$_7$	0.5	4×10^{-13}–2×10^{-12}	1.4×10^{-12}	8.6×10^{-12}	$10\text{-}9$–$2\ 9\ 10^{-5}$	1.2×10^{-6}	9.4×10^{-7}	2.1–2.6	2.3
CR										
C1–7	I$_1$	4.3	1×10^{-10}–1×10^{-9}	5.0×10^{-10}	5.7×10^{-9}	$1\ 9\ 10^{-8}$–$1\ 9\ 10^{-4}$	8.2×10^{-6}	6.2×10^{-5}	2.0–3.0	2.1
C2–2	I$_2$	14.2	4×10^{-13}–8×10^{-11}	3.9×10^{-12}	3.5×10^{-11}		1.2×10^{-6}	9.0×10^{-5}	1.4–2.7	1.95
C3–3	I$_3$	0.7	1×10^{-13}–2×10^{-12}	9.9×10^{-13}	1.6×10^{-12}	$3\ 9\ 10^{-8}$–$6\ 9\ 10^{-5}$	1.5×10^{-5}	4.9×10^{-5}	1.5–3.0	1.9
C4–3	I$_4$	1.4	4×10^{-14}–5×10^{-12}	2.4×10^{-12}	3.0×10^{-12}	$4\ 9\ 10^{-8}$–$3\ 9\ 10^{-4}$	1.2×10^{-5}	4.0×10^{-5}	1.9–3.0	2.1
C5–3	I$_5$	1.8	7×10^{-14}–9×10^{-12}	8.1×10^{-13}	1.5×10^{-11}	$1\ 9\ 10^{-7}$–$3\ 9\ 10^{-5}$	8.9×10^{-5}	2.4×10^{-5}	1.9–3.0	2.3
C6–3	I$_6$	0.5	1×10^{-14}–4×10^{-12}	2.2×10^{-13}	1.1×10^{-12}	$1\ 9\ 10^{-7}$–$9\ 10^{-5}$	7.7×10^{-6}	9.9×10^{-5}	1.5–2.9	2.5
C7–3	I$_7$	0.6	1×10^{-13}–1×10^{-12}	4.4×10^{-13}	8.2×10^{-13}	$3\ 9\ 10^{-8}$–$9\ 10^{-6}$	8.5×10^{-6}	2.3×10^{-5}	2.1–3.0	2.7

Shaded cells represent unrealistically wide range of uncertainties
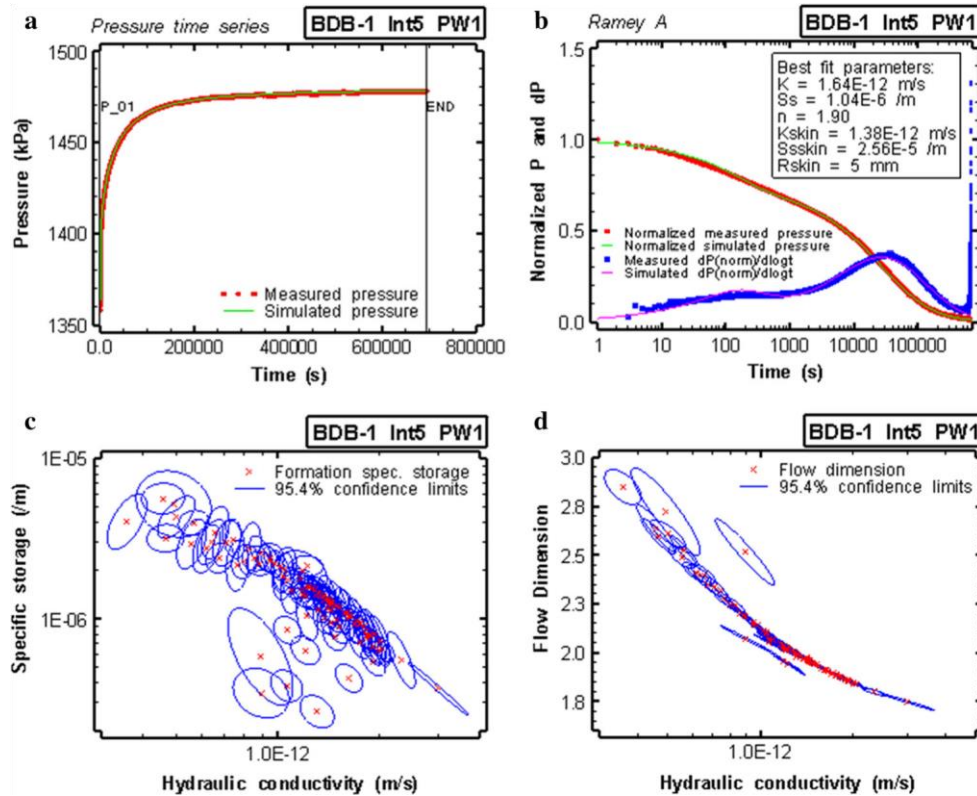
Fig. 10 a Simulation of a pulse test performed on BDB-1 Interval 5 located in the upper shaly facies of Opalinus Clay and **b** associated Ramey A plot with best fit parameters. Results of 200 perturbation analyses and their confidence regions (**c** and **d**)

permeability values in the shaly facies than in the sandy facies of Opalinus Clay.

Specific storage and flow dimension estimates are highly variable. One issue with single well hydraulic testing is that the volume of tested rock is limited to the immediate vicinity of the well.

5.3 Hectometer scale: tidal analysis

5.3.1 Tidal identification in BDB-1 pore pressure series

Detection of tidal components was performed on the pore pressure time series monitored by the sensors placed in BDB-1 borehole, with an acquisition time step set at 15 min. The four largest amplitude tidal components, O_1, K_1, S_2 and M_2 appear on all processed signals at the exact expected frequencies for time series between September 1st 2014 and March 10th 2015 (Fig. 11).

The form ratio is defined as the sum of the two main diurnal component amplitudes, K_1 and O_1, divided by the sum of the two main semi-diurnal component amplitudes, M_2 and S_2 (Wiegel 1964). Tidal deformation through the Opalinus Clay at Mont Terri is characterised by a form ratio varying between 0.84 and 1.04, which indicates a mixed, mainly

Fig. 11 Estimated Root Mean Square spectrum of pore pressure ▶ time series measured in BDB-1 borehole between 01/09/2014 and 10/03/2015. The following tides are observable: principal lunar semidiurnal tide M_2 (2.236×10^{-5} Hz) and solar semidiurnal tide S_2 (2.315×10^{-5} Hz), lunar diurnal tides K_1 (1.161×10^{-5} Hz) and O_1 (1.076×10^{-5} Hz), and the solar diurnal components S_1 (1.157×10^{-5} Hz) and P_1 (1.154×10^{-5} Hz)

semi-diurnal tide (Table 4). The maximum value is found in the interval located in the Passwang Formation, for which the diurnal components have slightly higher amplitudes than the semi-diurnal ones. Except for this interval, the M_2 tide presents the highest amplitude among the four major tides.

5.3.2 Hydraulic parameters computation

The results of specific storage coefficient computation are given in Table 5. Specific storage values are ranging between 1.1×10^{-6} and 1.6×10^{-6} m^{-1} in the Opalinus Clay and are higher for the adjacent formations (2.4×10^{-6} m^{-1} for the Lower Dogger limestone and 3.1×10^{-6} m^{-1} for the Staffelegg Formation). These estimates are consistent with the range given in the literature, deduced from in situ packer tests and permeameter tests for the OpalinusClay
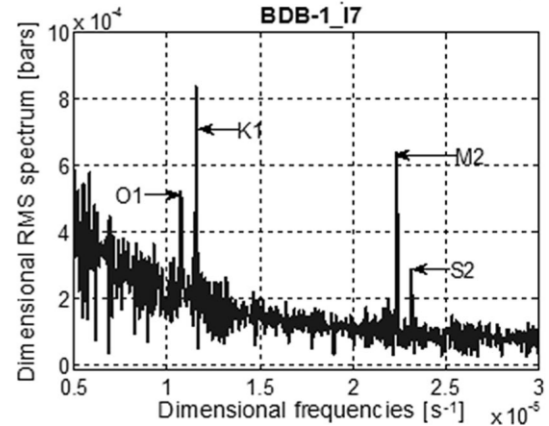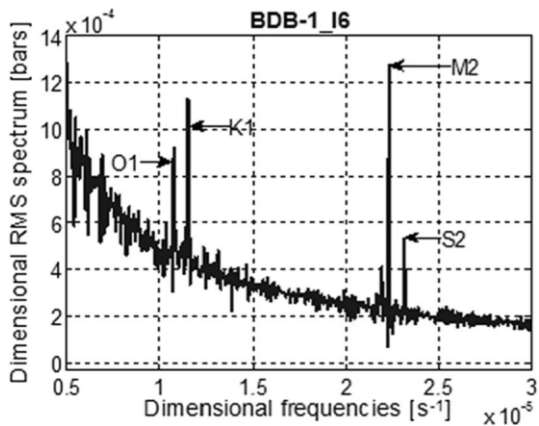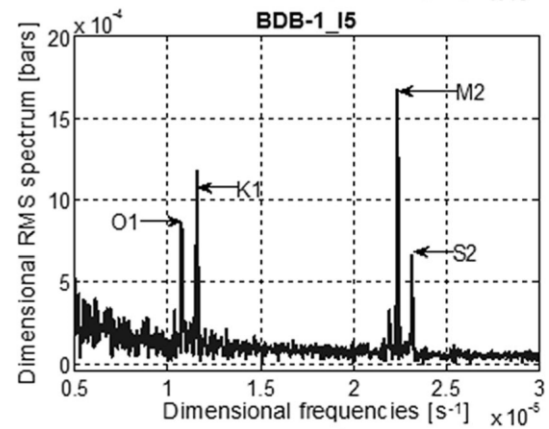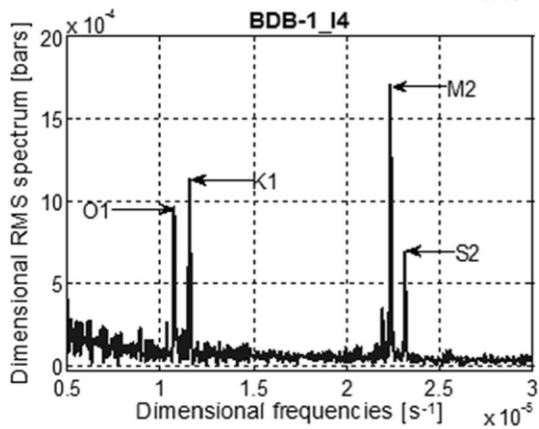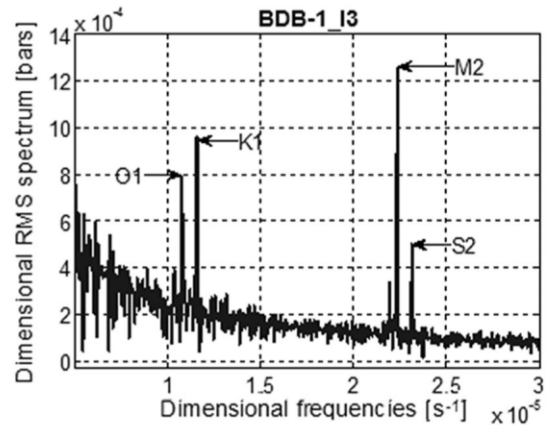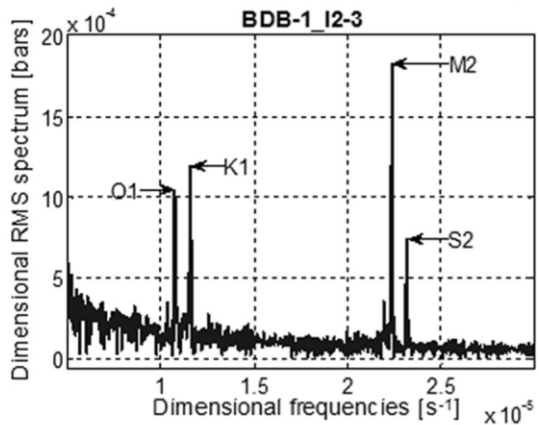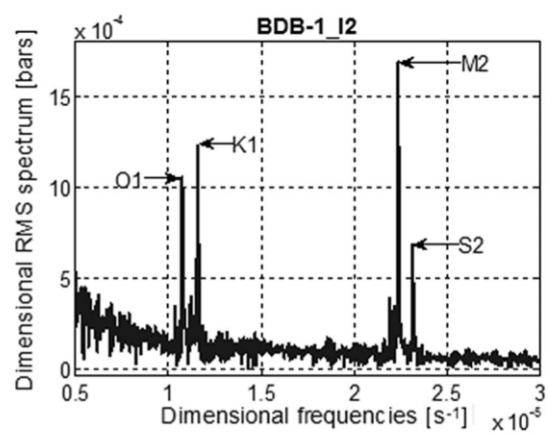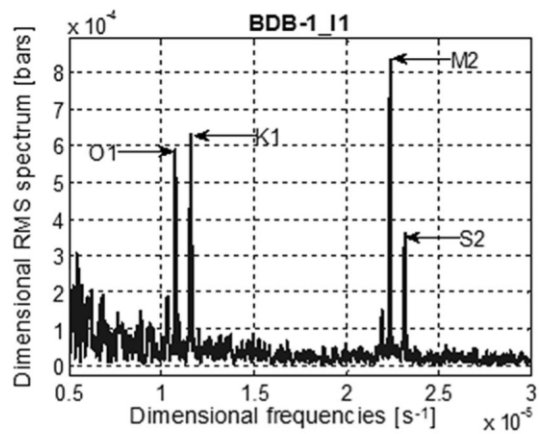
Table 4 Amplitudes of the tidal components with associated frequencies observed on BDB-1 pore pressure time series between 01/09/2014 and 10/03/2015

Formation/associated chamber	Amplitude on the RMS spectrum [bars]				Form ratio
	O_1 $(1.076 \times 10^{-5}$ Hz)	K_1 $(1.161 \times 10^{-5}$ Hz)	S_2 $(2.315 \times 10^{-5}$ Hz)	M_2 $(2.236 \times 10^{-5}$ Hz)	
Staffelegg formation/I_1	5.886×10^{-4}	6.326×10^{-4}	3.606×10^{-4}	8.353×10^{-4}	1.02
OPA-shaly facies/I_2	1.054×10^{-3}	1.230×10^{-3}	6.848×10^{-4}	1.696×10^{-3}	0.96
OPA-shaly facies/I_{2-3}	1.041×10^{-3}	1.192×10^{-3}	7.390×10^{-4}	1.823×10^{-3}	0.87
OPA-carbonate-rich facies/I_3	7.905×10^{-4}	9.553×10^{-4}	5.014×10^{-4}	1.255×10^{-3}	0.99
OPA-shaly facies/I_4	9.560×10^{-4}	1.133×10^{-3}	6.838×10^{-4}	1.701×10^{-3}	0.88
OPA-shaly facies/I_5	8.591×10^{-4}	1.084×10^{-4}	6.546×10^{-4}	1.670×10^{-3}	0.84
OPA-sandy facies/I_6	8.637×10^{-4}	1.205×10^{-3}	5.329×10^{-4}	1.278×10^{-3}	1.04
Passwang formation/I_7	5.200×10^{-4}	7.206×10^{-4}	2.825×10^{-4}	6.360×10^{-4}	1.35

Table 5 Specific storage coefficients (S_s) estimated from absolute pore pressure signals for BDB-1 borehole measuring intervals with corresponding formations and amplitudes of pressure head fluctuations Δh

Formation	Chamber	Δh [bar]	Δh [m]	S_s [m^{-1}]
Upper toarcian-Staffelegg Formation	I_1	8.353×10^{-4}	8.52×10^{-3}	2.4×10^{-6}
Upper toarcian/lower aalenian-Opalinus Clay –shaly facies	I_2	1.696×10^{-3}	1.73×10^{-2}	1.2×10^{-6}
Upper toarcian/lower aalenian-Opalinus Clay –shaly facies	I_{2-3}	1.823×10^{-3}	1.86×10^{-2}	1.1×10^{-6}
Lower aalenian- Opalinus Clay –carbonate-rich facies	I_3	1.255×10^{-3}	1.28×10^{-2}	1.6×10^{-6}
Lower aalenian Opalinus Clay –shaly facies	I_4	1.701×10^{-3}	1.73×10^{-2}	1.2×10^{-6}
Middle aalenian- Opalinus Clay –shaly facies	I_5	1.670×10^{-3}	1.70×10^{-2}	1.2×10^{-6}
Upper aalenian-Opalinus Clay–sandy facies	I_6	1.278×10^{-3}	1.32×10^{-2}	1.5×10^{-6}
Upper aalenian-Passwang Formation	I_7	6.360×10^{-4}	6.49×10^{-3}	3.1×10^{-6}

Table 6 Spectral coherence function (Coh), arithmetic mean of the specific storativity coefficient ($\tilde{S}_s$), amplitude of the pore pressure signal 1 (A_{z1}), and of the pore pressure signal 2 (A_{z2}), vertical effective amplitude hydraulic conductivity ($\tilde{K}_v^{Amp}$) and vertical effective phase hydraulic conductivity ($\tilde{K}_v^{D_t u}$), effective dynamic porosity (x) obtained for the M_2 earth tide for different couples of sensors in BDB-1 borehole

Chamber	Coh	$\tilde{S}_s$	A_{z1}	A_{z2}	$\Delta\varphi$	$\tilde{K}_v^{Amp}$	$\tilde{K}_v^{\Delta\varphi}$	B	ω	$\omega_{water\,loss}$
	[-]	[m^{-1}]	[bar]	[bar]	[rad]	[m s^{-1}]	[m s^{-1}]	[-]	[-]	[-]
I_1 vs. I_2	0.9985	1.8×10^{-6}	8.35×10^{-4}	1.70×10^{-3}	-0.18220	4.7×10^{-8}	7.2×10^{-7}	0.2520	0.09	0.18
I_2 vs. I_{2-3}	0.9992	1.1×10^{-6}	1.70×10^{-3}	1.82×10^{-3}	0.03573	2.5×10^{-6}	1.0×10^{-5}	1.0350	0.24	0.15
I_{2-3} vs. I_3	0.9986	1.3×10^{-6}	1.82×10^{-3}	1.26×10^{-3}	0.07658	1.4×10^{-7}	3.3×10^{-6}	0.3949	0.11	0.13
I_3 vs. I_4	0.9977	1.4×10^{-6}	1.26×10^{-3}	1.70×10^{-3}	-0.06768	2.9×10^{-7}	5.8×10^{-6}	4.6810	1.33	0.12
I_4 vs. I_5	0.9930	1.2×10^{-6}	1.70×10^{-3}	1.67×10^{-3}	0.02158	5.7×10^{-5}	4.1×10^{-6}	0.4758	0.12	0.14
I_5 vs. I_6	0.9965	1.4×10^{-6}	1.67×10^{-3}	1.28×10^{-3}	-0.05037	6.4×10^{-7}	1.8×10^{-5}	0.2889	0.08	0.13
I_6 vs. I_7	0.9965	2.3×10^{-6}	1.28×10^{-3}	6.36×10^{-3}	0.50810	3.9×10^{-8}	7.3×10^{-8}	1.6290	0.79	0.13

Mean water-loss porosity ($\omega_{water\,loss}$) is given for comparison purposes
Shaded cells indicate spurious values

shaly facies: between 1×10^{-7} and 1×10^{-4} m^{-1}, with a best estimate at 2×10^{-6} m^{-1} (Bossart and Thury 2008).
Effective dynamic porosity values obtained using the M_2 tide (Table 6) are globally in well agreement with those obtained from petrophysical measurements. Indeed, coherent values between 8 and 24% are obtained by cross-analyses of measuring intervals located in the Opalinus Clay. Statistical analysis carried out in previous studies on

Mont Terri samples (Fatmi 2009; Bailly and Matray 2015) revealed very low range values between 1 and 4% at the tunnel level. These unexplained low values could be related to the hydraulically disturbed state of the studied area and desaturation phenomena.

Hydraulic conductivity values obtained in the saturated part of the claystone by cross-analysis (Table 6) are much higher than those obtained by other techniques. Indeed, high conductivities ranging between 5.7×10^{-5} and 1.4×10^{-7} m s^{-1} are found in the Opalinus Clay. These values are 6 to 8 orders of magnitude higher than the range expected from literature data, suggesting that the method is not appropriate for this formation. Discrepancies up to three orders of magnitude between laboratory hydraulic conductivity results and tidal analysis results were also reported by Boldt-Leppin and Hendry (2003) who studied the King site claystone formation (Canada). These discrepancies were explained by scale factor effects and the presence of fractured area.

Bailly and Matray (2015) performed statistical analysis on pore pressure time series acquired in the BCD-3 borehole located at the Mont Terri tunnel level. They obtained hydraulic conductivities ranging between 1.9×10^{-10} and 7.5×10^{-11} m s^{-1} in the unsaturated part of the Opalinus Clay by applying the same method on the S_1 solar diurnal tide. The M_2 tide was not found in the studied pore pressure time series due to suction conditions associated to the rock laboratory level. The study also suggested that the structures observed in this borehole were hydraulically conductive, meaning that the Opalinus Clay true permeability should be even lower than the range given by tidal analysis.

6 Discussion

6.1 Comparability of laboratory tests and in situ tests results

Reliable estimates of permeability and specific storage that describe the bulk hydraulic behaviour are needed for the evaluation of radionuclide transport in geological formations. Linking the results of laboratory tests to bulk characteristics at the regional scale is not straightforward and the meaning of measured values has to be interpreted. Sedimentary rocks are generally associated with anisotropic properties such as permeability, diffusion coefficient and mechanical features. In the Opalinus Clay, which is an overconsolidated clay, a moderate permeability anisotropy ratio of 5.5 was estimated based on laboratory permeameter tests (Muñoz et al. 2003; Croisé et al. 2004; Fernàndez Garcia et al. 2007).

The petrophysical model is based on a conceptual parallel plane geometry which would be associated to a flow orientation parallel to bedding planes. Since BDB-1 borehole was drilled perpendicular to bedding plane, the main solicited direction for fluid flow during hydraulic testing is also parallel to stratification. For its part, tidal analysis is mainly based on gravitational forces that propagate radially from the center of the Earth and should result, given the setting of the Mont Terri anticline, in composite values of parallel and perpendicular to bedding permeabilities.

Although the petrophysical model may be unsuited to carbonated formations, calculation was also performed on the Passwang Formation and the Staffelegg Formation, which shows similar petrophysical parameters. Another questionable point is the use of a constant value for the Archie's exponent since this parameter depends on the nature of the porous medium. Consequently, adapted values should be taken in the future according to the evolution of rock facies along the stratigraphic sequence. Conductivities values obtained in BDB-1 with variable cementation factor (Fig. 12a) are only indicative and not qualityassured, given the uncertainties linked to data acquisition. Indeed, the Opalinus Clay was in the air-drilled section of the borehole, giving constraints for in situ determination of cementation factor.

Fitting the cementation factor by comparing petrophysical results and estimates from hydraulic tests can be debatable. Indeed, the volume of solicited rock is higher in the latter case and takes greater account of formation heterogeneities and local potentially open fractures. This point is clearly illustrated by the discrepancies observed for the Staffelegg Formation, in which many fractures were evidenced by drillcore mapping. Indeed, petrophysical measurements on centimetre-scale samples do not take into account these hydraulically conductive structures and underestimate the values of bulk properties.

Archie's law is rigorously an empirical relationship that links the electrical resistivity of saturated clay-free rocks and their porosity. However, an analogy can be made between the electrical potential and the concentration. It has been shown that effective diffusion coefficient could be predicted by this relationship in a variety of clays and shales with a cementation factor ranging between 2 and 3 (Boving and Grathwohl 2001; Van Loon et al. 2003; Mazurek et al. 2009). Best fit values of hydraulic conductivity obtained from hydraulic testing are generally higher that those computed with the petrophysical law (Fig. 12a). Hydraulic conductivities higher than 10^{-12} m s^{-1}
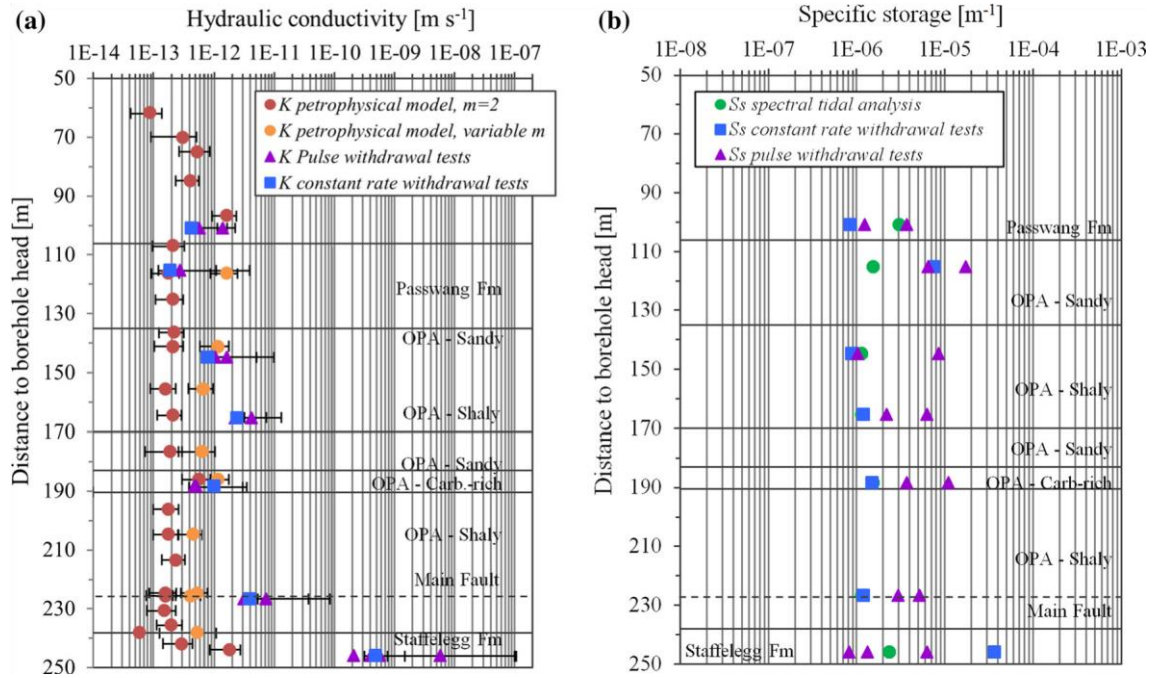
Fig. 12 Comparison of results obtained by petrophysical analysis, in situ hydraulic testing and tidal spectral analysis performed on BDB-1 borehole: **a** hydraulic conductivity **b** specific storage

found in the Opalinus Clay shaly facies would be associated to illogical values of cementation factor inferior to 1.3, which was given for clean unconsolidated sand packs by Archie (1942).

Whether it be for pulse or constant withdrawal tests, the numerical interpretation of hydraulic tests suggests rather wide and unrealistic ranges of uncertainties for hydraulic conductivity and specific storage. Covering several orders of magnitude and not tightly around the best estimates (Table 3), these uncertainties are probably linked to thelarge number of fitted parameters. Tidal analysis may be more representative than single well hydraulic testing for specific storage estimation (Fig. 12b), since the tidal deformation is applied to the entire rockmass. The highest values for specific storage obtained from pulse testing should be taken with caution since the sensitivity to this parameter is low for this kind of test (Cooper et al. 1967).

6.2 Consistency with previous results

Numerous in situ and laboratory investigations have been carried out at the Mont Terri rock laboratory to characterize the hydraulic properties of the Opalinus Clay. Laboratory permeameter tests revealed conductivity values ranging from 6 to 12×10^{-14} m s^{-1} with high associated storage coefficient of 4.8×10^{-4} m^{-1} (Croisé et al. 2004).

Figure 13 shows a compilation of hydraulic conductivity results obtained from packer tests (pulse, constant head and constant rate) performed previously at the Mont Terri site (Lavanchy and Mettier 2012), along with data collected in BDB-1 borehole. Tests were mainly performed in boreholes oblique or normal to bedding drilled in area unaffected by the excavation damaged zone of the tunnel. Previous permeability values measured at the rock laboratory level range from 1.5×10^{-14} to 1.1×10^{-9} m s^{-1} with 55% of the values in the order of 10^{-13} m s^{-1}. The high values above 1.1×10^{-10} m s^{-1} of the shaly facies from previous studies might be affected by the excavation damaged zone (EDZ) and are not quality assured. The best fit values obtained from BDB-1 hydraulic testing fall virtually in the expected range with higher values in the order of 10^{-12} m s^{-1} characterising the Opalinus Clay shaly facies.

Specific storage coefficients obtained by tidal analysis are rather homogeneous within the Opalinus Clay with values in the order of 10^{-6} m^{-1}, which are comparable to the range of 2×10^{-6} to 5×10^{-6} m^{-1} found by Bailly and Matray (2015).

No significant correlation between the hydraulic conductivity and the different lithological facies was highlighted by Croisé et al. (2004), Nussbaum and Bossart (2004) and Lavanchy and Mettier (2012) due to a lack of data from the sandy facies. Although best fit values obtained from BDB-1 borehole indicate higher values in
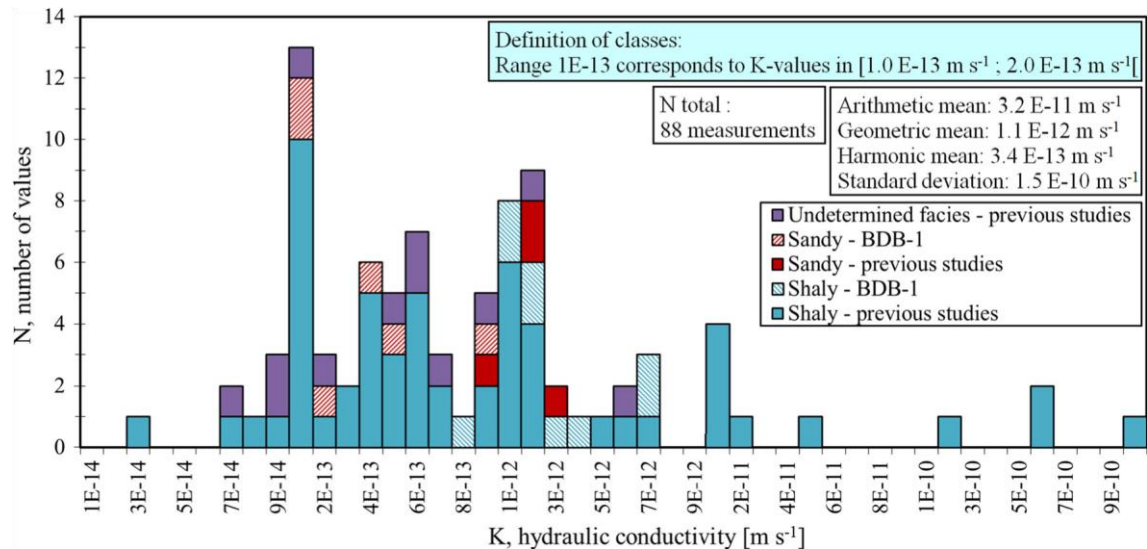
Fig. 13 Compilation of results from hydraulic borehole packer tests performed on the Opalinus Clay at the Mont Terri rock laboratory. The high values of the shaly facies from previous studies might be affected by the EDZ and are not quality assured (modified from Lavanchy and Mettier 2012)

the shaly facies, uncertainty ranges make it difficult to conclude on a possible contrast. Numerical simulations show that sandstone lenses embedded in clay rich strata do not compromise the barrier function of the Opalinus Clay since low hydraulic conductivity values characterise the entire formation. Furthermore, Opalinus Clay sandy layers are better cemented and display lower porosities (Fig. 5a). Microscopic observations in the sandy facies revealed precipitation of authigenic quartz, carbonates and kaolinite (Peters et al. 2011). On the other hand, porosity values measured in BDB-1 borehole are globally lower than those obtained at the rock laboratory tunnel level and may reflect the deconfinement and relaxation of stresses occurring at the latter location.

The Main Fault that intersects the laboratory does not impact the barrier function of the Opalinus Clay. Indeed, the sealing of fault planes by calcite shear fibres and clay minerals induce small effect of tectonic deformation on the hydraulic properties of the Opalinus Clay (Nussbaum et al. 2011). This observation is supported by the consistency between the hydraulic tests performed in the intact shaly facies and those carried out in the interval crossing the fault zone. Similarly, no contrast can be identified on the different profiles obtained with the petrophysical model.

7 Conclusions

The deep borehole (DB) experiment enabled the acquisition of data in a fresh borehole penetrating the entire hydraulically undisturbed Opalinus Clay at Mont Terri. Therefore, the presented results are unique, because other hydraulic data at Mont Terri are or might be influenced by tunneling and experimental activities. Three methods with different investigation volumes were carried out and compared.

A model that links intrinsic permeability to petrophysical parameters gives intrinsic permeability values ranging between 2×10^{-21} and 6×10^{-20} m^2 for a cementation factor varying between 2 and 3, corresponding to hydraulic conductivities between 2×10^{-14} and 6 9 10^{-13} m s^{-1}. Tidal analysis revealed itself not to be an appropriate method to compute hydraulic conductivity in our study, giving values overestimated of several orders of magnitudes. However, this approach gives reasonable values for specific storage and effective porosity. As a third method, in situ hydraulic testing was performed using the multipacker system installed in BDB-1 borehole. Hydraulic conductivity values obtained by numerical inversion from pulse tests are consistent with those deduced from constant rate withdrawal tests, and suggest a slight vertical variability across the formation in the range of 1×10^{-13} to 7×10^{-12} m s^{-1}, possibly due to local variations of the matrix structure, composition and cementation, or the presence of fractures. In conclusion, the hydraulic conductivity values of the deep borehole (DB) experiment agree well with previous hydraulic testing results performed in the hydraulically disturbed Opalinus Clay around the Mont Terri rock laboratory. Therefore, future hydraulic testing in the laboratory outside the excavated damaged zone can be rated as comparable to undisturbed conditions. However, results obtained in BDB-1 borehole show higher values (in the order of 10^{-12} m s^{-1}) for the Opalinus Clay shaly facies than its sandy facies (in the order of 10^{-13} m s^{-1}), which is consistent with previous microscopic observations (Peters et al. 2011). Further laboratory experiments using Hassler

cells will be performed to characterise the Opalinus Clay permeability anisotropy in the future.

Petrophysical analysis of drillcores and time-series analyses are complementary to hydraulic testing. These techniques involve different volumes of investigation. Core analysis, as well as laboratory permeameter tests, give the homogeneous matrix hydraulic properties but do not account for larger scale heterogeneities such as sedimentary and tectonic features. Moreover, analyses on core samples might be influenced by deconfining and alteration of the core material, thus resulting in biased values. Therefore, hydraulic testing in a fresh borehole is the recommended method for determination of hydraulic conductivity in overconsolidated clays. However, the pressure perturbations e.g., induced by drilling activities have to be taken into account for design and analyses of hydraulic testing. The dissipation of drilling and installation of instrumentation induced pressure pertubations can be identified by the tidal components in the pore pressure time series. Our study showed that drilling the BDB-1 borehole with air as drilling fluid and a saturation with artificial pore-water was an appropriate choice for our application, because: (1) no mud-cake was created, (2) no artificial osmotic effects and borehole convergence were observed so far, (3) future water sampling can be carried out since there was no contamination with drilling mud, and (4) we reached fully undisturbed formation pressures after several months. The latter was possible to do so in an underground laboratory experiment, due no time and financial constraints, which are limiting factors on drill site for exploration boreholes. Therefore, in clay formations, particular care should be taken in the choice of drilling method and drilling fluid as well as borehole instrumentation materials, in order to obtain accurate hydraulic parameters.

References

Ababou, R., Fatmi, H., Matray, J. M., Nussbaum, C., & Bailly, D. (2012). Statistical analyses of pore pressure signals in claystone during excavation works at the Mont Terri Underground Research Laboratory. In R. Abdel Rahman (Ed.), Radioactive waste (pp. 373–430). Publisher: InTech.

Altinier, M. V. (2006). Etude de la composition isotopique des eaux porales de l'argilite de Tournemire : intercomparaison des méthodes de mesure et relations avec les paramètres pétrophysiques. Ph. D. dissertation, Université Paris-Sud, Orsay, France, pp. 200

Archie, G. E. (1942). The electrical resistivity log as an aid in determining some reservoir characteristics. Transactions of the American Institute of Mining Metallurgical, and Petroleum Engineers, 146, 54–62.

Bailly, D., Matray, J. M., & Ababou, R. (2014). Temporal behavior of a ventilated claystone at the Tournemire URL: Cross-spectral analyses focused on daily harmonics. Engineering Geology, 183, 137–158.

Bailly, D., & Matray, J.-M. (2015). LP-A Experiment: Phase 20, Statistical analysis of time series acquired in the EZ-B Niche and at the Main fault. Mont Terri Technical Note, TN 2014-59, 79 pp. Federal Office of Topography (swisstopo), Wabern, Switzerland. www.mont-terri.ch.

Barker, J. A. (1988). A generalized radial-flow model for hydraulic tests in fractured rock. Water Resources Research, 24(10), 1796–1804.

Beauheim, R. L., Roberts, R. M., & Avis, J. D. (2004). Well testing in fractured media: flow dimensions and diagnostic plots. Journal of Hydraulic Research, 42, 69–76.

Beauheim, R. L., & Roberts, R. M. (2004). Well-test analysis techniques developed for the Waste Isolation Pilot Plant. In Proceedings of the 66th EAGE Conference and Exhibition, Paris, France.

Blaesi, H.-R., Peters, T. J., & Mazurek, M. (1991). Der Opalinus-Ton des Mt. Terri (Kanton Jura): Lithologie, Mineralogie und physiko-chemische Gesteinsparameter. Nagra Interner Bericht, (pp. 90–60). Nagra, Wettingen, Switzerland. www.nagra.ch.

Boldt-Leppin, B. E. J., & Hendry, J. (2003). Application of Harmonic Analysis of Water Levels to Determine Vertical Hydraulic Conductivities in Clay-Rich Aquitards. Ground Water, 41(4), 514–522.

Bossart, P., & Thury, M. (2008). Mont Terri Rock Laboratory. Project, Programme 1996 to 2007 and Results. Reports of the Swiss Geological Survey, No. 3, p 445. Federal Office of Topography (swisstopo), Wabern, Switzerland. www.mont-terri.ch.

Bossart, P., Bernier, F., Birkholzer, J., Bruggeman, C., Connolly, P., Dewonck, S., Fukaya, M., Herfort, M., Jensen, M., Matray, J-M., Mayor, J. C., Moeri, A., Oyama, T., Schuster, K., Shigeta, N., Vietor, T., & Wieczorek, K. (2017). Mont Terrirock laboratory, 20 years of research: introduction, site characteristics and overview of experiments. Swiss Journal of Geosciences, 110. doi:10.1007/s00015-016-0236-1 (this issue).

Boulin, P. F., Bretonnier, P., Gland, N., & Lombard, J. M. (2012). Contribution of the steady state method to water permeability measurement in very low permeability porous media. Oil and Gas Science and Technology, 67, 387–401.

Boving, T. B., & Grathwohl, P. (2001). Tracer diffusion coefficients in sedimentary rocks: correlation between porosity and hydraulic conductivity. Journal of Contaminant Hydrogeology, 53(1), 85–100.

Bredehoeft, J. D. (1967). Response of well-aquifer systems to Earth tides. Journal of Geophysical Research, 72(12), 3075–3087.

Bredehoeft, J. D., & Papadopoulos, S. S. (1980). A method for determining the hydraulic properties of tight formations. Water Resources Research, 16(1), 233–238.

Butler, J. J. (1998). The design and performance, and analysis of slug tests (p. 252). Boca Raton: Lewis Publishers (imprint of CRC Press LLC).

Chapuis, R. P., & Aubertin, M. (2003). Predicting the Coefficient of Permeability of Soils Using the Kozeny-Carman Equation (p. 35). Montréal: Ecole Polytechnique de Montre´al.

Clauer, N., Techer, I., Nussbaum, C., & Laurich, B. (2017). Geochemical signature of paleofluids in microstructures from ''Main Fault'' in the Opalinus Clay of the Mont Terri rock laboratory, Switzerland. Swiss Journal of Geosciences, 110.

doi:10.1007/s00015-016-0253-0 (this issue).

Cooper, H. H., Bredehoeft, J. D., & Papadopulos, I. S. (1967). Response of a finite-diameter well to an instantaneous charge of water. Water Resource Research, 3, 263–269.

Croisé, J., Schilckenrieder, L., Marschall, P., Boisson, J. Y., Vogel, P., & Yamamoto, S. (2004). Hydrogeological investigations in a low permeability claystone formation: the Mont Terri Rock Laboratory. Physics and Chemistry of the Earth, 29, 3–15.

Cutillo, P. A., & Bredehoeft, J. D. (2011). Estimating aquifer properties from the water level response to earth tides. Ground Water, 49(4), 600–610.

Doodson A. T., & Warburg, H. D. (1941). Admiralty manual of tides. Her Majesty's Stationary Office, London, xii, p 270.

Fatmi, H. (2009). Méthodologie d'analyse des signaux et caractérisation hydrogéologique: application aux chroniques de données obtenues aux laboratoires souterrains du Mont Terri, Tournemire et Meuse/Haute-Marne. Ph.D. dissertation (p. 249). Université de Toulouse.

Fatmi, H., Ababou, R., & Matray, J.-M. (2008). Statistical preprocessing analyses of hydrometeorological time series in a geological clay site (methodology and first results for Mont Terri's PP experiment). Journal of Physical Chemistry Letters A/B/C, 33, S14–S23.

Fernàndez-Garcia, D., Gómez-Hernández, J. J., & Mayor, J. C. (2007). Estimating hydraulic conductivity of the Opalinus Clay at the regional scale: Combined effect of desaturation and EDZ. Physics and Chemistry of the Earth, Parts A/B/C, 32(8), 639–645.

Fierz, T., & Rösli, U. (2014). Mont Terri DB Experiment: Installation of a 7-interval multi-packer system into borehole BDB-1. Instrumentation Report. Mont Terri Technical Note, TN 20414-23. p 37. Federal Office of Topography (swisstopo), Wabern, Switzerland. www.mont-terri.ch.

Gautschi, A. (2001). Hydrogeology of a fractured shale (Opalinus Clay): Implications for the deep disposal of radioactive wastes. Hydrogeology Journal, 9, 97–107.

Horseman, S. T., Higgo, J. J. W., Alexander, J., & Harrington, J. F. (1996). Water, Gas and Solute Movement Trough Argillaceous Media. Nuclear Energy Agency Rep., CC-96/1, OECD, Paris, p 306.

Hostettler, B., Reisdorf, A. G., Jaeggi, D., Deplazes, G., Bläsi, H.-R., Morard, A., Feist-Burkhardt, S., Waltschew, A., Dietze, V., & Menkveld-Gfeller, U. (2017). Litho- and biostratigraphy of the Opalinus Clay and bounding formations in the Mont Terri rock laboratory (Switzerland). Swiss Journal of Geosciences, 110. doi:10.1007/s00015-016-0250-3 (this issue).

Jiang, Z., Martiethoz, G., Taulis, M., & Cox, M. (2013). Determination of vertical hydraulic conductivity of aquitards in a multilayered leaky system using water-level signals in adjacent aquifers. Journal of Hydrology, 500, 170–182.

Johns, R. T., Vomvoris, S. G., & Löw, S. (1995). Review of hydraulic field tests in the Opalinus Clay of Northern Switzerland. Nuclear Energy Agency: Hydraulic and hydrochemical characterisation of argillaceous rocks.

Kell, G. S. (1975). Volume properties of ordinary water. In R. C. Weast (Ed.), Handbook of chemistry and physics (56th ed.). Cleveland: CRC Press.

Keller, C. K., Van der Kamp, G., & Cherry, J. A. (1989). A multiscale study of the permeability of a thick clayey till. Water Resources Research, 25(11), 2299–2317.

Kostek, S., Schwartz, L., & Johnson, D. (1992). Fluid permeability in porous media: Comparison of electrical estimates with hydrodynamical calculations. Physical Review B, 45(1), 186–194.

Lavanchy, J. M., & Mettier, R. (2012). HA (Hydrogeological analysis) Experiment: Hydraulic database, Phases 1-16, Version 1.0. Mont Terri Technical Note, TN 2010-74, p 22. Federal Office of Topography (swisstopo), Wabern, Switzerland. www.mont-terri.ch.

Marschall, P., Horseman, S., & Gimmi, T. (2005). Characterisation of gas transport properties of the Opalinus Clay, a potential host rock formation for radioactive waste disposal. Oil and Gas Science and Technology, 60(1), 121–139.

Matray, J.-M., Savoye, S., & Cabrera, J. (2007). Desaturation and structure relationships around drifts excavated in the wellcompacted Tournemire's argillite (Aveyron, France). Engineering Geology, 90, 1–16.

Mazurek, M., Hurford, A., & Leu, W. (2006). Unravelling the multistage burial history of the Swiss Molasse Basin: integration of apatite fission track, vitrinite reflectance and biomarker isomerisation analysis. Basin Research, 18, 27–50.

Mazurek, M., Alt-Epping, P., Bath, A., Gimmi, T., & Waber, H. N. (2009). Natural tracer profiles across argillaceous formations: The CLAYTRAC Project (p. 365). Paris: Nuclear Energy Agency report, OECD.

Mejı́as, M., Renard, P., & Glenz, D. (2009). Hydraulic 652 testing of low-permeability formations: A case study in the granite of Cadalso de los Vidrios, Spain. Engineering Geology, 107, 88–107.

Melchior, P. (1978). The tides of the planet Earth (p. 609). Oxford: Pergamon Press.

Mercer, J. W., Pinder, G. F., & Donalson, I. G. (1975). A Galerkinfinite element analysis of the hydrothermal system at Wairakei, New-Zealand. Journal of Geophysical Research, 80, 2608–2621.

Merritt, M. L. (2004). Estimating hydraulic properties of the Floridan aquifer system by analysis of earth-tide, ocean-tide, and barometric effects. Collier and Hendry Counties, Florida. U.S. Geological Survey Water-resources investigations Report 03-4267, p 70.

Monnier, G., Stengel, P., & Fies, J. C. (1973). Une me´thode de mesure de la densite´ apparente de petits agglome´rats terreux. Application a` l'analyse de syste`me de porosite´ du sol. Annales Agronomiques, 24, 533–545.

Munõz, J. J., Lloret, A., & Alonso, E. (2003). Laboratory Report: Characterization of hydraulic properties under saturated and non saturated conditions. Project Deliverable, 4.

Nagra (2002). Projekt Opalinuston: Konzept fu¨r die Anlage und den Betrieb eines geologischen Tiefenlagers: Entsorgungsnachweis für abgebrannte Brennelemente, verglaste hochaktive sowie langlebige mittelaktive Abfälle. Nagra Technical Report, 02-02, p 24. Nagra, Wettingen, Switzerland. www.nagra.ch.

Neuzil, C. E. (1982). On conducting the modified 'slug' test in tight formations. Water Resources Research, 18(2), 439–441.

Neuzil, C. E. (1994). How permeable are clays and shales? Water Resources Research, 30(2), 145–150.

Neuzil, C. E. (2000). Osmotic generation of ''anomalous'' fluid pressures in geological environments. Nature, 403, 182–184.

Nussbaum, C., & Bossart, P. (2004). Compilation of K-values from packer tests in the Mont Terri rock laboratory. Mont Terri Technical Note, TN 2005-10, p 29. Federal Office of Topography (swisstopo), Wabern, Switzerland.

Nussbaum, C., Bossart, P., Amann, F., & Aubourg, C. (2011). Analysis of tectonic structures and excavation induced fractures in the Opalinus Clay, Mont Terri underground rock laboratory (Switzerland). Swiss Journal of Geosciences, 104, 187–210.

Nussbaum, C., Kloppenburg, A., Caer, T. & Bossart, P. (2017). Tectonic evolution of the Mont Terri anticline based on forward modelling. Swiss Journal of Geosciences, 110. doi:10.1007/s00015-016-0248-x (this issue).

Pape, H., Clauser, C., & Iffland, J. (1999). Permeability prediction based on fractal pore-space geometry. Geophysics, 64, 1447–1460.

Pearson, F. J., Arcos, D., Boisson, J-Y., Fernández, A. M., Gäbler, H.E., Gaucher, E., Gautschi, A., Griffault, L., Hernán, P., & Waber, N. (2003). Mont Terri Project-Geochemistry of water in the Opalinus Clay Formation at the Mont Terri Rock Laboratory. Reports of the Swiss Geological Survey, No. 5, p 143. Federal Office of Topography (swisstopo), Wabern, Switzerland. www. mont-terri.ch.

Peters, M., Mazurek, M., Jaeggi, D., & Müller, H. (2011). WS-H Experiment: Heterogeneities in the sandy facies of Opalinus Clay on a scale on millimetres to centimeters. Mont Terri Technical Note, TN 2010-76, p 66. Federal Office of Topography (swisstopo), Wabern, Switzerland.

Terzaghi, V. K. (1936). The sheering resistance of saturated soils and the angle between the planes of shear. First International Conference of Soil Mechanics, Harvard University Press, 1, 54–56.

Timms, W. A., & Acworth, R. I. (2005). Propagation of pressure change through thick clay sequences: an example from Liverpool Plains, NSW, Australia. Hydrogeology Journal, 13(5–6), 858–870.

Tremosa, J. (2010). Influence of osmotic processes on the excess hydraulic head measured in the Toarcian/Domerian argillaceous formation of Tournemire. Ph.D. dissertation (p. 322). Paris: Université Pierre et Marie Curie.

UNESCO. (1981). Tenth report on the joint panel on oceanographic tables and standard. UNESCO Technical Paper in Marine Science, 36, 28.

Ullman, W. J., & Aller, R. C. (1982). Diffusion coefficients in nearshore marine sediments. Limnology and Oceanography, 27, 552–556.

Van Loon, L. R., & Mibus, J. (2015). A modified version of Archie's law to estimate effective diffusion coefficients of radionuclides in argillaceous rocks and its application in safety analysis studies. Applied Geochemistry, 59, 85–94.

Van Loon, L. R., Soler, J. M., Jakob, A., & Bradbury, M. H. (2003). Effect of confining pressure on the diffusion of HTO, $^{36}Cl^-$ and $^{125}I^-$ in a layered argillaceous rock (Opalinus Clay): diffusion perpendicular to the fabric. Applied Geochemistry, 18, 1653–1662.

Van der Kamp, G. (2001). Methods for determining the in situ hydraulic conductivity of shallow aquitards–an overview. Hydrogeology Journal, 9, 5–16.

Wiegel, R. L. (1964). Tsunamis, storm surges, and harbour oscillations. In Oceanographical Engineering (pp. 95–127). Englewood Cliffs: Prentice Hall.

Yu, L., Rogiers, B., Gedeon, M., Marivoet, J., Craen, M. D., & Mallants, D. (2013). A critical review of laboratory and in situ hydraulic conductivity measurements for the Boom Clay in Belgium. Applied Clay Science, 75, 1–12.

Bayesian inversion of a chloride profile obtained in the hydraulically undisturbed Opalinus Clay: mass transport and paleo-hydrological implications

Catherine Yu[1) 2)], Julio Gonçalvès[2)], Jean-Michel Matray[1)]

1) Institut de Radioprotection et de Sûreté Nucléaire, 31 Allée du Général Leclerc, F92260 Fontenay-aux-Roses, France

2) Aix Marseille Univ., CNRS, IRD, Coll. De France, CEREGE, Aix-en-Provence, France

Corresponding author: Catherine Yu. E-mail: ji.catherine@gmail.com

Abstract

The BDB-1 deep inclined borehole was drilled at the Mont Terri rock laboratory (Switzerland) and enabled to acquire relevant data on porewater composition through the Opalinus Clay (OPA) and its bounding formations. Petrophysical measurements were carried out and included water content, water accessible porosity and grain density determination. Conservative anion profiles were obtained by aqueous leaching and out diffusion experiments performed on drillcore samples, and revealed to be consistent with previous studies carried out at the rock laboratory level. Diffusive properties were also investigated using three experimental setups: cubic out diffusion, radial diffusion and through diffusion. These transport parameters were used as *a priori* values in a Bayesian inversion using a Markov Chain Monte Carlo method to interpret the chloride profile in the Opalinus Clay. Based on a Peclet number analysis using the transport parameters formerly acquired, a purely diffusive scenario enabled specifying the paleohydrogeological evolution of the Mont Terri site from the folding and thrusting of the Jura Mountains to present time and transport parameters.

1 Introduction

The Swiss National Co-operative for the Disposal of Radioactive Waste (Nagra) selected the Opalinus Clay (OPA) as a potential host rock suitable for a deep geological repository for high-level radioactive waste and long-lived-intermediate-level waste. The evaluation of the confinement properties of this formation has been ongoing since 1996 in the Mont Terri rock laboratory, which is located in the Jura Mountains in north-western Switzerland. An overview of the safety aspects covered by this international research program and its contribution to the understanding of argillaceous formation behaviour is given by Bossart et al. (2017).

Solute transport is considered to be dominated by diffusion in compacted claystones due to their low permeability (Patriarche et al., 2004b; Mazurek et al., 2011). Limited water flow in these formations make standard sampling of porewater non applicable. Unconventional extraction processes based on physical or chemical extraction were developed and include centrifugation, squeezing, leaching, advective displacement and diffusive equilibration (Sacchi et al., 2001). Natural tracer profiles across argillaceous formations give information on fluid flow and transport properties, as they result from a long-term exchange between the aquitard and the bounding aquifers porewaters (Mazurek et al., 2011; Bensenouci et al., 2013). The example of

the Opalinus Clay was studied through the interpretation of several natural tracers (Cl-, 2H and He) profiles by Mazurek et al. (2011). This study concluded thata purely diffusive transport model could explain the present profiles and proposed values for activation times of the Opalinus Clay bounding aquifers and initial chlorinity. However, i) the predominance of diffusion over advection for mass transport behavior was tested by performing a sensitivity test on advection using plausible Darcy's velocity values, which were not based on global driving forces (pressure, temperature, salinity gradients; ii) no corresponding Peclet number calculation was made; iii) only a single value of the diffusion coefficient was applied to the stratigraphic column; and iv) no uncertainties were associated with the fitting parameters.

At the end of 2014 and in the framework of the Deep Borehole experiment (DB), a 247.5 m long 45° downward inclined borehole named BDB-1 was drilled through the Opalinus Clay and the bounding formations. The aim of the experiment was to develop and validate a methodology for assessing the confinement properties of a thick argillaceous unit using the Opalinus Clay as an example. In this framework, conservative anion profiles were acquired by leaching and out diffusion experiments and diffusive transport parameters (effective diffusion coefficients and accessible porosities) were also identified by radial and through diffusion experimental setups.

This paper presents an exhaustive and self-consistent acquisition of transport parameters and natural tracer profiles in the hydraulically undisturbed (i.e. unaffected by the drainage effects of underground structures happening at the tunnel level) zone crossed by the BDB-1 borehole. The chloride profile was interpreted by means of a purely diffusive 1D numerical model. The assumption of purely diffusive mass transport phenomena was verified by estimating the Peclet number including osmotic processes in the advection term. A Bayesian inversion using a Markov Chain Monte Carlo algorithm based on effective diffusion coefficients, initial value of the chloride concentration and two exhumation and thus hydraulic activation times for the two bounding aquifers (10 parameters) allowed to evaluate the best fit parameter sets and their uncertainties not evaluated so far.

Obtaining a relevant interpretation of the chloride profile is crucial for water flow and flow characterisation. Hence, pressure anomalies (pore pressure exceeding or inferior to the hydrostatic or surrounding aquifer ones) were recognised in the Opalinus Clay. At first, long-term monitoring at the Benken site revealed overpressures that were assumed to be remnant from the formation burial history (Bruel and Küpfer, 2002; Mazurek et al., 2002, 2006). However, further measurements obtained after replacing the hydraulic multipacker system in 2009 do not support these interpretations. Indeed, the latest measurements tend to show instead that the Opalinus Clay is underpressured at the Benken site. Compaction disequilibrium (e.g. rebound in response to glacial unloading) and the impact of tectonic strain are suggested as possible causes of the anomalous pressures (Beauheim, 2013). At the Mont Terri site, measurements obtained so far from the BDB-1 borehole sensors are supporting an overpressurised state of the Opalinus Clay. The influence of osmotic phenomena (water flow due to salinity or temperature gradients) on the pressure anomaly has not been investigated yet and depends strongly on the porewater composition. Therefore, understanding the salinity profile and its transient geological evolution across the formation is a necessary prerequisite for further transient interpretation of pressure profile (Gonçalvès et al., 2004).

Section 2 focuses on the geological setting of the Opalinus Clay, followed by a description of the Mont Terri Deep Borehole experiment and the acquisition methods in section 3. The different results and associated discussions are reported in section 4, followed by concluding remarks given in section 5.

2 Geological setting
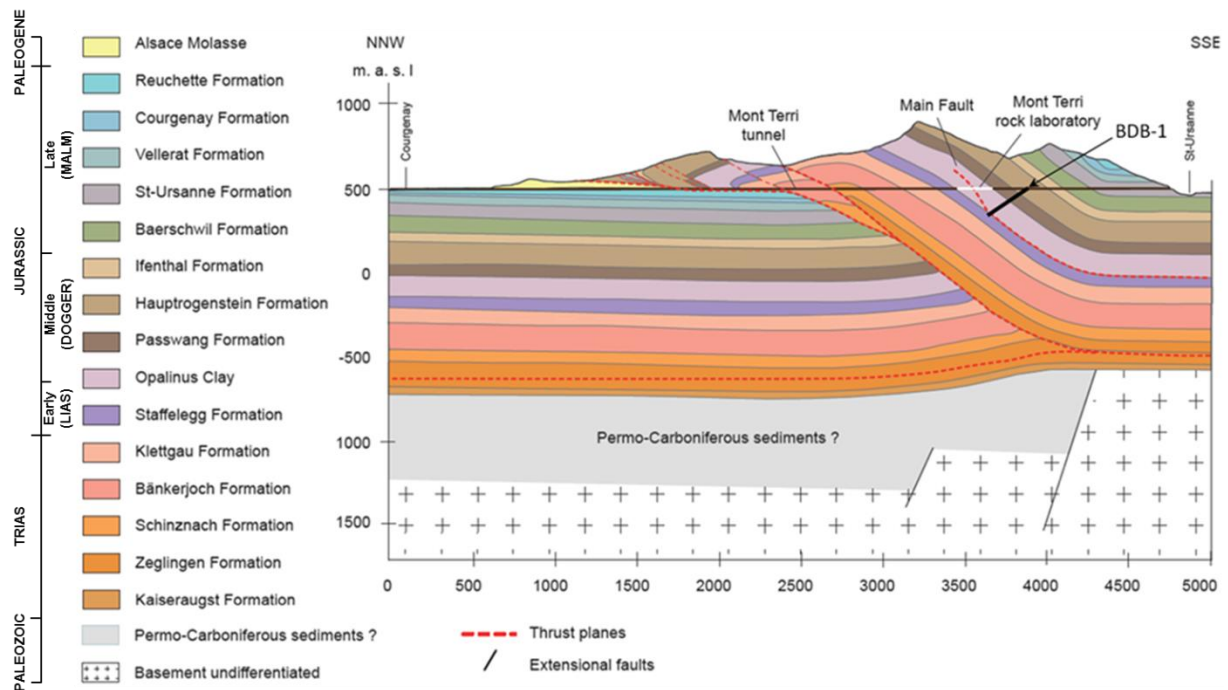
Fig. 1. Geological cross-section of the Mont Terri anticline. Location of the rock laboratory is indicated by a white line. The BDB-1 deep borehole, represented by a thick black line, crosses the lower part of the Middle Jurassic aquifer, the entire Opalinus Clay formation and the upper part of the Early Jurassic marls (adapted from Nussbaum et al., 2017).

The Opalinus Clay at the Mont Terri site is an overconsolidated claystone of Aalenian-Toarcian age, overlain by 800 m of Middle to Late Jurassic limestones, marls and shales, and underlain by 400 m of Early Jurassic to Triassic marls and limestones, dolomites and anhydrites (Figure 1). The thickness of the Opalinus Clay in the Mont Terri anticline varies between 130 m in the BDB-1 borehole and 150 m at rock laboratory level, depending on the tectonic contribution. This corresponds to a sedimentary thickness of about 120 m, when corrected for tectonic overthrusting (Bossart et al., 2017; Hostettler et al., 2017). The Opalinus Clay reached a burial depth of 1350 m about 120 Ma ago during early Cretaceous, which resulted in a maximum temperature of 80-90°C (Mazurek et al. 2006).

A period of marine regression occurred between 100 and 40 Ma, leading to a subaerial exposure of the top of the Late Jurassic limestone. Starting about 40 Ma, the rifting of the Rhine Graben affected Northern Switzerland, resulting in considerable subsidence of the area in the mid-Tertiary, which brought the Opalinus Clay sequence back to about 500 m depth. According to Clauer et al. (2017), two sea invasions into the Mont Terri area took place during Priabonian (37 to 34 Ma) and during the Rupelian (34 to 28 Ma). Mazurek et al. (2017) proposed that the Late Jurassic limestones, represented by the Baerschwil Formation, acted as a fresh-water boundary that induced a decrease of the Opalinus Clay porewater salinity to half the original value at the end of the Paleogene (23 Ma). Partial evaporation potentially occurred in the Chattian/Aquitanian and afterwards, brines would have diffused in the underlying formation, resulting in a salinity increase in the Opalinus Clay before Late Alpine folding during the late Miocene to Pliocene (about 12 to 3 Ma) that formed the Jura Fold-and-Thrust Belt. Erosion exposed the core of the Mont Terri anticline between 6 and 2.5 Ma, and activated the Middle Jurassic limestones aquifer (overlying the Opalinus Clay), causing a porewater flushing. Similarly, infiltration to the Early Jurassic limestones would have started in the Quaternary, between 0.5 and 0.2Ma ago (Pearson et al., 2003, Mazurek et al., 2011).

Three main facies were identified within the Opalinus Clay (Blaesi et al., 1991): a shaly facies in the lower part of the sequence, a thin carbonate-rich sandy facies in the middle part of the formation, and a sandy facies interstratified with shaly facies in the upper sequence.The shaly facies mineral composition includes 27-78% of clay minerals (illite, chlorite, kaolinite and illite-smectite mixed layers), 4-29% of carbonates, 10-32% of quartz, and accessory feldspars, pyrite and organic matter (Bossart and Thury, 2008).

Several minor tectonic faults and a larger fault zone called "Main Fault" can be observed in the Opalinus Clay (Nussbaum et al., 2011; Jaeggi et al., 2017). Nagra's investigations in deep boreholes at Riniken, Weiach, Schafisheim and Benken revealed that the tectonically disturbed zones are hydraulically similar to the undeformed matrix (Johns et al. 1994; Gautschi 2001, 2017). This conclusion was also confirmed by hydraulic investigation in the BDB-1 borehole at Mont Terri (Yu et al., 2017).

3 Material and methods

3.1 Sampling

The stratigraphic sequence crossed by the BDB-1 borehole is presented in Figure 2 and is described in detail in Hostettler et al. (2017). The Opalinus Clay section was drilled with air as drilling fluid. Drilling was immediately followed by the installation of a multipacker system (Fierz and Rösli, 2014) with pressure and temperature sensors. The borehole was entirely cored for lithostratigraphic, petrophysical, mineralogical and geochemical studies. Cores sent for analysis were sampled every 10 m along the borehole. Their preservation was ensured by nitrogen flushing and sealing after vacuum with plastic foil in aluminum coated plastic bags, in order to avoid further evaporation and contact with the atmosphere.

3.2 Petrophysical characterisation

Determination of petrophysical parameters (water content, porosity, apparent density, degree of saturation etc.) were performed in laboratory on representative elementary volume samples taken from the central part of the cores. Water contents were determined by weighing before and after oven-drying at 105°C until mass stabilization. Density and degree of saturation were calculated based on Archimede's principle after sample immersion into kerdane (de-aromatized hydrocarbide), following the experimental protocol first proposed by Monnier et al. (1973) and adapted to Tournemire and Mont Terri claystones (Matray et al., 2007; Matray and Möri, 2010). Grain density was evaluated using a helium pycnometer (Micromeritics Accupyc II 1340) on oven-dried samples.

3.3 Aqueous leaching

Leaching consists in diluting porewater solutes contained in a powdered rock sample into a leaching solution (Sacchi et al. 2001, Koroleva et al. 2011). Samples were crushed, sieved (< 100 μm) and placed together with deionised water at solid/liquid ratio of 1:2 in centrifuge vessels. The procedure took place under controlled atmospheric condition in a glove box (N2 atmosphere). Centrifuge tubes were placed in a hermetic glass jar and stirred out of the glove box using an end-over-end agitator for 2 hours. Then, samples were centrifuged at 10,000 rpm for 15 minutes and placed again inside the glovebox to be filtered with 0.22 μm syringe filter. Leachates were analysed by liquid ion chromatography using a Metrohm 861 Advanced Compact IC with an accuracy of 10%.
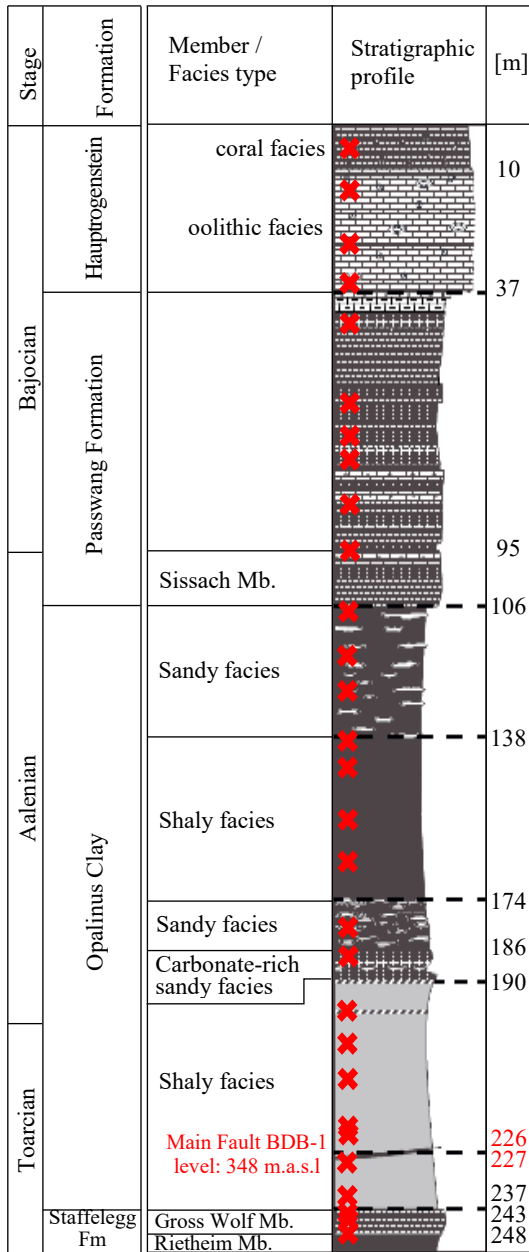
Fig. 2. Lithostratigraphy of the formations crossed by BDB-1 borehole (adapted from Hostettler et al., 2017) and approximative location of the studied samples represented by red crosses.

The following formula was used to calculate solute concentrations in porewater:

$$[X]_{PW} = \frac{[X]_l}{\frac{m_r}{m_l} WC_{bulk,wet} P_a}$$

(1)

where $[X]_{PW}$ [ppm] and $[X]_l$ [ppm] are respectively the concentrations of element X in porewater and in leachate, m_l [g] is the mass of liquid (sum of porewater and added leaching solution), m_r [g] is the mass of powdered rock sample, $WC_{bulk,wet}$ [-] is the gravimetric bulk water content and P_a [-] is the ratio between accessible porosity to anions and total porosity.

Water contents were recalculated from laboratory measurements (weighing, drying, density measurements etc.), considering a full saturation state for all samples. This recalculation was made due to the fact that desaturation of

samples during core drilling and sample handling can lead to a strong overestimation of the porewater concentrations.

Pa was assumed to equal 1 in the upper carbonated aquifer (Hauptrogenstein Formation) and 0.55 elsewhere, considering the anion exclusion in clay-bearing formations (Pearson et al. 2003).

3.4 Diffusion experiments

Schematic views of the alternative experimental setups used to characterise the Opalinus Clay are shown in Figure 3.
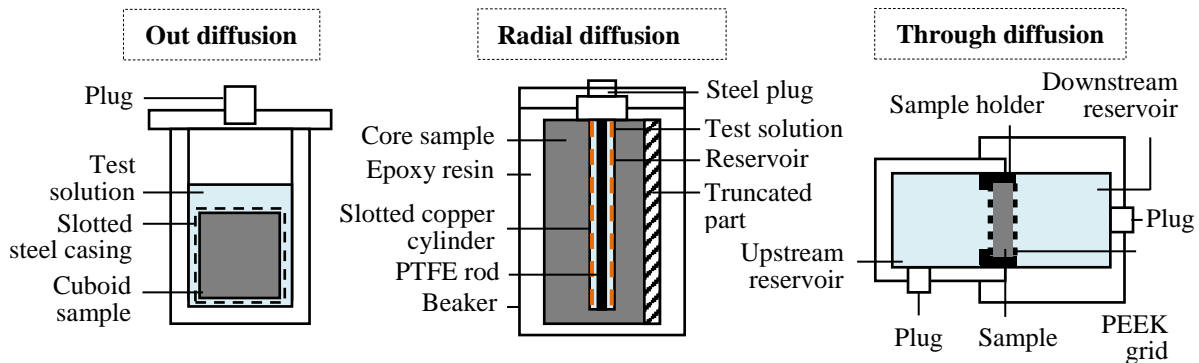
Fig. 3. Schematic views of the diffusion cells used in this study to characterise the Opalinus Clay diffusive properties.

3.4.1 In and out-diffusion

In cubic configuration, an out-diffusion experiment consists in immersing a cubic-shaped sample into a synthetic solution and sampling the solution until reaching diffusive equilibrium. In order to limit the chemo-mechanical effects that could disturb the sample integrity, test solutions were prepared to present a similar ionic strength to the porewater one by adding $NaHCO_3$ to milliQ water, based on chloride contents obtained from leaching experiments (Table 1).

Table 1. $NaHCO_3$ concentrations used for synthetic solutions of cubic out diffusion experiments, based on chlorinity acquired by leaching experiments.

Formation	Distance [m]	[Cl$^-$] [mol L^{-1}]	Ionic strength [mol L^{-1}]	[NaHCO$_3$] [g L^{-1}]
Hauptrogenstein	24.98	0.306	0.398	25.67
Passwang Formation	96.07	0.085	0.109	7.14
OPA - Sandy	116.24	0.089	0.114	7.48
OPA - Shaly	141.1	0.195	0.252	16.38
OPA - Shaly	155.1	0.234	0.303	19.66
OPA - Sandy	176.48	0.357	0.466	29.99
OPA - Carbonate-rich	185.97	0.354	0.462	29.74
OPA - Shaly	204.73	0.384	0.503	32.26
OPA - Shaly	213.23	0.393	0.515	33.01
Staffelegg Formation	238.2	0.414	0.543	34.78

The method has been employed on argillite from Tournemire rock laboratory (France) by Patriarche (2004a) and enables the estimation of initial halide concentrations in porewater with a mass balance equation, as well as pore diffusion coefficient of the tested samples.

The mass balance equation of the system writes:

$$C_{pw}m_{pwa} = \left(m_{ftw} + m_{pwa}\right)C_{eq} + \sum_{i=1}^{n} m_i C_i \qquad (2)$$

where C_{pw} [ppm] is the solute concentration in porewater, m_{pwa} [mg] is the mass of porewater accessible to anions, m_{ftw} [mg] is the final mass of test solution, C_{eq} [ppm] is the equilibrium concentration, n [-] is the number of samples, m_i [mg] is the mass of sample i and C_i [ppm] is the concentration of sample i. The mass $m_{pwa}$is deduced considering the water loss porosity obtained by petrophysical measurements and assuming an anion accessible fraction of 0.55. This fraction was used to calculate anion contents in accessible porewater at all depths, except in the Hauptrogenstein Formation.

Eighteen samples measuring about 5 cm wide were prepared with a diamond wire saw. They were constrained by placing a metallic grid, after being coated with epoxy resin on four faces to impose a single diffusion direction (perpendicular or parallel to the bedding). Test solutions were monitored for halides (Cl-, Br-) and sulphate concentrations by ionic chromatography using a Metrohm Advanced Compact IC 861.

A radial diffusion experiment consists in diffusive equilibrium between porewater contained in a drillcore and a test solution with known composition placed in an axial drilled reservoir (Van der Kamp et al. 1996, Savoye et al. 2006a and 2006b). It enables the determination of both diffusion coefficient and accessible porosity to the chosen tracer. A total of ten samples were prepared, each consisting of a core portion cut with a circular saw with a diameter of 10.2 cm or 8.5 cm and a length between 6.7 and 10 cm. A 24 mm diameter reservoir was drilled with a drill pressin each sample, in which was inserted a 22 mm outer diameter copper tube with horizontal slots in order to prevent sample swelling. A 18 mm diameter polytetrafluoroethylene (PTFE) rod was also placed in the reservoir to minimise the solution volume used for the experiment and the time required to reach diffusive equilibrium. Solutions were analysed for anions (Cl-, SO_4^{2-} and Br-) by ionic chromatography using a DIONEX ICS-1000, and for stable isotopes (^{18}O and ^{2}H) using a Las Gatos Research LWIA-24IEP. The analytical uncertainties of these analysis are $\pm$ 5-10 % for anions, $\pm$ 1 ‰v-SMOW for δ^2H and $\pm$ 0.6 ‰ v-SMOW for δ^{18}O.

3.4.2 Through diffusion

Through diffusion cells consisted of a polypropylene sample holder, two polypropylene reservoirs for liquid phase (upstream and downstream, with respective capacities of 180 mL and 90 mL), two supporting grids and two sampling openings. Six cylindrical samples of approximatively 10 mm thickness and 30 mm diameter were prepared from core samples by sawing with a diamond wire saw. These samples were confined between porous polyether ether ketone (PEEK) grids in order to control clay mineral swelling and the assembly was fixed to the sample holder using Sikadur® epoxy adhesive. After a resaturation phase with synthetic porewater, the solutions were replaced with fresh ones and the upstream reservoir added with conservative radioactive tracers (HTO and ^{36}Cl-). The effective diffusion coefficient can be determined from the flux data during the steady-state case and the accessible porosity from the break-through time (Van Loon et al., 2012). The flux of radioactive species between the reservoirs was monitored as a function of time by liquid scintillation using a Packard Tri-carb 3100 TR counter. The accuracy of activity measurement, in Bq L^{-1}, is estimated at 6.4 % for HTO and 3.5 % for ^{36}Cl-.

3.4.3 Modelling of the diffusion experiments

Cubic out diffusion and through diffusion experiments were modelled numerically using the chemistry-transport coupled model code HYTEC (Van der Lee et al. 2003), which is based on finite volumes method. In purely diffusive system and for conservative components, the transport equation writes:

$$\omega \frac{\partial c_i}{\partial t} = \text{div}(D_e \nabla c_i) \tag{3}$$

where c_i is the total concentration of component i, ω [-] is the diffusion accessible porosity for conservative components, and D_e [m²s⁻¹] is the effective diffusion coefficient with $D_e = \omega D_p$, where D_p is the pore diffusion coefficient accounting for the tortuosity of the porous media.

For cubic out diffusion experiments, pore diffusion coefficient and initial concentration in the sample porewater were fitted while the accessible porosity was set, assuming an anion accessible fraction at 0.55 based on litterature data (Pearson et al., 2003). Initial concentrations in reservoirs were known in through diffusion cells while diffusion coefficients and accessible porosities were fitting parameters.

For radial diffusion experiments, a numerical inversion of the semi-analytical solution of equation (3) in radial coordinates given by Novakowski and Van der Kamp (1996) and Savoye et al. (2006b) was applied using Mathematica 5.2©.

All simulations were visually fitted to experimental data by adjusting input parameters (diffusion coefficients, accessible porosities or initial concentrations) by trial and error.

3.5 Markov Chain Monte Carlo method

The chloride profile acquired by cubic out diffusion experiments on samples from the BDB-1 borehole was interpreted using a finite difference numerical resolution of the transport equation (3). This numerical treatment, which includes a statistical inversion process using a Markov Chain Monte Carlo (MCMC) approach, was implemented using Python©. MCMC methods are probabilistic sampling techniques for Bayesian parameter estimation and uncertainty quantification. The basic principle consists in an oriented random walk exploration of the parameter space in order to avoid large time-consuming and even unrealistic systematic (using regular steps) sampling of parameters sets that allow reproducing the chloride profile. Each selected parameters set throughout the random walk is introduced in direct transport simulations. Therefore, these algorithms generate a sequence of model parameter sets and compare the model-based predictions to a given set of observed measurements (Tarantola, 2005; Gallagher et al. 2009; Petersen et al. 2014). The model parameters are constrained to minimise the misfit between simulated (sim_i) and measured values (obs_i), represented here by the mean squared error function $S(\boldsymbol{m})$:

$$S(\boldsymbol{m}) = \frac{1}{n}\sum_i (obs_i - sim_i)^2 \tag{4}$$

where n is the number of measurements and $\boldsymbol{m}$ $(m_1...m_n)$ is the vector of model parameters.

The random walk is based on sorted values in the *a priori* probability density function (pdf) $\rho(\boldsymbol{m})$ of each parameter while the forward modelling identifies a set of parameters allowing a good agreement between simulated and observed chloride values. This set of successful parameters samples the *a posterior* joint pdf $\sigma(\boldsymbol{m})$ which describes the updated parameters distribution (after forward modelling and data comparison) yielding the best simulations. Then, marginal pdfs have to be identified for each parameter to estimate e.g., its mean value

and associated uncertainty. The marginal distributions were simply identified by a statistical treatment of all the parameters samples that satisfies an acceptance criterion (fraction of best simulations, misfit threshold).

Let's now consider a current step of the MCMC algorithm characterised by a position m_i of the random walk in the parameter space, and a potentially new position m_j created by means of a random perturbation of m_i. The acceptance of the displacement from a former parameter set m_i to the posterior one m_j follows the probabilistic rule (probability of acceptance P):

$$P \begin{cases} 1 & if\ S(m_i) > S(m_j) \\ \dfrac{L(m_j)}{L(m_i)} = \exp\left(-\dfrac{\Delta S}{\alpha}\right) & if\ S(m_i) < S(m_j) \end{cases} \qquad (5)$$

where $L(m)$ is the likelihood function defined by:

$$L(m) = k \times e^{-\frac{S(m)}{\alpha}} \qquad (6)$$

where k is a normative constant that ensures that the integral of $\sigma(m)$ over the parameter space equals 1, α is a convergence parameter to be set here by trial and error to ensure effective decreasing error, and $exp(-\Delta S/\alpha) = exp(-(S(m_j)-S(m_i))/\alpha)$.

The first option in equation (5) just states that if the displacement yields a lower error between the direct model results and the observations, the displacement is accepted. The second one states that an unfavourable displacement can be accepted in order to leave local minimum values of the objective function and to explore other regions of the parameter space. This second option is practically treated by sorting a value in a uniform distribution between 0 and 1: if it is lower than $exp(-\Delta S/\alpha)$, which occurs with a probability $exp(-\Delta S/\alpha)$, then the unfavourable displacement is accepted and the algorithm (Eq. 5) is satisfied. This algorithm globally favours the displacements within the parameter space in the direction of decreasing misfits (Mosegaard and Tarantola, 1995). After a first convergence stage of the method, which consists in reaching the regions of the parameter space where the error is minimum, the MCMC algorithm provides a set of accepted parameters which allow the best simulations.

4 Results and Discussion

4.1 Transport parameters

4.1.1 Porosities

Porosity values obtained from petrophysical analysis and diffusion experiments are reported in Figure 4.

The mean water accessible porosity determined by density measurements is 13.0% in the Opalinus Clay, with a lower average porosity of 12.0% in the sandy facies compared to the shaly facies, which shows a mean porosity of 13.5%. These values are lower than the mean value of 18% suggested by previous studies performed at the Mont Terri tunnel level (Bossart et al. 2017). The Passwang Formation presents slightly lower porosity values ranging between 8.1% and 14.6% with a mean value of 12.2%. The Hauptrogenstein is characterised by the lowest porosity with a mean value of 3.9%.

Except for the carbonate-rich sandy facies, porosity values obtained by radial diffusion for stable water isotopes in the Opalinus Clay (up to 22 %) are higher than the values obtained by density measurements (maximum value
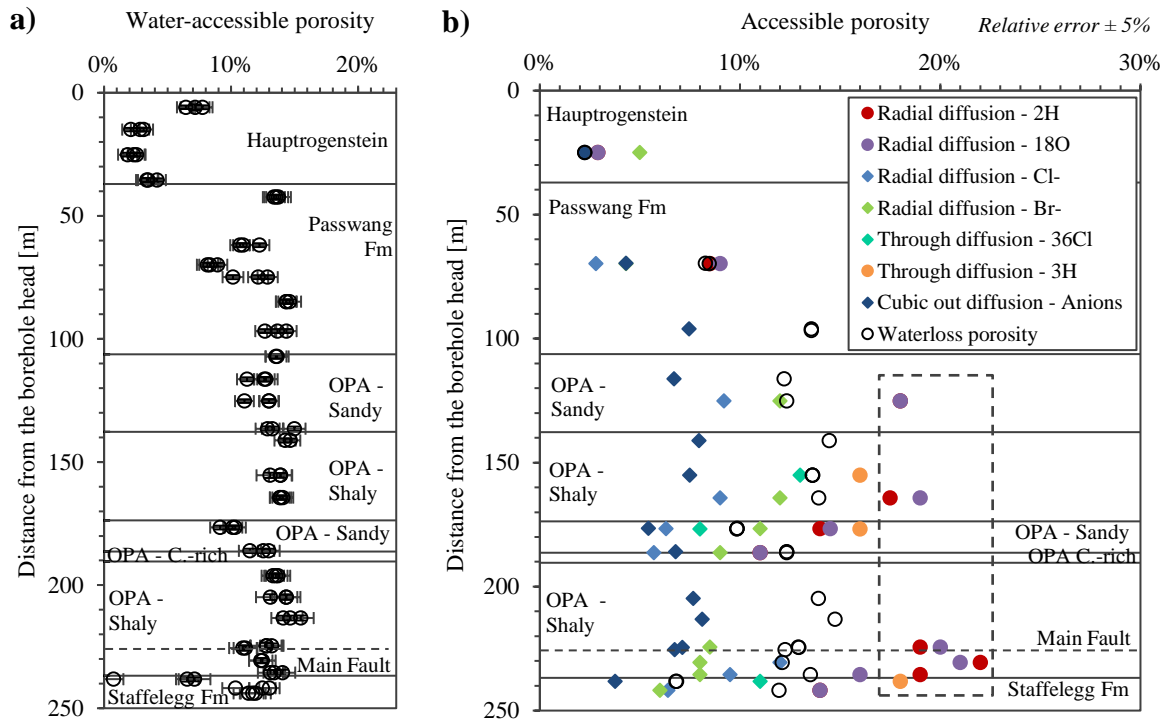
Fig. 4 a) Water accessible porosity acquired by oven-drying at 105°C of BDB-1 borehole samples and **b)** accessible porosity to anions (Cl⁻, Br⁻), radioactive tracers (HTO, ³⁶Cl⁻) and stable water isotopes (²H, ¹⁸O) determined by laboratory-scale diffusion experiments. Values framed by a dashed line are probably overestimated due to swelling or microcracks.

of 15 %). Sample preparation steps, such as drilling, may have brought additional porosity by creating microcracks.Values obtained for ²H and ¹⁸O are globally comparable and the anion exclusion (ratio of anion to water accessible porosities) is in the range of 51 % to 55 % in the OPA shaly facies and between 45 % and 51 % in the sandy facies. These results are consistent with the ratio of 55%, which was chosen in out diffusion experiments to calculate anion contents in porewater and based on literature data (Pearson et al. 2003). Chloride and bromide diffusion accessible porosities are also comparable with values ranging between 6 % and 12 % and a best estimate at 8%.

4.1.2 Diffusion coefficients

Deduced from radial diffusion experiments, chloride and bromide effective diffusion coefficient parallel to the bedding are in the order of 4.0×10^{-11} m² s⁻¹ in the Opalinus Clay, which is in good agreement with the range of 1.7×10^{-11} to 4.5×10^{-11} m² s⁻¹ for bromide and 1.8×10^{-11} to 6.8×10^{-11} m² s⁻¹ for chloride reported in previous studies (Bossart et al. 2011). Reasonable values from 3.0×10^{-11} to 1.1×10^{-10} m² s⁻¹ are obtained for stable water isotopes. Values obtained by through diffusion experiments are also in good agreement with literature data. In the Opalinus Clay shaly facies, values of 9.6×10^{-11} m² s⁻¹ for tritium and 1.4×10^{-11} m² s⁻¹ for ³⁶Cl are obtained parallel to the bedding. In the sandy facies, simulations give 1.9×10^{-11} m² s⁻¹ for tritium and 5.1×10^{-12} m² s⁻¹ for ³⁶Cl perpendicular to the bedding (Figure 5). Due to experimental artefacts linked to sample preparation, only three out of the six through diffusion cells provided relevant data.

The diffusion anisotropy ratio is the ratio between the effective diffusion coefficients parallel and perpendicular to the bedding. Based on out diffusion experiments, a low anisotropy ratio of 2.4 was estimated for chloride effective diffusion coefficient in the Opalinus Clay sandy facies, which is lower than the value of 4 reported by Van Loon et al. (2004) on a shaly facies sample. Diffusion anisotropy ratios were also determined in a field scale

experiment at Mont Terri within the Diffusion and Retention Experiment and revealed values of 3.8 for iodide and 2.56 for bromide, lower than the ratios of 5.06 derived for HTO in the same experiment (Gimmi et al., 2014).

Although BDB-1 borehole core samples were extracted from an hydraulically undisturbed zone of the Mont Terri site, one can argue on the representativeness of the acquired transport parameters. Indeed, the steps of extraction, conditionning and preparation of centimeter- to decimeter-scale samples at laboratory induce disturbances (e.g. desaturation, deconfinement, creation of microcracks) that would tend to increase the values of accessible porosity and diffusion coefficients compared to those characterising the in situ formations. The great brittlemess of the Opalinus Clay also led to difficulties to obtain a whole reliable set of proper measurements. As an example, anisotropy of diffusive parameters could not be determined in the shaly facies crossed by BDB-1 borehole due to sample cracking and other unloading artefacts.
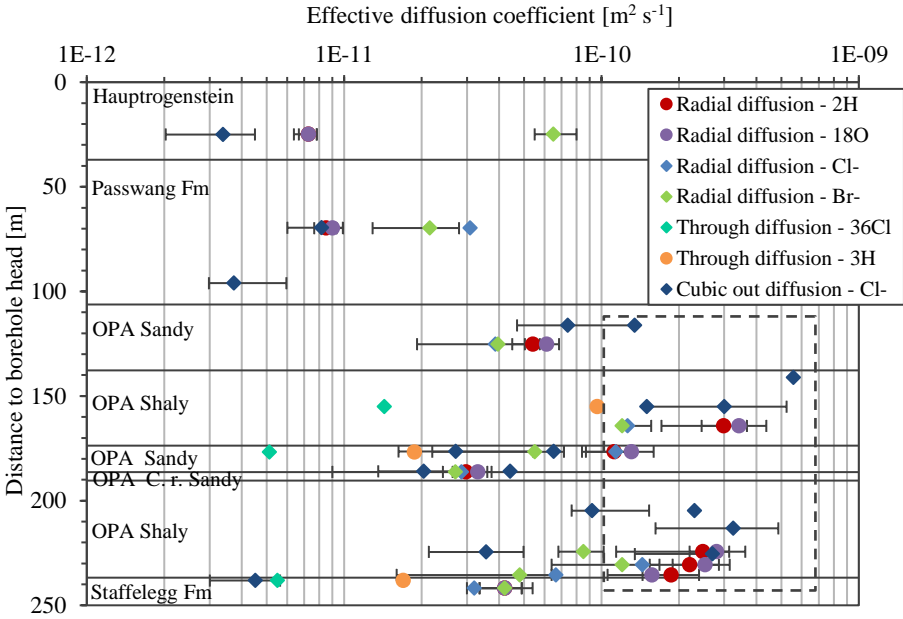
Fig. 5 Effective diffusion coefficients acquired on BDB-1 borehole samples. Values framed by a dashed line are probably overestimated due to swelling or microcracks.

Diffusion parameters (accessible porosities, diffusion coefficients) derived from the experiments conducted in this study are reported in Table 2.

Table 2 Effective diffusion coefficients D_e and accessible porosity ω for HDO, $H_2^{18}O$, Cl^-, Br^-, $^{36}Cl^-$ and HTO acquired on BDB-1 samples. D.O. stands for Diffusion Orientation with respect to the bedding plane. Shaded numbers are probably affected by experimental artefacts. Values with an asterisk were retained for chloride profile modelling.

Distance to borehole head [m]	Formation	Tracer	D.O.	D_e [m²/s] (× 10⁻¹¹)	ω	Acquisition method
24.95	Hauptrogenstein	HDO	//	0.725 ± 0.058	0.029	Radial out diffusion
24.95		$H_2^{18}O$	//	0.725 ± 0.0725	0.029	Radial out diffusion
24.95		Br^-	//	6.5 ± 1.25	0.05	Radial in diffusion
24.98		Cl^-	⊥	0.34 ± 0.12	0.022	Cubic out diffusion
69.6	Passwang Formation	Cl^-	⊥	0.817* ± 0.19	0.083	Cubic out diffusion
69.78		HDO	//	0.85 ± 0.085	0.085	Radial out diffusion
69.78		$H_2^{18}O$	//	0.9 ± 0.09	0.09	Radial out diffusion
69.78		Cl^-	//	3.08 ± 0.08	0.028	Radial out diffusion
69.78		Br^-	//	2.15 ± 0.75	0.043	Radial in diffusion
96.07		Cl^-	⊥	0.373 ± 0.15	0.136	Cubic out diffusion
116.24	OPA – Sandy facies	Cl^-	⊥	7.38* ± 4.36	0.122	Cubic out diffusion
116.24		Cl^-	//	13.4 ± 6.71	0.122	Cubic out diffusion
125.21		HDO	//	5.4 ± 0.63	0.18	Radial out diffusion
125.21		$H_2^{18}O$	//	6.12 ± 0.9	0.18	Radial out diffusion
125.21		Cl^-	//	3.86 ± 0.63	0.092	Radial out diffusion
125.21		Br^-	//	3.96 ± 1.8	0.12	Radial in diffusion
141.1	OPA – Shaly facies	Cl^-	⊥	55.6	0.145	Cubic out diffusion
155.1		Cl^-	⊥	29.9 ± 18.7	0.136	Cubic out diffusion
155.1		Cl^-	//	15.0 ± 7.48	0.136	Cubic out diffusion
155.1		$^{36}Cl^-$	//	1.43*	0.13	Through diffusion
155.1		HTO	//	9.6	0.16	Through diffusion
164.29		HDO	//	29.8 ± 6.13	0.175	Radial out diffusion
164.29		$H_2^{18}O$	//	34.2 ± 13.3	0.19	Radial out diffusion
164.29		Cl^-	//	12.6 ± 6.13	0.09	Radial out diffusion
164.29		Br^-	//	12.0 ± 7.8	0.12	Radial in diffusion
176.48	OPA – Sandy facies	Cl^-	⊥	2.71* ± 1.9	0.099	Cubic out diffusion
176.48		Cl^-	//	6.51 ± 1.36	0.099	Cubic out diffusion
176.60		HDO	//	11.2 ±2.45	0.14	Radial out diffusion
176.60		$H_2^{18}O$	//	13.1 ± 3.63	0.145	Radial out diffusion
176.60		Cl^-	//	11.3 ± 2.45	0.063	Radial out diffusion
176.60		Br^-	//	5.5 ± 2.4	0.11	Radial in diffusion

Distance to borehole head [m]	Formation	Tracer	D.O.	D_e [m²/s] (× 10⁻¹¹)	ω	Acquisition method
176.84	OPA Sandy facies	$^{36}Cl^-$	//	1.43	0.08	Through diffusion
176.84		HTO	//	9.6	0.16	Through diffusion
185.97	OPA – Carbonate-rich sandy facies	Cl^-	⊥	2.04 ± 0.68	0.123	Cubic out diffusion
185.97		Cl^-	//	4.41 ± 2.04	0.123	Cubic out diffusion
186.27		HDO	//	2.97 ± 0.33	0.11	Radial out diffusion
186.27		$H_2^{18}O$	//	3.3 ± 0.66	0.11	Radial out diffusion
186.27		Cl^-	//	2.85 ± 0.33	0.057	Radial out diffusion
186.27		Br^-	//	2.7 ± 1.35	0.09	Radial in diffusion
204.73	OPA – Shaly facies	Cl^-	⊥	9.19 ± 3.83	0.139	Cubic out diffusion
204.73		Cl^-	//	23.0 ± 11.5	0.139	Cubic out diffusion
213.23		Cl^-	⊥	32.4 ± 16.2	0.147	Cubic out diffusion
224.40		HDO	//	24.7 ± 9.98	0.19	Radial out diffusion
224.40		$H_2^{18}O$	//	28.0 ± 7.1	0.20	Radial out diffusion
224.40		Br^-	//	8.5 ± 1.7	0.085	Radial in diffusion
224.49		Cl^-	⊥	3.56* ± 1.42	0.129	Cubic out diffusion
225.5		Cl^-	⊥	27.0	0.123	Cubic out diffusion
230.64		HDO	//	22.0 ± 6.6	0.22	Radial out diffusion
230.64		$H_2^{18}O$	//	25.2 ± 6.3	0.21	Radial out diffusion
230.64		Cl^-	//	14.4 ± 6.6	0.12	Radial out diffusion
230.64		Br^-	//	12.0 ± 5.2	0.08	Radial in diffusion
235.48		HDO	//	18.6 ± 4.75	0.19	Radial out diffusion
235.48		$H_2^{18}O$	//	15.7 ± 4.4	0.16	Radial out diffusion
235.48		Cl^-	//	6.65 ± 4.75	0.095	Radial out diffusion
235.48		Br^-	//	4.8 ± 2.4	0.08	Radial in diffusion
238.2	Staffelegg Formation	Cl^-	⊥	0.451* ± 0.132	0.068	Cubic out diffusion
238.2		$^{36}Cl^-$	⊥	0.55	0.11	Through diffusion
238.2		HTO	⊥	1.69	0.18	Through diffusion
241.83		HDO	//	4.2 ± 0.77	0.14	Radial out diffusion
241.83		$H_2^{18}O$	//	4.2 ± 0.77	0.14	Radial out diffusion
241.83		Cl^-	//	3.2 ± 0.77	0.064	Radial out diffusion
241.83		Br^-	//	4.2 ± 1.2	0.06	Radial in diffusion

4.2 Anion profiles

Chloride, bromide and sulphate profiles acquired by leaching and out diffusion experiments on BDB-1 samples are presented in Figure 6 and confirmthe vertical variability of porewater composition along the stratigraphic column.
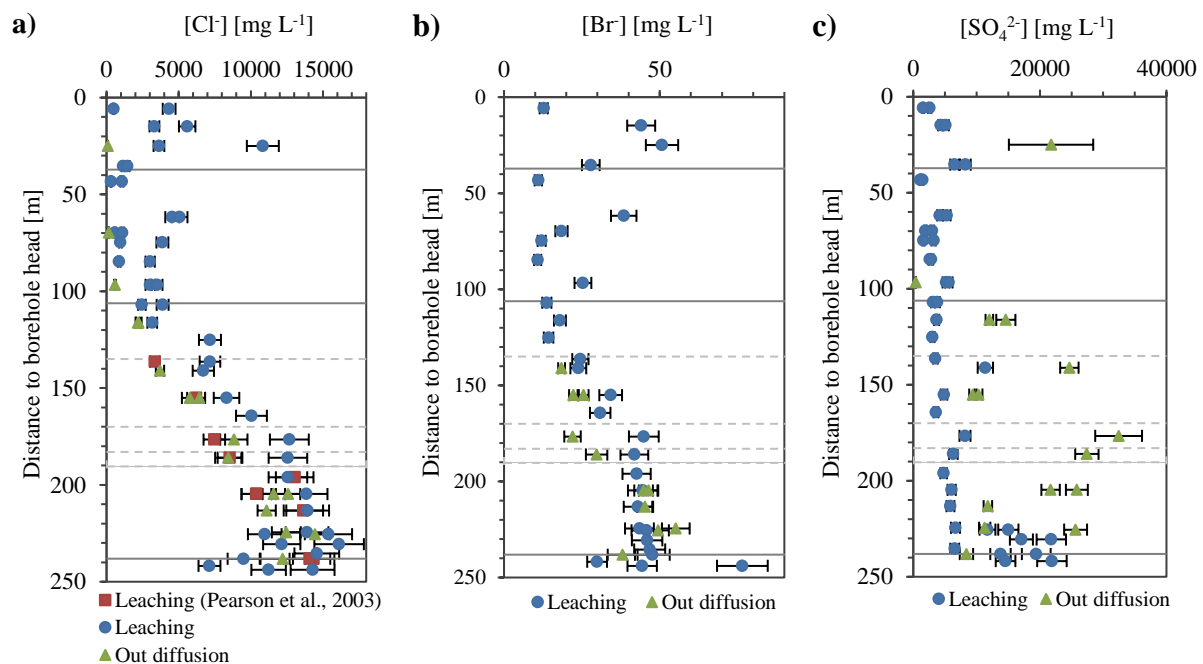

Fig. 6. a) Chloride, **b)** bromide and **c)** sulphate profiles acquired along BDB-1 borehole by leaching experiments and out diffusion tests.

Chloride and bromide values obtained by aqueous leaching are systematically higher compared to out diffusion results. Higher values of halides given by aqueous leaching compared to out diffusion are likely due to mineral dissolution or release of elements initially contained in inaccessible porosity. However, the two methods reveal similar curved profiles with increasing chlorinity towards the basal part of the Opalinus Clay (up to 16.1 gL^{-1}from leaching experiments). Out diffusion experiments give a range between 2.1 ± 0.3 g L^{-1} and 14.4 ± 1.0 g L^{-1} for chloride contents withmaximum concentrations found in the basal shaly facies of the Opalinus Clay. Scattered chloride values are found in calcareous lithologies and much higher than in groundwater samples, which amount to about 4 mg L^{-1} between 50 and 51 m depth in the Passwang Formation, and 8 mg L^{-1} in the Hauptrogenstein (as artesian inflow). The discrepancies can be explained by the heterogeneity of the hydrochemical composition within the limestone aquifer. In this study, samples tested in diffusion and leaching experiments were prepared from intact drillcores distant to flowing fractures. The composition of matrix porewater, more stagnant than flowing groundwater, varies depending of the distance to these fractures. Moreover, milling in the course of leaching experiments can release solutes from secondary reservoirs contained for example in closed porosity.

The sulphate profile along BDB-1 borehole also shows an increasing trend with depth, but even when extraction was performed under anoxic conditions, a potential effect of oxidation on measured concentrations cannot be excluded.Artificial increase of sulphate contents can be induced by artefacts linked to experimental procedures: pyrite oxidation during the sample preparation or equilibration process, and dissolution of sulphate-bearing minerals such as gypsum or celestite (Pearson et al., 2003; Wersin et al., 2013). For sulphate, out diffusion results are consistently higher than leaching results, in contrast to chloride and bromide data. The overestimation is due to the fact that diffusion experiments were performed at ambient conditions, enhancing thus redox effects. Aqueous extraction and out diffusion are relevant to quantify conservative anions but unsuitable for reactive anions.

Previous studies conducted at the tunnel level also concluded to a maximum value ranging from 13.6 to 14.4 g L^{-1} for chloride content, found at the limit between the Opalinus Clay and the Staffelegg Formation (Pearson et al.

2003). The halide concentration ratios are consistent with a marine origin of the Opalinus Clay porewater. This observation was also stated in earlier studies (e.g. Pearson et al., 2003) but other ratios such as stable water isotopes are not fully consistent with marine origin (Mazurek et al, 2011).

4.3 Chloride profile modelling

4.3.1 Modelling assumptions and scenario

Although the predominant character of diffusion among other transport processes in low permeability formations is generally claimed, such assumption, which greatly simplifies transport numerical calculations, must be verified using the Peclet number (Soler, 2001):

$$Pe = \frac{qL}{D_e} \qquad (7)$$

Where q [m s^{-1}] is the specific discharge (Darcy's velocity), L [m] is a characteristic distance for transport, here taken to be the formation half thickness, and D_e [m^2 s^{-1}] is the effective diffusion coefficient. It is classically stated that for Pe < 1, diffusion dominates over advection and advection is dominant over chemical diffusion if Pe >1. However, in their discussion of transport phenomena in low permeability environments, Huysmans and Dassargues (2005) show that for Peclet numbers (Eq. 7) as high as 10, numerically simulated salinity profiles considering advection and diffusion or diffusion alone only differed by 10% pointing to a negligible advective contribution. Consequently, one can consider that below a value of 10 for Pe, diffusion models are sufficiently accurate for salinity profile interpretations.

The Opalinus Clay formation is characterised by maximum pressures (or hydraulic head h) and chlorinity values within the formation yielding corresponding differences with the surrounding aquifers of at least 5 bars (Δh = 50 m), ΔT = 4°C, and Δc = 0.42 mol L^{-1} respectively. Note that in fact, a monotonic cross-formational temperature difference of 8.5°C per 100 m is observed.

Considering that osmotic processes are at work in the Opalinus Clay, the 1D Darcy's velocity accounting for osmotic terms can be expressed as (Gonçalvès et al., 2015):

$$q = -K\frac{\partial h}{\partial z} + \frac{vRT\varepsilon_c K}{\rho g}\frac{\partial c}{\partial z} - \frac{\varepsilon_T}{\rho g}K\frac{\partial T}{\partial z} \qquad (8)$$

where K [ms^{-1}] is the cross-formational hydraulic conductivity, z is the axis perpendicular to the bedding, h [m] is the hydraulic head, ρ is the porewater density [kg m^{-3}], g [9.81 m s^{-2}] is the gravitational acceleration, ε_c[-] and ε_T [Pa K^{-1}] are respectively the chemical osmotic efficiency and the thermo-osmotic coefficient, v is the number of dissociated species for a salt (e.g. 2 for NaCl), R [8.32 m^3 Pa K^{-1} mol^{-1}] is the gas constant, T [K] is the temperature, and c [mol m^{-3}] is the chloride concentration.Note that for this first-order calculation, no gravity effect due to salinity is considered enabling the use of the hydraulic head h.

The first term in the right-hand side of Equation (8) is related to purely darcian fluid flow, the second and third terms to the chemical and thermal osmosis, i.e. fluid flow driven by salinity and temperature gradients. The petrophysical parameters of the Opalinus Clay together with the thermo-osmotic model by Gonçalvès et al. (2015) points to a negligible thermo-osmotic term here. For the two remaining terms, simple gradients given by $\Delta h/L$ and $\Delta c/L$ can be introduced in Eqs (7) and (8). Peclet calculations require equivalent transport parameters (harmonic means across the formation, perpendicular to the bedding). Using the data of this study and of Yu et al. (2017), a harmonic mean of 10^{-11} m^2 s^{-1} and 1.85 × 10^{-13} m s^{-1} is found for D_e and K. Using these values for an equivalent NaCl (v =2) system and ε_c between 0.036 and 0.081 (Noy et al., 2004) yields a Peclet number of between 1.3 and

1.5. It can thus be concluded that transport is likely dominated by diffusion for the Opalinus Clay. Therefore, mass transport calculations can be made by solving Equation (3) using a simple and robust finite difference numerical scheme.

The paleohydrogeological evolution was chosen accordingly to the conclusions of Bossart and Wermeille (2003), who constrained the erosion and thus the exhumation of the Middle Jurassic limestone overlying the Opalinus Clay between 10.5 and 1.2 Ma (time t_0 hereafter). At that time, the subsequent rapid flushing of the Middle Jurassic limestone porewater by meteoritic water brought the salinity to zero which constitutes a boundary condition for the transport model. The activation of the Early Jurassic limestone aquifer underlying the Opalinus Clay occurred between 0.5 and 0.2 Ma (time t_1). A plausible range between 14 and 23 g L^{-1} was chosen for the initial chlorinity C_0 prior to the Jura folding and thrusting (Mazurek et al., 2011). Cross-formational diffusive transport parameters, namely effective diffusion coefficient and diffusion accessible porosity, were deduced from laboratory experiments carried out on BDB-1 samples and described in section 5.1. Exhumation times t_0 and t_1 together with the initial chlorinity are used for boundary and initial conditions definition of the 1D diffusion model. At initial time t_0, the chlorinity is set to C_0 within the Opalinus Clay, the upper and lower concentration boundary conditions are 0 and C_0, respectively. Then, when the simulation time reaches t_1, the lower boundary condition is set to zero. These boundary conditions allow simulating diverging diffusive mass transport from the Opalinus Clay towards first the upper aquifer alone then towards both aquifers. The model takes into accounts 7 formations showing different properties listed in Table 3.

4.3.1 Modelling results

The parameters to be calibrated must be chosen carefully since for more than 10 parameters, implementing MCMC methods becomes hazardous (convergence issues). Porosities, being relatively well constrained, were kept constant for each formation. From a practical standpoint, the calibrated parameters were the cross-formational effective diffusion coefficient for each of the 7 formations D_e (in fact D_p since ω is fixed, see above), t_0, t_1 and C_0 which are all considered uncertain. Uniform *a priori* distributions were considered for these 10 parameters using lower and upper boundaries described in Section 4.3.1 for t_0, t_1 and C_0, and boundaries encompassing the measurements for the 7 formation D_e values (see Table 3)

In the course of the MCMC inversion process involving 10 parameters (a priori values in Table 3), the misfit function reached a plateau after about 2000 iterations for 150000 performed iterations (Figure A.1, Appendix A). The convergence, which corresponds to the effective sampling of the stationary and unique posterior distribution, was simply assessed by verifying that stabilised parameter values were sampled: around the mean value for unimodal posterior distributions and values alternating around the modes for multi-modal ones. Uniqueness was empirically verified by implementing three starting positions for short chains yielding the same range of accepted parameter values. Only about 1500 random moves were accepted, indicating a relatively low number of parameter sets that fit the experimental data. Only chloride concentrations obtained by out diffusionwere considered for the misfit function calculation, since they can be considered to be more representative and reliable than leaching experiment results, with limited mechanical disturbances, low liquid to solid ratio and higher volume of tested sample. The sets of parameters leading to misfit values below 0.8 were used to establish the *a posteriori* marginal distributions of the ten parameters shown in Fig 2.A of Appendix A. Both multimodal and unimodal distributions are obtained. Multimodal distributions were fitted by gaussian mixture distributions, all unimodal variables were fitted by a gaussian model except for C_0 that is described by a log normal distribution (see Appendix A). Mean values and 95% confidence intervals for each parameter were calculated using the fitted distributions (see Table 3). For multimodal distributions, the weights and means of each fitted normal distribution component are used to

calculate an "overall mean" for a given parameter as the weighted average of the mean values (see Appendix A). Therefore, the relative importance of each gaussian distribution within the gaussian mixture is respected. Note that the low number of sampled values in the parameter space is likely a limitation for the a posteriorimarginal pdfs identification method described in Section 3.5. However, taking more samples (40% of accepted displacements) yields the same type of marginal distributions but with slightly different statistical parameters and a larger misfit when the mean parameters values are used in a direct simulation.

Table 3 Input parameters and associated uncertainties involved in the MCMC inversion process. Accessible porosities and formation thicknesses were kept constant. CI stands for Confidence Interval.

| Formation | Thickness [m] | ω [vol.%] | De [m²/s] ($\times 10^{-11}$) | | |
			Measurements	*A priori*	*A posteriori Mean and 95% CI*
Passwang Formation	69	7.5	D_e^7: 0.817 ± 0.2	$[10^{-1}$-20]	2.66 [1.51; 4.81]
OPA – Sandy facies	29	6.9	D_e^6: 7.38 ± 4.36	$[10^{-1}$-20]	6.55 [3.92; 11.61]
OPA – Shaly facies	35	7.6	D_e^5: 0.597 ± 0.2	$[10^{-1}$-20]	0.30 [0.18; 0.41]
OPA – Sandy facies	14	5.4	D_e^4: 2.71 ± 1.9	$[10^{-1}$-20]	1.91 [0.59; 4.12]
OPA – Carbonate-rich Sandy facies	6	6.8	D_e^3: 2.04 ± 0.68	$[10^{-1}$-20]	2.91 [0.39; 4.84]
OPA – Shaly facies	47	7.7	D_e^2: 3.56 ± 1.42	$[10^{-1}$-20]	0.33 [0.04; 0.62]
Staffelegg Formation	63	4.5	D_e^1: 0.451 ± 0.132	$[10^{-1}$-20]	0.59 [0.15; 1.04]

| Parameter | Value | Range | | | |
	A priori				*A posteriori*
Activation time [Ma]					
Middle Jurassic aquifer t_0 (upper boundary)	-5	[-10.5; -1.2]			-4.54 [-6.77; 1.7]
Early Jurassic aquifer t_1 (lower boundary)	-0.25	[-0.5; -0.2]			-0.24 [-0.3; -0.2]
Initial chlorinity C_0 [g L⁻¹]	19	[14; 23]			19 [17.3; 22]

As shown in Figure 7a, the simulation of diffusion for chloride matches fairly well the experimental dataconsidering the mean a posteriori values for the parameters (Table 3). Except for two diffusion coefficients values (Passwang Formation and Opalinus Clay basal shaly facies), the fitted parameters are highly consistent with the measurements and exhumation time expectations (Fig. 7b). The misfit for diffusion coefficients can be due to an imperfect mechanical confining of the Opalinus Clay sample leading to an overestimation of the measured D_e for the Opalinus Clay shaly facies. On the other hand, the Passwang Formation is more heterogeneous compared to the different facies of the Opalinus Clay. Lithostratigraphic investigation carried out by Hostettler et al. (2017) on BDB-1 drillcores showed that this formation exhibits variable lithology (silty to fine sandy marls, quartz sand and biodetrital sandy limestones, ferruginous limestones, iron oolithic marls and limestones). The number of samples investigated in laboratory-scale diffusion experiments was likely insufficient to reflect this variability in the present study.
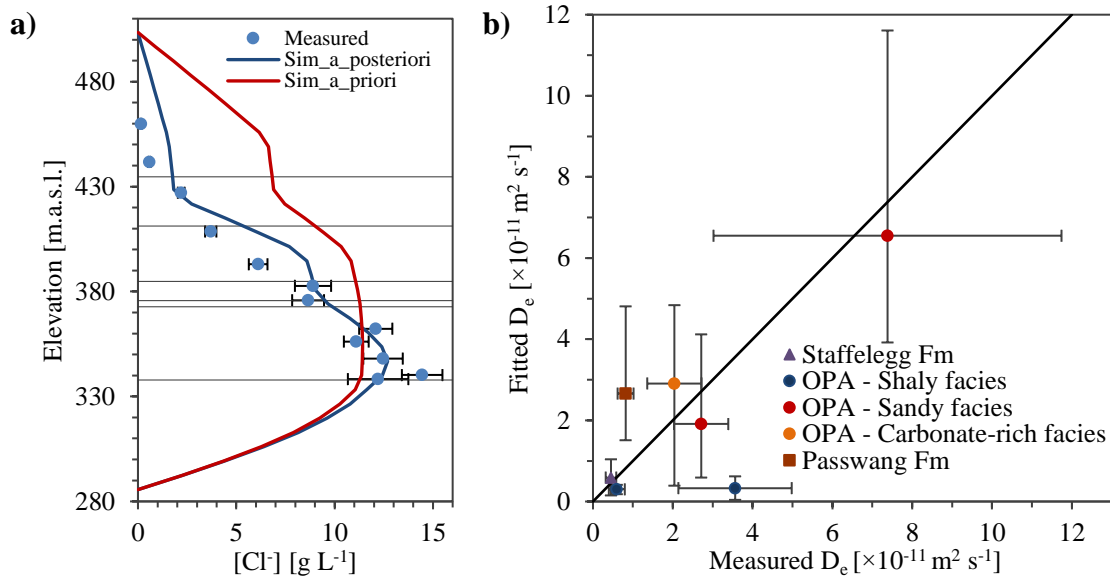
Fig. 7. Comparison between **a)** experimental and simulated chloride profile obtained with the mean *a posteriori* values for the parameters and **b)** experimental and fitted diffusion coefficients, error bars represent 95% confidence interval.

The sensitivity of the MCMC approach was assessed and devoted to the analysis of the influence of the fitted parameters and the effect of their uncertainties. The uncertainty range for each of the fitted parameters was independently tested. The resulting plots are presented in Figure 8. With a time range of several million years, changes in activation time for the upper aquifer (t_0) induce moderated effect on the envelope profiles, relatively to variations of the lower aquifer activation time (t1), which only extend on 300 thousand years. In the lower part of the stratigraphic column, the simulated chloride profile is mainly constrained by the lower boundary condition and the Staffelegg Formation effective diffusion coefficient (D_e^1), as experimental data are lacking in this section. In a first run, we maintained the porosity constant and modify the pore diffusion coefficient D_p and in a second run we kept the Dp values constant and we modified the porosities, which shows a very moderate influence as expected from the transport equation. For a same authorized variation range of effective diffusion coefficients (1×10^{-12} to 2×10^{-10} m² s⁻¹), the most pronounced impact of parameter change on the fit is observed for the Staffelegg Formation and the upper part of the column (D_e^5 and D_e^6 in the Opalinus Clay, and D_e^7 in the Passwang Formation).
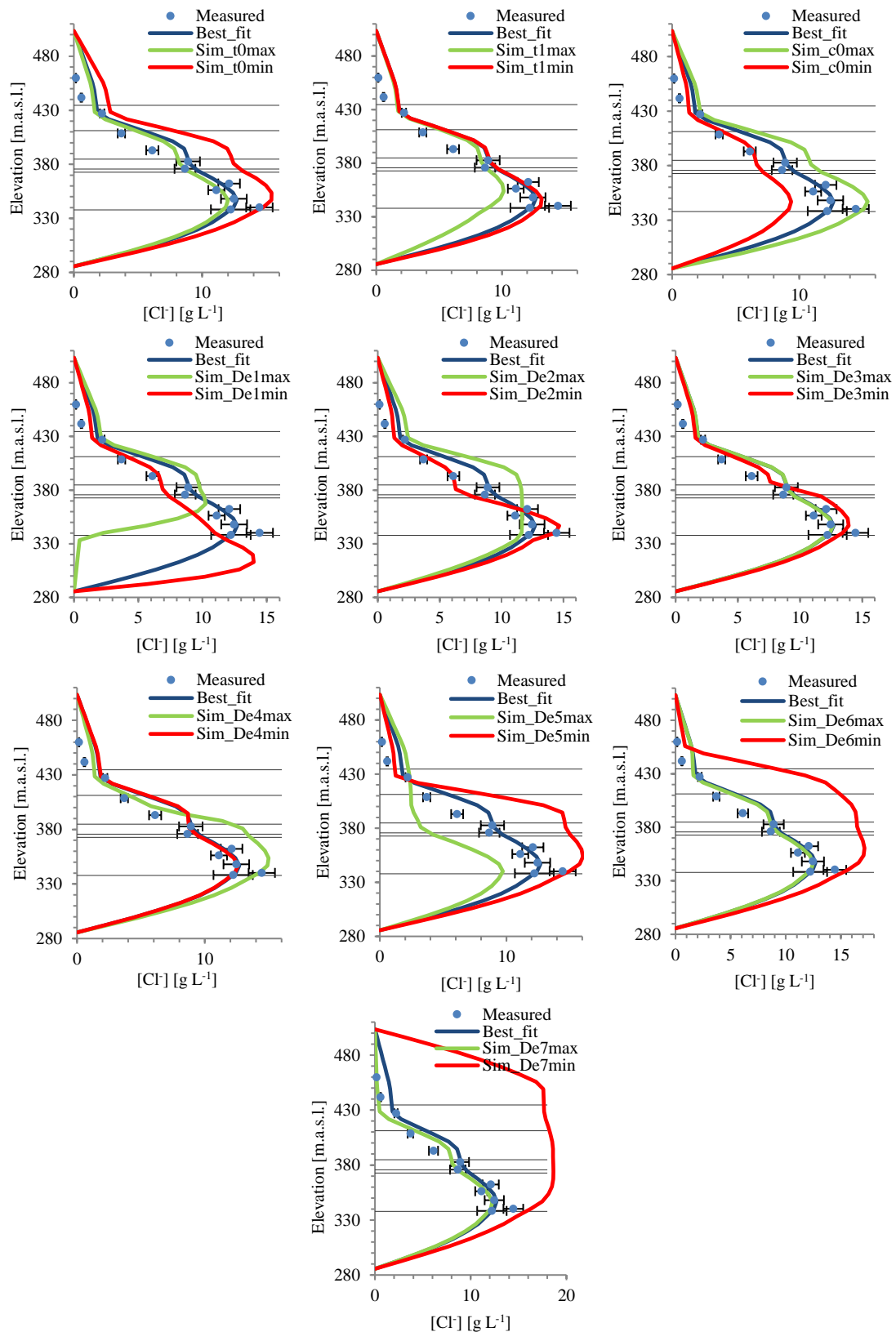
Fig. 8 Results of the sensitivity analysis on the fitted parameters: influence of the aquifers activation times, initial concentration and effective diffusion coefficients on the simulated chloride profile.

The modelling results are globally consistent with previous studies carried out at the Mont Terri rock laboratory. A lower equivalent effective diffusion coefficient for anions of 4.6×10^{-12} m² s^{-1} was used in Mazurek et al. (2011) for the Opalinus Clay and the directly adjacent formations, whereas different diffusion coefficient values were

considered for each unit along the rock sequence in the present study. A higher cross-formational equivalent diffusion coefficient of 6.3×10^{-12} m² s^{-1} for the Opalinus Clay explains the shorter time obtained for the adjacent aquifers activation in comparison with the study of Mazurek et al. (2011): 4.5 Ma compared to 6 Ma for the upper aquifer and 0.246 Ma compared to 0.5 Ma for the lower aquifer. However, the activation age at -4.54 Ma proposed here is close to one of the major morpho-tectonic event proposed by Kuhlemann and Rahn (2013) at -4.2 Ma. This event corresponds to the Aare-Danube river system catchment by a tributary of the Rhône-Doubs river system, leading to the formation of a planation surface.

5 Conclusions

An integrated study from BDB-1 borehole samples characterisation on the Opalinus Clay transport capabilities and transport modelling was performed. Petrophysical analysis enabled the acquisition of water loss porosity, grain density and water content along the rock sequence. Out diffusion and aqueous leaching techniques were used to obtain chloride concentrations of porewater in the Opalinus Clay and its bounding formations. Effective diffusion coefficients and diffusion accessible porosities were also investigated by radial diffusion and through diffusion experiments.

The measured chloride contents are in good agreement with previous investigation performed at the Mont Terri tunnel level, and show an asymmetric bell-shaped trend increasing to a high chloride concentration of 14.4 g L^{-1} towards the bottom of the Opalinus Clay. Moreover, chloride to bromide ratios reflect a marine signature in the clay rock. The chloride profile suggests a diffusive exchange between the argillaceous formation and the adjacent aquifers, with deferred activation times of the fresh-water sources linked to the surface erosion of the geological formations. This scenario was implemented in a Markov Chain Monte Carlo inversion method, which enabled to assess the best fitting set of parameters (initial chloride content, aquifer activation times and diffusion coefficients) and associated confidence intervals explaining the present-day chloride profile. Experimental and simulated data are comparable for respective diffusion times of 4.54 Ma and 0.246 Ma between the Opalinus Clay and the Middle Jurassic (overlying) and Early Jurassic (underlying) limestones.

The present study confirms the paleohydrogeological evolution of the Mont Terri site from the folding and thrusting of the Jura Mountains to present time. This scenario is fundamental to constrain our future transient modelling of the overpressure regime observed in the Opalinus Clay to fully characterise transport processes in this formation.

Appendix A

The convergence of the MCMC approach is characterised by a sharp decrease of the misfit function value from almost 7 to 1.5 on average after 2000 iterations (almost 200 accepted movements) of the random walk as shown in Figure A.1.
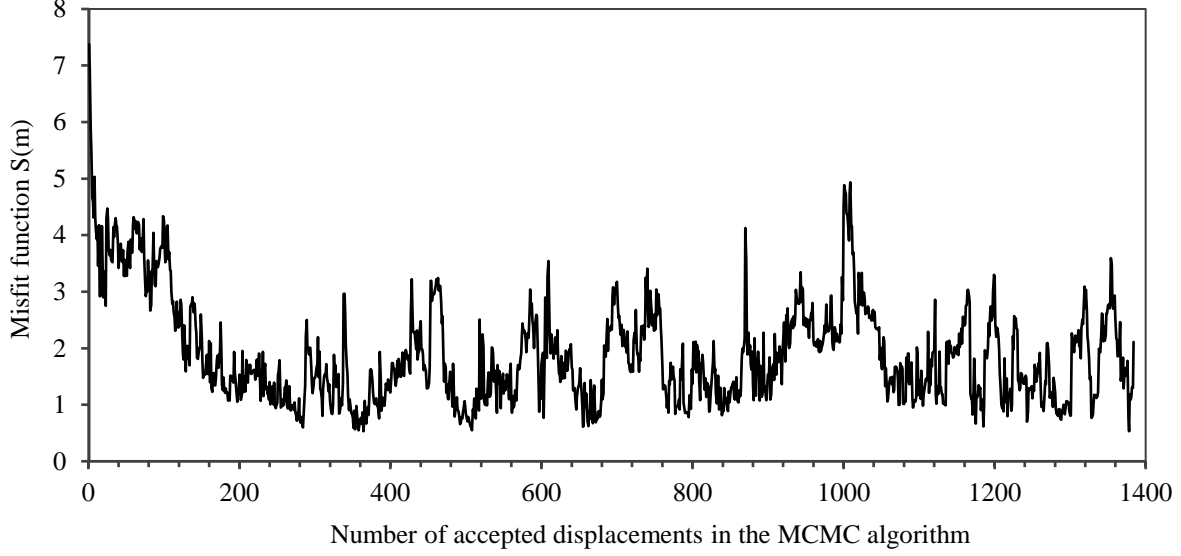
Misfit function S(m)

Number of accepted displacements in the MCMC algorithm

Fig. A.1 Misfit function as a function of the number of accepted displacements in the MCMC algorithm.

The sets of parameters leading to the 5% lower misfit values (errors lower than 0.8) were used to establish the *a posteriori* marginal distributions (Figure A.2).

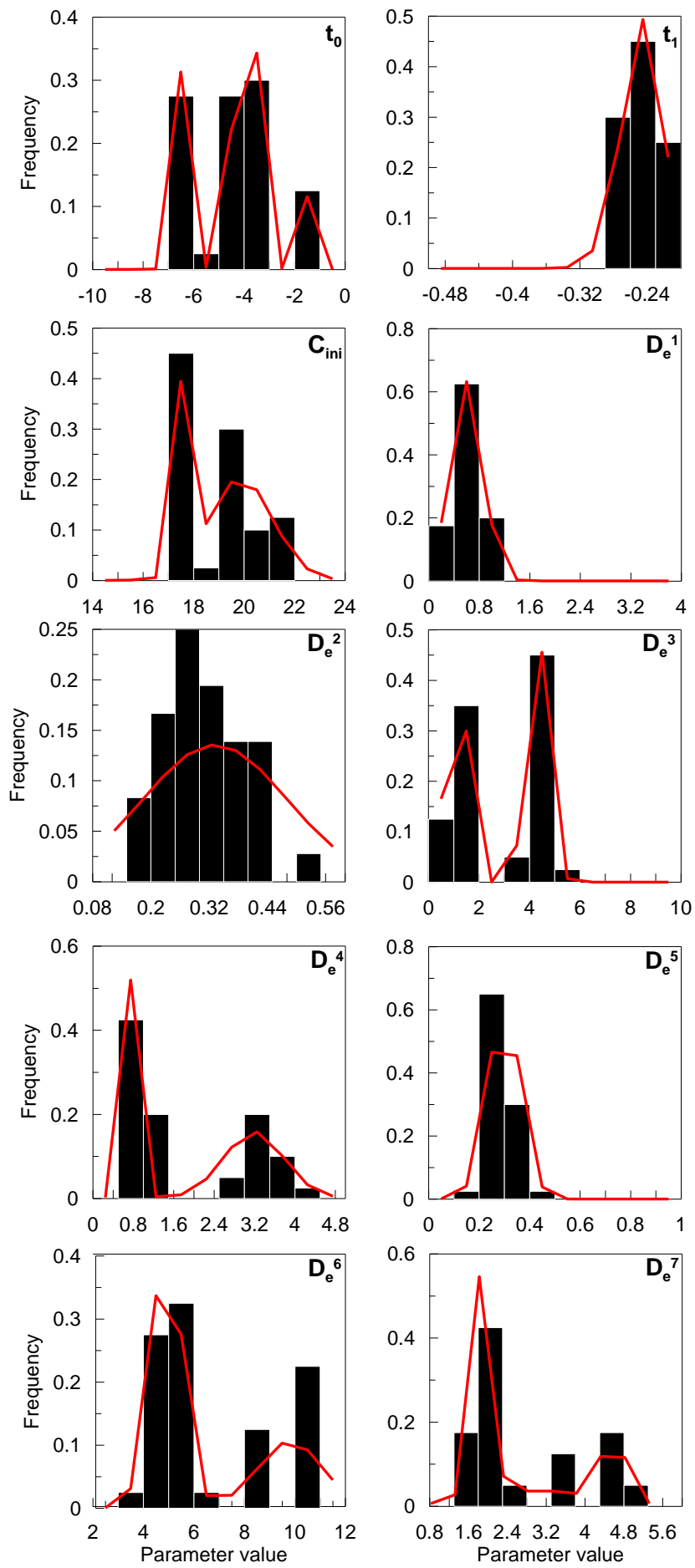Multimodal distributions were fitted by gaussian mixture distributions:

$$\alpha G(\mu_1, \sigma_1) \; + \; \beta G(\mu_2, \sigma_2) \; + \; \gamma G(\mu_3, \sigma_3) \tag{A.1}$$

where $G(\mu_i, \sigma_i)_{i=[1,...3]}$ are Gaussian distributions and α, β, and γ are the respective weights. The fitted distribution parameters are listed in Table A.1.

Fig. A.2 *A posteriori* distributions (pdfs) for each parameter of the diffusion model. Parameters values in $[\times 10^{-11} \text{ m}^2 \text{ s}^{-1}]$ for D_e, [g L^{-1}] ▶ for C_0, and [Ma] for t_0 and t_1. The histograms result from the MCMC approach (Section 3.5). In red, the fitted theoretical distributions (Gaussian mixtures: t_0, C_0, D_e^3, D_e^4, D_e^6, and D_e^7, Gaussian: D_e^1, D_e^2, and D_e^5, and Lognormal: t_1)

Table A.1 Parameters of fitted pdf with effective diffusion coefficients D_e $[\times 10^{-11} \text{m}^2\text{s}^{-1}]$, activation times t_0 and t_1 [Ma], and initial chloride concentration C_0 [g L^{-1}].

Variable	α	β	γ	μ_1	σ_1	μ_2	σ_2	μ_3	σ_3
t_0	0.32	0.56	0.12	-6.45	-3.95	-1.78	0.19	0.22	0.10
$\text{Log}(-t_1)$	1	0	0	-0.61	0.04	-	-	-	-
C_0	0.37	0.63	0	17.48	19.87	1.22	0.09	-	-
D_e^1	1	0	0	0.60	0.22	-	-	-	-
D_e^2	1	0	0	0.33	0.14	-	-	-	-
D_e^3	0.16	0.3	0.54	0.48	1.74	4.33	0.08	0.08	0.3
D_e^4	0.53	0.47	0	0.75	3.18	0.57	0.10	-	-
D_e^5	1	0	0	0.3	0.06	-	-	-	-
D_e^6	0.67	0.33	0	4.91	9.83	1.24	0.55	-	-
D_e^7	0.58	0.22	0.2	1.86	3.08	4.58	0.14	1.19	0.14

References

Beauheim, R.L., 2013. Hydraulic conductivity and head distributions in the host rock formations of the proposed siting regions. *Nagra Interner Bericht, 13-13.* Nagra, Wettingen, Switzerland. <www.nagra.ch>

Bensenouci, F., 2010. Apport des traceurs naturels à la compréhension des transferts au sein des formations argileuses compactées. Thesis, Université Paris-Sud XI, Orsay, France, 194 pp.

Bensenouci, F., Michelot, J.L., Matray, J.M., Savoye, S., Tremosa, J., Gaboreau, S., 2013.Profiles of chloride and stable isotopes in pore-water obtained from a 2000 m-deep borehole through the Mesozoic sedimentary series in the eastern Paris Basin. *Phys. and Chem. of the Earth*, *65*, 1-10.

Blaesi, H.-R., Peters, T. J., Mazurek, M., 1991. Der Opalinus-Ton des Mt. Terri (Kanton Jura): Lithologie, Mineralogie und physiko-chemische Gesteinsparameter. *Nagra Interner Bericht, 90-60.* Nagra, Wettingen, Switzerland. <www.nagra.ch>

Bossart, P., Wermeille, S., 2003. Paleohydrological study of the Mont Terri rock laboratory. In: Heitmann, P., Tripet, J.P. (Eds.), Mont Terri Project-Geology, paleohydrogeoogy and stress field oft he Mont Terri region. Federal Office for Water and Geology Rep. 4, Bern, Switzerland, 45-64. <www.swisstopo.admin.ch>

Bossart, P., Thury, M., 2008. Mont Terri Rock Laboratory. Project, Programme 1996 to 2007 and Results. *Reports of the Swiss Geological Survey, No. 3*, 445 pp. Federal Office of Topography (swisstopo), Wabern, Switzerland. <www.mont-terri.ch>

Bossart, P., Bernier, F., Birkholzer, J., Bruggeman, C., Connolly, P., Dewonck, S., Fukaya, M., Herfort, M., Jensen, M., Matray, J.-M., Mayor, J.C., Moeri, A., Oyama, T., Schuster, K., Shigeta, N., Vietor, T., Wieczorek, K., 2017. Mont Terri rock laboratory, 20 years of research: introduction, site characteristics and overview of experiments. *Swiss J. of Geosci.*, *110*, doi:10.1007/s00015-016-0236-1

Bruel, D., Küpfer, T., 2002. Modelling the overpressure regime in the Opalinus clay, at Benken (CH): Implications for the present day hydrogeological parameters. Clays in Nat. and Eng. Barriers for Radioact. Waste Confinement, ANDRA, Reims, France, 155-156.

Clauer, N., Techer, I., Nussbaum, C., Laurich, B., 2017. Geochemical signatures of paleofluids in microstructures from Main Fault of the Opalinus Clay, Mont Terri rock laboratory, (Switzerland). *Swiss J. of Geosci.*, *110*, doi:10.1007/s00015-016-0253-0

Fierz, T., Rösli, U., 2014. Mont Terri DB Experiment: Installation of a 7-interval multi-packer system into borehole BDB-1. Instrumentation Report. *Mont Terri Technical Note*, TN 20414-23. 37 pp. Federal Office of Topography (swisstopo), Wabern, Switzerland. <www.mont-terri.ch>

Gallagher, K., Charvin, K., Nielsen, S., Sambridge, M., Stephensen, J., 2009. Markov chain Monte Carlo (MCMC) sampling methods to determine optimal models, model resolution and model choice for Earth Science problems. *Mar. and Pet. Geol.*, *26*, 525-535.

Gautschi, A., 2001. Hydrogeology of a fractured shale (Opalinus Clay): Implications for the deep disposal of radioactive wastes. *Hydrogeol. J., 9*, 97-107.

Gautschi, A., 2017. Safety-relevant hydrogeological properties of the claystone barrier of a Swiss radioactive waste repository: An evaluation using multiple lines of evidence. *Grundwasser – Zeitschrift der Fachsektion Hydrogeologie,* doi: 10.1007/s00767-017-0364-1

Gimmi, T., Leupin, O.X., Eikenberg, J., Glaus, M.A., Van Loon, L.R., Waber, H.N., Wersin, P., Wang, H.A.O., Grolimund, D., Borca, C.N., Dewonck, S., Wittebroodt, C., 2014. Anisotropic diffusion at the field scale in a 4-year multi-tracer diffusion and retention experiment – I: Insights from the experimental data. *Geochemica et Cosmochimica Acta*, *125*, 373-393.

Gonçalvès, J., Violette, S., Wendling, J., 2004. Analytical and numerical solutions for alternative overpressuring processes: applications of the Callovo-Oxfordian argillite in the Paris Basin, France. *J. of Geophy. Res.*, *109(B2)*, doi: 10.1029/2002JB002278

Gonçalvès, J., Adler, P.M., Cosenza, P., Pazdniakou, A., de Marsily, G., 2015. Semi-permeable membrane properties and chemo-mechanical coupling in clay barriers. *Nat. and Eng. Clay Barriers*, 269-327.

Hostettler, B., Reisdorf, A. G., Jaeggi, D., Deplazes, G., Bläsi, H.-R., Morard, A., Feist-Burkhardt, S., Waltschew, A., Dietze, V., Menkveld-Gfeller, U., 2017.Litho- and biostratigraphy of the Opalinus Clay and bounding formations in the Mont Terri rock laboratory (Switzerland). *Swiss J. of Geosci.*,*110*, doi:10.1007/s00015-016-0250-3

Huysmans, M., Dassargues, A., 2005. Review of the use of Péclet numberstodetermine the relative importance of advectionand diffusion in low permeability environments. *Hydrogeol. J.*, *13* (5–6), 895–904.

Jaeggi, D., Laurich, B., Nussbaum, C., Kristof Schuster, Connolly, P., 2017. Tectonic structure of the "Main Fault" in the Opalinus Clay, Mont Terri rock laboratory (Switzerland). *Swiss J. of Geosci.,110*, doi:10.1007/s00015-016-0243-2

Johns, R. T., Vomvoris, S. G., Löw, S., 1994. Review of hydraulic field tests in the Opalinus Clay of Northern Switzerland. *Hydraul. and hydrochem. Charact. of argillaceous rocks*, Proc. Int. Workshop, Nottingham (UK), 7-9 June 1994, OECD/NEA, Paris, pp. 167-177.

Koroleva, M., Lerouge, C., Mäder, U., Claret, F., Gaucher, E.C., 2011. Biogeochemical processes in a clay formation in situ experiment: Part B - Results from overcoring and evidence of strong buffering by the rock formation. *Appl. Geochem.*, *26 (6)*, 954-966.

Kuhlemann, J., Rahn, M., 2013. Plio-Pleistocene landscape evolution in Northern Switzerland. *Swiss. J. Geosci.*, *106*, 451-467.

Mazurek, M., Elie, M., Hurford, A., Leu, W., Gautschi, A., 2002. Burial history of Opalinus Clay. *Clays In Nat. And Eng. Barriers For Radioact. Waste Confinement*, December 9-12, Reims, France.

Mazurek, M., Hurford, A., Leu, W., 2006. Unravelling the multi-stage burial history of the Swiss Molasse Basin: intergration of apatite fission track, vitrinite reflectance and biomarker isomerisation analysis. *Basin Res., 18*, 27-50.

Mazurek, M., Alt-Epping, P., Bath, A., Gimmi, T., Waber, H.N., Buschaert, S., De Cannière, P., De Craen, M., Gautschi, A., Savoye, S., Vinsot, A., Wemaere, I., Wouters, L., 2011. Natural tracer profiles across argillaceous formations. *Appl. Geochem.*, *26*, 1035-1064

Mazurek, M., de Haller, A., 2017. Pore-water evolution and solute-transport mechanisms in Opalinus Clay at Mont Terri and Mont Russelin (Canton Jura, Switzerland). *Swiss J. of Geosci.*, 110, doi:10.1007/s00015-016-0249-9.

Mills, R.L., and Lobo, V.M.M., 1989. Self-diffusion in Electrolyte Solutions - A Critical Examination of Data Compiled from the Literature. Elsevier.

Mosegaard, K., and Tarantola, A., 1995. Monte Carlo sampling of solutions to inverse problems. J. Geophys. Res., 100(B7), pp 12431-12447. doi:10.1029/94JB03097.

Novakowski, K.S., Van der Kamp, G., 1996. The radial diffusion method 2. A Semianalytical model for the determination of effective diffusion coefficients, porosity and adsorption. Water Resour. Res., 32, No. 6, 1823-1830.

Noy, D., Horseman, S., Harrington, J., Bossart, P., Fisch, H., 2004. An Experimental and modelling study of chemico-osmotic effects in the Opalinus Clay of Switzerland. In: Heitzmann, P. ed. (2004) Mont Terri Project - Hydrogeological Synthesis, Osmotic Flow. *Rep. of the Fed. Off. for Water and Geol.* (FOWG), Geology Series (6), 95–126.

Nussbaum, C., Bossart, P., Amann, F., Aubourg, C., 2011. Analysis of tectonic structures and excavation induced fractures in the Opalinus Clay, Mont Terri underground rock laboratory (Switzerland). *Swiss J. of Geosci., 104*, 187-210.

Nussbaum, C., Kloppenburg, A., Caer, T., Bossart, P., 2017. Tectonic evolution of the Mont Terri anticline based on forward modelling. *Swiss J. of Geosci.*, 110, doi:10.1007/s00015-016-0248-x

Patriarche, D., Michelot, J.L., Ledoux, E., Savoye, S., 2004a. Diffusion as the main process for mass transport in very low water content argillites: 1. Chloride as a natural tracer for mass transport – Diffusion coefficient and concentration measurements in interstitial water. *Water Resour. Res.*, 40, W01516, doi:10.1029/2003WR002700.

Patriarche, D., Michelot, J.L., Ledoux, E., Savoye, S., 2004b. Diffusion as the main process for mass transport in very low water content argillites: 2. Fluid flow and mass transport modeling. *Water Resour. Res.*, 40, W01517, doi:10.1029/2003WR002700.

Pearson, F. J., Arcos, D., Boisson, J-Y., Fernández, A. M., Gäbler, H.E., Gaucher, E., Gautschi, A., Griffault, L., Hernán, P., Waber, N., 2003. Mont Terri Project - Geochemistry of water in the Opalinus Clay Formation at the Mont Terri Rock Laboratory. *Rep. of the Swiss Geol. Survey, No. 5*, 143 pp. Federal Office of Topography (swisstopo), Wabern, Switzerland. <www.mont-terri.ch>

Petersen, J.O, Deschamps, P., Gonçalvès, J., Hamelin, B., Michelot, J.L., Guendouz, A., Zouari, K., 2014. Quantifying paleorecharge in the Continental Intercalaire (CI) aquifer by a Monte-Carlo inversion approach of [36]Cl/Cl data. *Appl.Geochem*, *50*, 209-221

Sacchi, E., Michelot J-L., Pitsch, H., Lalieux, P., Aranyossy, J-F., 2001. Extraction of water and solutes from argillaceous rocks for geochemical characterisation: Methods, processes, and current understanding, *Hydrogeol. J.*, *9*, 17-33.

Soler, J.M., 2001. The effect of coupled transport phenomena in the Opalinus Clay and implications for radionuclide transport. *J. of Contam. Hydrol.*, 53, 63–84

Tarantola, A., 2005. Monte Carlo Methods. Chapter 2 in Inverse Problem Theory and Methods for Model Parameter Estimation. *Soc. for Ind. and Appl. Math.*, 41-56.

Van der Kamp, G., Van Stempvoort, D.R., Wassenaar, L.I., 1996. The radial diffusion method 1. Using intact cores to determine isotopic composition, chemistry, and effective porosities for groundwater in aquitards. *Water Resour. Res.*, *32*, *No. 6*, 1815-1822.

Van der Lee, J., De Windt, L., Lagneau V., Goblet, P., 2003. Module-oriented modeling of reactive transport with HYTEC. *Comput. & Geosci.*, *29-3*, 265-275.

Van Loon, L.R., Soler, J., Müller, W. and Bradbury, M. H., 2004. Anisotropic diffusion in layered Argillaceous Rocks: a case study with Opalinus clay. *Environ. Sci. Technol.*,*38*, 5721–5728.

Van Loon, L.R., Glaus, M., Ferry, C., Latrille, C., 2012. Studying radionuclide migration on different scales: The complementary roles of laboratory and in situ experiments. In: Radionuclide Behaviour in the Natural Environment: Science, Implications and Lessons for the Nuclear Industry, Woodhead Publishing Series in Energy, pp 446-483.

Wersin, P., Waber, H.N., Mazurek, M., Mäder, U.K., Gimmi, T., Rufer, D., Traber, D., 2013. Resolving Cl and SO_4 profiles in a clay-rich rock sequence. *Procedia Earth and Planet. Sci*,.7, 892-895.

Yu, C., Matray, J.M., Gonçalvès, J., Jaeggi, D., Gräsle, W., Wieczorek, K., Vogt, T., Sykes, E., 2017. Comparative study of methods to estimate hydraulic parameters in the hydraulically undisturbed Opalinus Clay (Switzerland). *Swiss J. of Geosci.*,*110*, doi:10.1007/s00015-016-0257-9**)**